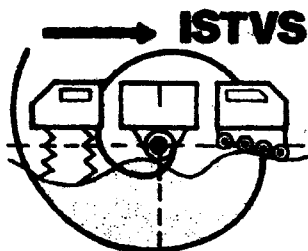


AD-A254 619



R.D 6659-EN-02



International  
Society for  
Terrain-  
Vehicle  
Systems

DTIC  
ELECTE  
JUL 01 1992  
S A D

## 5th EUROPEAN CONFERENCE

DAJ45-91-M-0211

Budapest, Hungary

September 4-6, 1991

PROCEEDINGS  
VOLUME I

This document has been approved  
for public release and sale; its  
distribution is unlimited.



SCIENTIFIC SOCIETY OF  
MECHANICAL ENGINEERS



UNIVERSITY OF AGRICULTURAL SCIENCES  
AGRICULTURAL ENGINEERING FACULTY  
Department of Agricultural Vehicles and Engines

92 6 30 060

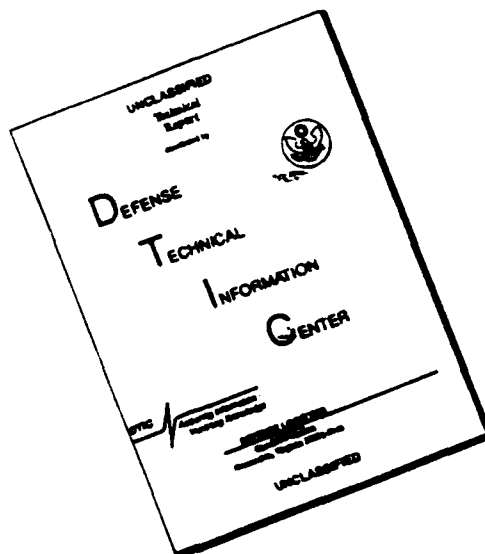
92-17225



391809

343 pg.

# DISCLAIMER NOTICE



THIS DOCUMENT IS BEST QUALITY AVAILABLE. THE COPY FURNISHED TO DTIC CONTAINED A SIGNIFICANT NUMBER OF PAGES WHICH DO NOT REPRODUCE LEGIBLY.

# 5th EUROPEAN CONFERENCE

Budapest, Hungary  
September 4-6, 1991

PROCEEDINGS  
VOLUME I

Accession For	
NTIS CRA&I	<input checked="" type="checkbox"/>
DTIC TAB	<input type="checkbox"/>
Unannounced	<input type="checkbox"/>
Justification	
By <i>perform 50</i>	
Distribution /	
Availability Codes	
Dist	Avail and/or Special
<i>A-1</i>	



## **PROFILE OF BUDAPEST**

**Budapest is the capital of the Republic of Hungary. Its population is around two million. The city is located on both sides of the second largest river in Europe, the Danube. It is spanned by 8 bridges and, in addition, a subway line crosses under the river.**

**Budapest is the cultural center of Hungary. Its eight universities and four colleges await eager-to-learn students. Foreign students are very much interested in studying at these institutions, especially at the Technical University and at the University of Medical Sciences.**

**The yearly Spring Festival of Budapest draws extraordinary international attention. The program is rich in concerts, ballet performances and plays. Famous artists from all around the world appear in these productions.**

**Budapest is also the city of museums. The "Castle Quarter" (the area around the restored castle of former Hungarian kings) deserves special notice by those interested in the treasures of the past.**

**The Square of Heroes provides a splendid spectacle. There are a great many churches, including the incomparable St. Stephen Cathedral. The hotel row along the east bank of the river is aesthetically pleasing. But in contrast, it is also worth while to frequent the small inns in Obuda (the old city), whose unique atmosphere stems from fine Hungarian dishes and "schrammel" music.**

**Budapest is also very beautiful at night. The best night spots are the Moulin Rouge and the Maxim, featuring pretty dancers, excellent music and outstanding entertainment.**



## INVITATION

We are pleased to invite you to the 5th European Conference of the International Society for Terrain Vehicle Systems to be held in Budapest, Hungary, from 4-6 September, 1991. The Conference will include plenary lectures, a short presentation of all papers, and posters showing allowing an opportunity to discuss the presented material in detail. Social events and a technical visit are also being arranged. We believe that you will acquire valuable scientific experiences at the Conference and, at the same time, you may enjoy the special charm of Budapest.

We are looking forward to seeing you at our Conference in Budapest

sincerely yours.

G. Sitkei.  
Chairman of  
Organizing Committee

**These Proceedings are published in two volume by the Organizing Committee of the 5th European Conference of the ISTVS**

**CONFERENCE ORGANIZING COMMITTEE**

**Prof. G. Sitkei (chairman)  
Prof. G. Kománde (programme chairman)  
Dr. L. Laib (secretary)**

**The Conference was jointly organized by the Agricultural Machine Industry Division of the Scientific Society of Mechanical Engineers and by the Department of Tractors and Automobiles, University of Agricultural Sciences Gödöllő.**

**Acknowledgement is made to the European Office of ISTVS, Stockholm, and to the European Research Office of the US Army, London, for their support of the Conference.**

**Further copies of the proceedings may be obtained from:**

**Main Office ISTVS  
c/o USA CREEL  
72 Lyme Road  
Hanover, NH 03755  
USA  
Fax: (603)646-4278**

**European Office ISTVS  
SFM/FOA2  
P.O. Box 27322  
102 54 Stockholm  
Sweden  
Fax: xx46-(0)8 6675559**

**University of Agricultural Sciences  
College of Agroculural Engineering  
Department of Tractors and Automobiles  
Gödöllő, Péter Károly u. 1.  
2103 – Hungary  
Fax: 36-(28)-10-804**

# TABLE OF CONTENTS

## VOLUME I.

### PLENARY LECTURE

<b>The Role of Simulation in the Research, Development and Acquisition of Military Vehicles</b> Z. J. János, Warren, USA .....	1
---	---

### SESSION 1: SOIL PROPERTIES

<b>Application of the Finite Element Method on Soil Mechanical Processes</b> Th. Aubel, Hamburg, Germany .....	9
<b>The Prediction of Soil Strength with the Aid of Climatic Data</b> D. Hintze, Hamburg, Germany .....	17
<b>Automatic Data Recording and in Situ Statistical Survey of Cone Penetrometer Tests</b> G. Hefer and G. Heimig, Hamburg, Germany .....	25
<b>Bearing Capacity and Sinkage Mechanism of Loose Sand</b> W. Qingnian, Li Ying and Gui Longming, Jilin University, P. R. of China .....	33
<b>Advanced Study on the Performance of Lug Configuration and Arrangement for Powered Wheel of Powered Tiller in Paddyfield</b> Yao Jian Shao, Xiwen Luo and Hua Zhong Lu, South China Agr. University, P. R. of China .....	41
<b>Numerical Prediction of Soil Behavior under Rigid Wheel</b> A. Jarzebowski, Y. Nohse, K. Uchiyama, K. Hashiguchi, M. Ueno, M. Kamei and F. Koyama, Sakai Heavy Ind., Japan .....	49
<b>Calculation of Soil Compaction Caused by Vehicles Action</b> A. Miroshnichenko, Moscow, USSR .....	57
<b>A Model of Vehicle-Soil Interaction</b> A. Miroshnichenko, V. Gromov, V. Grushin and V. Mehanuk, Moscow, USSR .....	63
<b>Effect of Agricultural Machinery on Oxygen Diffusion Rate in Loamy Sandy Soil</b> L. Nozdrovicky, Nitra, Czechoslovakia .....	72
<b>Adaptiv Hydroactuator for Soil Testbench</b> S. Sitnikov Moscow, USSR .....	78

### SESSION 2: SOIL-VEHICLE INTERACTION, TIRES AND TRACKS

<b>The Influence of Wheel Configuration on Ground Pressure of Agricultural Vehicles</b> F. Tijink, Wageningen, The Netherlands .....	89
<b>The Effect of Tire-Soil Interface Shape on the Prediction of Vehicle Off-Road Performance</b> M. Mahmoud and M. Dwyer, Silsoe, UK .....	97

<b>Friction Between Rubber Track Pads and Ground Surface with Regard to the Turning Resistance of Tracked Vehicles</b>	
St. Pott, Hamburg, Germany .....	105
<b>The Calculation of Pressure-Sinkage Curves Based on Shear Strength Measurements</b>	
P. Wagner, Hamburg, Germany .....	113
<b>The Ways to Improve the Trafficability of Vehicles on Sand</b>	
J. Zhuang, Z. Wang and J. Liu, Jilin University, P. R. China .....	121
<b>Considerations on the Wheel-Soil Interaction and its Role in Soil Compaction</b>	
N. Tecusan, Timisora, Romania .....	127
<b>Measurements of Tractive Capacity of Rubber Treads on Grass</b>	
A. Grecenko, Prague, Czechoslovakia .....	133
<b>Soil-Track Interaction Relation for the Motion of Tracked Vehicles on Dry Sand</b>	
K. Watanabe, M. Kitano, and H. Murakami, Hashirimizu Yokosuka, Japan .....	141
<b>Approximation for the TDF-Value of a New Tire-System</b>	
P. Parringer, Ottobrunn, Germany .....	149
<b>Investigations on Dependence of the Soil Compaction on Unit Pressure of the Tire</b>	
Z. Blaszkiewicz, Poznan, Poland .....	157
<b>Soil Pressure and Soil Compaction under Agricultural Tires</b>	
H. Schwanghart, München, Germany .....	163
<b>Wear Investigation on Crawlers of Earth Moving Machinery</b>	
W. Poppy and C. Segieth, Berlin, Germany .....	171
<b>The Maximum Efficiency of the Tractor and Implement Combination</b>	
A. Fekete, Gödöllő, Hungary .....	179
<b>Measurements of Combined Lateral and Longitudinal Forces Generated by Off-Road Tyres</b>	
D. Crolla, Leeds, UK, A. El-Razaz Minia, Egypt. ....	187
<b>Cone Resistance Measuring System for Generating Cone Resistance Distribution Map</b>	
K. Ohmiya, Sapporo, Japan .....	207
<b>Determining of Drawbar Parameters of Agricultural Wheeled Tractors</b>	
R. Nikolic, Novi Sad, Yugoslavia .....	215
<b>Analytical Modelling of the Performance of a Snow Deposit under Compression Loading</b>	
R. Yong, A. Mohamed and A. Murcia, Moantreal, Canada .....	222
<b>One Simple Laboratory Method for Relative Estimations of Tractor Tires Performances</b>	
D. Rónai and V. Muzikravic, Novi Sad, Yugoslavia .....	234
<b>Basic Energy Analysis in Soil-Crawler Interaction.</b>	
K. Kogure and Y. Ohira, Hashirimizu Yokosuka, Japan .....	241
<b>Trafficability of Deep-Sea Floor</b>	
G. Dörfler, Karlsruhe, Germany .....	249
<b>Compaction of Agricultural Soils with Viscoelastic Behavior under Confined and Unconfined Conditions</b>	
G. Sitkei, Sopron, Hungary .....	257
<b>The Relationship between the Technical, Agrotechnical and Energy Parameters of Medium-Deep Tillage Implements</b>	
I. Jóri and S. Soós, Gödöllő, Hungary .....	265

<b>The Effects of Various Design Parameters on the Tractive Performance of Rubber Tracks</b> M. Dwyer, J. Okello and F. Cottrell, Silsoe, UK .....	278
<b>On the Kinematically Admissible Solutions for Soil-Tool Interaction Description in the Case of Heavy Machines Working Process</b> W. Trampczynski and J. Maciejewski, Warsaw, Poland .....	286
<b>Shear Strength Properties from Cone Index Tests</b> J. Farr, Vicksburg, USA .....	304
<b>Analysis of Soil-Track Interaction for Tank Steerability</b> J. Peters and N. Murphy, Vicksburg, USA .....	312
<b>Improved Calculation of Sinkage of a Wheel on Soft Ground</b> I. Schmid and J. Ludewig, Hamburg, Germany .....	318
<b>Mathematical Models for Predicting the Tractive Characteristics of Tractor Tires</b> E. Elashry, Alexandria, Egypt .....	3

## VOLUME II.

### **SESSION 3: Instrumentation and Computer Control of Traction and Transport System**

<b>Electro-Hydraulic Draft, Position and Combined Control System</b> A. Fekete, Gödöllő, Hungary .....	334
<b>Engine Load Monitor and Load Control System</b> A. Fekete, Gödöllő, Hungary .....	343

### **SESSION 4: Simulation and Modeling for the Prediction of the Performance of Cross-Country Vehicles.**

<b>Interactive Simulation of the Driver-Vehicle-Terrain System</b> K. Ruff, Hamburg, Germany .....	351
<b>Predicting Vehicle Stability Using Portable Measuring Equipment</b> G. Owen, A. Hunter and C. Glasbey, Penicuik, Scotland UK. ....	359
<b>A Method of Study of Wheel-Ground Phenomena in the Presence of Vibrations</b> A. Orlandi, G. Capitani and M. Matassa, Bologna, Italy .....	367
<b>Using a Computer Model to Determine Speed and Acceleration of Wheeled Off-Road Vehicles</b> G. Hohl, Vienna, Austria .....	375
<b>Modelling the Loads in a Non-Linear Tractor and Mounted Implement System Using ADAMS</b> T. Collins, Silsoe, UK .....	383
<b>Tread Dynamics and Wear of Agricultural Tires and its Influence on the Driving Comfort</b> T. Siefkes and H. Göhlich, Berlin, Germany .....	391

<b>Tire Simulation as a Basis for Vehicle Performance Prediction</b> T. Siefkes and H. Göhlich, Berlin, Germany .....	399
<b>Improved Method of Simple Calculation of the Tracked Vehicle Performance</b> M. Poncyliusz, Warsaw, Poland .....	407
<b>The Application of Analytical Simulation to the Development of a Military Vehicle Simulator</b> R. Beck, Warren, USA .....	413
<b>Rolling Tire Characteristics and their Effect on Prediction of Unsuspended Vehicle Ride.</b> J. Lines, Silsoe, UK .....	421
<b>Full Scale Computer-Based Modeling, Simulation and Analysis of the On and Off-Road Performance of a Heavy Tractor/Semitrailer Line Haul System.</b> M. Letherwood and R. Wehage, Warren, USA .....	428
<b>Computation of Drawbar Pull Acceleration Ability of Four Wheel Driven Vehicles</b> P. Marteau, Viena, Austria .....	436

## **SESSION 5: New Cross-Country Vehicles**

<b>Design and Evaluation of a Rubber-Tracked Agricultural Tractor</b> J. Reed and A. Scarlett, Silsoe, UK .....	444
<b>A 4x4 Trailer for Forestry Use</b> R. Chaplin, Lancaster, UK .....	452
<b>Gantry Vehicles for Agriculture: International Development and Potential</b> J. Taylor, Auburn, USA .....	460
<b>Form Index as possible Criterion for Classification of Forest Off-Road Vehicles</b> S. Sever and I. Knezevic, Zagreb, Yugoslavia .....	468
<b>Susitracks: A Newlight-Weight Flexible Terrain Carpet and Fascine System</b> D. Douwes Dekker and H. Brockhoff, Breda, The Netherlands. ....	477
<b>A Modulated Carrier-Concept for Army-Engineer Equipment</b> I. Holm and I. Schmid, Hamburg, Germany .....	485
<b>Design Principles for Off-Road Motorcycles</b> R. Jelemensky, Steyr, Austria .....	493
<b>NOKIKER – A New Horse in the Stable of Steyr-Daimler-Puch Fahrzeugtechnik</b> P. Resele, Graz, Austria .....	501

## **Late papers.**

<b>Analysis of the Mechanical Properties of Legged Vehicle Walking Parts</b> J. Zhuang, X. Qiu, P. Xu, Z. Wang, J. Li. filin University. P. R. China	
<b>Off-Road Mobility of Cross-Country Vehicles</b> L. Laib. Gödöllő, Hungary	
<b>Analysis of Technological Processes on Improved Roads and in the Field by Means of a New Test Apparatus</b> Gy. Komándi, Gödöllő, Hungary	

# **PLENARY LECTURE**

**THE ROLE OF SIMULATION IN THE RESEARCH,  
DEVELOPMENT AND ACQUISITION OF MILITARY VEHICLES**

by

Zoltan J. Janosi

U.S. Army Tank-Automotive Command

It is indeed an honor to be asked by the Organizing Committee to deliver the introductory presentation at this conference. I am grateful for their confidence, and I hope that I will be able to make a contribution that most of you will find useful, at least to a certain degree.

The Committee left the selection of the topic up to me. After some thought, I decided to talk about what I am most closely associated with, namely, how analytical simulation is used in the military vehicle business.

I have been working for the U.S. Army Tank-Automotive Command (TACOM) since 1957. This organization is responsible for research, development, acquisition, manufacturing, maintenance and field support relative to all military vehicles used by the Armed Forces of the United States. The gamut runs from a modified Chevrolet Blazer (called the Commercial Utility Cargo Vehicle) to the M1 Heavy Combat Vehicle (tank).

The purpose of this presentation is to give you a short description of how TACOM uses modern computer-based simulation techniques in the military vehicle design, development, acquisition and product improvement processes. While I realize that most of you are not in the military vehicle business, I believe that many of the ideas in my presentation are applicable to other engineering fields.

In the past, military vehicle research and development relied heavily on building and testing prototypes or test beds. This approach constrained engineers to evaluating a limited number of design ideas (based largely on empirical knowledge) under restricted field conditions. This was referred to as the "build-test-break-fix" prototype based development.

Army leadership and TACOM have long recognized the value of computer-based simulation as a means for reducing the cost and time associated with traditional ways of developing vehicles. As a result, the application of simulation technology has become an integral part of the Army's combat and tactical vehicle research, development and acquisition process. Analytical simulation, however, is conducted by simulation experts at TACOM and not by our vehicle designers.

In the near future, TACOM plans to integrate performance simulation and vehicle data bases into an environment in which the evaluation of vehicle systems and subsystems becomes a routine



engineering task, rather than a problem which can only be addressed by simulation specialists. This, we believe, will

- revolutionize the vehicle design process
- shorten vehicle development time
- reduce developmental and operational support cost and
- make TACOM a smarter buyer.

Previously, our requirement documents soliciting bids from industry have often contained vague performance specifications concerning off-the-road mobility, ride quality, weapon platform stability, roll and maneuver stability and other aspects of military vehicle behavior. One would often find such vague specifications as "the vehicle must negotiate mud, sand and snow" or "the vehicle must be as mobile as the M113 Armored Personnel Carrier". As a result, decisions were made largely on a judgmental basis using engineering experience.

Because prototype-based design inhibits the investigation of design alternatives, advanced technology systems, with their higher degree of uncertainty and pay-off, were not given the fullest consideration, since empirical design guidelines (or rules of thumb) did not apply to them. Advanced component technology was often set aside in favor of better understood conventional methods, leading to conservative designs. The result was a slow and costly process which, in addition, did not ensure optimum design solutions.

Beginning in the late 1960s and early 1970s, complex theoretical mathematical models relating aspects of vehicle performance, the terrain and the human occupants were no longer confined to the pages of research reports. The availability of computers and higher level programming languages (such as FORTRAN) ushered in new analytically-based simulation methodologies. Detailed computer simulations have become practical tools for predicting vehicle behavior, even in the concept stage.

The first such model was the U.S. Army-developed cross-country mobility simulation which is now used by many NATO countries and is referred to as the NATO Reference Mobility Model or NRMM. Another significant tool jointly developed by TACOM and the University of Iowa is a high-resolution three-dimensional vehicle dynamics simulation methodology called the Dynamic Analysis and Design System or DADS. Currently TACOM and its contractors use a large variety of simulations covering such disciplines as

- dynamics and controls
- mobility
- survivability
- different vehicle subsystem evaluation tools  
(example: detailed track models)
- structural analysis

- cost.

In fact, various TACOM organizations are now using so many simulation methods and different models that it has become necessary to publish a catalog listing the models, their short description, input requirements, output data and computer hardware requirements. The purpose was to inform different Army organizations about the availability of simulation capabilities at TACOM so that they could apply them in their work and, also, to minimize duplications.

The fact that different TACOM organizations use their own models and input data files leads to less-than-ideal situations, since the input data bases used by these models are generally incompatible. A common input data base and "electronic transportability" of output data from one model to another are clearly needed. This is why one of the most pressing goals of the System Simulation and Technology Division (the TACOM organization responsible for managing the engineering simulation capabilities of the Command) is the establishment of an **Integrated Simulation Software Environment (ISSE)**.

However, before I discuss our plans and progress toward this goal, I would like to explain how simulation is currently used in the military vehicle **acquisition process**. This is a very important subject for us, because TACOM spends large sums of the American taxpayer's money for buying military vehicles. First of all, I would like to point out that TACOM's policy is to use simulation in the acquisition process to the maximum extent possible.

The Government does not operate production facilities and, therefore, manufacturing of military vehicles is done by private industry in the United States. After the Army establishes the need for a new vehicle or trailer, detailed specifications are developed and interested manufacturers prepare proposals describing their approach to meet the specifications.

Simulation specialists are heavily involved in the preparation of technical specifications. The user states, for example, that the new vehicle should have the same cross-country mobility as an existing vehicle. By means of NRMM, simulation experts determine several quantitative performance specifications for the existing vehicle, such as the well known Vehicle Cone Index, or the ride quality for given terrain profiles, or the percent of area where the vehicle cannot move (relative to a large geographic area). The new vehicle must meet these performance parameters computed via the NRMM. Needless to say that, depending on the mission of the vehicle to be procured, many other models may be employed to prescribe other important aspects of its performance.

Naturally, private companies intending to offer one of their existing vehicles or planning to build a new design must be able to

execute the computer models TACOM uses for determining the quantitative specifications; otherwise, they will not know whether their bid can meet the requirements. Also, they are required to include in their documentation engineering data in a form which TACOM can use for evaluating the proposals.

To solve this problem, in case of the NRMM, TACOM held extensive seminars for engineers of interested companies and taught them how to use the model. Potential contractors may obtain the NRMM source code from TACOM. Other models or modeling methodologies, such as the aforementioned DADS, are owned by commercial software companies, so that the vehicle manufacturer must either lease the model or hire a software company to run the model for them. Yet other models can be purchased outright, because they are very mature, commercially available and well known industry wide. (Example: finite element codes.)

Once all proposals are in, TACOM gathers a group of in-house experts into a so-called "Source Selection and Evaluation Board". The Board works intensively, sometimes for several months, going through the offerors' documents and drawings with a fine tooth comb. Simulation experts serving on the Board evaluate the different designs by creating models and running computer simulations to see whether the specifications are being met. Some of the offerings may be eliminated when simulation detects severe deficiencies. The results of these simulations are heavily relied upon by the final decision makers, making TACOM a smarter buyer of military vehicle hardware.

Once a winner has been selected and, subsequently, the hardware becomes available, it goes through different test cycles. The simulation expert can be valuable in the determination of detailed test plans, because he can pinpoint critical conditions which should be thoroughly examined and determine areas of high confidence where extensive testing would be wasteful.

Let me turn to the discussion of our work aimed at the establishment of the **Integrated Simulation Software Environment**. As I mentioned earlier, simulations are currently performed by specialists who are intimately familiar with the physical and empirical laws influencing the particular problem, know the computer code and the underlying assumptions, and have a good feel for judging whether the output data are realistic or not. (Remember the well known acronym: GIGO, or garbage in, garbage out!) These specialists, however, do not have expertise in vehicle hardware design, nor are they trained and qualified to develop new vehicle concepts.

TACOM does not design nor manufacture the military vehicles intended to be handed over to the troops or, as we say, which are to be "fielded". However we do design and fabricate prototypes and we are heavily engaged in the development of advanced military

vehicle concepts. Therefore, our concepts organization and our design engineers need to employ simulation to a great extent.

It is not hard to see that a dichotomy exists here: on one hand, we have simulation experts who can develop sophisticated models, but are not qualified to do concept development or design work; and on the other hand, we have concept developers and designers who are only superficially familiar with the available simulation software and cannot create models or run the simulations independently and reliably. This is why we need an ISSE.

Let me describe the integrated simulation software environment which is being developed by us and by the University of Iowa. It should be clear by now that the ISSE is a computer software environment designed to facilitate engineering analysis and manage related engineering data.

The ISSE provides these features:

- Engineering database
- Database administration
- Network computing environment
- Graphical interface for analysis tools
- External link to analysis tools
- External interface to computer aided design systems
- External interface to test hardware
- Simulation output processing.

The fundamental component of the ISSE is the **database** which serves as a computer aided engineering information repository. Vehicle engineering data are grouped in a manner which is analogous to the real world system it pertains to. For example combat vehicle data would be grouped as turrets, hulls, guns and suspensions. The term used to describe a related group of data is an "object".

The ISSE database is designed to be independent of a particular model. It achieves this independence by using the concept of objects. As with real-world objects, there are different perspectives from which one can view them. Depending on its use, different sets of information are revealed about an object. For a tracked vehicle, we would have a turret, a hull, suspension, track, and others. For example, if we think about the hull object from the viewpoint of vehicle dynamics modeling, the data of interest are the mass, center of gravity location, moments of inertia and geometry and type of the joints connecting it to other vehicle objects. A vehicle signature modeler, on the other hand, needs detailed surface geometry, thermal radiation descriptors, radar reflectivity information and other similar data. The idea of viewing data in different contexts is also important for determining how information can best be graphically displayed by the ISSE. The system provides a **"graphical user interface"** so its capabilities can be invoked graphically using symbols called

"icons". (These are small pictures representing an operation, which can be activated by a device called a "mouse". Sometimes, invoking an operation produces further choices in the form of new sets of icons or "pull down menus.") The intent of this interface is to provide a consistent and easy-to-learn method of using different features of the ISSE. The icons are used to perform simulation functions, such as starting a simulation, viewing simulation data or displaying data from the database. Inherent in the database is the flexibility of the information display. For example, suspension spring force versus deflection information can be displayed graphically as a function (or a curve), or it can be represented as two columns of numbers. The ISSE "knows" the type of data in the database and will display them in an appropriate format. At present, the data can be viewed as vectors, arrays, simple animations or curves.

Another major feature of the ISSE is **network computing**. The ISSE provides utilities to develop applications which can be distributed across a network of engineering workstations, a supercomputer and high-quality graphics workstations. Different aspects of the analysis process are distributed to appropriate machines across the network without the direct involvement of the user. A simulation model can run on the supercomputer, gather data from a database machine and display simulation results on a workstation. Most of the network activities take place automatically in a "transparent" manner. (That is, the user does not have to know the details of the operations taking place throughout the network and in the different computer hardware involved in the process.)

The **TACOM Tracked Vehicle Workstation (TVW)** project is the first application developed using the ISSE system. The TVW software was created for a military vehicle designer. It allows a vehicle designer to use computer simulations and engineering analysis tools to evaluate alternative vehicle designs.

Figures 1-4 represent a sequence of four steps which are the ingredients of the process. To create a dynamics model, the engineer selects vehicle components from a library of existing computer aided representations of those components. In the case of a tank, the engineer would select a gun, a hull, a turret and a suspension system. (Fig. 1.)

Based on the specific vehicle mission requirements the designer would select a "test scenario". (We really mean a scenario which simulates actual tests.) Several simulation test scenarios are available to assess different performance aspects, such as steering characteristics, gun firing dynamics, cross-country ride or cross-country mobility. (Fig. 2.)

Once the vehicle dynamics model has been constructed and the test plan selected, the engineer would execute a run. At this point

the workstation software would assemble the simulation representation of the vehicle, which in our example is an input data file needed to run the dynamic ride simulation by means of the DADS methodology. While the simulation is running, the engineer can monitor the process. A simple three dimensional representation of the vehicle is displayed showing the vehicle moving along the course. The time history of certain data of interest are also displayed. (For example, acceleration at the driver's location and others.) See Fig. 3.

When the simulation is complete, the results are returned to the database. They can be viewed in different formats, for example x-y plots, time history data or high quality animation. (Fig. 4.)

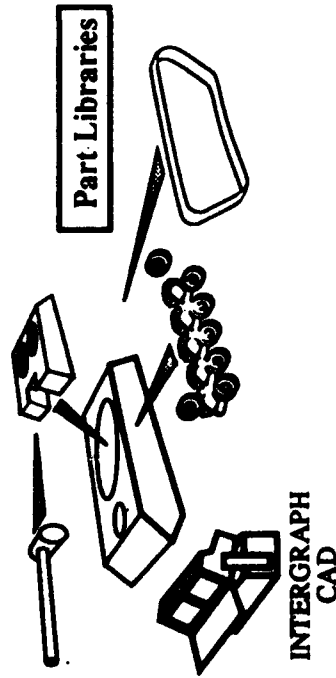
At the time of writing this paper, the tracked vehicle military workstation was not complete. The database needs to be expanded substantially and we have to implement several simulations beyond the three dimensional vehicle dynamics methodology (DADS). TACOM is fully aware of the importance of the TVW and, consequently, it sustains a significant effort toward its full development.

Next, I would like to emphasize that simulation is also applied to remedying problems encountered by fielded vehicles, that is in **product improvement** programs. The analytical evaluation of proposed design modifications is not different, from the viewpoint of the simulation expert, from examining new designs. Another frequently used type of application is the determination of safe operational conditions. The Army has experienced stability problems with some of its older trailers still in use. In many cases it would be impractical to redesign and modify them. TACOM analysts have often been tasked to determine what is called a safe operational envelope for these vehicles. We have, for example, determined via simulation what the maximum safe speed would be in a sharp turn, or how loads should be configured to keep the center of gravity low.

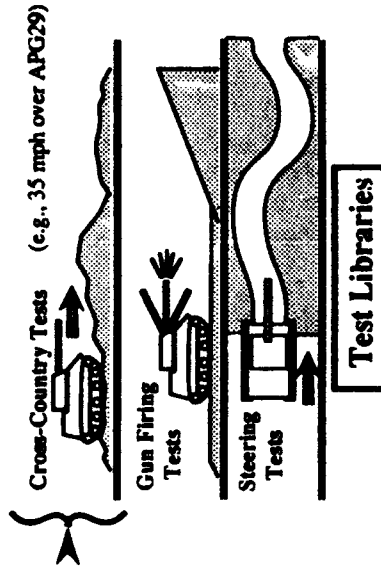
Finally, I should mention **physical simulation**. However, I will not go into details here because my colleague, Dr. Beck, has a paper on this topic, which is part of the conference material.

I hope this short presentation contained some information useful to most of you. I do not believe that anyone needs convincing about the importance and usefulness of simulation in engineering and in many other scientific disciplines. The rapidly improving tools, computers, workstations, physical simulation equipment and the accompanying methodology development open an ever-widening horizon for the engineer. It is up to him how well these opportunities offered by this computer age will be utilized.

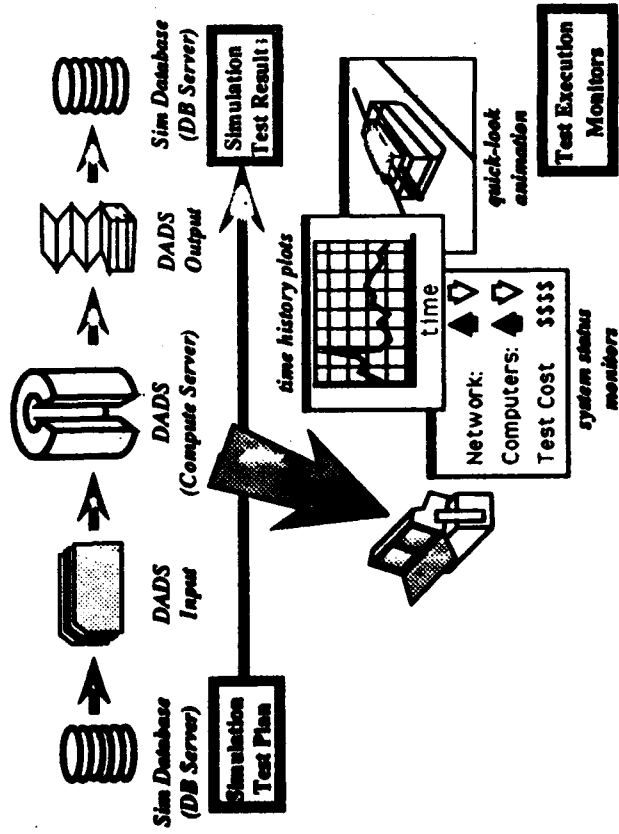
## 1. Assemble Concept Tracked Vehicle



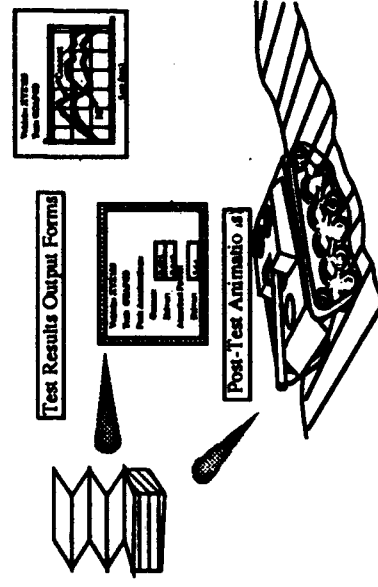
## 2. Select/Define Dynamic Test Scenario



## 3. Execute/Monitor Simulated Test



## 4. Review Test Results



# **SESSION 1**

## **SOIL PROPERTIES**



# **APPLICATION OF THE FINITE ELEMENT METHOD ON SOIL MECHANICAL PROCESSES**

**Th. Aubel**

**University of the Federal Armed Forces Hamburg, Germany  
Institute of Automotive Engineering**

## **SUMMARY**

By the prediction of off-road-mobility for vehicles on soft ground usually soil penetration tests with cones or plates are carried out. From the pressure-sinkage curves special empirical soil parameters, which are used as input datas for several analytical models, can be calculated. In addition to the knowledge of these integral parameters it is important for the basic research to investigate the internal stress-strain behaviour of the soil during the penetration.

The utilization of the Finite Element Method (FEM) is examined to describe and simulate these soil processes. Therefore the available program ABAQUS with the facility of nonlinear analysis was used. The simulation of the two most different types of soil - frictional and cohesive - is based on two material laws with an elastic and plastic part, a yield function, a flow and a softening/ hardening rule.

After the introduction into the theory of the used models some results of a typical soil test with large plastic deformation are presented and compared with original measurements. This work shows, that the FE method is suitable for the simulation of soil mechanical processes. The presented theories and their models are able to simulate original soil tests with a good correlation.

In future the use of FEM as a tool for the simulation of dynamic processes will be investigated.

## **1. INTRODUCTION**

It is important for the examination of the terrain mobility to know the values of vehicle sinkage and attainable driving speed, because the performance is limited by these parameters.

For the prediction of sinkage the deformation resistance of soils is measured by penetration tests with cones or plates. First Bekker [1] introduced a method to investigate empirical soil parameters from these curves and to calculate the sinkage as a function of loading. Based on this idea Grahm [2] extended Bekker's quasi static relation by a dynamic term, which considers the driving velocity of a rigid wheel.

Up till now a lot of work was done in this research field, but nearly all are based on integral soil parameters. For the understanding of the soil reaction it seems to be logical, to investigate the causal influence to the deformation resistance.

Due to the problem of measuring the stress-strain behaviour of a soil in natural state the possibility of simulation has to be investigated, especially the use of FEM.

In this paper only Bekker's quasi static method for prediction of sinkage is simulated, the opportunity to use FEM for the dynamic simulation will be investigated later.

## 2. FINITE ELEMENT METHOD

The procedure is described fundamentally by Zienkiewicz [3]. A continuum with endless degrees of freedom will be divided into a final number of parts. The connection between these elements are realised by nodes at their borders. As the basic parameter the displacement of the nodes is chosen. From the node transformation it is possible to calculate the shifting and distortion state of every finite element with known system functions.

The deformation of a medium can mathematically be described by a Lagrangian treatment

$$\Delta S_{ij} = \Delta D_{ijkl} \Delta E_{kl} \quad (1)$$

with  $\Delta S_{ij}$  incremental Kirchhoff stress tensor  
 $\Delta E_{kl}$  incremental Green strain tensor  
 $D_{ijkl}$  known function of current state

In [4] it is shown, that it is possible to apply this solution method to the deformation behaviour of an elasto-plastic soil.

## 3. THEORIES OF THE APPLIED MODELS

In distinction of their grainstructure soils can be classified in two different types: cohesive ones like clay and frictional ones like sand.

The ability to store water leads to a different mechanical behaviour. For a loam there is a big influence, for sand it is less. As the result of a loading cohesive soils react with a bigger change of volume, while a granular material will be displaced under the effect of friction. So for the research of soilmechanical processes it is very important to know the elasto-plastic behaviour and to be able to describe the point of failure.

Based on this, two different theories are chosen. They will be presented and failure criterion will be developed considering the stress-strain relations.

### (1) Plasticity model for frictional materials by Drucker-Prager [5]

For the calculation the soil behaviour will be idealized by two phases: at first the material reacts elastically up to a definite stress state, later on it begins to slide or to flow.

The total strain rate

$$d\epsilon = d\epsilon^{el} + d\epsilon^{pl} \quad (2)$$

is decomposed in the elastic  $d\epsilon^{el}$  and the plastic part  $d\epsilon^{pl}$ , which are separated by the failure surface.

Therefore the elastic constitutive behaviour is assumed to

$$\sigma = D : \epsilon^{el} \quad (3)$$

with  $D$  as a linear elasticity matrix.

A simple plasticity model is the Mohr-Coulomb's representation of yield. Based on this theory Drucker and Prager introduced the equivalent pressure stress in addition to the Mises yield criterion.

By this proper generalization they postulated the yield function as

$$q - \alpha \cdot p - k = 0 \quad (4)$$

with the equivalent pressure stress  $p = -1/3 \text{ trace}(\sigma)$

and the Mises equivalent stress  $q = \sqrt{3/2 (S : S)}$

$$S = \sigma + p \cdot I$$

I: unit matrix

Both are stress invariants and  $\alpha$  and  $k$  are positive material constants. A geometrical interpretation of this idea is shown in fig. 1.

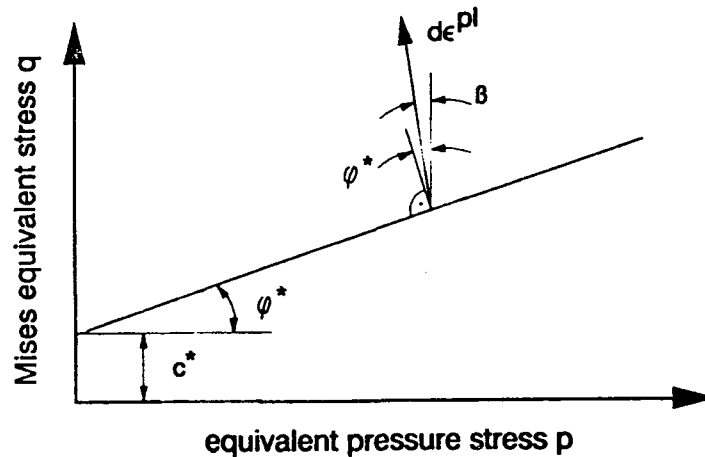


Fig 1: Schematic representation of the Drucker-Prager model

The failure surface is defined as

$$q - p \cdot \tan \varphi^* - c^* = 0 \quad (5)$$

and includes the characteristic soil parameters like the internal angle of friction  $\varphi^*$  and the cohesion  $c^*$ .

By this modification the Drucker-Prager theory represents a smooth yield function, while the Mohr-Coulomb model does not. Fig. 2 shows the difference in the principal stress space a) and the deviatoric plane b).

So the Drucker-Prager model is simpler to handle numerically. But it is a disadvantage, that this model restricts possible flow patterns, when the stress point is at a vertex of the Mohr-Coulomb model. For materials, in which the plastic flow direction wants to change rapidly with the load, ABAQUS [6] extended the theory by introducing a non associated flow rule. This means that the vector of plastic strain  $d\epsilon^{Pl}$  is not rectangular to the failure surface.

The flow rule has the form

$$d\epsilon^{Pl} = d\lambda \cdot \partial q / \partial \sigma \quad (6)$$

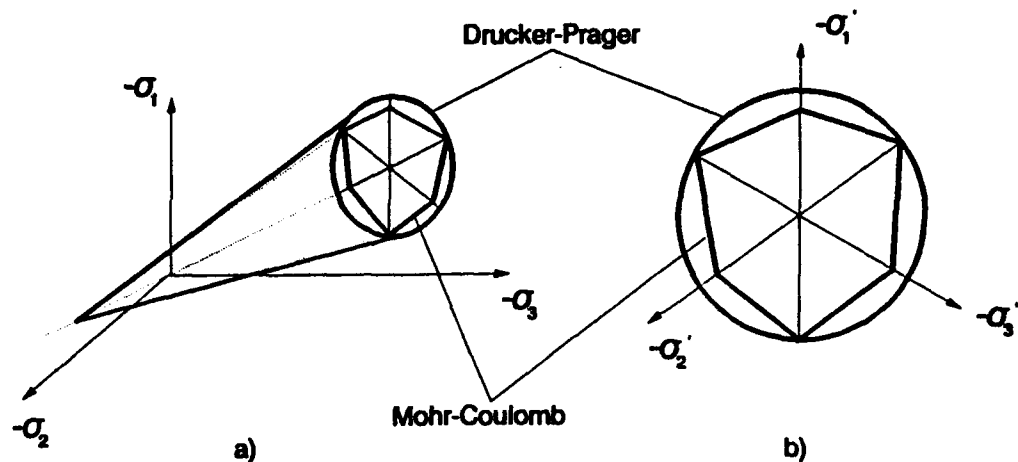


Fig. 2: Comparison of the different plasticity criterions by Drucker-Prager and Mohr-Coulomb

where  $d\lambda$  is a scalar determined by the magnitude of deformation and  $g$  is the flow potential, chosen in this model as

$$g = q - p \cdot \tan \beta \quad (7)$$

$\beta$  is the dilation angle and takes the volume change as a function of shear stress into consideration.

The geometric influence of  $\beta$  can be seen in fig. 1.

In addition to the extension of the dilation in ABAQUS it is possible to use the effect of the third stress invariant. The experimental datas of friction angle and cohesion are often obtained from triaxial tests and are determined like the presentation in the Mohr's circle. To match the Drucker-Prager constants  $\varphi^*$  and  $c^*$  to the Mohr-Coulomb model it is necessary to use simple relations for  $\alpha$  and  $k$ , which are introduced in equation (4).

## (2) Plasticity model for cohesive soils by Roscoe [7]

This model is developed around a plastic critical state theory. The main reflection is the division into an elastic part, which has a nonlinear stiffness in dependence of loading, and a plastic part, which includes the possibility of changing the flow surface size as a softening/hardening feature.

The basic parameter of this theory is the total volume alteration

$$\Delta V = \Delta V^g \cdot \Delta V^{el} \cdot \Delta V^{pl} \quad (8)$$

with  $\Delta V^g$  change of the grain volume  
 $\Delta V^{el}$  elastic volume change  
 $\Delta V^{pl}$  plastic volume change

These values are respectively the ratio of the current and the original volume.

With the definition of the volumetric strains

$$\epsilon_{vol}^i = \ln \Delta V^i$$

as the logarithm of the correspondending volume alteration the total strain rate follows to

$$d\epsilon = d\epsilon_{vol}^g \cdot I + d\epsilon^{el} + d\epsilon^{pl} \quad (9)$$

where  $I$  is the unit matrix.

Experimental results have shown, that the elastic part of the volume change is a function of the logarithmic equivalent pressure stress. That leads to the expression

$$\Delta v^{el} = 1 - \kappa \cdot \ln(p/p_0) \quad (10)$$

where  $p_0$  is the initial value of  $p$  and  $\kappa$  is the logarithmic elastic bulk modulus.

The plastic behaviour of this model is also developed by the stress invariants and is described by the yield function as

$$\frac{1}{\beta^2} \left[ \frac{p}{a} - 1 \right]^2 + \left[ \frac{t}{M \cdot a} \right]^2 - 1 = 0 \quad (11)$$

with parameter for controlling the failure surface size  $a$   
value for variation of the failure surface shape  $\beta$   
gradient factor of the critical state line  $M$

Fig. 3 shows this relation in the  $p/q$ -plane.

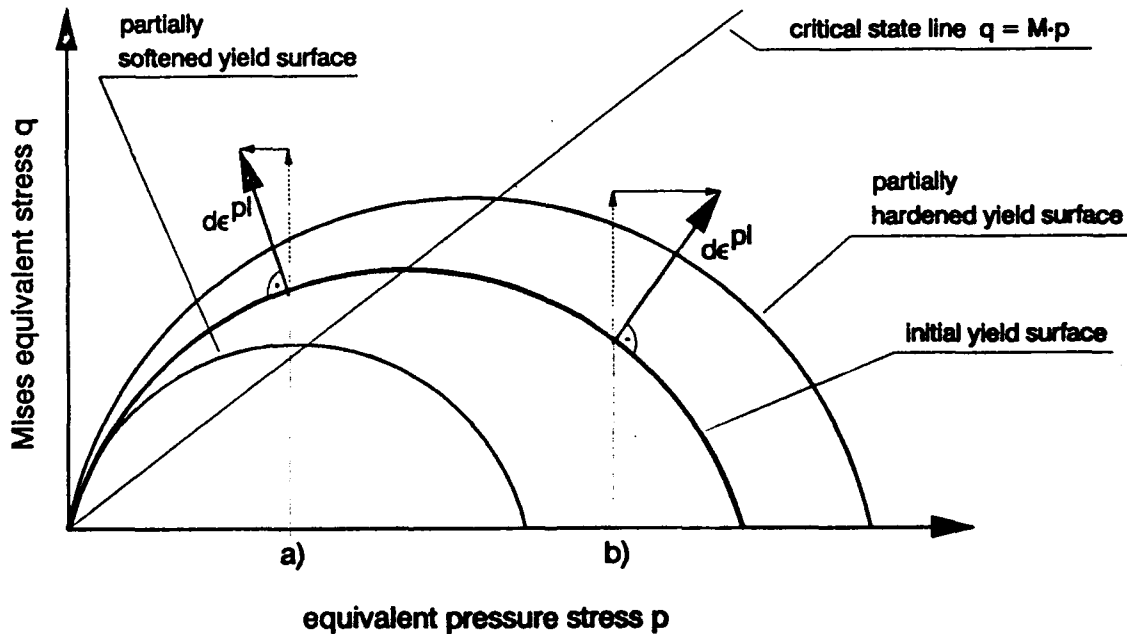


Fig. 3: Yield and critical state surface of the Roscoe plasticity model

In this plane the initial yield surface is an elliptic arc. The introduction of a critical state surface leads to the development of the softening and hardening function as the main feature of this model. The critical state surface in the  $p/q$ -plane appears as a straight line with the slope  $M$  passing through the origin and the vertex of the elliptic arc. So the initial failure surface is divided into two parts.

Under the condition of associated plastic flow, two horizontal components of  $d\epsilon^p$  with different directions results for the upper and the lower part of the critical state line. So compression of the soil body effects a growing, and volume enlargement a shrinking of the yield surface.

By constant equivalent pressure stress the two different cases

- a)  $q > M \cdot p$  leads to softening
- b)  $q < M \cdot p$  leads to hardening

of the material; both are marked in fig. 3.

In addition to this theory ABAQUS extended the model by dependence of the third stress invariant and of the yield surface shape. Furthermore it is possible to introduce initial conditions like the density as a function of depth and constant void ratios.

#### 4. SIMULATION OF THE PLATE PENETRATION TEST ON A FINITE SOIL BODY

The actual pressure sinkage tests were carried out in a soil bin with a hydraulic penetrometer at the Institute of Automotive Engineering in Hamburg. Fig. 4 shows the geometric reproduction of the test procedure simulated by a FEM-mesh.

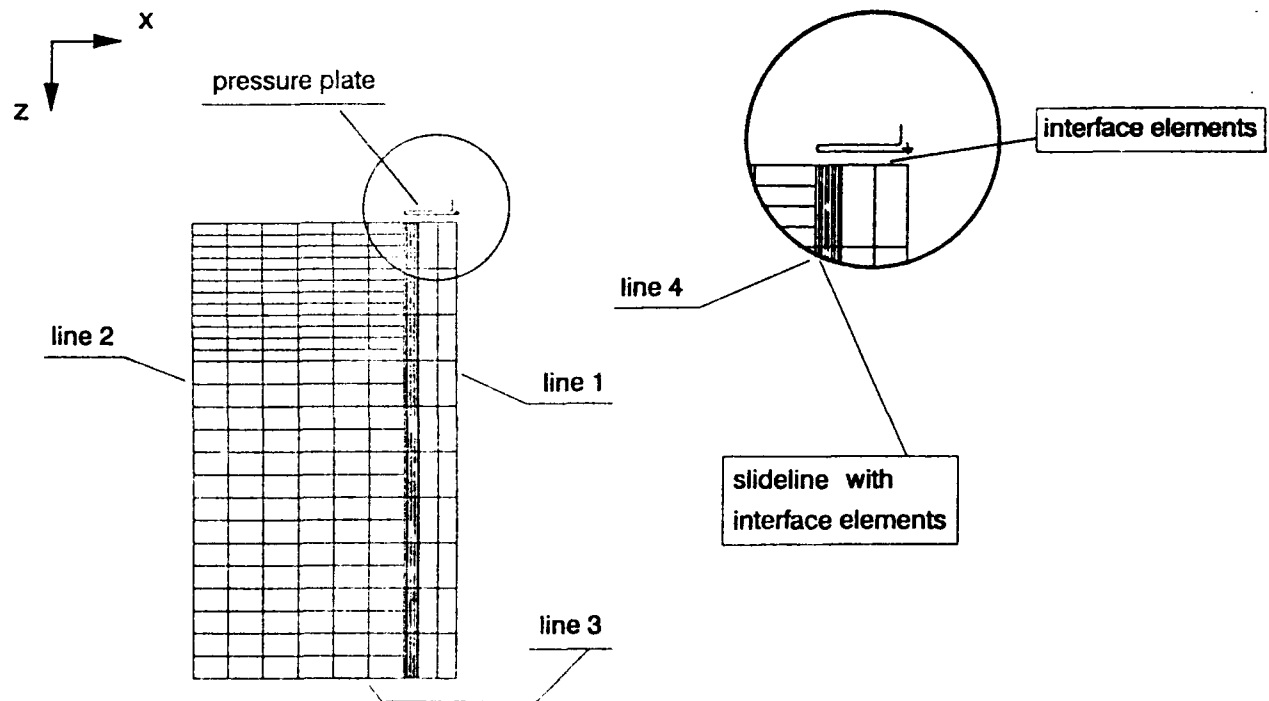


Fig. 4: FEM-mesh of the soil body with pressure plate

In order to save CPU-time only one plane of the axialsymmetric halfspace is computed. Line 1 is the axis of symmetry and their degree of freedom is restricted in the x-direction. The same is done for line 2, which simulates the rigid wall of the soil bin. The ground (line 3) is fixed in the z-direction.

The plate, which is computed as a rigid steel body, is placed at the top of the soil medium. The problem of contact between plate and soil is solved by using interface elements. They also realize the friction between steel and soil as a function of the soil type.

In case of plate shifting  $\Delta z$  a soil fraction results at the border of the steel plate along the z-axis. At this place an imaginary fraction line (4) is introduced to simulate this effect. In requirement of a homogeneous soil this line is computed with the same material properties like the total body. The fraction and contact solution will be done by a slideline and opposite interface elements. Especially in this critical area the mesh is computed with very small elements.

For the different types of soil the elements have the material definitions as shown in chapter 3 of this paper.

## 5. FIRST TEST RESULTS

For the simulation a circular plate with an area of  $A=600\text{cm}^2$  is used and penetrated into the soil up to a depth of  $\Delta z=20\text{cm}$ . As output value the reaction force at the plate bar is measured.

The simulated sand is described by the characteristic parameters of friction angle  $\varphi=39^\circ$  and cohesion  $c=1.3\text{N/cm}^2$ . Fig. 5 shows the calculated results compared with original measurements. The calculation is done with the basic Drucker-Prager model by using the same value for dilation and friction angle and without regard of the third stress invariant. The simulated pressure-sinkage curve for sand correlates very good with the measurements [8].

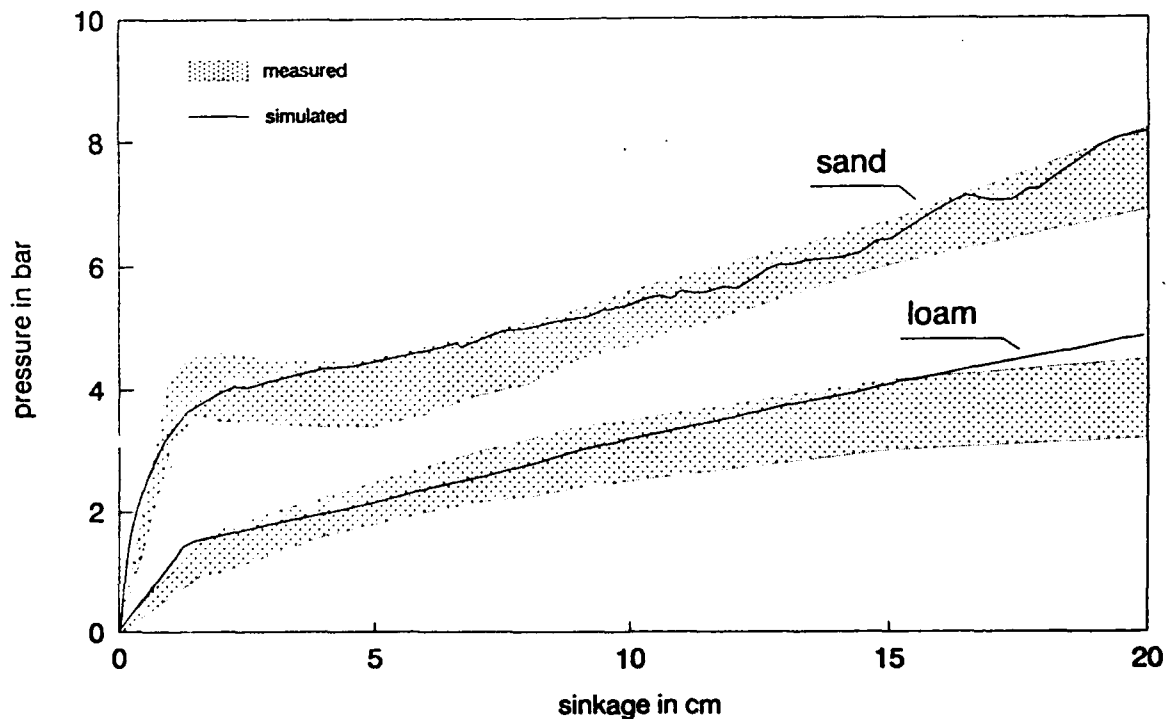


Fig. 5: Results of the penetration tests from original measurements and simulation

The loam is calculated with the Roscoe model. The characteristic parameters are logarithmic plastic bulk modulus  $\lambda=0.2$ , density  $\zeta=2.03\text{g/cm}^3$  and initial void ratio  $e_0=0.49$ . The correlation is not so good as in the case of the sand. An additional disadvantage of this model is the difficulty in measuring the input datas. The determination of the Drucker-Prager constants is much easier.

So in the future the usefulness of the Drucker-Prager model for all kinds of soil is to be investigated.

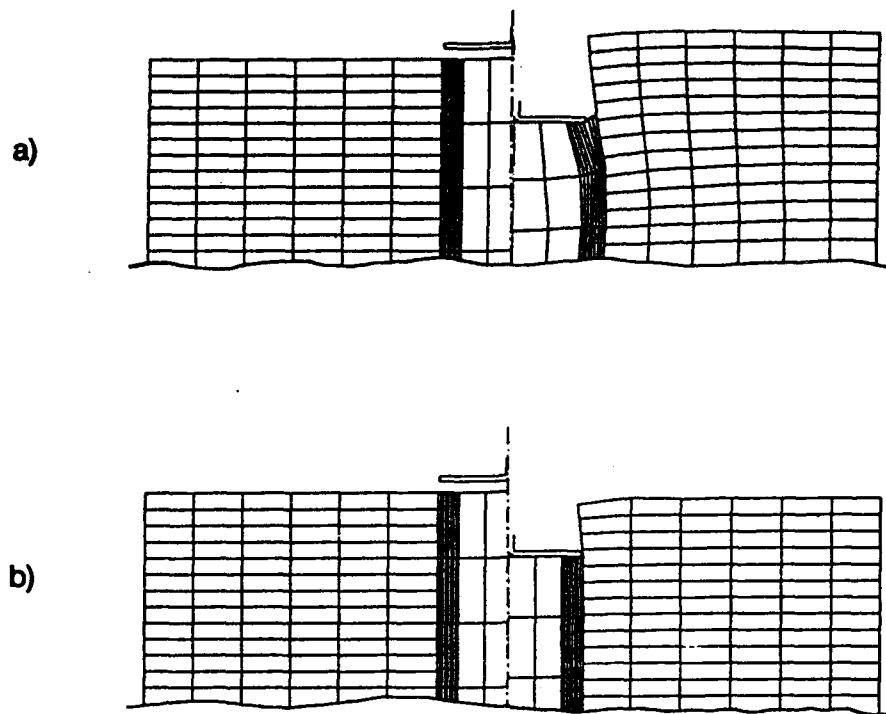


Fig. 6: Deformed soil bodies for sand a) and loam b) compared with undeformed mesh

Fig. 6 shows the deformation of both soil types at a sinkage depth of  $\Delta z = 10\text{cm}$ . The basic difference between the two appicated models is obvious by consideration of the volume alteration. In the case of the sand there is a big material displacement, while the loam is compressed only.

## 6. REFERENCES

- [1] BEKKER, M.G.: "Theory of Land Locomotion", The University of Michigan Press, Ann Arbor, Michigan 1956
- [2] GRAHN, M.: "Prediction of Sinkage and Rolling Resistance for Off-The-Road Vehicles Considering Penetration Velocity", 10th Intern. Conf. ISTVS, Kobe 1990, Proc., Vol. II, pp. 371 - 381
- [3] ZIENKIEWICZ, O.C.: "Methode der finiten Elemente", Carl Hauser Verlag München, Wien 1975
- [4] CARTER, J.P.; BOOKER, J.R.; DAVIS, E.H.: "Finite Deformation of an Elasto-Plastic Soil", International Journal of Numerical and Analytical Methods in Geomechanics, Vol. 1, pp. 25 - 43, 1977
- [5] DRUCKER, D.C.; PRAGER, W.: "Soil Mechanics and Plastic Analysis or Limit Design", Quarterly of Applied Mathematics, 1952, Vol. 10, pp. 157 - 165
- [6] HIBBIT, KARLSSON & SORENSEN, Inc.: "ABAQUS Manuals", Version 4.8, Providence, Rhode-Island, 1989
- [7] ROSCOE, K.H.; BURLAND, J.B.: "Stress-strain Behaviour of 'Wet Clay'", Engineering Plasticity, Cambridge University Press, 1968
- [8] HOLM, C.; HINTZE, D.; HEFER, G.J.: "Einfluß der Form und Größe des Eindringkörpers auf die Druck-Einsinkungsbeziehung in weichen Böden", IKK-Bericht 87-06, Hamburg 1987



# **THE PREDICTION OF SOIL STRENGTH WITH THE AID OF CLIMATIC DATA**

**D. Hintze**

**University of the Federal Armed Forces Hamburg, Germany  
Institute of Automotive Engineering**

## **SUMMARY**

The mechanical properties of a given soil depend on its moisture content. It is of importance in terrain-vehicle evaluation that soil strength decreases with the increase of moisture content. Soil moisture and therefore also soil values change in time because of seasonal fluctuations of the climate.

This presentation shows, how the future moisture content of a given soil can be predicted, knowing a past moisture content and the development of climatic data. Further it is shown, that the pressure-sinkage curves for a given soil can be calculated, knowing the moisture content.

Hence it is possible to predict soil strength for a given soil just knowing the past moisture content and future climatic data, like precipitation and evaporation.

## **1. INTRODUCTION**

Off-the-road mobility is dependent on soil strength. The specification factors for the soil strength are soil type, soil density and moisture content. On natural soils the soil class and the soil density are nearly constant sizes for a defined small area. For this area the moisture content is decisive for the soil strength [1].

The change of moisture content is a result of the weather situation. The weather determines with the precipitation and dryness the moisture content in the soil. Therefore it seems logical to assume that moisture content can be derived from climatic data and that soil strength can be derived from moisture content. These relationships will be presented in two models, A and B.

At the Institute tests were carried out over a long period of time in natural soils in order to collect data for the models. Precipitation  $N$  [mm], temperature  $T$  [°C], moisture content  $w$  [%] and soil strength as Cone-Index [bar] were measured daily in a defined area of a plastic soil and a coarse grained soil. The plastic soil, a sandy silt with 9% organic materials, consists of 25% silt and 75% sand. The coarse grained soil consists of fine and middle sand without any organic

materials. Some of the results of the prediction of moisture content and of pressure-sinkage curves are presented here for the more difficult plastic soil.

## **2. Model A: Theory of predictability of the moisture content by climatic data**

Moisture content is dependent on many factors, namely climatic factors as humidity, temperature, air pressure, altitude, transpiration of plants, evaporation, precipitation and soil factors as for example dry bulk density, organic matter, ability to store water in soil, position of groundwater table and amount of the groundwater and impounded water. The factors influence each other. These influences vary considerably.

Humidity, temperature, dry bulk density and the ability to store water in certain limits are taken into account and will pass into a basic equation. In order to predict the future moisture content,  $w$ , several factors must be considered in a mathematical equation. These are the present moisture content  $w_1$  and the change of moisture content in the future. The change of moisture content consists of two parts, the input and output of water. In a general form the mathematical equation is written as:

$$w = w_1 + \text{precipitation} - \text{watertransfer} \quad (1)$$

Water movement or moisture transfer in soils may be divided into two particular systems for general consideration: a) the saturated system where all the voids are filled with water and b.) the partly-saturated system where both air and water are present. It is to be remarked that the moisture content varies between an upper and a lower limit. These limit values depend on the soil type. Their difference defines the capability of the soil to store water in the pores. Precipitation and watertransfer determine the amount of moisture content.

The factors in equation (1) are:

### **2.1 Present moisture content $w_1$**

The present moisture content  $w_1$  reflects the influence of the weather in the past. Usually it is given in percent of masses. Because the precipitation is given in mm the moisture content must be converted from percent into mm using equation (2).

$$w \text{ (mm)} = w(\%) \cdot \rho_d \quad (2)$$

The conversion factor, the dry bulk density  $\rho_d$ , is valid for a soil layer of 10 cm.

### **2.2 Precipitation**

Precipitation takes place as rainfall, snow, wet fog or dew. It may fill up the water reservoir in the pores till its upper limit. In this case additional precipitation does not change the moisture content. The water percolates, drains off the surface or stays on soil surface and evaporates.

These situations are unimportant for soil strength because they do not change the moisture content in the soil. The percolating water displaces the bounded water in the pores from the upper zone into the lower one [2].

Because the moisture content has an upper limit the additional precipitation has to be limited in the model by means of a reduction factor  $i(S_r)$ , which depends on the degree of saturation  $S_r$ . For plastic soils the upper limit of the degree of saturation  $S_r$  runs to ~95% according to experimental results in literature and own measured values. For coarse grained soils it is considerably smaller.

### 2.3 Watertransfer

The watertransfer consists of percolation, surface drainage and evaporation. The important parameter for the decrease of the moisture content is the evaporation. It depends on soil type, its water reservoir by capillarity, and climatic data. The climatic data are temperature  $T$ , humidity  $F$ , air pressure and wind [3].

As is well-known, only a limited amount of water vapour can be contained in a given quantity of air, and this limit is determined by the temperature. At very low temperatures only a small amount of water vapour can remain in the air; at very high temperatures a much larger amount is able to remain. Air with a certain absolute humidity that is cooled continuously will eventually reach a temperature  $T_D$  at which it can contain no more vapour, it becomes saturated. The humidity of the air then is 100% and the corresponding temperature is called dew point  $D$ . At this dew point, water condenses on particles, which grow and become visible as clouds or precipitation.

Most of the time the air is unsaturated, that is to say, its temperature is  $T > T_D$ . The relationship between the absolute values of unsaturated and saturated humidity  $H$  is the relative humidity  $R$ . Evaporation  $V$  is only possible if a difference is present between absolute and relative humidity. The temperature dependent difference determines the amount of evaporation  $V$ , as can be seen in equation (3) and figure 1.

$$V = a \cdot (H - R) \quad (3)$$

The factor "a" considers further specific factors, namely soil type, capillarity and wind and can be found by the best fit between measured and calculated points using the method of least squares.

The weather stations register temperature and dew point. The daily mean values of  $(H-R)$  (same as  $(H-D)$ ) can easily be called up or measured. Equation (4) describes the daily evaporation for a time intervall  $dt$  of one hour.

$$v = a * \frac{1}{24} \int (H - D) dt \quad (4)$$

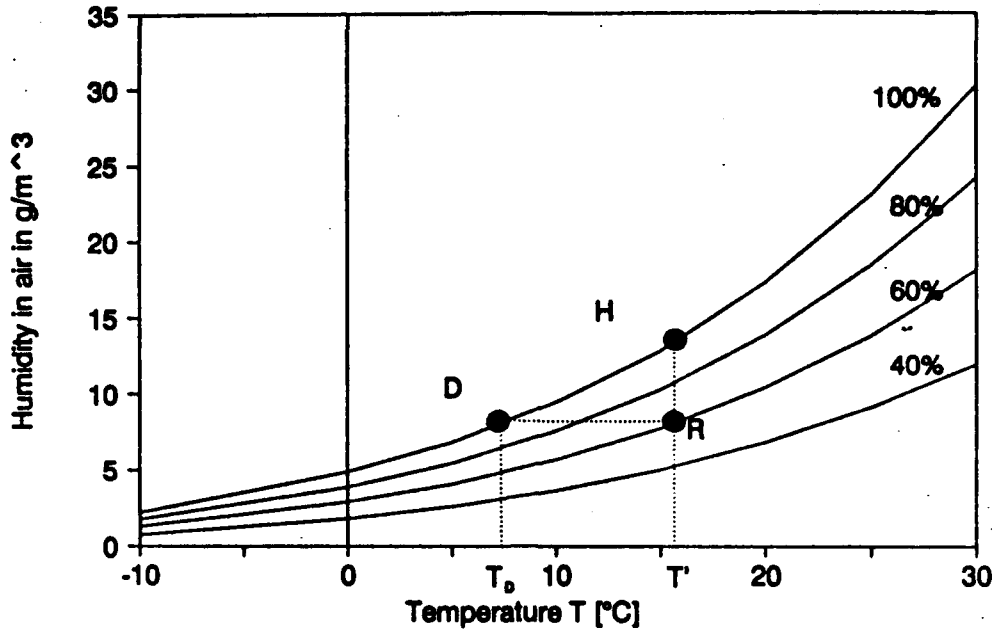


Fig. 1: Humidity as function of temperature

#### 2.4 Model A: Predictability of the moisture content by climatic data

Using the extended expressions for precipitation and watertransfer in equation (1) the moisture content  $w$  after a period of  $n$  days is expressed by equation (5).

$$w \text{ [mm]} = w_1 + \sum_1^n N * i(S_r) - \sum_1^n a * \frac{1}{24} \int (H - D) dt \quad (5)$$

Figure 2 shows the agreement of the measured and calculated points over a long period in 1990. For the calculated curve a fixed starting point, the present moisture content  $w_1$ , at the first day was used and then over the whole period only climatic data namely precipitation, dew point and absolute humidity by given temperature of the next weather station were considered. The values of the weather station are usually valid for a large region. In equation (2)  $w$  is valid for a soil layer of 10 cm. For a soil layer of any size  $d_i$  the equation (5) is to be multiplied with the soil layer  $d_i$  in unit [dm].

If the climatic data of the nearest weather station are not available, it is also possible to register the temperatures and the rainfall measurement in situ. Equation (4) can be replaced by the following equation (6) because humidity is connected with temperature.

$$v = b * \frac{T_{min} + T_{max}}{2} \quad (6)$$

In this equation factor "b" has a similar meaning as factor "a" in equation (3) and the daily evaporation  $V$  will be expressed by the mean value of the minimum and maximum temperature. This investigation leads to comparable results as figure 2 shows.

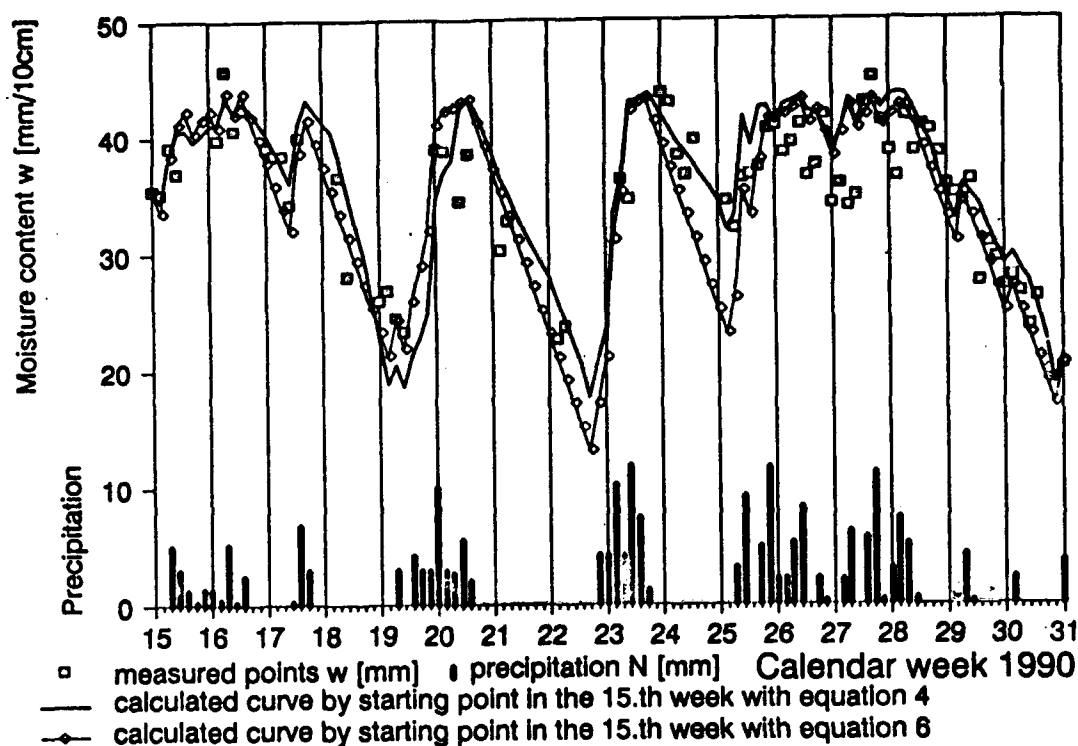


Fig. 2: Comparison of measured and calculated moisture content

### 3. Model B: Theory of predictability of soil strength by moisture content

Usually pressure-sinkage curves are presented as function of depth,  $p = f(z)$  [4]. The pressure-sinkage relationship depends on moisture content. Figure 3 shows the measuring points and the linear regression of CI-values in two depths as a function of moisture content of the plastic soil area. According to this a relationship,  $p = f(z, w)$ , has to be developed in an equation, based on data from figure 3.

The measured curves of plate and cone tests show three different fundamental shapes of curve, illustrated by curve A, B and C, shown in figure 4. Curve A is valid for cone- and plate-tests in a coarse grain soil, curves B, C and D for plastic soils. Plate penetrometer tests lead to curve B, cone penetrometer to type C. Curve C and D have a similar shape but a different upper  $p_{max}$  and lower limit  $p_{lim}$ .

While the results of plate penetrometer tests are mainly due to main stresses the results of cone penetrometer tests are based on a combination of shear and main stresses. Therefore curve B is usually described by equation (7). The shape of the more complicated curve C and D is expressed by equation (8).

$$p(z) = k \cdot z^n \quad (7)$$

$$p(z, w) = p_{lim} [1 + k_3 e^{-z/k_4}] \cdot [1 - e^{-z/k_4}] \quad (8)$$

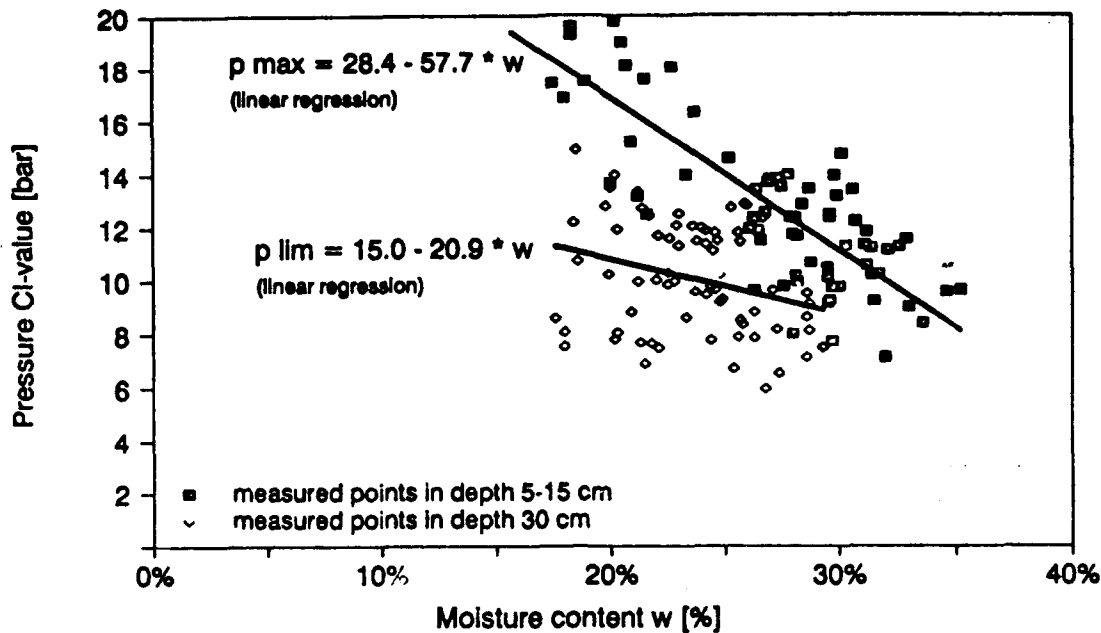


Fig. 3: Linear regression of CI-values to moisture content in two depths

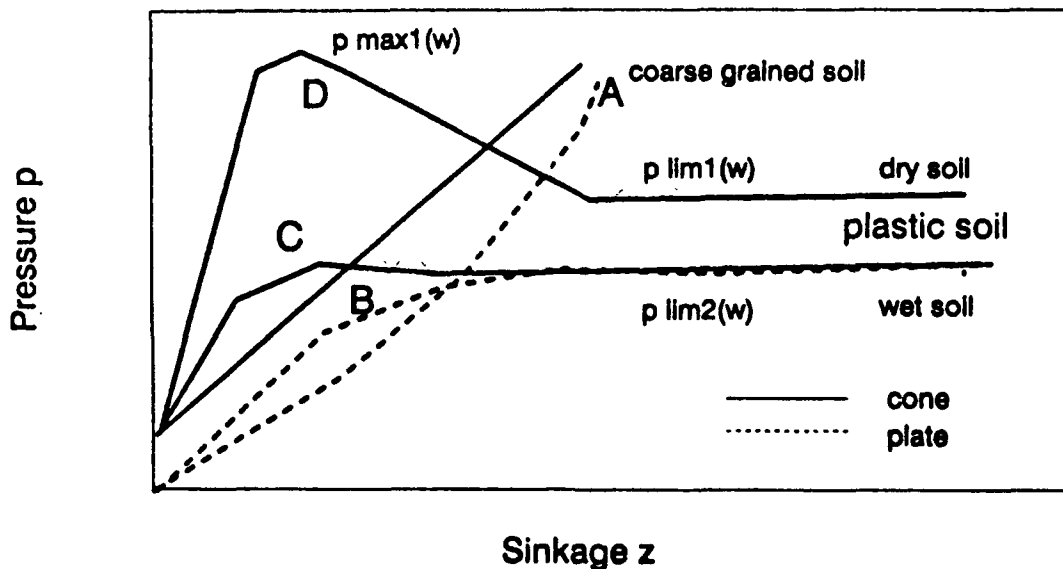


Fig. 4: Fundamental forms of pressure-sinkage curves

The similar curves C and D are measured in the same area but under different conditions, namely wet or dry soil. It is the objective to express the pressure-sinkage curves as a function of depth and moisture content. This can be done with the aid of the empirical data in fig. 3 and by formula (8). The parameters  $k_3$  and  $k_4$  describe the peak and shape of the curves dependent on soil type and moisture content. The limit value  $p_{lim}$  is also a function of  $w$ .

A comparison of predicted and measured pressure-curves is shown in figure 5. The important influence of moisture content is visible in the measured and calculated curves. Further it is remarkable that the influence of shear stresses is higher in dry soils than in wet soils. The amount of shear stress involved in the pressure-sinkage curve increases with the dryness of the soil. This is the reason why differences between cone- and plate-curves are less in wet soils.

Since the prediction of the pressure-sinkage curves is good, it is possible to predict soil strength on the basis of moisture content [5].

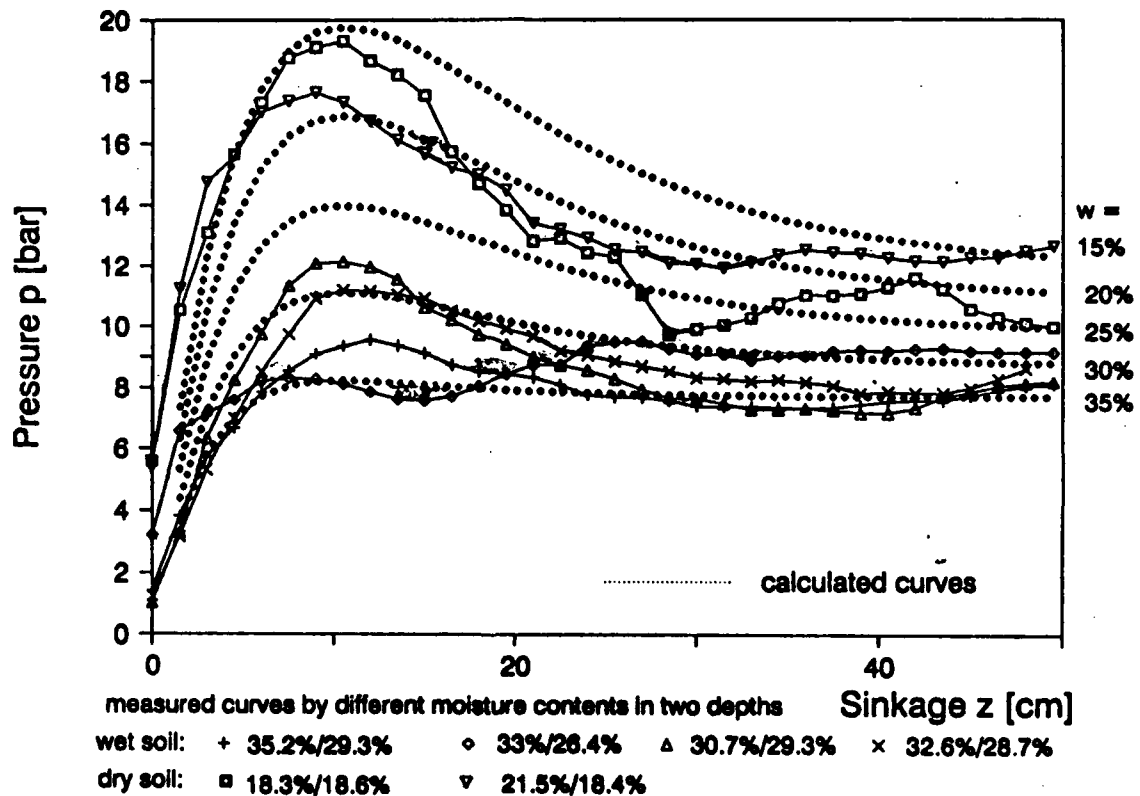


Fig. 5: Comparison of calculated and measured pressure-sinkage curves of a wet and dry plastic soil

The pressure development can also be predicted over a longer period of time. The pressure is then described by an equation of the form  $p = f(w\%)$ , as seen in figure 3, and using model A. The pressure is calculated only on the basis of the climatic data. The development of the measured data, temperature, dew point and precipitation are seen in figure 6. Figure 7 shows the good correlation of measured and calculated CI-values over a period of four months.

Hence it is possible to predict soil strength of a given soil without field measurements using only the development of climatic data.

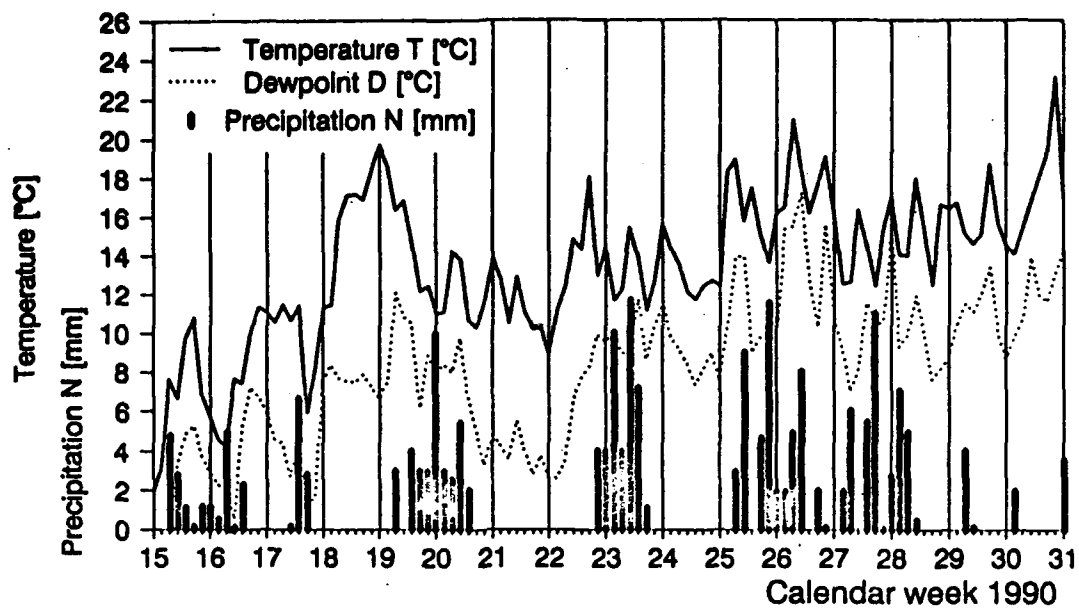


Fig. 6: Used climatic data in model A

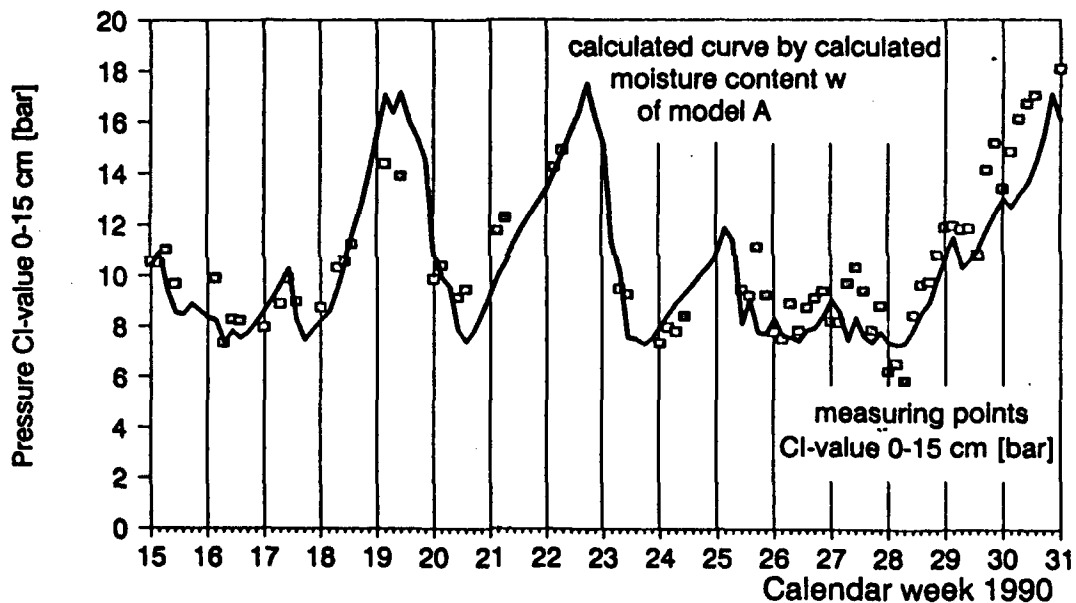


Fig. 7: Comparison of measured and calculated CI-values [bar]

## 5. REFERENCES

- 1 HINTZE, D.: The influence of seasonal moisture changes on soil strength, Proceedings of 10th International Conference of the ISTVS, Kobe, Japan, Volume 1, p. 107-116, 1990
- 2 KEZDI, A.: Handbuch der Bodenmechanik, Band 1, Bodenphysik, VEB Verlag für Bauwesen Berlin, Verlag der Ungarischen Akademie der Wissenschaften Budapest, 1971
- 3 WECHMANN, A.: Hydrologie, Verlag für Bauwesen, Berlin 1964
- 4 BEKKER, M. G.: Introduction to Terrain-Vehicle Systems, University of Michigan Press 1969
- 5 HINTZE, D.: Ph. D.- Thesis in preparation; "Einfluß der Witterung auf die Befahrbarkeit natürlicher Böden"



# **AUTOMATIC DATA RECORDING AND IN SITU STATISTICAL SURVEY OF CONE PENETROMETER TESTS**

**G.J. Hefer, G.W. Heiming**

**University of the Federal Armed Forces Hamburg, Germany  
Institute of Automotive Engineering**

## **SUMMARY**

At the Institute of Automotive Engineering in Hamburg an automatized cone penetration test device has been developed, in order to ease the operation and make the measurements more efficient. A small computer unit to manage data recording and data storage was installed in the top case of a Bush Cone Penetrometer. Now the penetration tests can be carried out by one man alone. As the measurements can be carried out very quickly, it is possible to obtain more data, in order to consider the requirements of statistics. All the data are recorded and stored by the new device. This enables the operator to get the data without using any other devices, to transfer the stored data to a main computer by serial data transfer and to use the data profitably for further evaluation. It is possible to produce a statistical survey of the data, using the build-in computer. Due to the large scattering of the measured data it was always difficult to decide how many penetration tests should be carried out for a satisfying result. Now the required amount of measurements are automatically precalculated parallel to the tests. As input values the acceptable standard-deviation and the required confidence factor have to be chosen.

## **1. INTRODUCTION**

The NATO Reference Mobility Model (NRMM) is a common model to predict the mobility of a vehicle on soft ground. As a criteria for mobility the Cone Index (CI), measured with a cone penetrometer is used. The cone is pressed into the soil in order to measure the force in relation to the sinkage. By the mechanical kind of penetrometer either the pressure sinkage curve is plotted directly on a paper (i.e. STIBOKA Penetrograph), or the measured values are shown by analog displays (i.e. FARNELL or EIJKELKAMP Penetrometer). At the Institute an electronic kind of penetrometer (BUSH) with digital display for force and sinkage is used.

## **2. PREVIOUS PROCEDURE**

As a reference for the bearing capacity of a soil cone penetration tests were carried out in the field by using a grid of 40x40 m with 255 intersections. The number of measurements in such a grid was regarded as sufficient representative for the whole area. All the data (up to 32 values in the depth from one penetration test) had to be read from the display by the operator and noted on paper by another person. For further processing, the data had to be transferred to a personal computer by data typing. It was our objective to improve this operation with the development of a new penetration device and an improved prediction procedure.

### 3. REQUIREMENTS FOR THE ELECTRONIC DATA RECORDING AND STORAGE

In order to optimize the data recording and storage the use of electronic data processing devices is required. Concerning the hardware a high grade of reliability of the system due to the rough conditions of field measurements has to be taken into account. The handling and the operation of the device must be easy. Concerning the software some demands have to be placed. A program is needed for conventional operation under the consideration of all possibilities. But the build-in computer should not only be used to record and store the data. As a further requirement operational errors must be controlled and the statistical properties of the soil have to be taken into account. During measurement the necessary number of samples should be calculated as a function of the standard deviation and a pre-selected statistical certainty.

### 4. STATISTICAL SURVEY

A typical feature while measuring soil properties is the broad scattering of values varying in a different manner on different soil types. For the characterization of a terrain sector, several measurements are required, which are statistically combined after completion of measurements. In statistic terms this means: The statistic parameters of the population are assessed on the basis of a sample.

The testing of a large quantity of different types of soil and of various characteristic soil values has shown, that an adequately accurate description of the distribution function of the values as measured is possible on the basis of the normal distribution.

In order to identify the distribution shape of an existing sample it is necessary to determine the distribution parameters from this sample. The level of accuracy of this assessment is the higher, the less this sample differs from the population.

This fact is described by the distribution of the t-values defining the random t variables, SACHS [1].

$$t = \frac{x - \mu}{s / \sqrt{n}} \quad (4.01)$$

which by conversion results in

$$x - \mu = \frac{t \cdot s}{\sqrt{n}} \quad (4.02)$$

Regarding great n-values,  $(x - \mu)$  tends towards zero. This means that with regard to an adequate size 'n' of the sample mean 'x' tends towards the population mean  $\mu$ .

By allowing a deviation  $d_x = x - \mu$  for the mean, assessed on the basis of the sample, the minimum size  $n_x$  of the sample can be determined on the basis of equation (4.02), if the appropriate normal distribution bound  $z_\alpha$  is inserted in replacement of 't'.

$$n_x = (z_\alpha/d_x)^2 \cdot \sigma^2. \quad (4.03)$$

The factor  $d_x$  represents half the width of the confidence interval valid for the mean 'x'. This means, that the range within the true mean may be expected at the selected confidence level.

Figure 1, right side, indicates that it is not possible to determine the optimum size of a sample in order to obtain a minimum confidence interval width in respect of the mean. If the size of the sample is above 25, the width of the confidence interval can only be reduced by large increases in the size of the sample.

An evaluation of the confidence intervals shown in figure 1 reflects, that based on equation (4.03) these intervals also depend on the standard deviation.

Measurements in terrain soils have shown, that due to the large number of factors it is not possible to forecast the standard deviations of the soil parameters as measured. For this reason one has to start out from an - also unknown - standard deviation.

With regard to the number of measurements required to achieve an accuracy  $d_s$  (i.e. half the confidence interval width) of the assessed standard deviation SACHS [1], indicates the equation

$$n_s \approx 1 + 0.5 \cdot (z_\alpha/d_s)^2 \quad (4.04)$$

in which  $d_s = (s - \sigma) / \sigma$ .

Figure 1, left side, shows the same relations in terms of quality as already described with regard to the mean. The confidence interval width of the standard deviation, however, is smaller than that of the the mean.

The bound  $z_\alpha$  of the normal distribution, which exists both in equation (2.03) and (2.04) depends on the confidence factor. The confidence factor expresses the level of probability at which the statistic statement can be expected to be true. With regard to a confidence level of 90%, the value of  $z_\alpha$  is 1,64. Further values may be taken from appropriate tables.

The statistical survey aims at assessing the distribution of soil values on the basis of a limited number of measurements. As already pointed out, uncertain values in terms of the mean and the standard deviation are available for this purpose. The selected confidence level can therefore only indicate a range, within the true distribution of soil values may be expected.

Figure 2 indicates such ranges with regard to the distribution of the cumulative frequency of characteristics, the parameters of which have been assessed on the basis of a limited number of values. In the case of equal levels of statistical probability, the spread is determined by the size of the sample and the standard deviation value. The spread is decreased if the size of the sample is increased. It is reduced to a single curve again, if the size of the sample is infinite. An increase of the standard deviation results in a broader spread of the values.

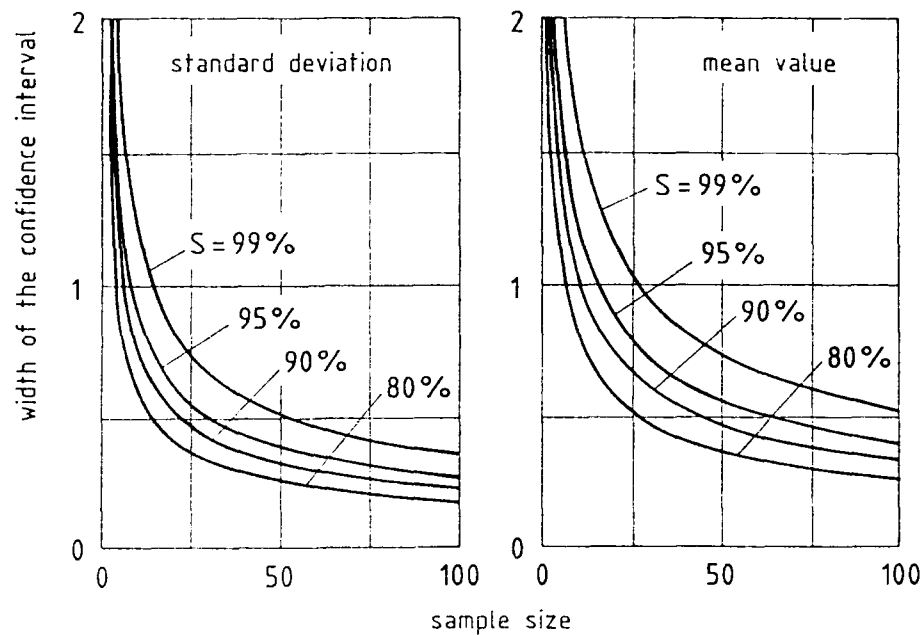


Fig. 1: The confidence intervals of the standard deviation (left) and the mean (right) of a sample depending on the size of the sample and the selected confidence level.

This means, that the number of measurements required can be determined on the basis of the selected width of the confidence interval and the selected confidence level. Due to the fact, that the number of measurements depends, among others, on the standard deviation of the values measured, a statistical evaluation of the data is already required while the measurements are taken. The result of this evaluation enables the test operator to perform the exact number of measurements required.

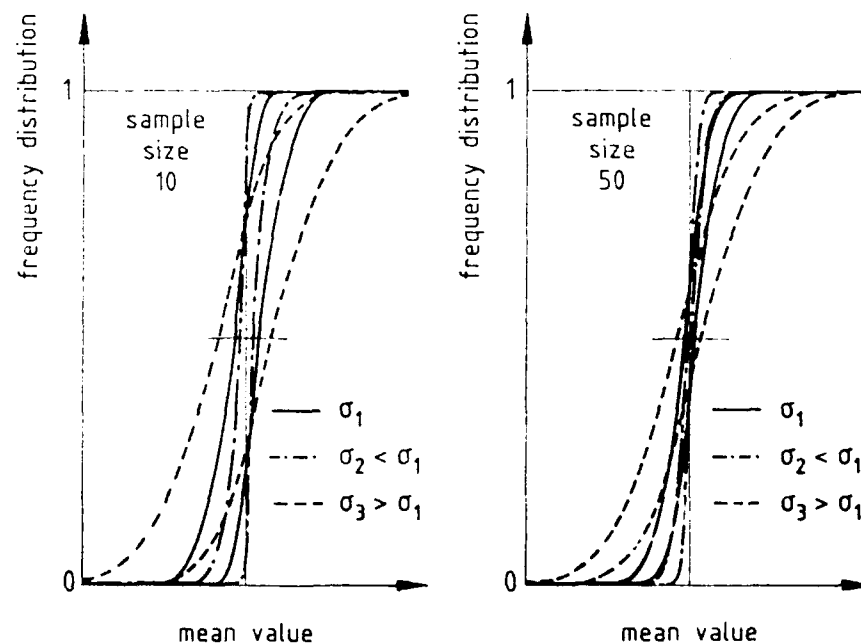


Fig. 2: Spread of the frequency distribution regarding normal distribution on the basis of an uncertain mean and an uncertain standard deviation (90% confidence level).

Based on the relations as described above, a program was generated for the penetrometer-integrated computer. Having entered the confidence level (default 90%) and the confidence interval width, that can be tolerated on the basis of the mean, the required number of measurements is calculated.

While the data is recorded, it is constantly checked whether the standard deviation of the measured values requires an increase of the number of measurements to be performed. At the completion of the data run, the mean, its confidence interval width, the standard deviation (ignoring its confidence interval width) and the number of measurements performed are displayed and stored.

## 5. HARDWARE

It is common and economic for the development engineer to use commercial elements for a new design. Based on the existing Bush Penetrometer an electronic data recording and storage device was developed. The data storage unit available from the manufacturer was not appropriate because this device only stores mean values of several measurements, has no possibility to control the measurement, is sensitive to field measurement conditions like weather, dynamic shocks etc., is very big and has an additional weight of app. 6 kg.

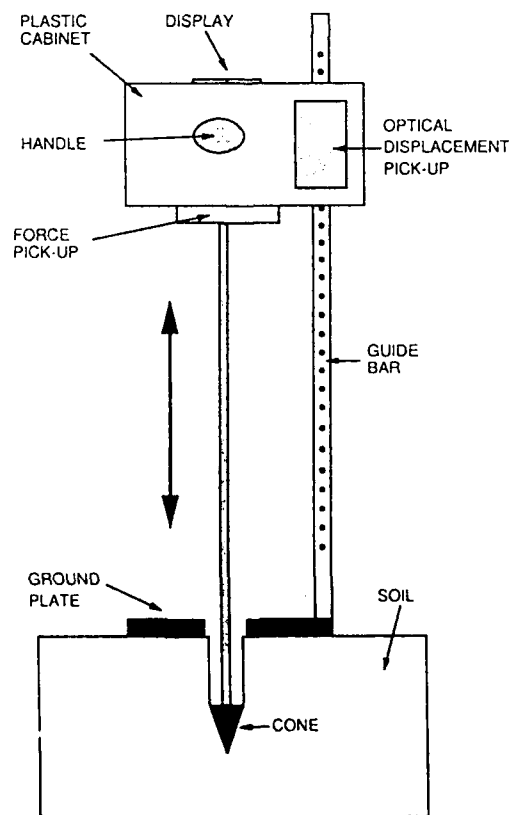


Fig. 3: Schematic of the BUSH Cone Penetrometer.

The sinkage is controlled by an optical displacement pick-up, the applied force is measured by a force pick-up. The signals are passing a signal amplifier and an A/D transducer and are shown on a digital display on top of the case. The method to obtain the data was not modified, but now the electrical signals are joined together on the single board computer. This single board was housed into a common cabinet with the original parts of the penetrometer. The organisation of the computer and the peripheral devices can be seen in figure 4.

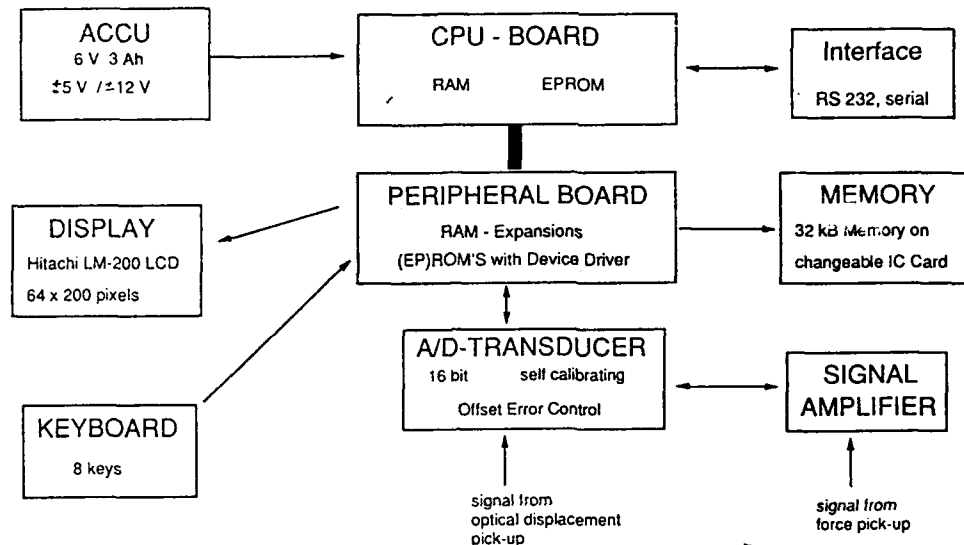


Fig. 4: Organisation of the single board computer and the peripheral devices.

The computer is based on a usual 8052AH Basic CPU, the operating system is Basic and user programs are stored in EPROM's. An 8 kB BASIC-Interpreter and all necessary functions for EPROM programming are available. The internal structure is shown in figure 5.

The adressable memory is build by three blocks of 32 kb each. These are

- Program Code Memory ( ROM/EPROM ) with 8 kB reserved for the interpreter
- Program Memory ( RAM ) to be used as conventional memory
- EPROM Programming area and BASIC Program Memory ( RAM / ROM / EPROM )

User written programs for measurement data processing are stored in the EPROM area.

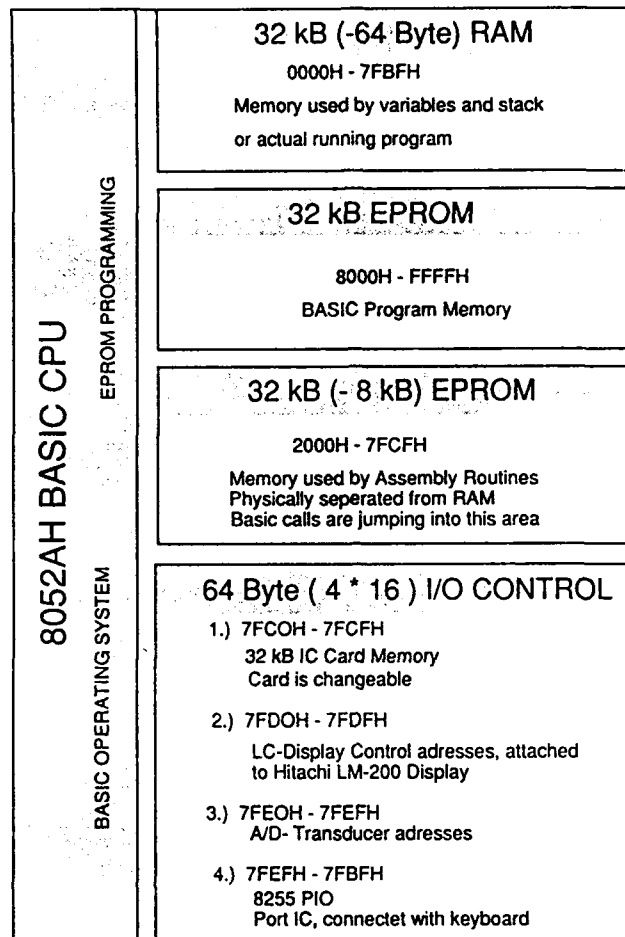


Fig. 5: Architecture of the 8052AH BASIC CPU

The signals are passing a signal amplifier and an A/D transducer and then are ready to be interpreted by the peripheral board. The peripheral board manage the display and the storage on the IC-Card. The desired measurement program can be chosen by the keyboard from outside. Main functions are

- start / stop of measurement
- switch between graphic and text mode
- storage of measured data
- transfer data to main computer via RS232

Before starting a measurement, the operator sets all variables and the desired graphic or text mode. After the initialisation of the display the penetrometer is ready for use. While the measurement is running, the electrical signals are transduced in proportioned values and stored in the RAM and simultaneously shown on the graphic or text display. At the end of each measurement the operator gets an information about possible errors (i.e. too fast penetration) and he can decide wether to store the data or not. After all measurements the data can easily be transfered to a personal computer by using the serial RS232 interface or using a PC with a build-in card reader/writer. The original display was changed by a Hitachi LC-Display which allows the data presentation in text or graphic mode. The brightness of the display can be

manipulated. Below this display the keyboard with eight keys is arranged. On the left side of the top the IC-Card card "drive" is fitted. The card has a capacity of 32 kB storage, this represents 16,000 measurement values. The read/write operations are performed fully contactless by coils without any moving parts. On the upper left the on/off switch is found. The AC/in and the serial interface are fitted at the box side.



FIG. 6: Operating of the manipulated penetrometer. The accumulators are carried by the operator.

## 6. REFERENCES

- [1] Sachs, L.: Statistische Methoden, Springer Verlag, Berlin, 1984
- [2] Hefer, G.J.; Heiming, G.W.: Beschreibung eines Meßsystems für die Erfassung und Auswertung von Bodenkennwerten und der Befahrbarkeit von Geländeböden, IKK-Bericht 87-08, UniBwH, Hamburg, 1987
- [3] Hefer, G.J.: Ein rechnerunterstütztes Kegelpenetrometer für die Messung und Auswertung statistisch verteilter Kegel-Index-Werte, 5. Arbeitstreffen der Auftragnehmer von BMVg-Rü III 5, München, 1989
- [4] Heiming, G.W.: Erfassen von Bodenkennwerten unter Berücksichtigung deren statistischer Verteilung, IKK-Bericht 89-22, UniBwH, Hamburg, 1990
- [5] Auel, Th.; Ruff, K.: Entwicklung eines mobilen Penetrometers mit Erfassung und Speicherung der Meßdaten sowie in-situ Bestimmung der erforderlichen Zahl der Messungen, IKK-Bericht 89-21, UniBwH, Hamburg, 1990



# BEARING CAPACITY AND SINKAGE MECHANISM OF LOOSE SAND

Wang Qingnian, Li Ying and Gui Longming  
Automobile Engineering Department, Jilin University of Technology  
Changchun, Jilin Province, People's Republic of China

## ABSTRACT

By limiting the lateral flow of the sand beneath plate, the load-sinkage mechanism of plates in different size has been examined. It has been shown by experiments that for the loose sand, the sinkage, in a large degree, about to 75 percent, results from the lateral flow of the sand beneath plate, and the sinkage caused by sand compaction is only near to 25 percent. Therefore, limiting the lateral flow of sand can effectively reduce the sinkage and enhance the bearing capacity.

## INTRODUCTION

The tractive effort of a wheeled vehicle on sand is largely dependent on the sinkage of its wheels. Therefore, how to reduce the sinkage of wheels has been of great interest in the area of soil-vehicle system mechanics. A number of efforts have been made in recent years in many countries in order to find out a practicable method. For a long time, it has been considered that the wheel sinkage is mainly formed by sand compaction, as pointed out by Bekker and others<sup>[1]-[2]</sup>. And so, the low inflation tires with larger diameter and wider section have been widely used to improve the tractive performance of wheeled vehicles on sand. But many experiments and theoretical analysis<sup>[3]-[6]</sup> have shown that for soft soil, particularly for the loose sand, the wheel sinkage depends on not only the sand compaction but also the lateral flow of the sand beneath it. It means that it is still necessary for us to study further the sinkage mechanism of the wheel on sand in order to approach a more effective way to reduce the wheel sinkage.

In this paper, the load-sinkage relation of plates in different size with the various lateral limit conditions, which limits the lateral flow of the sand beneath the plate, has been examined, in order to get a good insight of the plate sinkage mechanism on the sand under different conditions.

## THE LOAD-SINKAGE TESTS OF PLATES

As plate sinkage tests represent a useful tool for evaluating the soil bearing capa-

city and its load-sinkage relation, a series of such tests under different lateral limit conditions was made in order to separate sinkage components caused by the compaction and the lateral flowing of the sand the plate from the total sinkage.

1. plate tests without the lateral limit;
2. the lateral flow in one direction, longitudinal or transverse, was limited;
3. the lateral flow in all directions was limited.

The tests were made in the indoor simulative bin. In tests the effects of the plate dimensions on its load-sinkage property was investigated by using four plates with different ratio aspect, as shown in Tab. 1.

Tab. 1 Dimensions of the plates used in tests.

No.	1	2	3	4
length L (mm)	72	108	150	216
width B (mm)	72	72	72	72
ratio L/B	1	1.5	2.1	3

Fig. 1 shows the schematic of the equipment and the apparatus used in tests. the experimental soil was a kind of dry fine sand gradation curve of which was shown in Fig. 2. The measured Bekker's soil parameters are as follows:

$$\begin{array}{lll} n = 1.03 & k_c = 0 & k_\phi = 1.47 \text{ N/cm}^{n+1} \\ c_o = 0 & \phi = 31 & k = 1.43 \text{ cm} \end{array}$$

In tests, the limiting lateral flow of the sand beneath the plate was implemented by mounting two limiting plates to the two sides of plate in different directions according to the requirement of the test, as shown in Fig. 3.

## TEST RESULTS AND DISCUSSION

Fig. 4 ~ Fig. 7 show that the load-sinkage relations of the plates in different size under various limit conditions. By comparing these measured results we can see that the bearing capacity can be remarkably increased by limiting the lateral flow of sand beneath the plate. For a rectangular plate, limiting the longitudinal flow of sand is more effective to increase the bearing capacity than limiting the transverse flow of sand. While the lateral flow of sand beneath the plate in all directions was limited, the increment of the bearing capacity reached the maximum.

For the rectangular plates described above, to the same sinkage, for example 2cm, the load they can support increases by an average of 151% (longitudinal limit), 257% (transverse limit) and 561% (limit in all directions) respectively, compared with values without the lateral limit. On the other hand, in the conventional plate sinkage test, the bearing capacity of the plate, as we all know, is proportional to its area. Thus it can be seen that to limit the lateral flow of sand can more effectively raise the bearing capacity than to increase the plate area. As to the reducing percent of the plate sinkage compared with the

that is,

$$Z_{OL} = Z_C + Z_L \quad (4)$$

and so

$$Z_L = Z_{OL} - Z_C \quad (5)$$

Where,  $Z_{OL}$  -- the sinkage component measured, when the transverse flow of the sand was limited

When the  $Z_T$  and  $Z_L$  are determined, then the sinkage component caused by sand compaction,  $Z_C$  can be separated from the total sinkage  $Z_O$  by using equation (1). Here,  $Z_O$  is assumed to equal the value of plate sinkage measured when the lateral flow of sand in all directions was not limited. The calculation results of  $Z_O$ ,  $Z_T$  and  $Z_L$  was shown in Tab. 3.

Tab. 3 Calculation results of the sinkage components  
(plate 150mm×72mm).

sinkage components (cm)	unit pressure (10 <sup>5</sup> pa)		
	0.5	1.0	1.5
$Z_O$	3.1	5.9	8.3
$Z_C$	0.72	1.32	1.82
$Z_C/Z_O$ (%)	23.2	22.3	21.9
$Z_L$	0.73	1.43	2.12
$Z_L/Z_O$ (%)	23.5	24.2	25.5
$Z_T$	1.38	2.68	4.05
$Z_T/Z_O$ (%)	44.5	45.4	48.8
$Z_O - (Z_C + Z_L + Z_T) / Z_O$	8.7%	8%	3.7%

The error analysis in Tab. 3 indicates that it is possible to separate the sinkage components from the total sinkage of the plate based on the four times measured results under different lateral limit conditions. The maximum error is less than 10%.

From Tab. 3 it can be seen, although the various sinkage components increase with the unit pressure, its proportion to the total sinkage is nearly to be a constant. The compaction component is only about 25 percent of the total sinkage and the lateral flow component, the sum of the longitudinal and transverse flow components, is unexpectedly high to 75 percent. Furthermore, for a rectangular plate, limiting the transverse flow can more efficiently increase the bearing capacity and reduce the sinkage than limiting the longitudinal flow.

Under the test condition, the effect of the aspect ratio of the plates on the sinkage components was shown in Fig. 10. The aspect ratio had nearly no influence on the compaction component. Nevertheless, the transverse flow component increased with it and the longitudinal flow component reduced with it. But the sum of these two kinds of flow components basically did not change with the aspect ratio of the plate, as shown in Fig. 10.

measured values without limit was shown in Tab. 2.

Tab. 2 The reducing percent of the plate sinkage under different lateral limit conditions compared with the value without lateral limit ( $q = 0.75 \cdot 10^5 \text{ Pa}$ ).

reducing percent of sinkage	plate dimensions (mm-mm)			
	72*72	108*72	150*72	216*72
limit transverse flow	41%	50.6%	54.6%	63.1%
limit longitudinal flow	41%	35.1%	32.3%	28.9%
limit the lateral flow in all the directions	79.9%	76.2%	74.6%	74.8%

The above test results show that limiting the lateral flow of the sand beneath plate is an effective path to increase the bearing capacity and reduce the sinkage. It means that to approach a new type of running gear which has the function of avoiding the lateral flow of the sand beneath it is of fundamental importance to the development of the desert-vehicle.

Furthermore, to the loose sand, as shown by above experiments, not all the plat sinkage is caused by the sand compaction. In fact, the sinkage component caused by the lateral flow of the sand beneath the plate holds a quite large part in the total sinkage, as shown in Fig. 8 and Fig. 9. So it is significant to determine quantitatively the sinkage components caused by the compaction and the lateral flow of the sand beneath the plate in different directions. Based on the measured results, the values of sinkage components and its proportion to the total sinkage were approximately estimated by following method.

Assume the total sinkage of the plate is expressed as follows

$$Z_0 = Z_c + Z_T + Z_L \quad (1)$$

Where,  $Z_0$ -- total sinkage of the plate;

$Z_c$ -- sinkage component caused by the sand compaction;

$Z_T$ -- sinkage component caused by the transverse flow of the sand;

$Z_L$ -- sinkage component caused by the longitudinal flow of the sand.

From the above definition, when the longitudinal flow of the sand is limited, it means the  $Z_L$  in the equation (1) is equal to zero. If denote the sinkage measured under this condition as  $Z_{0T}$ , then from the equation (1)

$$Z_{0T} = Z_c + Z_T \quad (2)$$

thus, the sinkage caused by the transverse flow of the sand is

$$Z_T = Z_{0T} - Z_c \quad (3)$$

In same way, when the transverse flow of the sand is limited,  $Z_T$  is equal to zero,

## CONCLUSIONS

1. For the loose sand the plate sinkage can be divided into two parts. The first part caused by the compaction is only about 25 percent of the total sinkage and the second part caused by the lateral flow of the sand beneath the plate is near to 75 percent.

2. Limiting the lateral flow of the sand can largely reduce the plate sinkage and increase the bearing capacity. For a rectangular plate, to limit the transverse flow is more effective than to limit the longitudinal flow.

3. The work described in this paper indicates that as compared with merely increasing the contacting area, to develop a new type of the running gear, which can, at some extent, avoid the lateral flow of the sand beneath it, may be a more effective way to improve the tractive performance of vehicles on sand. But it still needs to approach further, particularly, the penetrating depth of the limit plate into the sand on the bearing capacity of sand and the plate sinkage. About this problem and the relative experiment results will be discussed in another paper.

## ACKNOWLEDGEMENT

The work described in this paper formed part of a programme "A Study of the Dynamic Property of the Sand-Vehicle System and Its Trafficability", financed by the National Committee of Natural Science Foundation of People's Republic of China.

## REFERENCES

- [1] M. G. Bekker, Introduction to Terrain-Vehicle System, Ann Arbor, University of Michigan Press, 1969
- [2] L. L. Karafaith and E. A. Nowatzk, Soil Mechanics for Off-Road Vehicle Engineering, Trans. Tech. Publications, 1978
- [3] Gao Dashui, Yu Qun and Yu Guyuan, Research in Slip-Sinkage of Tractor Driving wheel and Its Effect on Traction Performance, J. of Beijing Institute of Agricultural Engineering, No. 1, 1985
- [4] J. Y. Wong, Behaviour of Soil Beneath Wheels, J. Agric. Engng. Res. No. 4, 1967
- [5] K. wiendick, Stress-Displacement Relations and Terrain-Vehicle Mechanics--A Critical Discussion, J. Termechan. No. 3, 1968

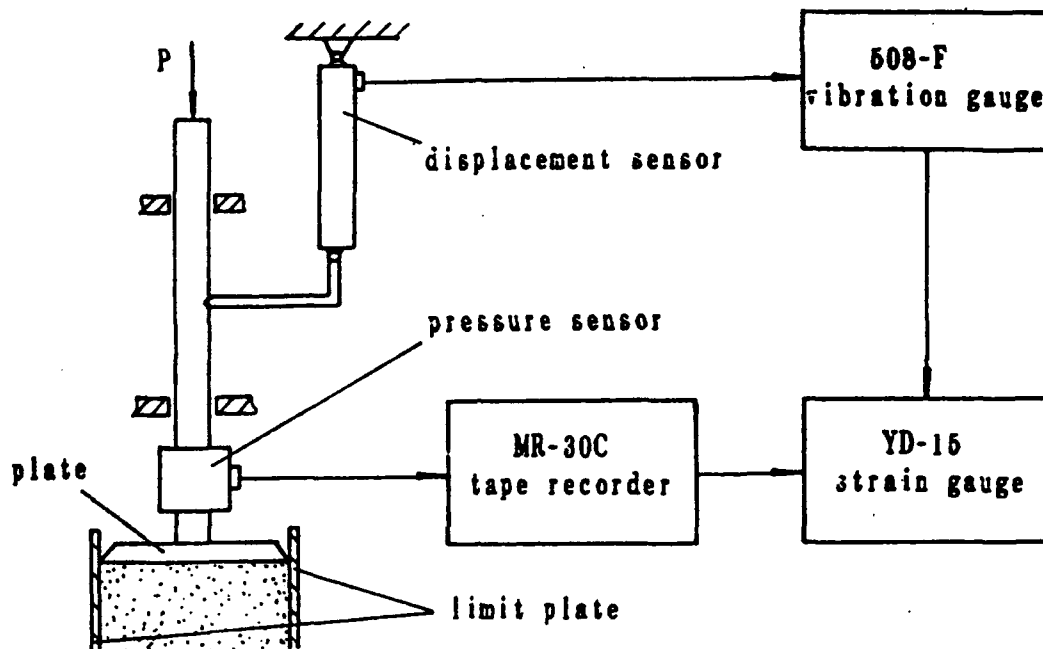


Fig. 1 Schematic view of the measuring system used in tests.

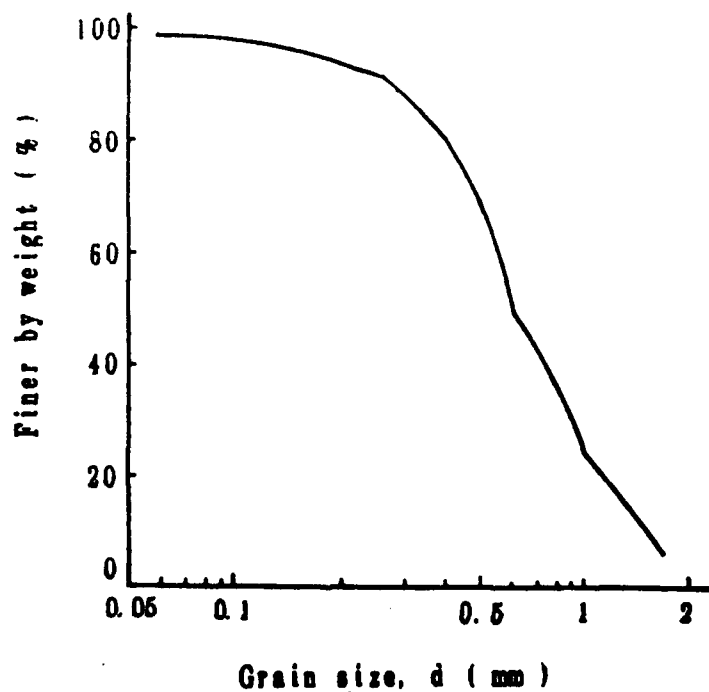


Fig. 2 Grain size distribution.

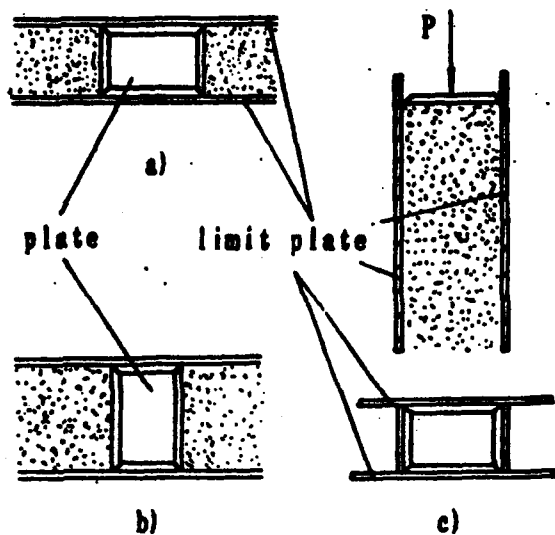


Fig. 3 Schematic of the plate test with the limiting plates.  
 a) limit the transverse flow;  
 b) limit the longitudinal flow;  
 c) limit the lateral flow in all directions.

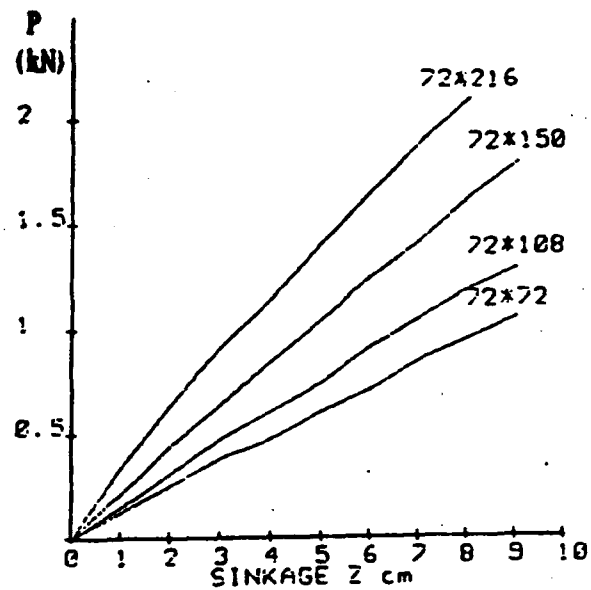


Fig. 4 Load-sinkage relations with longitudinal limit.

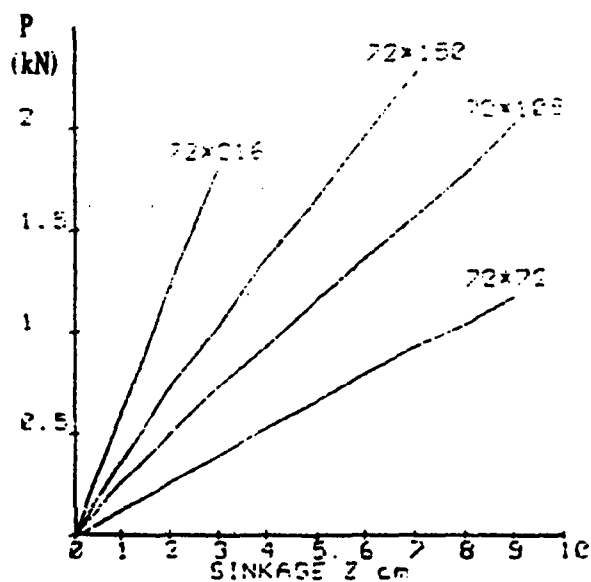


Fig. 5 Load-sinkage relations with transverse limit

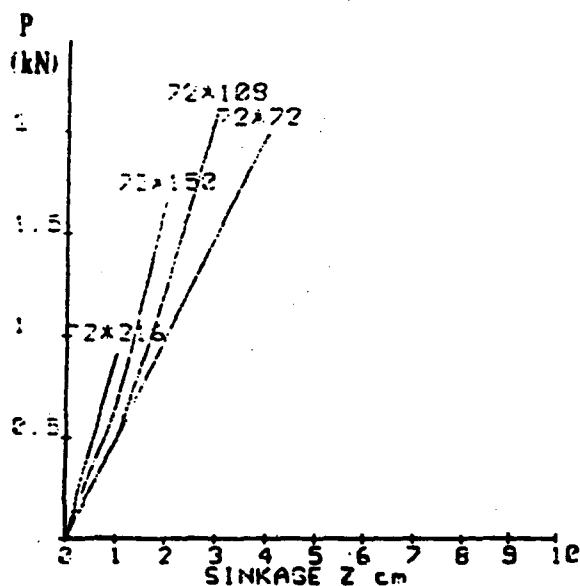


Fig. 6 Load-sinkage relations with the lateral limits in all directions.

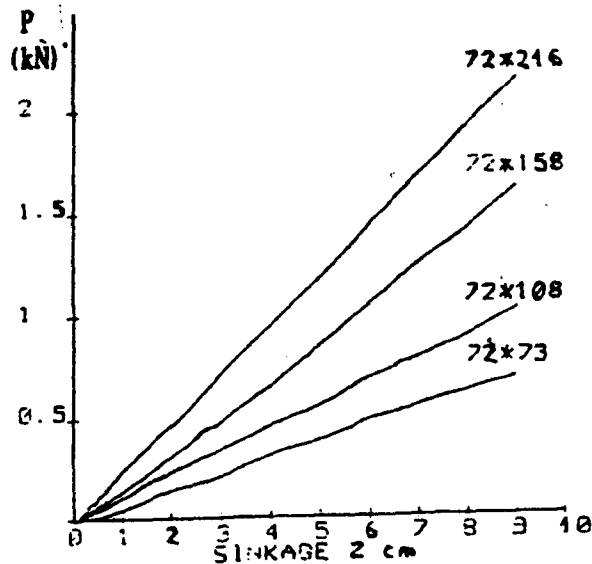


Fig. 7 Load-sinkage relations without the lateral limit.

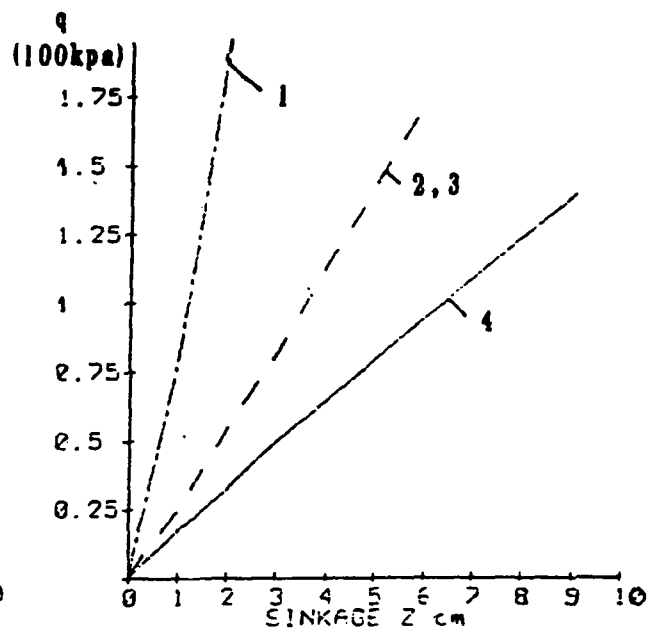


Fig. 9 Load-sinkage relations under the different lateral limit conditions (plate dimension - 72mm\*72mm).

- 1- limit lateral flow in all directions;
- 2- limit transverse flow;
- 3- limit longitudinal flow;
- 4- without lateral limit.

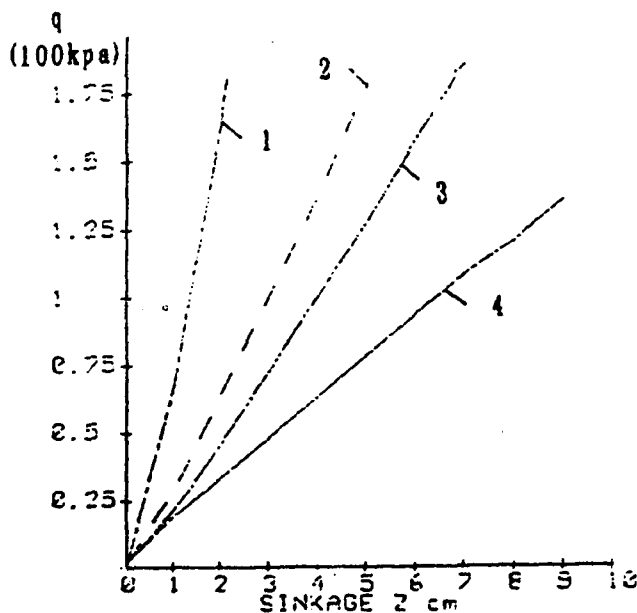


Fig. 8 Load-sinkage relations under the different lateral limit conditions (plate dimension - 108mm\*72mm).

- 1- limit lateral flow in all directions;
- 2- limit transverse flow;
- 3- limit longitudinal flow;
- 4- without lateral limit.

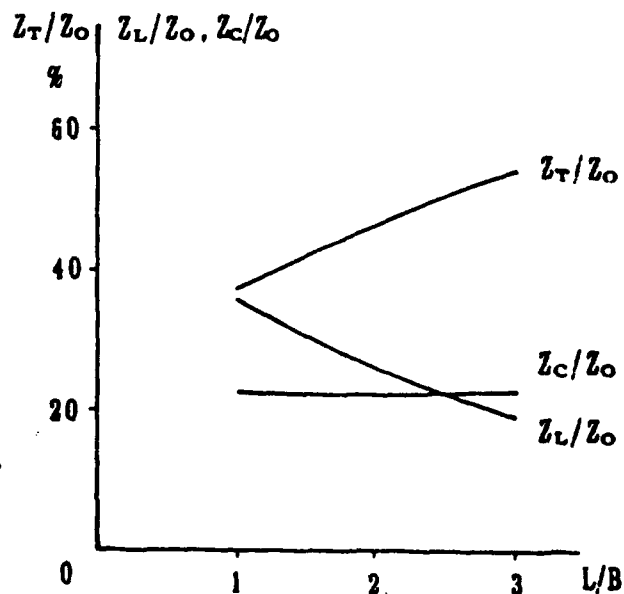


Fig. 10 Relations of the sinkage components and the ratio aspect of the plate.



# ADVANCED STUDY ON THE PERFORMANCE OF LUG CONFIGURATION AND ARRANGEMENT FOR POWERED WHEEL OF POWERED TILLER IN PADDYFIELD

Yao Jian Shao   Xiwen Luo   Hua Zhong Lu  
(South China Agricultural University, P.R. China)

## SUMMARY

The 2-3kw diesel powered tillers are now very popular in South China for farmers who own very small plot area of paddyfield. A research project was conducted to improve the performance of its single wheel. The effect of lug profile (curved or flat), lug height, lug angle, and lug number on wheel was investigated. It was observed that the profile, height, lug angle, lug number on wheel, sinkage and slip gave very strong effect on lug forces and performance of powered tiller. The optimized design on lug configuration for powered wheel was developed.

## INTRODUCTION

The 2-3kw diesel powered tillers are now very popular in South China for farmers who own very small plot area of paddyfield. The population of the on farm powered tillers in South China is growing to 300,000 sets. They are inexpensive and easy to fabricate. A powered tiller worths the same price as a water buffalo but works double and needs only half the feeding and managing costs. That is the reason why so many farmers buy them instead of their water buffalos.

Most powered tillers have only one driven wheel of which its top diameter is so small as 0.72m.

This research project is to design the lug wheel with optimum geometrical parameters to meet the need of general flooded paddyfield with hard pan layer, dry state paddyfield and very soft flooded paddyfield without hard pan layer near lakeshore or seashore.

The lug of a powered wheel is the basic element to interact with soil and its geometrical parameters play most important role to give better performance for powered wheel.

The purpose of this paper is mainly on an advanced study of optimum selection on lug angle, lug height, curved or flat lug, and lug number for powered wheel of this small powered tiller based on the recent study and experiments on soil behaviours and measured lug forces.

## PREVIOUS WORK

According to the Law of conjugate action between meshing profiles and the kinematics of lug, Shao (1) proposed nine equations for geometrical parameters of lug with respect to slip. The dynamic performance of single lug was studied by Zhang and Shao (2). The soil flow beneath lugs on sand and clay was studied by Shao and Wong (3) at Carleton university Canada in 1983. The soil flow as well as soil reaction beneath single lug and multi-lug were studied by Lu and Shao (4). The interference between lugs was studied by Luo and Shao (5). The Phd dissertation thesis of Lu (6) supervised by Shao discusses and analyses the soil behaviours, the measured soil reaction forces, the models of passive soil failure and the prediction of pull and lift forces for single lug and multi-lug, curved and flat lug of powered wheel at various slip from 10% to 100% on dry pure sand, saturated pure clay and wet paddy soil with comparison to plain moving blade in 1991.

Gee-Clough and Chancellor (7) measured the lug forces developed by a single lug of a cage wheel in Maahas clay loam soil. It was observed that soil moisture content, lug angle,

lug width, lug shape, sinkage and travel reduction had a strong effect on lug forces. Gee-Clough and later with Salokhe (8) in their studies on the effect of lug angle on performance found that 30 degree obtained the best performance in Thailand paddy soil. They also studied the soil behaviour under lug soil interaction at 50-100% slip for single lug and found the elliptical soil wedge in contrast to the prismatic soil wedge assumed in conventional theory (9). They studied the pull and lift forces acting on single lug of cage wheel and found the measured lug forces when compared with those predicted by the theory of conventional theory of passive soil failure did not suit accurately.

#### APPARTUS AND EXPERIMENTAL DETAILS

The experiments of soil behaviours and soil reaction forces beneath lug of model wheel were conducted in a specially designed set of apparatus. A 1200x600x125mm glass sided soil box was filled with pure dry sand, or wet pure clay, or Guangzhou paddy soil in different moisture content. The physical properties and mechanical parameters of sand, clay and paddy soil are shown in Table 1 and Table 2.

Table 1 Physical properties of experimental soils

Particle size distribution:				
Grain size	Soil particle	Pure seived sand	Pure clay	Paddy soil
0.001	Clay	-	61.78%	19.57%
0.05-0.001	Silt	-	32.82%	24.79%
0.25-0.05	Sand	-	5.4%	55.64%
<0.01	Physical clay	-	90.74%	33.92%
>0.5	Coarse sand	100%	-	-
Consistency limits (db):				
	Liquid limit	-	51.40%	35.40%
	Plastic limit	-	33.80%	22.80%
	Plastic index	-	17.60%	12.60%

Table 2 Mechanical parameters of experimental soils

Soil type	Unit weight	Cohesion	Internal friction	Soil metal friction	Adhesion	Cone index	Moisture content
	kN/m <sup>3</sup>	c kpa	angle $\phi$	angle $\phi$	Ca kpa	kpa	%
Pure sand	14.7	-	28	18.5	-	-	-
Pure clay	16.8	4	5	2.5	2.8	-	56
Paddy soil	17.36	2.5	12	10	2.1	105	37
	17.2	1.85	8	6	1.2	62.5	52

The rotation and plain motion of the model wheel was driven by a 1.5m long lathe and so the wheel had various necessary speeds and slips. The desired speed was controlled by the gear box of lathe and a pair of gear one of which rotated and moved along a splined shaft clamped on the chuck and spindle set of lathe. The desired slip was obtained by controlling the selected feeding speed of apron on which a worm gear box and frame was attached.

The model wheel had a steel disc (10mm thick and 150mm diameter) on which attached an octagonal transducer with different tested lugs. In this study, 25 and 30 degree involute curved lugs, 12.6, 14.6, 20, 25, 30 degree flat lugs, all with a constant top radius 250mm were compared on lug forces and dynamic performance, and found the optimum lug height, lug angle, lug profile, lug number, slip and sinkage for the powered wheel of small powered tiller. Figure 1 shows the experimental setup of soil box and model wheel. The transducer was calibrated before use. The signals of measured torques and forces were amplified by strain amplifier and recorded by magnetic recorder. All signals recorded were entered into a microprocessor to take out the normal, tangential forces and torques and then calculated to obtain the pull and lift forces and efficiency of lug. The curves of torques, pull and lift forces vs rotation angle of wheel are drawn by microcomputer and printer. Figure 1 shows the experimental set up of soil box and model lug wheel.

Besides model lug studies, there were experiments of full size lug wheels on paddy soil bin for tractive performance, and also plough work tests on paddyfield of Guangzhou and Hunan Province. Figure 2 shows the soil bin experiment of full size lug wheel and Figure 3 shows the tests of different lug wheels on paddyfield in Hunan Province. Figure 4 shows the penetration resistance with respect to the depth of experimental paddyfield.

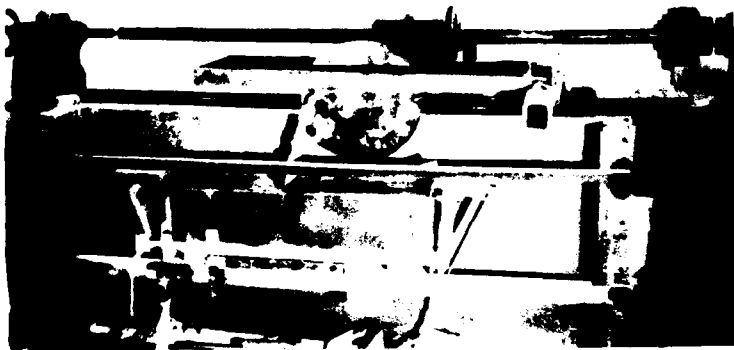


Figure 1

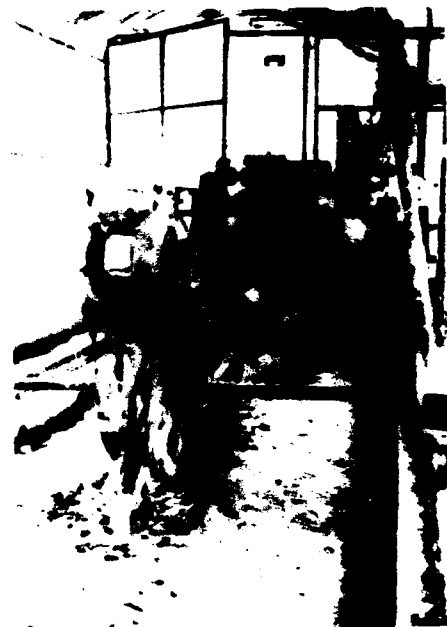


Figure 2

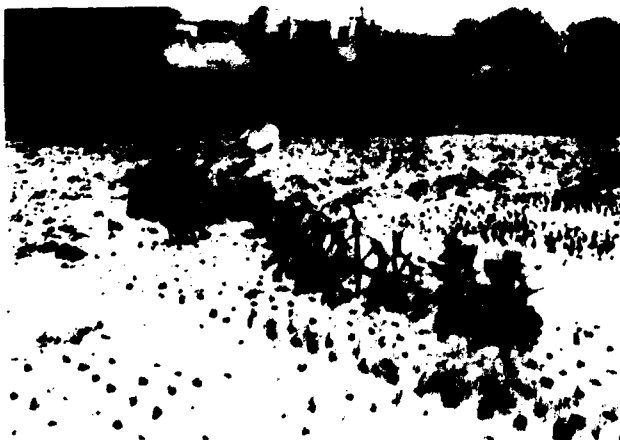


Figure 3

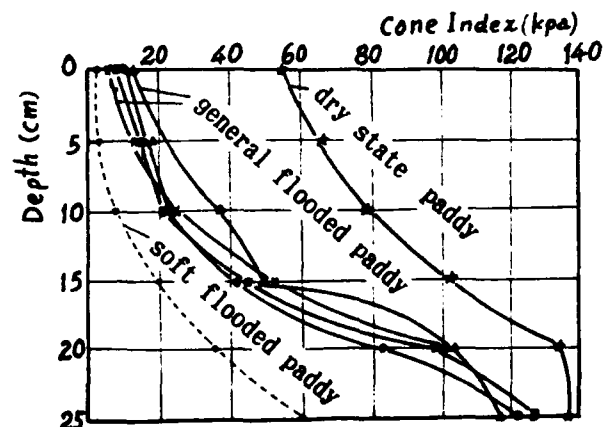


Figure 4

## EXPERIMENTAL RESULTS

### Effect of slip on measured forces

Figure 5 compares the curves of pull forces obtained at slips 10%, 15%, 20%, 35%, 50%, and 100%. Figure 6 compares the curves of lift forces obtained at above slips. It was observed that the pull and peak pull forces were increased with the slip much higher than lift and peak lift forces. The optimum slip in the experiment of model lug wheel was about 15% while the lug efficiency reached its maximum value. This was proved by the full size wheel test in soil bin and in paddy field farm. It should be noted that in this paper the definition of slip  $i$  is ratio of  $(R_o - R)$  over  $R_o$ , that is:

$$i = (V_o - V) / V_o = (R_o - R) / R_o \quad (1)$$

where  $V_o, R_o$  are the top velocity and top radius;  
 $V, R$  are velocity and rolling radius.

THE PULL FORCE AT VARIOUS SLIPS

(  $n=1$ , sinkage=60 )

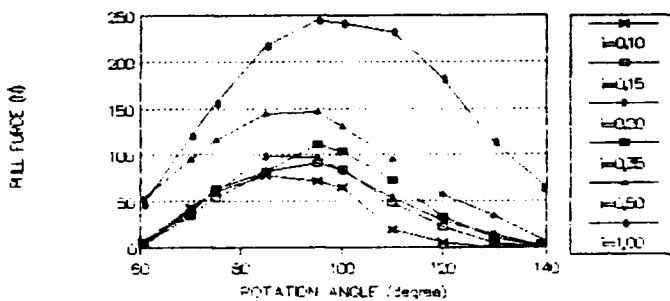


Figure 5

THE LIFT FORCES AT VARIOUS SLIPS

(  $n=1$ , sinkage=60 )

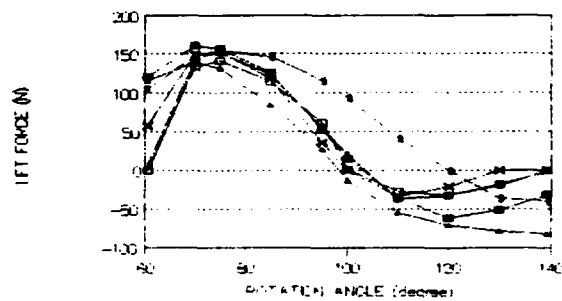


Figure 6

### Comparison of measured lug forces for curved lug and flat lug

Figure 7,8, shows the measured pull forces and lift forces of model wheel at 6cm sinkage, 15% slip and 37% moisture content paddy soil. The experiments were repeated three times and the average values were plotted by computer and printer. As shown in figure, the peak pull force of 25° curved lug is 35% larger than that of flat lug with 14.6° lug angle at 95% level of significance. Another measured peak pull force of 30° curved lug is 32.6% larger than that of flat lug with 12.6° lug angle. It is necessary to point out that the peak lift force of curved lug is 45-64.5% larger than that of flat lug, so that the distributed weight on powered wheel should be larger in proportion.

THE PULL FORCE OF CURVED AND FLAT LUG

(  $n=1$ , sinkage=60, slip=15% )

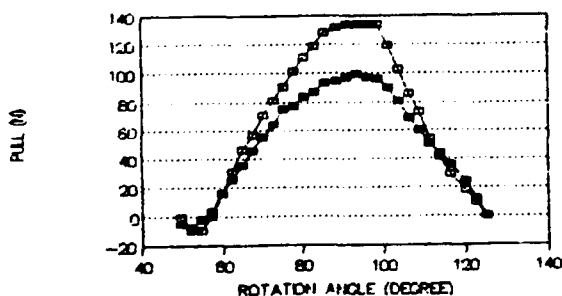


Figure 7

THE LIFT FORCE OF CURVED AND FLAT LUG

(  $n=1$ , sinkage=60, slip=15% )

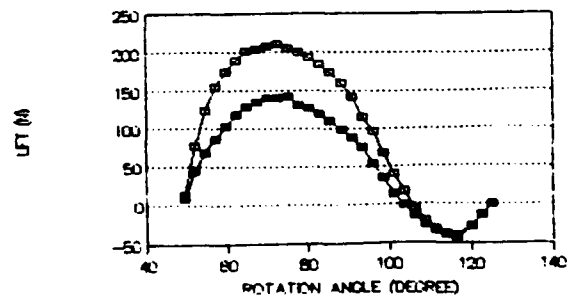
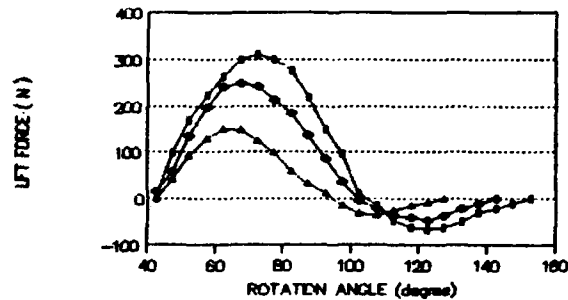


Figure 8

### EFFECT OF SINKAGE ON LIFT FORCES

( n=1, t=15% )



**Figure 10**

Figure 9.10 shows that the effect of lug sinkage on lug forces. Three lug sinkages (4cm, 6cm, 8cm) were compared in experiments. The lug slip and soil moisture content were kept constant at 15% and 37% respectively. The effect of sinkage on lug forces for curved lug and flat lug had similar results. It was observed that at 4cm, 6cm and 8cm sinkage the peak pull forces were 146N, 215N, 270N and the peak lift forces were 150N, 240N, 310N respectively. All lug forces were increased in proportion with sinkage in test range. It is evident that the lug sinkage in test range affects the lug force significantly at 95% level of significance on statistical analysis.

According to the conventional theoretical kinematic analysis on lug-soil interaction, when the lug tip was at its lowest point ( $\theta=90^\circ$ ), the zero lift force would be presented, and the instant point of vertically leaving of lug from soil should be at this instant point. Based on our study of soil flow and passive failure under lug wheel, it was observed that when the rotation angle of wheel was at 100-103 degree, the zero lift force was presented as shown in Figure 6 for slips from 10% to 35%, so we took the instant of first measured zero lift force as the instant point of vertically leaving of lug from soil.

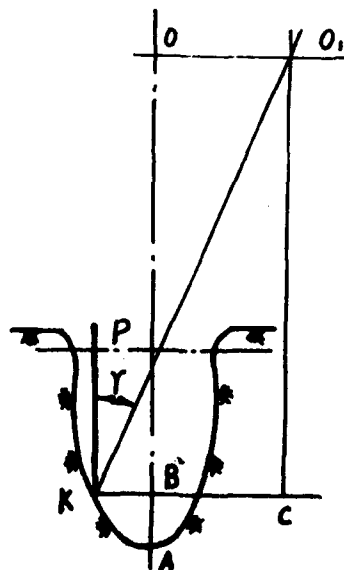


**Figure 12**

Figure 11 shows the geometrical relation to decide the lug angle using  $i$  as the instant point of lug leaving for flat lug. An expression to determine the appropriate lug angle is:

$$\begin{aligned} R_D &= R_o (1 - i) \cos \alpha = R_o \cos (\alpha + \gamma) \\ (1 - i) \cos \alpha &= \cos (\alpha + \gamma) \\ i &= 1 - \cos (\alpha + \gamma) / \cos \alpha \end{aligned} \quad (2)$$

where  $\alpha$  and  $\gamma$  are the pressure angle and lug angle in degree respectively.

If  $i = 0.15$ , and pressure angle takes 25 and 30 degree, the lug angle may be calculated as 14.6 and 12.6 degree respectively.

Another simple expression for lug angle with respect to slip was developed on another geometrical conception with sufficient accuracy as shown in Figure 12:

$$\cos \gamma = 1 - i^2 \quad (3)$$

#### *The appropriate lug number*

In order to determine the lug number on powered wheel, it is necessary to make use of maximum rupture length of soil failure zone beneath lug.

There are three principles to determine the appropriate lug number on powered wheel:

1. To ensure enough space and length between two adjacent lugs based on the maximum rupture length on soil failure experiments beneath single lug and multi-lug. During the special study on soil behaviour under single lug and multi-lug, photographic results clearly showed that the maximum rupture length was found at a lug position of 65-72 degree after entering into paddy soil. The sign of maximum rupture length was that the up heave of soil reached its maximum value in continuous photographs.

2. To ensure the maximum soil reaction forces obtained.

3. To ensure that there would be no soil packing between adjacent lugs and that a self cleaning of soil between lugs under lug-soil interaction.

The appropriate lug number of powered wheel depended on the geometrical parameters of wheel (top radius  $R_o$ , lug height  $h$ ), working condition (slip  $i$ , sinkage  $z$ ) and parameters of soil. The soil bin experiments and on farm paddyfield tests of powered wheel are needed to check the appropriate lug number of wheel. Figure 13 shows the geometrical relation of soil failure zone, maximum rupture length, loop width of locus for lug tip at optimum slip for the determination of appropriate lug number of powered wheel.

An expression was developed to determine appropriate lug number  $n$  as follows:

$$2R_o(1 - i)/n = L_{\max} \pm B \quad (4)$$

where  $L_{\max}$  is the maximum rupture length,

$B$  is the width of loop of lug tip at given slip.

As shown in Figure 13,  $L_{\max}$  may be calculated by conventional theory of passive soil failure theory at trustable agreement with measured values.

$$L_{\max} = 2 r_s \cos (45 - \phi/2) \quad (5)$$

$$\text{where } r_s = r_o \exp (\omega \tan \phi) \quad (6)$$

$$r_o = h / \sin \beta \quad (7)$$

$$\omega = \pi - (\pi/4 - \phi/2) - \beta \quad (8)$$

The width of loop could be calculated by the kinematics analysis of locus of lug tip by the following expression using the XY coordinate with origin at instant center of a slip wheel.

$$\begin{cases} x = R_o (1 - i) \theta - R_o \sin \theta \\ y = R_o (1 - i) - R_o \cos \theta \end{cases} \quad (9)$$

$$B = 2 R_o (1 - i) \theta y = 0 - 2 R_o \sin \theta y = 0 \quad (10)$$

Width of loop could be calculated using the following experience formula with enough accuracy at optimum slip 15%:

$$B = 0.1104 R_o \quad (11)$$

Substitute (5),(6),(7),(8) into (4) at optimum slip 15%, A general expression could be obtained:

$$n = \frac{2\pi R_o (1-i)}{\frac{2h}{\sin \beta} \cdot e^{(\frac{3}{4}\pi + \frac{\phi}{2} - \beta) \tan \phi} \cdot \cos(45 - \frac{\phi}{2}) \pm B} \quad (12)$$

To enter Formula (12) with  $P_o = 362.5 \text{ mm}$ ,  $h = 100 \text{ mm}$ ,  $\beta = 65^\circ - 72^\circ$ ,  $\phi = 12^\circ$ . We obtained the appropriate lug number of powered wheel for powered tiller  $n = 9 - 11$ .

#### The appropriate lug height

From formula (12) we know that the lug height decreased in proportion with increase of lug number. According to calculation, while  $h = 100 \text{ mm}$ ,  $n = 10 - 11$ , while  $h = 125 \text{ mm}$ ,  $n = 9 - 10$ . In general flooded paddy soil, 125mm lug height was sufficient to give about 1300N traction force at more than 50% tractive efficiency and good enough for single bottom plow work at 20mm width x 15mm depth.

We design the 125mm height flat lug for flooded paddy soil with hard pan layer and dry state paddy soil ( $n = 9$ ), and design the 150mm height involute curved profile lug for soft paddy soil without hard pan layer ( $n = 9$ ).

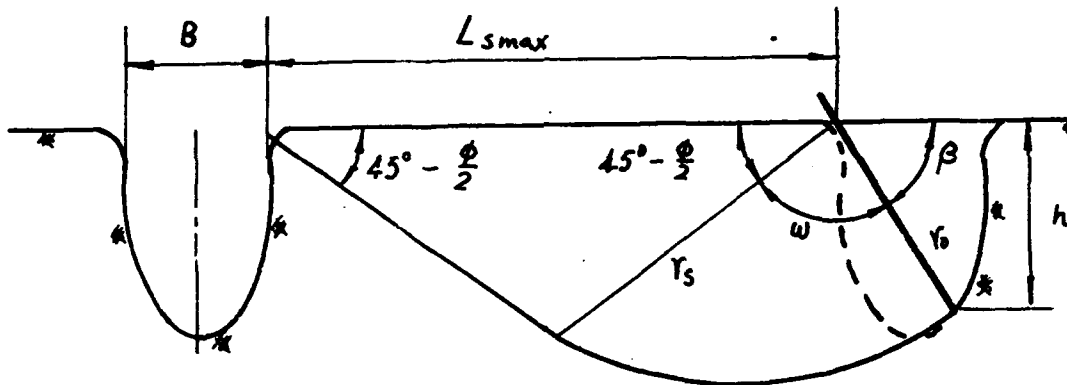


Figure 13

#### PERFORMANCE OF POWERED WHEEL ON PADDY SOIL BIN AND PADDY FIELD

We designed seven sets of lug wheels in which two sets with involute curved profile lug for deep and soft paddy field without hard pan and five sets with flat lugs. All these wheel were put into tests for performance on paddy soil bin and paddy field. Figure 14 shows the curves of traction force with respect to slip, velocity, traction power, fuel consumption, and unit power fuel consumption. As the traction force of powered tiller reached to a peak value at about 1700N to meet the need of traction forces for plough work and a traction force about 1300N at a tractive efficiency of more than 50% and slip 15% in general flooded paddy soil with hard pan. This results seemed to be satisfied as better performance in paddy field.

#### CONCLUSION

1. This paper introduces the research to design the lug with appropriate geometrical parameters such as lug angle, lug profile, lug height and lug number for powered wheel of powered tiller based on our recent experiments on soil behaviour, soil reaction forces

measurements and performance tests in soil bin and paddy field.

2. Based on the effect of slip on lug forces in experiments and the performance tests, the optimum slip 15% is recommended in designing the geometrical parameters of lug.

3. Based on the experiments of soil flow and soil reaction forces beneath single lug, we found the instant point K for vertical leaving of lug at  $100-103^\circ$  but not  $90^\circ$  when zero lift force was presented. This paper developed a methods in using the instant point K to determine the lug angle of flat lug and involute profile curved lug.

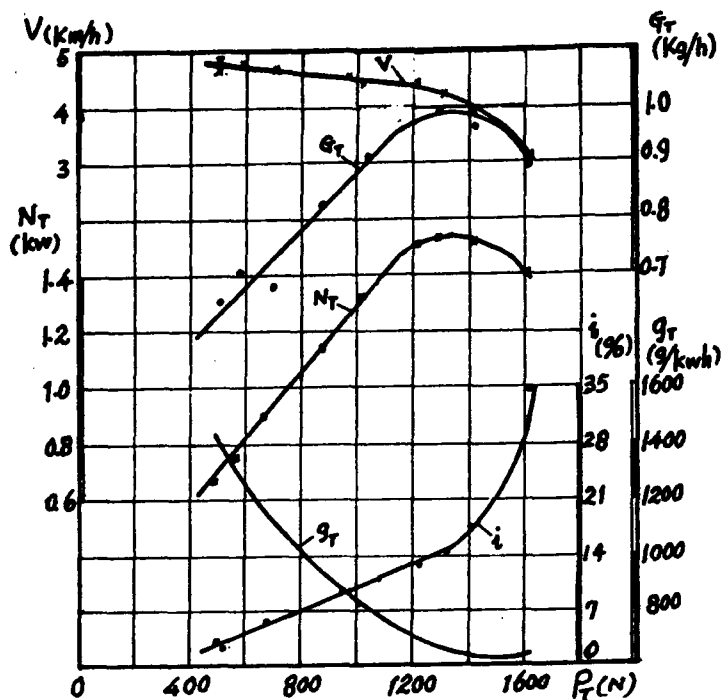


Figure 14

4. The pull and lift force of the involute curved lug KG ( $25^\circ$  or  $30^\circ$  pressure angle) are 35% and 32% significantly higher than those of the flat lug KF.

5. Based on the maximum rupture length of passive soil failure beneath single lug and multi-lug, this paper developed a general expression to determine the appropriate lug number and lug length for powered wheel.

6. The field tests on the performance of powered wheel with the appropriate lug parameters gave satisfactory tractive efficiency and farm work.

#### REFERENCES

1. Y.J. Shao, Advanced analysis on the design of geometrical parameters of the blade for the paddyfield wheel tractor, Proc. 7th Int. Conf. ISTVS, Calgary Canada, pp1509-1552 (1981)
2. T.L Zhang and Y.J. Shao, The analysis of the dynamic performance of a single lug, Proc. 8th Int. Conf. ISTVS, Cambridge UK, pp507-519 (1984)
3. H.Z. Lu and Y.J. Shao, Experimental research on the soil reaction beneath lugs of powered wheel, Proc. 9th Int. Conf. ISTVS, Barcelona, Spain (1987)
4. Y.J. Shao and J.Y. Wong, Experimental research on soil flow beneath lugs of powered wheel, Proc. Int. Conf. 1st Asian Pacific ISTVS, Beijing PR China, (1986)
5. X.W. Luo and Y.J. Shao, The study on the interference of lugs on the paddy wheel, Proc. 2nd Conf. CSAE (1983)
6. H.Z. Lu, Phd dissertation thesis of lug soil interaction (1991)
7. D. Gee-Clough and W.J. Chancellor, Pull and lift characteristics of single lug on rigid wheels in wet rice soil, Trans. ASAE 19 (3) 433-441, 447 (1976)
8. D. Gee-Clough etc, Recent research into vehical performance in wetland conditions, Proc. 7th Int. Conf. ISTVS, Calgary Canada, pp295-237, (1981)
9. V.M. Salokhe and D. Gee-Clough, Formation of a boundary wedge on a single lug in wet clay soil, Journal of Agr. Engng. Res., 37(4), pp255-266, (1987)
10. V.M. Salokhe, S. Mansoor, and D. Gee-Clough, Pull and lift forces acting on single cage wheel lugs, Journal of Terramechanics, Vol. 27, No. 1 pp. 25-39, (1990)
11. X.W. Luo and Y.J. Shao, Studies on geometrical parameters of powered wheel for powered tiller, Proc. 7th Chinese STMS, Xian, China, (1990)



# NUMERICAL PREDICTION OF SOIL BEHAVIOR UNDER A RIGID WHEEL

A. Jarzębowski\* , Y. Nohse\*\* , K. Uchiyama\*\* , K. Hashiguchi\*\*\* ,  
M. Ueno\*\*\*\* , M. Kamei\*\*\*\*\* , F. Koyama\*\*

## Abstract

A new finite element method program was developed to enable the precise prediction of stress and strain distribution beneath a rolling wheel as well as the mechanical properties concerned with the tractive performance of off-road vehicles, e.g., drawbar pull, axle torque, slip and sinkage. In order to describe the elasto-plastic deformation of soil, the extended Subloading Surface Model was introduced into the program. Some new algorithms using the Corrected Euler Method and the Conjugate Gradient Method were formulated to improve the accuracy of predictive quantities. Some results for the stress and the strain distribution in the soil beneath the wheel and the tractive performance of the wheel are compared subsequently with the ones from laboratory model tests.

## INTRODUCTION

An elucidation of the deformation of soils under a rolling wheel is required to improve the tractive performance of off-road vehicles and also a soil compaction performance of road construction machinery, whereas the soil compaction beneath wheels of farm vehicles causes a damage of soil structures which influences the growth of plant roots. This study aims at developing an effective numerical solution which is capable of describing the behavior of the soil, i.e., the stress and the strain distribution beneath the rigid rolling wheel and its tractive performance.

As the numerical solutions to predict the soil deformation behavior, several finite element method programs have been developed. Such programs have not been satisfactorily accurate as yet. First of all, most of constitutive equations incorporated in the programs have been inadequate and able to predict only the simplest phenomena of soils [1] or the monotonic loading [2]. Although more advanced constitutive equations for soil under monotonic and cyclic loadings were developed [3,4], they have been hardly applied to the finite element analysis of the soil deformation under the wheel. Recently, an attempt at using the initial Subloading Surface Model was presented [5]. A more accurate prediction of some engineering problems by incorporating the extended Subloading Surface Model for sand [4] is one of the purposes of the present study.

A proper description of the boundary condition is also a difficult problem, and even the most advanced studies for the numerical solution treat the boundary friction problems with a great simplification, though it has a direct influence on the accuracy of calculations [6,7]. In

\*Polish Academy of Sciences, Warsaw, Poland, presently visiting researcher  
at Tech. Laboratory, Sakai Heavy Industries, Japan

\*\*Tech. Laboratory, Sakai Heavy Industries, Kurihashi, Saitama, 349-11, Japan

\*\*\*Dept. Agr. Eng., Kyushu Univ., Hakosaki, Higashi-ku, Fukuoka, 812, Japan

\*\*\*\*Dept. Agr. Eng., Ryukyu Univ., Nishihara, Okinawa, 903-01, Japan

\*\*\*\*\*Kyushu Agr. Exp. Sta., Izumi, Chikugo, Fukuoka, 833, Japan

the present paper considerable attention was paid to the modelling of the friction boundary conditions between the rigid wheel and the soil.

The numerical calculations were conducted under the plane strain condition and their results were compared with the experimental ones from the laboratory model tests realized under the same condition.

Although a number of studies investigating soil deformation by markers in soils [8,9] or the simultaneous measurement of stresses in soils have been reported [10], the precise measurement of the stress distribution have not been accomplished yet. Thus, the measurement and the analyzing systems for stress and strain beneath the wheel were developed [11, 12] and used in the present study.

### FINITE ELEMENT ANALYSIS

Based on the displacement method of the FEM [13], the computer program was formulated and developed under the plain strain condition. The 4-noded finite elements with a 4-point integration rule [14] were adopted. The finite element mesh and the boundary conditions assumed for the walls and the bottom of the soil bin are shown in Fig.1.

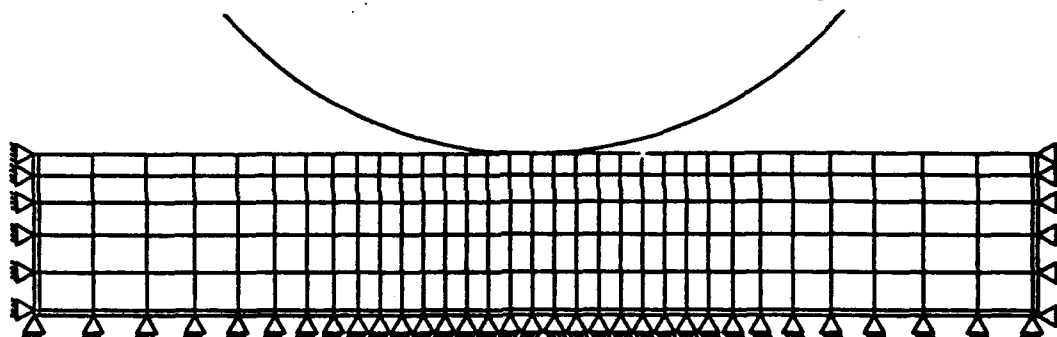


Fig.1. Finite element mesh and boundary conditions.

The mechanical property of soil was assumed to be an elasto-plastic one described by the extended Subloading Surface Model [4]. Since the constitutive equation has an incremental form, the incremental method was applied in the FEM program. When the sinkage stage of the wheel was executed, increments of vertical displacement were given to the centre of the wheel. Further, in the rolling stage the increments of rolling angle and of horizontal displacement were given to the wheel to realize a desired slip, while the increments of vertical displacement were additionally given to keep the contact load between the wheel and soil within the range of  $\pm 0.2\%$  of the assigned value.

The total stiffness matrix for the whole task was actualized after each step. Within each incremental step the so-called initial value problem [15] was solved using the Corrected Euler Method to improve the accuracy of calculated results. As the stress state components and their increments have to be calculated after each step, all components of the constitutive stiffness matrix for each integration point also have to be known. Thus, the Corrected Euler Method was realized according to the proposed formulae

$$[D]^{i+1} = ([D]_{Pre}^i + [D]_{Cor}^{i+1})/2 \quad (1)$$

$$[B]^{i+1} = ([B]_{Pre}^i + [B]_{Cor}^{i+1})/2 \quad (2)$$

$$[K]^{i+1} = \int [B]^{i+1T} [D]^{i+1} [B]^{i+1} dV \quad (3)$$

where  $[D]^{i+1}$  and  $[B]^{i+1}$  are the constitutive stiffness and the shape function matrix in every integration point at the actual step number  $i + 1$ ,  $[D]_{P,r}^i$  and  $[B]_{P,r}^i$  denote their values computed in the predictive part according to the stress and the strain state after the step number  $i$ , while  $[D]_{C,r}^{i+1}$  and  $[B]_{C,r}^{i+1}$  denote their values used in the corrective part of the actual step according to the stress and the strain state after the predictive part of the step number  $i + 1$ , and  $[K]^{i+1}$  is the total stiffness matrix in the actual step number  $i + 1$ . The total stiffness equation

$$\Delta f = [K]^{i+1} \Delta u \quad (4)$$

was solved by C.G.M. [15], where  $\Delta f$  and  $\Delta u$  denote the increment vectors of load and displacement, respectively, of the finite element system. At the initial stage of the calculation process, the stresses caused by the weight of the upper layers were superposed on every integration point.

The Coulomb friction law was applied to the interface nodes between the wheel and the soil after the incremental displacement was given. Whenever the friction law was violated at any node, the calculations were repeated until that law was satisfied in all nodes on the wheel surface.

In the sinkage and the rolling stage some nodal points newly came into contact with the wheel surface, and furthermore some nodal points separated from the wheel surface in its rear in the rolling stage. To detect new contact points the geometrical condition was applied, while to detect separating points from the wheel surface, the normal component of the nodal contact force was considered in addition to that condition. Thus, the whole number of contact points was not always kept constant during the calculation.

## RESULTS AND COMPARISON WITH EXPERIMENTS

Calculations were carried out for the rigid wheel of 300 mm diameter  $\times$  410 mm width and weight 215.6 N on the Toyoura sand (mean density 1578.0 kg/m<sup>3</sup>, internal friction angle 38 degrees). The friction coefficient between the wheel and the sand was 0.63. All dimensions listed above were specified from the conditions of experiment. The apparatus and the testing procedure were described in detail elsewhere [8], together with the initial laboratory test results [8,12]. The size of the finite mesh was 60 mm height  $\times$  370 mm width.

The relation between the contact load and the sinkage (the displacement of the centre of the wheel) during the sinkage stage is presented in Fig.2. As the number of nodes contacting with the wheel gradually increased during the calculations, the resultant relation is not smooth.

Calculations at various slips 5, 15 and 41% were performed in the rolling stage after the sinkage one. Results in the initial part of the rolling stage at various slips are presented in Fig.3, where the predicted values of sinkage and drawbar pull are compared. The significant influence of slip on the above-mentioned quantities in the initial stage of rolling is observed clearly, which coincides with the experimental one (cf. [8]).

The calculated displacement field and the stress and the strain distribution in the soil after the sinkage stage are shown in Figs.4 and 5. The corresponding strain distribution obtained from the laboratory test is presented in Fig.6. In these figures, to enable a direct comparison between theoretical and experimental results, the same isolines are drawn and the calculated displacements are magnified 16 times (cf. Fig.4.a). In the upper layer between 0 and 5 mm depth the strain field distribution were not available experimentally since it was technically difficult to put polyester film markers [8] in the soil close to the free surface. Both theoretical and experimental results (Fig.5 and 6, respectively) show similar zones, although it is sometimes difficult to detect their boundaries, especially in case of test results.

Because of the lack of space for the detailed comparison herein, only some theoretical and experimental results in the initial stage of rolling at 41% slip are presented in Fig.7 and 8, respectively. The predicted boundaries of the stress and the strain isolines tended to develop nonsymmetrically (cf. corresponding Figs.4.b, 5.c and Figs.7.a, b). In case of experimental data the same tendency was also observed (cf. Fig.6.c. and Fig.8). At the high slip value the zone of the compressive horizontal stress tended to move backwards the travelling direction.

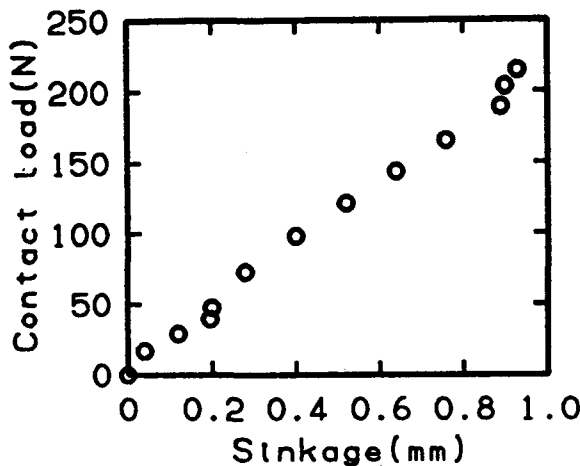


Fig.2. Contact load change during the sinkage stage.

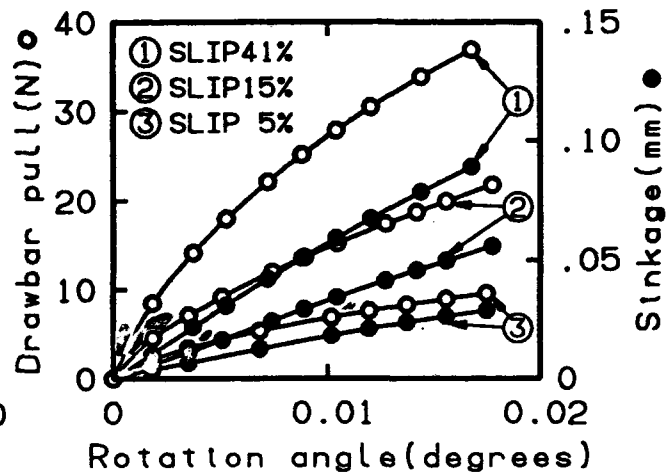


Fig.3. Drawbar pull and sinkage during the initial part of the rolling stage.

### CONCLUDING REMARKS

The theoretically predicted results coincide qualitatively and quantitatively with the experimental ones, although differences between some values are observed. For the more precise comparison additional laboratory tests under the same test conditions should be performed to investigate the repeatability of experimental data. The theoretical results presented above are those in the initial stage. Comparisons for the more advanced rolling stage and for various travelling conditions, i.e., slip, weight of wheel, friction coefficient between a wheel and soil and mean density of soil will be presented in the further study.

### REFERENCES

1. Nakashima, H., Tanaka, T. and Yamazaki, M., Finite element analysis of soil-lug interactions, *Proc. 10th Int. Conf. ISTVS, Kobe (Japan), 1990*, pp.277-288.
2. Kitano, M. and Tokita, M., Study on interaction between rigid wheel and soil, *Proc. 5th Japan. Conf. Terrain-Vehicle Systems, 1985*, pp.48-64 (in Japanese).
3. Jarzabowski, A. and Mróz, Z., A constitutive model for sands and its application to monotonic and cycling loadings, *Constitutive Relations for Granular Non-Cohesive Soils*, (Saada & Bianchini eds.), Balkema, Rotterdam, 1988, pp.307-323.

4. Hashiguchi, K., Subloading surface model in unconventional plasticity, *Int. J. Solids Structures*, 1989, Vol.25, No.8, pp.917-945.
5. Ueno, M., Hashiguchi, K., Nohse, Y., Koyama, F., Uchiyama, K. and Izumi, H., Analysis of soil-wheel interaction by elastoplastic finite element method, *Proc. 10th Int. Conf. ISTVS*, Kobe (Japan), 1990, pp.253-264.
6. Chung, T.J. and Lee, J.K., Dynamics of viscoelastoplastic soil under a moving wheel, *J. Terramechanics*, 1975, Vol.12, No.1, pp.15-31.
7. Yong, R.N., Fattah, E.A. and Boonsisuk, P., Analysis and prediction of tyre-soil interaction and performance using finite elements, *J. Terramechanics*, 1978, Vol.15, No.1, pp.43-63.
8. Nohse, Y., Shikanai, T., Hashiguchi, K., Ueno, M., Izumi, H. and Koyama, F., A measurement of basic mechanical quantities of off-the-road traveling performance, *Proc. 10th Int. Conf. ISTVS*, Kobe (Japan), 1990, pp.545-556.
9. Wong, J.Y., Behaviour of Soil Beneath Rigid Wheels, *J. Agric. Engng. Res.*, 1967, Vol.12, No.4, pp.257-269.
10. Burt, E.C., Bailey, A.C. and Wood, R.K., Tire dynamic load effects on soil-tire interface and soil profile stress, *Proc. 10th Int. Conf. ISTVS*, Kobe (Japan), 1990, pp.159-170.
11. Ueno, M., Hashiguchi, K., Nohse, Y., Kokubu, T., Uchiyama, K. and Shikanai, T., Deformation and Strain Analysis of Soil under the Wheel, *Proc. 10th Int. Conf. ISTVS*, Kobe (Japan), 1990, pp.253-264.
12. Ueno, M., Izumi, H., Kokubu, T., Hashiguchi, K. and Nohse, Y., Analyzing system of stress, strain and deformation of the soil under the rolling wheel, *Proc. 11th Japan Conf. Terrain-Vehicle Systems*, 1990 (in Japanese).
13. Zienkiewicz, O.C., Introductory Lectures on the Finite Element Method, *Int. Centre for Mechanical Sciences, Courses and Lectures*, No.130, Springer-Verlag.
14. Bathe, K.J. and Wilson, E.L., Numerical Methods in Finite Elements Analysis, Prentice-Hall Inc., 1976.
15. Beckett, R. and Hurt, J., Numerical Calculations and Algorithms, Mc Graw-Hill Book Comp.
16. Ye, Q., Bell and D.J., A conjugate gradient algorithm applied to plane stress-strain problems, *Comp. Meth. Appl. Mech. Eng.*, 1983, Vol.40, pp.127-136.

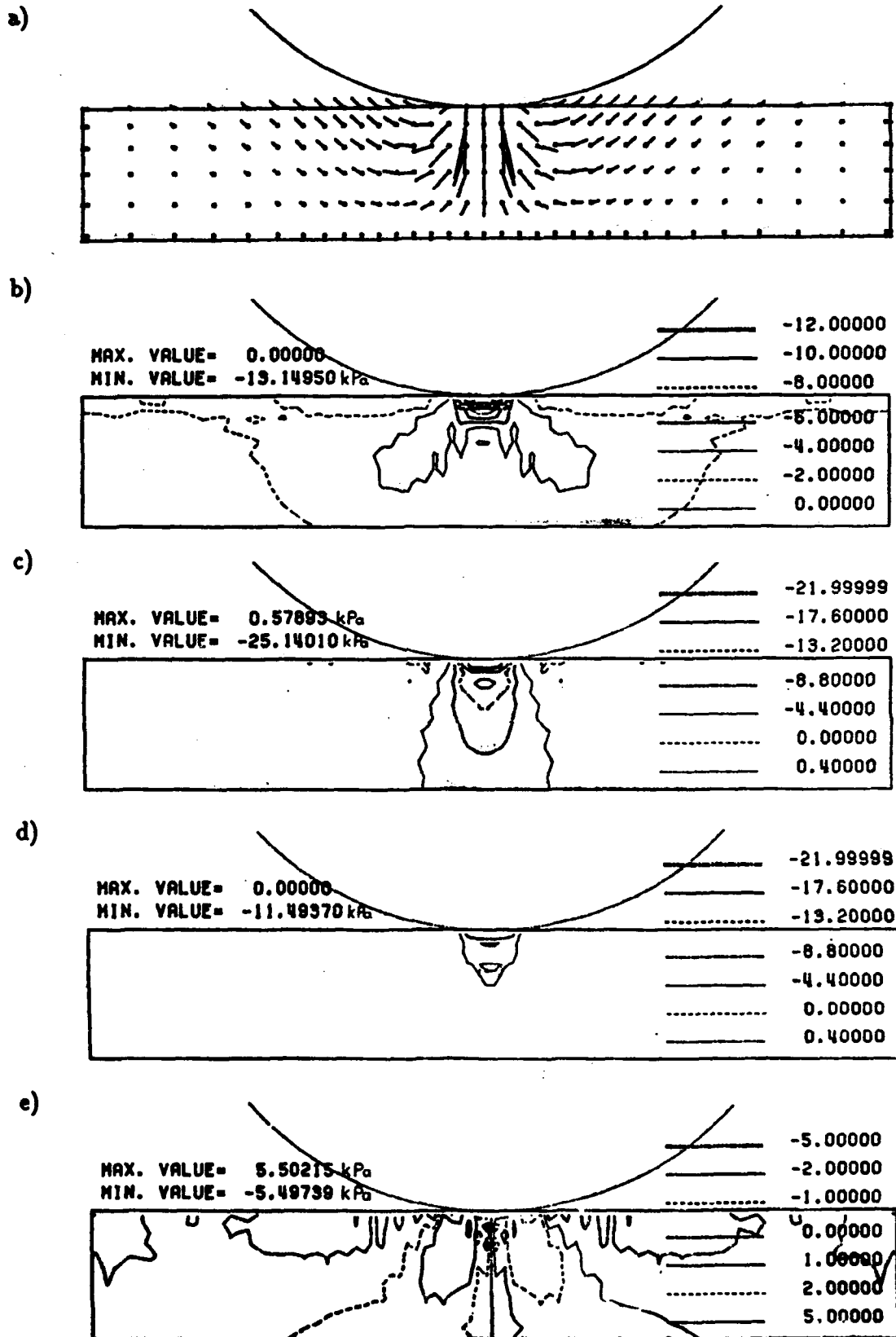


Fig.4. Theoretical results after the sinkage stage: a) displacement field, stress distribution : b) horizontal -  $\sigma_x$ , c) vertical -  $\sigma_y$ , d) lateral -  $\sigma_z$ , e) shear -  $\tau_{xy}$ .

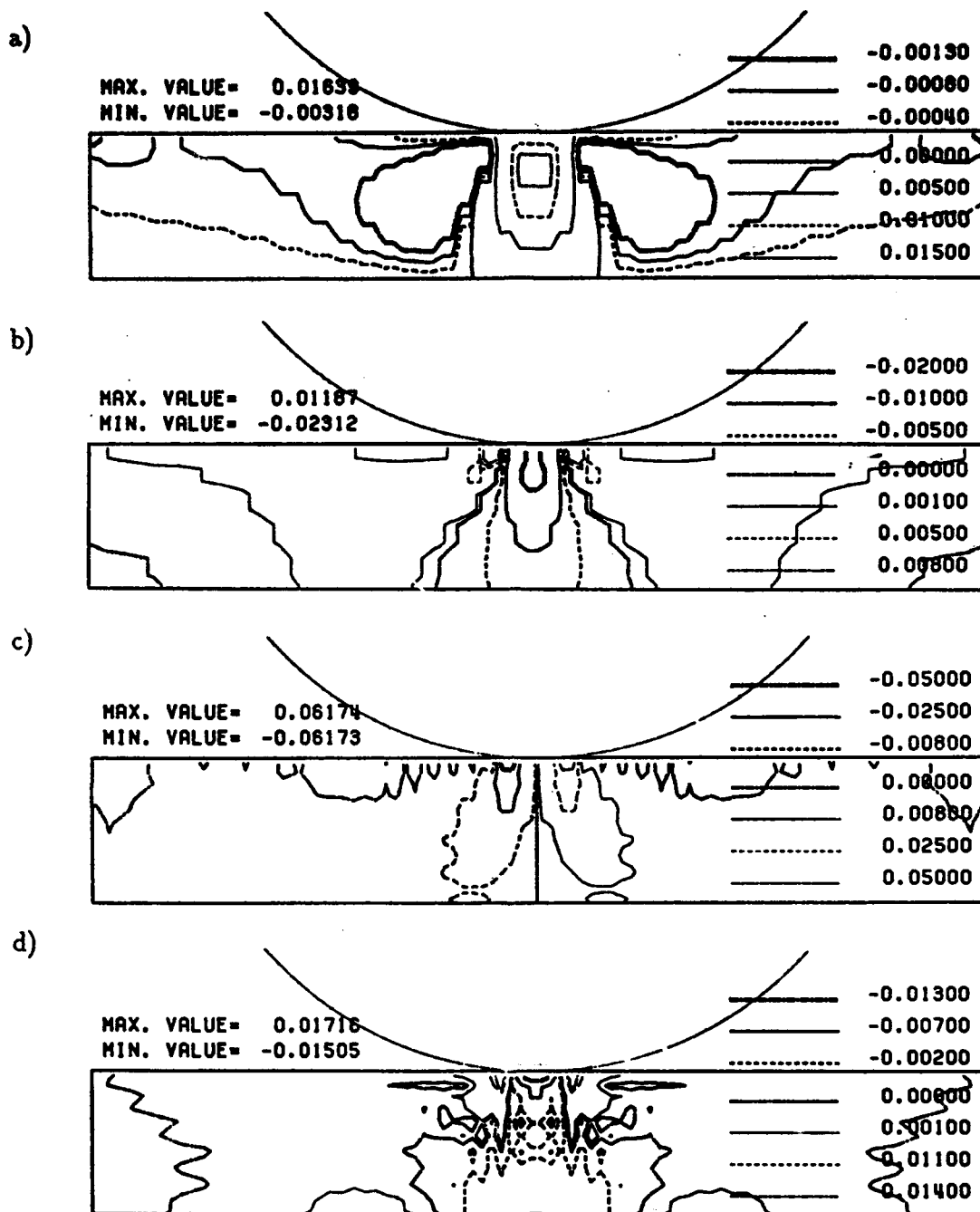


Fig.5. Theoretical results of strain distribution after the sinkage stage: a) horizontal -  $\epsilon_x$ , b) vertical -  $\epsilon_y$ , c) shear -  $\gamma_{xy}$ , d) volumetric -  $\epsilon_v$ .

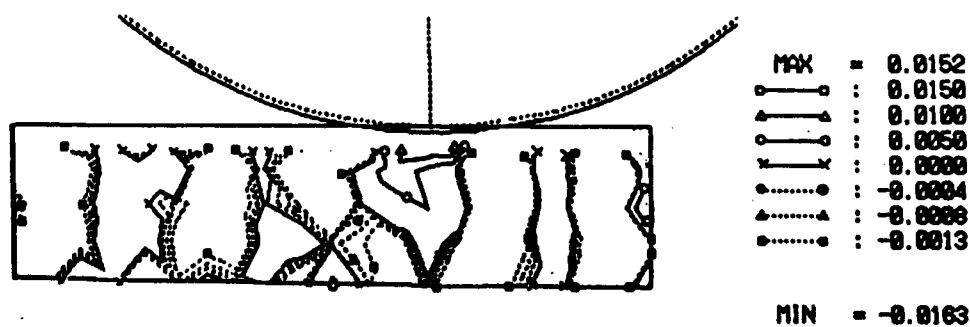


Fig.6. Experimental results of strain distribution after the sinkage stage: a) horizontal -  $\epsilon_x$ .

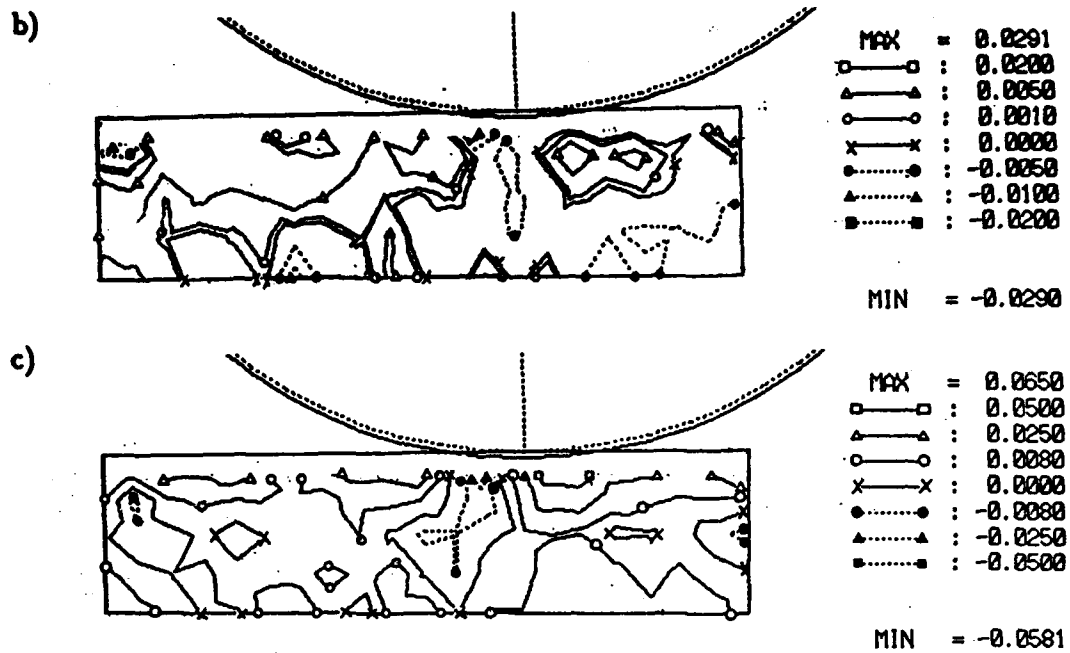


Fig.6. Experimental results of strain distribution after the sinkage stage: b) vertical -  $\epsilon_y$ , c) shear -  $\gamma_{xy}$ .

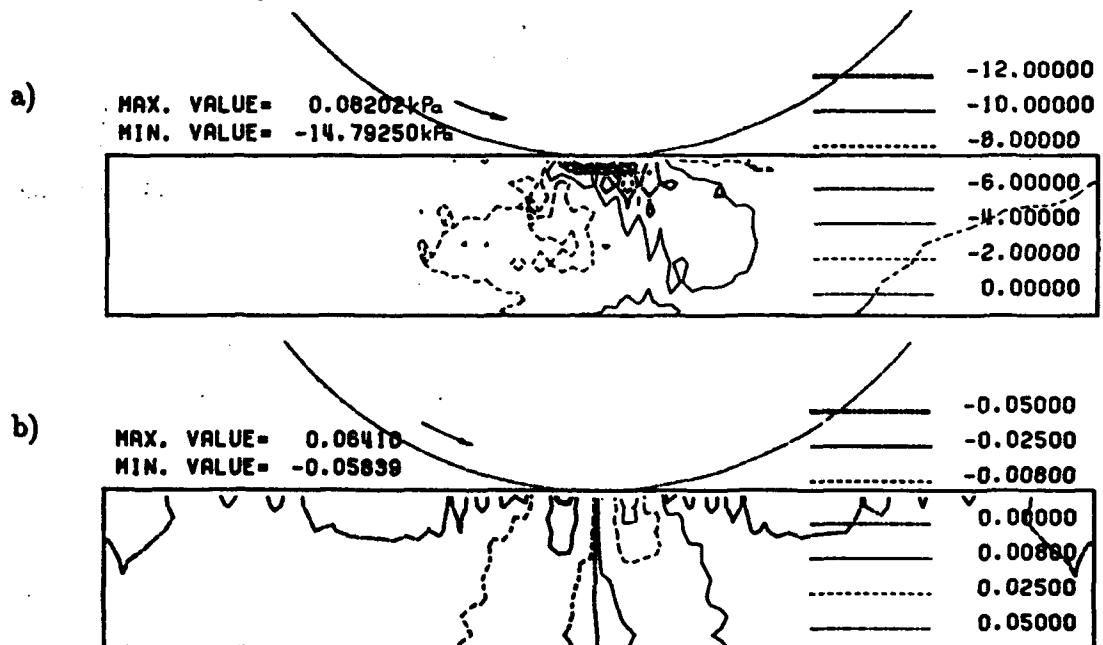


Fig.7. Theoretical results during the rolling stage: a) horizontal stress  $\sigma_x$  distribution, b) shear strain  $\gamma_{xy}$  distribution.

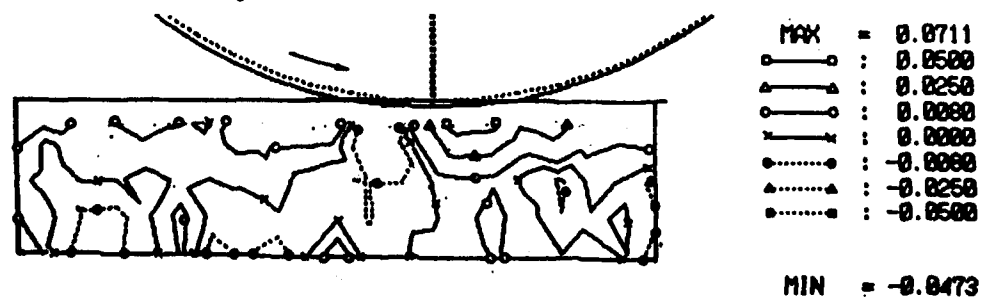


Fig.8. Experimental results of shear strain  $\gamma_{xy}$  distribution during the rolling stage.



## CALCULATION OF SOIL COMPACTION BY THE VEHICLE'S ACTION

Dr.A.V.Miroshnichenko

Mathematical model of soil deformation was worked out, which allows to describe the soil-vehicle interaction process and to estimate parameters of this process. It also allows to estimate the soil compaction, caused by the vehicle's action. With the help of this model the process of the plate penetration was studied and the deformation performance was established.

At the present time a special emphasis is being placed on the study of the vehicle's action on the soil with the view to investigating into the distruction of the top layer and compaction of soil. This is important for solving ecological problems and agricultural ones, where the land cultivation and good crop capacity are of concern.

To evaluate the vehicle's action both experimental methods of actual measuring of the soil density before and after passage of the vehicle, working under the field conditions, and laboratory measurements made in the soil bin where the action is simulated by using plates or a single wheel, were used.

In the present work a problem is posed to work out a method of calculation enabling investigation into the influence of the system's basic parameters, i.e. the vehicle-soil, on the compaction of soil, an attempt being made to give a close consideration to the mechanism of soil distruction.

Let's dwell upon the simplest task of interaction: penetrating of the flat plate into soil. This problem is traditional for terramechanics and is convinient for checking up adequacy of models designed.

Also, it should be pointed out that this problem is actual for the development of walking vehicles too; their application for the work on the soil is being studied.

Let a flat rectangular plate with dimensions of sides  $a$  and  $b$  penetrate into soil at a velocity  $U_p(t)$ . Then the consumption of soil  $Q_s$  for its penetration, displaced by the plate, equals:

$$Q_s(t) = S U_p(t) \quad (1)$$

where  $S = ab$  is the plate's area,  $t$  is the time.

Then, in penetrating of the plate by a quantity  $z_p$

$$z_p(t) = \int_0^t U_p(t) dt \quad (2)$$

the volume of the soil displaced  $V_s$  equals

$$V_s(t) = S z_p(t). \quad (3)$$

In this case two marginal variants of the soil behaviour are possible.

A first variant. Penetration of the plate goes along with displacement of soil in the lateral directions and density  $\rho$  is practically initial  $\rho \approx \rho_0$  throughout the whole process of deformation. This destruction occurs according to the general shear failure scheme.

A second variant. Here the deformation process takes place only at the expense of the variation in the density  $\rho$  and no soil displacement in the lateral directions occurs. This is the deformation according to the local shear failure scheme. We'll touch upon this case because it is for these soils that the compaction problem is really actual.

Shown in Fig.1 is an initial condition of the soil layer  $dx$ , with the coordinate  $x$  of the soil layer and time  $t$  being independent variables. In penetrating the plate by a quantity  $z_p$ , the soil layer is displaced by a quantity  $u(x, t)$  but then it will have a different thickness  $dx + du$ . Besides, if at the initial point the soil density equaled the quantity  $\rho_0$ , then by

the time  $t$ , the density equals  $\rho(t)$ . Assuming that no displacement of the soil in lateral directions occurs one can write down

$$\rho_0 dx = \rho(\partial x + \partial u) = \rho(1 + \partial u / \partial x) dx$$

or

$$\rho_0 = \rho(1 + \partial u / \partial x). \quad (4)$$

Now consider balance of the soil layer by using a second Newton's law (the product of soil mass by acceleration equals acting forces):

$$\rho_0 \partial x \frac{\partial^2 u}{\partial t^2} = -\partial q + \tau(x, t) \frac{2(\alpha + \beta)}{S} (\partial x + \partial u) \quad (5)$$

$\tau(x, t)$  are reactions occurring on the lateral surface of the soil layer.

If we are to assume that displacement of the soil layer occurs slowly and an inertia component of resistance to the deformation of soil is low, then an equation (5) takes the form:

$$\partial q = \frac{\pi}{S} (\partial x + \partial u) \tau; \quad \pi = 2(\alpha + \beta), \quad (6)$$

or

$$\frac{\partial q}{\partial x} = \tau \frac{\pi}{S} (1 + \frac{\partial u}{\partial x}). \quad (7)$$

Thus, we have obtained an equation (7) that shows that a drop in pressure  $q$  in the soil is completely determined by the friction of the displaceable soil column relatively to the whole soil mass.

In this connection, one can consider several presentations of tangential reactions  $\tau$ .

The simplest case is where a quantity  $\tau$  does not depend on the quantity of soil layer displacement and

$$\tau = \theta \varphi(q) + c \quad (8)$$

where  $\varphi(q)$  is lateral pressure i.e. a function of pressure on this soil layer;  $\theta$  is a tangence of the angle of internal friction,  $c$  is cohesion of soil.

A series of experimental studies have shown that in the range of pressures, real for transport vehicles, lateral pressure  $q_s$

can be presented by a linear function

$$q_s = \varphi(q) = \bar{\tau}_0 + \bar{\tau} q. \quad (9)$$

Then (7) takes the form

$$\frac{\partial q}{\partial x} = [\theta(\bar{\tau}_0 + \bar{\tau} q) + c] \frac{\pi}{S} \left(1 + \frac{\partial u}{\partial x}\right) \quad (10)$$

or

$$\int \frac{dq}{\theta \bar{\tau} q + \theta \bar{\tau}_0 + c} = \frac{\pi}{S} \int \left(1 + \frac{\partial u}{\partial x}\right) dx. \quad (11)$$

Having integrated the left term of the equation one obtains:

$$\frac{1}{\theta \bar{\tau}} \ln |\theta \bar{\tau} q + \theta \bar{\tau}_0 + c| = \frac{\pi}{S} \int \frac{\rho_0(x)}{\rho(x, t)} dx + C. \quad (12)$$

By holding the functions  $\rho_0(x)$  and  $\rho(x)$  we determine a function of  $q(x)$  from the soil depth or by holding the function  $q(x)$ , we determine the function  $\rho(x)$ .

If the function  $q = f(\rho, \rho_0)$  is given

$$q = q(\rho, \rho_0) \quad (13)$$

say from the testing results, on the given soil, one can determine, from equation (10), the distribution of density  $\rho(x)$  from the soil depth

$$\int \frac{\rho q' d\rho}{\rho_0 \{ \theta [\bar{\tau}_0 + \bar{\tau} q(\rho, \rho_0)] + c \}} = \frac{\pi}{S} \int dx. \quad (14)$$

It should be noted that the advantage of the dependence obtained (13) lies in the possibility of giving  $\rho_0(x)$ , that is in giving the initial distribution of density from the soil depth.

If the dependence of tangential reactions  $\tau$  has the form of Janosi - Hamamoto

$$\tau = [\theta \psi(q) + c] \left[ 1 - \exp\left(-\frac{u}{K_\tau}\right) \right] \quad (15)$$

then we write down the (6) as having the form:

$$\frac{\partial q}{\partial u} \frac{\partial u}{\partial x} = \tau \frac{\pi}{S} \left( 1 + \frac{\partial u}{\partial x} \right) \quad (16)$$

or

$$\int \frac{(\rho_0 - \rho) dq}{\rho_0 [\theta \psi(q) + c]} = \frac{\pi}{S} \int \left[ 1 - \exp\left(-\frac{u}{K_\tau}\right) \right] du \quad (17)$$

The dependence (17) enables us to determine the variation in the soil density  $\rho(x)$ , allowing for (13), depending on the quantity of displacement  $u$  and on the depth of the penetration of the deforming plate  $z_p = u (x = 0)$ .

Therefore, we have an opportunity to obtain a deformation characteristic  $q = q(z_p)$  allowing for the soil parameters  $c$ ,  $\theta$ ,  $K_\tau$  and to make an analysis of their influence on compactibility and on the distribution function  $\rho(x)$  over the soil depth.

Besides one can determine the magnitude of the soil layer in which compaction has occurred, induced by the action of a technical system, as well as relate the parameters of the action (kinematics, geometry and pressure on the interaction interface) with the density distribution in the soil.

The presented model of interaction enables treatment of a set of processes occurring in the vehicles' action on the soil.

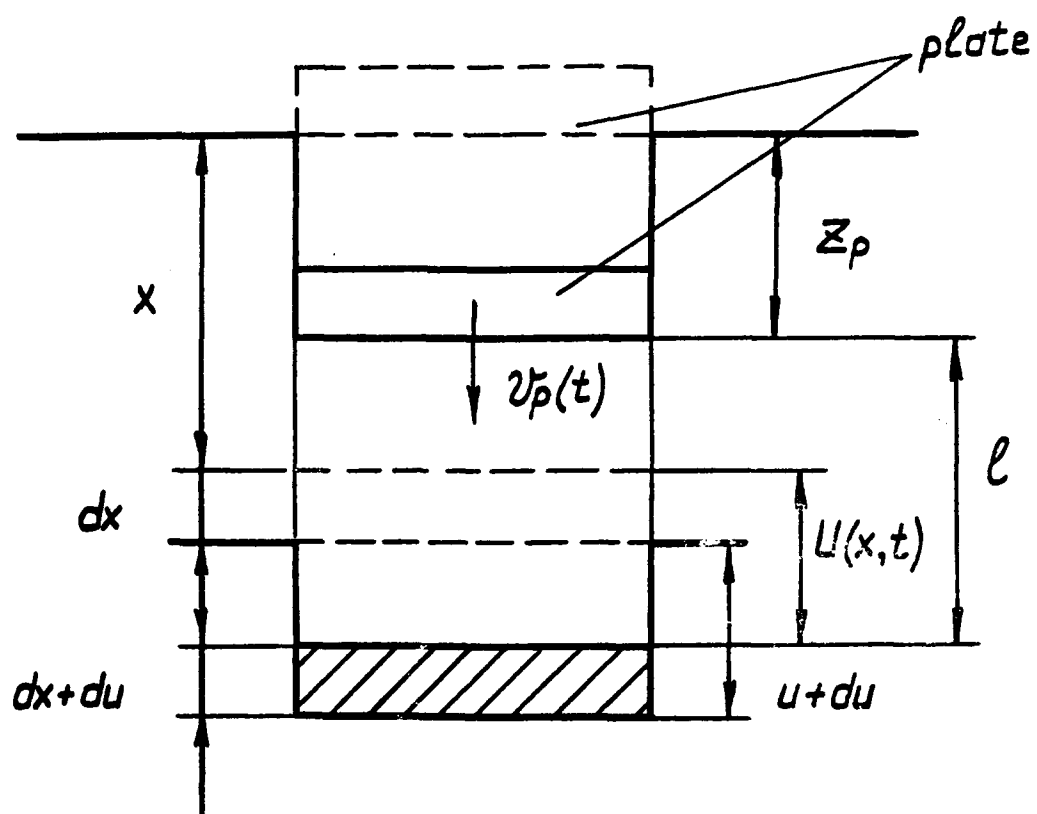


Fig. 1

## A MODEL OF VEHICLE - SOIL INTERACTION

Dr.A.V.Miroshnichenko, dr.V.V.Gromov, V.P.Grushin, V.N.Mehanuk

The process of vehicle-soil interaction was studied taking into account the influence of tangential reactions on the bearing capacity of soil. Mathematical model of the process was worked out and we made comparisons between experimental and calculated performances of multiwheeled vehicle.

The fundamental problem in the study of vehicle mobility is the development of methods to predict drawbar pull capacities and energy losses on vehicle motion.

Consider the interaction of a multiwheeled vehicle with a non-cohesive soil. We assume that the vehicle moves linearly over deformable soil at a constant velocity and the soil breaks down according to the general shear failure scheme (Fig.1).

In accordance with this scheme, soil failure precludes rigorous, one-to-one correspondence between the kinematics of the soil particles and that of the wheel's rim while a the vehicle's action on the soil specific weight  $\gamma$  and on the internal friction angle of soil  $\theta$  is insignificant.

In this case classical approach to the prediction of normal and shear stresses distribution under the wheel is not applicable here. On non-cohesive soil, displacements of each particle are caused by not only the rim's displacement but by mutual integral influence of the entire soil mass. Because this is so, normal and shear stresses achieve maximum values at a point  $H_j$ , with an  $\alpha_{mj}$  angular coordinate (Fig.2). The location of the point  $H_j$  depends upon the value of wheel slip  $i$ .

The location of maximum stress on the wheel - soil interface reaction distribution corresponds to the position where the two slip-

ping surfaces meet (Fig.2); these surfaces arise from the wheel's action on the soil.

This failure mode allows us to consider the soil deformation by the wheel as a penetration process of some equivalent plate into the soil. Using the approach based on the limit equilibrium theory and comparing a failure pattern beneath the plate and the wheel, one can show that the plate's sizes  $a$  and  $b$ , which are equivalent to the wheel equal to the following

$$a = B; b = \chi D; \quad (1)$$

$$D = 2R, \chi = D[(\cos \alpha_{oj} - \cos \alpha_{mj}) \operatorname{tg} \bar{\gamma}_j - \sin \alpha_{mj} + \sin \alpha_{oj}] \operatorname{ctg} \psi,$$

if  $\frac{B}{D} \gg \chi$  and

$$a = \chi D; b = B, \quad (2)$$

if  $\frac{B}{D} < \chi$ ; where  $\psi = \frac{\pi}{4} + \frac{\theta}{2}$ ,  $\bar{\gamma}_j = f(\alpha_{oj}, \alpha_{mj}, \theta)$  - characterize the failure geometry;  $R$  and  $B$  are a radius and a width of the wheel.

Then maximum normal stress  $q_{mj}$  can be considered as a sinkage function of the equivalent plate  $p = f(z)$  at the  $z_{mj}$  depth corresponding to the point of the wheel's rim with the coordinate  $\alpha_{mj}$  (Fig.2).

Since the sizes of the equivalent plate  $a$  and  $b$  depend on the wheel's geometry, soil performance and on the slip value  $i$ , it is necessary to have a pressure-sinkage dependence of the plate sizes to determine  $p$  analytically.

Basing on the previous works on the subject as well as on the research done by the authors with plates of various sizes, with dry sand, it was found, that pressure-sinkage dependence can in its general form be presented allowing for the plate's sizes

$$p = K_p R_h \left( \frac{z}{\sqrt{F}} \right)^n, \quad (3)$$



where  $R_h = ab / 2(a + b)$ ;  $F = a b$ ;  $K_\psi$  and  $n$  are an empirical coefficient and a sinkage exponent obtained from the experimental results.

In addition to the given experiments, the investigations were carried out into the influence of the wheel's action on the deformation characteristic on the non-cohesion soil (Fig.3) under different loads  $W_j = \text{var}$  on the vehicle and under different slip values  $i_j = \text{var}$ .

Taking into account the vehicle's action, pressure-sinkage characteristic of the non-cohesive soil can be presented as follows: for  $j = 1$

$$\rho = K_\psi R_{h1} \left( \frac{z}{\sqrt{F_1}} \right)^n \quad (4)$$

for  $j > 1$

$$\begin{aligned} \rho &= K_\psi \frac{R_{hj}}{\sqrt{F_j}} \left[ z_j - \sum_{k=1}^{j-1} z_{k(j)} \right], \quad z_j < z_{nj}; \\ \rho &= K_\psi R_{hj} \left( \frac{z_j}{\sqrt{F_j}} \right)^n, \quad z_j \geq z_{nj} \end{aligned} \quad (5)$$

where  $z_{k,j-1}$  is the rut depth after  $(j-1)$  wheel passage,  $K_\psi$  is an empirical coefficient.

Then, allowing for the condition  $q_m = p(a, b, z_m)$  we'll obtain: for  $j = 1$

$$q_{m1} = K_\psi R_{h1} \left( \frac{z_{m1}}{\sqrt{F_1}} \right)^n; \quad (6)$$

for  $j > 1$

$$\begin{aligned} q_{mj} &= K_\psi \frac{R_{hj}}{\sqrt{F_j}} \left( z_{mj} - \sum_{k=1}^{j-1} z_{k(j)} \right), \quad z_{mj} < z_{nj}; \\ q_{mj} &= K_\psi R_{hj} \left( \frac{z_{mj}}{\sqrt{F_j}} \right)^n, \quad z_{mj} \geq z_{nj}. \end{aligned} \quad (7)$$

Now, consider the effect of tangential reactions on the

bearing capacity of soil. We have performed two types of testing:

1) the plate was penetrated through applying a constant, vertical force followed by a displacement in tangential (horizontal) direction;

2) the plate was penetrated vertically with simultaneous displacement in horizontal direction.

The experimental results enabled the effect of tangential reactions on the soil bearing capacity to be described by the formula:

$$\tau^2 + \rho^2 = \rho_{\tau=0}^2 \cos^2 \beta \xi \quad (8)$$

where  $\beta$  is the angle of friction,  $\xi$  is a parameter of soil; these are shown in Fig.4.

Then, allowing for (8), reduction in  $q_{mj}$  to magnitude  $\bar{q}_{mj}$  will take place, which corresponds to quantity of  $\tau$  and to a sinkage value  $z$ .

When  $\bar{q}_{mj}$  is known, a real normal stress distribution can be approximated by using the functions with sufficient accuracy:

$$q_j(\alpha) = \bar{q}_{mj} \frac{\sin \frac{\alpha - \alpha_{oj}}{2}}{\sin \frac{\alpha_{mj} - \alpha_{oj}}{2}}, \quad \alpha_{oj} \leq \alpha < \alpha_{mj}; \quad (9)$$

$$q_j(\alpha) = \bar{q}_{mj} \frac{\sin \frac{\alpha_{kj} - \alpha}{2}}{\sin \frac{\alpha_{kj} - \alpha_{mj}}{2}}, \quad \alpha_{mj} \leq \alpha \leq \alpha_{kj}. \quad (10)$$

The condition of the soil flow distribution from the contact zone 11 (Fig.2)

$$Q_{11j} = \gamma V B (z_{kj} - z_{mj}) = \gamma V B R (1 - \sin \alpha_{mj}) \quad (11)$$

which is proportional to the areas of geometry failure beneath the wheel in the crosssection with the coordinate  $\alpha_{mj}$

$$\frac{Q_{kj}}{Q_{lj}} = \frac{S_{kj}}{S_{kj} + S_{lj} + S_{hj}} \quad (12)$$

where  $Q_{kj}$  is the soil flow for rut recovery,

allows determination the coordinate

$$\sin \alpha_{kj} = \sin \alpha_{mj} - \frac{R}{B} \operatorname{ctg} \psi (1 - \sin \alpha_{mj}) [(\cos \alpha_{oj} - \cos \alpha_{mj}) \operatorname{tg} \xi_j - \sin \alpha_{mj} + \sin \alpha_{oj}] \quad (13)$$

under the conditions:  $S_{lj} = S_{hj}$ ;  $\frac{S_{kj}}{S_{kj} + S_{lj} + S_{hj}} = 1 - \frac{R}{B} [(\cos \alpha_{oj} - \cos \alpha_{mj}) \operatorname{tg} \xi_j - \sin \alpha_{mj} + \sin \alpha_{oj}] \operatorname{ctg} \psi$ .

Preliminary excitation of the soil flow particles of the entire mass, at the beginning of the contact with the wheel, makes the pattern of the shear displacement formation <sup>still</sup> more complicated. An analysis of experimental distribution of stresses showed that with non-cohesive soil the relationship between shear and normal stresses  $\tau/q$  remained constant over the contact surface, including the frontal zone, with the slip coefficient remaining constant. The  $\tau/q$  ratio changes as a function:

$$\left(\frac{\tau}{q}\right)_j = \operatorname{tg} \theta \left[1 - \exp\left(-\frac{l_{\tau mj}}{K_{\tau}}\right)\right] \quad (14)$$

if  $l_{\tau mj}$  is assumed as a mean integral shear displacement over the wheel-soil interface for  $H_j$  point

$$l_{\tau mj} = R \int_{\alpha_{oj}}^{\alpha_{mj}} [1 - (1 - i_j) \sin \alpha] d\alpha \quad (15)$$

Given the assumption that the reactions over the width of the wheel are uniform then a vertical load on the wheel, free drawbar pull and moment will correspondingly equal:

$$W_j = RB \left[ \int_{\alpha_{oj}}^{\alpha_{kj}} q_j(\alpha, i_j) \sin \alpha d\alpha + \int_{\alpha_{oj}}^{\alpha_{kj}} \tau_j(\alpha, i_j) \cos \alpha d\alpha \right]; \quad (16)$$

$$P_j = -RB \left[ \int_{\alpha_{0j}(l_j, W_j)}^{\alpha_{kj}(l_j, W_j)} q_j(\alpha, l_j) \cos \alpha d\alpha - \int_{\alpha_{0j}(l_j, W_j)}^{\alpha_{kj}(l_j, W_j)} \tau_j(\alpha, l_j) \sin \alpha d\alpha \right]; \quad (17)$$

$$M_j = R^2 B \left[ \int_{\alpha_{0j}(l_j, W_j)}^{\alpha_{kj}(l_j, W_j)} \tau_j(\alpha, l_j) d\alpha \right]. \quad (18)$$

For  $j$  wheel, specific free drawbar pull  $\varphi_j$  is determined as:

$$\varphi_j = \frac{P_j}{W_j} \quad (19)$$

while energy losses on motion equal :

$$f_{W_j} = \frac{M_j}{W_j (1 - l_j) R} - \frac{P_j}{W_j} \quad (20)$$

Integrated solution of equations (13), (16) and the relation determining the position of the maximal reaction  $\bar{q}_{mj}$  permit evaluation of the quantities  $\alpha_0$ ,  $\alpha_m$  and  $\alpha_k$  allowing for a preceeding action ( $j-1$ ) of wheels on deformable soil. It also allows finding quantities  $P_j$ ,  $M_j$ ,  $\varphi_j$  and  $f_{W_j}$ , which characterize the interaction process.

Substitution of (16), (17), (18) in the equilibrium equations for a multiwheeled vehicle enables determining force and power parameters of motion over non-cohesive soil and subsequently making an analysis of the distribution of twisting moments and of the weighing on the interaction process of the wheeled vehicle with the given type of soil.

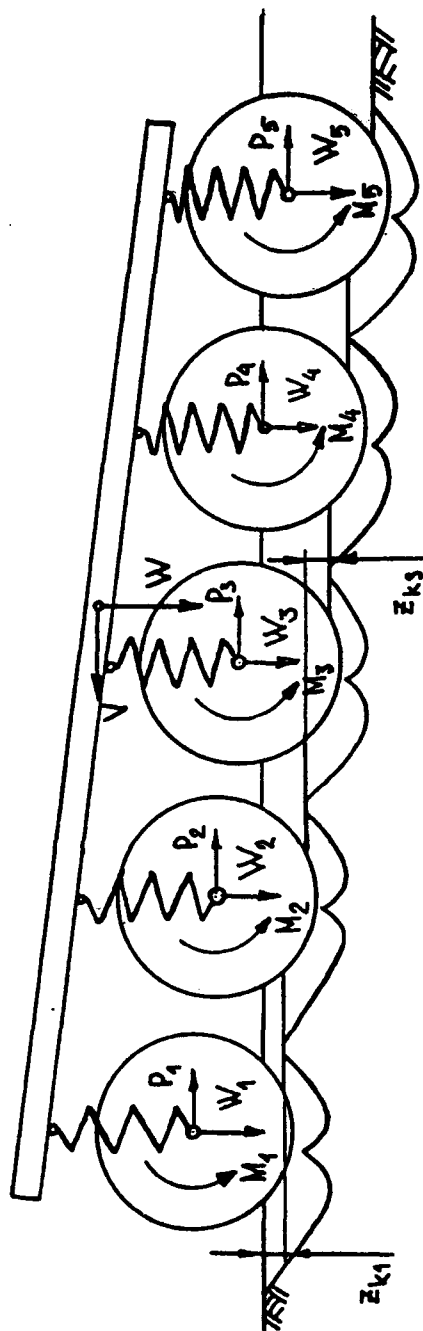
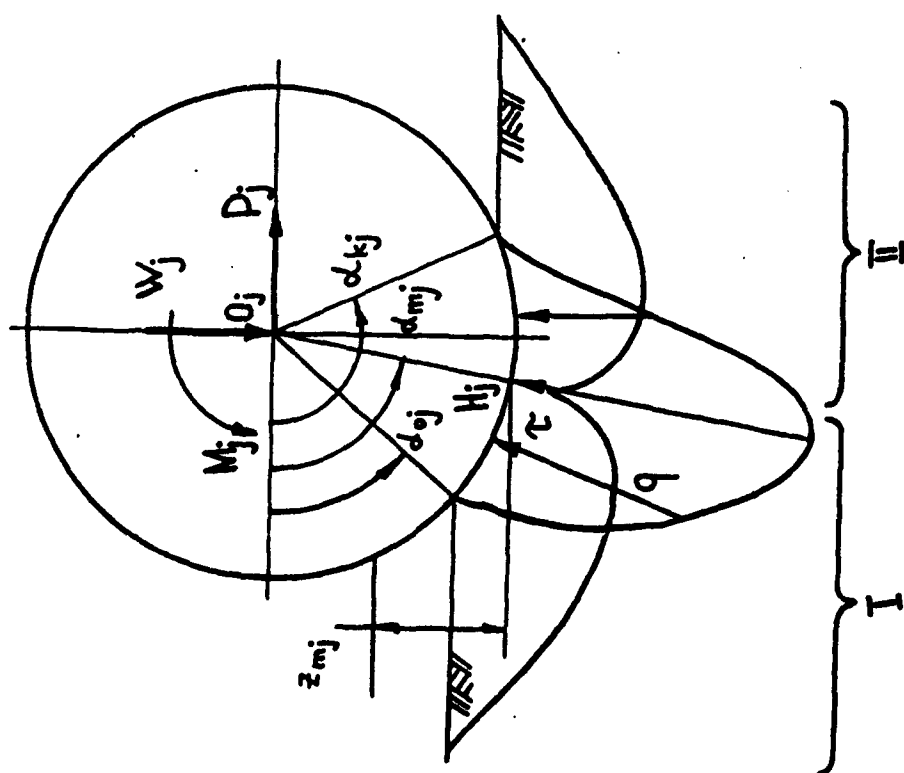
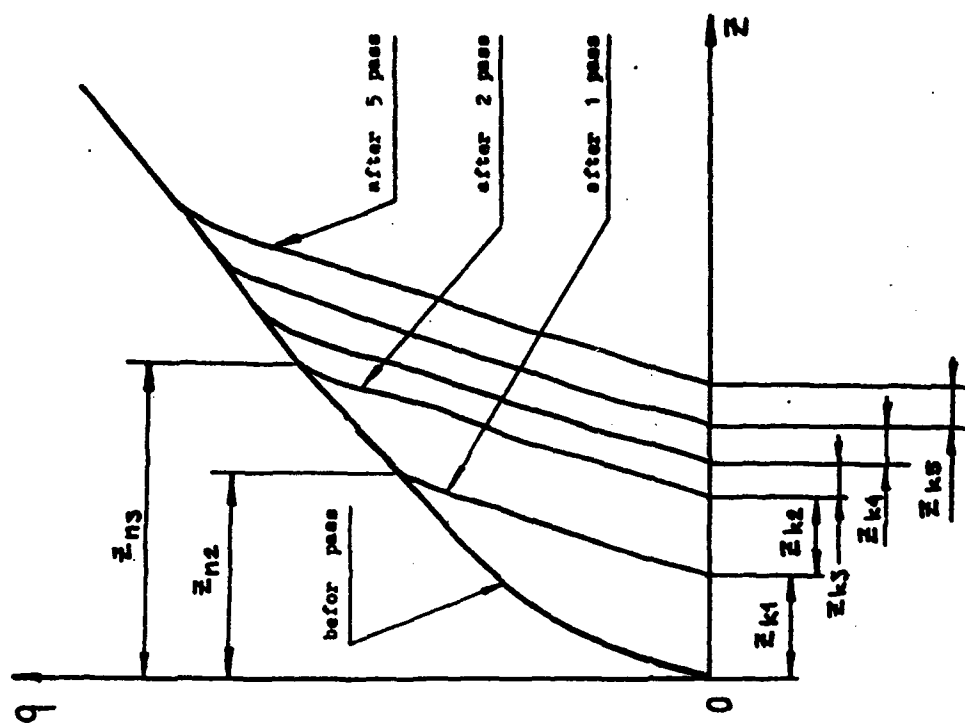


Fig. 1



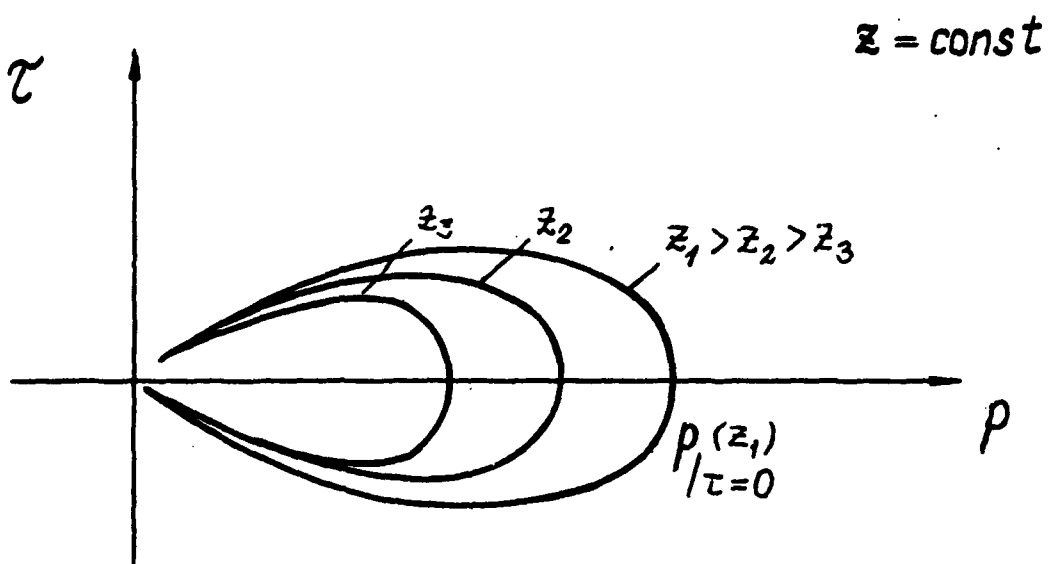


Fig. 4

# EFFECT OF AGRICULTURAL MACHINERY ON OXYGEN DIFFUSION RATE IN LOAMY SANDY SOIL.

Dr. Nozdrovický, L. Associate Professor  
Mihal, P. Research Fellow  
Department of Mechanization of Crop Production  
University of Agriculture, Nitra  
Czechoslovakia

## SUMMARY

High intensity agricultural production is accompanied by negative effects on the entire soil system, namely soil compaction, from tractors and other field machinery. Changes of oxidation-reduction soil regime in loamy sandy soil are analysed in the present paper in relation to tractor passes and soil cultivation.

An electronic measuring device equipped with a set of platinum and calomel microelectrodes was used to measure the soil oxygen diffusion rate (ODR).

During field experiments we investigated the effect of multiple passes of wheel-type tractor, Zetor 12 011, on the ODR in different depths of soil. After a statistical analysis of the field experimental data a functional relationship between compaction factors, ODR and soil properties (soil bulk density, porosity and soil penetration resistance) was obtained.

We analysed also the effect of two types of tillage tools (conventional chisel and arrow-shape deep-cultivator tyne both belonging to the Alform 290 chisel plough designed for deep ripping) on ODR.

## INTRODUCTION

By the characteristic feature of the field tasks related to the technological process in plant production are multiple passes of tractors, machines and means of transport. These passes are related to displacement of machines at main operations and also at secondary operations (rotation on the dead center). Field machines affect the whole set of soil regime defined by BEDRNA, Z. and coll. (1). Oxidation-reduction regime has important place in the category of soil regime characterizing the energetic state of soil. The oxidation-reduction soil regime is considered as a result of function of the complicated complex of factors. SOTÁKOVÁ, S. in (4) describes the ways of dynamics measurement of oxidation-reduction processes in soil. MALICKÝ, M. (3) gives the method for the ascertainment of potential intensity of oxygen diffusion in soil ODR (Oxygen Diffusion Rate) on the basis of current amperometric measuring of electrode reaction at partial oxygen reduction. This reaction is proceeding in soil solution on the surface of platinum electrode pushed into the soil. The practical results obtained on the basis of the applying of this method gives CZYŽ, E. (2).

From the mentioned analysis follows that variable ODR can serve as the reference indicator for the evaluation of oxygen accessibility for plant roots.

## MATERIAL AND METHODS

The observation of the effect of field technique on changes of oxidation-reduction regime in soil was intended on two aspects:  
- effect of multiple passes of wheel-type tractor Zetor 12 011 (engine power  $P_e = 88$  kW, weight  $G_1 = 4\ 820$  kg, front types 7.50/20



inflation pressure 250 kPa, rear tyres 18,4/ 15 - 34, inflation pressure 140 kPa/.

- effect of two types of tools for deep loosening of soil (conventional chisel and arrow-shape deep-cultivator tyne) on ODR.

The measurements were analyzed on loamy sandy soil. For this soil was found out its granular composition and content of humus. At every measurement were determined these basis soil parameters: soil moisture, specific and bulk density of soil, porosity, penetration resistance. The information about characterization and kind of soil gives the table 1.

Table 1. Granular composition and content of humus in the individual depths of soil profile.

grain size ( mm )	Depth, m		
	0,05-0,10	0,15-0,20	0,25-0,30
0,25	6,21	5,29	5,78
0,25-0,05	32,44	33,78	31,64
0,05-0,01	47,78	49,67	49,38
0,01-0,001	8,79	5,66	4,94
0,001	4,78	5,60	8,27
0,01	13,57	11,26	13,21
Content of humus, %	3,09	3,01	3,18

For the observation of the effect of wheel-type tractor Z-12 011 on the change of oxidation-reduction soil regime were realized the repeated passes in the experimental field and it in range 0,2x,4x passes. The mentioned tractor wasn't loaded by tractive force during the experiments. It moved by travelling speed 1.58-1.72 m.s<sup>-1</sup> at the simulated pressing of soil surface. The experimental plot was pressed down by way: "trace close by trace".

In the depth of the observed profile 0 - 30 cm were determined the following mean characteristics of soil: humidity 17.6 %, bulk density 1.44 g/cm<sup>3</sup>, porosity 47.5 %. Both types of shares that were at field experiments are the part of ALFARM 290 trailed chisel plough. This type of plough serves for autumn deep soil loosening into the depth 0.4 m. Its construction consists of sizeable square frame which carries 17 working shares (chisel respectively arrow-shape tynes). The total working gear of this tool is 3.8 m and at work is used in aggregation with tractor K-700 (effective engine power 170 kW). With regard to it, that this tool has considerable weight and size we used in our measuring only two operating organs which we have fastened on a frame of carrying plough from which were dismantled the original ploughing bodies. The axial distance of arrow-shape resp. chisel shares was 70 cm after this adjustment.

The electronic measuring device was used for the observation of changes of oxidation-reduction soil regime by the effect of affecting of passes of the choice tractor and using tool. On the figure 1 is shown the scheme of this device. Its function consist in current amperometric measuring of electrode reaction of partial oxygen on the surface of platinum electrode. The apparatus consists of the set of ten indicating platinum electrodes (cathode) and one saturated

calomel electrode, that has the function of reference element. Further metal electrode (anode) serves as donor of electrons. The using of this device facilitates to determine the value of oxygen diffusion that is expressed in  $\text{mg} \cdot \text{m}^{-2} \cdot \text{s}^{-1}$ . By this way in substance is expressed oxygen accessibility for plant roots.

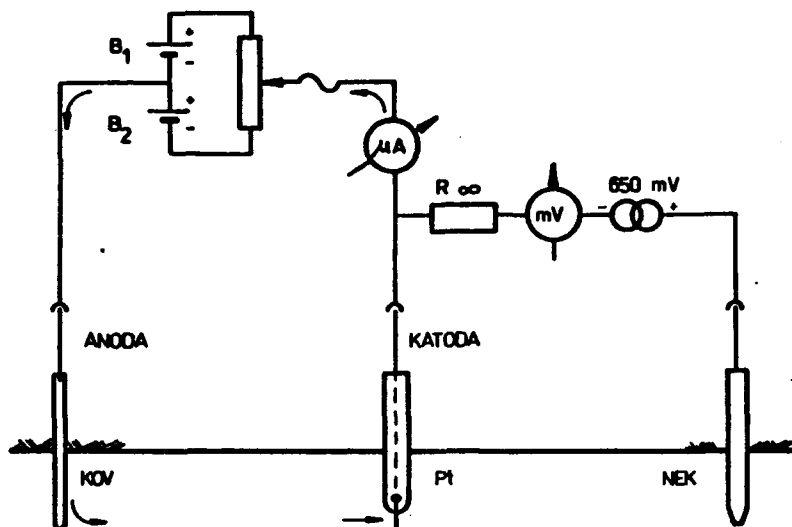


Fig. 1. Scheme for connection of device for oxidation-reduction soil regime determination.

## RESULTS AND DISCUSSION

In accordance with methodology was realized the series of measurements intended on determination of the effect of the repeated passes of wheel tractor Z - 12 011 on changes of oxygen diffusion in soil. The observed variable was determined in three different depths of soil profile with triple repeating. The measured values were statistically evaluated, what facilitated to determine the functional dependence of infusion variable on numerosness of passes. As follows from table 2 this relation is possible to describe with high exactness by means of linear functional dependence. That claim is proved by high values of regression coefficient.

The measuring and statistically elaborated data we have compared with limiting values of oxygen diffusion which relate to growth conditions of sugar beet. As CZYŻ, E (2) gives the optimal values OQR for sugar beet would be in the interval from 35 to 55  $\mu\text{g} \cdot \text{m}^{-2} \cdot \text{s}^{-1}$  in dependence on kind of soil.

At the observation of the affecting of two different types of deep cultivators was the main task to determine the distribution of oxygen diffusion values in whole cross profile cultivated by two shares. At the measurement was used ten platinum electrodes with spacing 17 cm, what facilitated to register the profile about width 153 cm. Because the working engagement of two shares was 140 cm the peripheral electrodes facilitated to measure the observed variable of oxygen diffusion in uncultivated part. The choice method gave the possibility to determine that what level participates soil cultivation by chisel resp. duckfoot share on values of oxygen diffusion in soil.

Table 2 Effect of number of tractor Z-12 011 passes on change of oxygen diffusion rate  $Y_{ODR}$  in soil

Number of tractor passes	Depth of measuring $h$ (m)	Oxygen diffusion rate $Y_{ODR} \frac{mg.m}{s}$	Functional dependance $Y_{ODR}=f(h)$	Parameters		Standard error	F-test	Level of significance	Regression coefficient	Correlation index	Standard error of function
				a	b						
0x	0,10	55	$y=a+b.h$	35		9,35	3,74	0,166	0,970	94,23	6,123
	0,20	65									
	0,30	90		1,75		0,43	4,04	0,154			
2x	0,10	45	$y=a+b.h$	36		1,87	19,24	0,03	0,990	98,97	1,22
	0,20	52									
	0,30	62		0,85		0,08	9,81	0,06			
4x	0,10	35	$y=a+b.h$	25,33		1,24	10,31	0,03	0,990	99,67	0,81
	0,20	46									
	0,30	55		1,0		0,05	17,32	0,03			

On the figures 2 and 3 is possible to see the explicit difference between cultivated and uncultivated soil as between individual types of working shares.

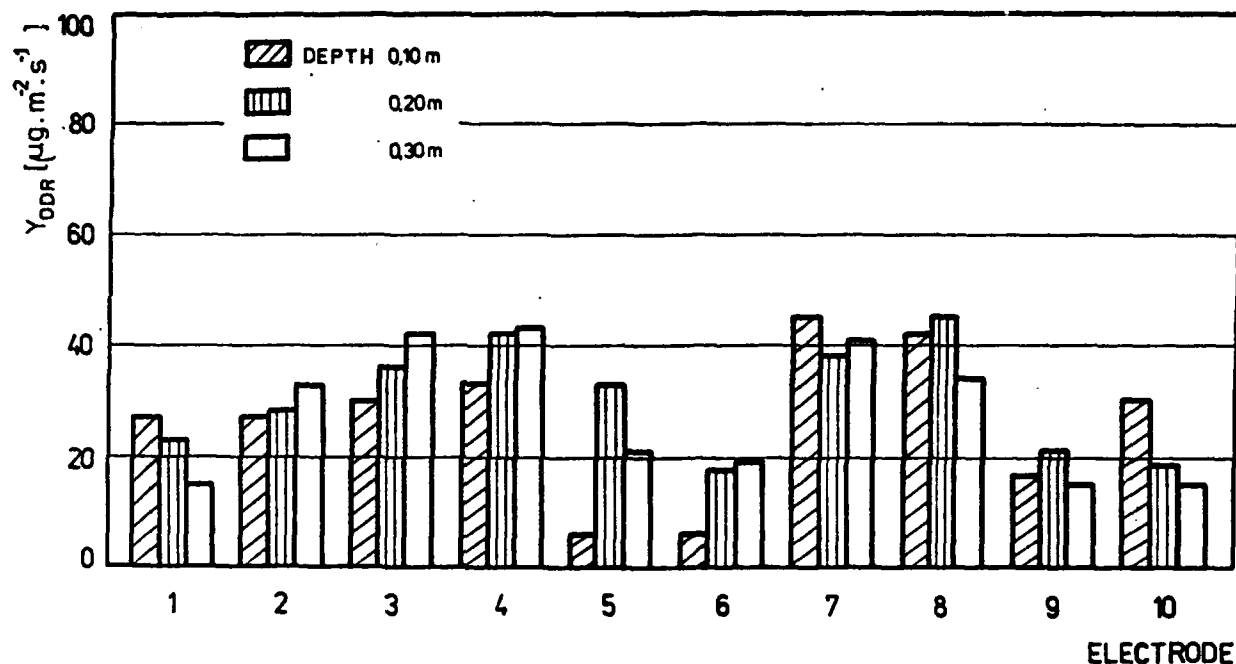


Fig. 2 The course of the oxygen diffusion rate in transversal profile after soil cultivation by chisel tynes

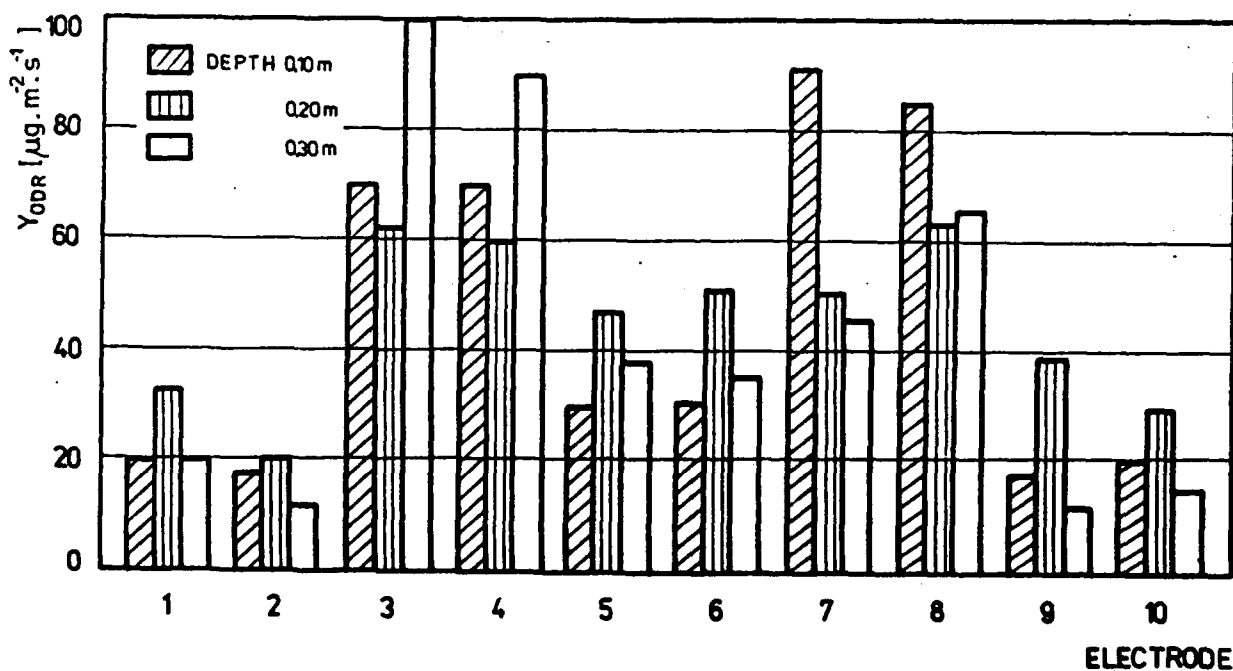


Fig. 3 The course of the oxygen diffusion rate in transversal profile after soil cultivation by arrow-shape tynes

From the figures 2,3 follows that places which aren't affect at the cultivation by chisel plough (the electrodes 1,2 and 9,10) were marked by mean level of ODR, which didn't lap  $30 \mu\text{g.m}^{-2}.\text{s}^{-1}$ .

We consider for the important zones in the cultivated profile the places in vicinity of electrodes 5,6 where occur to cumulation of soil tension. By the result is the increased soil pressing, what we consider for negative effect.

On the whole is possible to claim that using of duckfoot<sub>2</sub> share facilitates more intensive mean oxygen diffusion  $55 - 90 \mu\text{g.m}^{-2}.\text{s}^{-1}$ . Further from the mentioned figures is possible to calculate, that the highest values of oxygen diffusion were achieved in the places immediately affected by shares (electrodes number 3,4 and 7,8). The main meaning of these measurements therefore is the possibility to determine the optimal spacing of operating elements - shares on the frame as well as geometry of the active surfaces.

The mentioned method facilitates objectively and by quick way to determine the effects of machinery, tractors and the like in the concrete conditions on soil properties, that are conclusive for favourable growth of plants.

#### ACKNOWLEDGEMENT

The authors are grateful to Mrs. E.Czyż, scientist of the Institute of Soil Science and Plant Cultivation, Pulawy, Poland, for help with experimental field measurements.

#### REFERENCES

1. BEDRNA, Z. a kolektív: Pôdne režimy. Bratislava, Veda, vydavateľstvo Slovenskej akadémie vied, 1989, 224 s.
2. CZYŻ, E. : Effect of subsoiling and cultivation of double-wheeled tractor with soil openers on the aeration Conditions in soil. In.: Proceedings of the International Conference "Soil Conservation and Environment", Piešťany, 1989, 98-100
3. MALICKÝ, M.-WALCZAK, R.: A gauge of the redox potential and the oxygen diffusion rate in the soil with an automatic regulation of cathode potential. Zeszyty Problemowe Postupow Nauk Rolniczych, 1983, z.220: 447-451
4. SOTÁKOVÁ, S. a kol. : Návodý na cvičenia z geológie a pôdoznalectva. Bratislava, Príroda, 1988, 189 s.

## ADAPTIV HYDROACTUATOR FOR SOIL TESTBENCH

Dr. Sergey L. Sitnikov

In the testing machines with a hydroactuator it is necessary to provide high precision of laws of soil loading. However, due to the instability of the hydroactuator parameters and incomplete determination of the soil deformation characteristics this requirement cannot always be implomented without using new methods of dynamic objects control. Hydroactuator parameters instability is associated with a few factors such as the imperfection of the actuator circuit and elements design, the influence of technological errors, a variations in temperature and pressure in the working enviroument etc. The incomplete determination of the soil deformation characteristics may be caused both by insufficient information about the soil properties and the change of its properties during dynamic and repeated tests in particular.

One of the current methods of the instability compensation of the dynamic system parameters in the conditions of its characteristics incomplete determination is based on the adaptive control [ 1,2 ]. The self-tuning system (STS) with the model reference is characterised by good adaptivity to considerable changes in internal and external operation conditions, hish performance of the parametrs accomodation chanel and a relatively simple hardware implementation. It was that type of the STS that was used for a better control of the testing machine hydroactuator.

The diagram in Fig. 1 shows the hydroactuator which consists of a servo valve ( SV ) and an operating hydrocilinder ( HC ). The input is the electric signal  $U_{in}$ , the output is the displacement of slide  $x_{sv}$  of the servo valve and the effort on the HC rod which is equal to the product of the stress hardness  $C$  and the rod displacement  $y$  for the whole hydroactuator. ( For the research of the adaptive actuator control system the hardness of the soil is taken as a linear dependance  $P = C \cdot y$  .) In the diagram  $W_{sv}$ ,  $W_c$ ,  $K$  are the transfer functions of direct circuit elements and hydroactuator reverse communication coefficient. The effect of the diverse factors which cause the actuator characteristics instability is shown as parameter errors  $\delta_i$  ( $i = 1, 3$ ).

can generally be presented by a differential equation of the eighth order [ 3 ], Such a model is too complicated for designing a model reference. In order to simplify the model reference the mathematical description of the hydroactuator was reduced the equation of the second order. The approximation of the simplified mathematical model of the hydroactuator to the source one is implemented by means of the functional [ 4 ]:

$$J = \frac{1}{2\pi j} \int_{-j\omega}^{+j\omega} \frac{[W_8(j\omega) - W_2(j\omega)]^2}{j\omega} d(j\omega),$$

where

$$W_8(j\omega) = b_0 / \sum_{n=1}^8 [a_n(j\omega)^n + a_0] -$$

is an amplitude-phase frequency characteristic ( APFC ) for the source hydroactuator mathematical model of the eighth order ( $a_n = \text{const}$ ,  $a_0 = \text{const}$ ,  $b_0 = \text{const}$ );  $j = \sqrt{-1}$ ;  $\omega$  - is a circular frequency:

$$W_2(j\omega) = d_0 / (C_2 \omega^2 + jC_1 \omega + C_0) -$$

is a APFC for the simplified mathematical hydroactuator model of the second order;

the functional  $J$  allows to determine the coefficients  $C_0$ ,  $C_1$ ,  $C_2$  which minimize the difference at  $d_0 = b_0$ .

The transfer function of the source model  $W_m$  corresponds to APFS  $W_2(j\omega)$ .

In determining the STS structure first of all there appears a question about the type of the correcting links and their location in the system, as the efficiency of the actuator control and the complexity of the STS depend on this. You can answer this question if you estimate the influence of unstable hydroactuator parameters on the output quantity change and if you choose the adaptive parameters  $\alpha$ , which compensate the instability only of  $\beta$  hydroactuator parameters which exert the greatest influence on the output quantity. If the adapted parameters are chosen to compensate the instability of all hydroactuator parameters, the structure of the STS will be extremely complicated.

The degree of the influence of the hydroactuator unstable parameters on its static and dynamic characteristics was evaluated by means of sensitivity functions ( SF ), which are found from the

linear differential equation system with variable coefficients named sensitivity equations [ 1,5 ]:

$$\dot{u}_{ij} = \sum_{k=1}^n \frac{\partial \varphi_i}{\partial y_k} \cdot u_{kj} + \frac{\partial \varphi_i}{\partial \beta_j}, \quad (1)$$

where  $u_{ij}$  is SF of the  $i$  - variable of the  $j$  - unstable parameter  $i = \overline{1, n}$ ;  $\varphi_i$  is the right parts of the system differential equations, presented in the Koshi form;  $y_k$  is the system variables,  $k = \overline{1, n}$ ;  $\beta_j$  is unstable parameters;  $j$  - is the variables number in the differential equations, describing the dynamic system;  $j = \overline{1, m}$  (  $m$  - is the number of the system unstable parameters ).

For determining the sensitivity function the mathematical description of the hydroactuator according to the diagram shown in Fig.1 is used  $W_{SV}$  is taken equal to the amplification coefficient  $K_{SV}$ , and the whole closed loop of the hydroactuator is presented by the equation system [ 3 ]:

$$\dot{y}_1 = [(u_{in} - K y_3 C) K_{SV} - a_1 y_2 - y_1 a_2] / a_3; \quad (2)$$

$$\dot{y}_2 = y_1; \quad (3)$$

$$\dot{y}_3 = y_2, \quad (4)$$

$$\text{where } a_1 = T_H; a_2 = 2 f_c \cdot T_c \cdot T_H; a_3 = T_c^2 \cdot T_H; P = C y_3.$$

The parameters  $K_{SV}$ ,  $K$ ,  $a_1$ ,  $a_2$  are considered as unstable. The sensitivity function for the coefficient has not been determined as it has a very small value compared with other coefficients.

The joint solution of the sensitivity equations, which are derived from the equation (1) for the unstable parameters  $K_{SV}$ ,  $K$ ,  $a_1$  and  $a_2$  with the hydroactuator model equations allows to analyze the influence of the parameters instability on the hydroactuator output quantity very quickly. Fig.2 shows the computer calculations of the sensitivity function plots, In order to make the SF plots of the same dimensions the standardization was carried out by means of the relation



$$\bar{U}_{pj} = \frac{\partial P}{\partial \beta_j} \frac{\beta_{oj}}{P_{max}}$$

where  $\beta_{oj}$  is a stationary value of the  $j$  parametr of the hydroactuator;  $P_{max}$  is the maximum effort at the hydroactuator outlet.

The plots show that the output value of the hydroactuator is more sensitive to the parameter instability  $a_1$  and  $a_2$ ; the parametr instability can lead to a strong oscillation of the processes. The hydroactuator is less sensitive to the parameters  $K_{SV}$  and  $K$ , and the change of the parameter  $K$  leads to the set error. Analysing the SF particular attention should be paid to the system response time while changing the parameter, as the velocity of self-tuning is very important for STS control.

The  $a_1$  coefficient has been chosen as adapted parameter due to the greatest influence on the output quantity, its change velocity and the process stability. Considering  $a_1$  parameter an adapted one, let us write down the hydroactuator equations (2)-(4) as one equation:

$$[a_3 S^3 + a_2 S^2 + (a_1 + \alpha_1) S] P = K_{SV} C(U_{in} - K \cdot P), \quad (5)$$

where  $\alpha_1$  is an adapted parameter of STS hydroactuator control:  $S = d/dt$  - is a differentiation operator.

In the hydroactuator it is rather simple to regulate the  $\alpha_1$  parameter by means of an electric link, which is part of the reverse connection of the differentiating link. The quantity  $\alpha_1 P S$  in the equation (9) can be transferred to the right hand side:

$$(a_3 S^3 + a_2 S^2 + a_1 S) P = K_{SV} C(U_{in} - K P - \alpha_1 P S). \quad (6)$$

After choosing the adapted parameter let us consider the operation algorithm of nonsearch STS of the hydroactuator control with the model reference using the gradient method [1,2]. If the functional  $Q$  is taken as a factor of the self-tuning quality, then the adapted parameter change velocity  $\dot{\alpha}_1$  will be

$$\dot{\alpha}_1 = -\lambda \frac{\partial Q}{\partial \alpha_1} = -\lambda \frac{\partial Q}{\partial \mathcal{E}} \cdot \frac{\partial \mathcal{E}}{\partial \alpha_1}, \quad (7)$$

where  $\lambda$  is a coefficient of the self-adaptation velocity;

$\mathcal{E} = P_m - P$ —in a dynamic error between the output signal of the model reference  $P_m$  and hydroactuator  $P$ .

By means of the partial derivative  $\partial \mathcal{E} / \partial \alpha_1$  the auxiliary operator is determined, as the variable  $P_m$  does not depend on the main system parameters, then

$$\frac{\partial \mathcal{E}}{\partial \alpha_1} = - \frac{\partial P}{\partial \alpha_1}. \quad (8)$$

Let us introduce the operator  $\Phi_{py}$  of the main system (6) which depends on the arbitrary changing parameters and the self-tuning parameter  $\alpha_1$ . We get

$$P = \Phi_{py} \cdot U_{in}. \quad (9)$$

After the insertion of the equation (9) into the expression (8) we get

$$\frac{\partial \mathcal{E}}{\partial \alpha_1} = \left( - \frac{\partial \Phi_{py}}{\partial \alpha_1} \right) U_{in}.$$

The partial derivative  $\partial \Phi_{py} / \partial \alpha_1$  is the auxiliary operator, which can be implemented by a device (evaluator) with an operator  $W_e$ . Using the gradient method [ 2 ] the evaluator is formed as

$$W_e = W_m \cdot \frac{\partial W_c}{\partial \alpha_1} = \frac{d_0 \cdot S'}{C_2 S'^2 + C_1 S' + C_0}, \quad (10)$$

where  $W_c = \alpha_1 S'$ .

It should be pointed out that the equation (10) is derived in view of the change of the signal  $U_{in}$ , fed at the evaluator output, into the signal  $P$  from the hydroactivator output [ 2 ] according to the equation (9).

The exponent of the self-adaptation quality of the system under consideration is the disagreement square minimum between the outputs of the model reference and the hydroactivator:

$$Q(\mathcal{E}) = \mathcal{E}^2 / 2 \rightarrow \min.$$

If we substitute the transfer function of the evaluator (the signal  $P$  from the hydroactuator output is fed to the evaluator input) and the chosen quality exponent  $Q(\mathcal{E})$  to the expression (7),

after the cancellation of the differentiation operator  $S$  we get

$$\dot{\alpha}_1 = -\lambda \cdot \mathcal{E} \frac{d_0}{C_2 S^2 + C_1 S + C_0} P.$$

The resultant correlation determines the structure of the control STS with the model reference (Fig.3).

It should be pointed out that it is possible to feed the signals  $U_{in}$ ,  $P_m$  and  $\mathcal{E}$  to the evaluator input. It will cause the structure change of the STS, and what is very important, it may complicate the transfer function of the evaluator.

The computer calculations confirmed high efficiency of the adaptation algorithm proposed. During the computations we used a nonlinear mathematical model which simulates the practical hydroactuator and takes into consideration the instability of the hydroactuator and soil parameters. The computation result are shown in Fig.4, where  $P(t)$  is a transient process in the hydroactuator without the STS with a reverse effort connection at the output link of the hydrocylinder;  $P_m(t)$  is a signal from the model reference output;  $P_{STS}(t)$  is a transient process in the hydroactuator with the control STS. In the considered case the force 4 kH is a hained when the plate moves 50 mm in the soil. The diagrams show that having a stepped output influence, the transient effort process, which the hydroactuator develops, is aperiodic. The time of the transient process, when STS is available, is twice less as compared with the hydroactuator without the STS.

The competence of the  $\alpha_1$  parameter selection as an adapted parameter was estimated by means of a computer. We have calculated the transient processes in the hydroactuator with the control STS while adaptively various parameters in the correction links, which are included both into the direct and the reverse connection. These transient processes have long duration and tend to oscillate and the STS structure in the diagrams considered turned out to be more complicated than was shown in Fig.4.

### Conclusion

A simple STS for the hardware support can be obtained on the basis of the simplified hydroactuator mathematical model. The application of the sensitivity function allows to distinguish those STS parameters, which, when adapted, allow to get minimum

disagreement between the output signal of the model reference and the hydroactuator.

The nousearch gradient hydroactuator control STS with the model reference provides the improvement of dynamic characteristics of the testing machines.

1. Ходько С.Т. Проектирование систем управления с нестабильными параметрами. Л.: Машиностроение. 1987. 232 с.

2. Солодовников В.В., Шрамко Л.С. Расчет и проектирование аналитических самонастраивающихся систем с эталонными моделями. М.: Машиностроение. 1972. 270 с.

3. Попов Д.Н. Динамика и регулирование гидро- и пневмосистем. М.: Машиностроение. 1987. 464 с.

4. Автоматы - настройщики следящих систем/ Под ред. Б.В. Новоселова. М.: Энергия. 1975. 264 с.

5. Томович Р., Вукобратович М. Общая теория чувствительности. М.: Сов. радио. 1972 240 с.

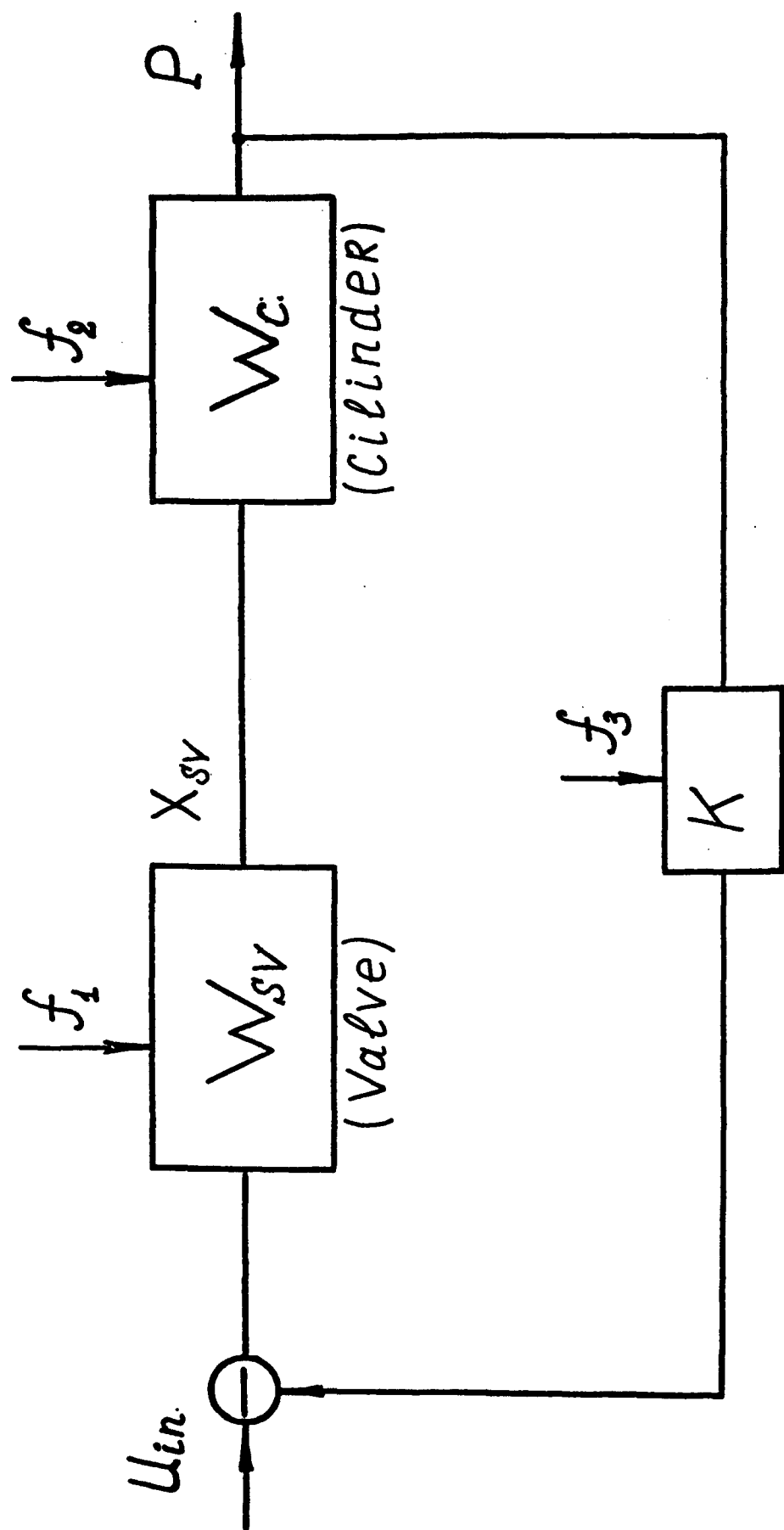


Fig. 1

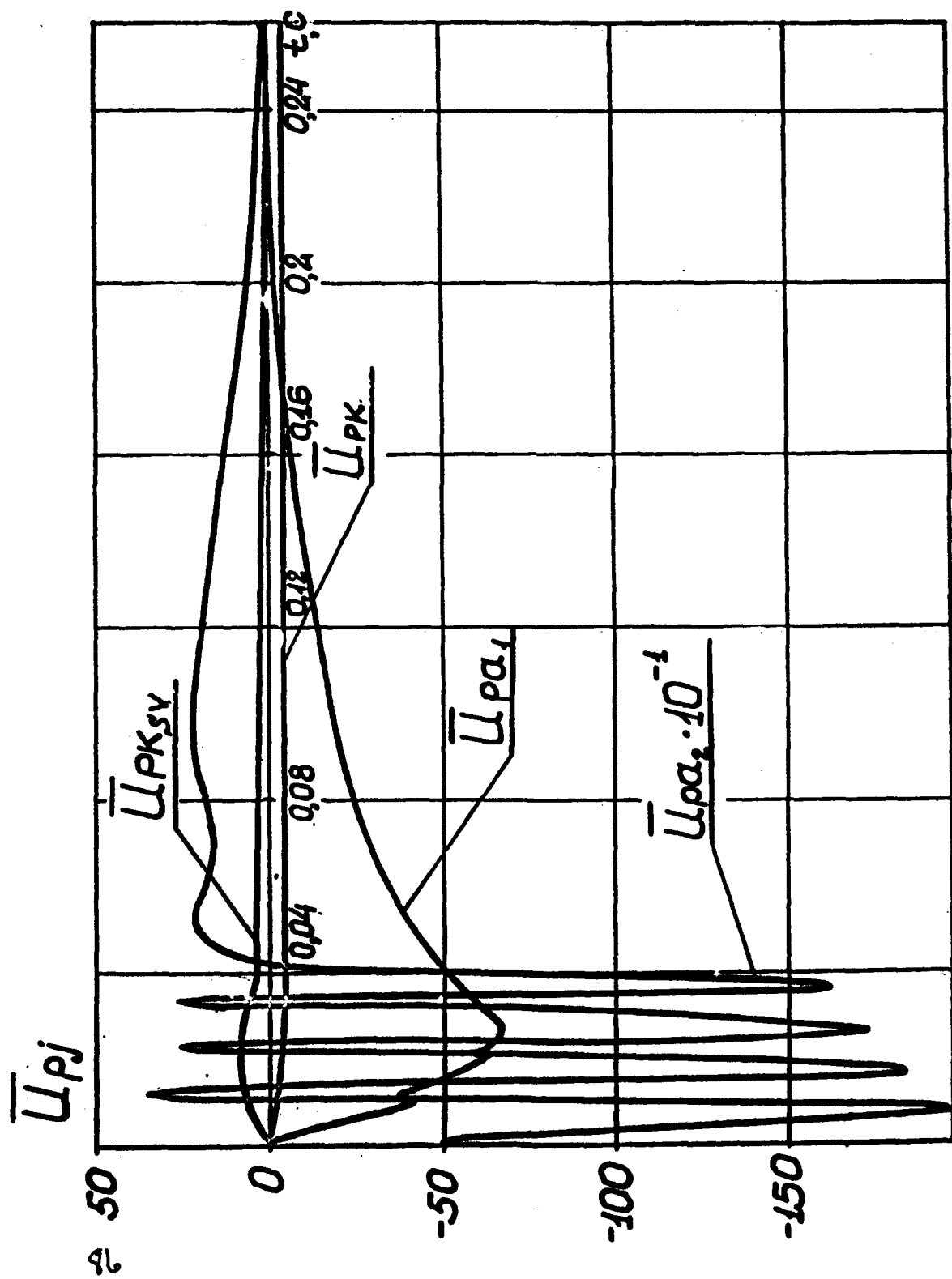


Fig. 2

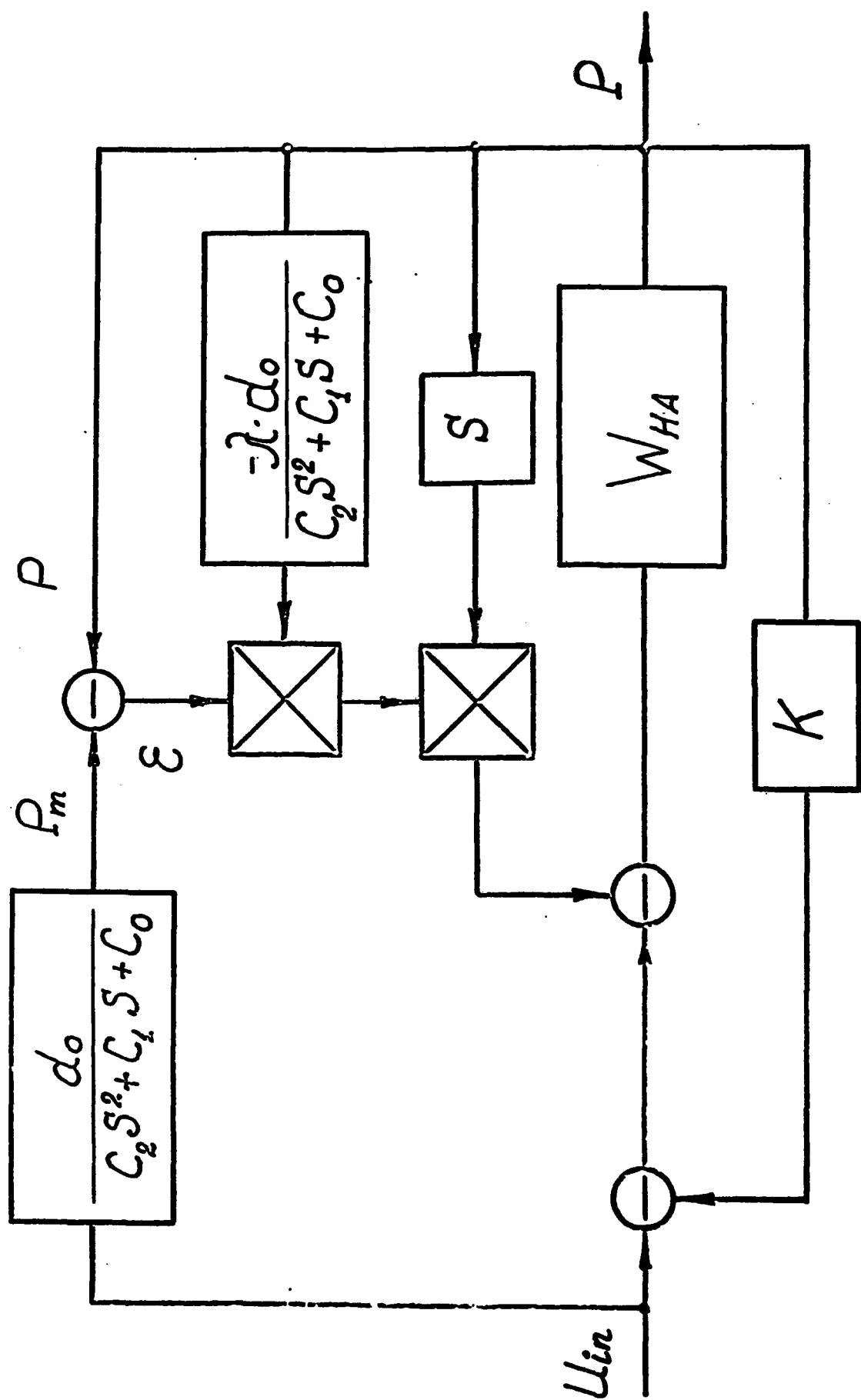


Fig. 3

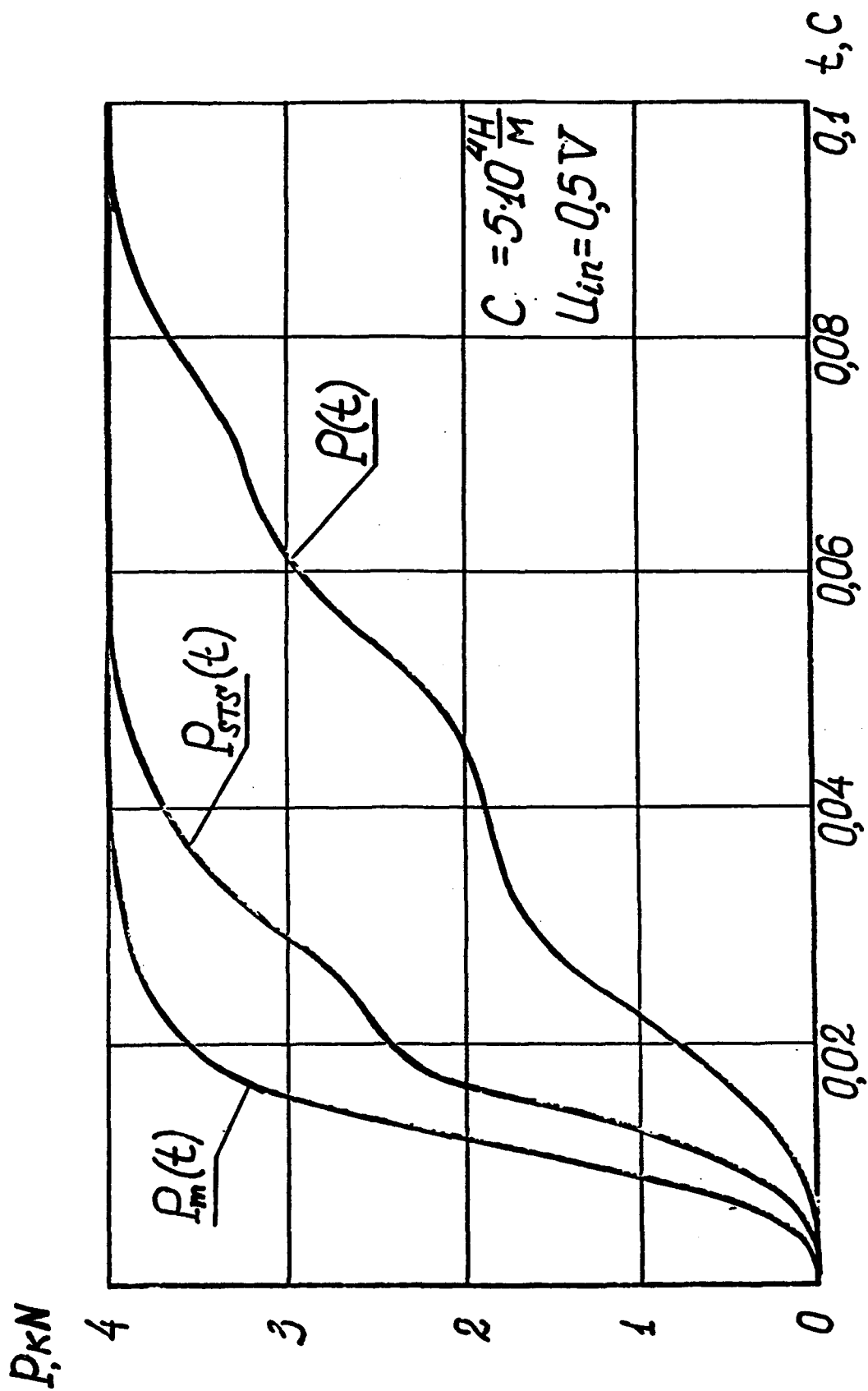


Fig. 4



## **SESSION 2**

**SOIL – VEHICLE INTERACTION,  
TIRES AND TRACKS**

# THE INFLUENCE OF WHEEL CONFIGURATION ON GROUND PRESSURE OF AGRICULTURAL VEHICLES

F.G.J. Tijink  
Institute of Agricultural Engineering (IMAG),  
P.O. Box 43, 6700 AA Wageningen, The Netherlands

## Abstract

Agricultural vehicles have a wide variety of wheel configurations (number of wheels, wheel loads, tyre sizes, number of axles, axle loads, central tyre inflation systems, etc.). During field traffic there must be a sound balance between the ground pressures exerted and the bearing capacity of the soil. A general rule of thumb is given for permitted average tyre contact pressure. The ground pressure of many vehicles is too high. The main problems are listed. Wheel configuration strongly influences contact pressure. This has been worked out for agricultural vehicles available in the Netherlands. The analyses show that trailers up to 30 Mg gross vehicle weight can be equipped to have an average contact pressure of 100 kPa.

## 1. PERMISSIBLE SOIL PRESSURES

Stresses occur at the tyre-soil interface during field traffic. The soil reaction to these stresses depends on soil parameters (soil type, bulk density, organic matter content, soil moisture, etc.) and technical parameters (wheel load, contact area, tyre inflation pressure, tyre construction, size and direction of stresses, driving speed, etc.). The interaction between all these parameters is very complex. In developing a traffic system, sustainability of a good soil structure for plant growth must be the point of departure. Two parameters are important when considering the untilled subsoil: soil moisture and the vertical pressure on the soil.

Fig. 1 gives a pressure-sinkage relationship for an untilled soil sample. Hooke's Law holds in part a of the curve [1]. This means that soil behaves elastically in this range. If the load is removed, the soil will recover to its original height. Irreversible sinkage will occur when the critical pressure is exceeded.

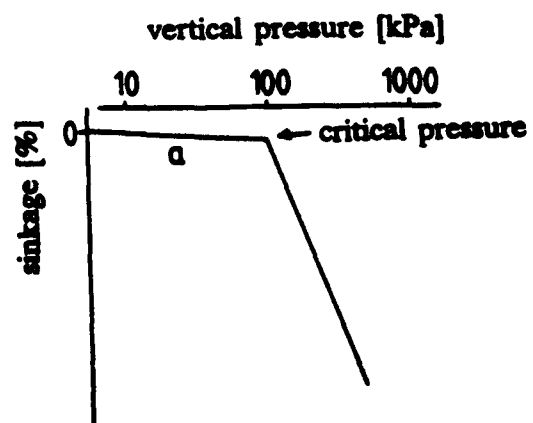


Fig. 1. Pressure-sinkage relationship for an untilled soil sample (schematized).

#### influence of soil moisture

Soil moisture is a major soil physical factor in the pressure-sinkage relationship [2]. This is illustrated schematically in Fig. 2. At pF2.5 (matric potential of -30 kPa) this soil has a critical pressure of 100 kPa. At pF1.8 (matric potential of -6 kPa) the critical pressure is less: 60 kPa. In the literature [3,4] critical pressures between 20 and 300 kPa are mentioned. A shift from pF2.5 to pF1.8 can easily result in a 50 kPa decrease of the critical pressure value.

#### influence of traffic system

Vertical soil pressure is a major engineering factor. Fig. 3 gives a schematic presentation. A 'soil-friendly' traffic system (e.g. all tyres at an inflation pressure of 40 kPa) achieves the critical pressure at a much higher moisture content than a 'soil-unfriendly' system (with all tyres at 250 kPa). A 'standard' traffic system (all tyres at 100 kPa) scores in between. Special vehicles (such as a gantry) do not touch the production zone and consequently do not affect this zone.

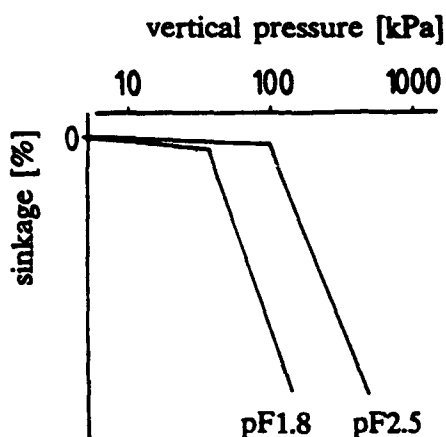


Fig. 2. Influence of pF value on the pressure-sinkage relationship and critical pressure (schematized).

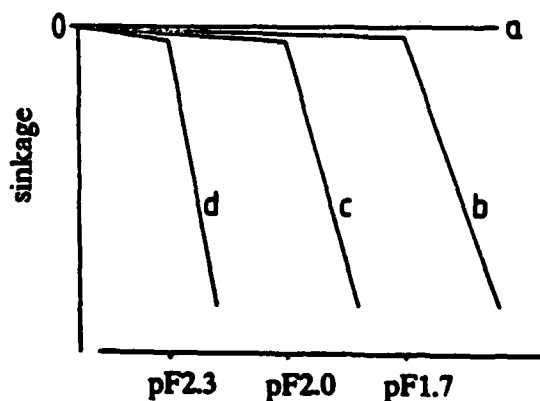


Fig. 3. Influence of traffic system on the relationship between pF and sinkage (schematized).

- a - gantry;
- b - 'soil-friendly' traffic system;
- c - 'standard' traffic system;
- d - 'soil-unfriendly' traffic system.

### average contact pressure

The average contact pressure is the load divided by the contact area. A load of 50 kN on a contact area of 1 m<sup>2</sup> means an average contact pressure of 50 kPa.

At IMAG, we use the following rules of thumb for the maximum permissible average contact pressures:

normal conditions: 100 kPa  
in spring on arable land: 50 kPa

The '100 kPa rule' aims at preventing compaction of the untilled subsoil. It is important that field operations on arable land in spring do not compress the topsoil unduly, and therefore permissible ground pressure for these operations is half the pressure permitted during other times of the year. At IMAG extensive trials have been done using these rules of thumb [5,6,7,8].

## 2. PERMISSIBLE WHEEL AND AXLE LOADS

An average contact pressure of 100 kPa is equivalent to a load of 10 Mg (=10 Metric tons) on a contact area of 1 m<sup>2</sup>. The biggest agriculture tyre (with a width of 1.10 m and an overall diameter of 1.86 m) has a contact area of 0.5 m<sup>2</sup> at proper settings of load and inflation pressure. This means that using the '100 kPa rule' results in a maximum wheel load of 5 Mg and a maximum axle load of 10 Mg.

EC legislation (74/151/EEC) also stipulates a maximum axle load of 10 Mg for wheeled agricultural tractors.

## 3. VEHICLES CAUSING PROBLEMS

Many agricultural vehicles have contact pressures that are much higher than the permissible contact pressures. The agricultural vehicles that pose greatest problem for Dutch conditions are presented in Table 1.

Table 1. Common average contact pressures of agricultural vehicles.

Transport vehicles	200 - 600 kPa
Front wheel of Two-Wheel-Drive tractors	200 - 300 kPa
Combine harvesters	200 - 300 kPa
Selfpropelled sugarbeet harvesters	200 - 300 kPa

## 4. REDUCTION OF CONTACT PRESSURE

The ground pressure exerted by agricultural vehicles can be reduced in one of two ways:

- reducing the total load (at a constant contact area)
- enlarging the contact area (at a constant load).

In this paper I will consider the latter option only. There are several ways of enlarging the contact area between vehicle and soil:

- a. using bigger tyres
- b. using more tyres: duals or more axles
- c. reducing tyre inflation pressure  
(Note: this affects load or speed)
- d. using rubber tracks.

Options a-c are discussed below. For a discussion of option d, see [9] and [10].

## 5. TRANSPORT VEHICLES

Tipping trailers and slurry tankers have particularly high contact pressures.

Wheel load can be calculated if the vehicle's payload capacity, empty vehicle weight, and vertical load on the trailer hitch are known. These specifications are available in the AGRIMACH database [11], for 35 tipping trailers (with a payload capacity of 6-25 Mg) and 40 slurry tankers (with a payload capacity of 4.2-30 m<sup>3</sup>). The wheel load at rated payload for all 75 vehicles was calculated, assuming that the vehicle weight was uniformly distributed over the wheels. The results are shown in Fig. 4, in which the influence of the number of axles is very clear.

Average contact pressures were calculated for the same vehicles. In all vehicles, using a standard tyre size (16/70-20) results in a ground pressure far above 100 kPa. Fig. 5 also gives the contact pressures when using the biggest tyre size (73x44.00-32). This shows the tremendous influence of tyre size and number of axles.

It is not yet common to use the biggest tyre sizes on vehicles with tandem and triple axles. Usually a 24R20.5 is the biggest tyre size for these vehicles. Further reduction of ground pressure can be achieved by using a central tyre inflation system (CTIS) and a weight transfer facility (WTF). In the Netherlands some tandem and triple axled trailers are equipped with these features.

CTIS and WTF will now be explained in more detail. Tyres have to meet different requirements for field traffic and road travel: driving on the road requires a high inflation pressure, but inflation pressure should be low in the field. It is common for road travel and field traffic to alternate, and therefore tyre inflation pressure is generally a compromise between the conflicting requirements of the two driving surfaces involved. Tyre manufacturers provide tables of tyre loading capacity and inflation pressure at 30 and 40 km/h. A considerable increase of tyre load is permitted at lower speeds. Table 2 illustrates this.

Table 2. Change in tyre loading capacity of tractor rear tyres in relation to driving speed (according to ETRTO standards [12]).

Tyre marking*:	PR	A6	A8
40 km/h	80%	90%	100%
35 km/h	90%	95%	103%
30 km/h	100%	100%	107%
25 km/h	107%	111%	111%
20 km/h	120%	123%	123%
8 km/h		150%	150%

\*: PR=Ply Rating; A6=30km/h; A8=40 km/h

It is also possible to change tyre inflation pressure (at constant tyre load) instead of changing tyre load (at constant inflation pressure). This is an interesting option for reducing ground pressure. With a CTIS it is possible to change inflation pressure on the go. In practice the change will be made between two extremes: high inflation pressure on the road and low inflation pressure in the field.

As an example, consider a 650/75R34 tractor rear tyre with a load of 4500 kg. The tyre manufacturer specifies an inflation pressure of 140 kPa at 40 km/h. An inflation pressure that is 30 kPa higher is needed when much road travel is done. Tyre specifications allow an inflation pressure of 80 kPa at 8 km/h in the field. With a CTIS the inflation pressure will be 80 kPa in

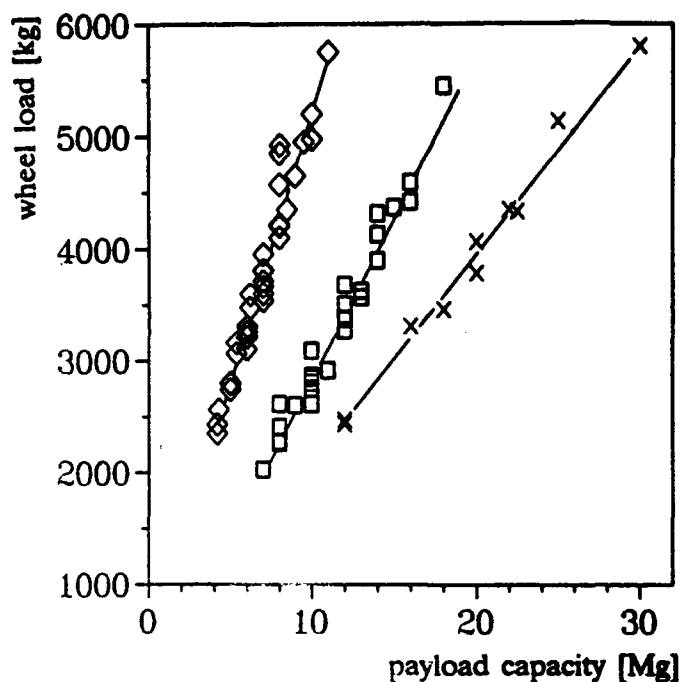


Fig. 4. Wheel load of tipping trailers and slurry tankers.

- ◇ - 2 wheels (single axle)
- - 4 wheels (steered tandem axle)
- × - 6 wheels (steered triple axle)

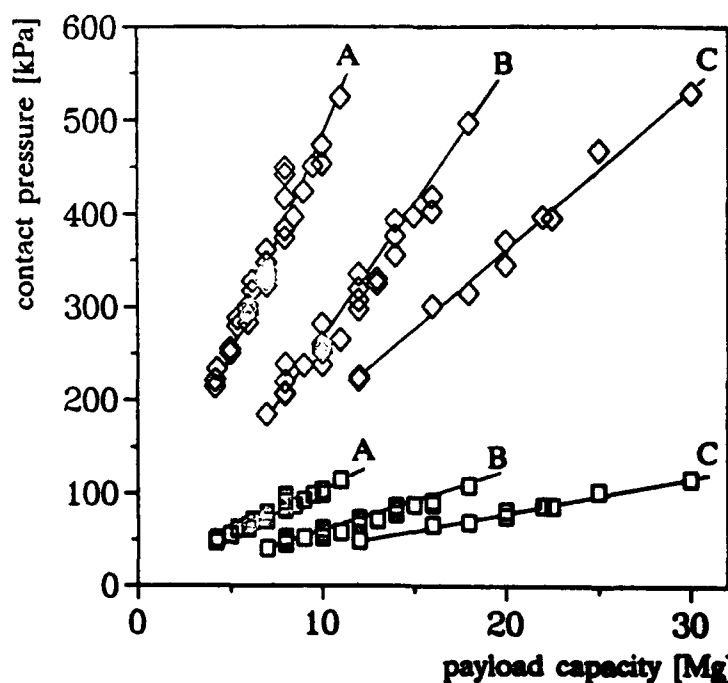


Fig. 5. Influence of wheel configuration on average contact pressure of agricultural trailers.

- ◇ - standard tyres (16/70-20; 0.42 m wide and 1.08 m diameter)
- - biggest tyres (73x44.00-32; 1.10 m wide and 1.86 m diameter)
- A - single axle; B - steered tandem axle; C - steered triple axle.

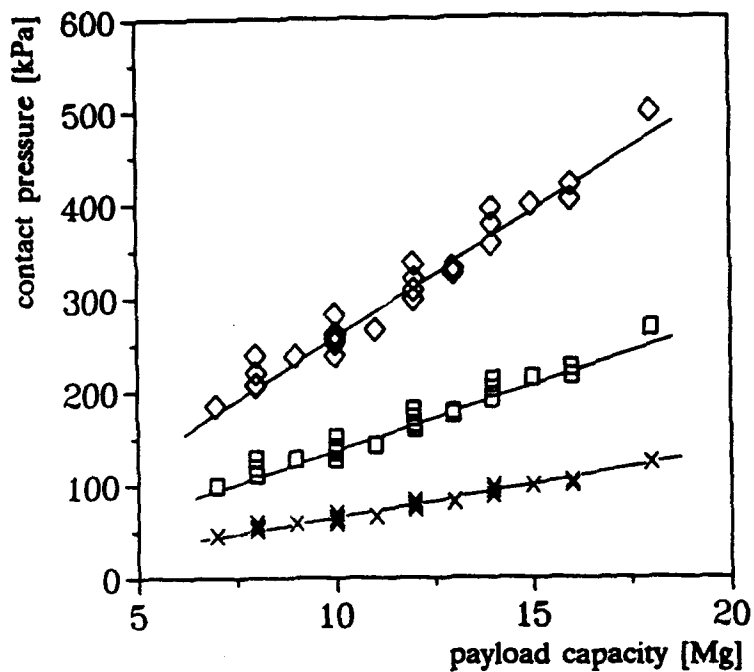


Fig. 6. Influence of wheel configuration on average contact pressure of trailers with steered tandem axle.

◇ - tyres: 16/70-20 (0.41 m wide and 1.08 m diameter)  
 □ - tyres: 24R20.5 (0.60 m wide and 1.37 m diameter)  
 × - 24R20.5 tyres + CTIS + WTF.

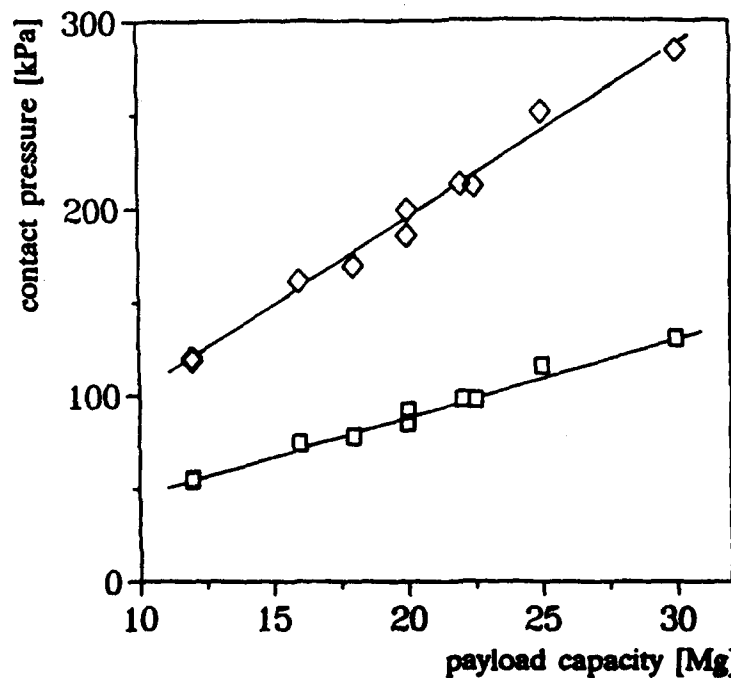


Fig. 7. Influence of wheel configuration on average contact pressure of trailers with steered triple axle.

◇ - tyres: 24R20.5 (0.60 m wide and 1.37 m diameter)  
 □ - 24R20.5 tyres + CTIS + WTF.

the field and 170 kPa on the road. This provides traffic without compromises between field and road. A proper use of CTIS can result in soil-friendly field traffic and less tyre wear on the road. Using a WTF as well as CTIS can reduce ground pressure further. With a WTF, on the road almost all the payload will be supported by the trailer. In the field the WTF shifts part of the payload (e.g. 5 Mg) on to the tractor. The tractor tyres have an additional loading capacity at low speeds (see Table 2), which is used by the WTF. The WTF also provides better traction in the field. The lighter load on the trailer allows the inflation pressure of the trailer tyres to be reduced further. An inflation pressure of 60 kPa is possible for all tyres of a well designed combination of tractor and 16 m<sup>3</sup> slurry tanker, equipped with CTIS and WTF. Inflation pressures of 80 kPa are possible for a 22 m<sup>3</sup> combination. The influence of using CTIS and WTF is also presented in Figs 6 and 7. From Figs 5-7 it can be concluded that trailers up to 30 Mg gross vehicle weight can be equipped to have an average contact pressure of 100 kPa. Maximum loads for single, tandem and triple axled trailers are summarized in Table 3.

Table 3. Maximum permitted vehicle loads at an average contact pressure of 100 kPa. (1 Mg= 1 Metric ton= 1000 kg)

	single axle	steered tandem axle	steered triple axle
Maximum payload	8.5 Mg	15 Mg	22 Mg
Maximum gross vehicle weight	10 Mg	20 Mg	30 Mg
Maximum axle load	10 Mg	10 Mg	10 Mg
Maximum wheel load	5 Mg	5 Mg	5 Mg

## 6. CONCLUDING REMARKS

- wheel configuration strongly influences the average contact pressure of agricultural vehicles;
- the parameter 'average contact pressure' is very useful in selecting wheel equipment;
- agricultural trailers up to 30 Mg gross vehicle weight can be equipped to have an average contact pressure of 100 kPa.

## LITERATURE

- [1] Hartge, K.H. und Horn, R., 1984. Untersuchungen zur Gültigkeit des Hooke'schen Gesetzes bei der Setzung von Böden bei wiederholter Belastung. Zeitschrift für Acker- und Pflanzenbau 153:200-207.
- [2] Tijink, F.G.J., 1988. Load-bearing Processes in Agricultural Wheel-Soil Systems. Doctoral thesis Agricultural University, Wageningen, 173 pp.
- [3] Koolen, A.J. and Kuipers, H., 1989. Soil deformation under compressive forces. In: W.E. Larson, G.R. Blake, R.R. Allmaras, W.B. Voorhees and S.C. Gupta (Editors), Mechanics and related processes in structured agricultural soils. NATO ASI Series, E: Applied Science 172:37-52. Kluwer, Dordrecht.
- [4] Lebert, M., 1989. Beurteilung und Vorhersage der mechanischen Belastbarkeit von Ackerböden. Doctoral Thesis University Bayreuth, 131 pp.
- [5] Vermeulen, G.D., Arts, W.B.M. and Klooster, J.J., 1988. Perspective of reducing soil compaction by using a low ground pressure farming system; selection of wheel equipment. Proceedings 11th Int. Conf. ISTRO, Edinburgh, Scotland, Volume 1:329-334.



- [6] Chamen, W.C.T., Vermeulen, G.D., Campbell, D.J. and Sommer, C., 1990. EEC cooperative project on reduction of soil compaction. ASAE paper 90-1073, 28pp.
- [7] Vermeulen, G.D. and Klooster, J.J., 1991. Lagedruk berijding. Landbouwmecanisatie 42(1):9-12.
- [8] Vermeulen, G.D., 1991. Topsoil and crop responses to a low ground pressure farming system on a marine loam in the Netherlands. Paper to be presented at the 12th Int. Conf. ISTRO, Ibadan, Nigeria.
- [9] Tijink, F.G.J., Koolen, A.J. and Arts, W.B.M., 1990. Banden tussen voertuig en grond. In: F.G.J. Tijink (ed.), Themadag Management Bodemstructuur, IMAG, Wageningen:9-23.
- [10] Tijink, F.G.J., Arts, W.B.M. and Koolen, A.J., 1990. Rijden over land, deel 2: ontwikkelingen op voertuiggebied. Landbouwmecanisatie 41(12):7-9.
- [11] Mengmestverspreiders, Agrimach Databank. Nota 471, IMAG, Wageningen, 1990:117 pp.
- [12] ETRTO standards manual 1990. The European Tyre and Rim Technical Organization, Brussels: A1-A31.

# THE EFFECT OF TYRE-SOIL INTERFACE SHAPE ON THE PREDICTION OF VEHICLE OFF-ROAD PERFORMANCE

M.A-M.Mahmoud\*, M.J.Dwyer\*\*

\*Automotive Department, Helwan University, Cairo, Egypt. (Visiting Worker, Silsoe Research Institute)

\*\*Silsoe Research Institute, Silsoe, Bedford, England

## ABSTRACT

Three two-dimensional models were developed to predict the tractive performance of a tractor driving wheel, by integrating the forces over the interface with the soil. Each model used a different assumed shape for the interface; a horizontal plane plus part of the undeflected circumference, a sloping plane joining the frontmost and rearmost points of contact between the tyre and the soil and part of the circumference of a circle larger than the tyre. Results predicted from the three models were compared with data from experiments using a single wheel tester to measure the tractive performance of three different sizes of tractor driving wheels in the field. The best agreement between measured and predicted results was obtained with the model which assumed a sloping plane interface. It would be necessary to take account of torsional deformation of the tyre to improve the accuracy of the prediction method.

## 1-INTRODUCTION

There have been many attempts in the past to describe a realistic deflected tyre-soil model to enhance the accuracy of predicting the performance of off-road vehicles. However, nothing is yet known about the exact shape of the tyre-soil interface because of the complicated nature of the soil as well as of rubber tyres. Bekker [1,2] suggested a mathematical model for wheeled vehicles to predict sinkage and rolling resistance of tyres. Wong and Reece [3,4] produced mathematical models for predicting the performance of rigid wheels in both driven and towed conditions. Karafiath [5] proposed tyre-soil models for both driven and towed wheels. The deflected portion of the tyre was assumed to consist of a flat portion and a logarithmic spiral portion. A mathematical model of tyre-soil interaction has been derived by Baladi and Rohani [6]. The deformed boundary of the tyre was assumed to be an arc of a larger circular wheel, Fig.3. A similar tyre-soil interface shape was used to develop a mathematical model for predicting tyre performance on soil by Steiner [7]. Qun et al [8] suggested two different tyre-soil interface shapes, depending on the relative stiffness between the tyre and the soil. One of them is as described above, Fig.3, and the other is formed by a horizontal plane connected to a spiral. Okello [9] also used this latter assumption.

Different shapes of the interface between the tyre and the soil have been suggested in developing mathematical models for tyre performance prediction on soil. However, nothing is known about the sensitivity of the prediction of tyre performance in different soil conditions to the assumptions made regarding the shape of the interface. The work described here examines the effect on the prediction of assuming different shapes for the tyre-soil interface.

## 2-DESCRIPTION OF TYRE-SOIL MATHEMATICAL MODELS

Three different wheel-soil geometries have been chosen for tyre off-road tractive performance prediction. The first model considers the interface to be formed by a rounded section and a flat part, Fig.1. The second considers the interface simply as a straight line which connects the entry and rear points of contact, Fig.2. The third assumes the interface to be formed by an arc of a circle larger in diameter than the original wheel, Fig. 3. The forces generated at each point on the tyre-soil interface have been calculated using a method described by Okello[9], by determining the path of each point on the interface and the soil deformation at that point. Bekker's pressure-sinkage and shear stress-deformation relationships:

$$p = k_b z^n \quad (1)$$

$$\tau = (c + \sigma(\theta) \tan \phi) (1 - e^{-l/k}) \quad (2)$$

have been used to calculate vertical and tangential forces acting in the tyre-soil contact zone, by integrating these stresses along the contact patch.

Horizontal and vertical equilibrium equations have been formulated to calculate normal load,  $W$ , drawbar pull,  $Dp$  and rolling resistance,  $R$ .

The equilibrium equations for model No.1 are: (referring to Fig.1)

$$W = 2 \sigma B r \sin \alpha_r + \int_{\pi/2-\alpha_e}^{\pi/2+\alpha_r} (\sigma(\theta) \sin(\theta) + \tau(\theta) \cos(\theta)) B r d\theta \quad (3)$$

where:

$$\sigma = k_b z_o^n$$

$$\sigma(\theta) = k_b z^n = k_b (r \sin(\theta) - r \cos(\alpha_e))^n$$

and;

$$k_b = k_c/b + k_\phi$$

$$Dp = \int_{\pi/2-\alpha_e}^{\pi/2+\alpha_r} (\tau(\theta) \sin(\theta) - \sigma(\theta) \cos(\theta)) B r d\theta + \int_{\pi/2-\alpha_r}^{\pi/2+\alpha_r} \frac{\tau(\theta)}{\sin(\theta)} r_p B d\theta \quad (4)$$

where  $r_p$  is axle height

$$R = \int_{\pi/2-\alpha_e}^{\pi/2+\alpha_r} \sigma(\theta) \cos(\theta) B r d\theta \quad (5)$$

The equilibrium equations for model No.2 are given by: (referring to Fig.2)

$$W = \int_{\pi/2-\alpha_e}^{\pi/2+\alpha_r} (\sigma(\theta) \cos(\theta) + \tau(\theta) \sin(\theta)) B r_1 d\theta \quad (6)$$

where:

$$\theta = (\alpha_e - \alpha_r)/2$$

and;

$$r_1 = r \frac{\cos((\alpha_e + \alpha_r)/2)}{\sin(\theta + (\alpha_e - \alpha_r)/2)}$$

$$Dp = \int_{\pi/2-\alpha_e}^{\pi/2+\alpha_r} (\tau(\theta) \cos(\theta) - \sigma(\theta) \sin(\theta)) B r_1 d\theta \quad (7)$$

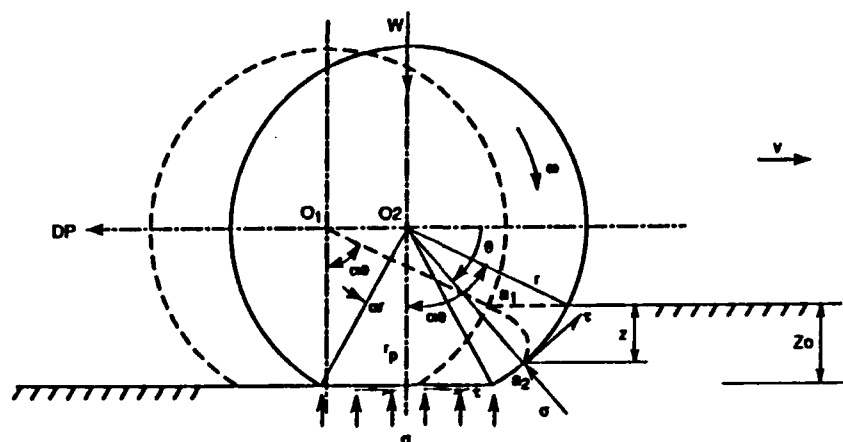


**FIG.1 TYRE-SOIL INTERACTION MODEL NO.1**

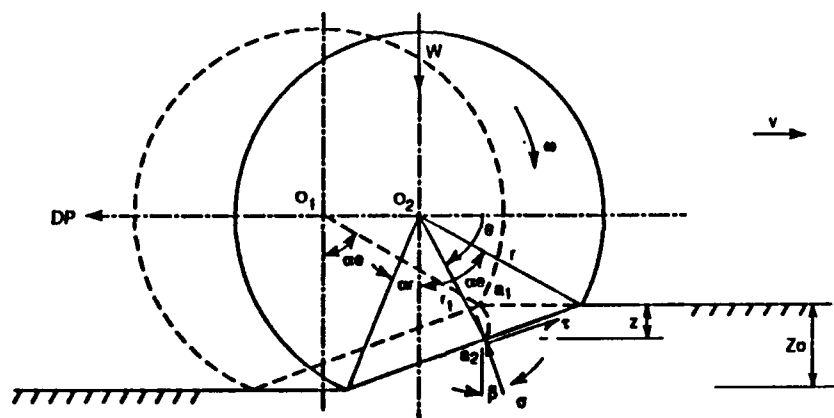


**FIG. 2 TYRE-SOIL INTERACTION MODEL NO.2**

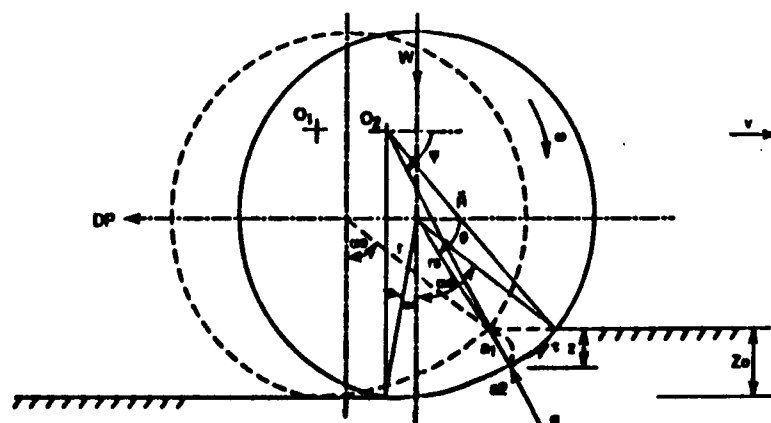


**FIG. 3 TYRE-SOIL INTERACTION MODEL NO.3**

The equilibrium equations for model No.3 are given by: (referring to Fig.3)

$$W = \int_{\pi/2-\alpha_e}^{\pi/2+\alpha_r} (\sigma(\theta)\sin(\psi) + \tau(\theta)\cos(\psi)) B r_s d\theta \quad (9)$$

where  $r_s$  is the radius at any point on the interface, given by:

$$r_s = R \frac{\cos(\psi+\beta)}{\cos(\beta+\theta)}$$

$$Dp = \int_{\pi/2-\alpha_e}^{\pi/2+\alpha_r} (\tau(\theta)\sin(\psi) - \sigma(\theta)\cos(\psi)) B r_s d\theta \quad (10)$$

$$R = \int_{\pi/2-\alpha_e}^{\pi/2+\alpha_r} \sigma(\theta)\cos(\psi) B r_s d\theta \quad (11)$$

Using the above equilibrium equations, tyre performance parameters in terms of coefficient of traction, coefficient of rolling resistance, and tractive efficiency in relation to tyre slip, for each model were calculated.

$$CT = Dp/W, \text{ and } CR = R/W$$



FIG. 4 SILSOE RESEARCH INSTITUTE SOIL PROPERTIES RIG.

### 3-EXPERIMENTAL WORK

A set of experiments has been conducted in the field, on sandy clay soil, to measure the tractive performance of tyres of sizes 12.4-36, 16.9-34, and 18.4-38 carrying loads of 15, 20, 20 kN using a single wheel tester [10]. Traction characteristics were measured and the coefficient of traction and coefficient of rolling resistance calculated. The mechanical properties of the soil in terms of  $c$ ,  $\phi$ ,  $k$ ,  $k_o$ ,  $k_\phi$ , and  $n$  were measured in situ using a soil properties rig shown in Fig.4.

Soil measurements were taken at four different sites along the test section of the field used. Shear strength and plate-sinkage tests were carried out to determine strength parameters  $c$ ,  $\phi$ ,  $k$  and pressure-sinkage parameters  $k_c$ ,  $k_\phi$ , and  $n$ , respectively.

The shear test is performed by pushing the shear head into the soil at specific normal pressure, and applying torque to it. Torque and angular displacement are recorded, through torque and displacement transducers and a tape recorder and shear stress versus shear deformation characteristics at different normal pressures were determined.

Figures 5 and 6 show examples of the relationship between shear stress and deformation and the corresponding maximum shear stress versus normal stress respectively.

Plate-sinkage tests were done using four different plate sizes: 50, 70, 100, 150 mm diameter. The test was performed by pushing the plate-sinkage ram into the soil while simultaneous recordings of normal load and vertical displacement were made. Pressure-sinkage characteristics as a plot of pressure versus sinkage for each plate size were obtained, Fig. 7.

In determining pressure-sinkage parameters a log-log plot for each pressure-sinkage curve was made and a line was fitted to the experimental data using linear regression to obtain the pressure-sinkage constant  $k_b$  and soil exponent  $n$ .

Having done that, a plot of  $k_b$  values versus  $1/b$  ( $b$  = plate radius) was obtained and, by fitting a line to  $k_b$  values, using linear regression, the soil values  $k_c$  and  $k_\phi$  were determined, Fig.8. Soil parameters of both shear and plate-sinkage tests are given in table I. These results were then used as input to a computer program for each model and the predicted performance parameters, for the three tyre sizes, were compared to the measured values obtained from the single wheel tester. It was found that the values of soil shear deformation modulus,  $k$ , calculated from the soil shear tests were too low to give good agreement with the measured results. It was necessary to assume a value of 0.03 m to obtain good agreement. This was considered to be due to the torsional deflection of the tyres adding to the effect of the deformation of the soil. Typical results are given in Figs.9, 10, and 11 and table II, assuming a value of 0.03 for  $k$ .

Table I: shear strength and plate-sinkage parameters for the tested sandy clay soil

Test Site	c kPa	$\phi$ deg.	k mm	$k_c$ $\text{kN/m}^{n+1}$	$k_\phi$ $\text{kN/m}^{n+2}$	n	m %
1	11.95	32.2	18.5	-	-	0.51	37.7
2	10.52	33.0	22.7	18.23	274.20	0.52	33.3
3	-	-	17.8	21.35	286.60	0.51	26.2
4	8.87	34.0	20.3	15.68	298.24	0.50	31.5
average	10.40	33.0	20.0	18.42	285.68	0.51	31.0

Table II: Predicted and measured CT at 20% and 50% slip and CR for the three tyre sizes

	16.9-34			12.4-36			18.4-38		
	CT*	CT**	CR	CT*	CT**	CR	CT*	CT**	CR
Model 1	0.451	0.558	0.073	0.436	0.545	0.076	0.480	0.571	0.063
Model 2	0.508	0.597	0.126	0.491	0.581	0.131	0.526	0.611	0.119
Model 3	0.578	0.643	0.085	0.563	0.631	0.088	0.592	0.653	0.080
Measured	0.476	0.624	0.119	0.376	0.499	0.141	0.490	0.587***	0.097

\*At 20% slip    \*\*At 50% slip    \*\*\*At 45.5% slip

#### 4-CONCLUSIONS

All three mathematical models predicted the general shape of the coefficient of traction-slip relationship in accordance with the measured results and values of coefficient of rolling resistance of the right order.

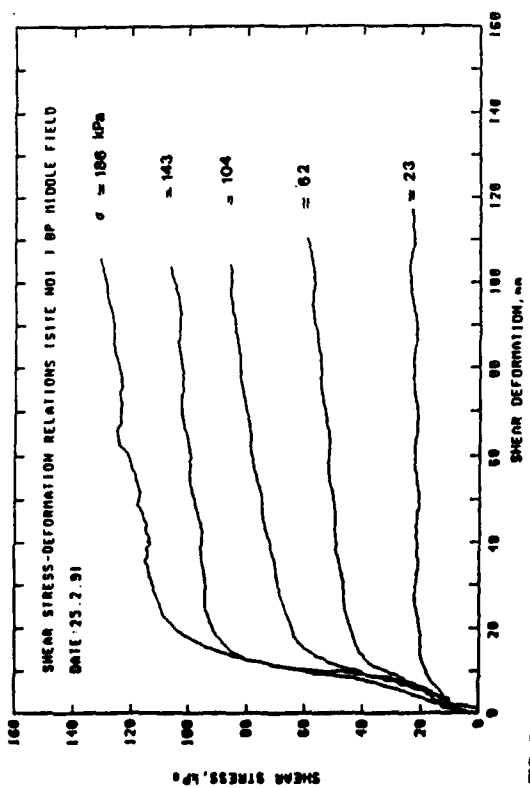


FIG. 5 SHEAR STRESS-DEFORMATION CHARACTERISTICS AT DIFFERENT NORMAL STRESSES.

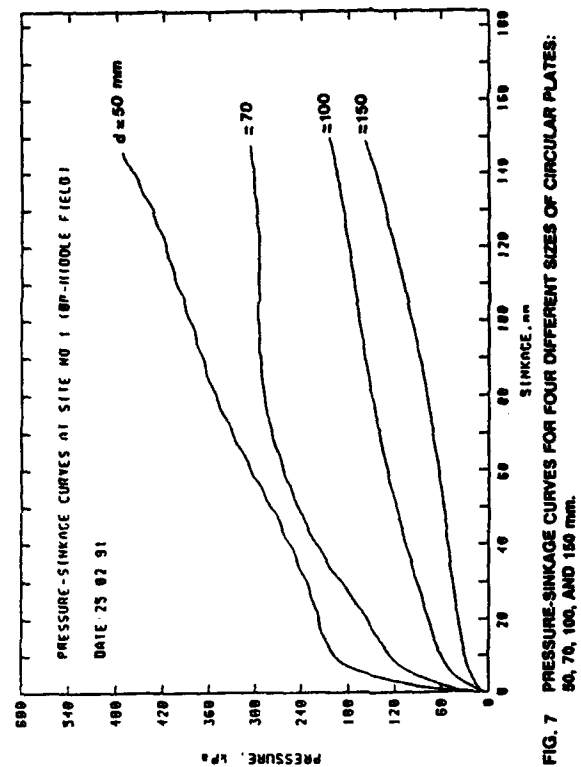


FIG. 7 PRESSURE-SINKAGE CURVES FOR FOUR DIFFERENT SIZES OF CIRCULAR PLATES: 50, 70, 100, AND 150 mm.

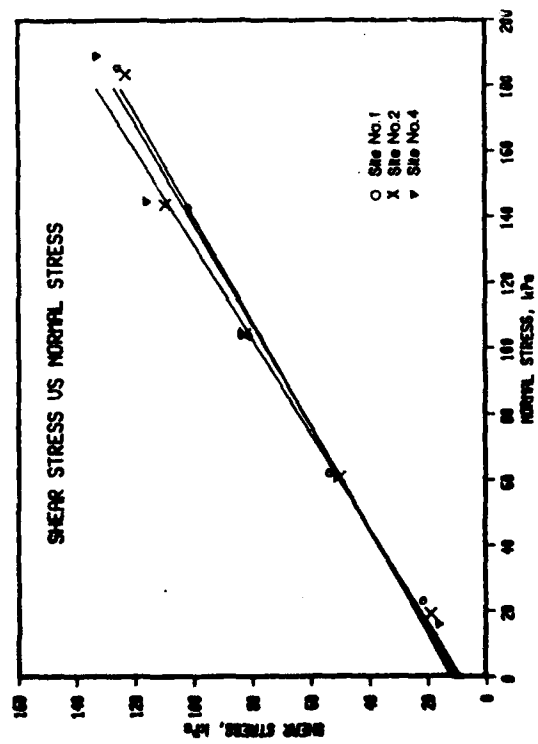


FIG. 6 MAXIMUM SHEAR STRESS VERSUS NORMAL STRESS.

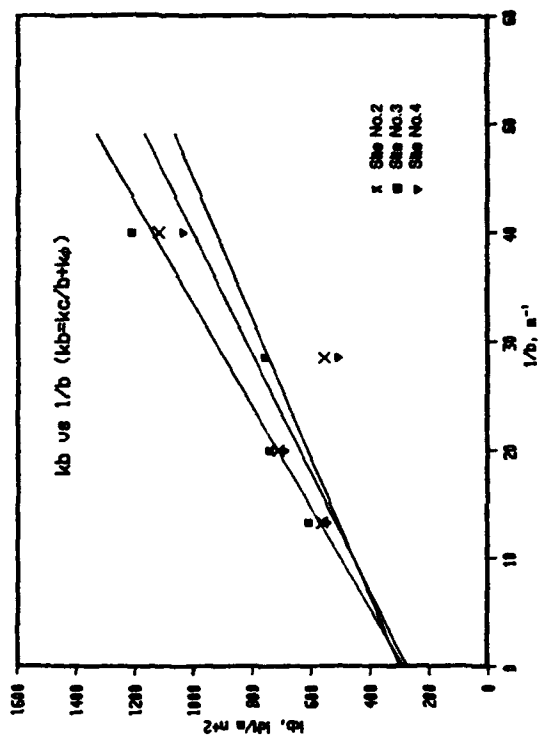


FIG. 8 PLOT OF  $K_b$  VERSUS  $1/b$  AT DIFFERENT SITES OF THE TESTED FIELD.

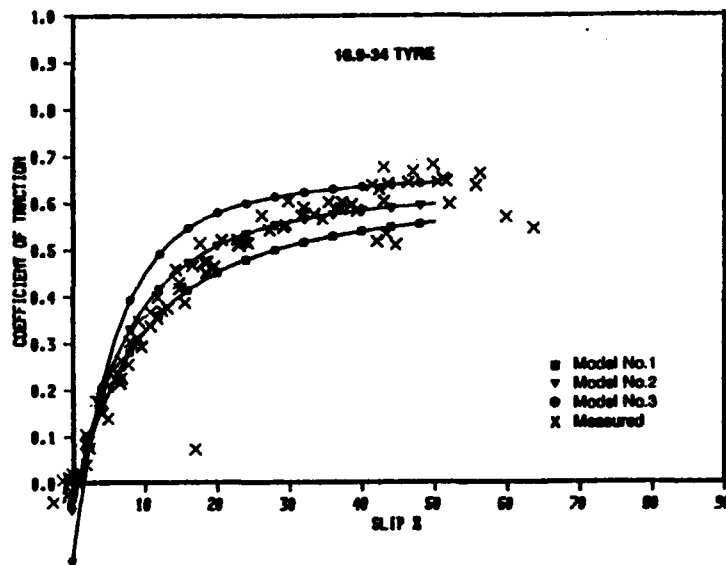


FIG. 9 PREDICTED AND MEASURED COEFFICIENT OF TRACTION-SLIP CHARACTERISTICS FOR 16.9-34 TYRE.

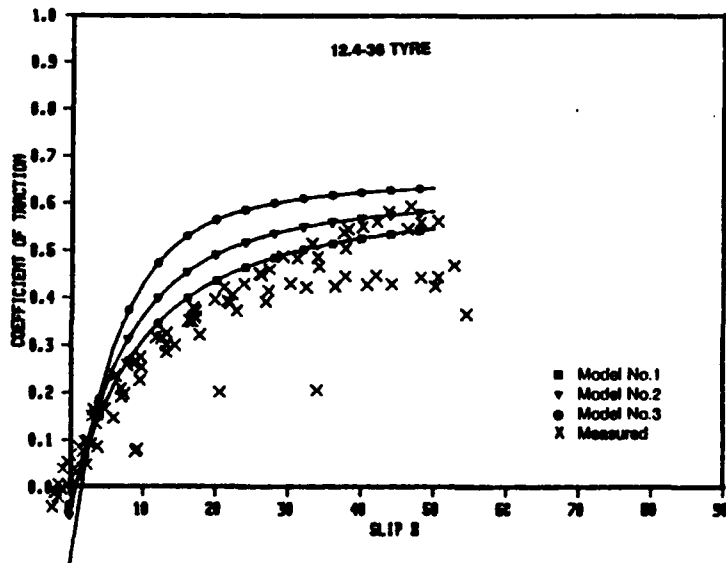


FIG. 10 PREDICTED AND MEASURED COEFFICIENT OF TRACTION-SLIP CHARACTERISTICS FOR 12.4-36 TYRE.

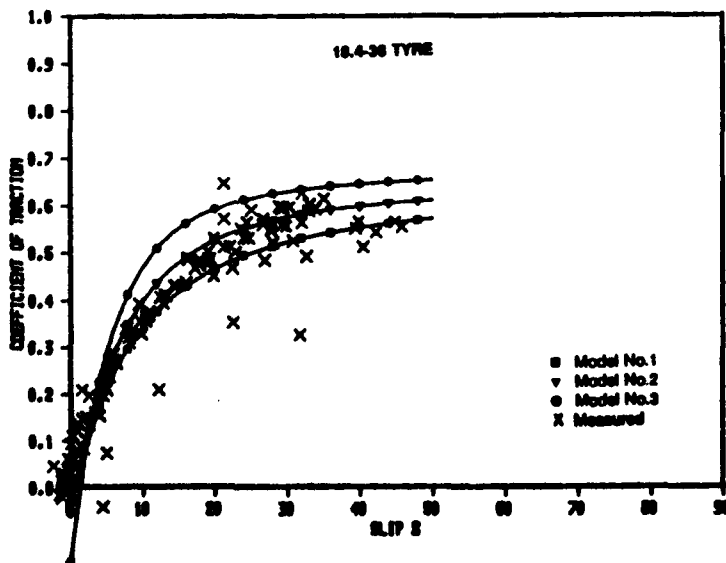


FIG. 11 PREDICTED AND MEASURED COEFFICIENT OF TRACTION-SLIP CHARACTERISTICS FOR 18.4-36 TYRE.



The best all round agreement between measured and predicted results was achieved with the second model, which assumed that the shape of the interface between the tyre and the soil was a sloping plane joining the frontmost and rearmost points of contact.

The exact shape of the coefficient of traction-slip relationship could only be predicted correctly if the soil shear deformation modulus,  $k$ , was increased from its calculated value of approximately 0.02 m to 0.03 m. This was believed to be because the theory assumes that all longitudinal deformation occurs in the soil, whereas, in practice, there is also torsional deformation of the tyre, which contributes to slip. Further research will be carried out to include this effect in the models and to compare the results with these predicted using Okello's assumed shape for the interface [9].

## 5-REFERENCES

- [1] M.G.Bekker "Theory of Land Locomotion" University of Michigan Press, Ann Arbor, Michigan, 1956
- [2] M.G.Bekker "Off-the-Road Locomotion" University of Michigan Press, Ann Arbor, Michigan, 1960
- [3] J.Y.Wong and A.R.Reece "Prediction of Rigid Wheel Performance Based on the Analysis of Soil-Wheel Stresses" Part I: Performance of Driven Rigid Wheels. J.Terramech., Vol.4, No.1, 1967
- [4] J.Y.Wong and A.R.Reece "Prediction of Rigid Wheel Performance Based on the Analysis of Soil-Wheel Stresses" Part II: Performance of Towed Rigid Wheels. J.Terramech., Vol.4, No.2, 1967
- [5] L.L.Karafiath "Running Gear-Soil Modeling for Off-Road Vehicles" Proceeding of 5th Int. Conference of ISTVS, 1975.
- [6] G.Y.Baladi, B.Rohani "Development of Soil-Wheel Interaction Model" Proceeding of 8th Int. Conference of ISTVS, 1984
- [7] M.Steiner "An Analysis of the Traction-Slip Curve of Tyres Calculated from the Loss Factors and Stress Distribution" Proceeding of 6th Int. Conference of ISTVS, 1978
- [8] Y.Qun, G.Sunrong and Y.Guyuan "On the Modelling and Simulation of Tyre-Soil System" Proceeding of 9th Conference of ISTVS, 1987.
- [9] J.A.Okello "Prediction of Force Distribution Between the Soil and The Wheel or Track" Proceeding of the International Conference of Agricultural Engineering, AG. ENG. 90, Berlin, 1990
- [10] W.P.Billington "The NIAE MKII Single Wheel Tester" J. Agric. Engng. Res., 1973, 18, 67-70

## NOTATION

- $b$  plate radius, m
- $B$  tyre section width, m
- $c$  soil cohesion, kPa
- CT coefficient of traction
- CR coefficient of rolling resistance
- $d$  tyre diameter, m
- $D_p$  drawbar pull, kN
- $j$  soil deformation, m
- $k$  soil shear deformation modulus (rate constant), m
- $k_b$  Bekker's pressure-sinkage constant,  $\text{kN/m}^{n+2}$
- $k_c$  soil cohesive modulus in Bekker's pressure-sinkage eq.,  $\text{kN/m}^{n+1}$
- $k_\phi$  soil frictional modulus in bekker's pressure-sinkage eq.,  $\text{kN/m}^{n+2}$
- $m$  soil moisture content, %
- $n$  soil exponent in Bekker's pressure-sinkage equation
- $p$  normal pressure on plate, kPa
- $r$  tyre radius, m
- $\bar{R}$  radius of a circle containing the deflected portion of the tyre, m
- $R$  rolling resistance, kN
- $s$  tyre slip
- $v$  forward speed, m/s
- $W$  wheel load, kN
- $z$  sinkage at any point on the interface, m
- $Z_0$  maximum wheel sinkage, m
- $\alpha_e$  entry angle (angle between front point of contact and vertical centre line), deg.
- $\alpha_r$  rear angle (angle between vertical centre line and rear point of contact), deg.
- $\phi$  soil angle of internal friction, deg.
- $\theta$  angle between horizontal centre line and any point on the interface, deg
- $\omega$  wheel angular speed, rad./sec
- $\tau$  soil shear stress, kPa
- $\sigma$  soil normal stress, kPa

# **FRICITION BETWEEN RUBBER TRACK PADS AND GROUND SURFACE WITH REGARD TO THE TURNING RESISTANCE OF TRACKED VEHICLES**

St. Pott

University of the Federal Armed Forces Hamburg, Germany  
Institute of Automotive Engineering

## **SUMMARY**

The turning resistance of tracked vehicles has been described in several analytical models. They use the principle of isotropic Coulomb's friction between a rubber track pad and the ground surface or the so-called turning resistance coefficient as an auxiliary. So far, the turning resistance coefficient has been obtained from measurements with the total tracked vehicle. It depends on the radius of the curve.

However, friction really does not depend on the turning radius. Therefore the physical phenomena, which result in the dependance of the turning resistance coefficient from the radius, are to be explored. Among those the lateral elasticity of the track pad was identified to be of great importance.

At the Institute of Automotive Engineering a test stand was built to examine lateral deformation and friction behaviour of a track pad. The following factors are changed during a test: ground pressure, slip angle, slip velocity, slip length and ground surface.

Some results will be presented in this paper. The friction coefficient does not clearly depend only on the ground surface but also on ground pressure, velocity and direction of slip. In the range of elastic pad deformation it also depends on slip length.

These results will be built into the analytical models describing the turning resistance.

## **1. INTRODUCTION THE TURNING RESISTANCE OF TRACKED VEHICLES**

During driving a curve with tracked vehicles the turning resistance is added to the motion resistances of straight ahead motion. The turning resistance is of special interest, because it is exacting to the propulsion system to realise high propulsion and braking forces at the tracks.

EHLERT [5,6,7] has improved analytical models of the turning resistance [1,2,3,4]. These models base either on the principle of isotropic Coulomb's friction between the rubber track pads and the ground surface or on empirical results, which are found by field measurements [5,6]. So the turning coefficient (fig. 1) is used as an auxiliary to determine the turning momentum of a tracked vehicle. It depends on the radius of a curve. It covers all the effects between the tracks and the ground surface.

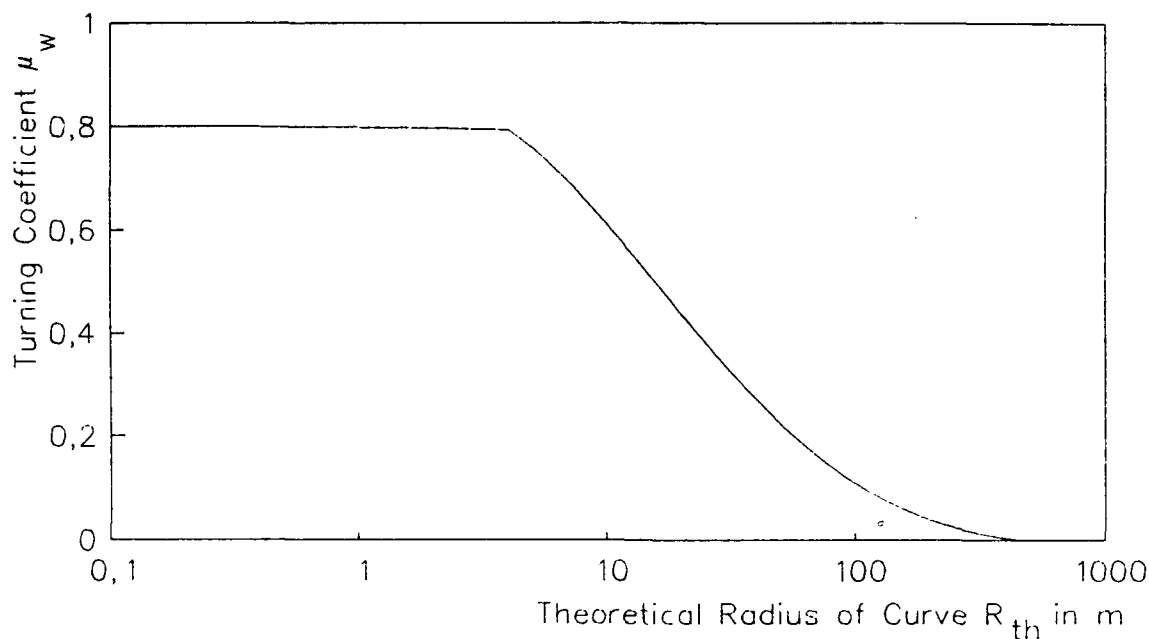


Figure 1: The turning coefficient of a 26-t-tank founded by EHLERT [6]

At the Institute of Automotive Engineering a test stand was developed to examine both lateral deformation of a rubber track pad and friction behaviour in the surface of contact between the tracks and the runway.

## 2. TEST STAND AND TEST CONDITIONS

The experiments to determine the coefficients of friction and the elasticity of a rubber track pad are carried out on a servo-hydraulic test stand (fig. 2).

This test stand is based on the principle of kinematical reversal: an element of road surface is pulled under a track shoe which is vertically loaded. The track shoe can be turned, so the angle of pull can be varied from  $0^\circ$  in longitudinal direction of the track upto  $90^\circ$  across.

The test piece was a rubber track pad DIEHL 228. The experiments are performed under the conditions of constant vertical load and slip velocity. The load was changed from  $F_z = 1 \text{ kN}$  (ground pressure  $p_B = 0.04 \text{ N/mm}^2$ ) to  $52 \text{ kN}$  ( $p_B = 2.26 \text{ N/mm}^2$ ). The maximum slip velocity had a value of  $25 \text{ mm/s}$ .

Measured values are the vertical load and the stroke, the horizontal force and the lateral deflection of the element of ground surface.

Figure 3 shows the horizontal force  $F_s$  versus lateral deflection  $s_s$ . In the beginning there is only elastic deformation of the rubber track pad without any slip motion. The horizontal force ascends nearly linear with the deflection. Further displacement leads to complete slipping between the pad and the ground surface,  $F_s$  is constant. After reaching the desired maximum of deflection the direction of pull was reversed. The rubber track pad is deformed elastically into the opposite direction until renewed steady slipping will be reached. There is still a horizontal force after reaching the starting position until entire removal of the vertical load.



Figure 2: Servo-hydraulic test stand to determine the transfer of force between a rubber track pad and the ground surface



Figure 3: Test cycle: Lateral force on a track pad versus horizontal movement

### 3. TEST RESULTS

Figure 4 shows the lateral stress  $p_s$  versus the displacement  $s_s$  depending on the ground pressure  $p_B$ . In these experiments  $p_B$  is considered as

$$p_B = \frac{F_z}{A} \quad (1)$$

and  $p_s$  is considered as

$$p_s = \frac{F_s}{A} \quad (2)$$

where  $A$  represents the basal surface of the rubber track pad.

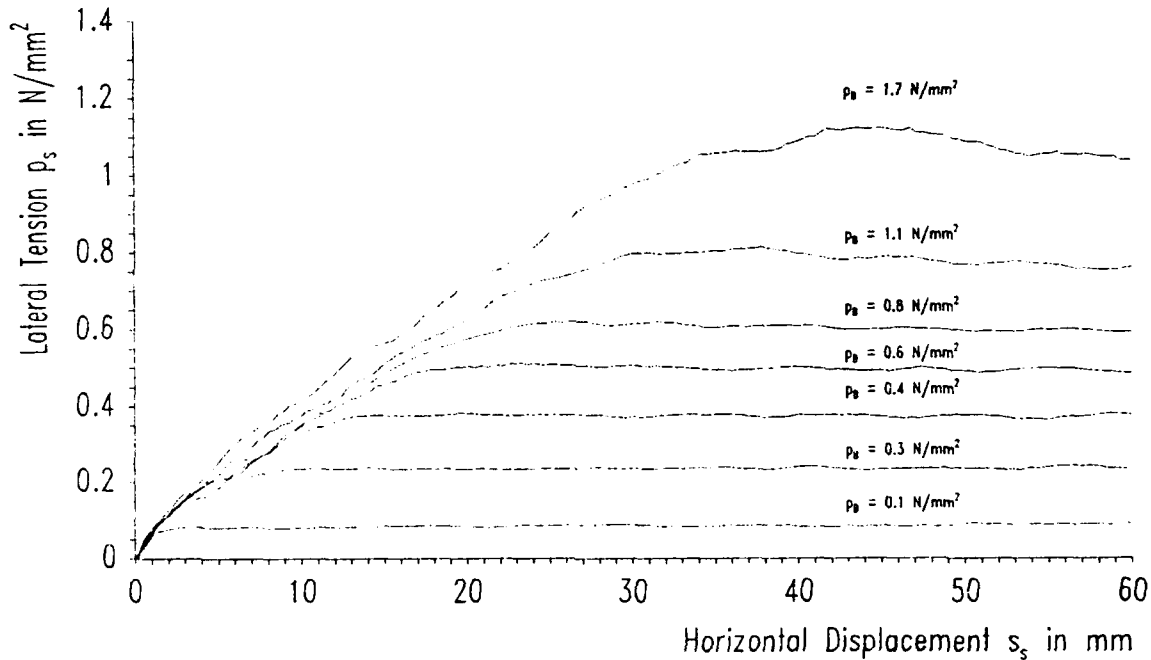


Figure 4: Lateral tension  $p_s$  depending on the displacement  $s_s$  at different ground pressures  $p_B$ , angle of pull:  $90^\circ$

The shape of the curves  $p_s = f(s_s)$  are similar in principle at different ground pressures. Elastic deformation of the pad can be observed in the range of small deflections. The maximum value of the elastic deformation depends on vertical load. After crossing the point of static friction the lateral tension is constant. The relation between the horizontal tension and the ground pressure can be described by the coefficient of friction  $\mu$ .

#### 3.1 THE COEFFICIENT OF FRICTION

Figure 5 shows the coefficient of friction as a function of ground pressure at different slip

angles. Increasing the ground pressure leads to a nearly linear descend of the coefficient. The Slip angle does not influence this behaviour.

This function can be described as

$$\mu = \mu_0 + a \cdot p_B \quad (3)$$

$$\text{with } \mu_0 = 0.93 \text{ and } a = -0.196 \text{ mm}^2/\text{N}.$$

Also this straight line is shown in figure 5.

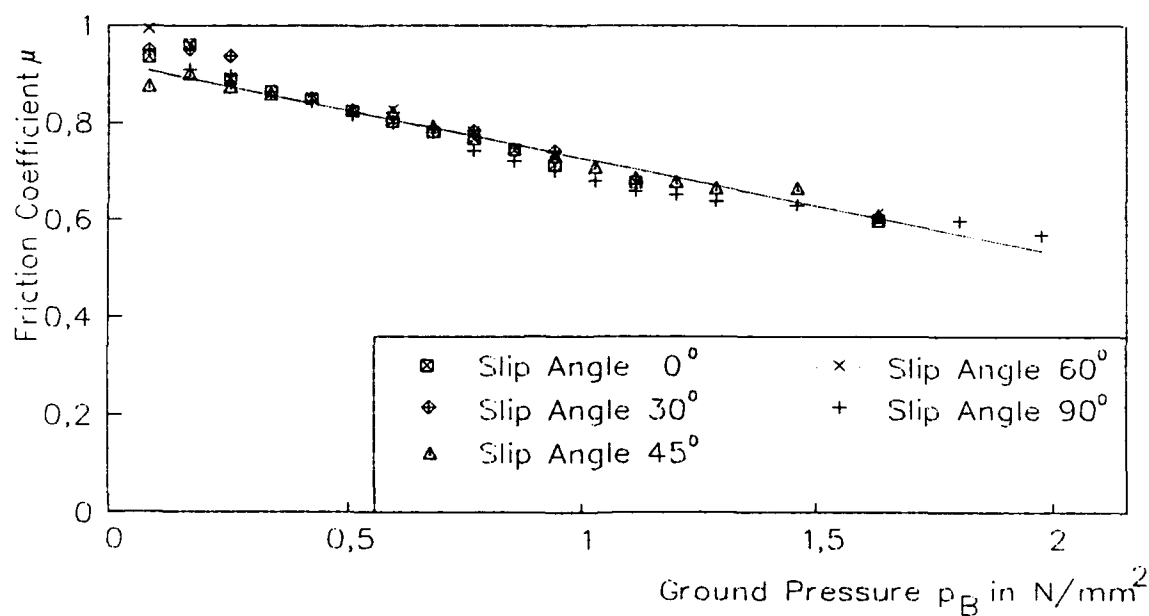


Figure 5: The coefficient of friction as a function of ground pressure

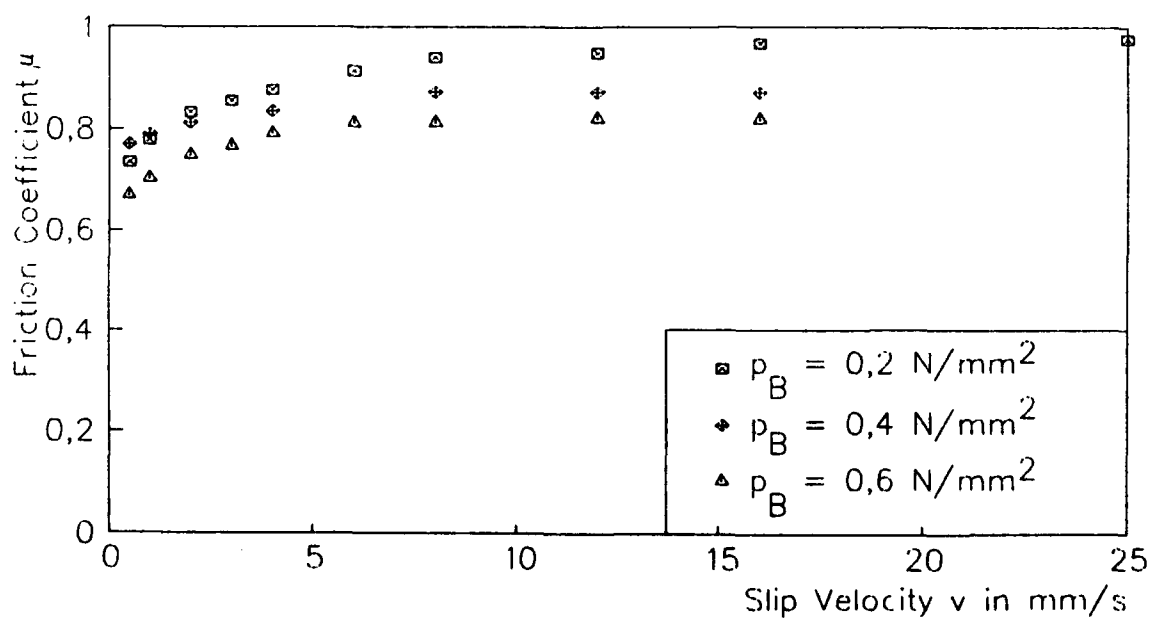


Figure 6: The coefficient of friction as a function of slip velocity

The coefficient of friction in the friction area between a rubber track pad and the concrete surface depends on the slip velocity (fig. 6). Within the range of small velocities ( $v < 10 \text{ mm/s}$ ) the measured curve rises in a degressive way. If the slip velocity is higher than  $10 \text{ mm/s}$  the coefficients of friction approach to a constant value. They only depend on ground pressure.

REIMPELL, SPONAGEL [8] and GEYER [9] examined the friction between rubber tires and ground surfaces. They made similar observations as the above observations on track pads. The coefficient of friction between a tire and concrete also depends on ground pressure and slip velocity. This is different from the classical physical laws of friction. It can be regarded, that the influence of the slip velocity is not as high between a rubber track pad and concrete as between a rubber tire and concrete.

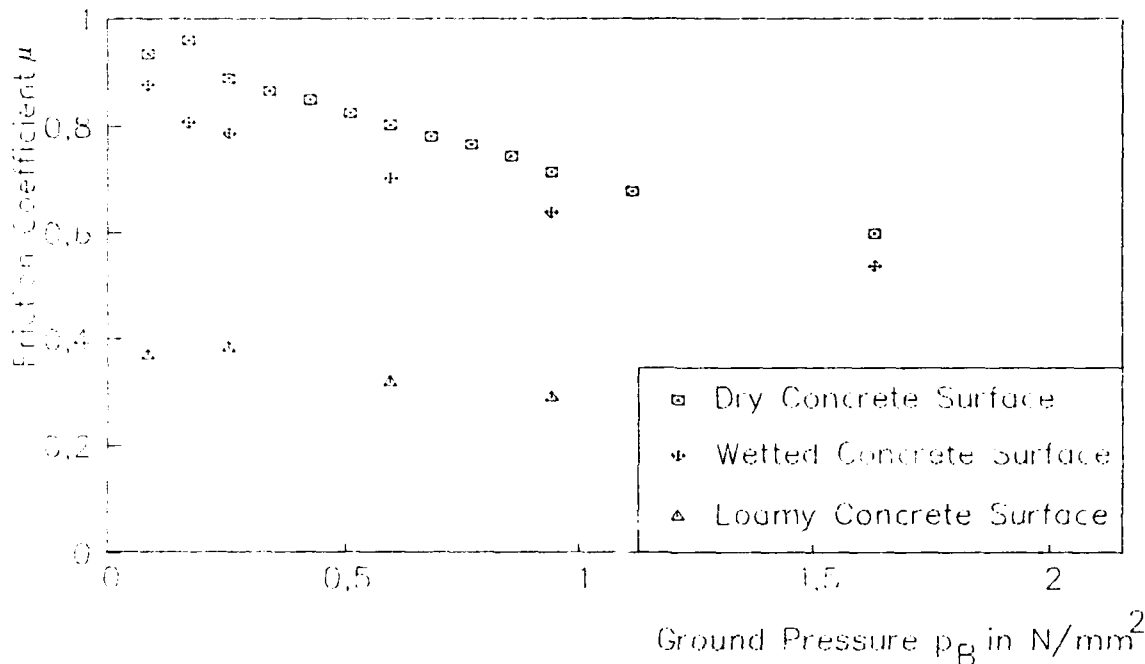


Figure 7: The coefficient of friction depending on ground surface

The influence of ground surface on the friction behaviour is shown in figure 7. The coefficient of friction is smaller on a wetted concrete surface than on a dry concrete surface. The linearity between coefficient of friction and ground pressure is valid. The conditions change on a dirty concrete surface. Only rather small coefficients of friction can be reached on a loamy concrete surface (fig. 7). They are below 0.4. An increased ground pressure does not influence the coefficient as much as on dry or wetted concrete surface.

### 3.2 THE ELASTIC DEFORMATION OF THE RUBBER TRACK PAD

The horizontal tension  $p_s$  is proportional to the horizontal deflection  $s_s$  until the coefficient of friction is reached (fig. 4). In this range of small deflections the tension  $p_s$  is independent of the ground surface. It only depends on the elastic deformability of the rubber without any sliding movements between track pad and ground surface. The deflection rate of elasticity  $c_s$  can be defined as:

$$c_s = \frac{dp_s}{ds_s} \quad (4)$$

$c_s$  is shown in figure 8:

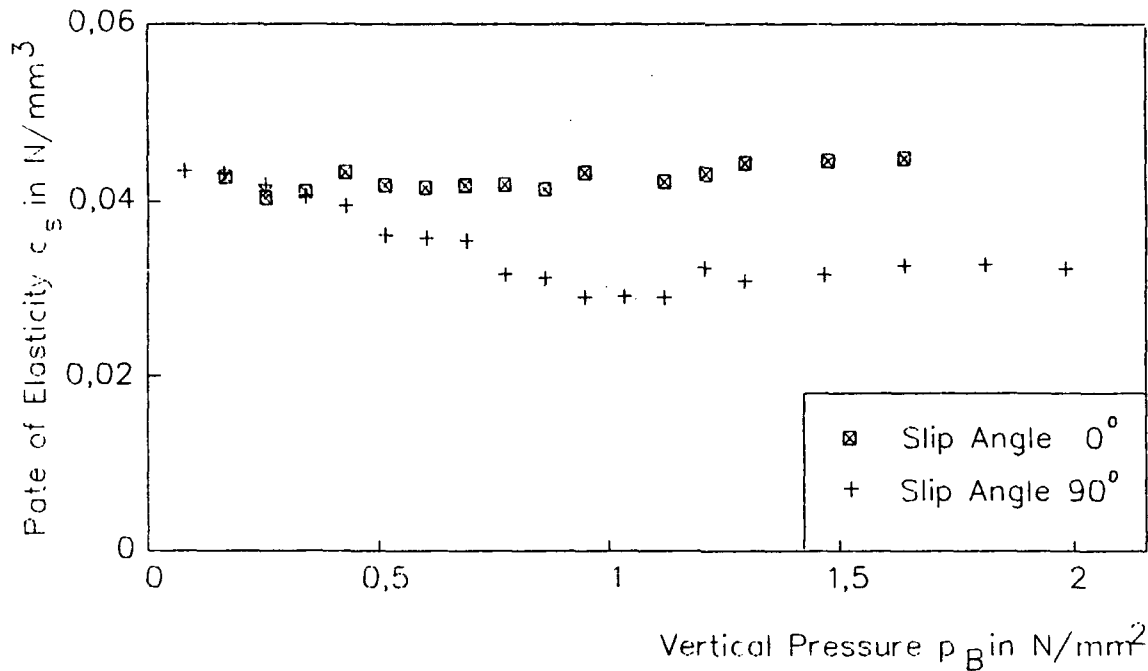


Figure 8: The rate of elasticity of the rubber track pad depending on vertical pressure

It was found, that the rate of elasticity depends on the angle of pull. During pull in the longitudinal axis of a track (0°) it ascends with higher vertical pressures. Crosswise to this direction (90°) it decreases with increasing vertical pressures. However it stabilizes on a reduced level. The design of the body of the considered track pad allows more elastic deformation crosswise to the longitudinal axis.

#### 4. CONCLUSIONS IN REGARD TO ANALYTICAL MODELS

Horizontal forces between a rubber track pad and the ground surface always are combined with horizontal displacement between the track and the ground surface.

The measurement results show, that elastic deformations of a rubber track pad can reach values up to 30 mm. The lateral movements of a track during a curve with a large turning radius will be picked up in this elasticity without sliding movements.

In the range of small deflections there is only elastic deformation of the rubber track pad without sliding movements between track pad and ground surface. The transmittable horizontal tensions depend on ground pressure, slip angle and on the quality of the ground surface.

Sliding movements between track and ground surface occur, if the horizontal deflection ex-



ceeds the deformation capability of the rubber. The coefficient of friction declines in a linear way depending on ground pressure, it depends on slip velocity and ground surface, but it is independent of angle of pull.

The experiments lay the basics for an analytical description of the real forces between a tracked vehicle and the ground surface with the goal to replace the empirical turning coefficient.

Further experiments were carried out to determine the hysteresis losses in the rubber track pads. These losses are of influence to the rolling resistance of a tracked vehicle.

## 5. REFERENCES

- [1] J. Hock: Lenkgetriebe für Kettenfahrzeuge, Firmenschrift, ZF Friedrichshafen, 1970
- [2] IABG, not published
- [3] M. Kitano, H. Jyozaki: A theoretical analysis of steerability of tracked vehicles, Journal of Terramechanics, 1976, Vol. 13, No. 4, pp. 241-258
- [4] M. Kitano, M. Kuma: An analysis of horizontal plane motion of tracked vehicles, Journal of Terramechanics, 1977, Vol. 14, No. 4, pp. 211-225
- [5] W. Ehlert, St. Pott: Bodenmechanische Einflüsse auf den Wendewiderstand von Gleiskettenfahrzeugen, IKK-Bericht Nr. 89-19, Universität der Bundeswehr Hamburg, 1989
- [6] W. Ehlert: Simulation der Fahrwiderstände von Gleiskettenfahrzeugen auf dem Prüfstand, insbesondere bei Kurvenfahrt, Universität der Bundeswehr Hamburg, Diss. 1990 (Entwurf)
- [7] W. Ehlert, B. Hug, I.C. Schmid: Field Measurements and Analytical Models as Basis of Test Stand Simulation of the Turning Resistance of Tracked Vehicles, Proc. of the 10th International Conference of the ISTVS, Kobe, Vol. III, pp. 601-612
- [8] J. Reimpell, P. Sponagel: Fahrwerktechnik - Reifen und Räder, Vogel-Verlag Würzburg, 1986
- [9] W. Geyer: Beitrag zur Gummireibung auf trockenen und nassen Oberflächen, Automobil-Industrie 4/70, S. 87-96

# THE CALCULATION OF PRESSURE-SINKAGE CURVES BASED ON SHEAR STRENGTH MEASUREMENTS

P.J.Wagner

University of the Federal Armed Forces Hamburg, Germany  
Institute of Automotive Engineering

## SUMMARY

The prediction of cross country mobility is based on different soil mechanics and vehicle specific parameters. According to the off-road-mobility model by Bekker the tractive effort and the rolling resistance are decisive for this prediction. The tractive effort is determined by the parameters of the shear strength, namely cohesion, angle of internal friction, further the contact-area between wheel and soil and the wheel-load. The rolling resistance depends on the wheel-sinkage. The calculation of this resistance is based till now on plate-pressure measurements in the field. These measurements require a lot of effort. The results are illustrated in pressure -sinkage curves.

A comparison between the results of shear strength measurements with accompanied pressure-sinkage curves from different soils, offers a clear correlation between pressure-sinkage and the shear strength properties, friction angle  $\varphi$  and cohesion  $c$ . This correlation can be explained with the MOHR's stress circle.

With a new model it is demonstrated, how to calculate pressure-sinkage curves independent of soil type, moisture content and soil density from the angle of internal friction  $\varphi$  and the cohesion  $c$ . With this model the calculation of tractive effort and rolling resistance are based on the results of shear strenght measurements only.

## 1. INTRODUCTION

The mechanical description of the soil strength to predict off-road-mobility is based till now on two different mechanical properties, the shear strength and the pressure-sinkage relationship. The shear strength  $\tau$  is described by MOHR using friction angle  $\varphi$  and cohesion  $c$  in the well known stress circle [1][2] (Fig. 1).

$$\tau = c + \tan\varphi * \sigma \quad (1)$$

$\sigma$  = ground pressure

The pressure-sinkage relationship is described in a pressure(p)-sinkage(z) curve. For this curve GORJATCHKIN [3] and BEKKER [4], [5] formulated the following equation:

$$p = k \cdot z^n \quad (2)$$

$k$  = Modulus of soil deformation

At the Institute of Automotive Engineering in Hamburg many shear and pressure-sinkage measurements were carried out with different soil types. The results of these measurements indicate a direct correlation between these two different kinds of soil strength measurements. In fine grain soils like clay and loam either the deformation resistance of the plate-pressure test or the shear strength is low. In contrast to these soft soils the shear strength and the plate-pressure resistance are high in coarse grain sands and gravels.

In order to find a systematic correlation between shear strength and pressure-sinkage relationship it is necessary to compare the results from measurements in the same soil with constant moisture content and density. Using this correlation a soil-mechanic model can be formulated to calculate pressure-sinkage curves with the shear strength parameters friction angle  $\varphi$  and cohesion  $c$ .

## 2. TEST PROCEDURE

In order to define the correlation between shear strength and pressure-sinkage relationship five different soils were chosen. The grain size distribution of the investigated soils reach from a clay over different loams to a fluvial sand [6].

The shear strength measurements were carried out with two different direct shear devices: a well-known standard simple shear device and a new field shear device, the Shear-pressure-cylinder (Fig.2), developed by the author. For the determination of friction angle and cohesion, 9 shear tests with rising ground pressures from 3N/cm<sup>2</sup> to 48N/cm<sup>2</sup> were carried out [7].

The plate-pressure tests were carried out in the field and in soil bins, which were filled with the prepared soils[8][9][10]. The sizes of the used circular plates reached from 150cm<sup>2</sup> to 900cm<sup>2</sup>.

## 3. TEST RESULTS

The correlation between shear and pressure-sinkage results is based on the stress distribution under the penetrating plate, Fig 3. The deformation pressure  $p$  of the plate-pressure test is defined as the main stress  $\sigma_1$ . The value of  $\sigma_1$  or  $p$  (3) depends on the calculated deflection angle  $\theta'(\varphi)$  and the cohesion  $c$  [11], see eqs. (3) and (4).

$$\sigma_1 = f(\theta', c) \quad (3)$$

$$\theta' = 45 + \frac{\varphi}{2} \quad (4)$$

According to equation (4) the deflection angle  $\theta'$  of soils with a friction angle of  $\varphi = 0^\circ$  amounts to  $45^\circ$ . Independent of the sinkage the maximum deformation pressure  $p$  or  $\sigma_1$  of a plate-pressure test is limited by the value of the cohesion  $c$ . In soils with friction angles  $\varphi > 0^\circ$  ( $\theta' > 45^\circ$ ) the deformation pressure increases continuously with rising sinkage over the value of the cohesion  $c$  (Fig 4).

In order to correlate the measured shear parameters ( $\theta'(\varphi)$  and  $c$ ) with the results of the plate-pressure tests the recorded pressure-sinkage curves are expressed in terms of two angles,  $\alpha_1$  and  $\alpha_2$ , as shown in fig. 5 and eqs. (5) and (6).  $\alpha_1$  and  $\alpha_2$  are related to the shape of the  $p(z)$  - curve in the following ranges of sinkage: 0cm - 10cm( $\alpha_1$ ) and 10cm - 30cm( $\alpha_2$ ). The cohesion  $c$  is subtracted from the  $p(z)$  - curve.

$$\alpha_1 = \frac{p_{10}}{z_{10}} \quad (5)$$

$$\alpha_2 = \frac{(p_{30} - p_{10})}{(z_{30} - z_{10})} \quad (6)$$

Fig. 6 shows the measured relationships between the rising-angles of the five investigated soils and the accompanied deflections angles  $\theta'(\varphi)$ . According to Fig 5 and 6 the pressure values  $p_{10}(z_{10})$ ,  $p_{30}(z_{30})$  can be calculated independent of the soil type from the following linear equations (7) and (8), using given values for  $\alpha_1(\theta')$  and  $\alpha_2(\theta')$ .

$$p_{10} = \tan \alpha_1(\theta') * z_{10} \quad (7)$$

$$p_{30} = p_{10} + \tan \alpha_2(\theta') * (z_{30} - z_{10}) \quad (8)$$

According to eq. 9, based on the equation by GORJATCHKIN and BEKKER (eq. 2), the pressure sinkage curve can be estimated from given values of  $p_{10}$ ,  $p_{30}$ ,  $\theta'(\varphi)$  and  $c$ .

$$p = k'(\theta', c) * \left[ \frac{z}{z_{10}} \right]^{n(\theta', c)} \quad (9)$$

$z$  = Sinkage [cm]

With this new soil-mechanic model it is possible to calculate pressure-sinkage curves independent of soil type, moisture content and density, using the shear strength properties deflection angle  $\theta'(\varphi)$  and cohesion  $c$ , only. Considering equation (9) at the points  $(z_{10}, p(z_{10}))$  and  $(z_{30}, p(z_{30}))$  the parameters  $k'$  and  $n$  can be calculated. This leads to the following equation for  $p(z)$ :

$$p = (p_{10} + c) * \left[ \frac{z}{z_{10}} \right]^{\frac{\ln((p_{30}+c)/(p_{10}+c))}{\ln(z_{30}/z_{10})}} \quad (10)$$

In Fig. 7 the results of measured (thin lines) and calculated (fat lines) pressure-sinkage curves are illustrated. All calculated curves from clay, loam and sand are very good positioned in the range of variation of the measured pressure-sinkage curves. According to this result it is possible to replace most of the plate-pressure tests, which require a lot of expenses and efforts, by simple handling shear strengths measurements (Shear-pressure-cylinder).

### REFERENCES

- [1] KEZDI, A.: Handbuch der Bodenmechanik Band 1, Bodenmechanisches Versuchswesen, VEB Verlag für Bauwesen, Verlag der Ungarischen Akademie der Wissenschaften Budapest, 1969.
- [2] KEZDI, A.: Handbuch der Bodenmechanik, Bodenphysik. VEB Verlag für Bauwesen Berlin, Verlag der Ungarischen Akademie der Wissenschaften Budapest, Bd 3, 1971.
- [3] GORIATCHKIN, B. P. et al: Teoria i proizvodstvo sielskohosiyaynih mashin (Theory and production of agricultural equipment), Moscow 1936.
- [4] BEKKER; M.G.: Theory of Land Locomotion. The University of Michigan Press, Ann Arbor, Michigan, 1956.
- [5] BEKKER, M.G.: Off-the-Road-Locomotion. The University of Michigan Press, Ann Arbor, Michigan, 1960.
- [6] WAGNER, P. J.: Einfluß bodenphysikalischer Kennwerte auf die Bodenfestigkeit. Tagungsband 6.Arbeitstreffen der Auftragnehmer von BMVg-Rü III 5, Bundesministerium der Verteidigung, Februar 1990.
- [7] WAGNER, P. J.: Beurteilung der Bodenbefahrbarkeit aufgrund der Korngrößenverteilung, Dichte und Feuchtigkeit. Institut für Kraftfahrwesen und Kolbenmaschinen der UniBWHH Bericht Nr. 90-02, Juni 1990.
- [8] HOLM, C.; HINTZE, D.; HEFER, G.: Einfluß der Form und der Größe des Eindringkörpers auf die Druck-Einsinkungsbeziehung in weichen Böden. Institut für Kraftfahrwesen und Kolbenmaschinen der UniBWHH Bericht Nr. 87-06, 1987.
- [9] GRAHN, M.; HEIMING, G.; HOLM, C.: Experimentelle und theoretische Vergleichsuntersuchung von Rollwiderstand und Zugkraft verschiedener Fahrzeuge in verschiedenen Böden. Institut für Kraftfahrwesen und Kolbenmaschinen der UniBWHH Bericht Nr. 87-12, 1987.

- [10] HOLM, C.: Das Verhalten von Reifen beim mehrmaligen Überfahren einer Spur auf nachgiebigem Boden und der Einfluss auf die Konzeption mehrachsiger Fahrzeuge. Diss. VDI-Verlag GmbH Düsseldorf, Reihe 14 Nr.17, 1972.
- [11] BÖLLING, H. W.: Zusammendrückung und Scherfestigkeit von Böden. Springer-Verlag Wien, New York, 1971.

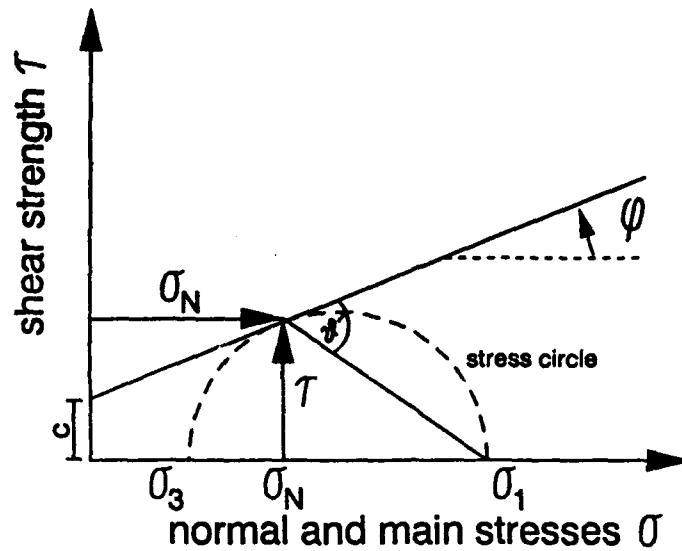


Fig. 1: Model of the MOHR's stress circle

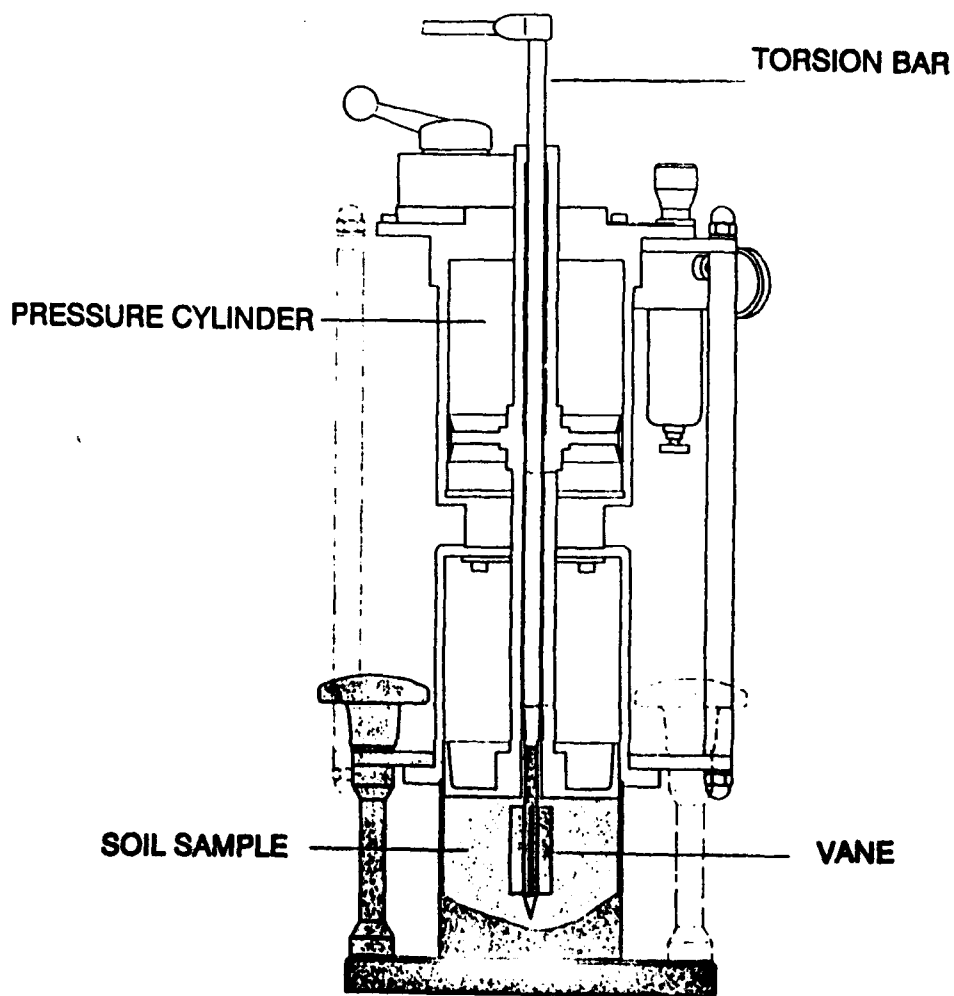


Fig. 2: Sketch of the new field shear device "Shear-pressure-cylinder"

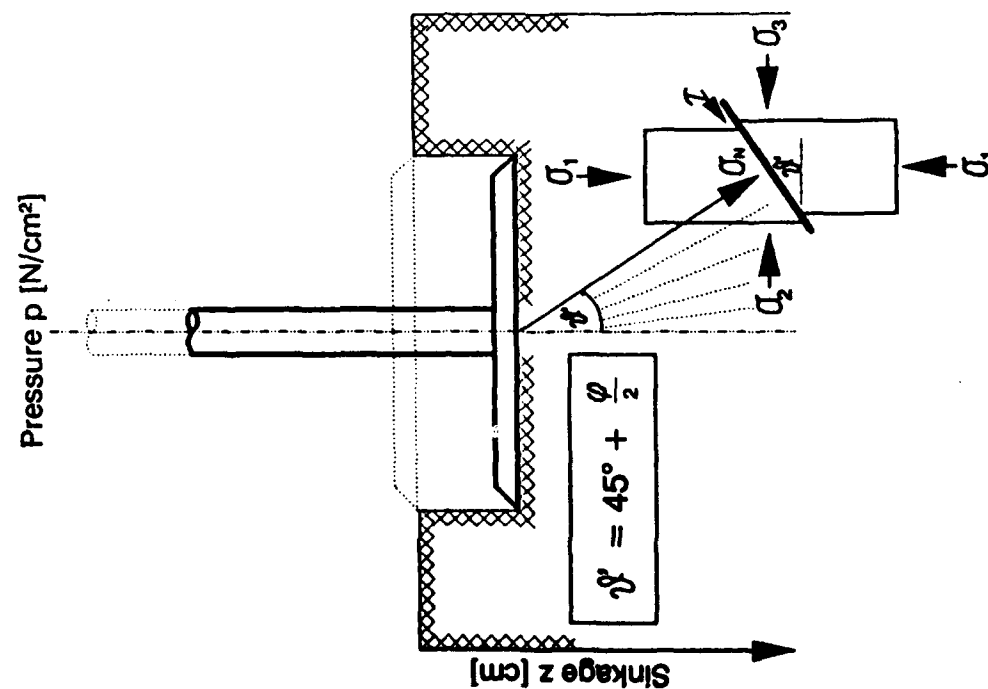


Fig. 3: Stress distribution under the penetrating plate

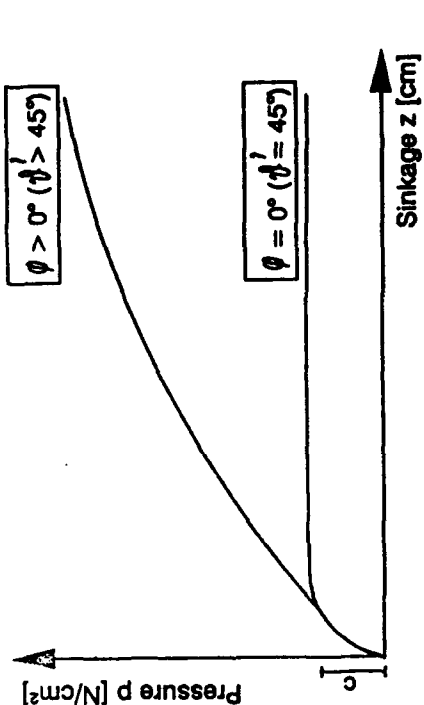


Fig. 4: Schematic influence of the cohesion and the deflection angle on the plate-pressure curves

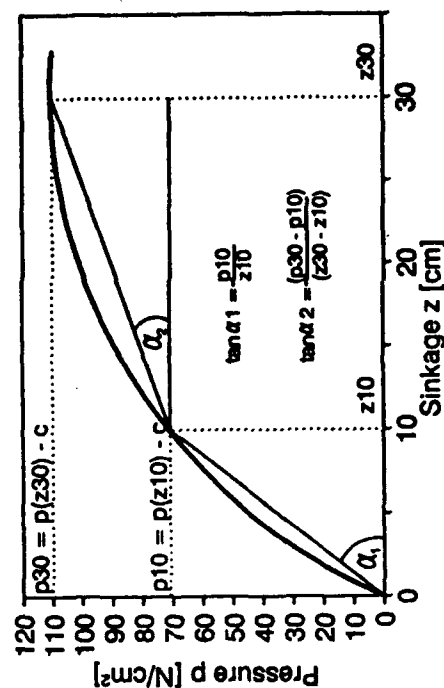


Fig. 5: Scheme of the mathematical description of the measured plate-pressure tests



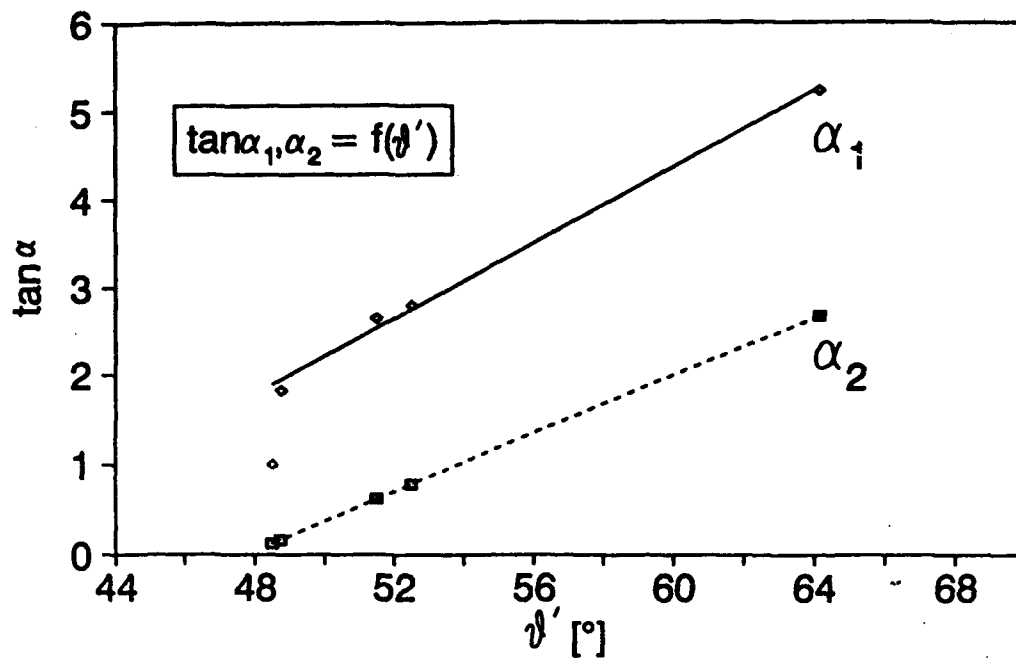


Fig. 6: Influence of the deflection angle  $\vartheta'$  on the two rising-angles  $\alpha_1$  and  $\alpha_2$

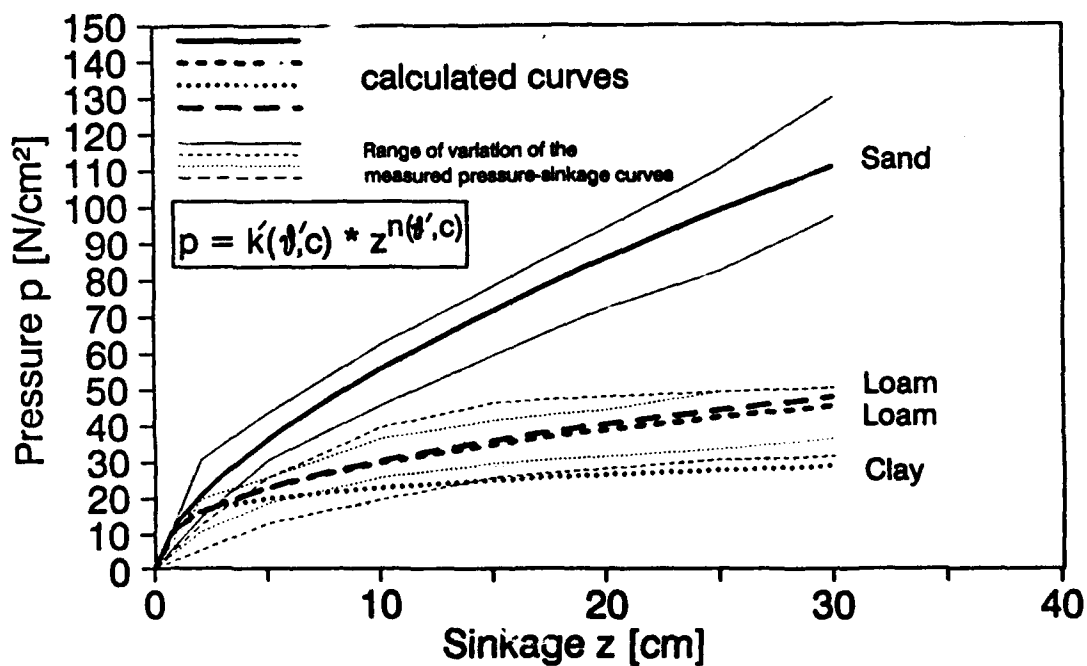


Fig. 7: Results of measured (thin lines) and calculated (fat lines) plate-pressure curves in different soils

# THE WAYS TO IMPROVE THE TRAFFICABILITY OF VEHICLES ON SAND

Zhuang jide Wang zhixing and Liu jude

Department of Automobile Engineering  
Jilin University of Technology  
Chang Chun, P.R. China, 130025

## ABSTRACT

In this paper, the mechanism of sinkage of running gear on sand was experimentally and theoretically studied. Its results indicated that reducing the flow failure of sand under the running gear of vehicle was the basic principle to reduce the sinkage and increase the tractive effort of vehicle. Based on this conclusion, some kinds of wheeled structure to improve the tractive performance of vehicle on sand were designed and evaluated by soil bin test. Finally, the direction of the running gear design to improve the trafficability of vehicle on sand was discussed by these results.

## 1 INTRODUCTION

The interaction of running gear and soft ground is the core of the study on the trafficability of vehicle on soft ground. A lot of work have been made by many scholars[1-3]. And many kinds of running gears such as track, low pressure tire, elastic wheel, etc. were developed to improve the trafficability of vehicle on soft ground. In order to develop a new vehicle used to transport on sand, the interaction of running gear-sand was studied.

This paper presents the results of an investigation into the mechanism of sinkage on sand and the ways to improve the trafficability of wheeled vehicle on sand by model test.

## 2 THE MECHANISM OF SINKAGE ON SAND

### (1) The results of load-sinkage test by plate

When the load applied to soil, generally, the deformation of soil consists of compaction and flow. One of the purposes of the test is to identify the components of sinkage on sand. The method of the test is shown in Fig.1. The results (shown in Fig.2) indicated that:

- a. The sinkage on sand is mainly caused by side flow.
- b. Under the state of two dimension confining, the sinkage is reduced about 50% compared with that of nonconfining. Under the state of three dimension confining, the sinkage is reduced about 80%.

### (2) The flow characteristics of sand under the wheel

The sinkage of wheel on sand includes load-sinkage and slip-sinkage. The dynamic characteristics of the interaction of sand-tire when wheeled vehicle travels on sand has been described in [4]. Here, the mechanism of sinkage on sand is analysed forwardly by model soil bin test.

The tractive performance test was carried out under following two conditions:

- a. The wheel travels on a narrow trough (width:80mm) which consists of two 1200mm(length) × 600mm(height) plates in sand.
- b. The wheel travels on sand and the flow of sand under the wheel isn't confined.

The test results is shown in Fig.3. It represents the relationship between the sinkage, rolling resistance coefficient of the wheel and slip. By this results, the slip-sinkage of wheel on sand is mainly caused by side flow of sand. The strength of sand can be increased remarkably by confining the side flow of sand.

(3) The mechanical analysis of the interaction between running gear and sand by FEM

As the FEM was developed quickly, theoretical approach to soil-structure interaction by FEM was also developed[5-6]. In this paper, the Duncan-Chang hyperbolic constitutive model [7] was used to represent the constitutive relationship of sand near the surface of the ground. The parameters of the model was tested by dynamic triaxial test equipment[8]. The nonlinear finite element method was used to calculate the relationship of load-sinkage, displacement and stress distribution etc. under different forms of confining flow. As one example, Fig.4 showed the displacement field in a increment, and the load--sinkage relationship by the calculation and related test results were shown in Fig.5. It represents that the FEM as well as Duncan--Chang model can be applied to analysis the sand--structure interaction.

To sum up, the sinkage on sand is produced by side flow of sand under load. In the case of slip-sinkage, the sinkage of wheel is also mainly the results of side flow of sand under the tangential force and vertical load applied by wheel. The sinkage can be reduced remarkably by confining the side flow. It is the following two properties of sand near the surface of the ground causing above phenomena:

- a. The compressibility of sand is very small.
- b. The results of triaxial test [8]: the volume of sand extends after shear failure.

However, these conclusion is only explanation to the mechanism of sinkage on sand. How the principle will be applied to wheel structure design is discussed in next chapter.

### 3 THE WAY TO IMPROVE THE TRAFFICABILITY OF WHEELED VEHICLE ON SAND

In the field of trafficability of vehicle on soft ground, generally, the tractive performance of vehicle was improved by decreasing the unit contact pressure of running gear and increasing its shear field. Track, multiwheel etc. are the example of it. These structures have been studied by many scholars. For the length of the paper is limited, prior and ours research about it will not be described in this paper.

Here, according to the conclusion of above chapter, some kinds of wheel with the structure of confining flow were designed and the tractive performance of them were evaluated by model soil bin test.

#### (1) The wheel with flanges (structure A)

The wheel with flanges is the simplest structure that above principle was applied to wheel. In this paper, five wheels with the height of flanges: 1,2,3,4 and 5 (cm) were tested. And the results indicated that, the sinkage of the wheel was decreased with the increasing of the height of flanges, but the rolling resistance can't be reduced always. When the height of flanges was higher than a value, the rolling resistance increases. For this size of wheel, the flanges with 2(cm) height was best. Fig.6 shows a part of results of test.

#### (2) The wheel with the structure of confining longitudinal and side flow of sand (structure B).

The characteristics of this structure were: the flow of sand under the wheel can be confined by side and longitudinal plates; If the torque of

wheel axle is greater than the maximum shear force produced by sand to the wheel, slip will be occurred between the wheel and the confining flow device. According to the results of last chapter, the height of side plates is 2(cm). And, the performance of this structure is compared with that of the wheel with rigid link between wheel and the confining flow device (structure C). The results (shown in Fig.7) tell us:

The tractive performance of wheel can be increased remarkably by confining the flow of sand. The tractive performance of structure B is higher than that of structure A and C.

(3) Discussion on the reasonable structure of wheel with high tractive performance.

Based on above results, the wheel used to travel on sand should have the structure of confining flow of sand beneath it. Generally, there are two flow zones of soil flow beneath a rolling wheel. Of the two zones, one is forward flow zone, the other is backward flow zone. The forward zone develops with the increasing of sinkage, the backward flow zone develops with the increasing of slip. The backward flow should be confined by the wheel with the structure of confining flow. And the forward flow zone should not be confined. So, the shear strength of sand beneath the wheel was enhanced and the horizontal ground deformation resistance didn't increase. The tractive performance of the wheel was improved. That is a design concept from the confining flow of sand point of view. Now we are studying the problem. Moreover, the structure of confining flow can also be applied to legged wheel or legged vehicle to improve its tractive performance.

In this paper, the research is only first step to explore ways and means of improving the trafficability of vehicle on sand, and has many problem to overcome.

#### 4. CONCLUSIONS

(1) Two important properties of sand near the surface of the ground are small compressibility and volume expand after failure. The sinkage of running gear on sand is mainly produced by flow. If the flow can be confined, the deformation of sand is decreased to a great extent.

(2) The structure of confining flow can be designed reasonably so as to improve the tractive performance of wheel. And, the design can be made under the direction of analysis of sand-wheel interaction by FEM.

#### REFERENCES

1. Bekker, M.G., 1969, Introduction to Terrain-Vehicle System. The University of Michigan press.
2. Wong, J.Y. 1978, Theory of Ground Vehicle. Jhon Wiley
3. Karafiath, L.L., Nowatzk, E.A. 1978, Soil Mechanics for Off-road Vehicle Engineering. Trans. Tech.Pull., Germany
4. J. Zhuang, Z. Wang and J. Liu, 1990, Study on the Dynamic Characteristics of Wheeled Vehicle on Sand. 2nd ASME Winter Symposium on Transportation System.
5. Perumpral, J.V., J.B. Liljedahl and W. Perloff, 1971, The Finite Element Method for Predicting Stress Distribution and Soil Deformation Under a Tractive Device. TRANSACTIONS of the ASAE. vol.14, No.6
6. Pollock, Jr. D., J.V.Perrumpral, J. Kappusamy, 1986, Finite Element Analysis of Multipass Effect of Vehicles on Soil Compaction. TRANSACTIONS of the ASAE, vol.29, No.1
7. Duncan, J.M., and C.Y. Chang, 1970, Nonlinear Analysis of Stress and Strain in Soil. J. Soil Mech. and Foundations Div., proc. of ASAE, 96(5)
8. Liu Jude et al, 1990 Study on the Strength Characteristics of Sands Journal of Jilin University of Technology, No.4, 1990

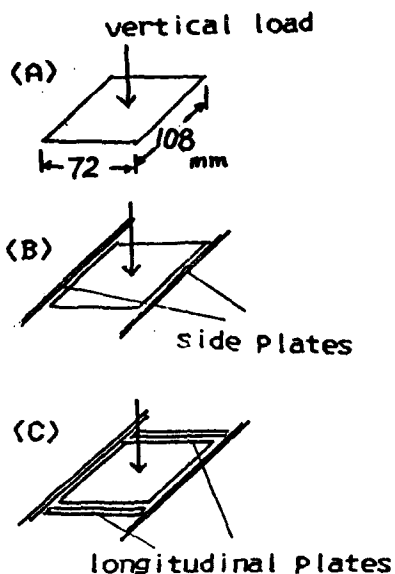


Fig.1 Three test conditions  
 (A) Nonconfining flow  
 (B) Two-dimension confining  
 (C) Three-dimension confining

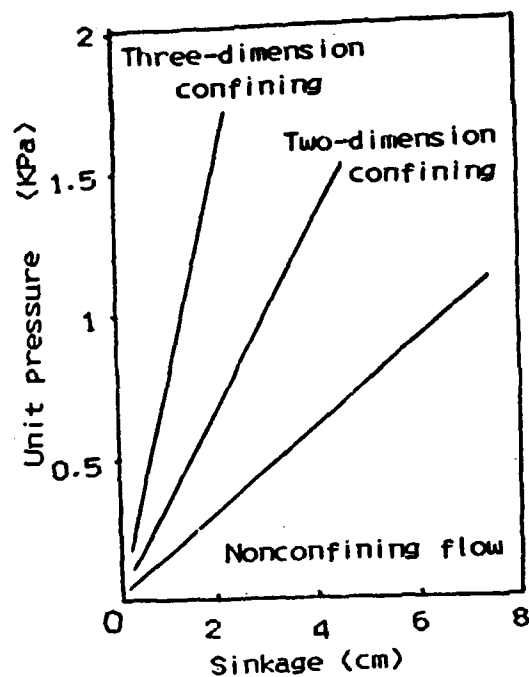


Fig.2 Comparison of results of test  
 under conditions: A, B and C

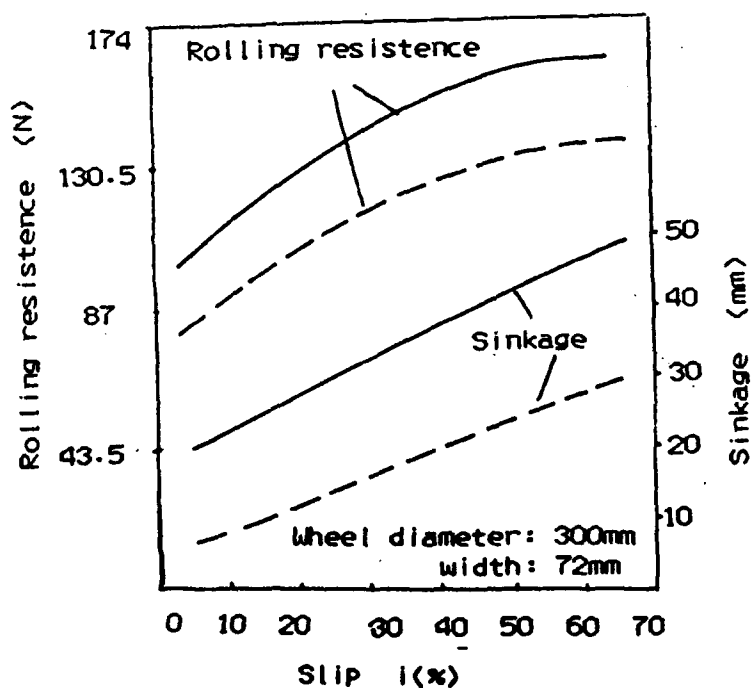


Fig.3 Relationship between rolling resistance,  
 sinkage and slip for two conditions:  
 (1) ——— Nonconfining flow  
 (2) ----- Traveling on narrow trough

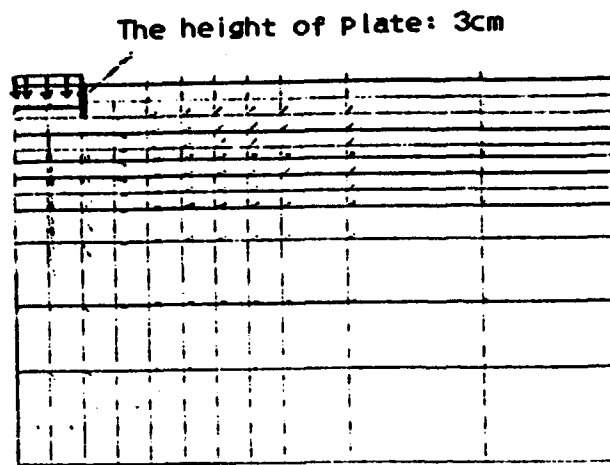


Fig.4 Displacement field beneath the plate with confining side flow os sand

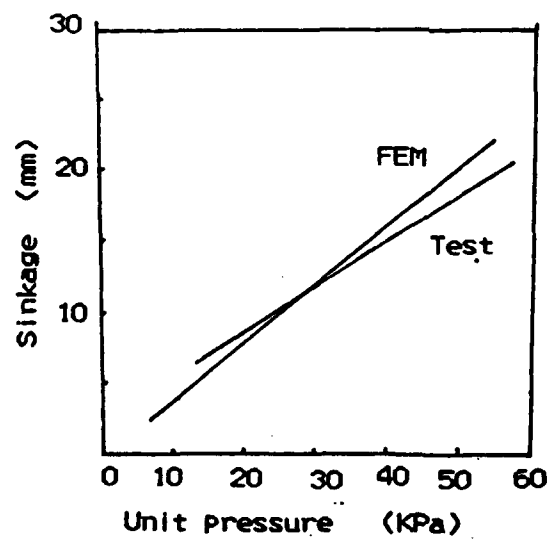


Fig.5 Comparison between test and caculation results by FEM

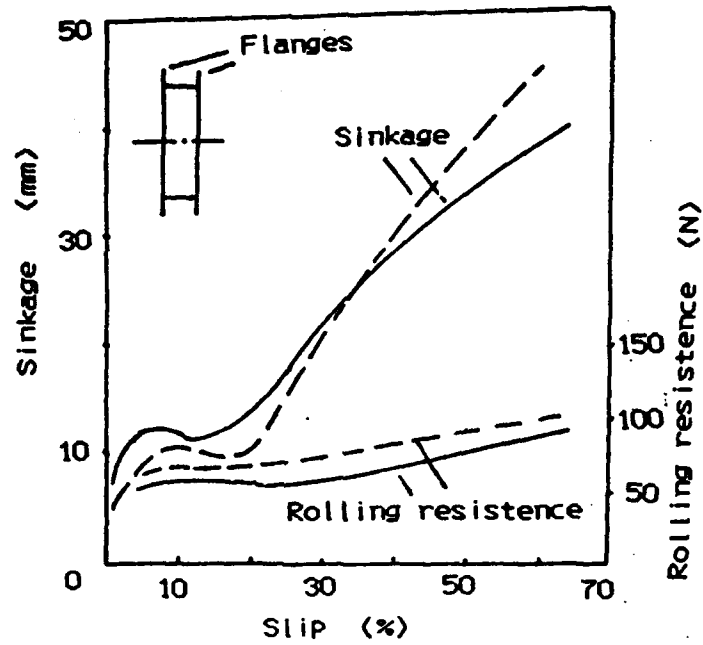


Fig.6 Comparison of the wheel with flanges  
 — The height of flanges: 2cm  
 - - - The height of flanges: 4cm

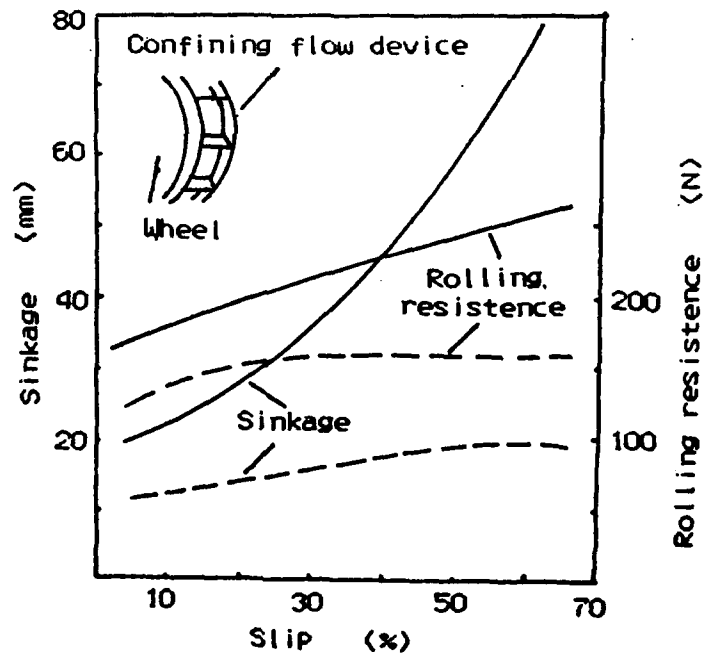


Fig.7 The test results of wheels with the structure of confining flow  
 — Rigid link between the wheel and the structure of confining flow  
 - - - Slip can be occurred between the wheel and the structure of confining flow

# CONSIDERATIONS ON THE WHEEL - SOIL INTERACTION AND ITS ROLE IN SOIL COMPACTION

D.E. Agr. NICOLAE TECUSAN  
professor at Polytechnical  
Institute of Timisoara,  
Romania

## I. INTRODUCTION

The problem of the role of the wheel-soil interaction in the appearance of soil compaction was in the attention of many researchers in the whole world, and especially in the Soviet Union, because it is generally known the negative effect of the wheels (of the tractors, agricultural machines, trucks and trailers) on the structure and compaction of soil, with the well known followings on the agricultural production.

It is well known that, as well the structure, as the cohesion and compaction of soil represent basic parameters that determine physical and mechanical properties of soil and its productive capacity.

In order to limit as much as possible the action of the wheels on the phenomenon of soil compaction, we must make the right choice of the tyres. The purpose of this work is to find methods which solve the dimensioning of the tyres.

## II. THEORETICAL AND PRACTICAL CONSIDERATIONS

It is well known by the specialists the undesired and hard to avoid phenomenon of the compaction of soil caused by the wheels and caterpillars of the tractors, agricultural machines and vehicles.

The introduction of complex aggregates in order to reduce the number of passings on the fields in agricultural production can not solve the whole problem, and the compaction phenomenon create the so-called hardpan. In the same time this complex aggregates need big tractors, which, because of their heavy weight, have a pressure on soil which exceeds the admissible value of 24 kPa.

Thus appears the necessity of the correlation between the elements of the tractors, agricultural machines and vehicles which



are in contact with soil in order to support their mass, especially with the contact surface of the tyre with soil, and the soil compaction phenomenon.

The contact surface of the tyre with the soil, which could be approximate by a cylindrical surface, has two distinct zone : the soil compression zone which has the  $R_1$  radius and  $\varphi_1$  angle of attack, and the soil decompression zone characterized by  $R_2$  radius and  $\varphi_2$  angle of attack.

Thus, the interaction between the deformation of soil and that of the tyre could be written as below (1):

$$\begin{aligned} R_1 &= R_r \left[ 1 + G/(C_s \cdot Z_1) \right] \\ R_2 &= R_r \left[ 1 + G/(C_s \cdot Z_2) \right] \end{aligned} \quad (1)$$

where :

$R_r$  is the radius of the tyre ;

$C_s$  is the coefficient which characterizes the radial deformation of the tyre;

$Z_1$  is the maximal deformation in the compression zone of soil;

$Z_2$  is the thickness of soil, after the decompression (because of the elasticity of soil).

The coefficient  $C_s$  could be expressed with the relation:

$$C_s = E(1 - \mu) / (k_1 - \mu - 2\mu^2) \quad (2)$$

where:

$E$  is the longitudinal elasticity modulus of soil;

$\mu$  is the Poisson coefficient;

$k_1$  is the penetration coefficient of soil;

$$k_1 = H / (R_1 \sin \varphi_1) \quad (3)$$

where :

$H$  is deformation deepness of soil.

The maximal strength which appears in soil is:

$$\tau_{\max} = C_s \operatorname{tg}(\varphi_1 / 2) \quad (4)$$

Analizing the constructive parameters of different type of tyres, we reproduce the values of some <sup>or</sup> their main parameters in table nr.1.

TABLE Nr.1

Dimension of the tyre	Type or trade mark	D/B mm	$Q_{min_N} / Q_{max}$	$F_c m^2$
6,00 - 15	Victoria	685/152	3,83/5,60	0,020
6,00 - 16	Victoria	710/152	3,83/6,05	0,022
6,50 - 16	Continental	736/165	3,68/6,03	0,027
6,50 - 20	Victoria	838/165	4,62/8,02	0,042
7,50 - 20	Victoria	889/190	5,23/10,20	0,056
9,50 - 20	Goodyear	990/241	6,24/12,24	0,062
11,2 - 20	F-32(URSS)	1076/284	7,50/11,3	0,065
11,2 - 23	Victoria	1153/284	7,50/12,3	0,068
12,40- 28	Victoria	1341/314	9,50/16,3	0,089
13,60- 28	Victoria	1402/345	11,4/18,5	0,095
13,60- 38	Victoria	1600/345	14,3/20,2	0,138
14,00 - 38	Victoria	1676/355	14,3/20,2	0,140
15,00 -38	Pirelli	1727/381	14,44/17,3	0,146
16,00-38	Klüber	1778/406	18,9/24,7	0,161
16,00- 38	Victoria	1778/406	18,9/24,7	0,161

The significances of the notations are:

D the diameter of the tyre ;

B the width of the tyre ;

$Q_{min}/Q_{max}$  the minimal/maximal value of the load;

$F_c$  the contact surface.

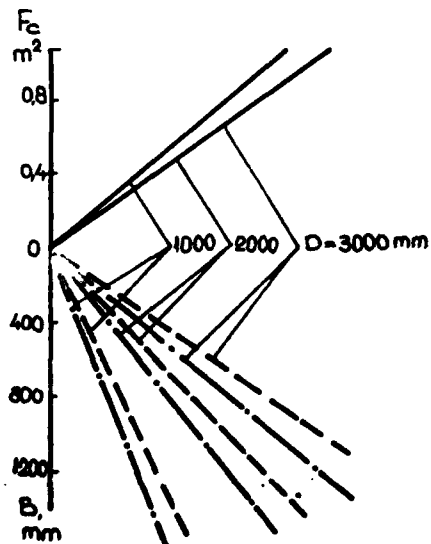


Fig.1.

As one can notice, both from Table nr.1 and from Fig.1, the width of the tyre B, has a determinant influence on the contact surface between the wheel and soil. The width of the tyre can be determined with an experimental relation:

$$B = 2F_c / ( \int \cdot k_1 \cdot \pi \cdot \sqrt{D \cdot f} )$$

(5) 129

where :

- $\left\{ \begin{array}{l} \text{is a correction coefficient, which has the value of 0.7;} \\ k_1 \text{ is a coefficient of load distribution on the contact} \\ \text{surface and} \\ f \text{ is the maximal camber of the tyre.} \end{array} \right.$

The data calculated with the relation (5) are presented in the Table nr.2. As one can observ, the width of the tyre B is a function of the tyre's diameter D, of the load Q and the characteristics of soil(humidity, crumbliness, a.s.o.).

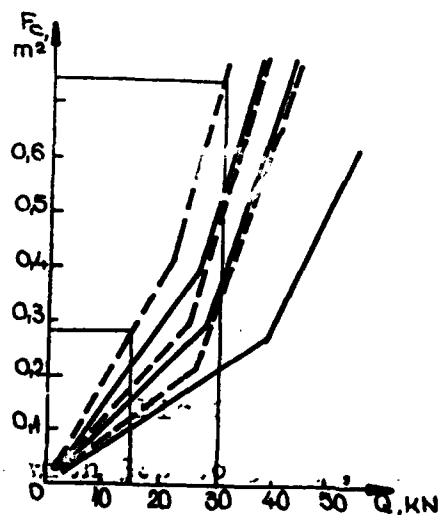
Also, the width B can be influenced by the lateral deformation of the tyre, wich is noticed by  $\gamma$ . The value of the coefficient  $\gamma$  is contained in the 0.14 - 0.25 interval, and can be adopted as  $\gamma$  0.22.

In the Fig.1, one can observ the manner of the influence of the coefficient  $\gamma$  on the tyre's width.

For the optimum choosing of the tyres(with given diameter D and width B) one can use the diagram presented in the Fig.2.

But all the showed facts relating to the functional dimensions of the tyres, especially in the case of the big tractors, must be correlated and subordinated to a very important parameter, the

ist be less than 25 k Pa. Nowadays, because



the neglecton of the above condition, one can observ an unnormal compaction of soil betwen. 50 and 70 cm depth, wich causes the destroying of the soil structure, crumbling the fraction with 0.25 - 1,0 mm diameter (wich are the ideal one for the agriculture).

In some cases, the real pression on soil is bigger than the admissible one (25 k Pa causes the diminution of the productions.

TABLE Nr.2

Season	D <sub>1</sub> mm	B <sub>1</sub> (mm)		Q(kN)	D mm	B <sub>2</sub> (mm)		Q(kN)
		50	40			30	20	
Spring	3000	1800/1050	1330/600	2000	1150/550	550/300		
	2000	2300/1550	1800/1100	1000	1550/900	950/450		
Autumn	3000	1350/400	950/300	2000	750/350	460/240		
	2000	1900/750	1450/500	1000	1200/550	800/370		

- x The numerator is the dimension B computed in the case of a soil with high humidity, and the denominator is in the case of a dry soil.

The practice confirmed that the exceeding of the admissible pression on soil, with 10 k Pa ( e.g. 35 k Pa) leads to a diminution of the production of 250 - 350 kg/ha for corn and with 10-12% for maize.

A great contribution in the soil compaction have the trucks and their trailers used in agricultural transportation. For exemple, the pression on the soil for the back wheels of a truck is approximatively 400 kPa, and for the front wheels is 750 kPa.

In order to verify the situation of the pression on the soil in the case of the main Rumanian tractors, we compute the values. The results are showed below:

Tractor	U - 650	112 k Pa
Tractor	U - 445	82 k Pa
Tractor	U -1010 and U 850	- 87 kPa.

As one can observ pression values are far bigger than the admissible one leading to a very important compaction phenomenon.

### III. CONCLUSIONS

From the above presented facts one can draw some practical conclusions, i.e. the following measures are proposed to be adopted: reducing of:

- the specific weight (reported to the engine power or to the field capacity) of the agricultural tractors and machines;
- redesigning of the agricultural tyres;
- filling of the tyres with a liquid material(for example milk of lime);
- using of double wheels;
- using of steel made wheels as the second wheel on the axle.

If one doesn't heed the above proposals, the phenomenon of the soil compaction could be increased, and as a consequence the crop productions will be diminished. In addition, the soil, compaction brings to the ploughing - resistance growing, with 3 - 5 %, wich

increases the energy-using with 3-10%. Because of the compaction, the structure of soil is continuously destroyed, and as a consequence the furrow will be more difficult to be crushed, and as such the seedbed preparation needs more tillage operations.

At least, to the losses one must - 10 - added the extra expense for the subsoiling, which is compulsory to realize in these conditions from five to five years.

#### B I B L I O G R A P H Y

1. Ageilin I.C. -Determining of the deformation and of the contact parameters between soil and the wheels.  
Automotive Industry, 5/1969.
2. Belkowskhi V.M. -The dimensions of the tyres and their action and soil. Tractor and Farm Machines, 5/1989.
3. Velez N. -Tractors and Automobiles.  
Agricultural Publishing Russe, 1980.
4. Tecusan N. -Tractors and Automobiles.  
Didactical Publishing Bucharest, 1982.

## MEASUREMENTS OF TRACTIVE CAPACITY OF RUBBER TREADS ON GRASS

A. Grečenko

Faculty of Mechanization, University of Agriculture

Prague 6 - Suchbát, Czechoslovakia

(reported work carried out in the Research Inst. of Agr. Engng.,  
Prague 4 - Chodov)

### Summary

As a part of the programme "Slope rating of agricultural vehicles" the measurements focused on the tractive capacity in different directions of 5 typical rubber tread patterns and 2 contact area forms on the grassy terrain.

The linear shear test procedure was implemented: contact area of a locked wheel with tyre was represented by a rubber-treaded plate with an area 252 cm<sup>2</sup>.

The results are presented mainly as the maximum coefficient of gross traction at angles 0-90° to the axis of the contact patch and as a function of the mean contact pressure.

### Introduction

Any vehicle crossing a slope has to cope, from the viewpoint of mechanics, with a set of external forces in the ground plane generating certain shear reactions in the running gear interface, e.g. wheel-ground contact area. The deviation of any such reaction from the wheel plane is specified by the angle  $\xi$ .

As I was interested to find more about the directional tractive capacity of various tread patterns, I have carried out during 1984-85 a set of experiments which will be reported in this paper.

Well known is the the friction circle e.g. of a wheel with tyre on the road which limits the maximum horizontal reaction  $U_{mf}$  from the ground related to the acting load  $Z$  in an arbitrary direction [1, p.196] :

$$U_{mf}/Z = f = \text{const} \quad (1)$$

In the soft ground traction theory a similar coefficient of gross traction has been introduced [2] based on the Coulomb's equation, indicating the maximum reaction  $U_m = (x^2 + y^2)_m^{1/2}$  transmitted through the shear in an arbitrary direction :

$$U_m/Z = \mu_m = (c/q_s) + \tan \varphi \quad (2)$$

where  $q_s$ ;  $c$ ;  $\varphi$  are mean contact pressure, soil cohesion and angle

of internal friction respectively. In this context the coefficient of traction according to ISTVS Standards [3] cannot be used.

The quantity  $\mu_m$  is the maximum value of the coefficient of gross traction  $\mu = U/Z$  in case that the combined tyre-ground displacements in the contact patch are equal and reach a certain length. Such a situation is represented by a towed locked wheel.

Some researchers including myself believed that a traction (friction) ellipse might have been the right answer [e.g.4, formula (14)].

### Experimental programme and observations

The experiments were designed to examine : a)  $\mu_m = f(f)$  ;  
b) the effect of the contact patch form on a) ; c)  $\mu_m = f(q_s)$  .

The contact area was represented by a rubber coated flat plate with tread. The device functioned as a linear shear apparatus with adjustable angular position of the treaded plate with respect to the direction of motion.

The dimensions of the plate with uniform area  $S_o = 251,7 \text{ cm}^2$  :  
- form O (oval) : length  $l_o = 21,2 \text{ cm}$ , width  $b_o = 13,8 \text{ cm}$   
the ratio  $b_o/l_o = 0,65$  is typical for conventional tyres ;  
- form C (circle) : diameter  $d = 17,9 \text{ cm}$  .

Kinds of tread patterns (Fig.1) made of rubber of hardness 65-70 Shore A :

- 0 ... smooth surface
- 1 ... lugs longitudinally, angle  $45^\circ$
- 2 ... lugs transversally, angle  $45^\circ$
- 3 ... three ribs (as for a front undriven tyre)
- 4 ... blocks (golf pattern)

The uniform tread density for all the patterns was 29% ; tread height 1,7 cm and the lug sides angle  $14^\circ$  [3].

The tested combinations were (plate form - tread) :  
O - 0, 1, 2, 3, 4 ; C - 4 .

The measuring apparatus (Fig.2) had to be simple and reliable to enable a quantity of time-saving measurements because a considerable scatter of data was expected. The meaning of position numbers : 1 - treaded plate, angularly adjustable by  $15^\circ$  all round, 2 - shearing head, 3 - adjustable double parallelogram, 4 - loading ram cylinder with hydro-pneumatic operation, 5 - pulling ram cylinder exerting the measured force F by means of a steel string 6, 7 - rollers for lateral guidance of the shearing head, 8 - anchored frame designed for transport by a

tractor three-point-hitch.

The measurements proceeded as follows : a desired angle  $\xi$  of the plate was adjusted, required contact pressure was set ( $q_s$  [kPa] = 43,8 p where p means pressure gauge reading in MPa). Then oil was supplied to the cylinder 5 by the hand pump so that the shear head velocity would not exceed 1 cm/s. Registered was the maximum coefficient of gross traction ( $\mu_m = 8,89 \times 10^{-3} \cdot F/p$ ) and the corresponding displacement.

Four series of measurements were carried out with  $\xi = 0 - 90^\circ$  (135, 180°) and  $q_s = 35, 53, 70, 88$  kPa. Every test was repeated 3 - 6 times. The ground was compact (wet bulk density 1,49 - 1,79 g/cm<sup>3</sup>, moisture content dry basis 26 - 53%) with dense turf, grass on the surface cut short.

Especially with lower contact pressure, the tread under pull penetrated the ground only after travelling certain distance. However, full shear always took place. Maximum pull was regularly observed within the interval of displacements 5 - 8 cm.

#### Results and their discussion

Of special interest from the 1st series of tests are the results for  $q_s = 53$  kPa appearing in the polar graph, Fig.3 - right-hand side (the number behind the oblique stroke indicates the contact pressure in kPa).

No difference between the thrust capacity of the oval and round treaded plate (O - 4, C - 4) was proved. The tread O - 2 behaved more efficiently than O - 1. The ribbed pattern O - 3 behaved for  $\xi = 0$  as the smooth plate O - 0 (force transfer only through friction ...  $f = \text{approx. } 0,81$ ) and for higher angles gradually attained the performance of O - 1 or O - 4 treads.

The results of the 2nd and 4th test series with the typical traction tread O - 1 were averaged due to their evident affinity while the mentioned difference in the moisture content did not show up (Fig.3 - left-hand side). This tread basically shows a marked reduction of thrust capacity at the angle  $\xi = 45^\circ$  (equal to the angle of lugs). The averaged results for O - 1 arrangement and all of the contact pressure values (except the doubtful result at  $q_s = 53$  kPa and  $\xi = 45^\circ$ ) give the following :

	$\xi^\circ$	0	45	90
average $\mu_m$		1,25	1,07	1,23
percentage ( $\mu_m$ )		100	86	98

This suggests that at  $\xi = 45^\circ$  only half of the contact area transmits the force through shear while the other half through friction.



The tests at  $\xi = 0^\circ$  with both kinds of traction tread pattern 0 - 1 and 0 - 4 (series 2 - 4) corroborate the general trend of  $\mu_m$  reduction with the increase of  $q_s$  (Fig.4). This indeed gives support to the old rule of terramechanics expressed e.g. by the formula (2).

The form of the polar graphs  $\mu_m = f(\xi)$  in Fig.3 reflects the considerable difference from the idealized traction (friction) circle or ellipse as mentioned in the introduction.

### Conclusions

From the measurements of the gross tractive capacity of rubber treaded plates on grass it follows :

1. the functions  $\mu_m = f(\xi)$  in polar coordinates have the form of deformed circles ;
2. the tractive capacity of traction tread patterns (lugs 0 - 1, 0 - 2 and blocks 0 - 4, C - 4) is very similar in the directions along and across the tread axis ( $\xi = 0^\circ, 90^\circ$ ) ;
3. the tread with lugs 0 - 1 when supporting through contact with ground an external force in the direction of lugs at one side of the pattern reduces its tractive capacity down to 86% of the value should this force act along the axis of the pattern ( $\xi = 0^\circ$ ) ;
4. the tractive capacity of a ribbed tread 0 - 3 gradually drops from 100% for  $\xi = 90^\circ$  (force acts perpendicularly to the ribs) to 69% at  $\xi = 0^\circ$  (force acts in the direction of the ribs) when the tractive capacity equals the force of friction of a smooth rubber tread ;
5. the maximum coefficient of gross traction  $\mu_m$  diminishes when the mean contact pressure in the contact area grows.

### References

1. Kamm, W.: Das Kraftfahrzeug. Springer, Berlin 1936 : 237 pp.
2. Grečenko, A.: Vehicle behavior in case when the resultant soil reactions comprise lateral components. Proceedings Internat. Conf. on Soil Dynamics, Auburn, Ala. 1985, Vol.4, p. 709-722.
3. ISTVS Standards. J. of Terramechanics 1977, 14(3), p.153-182.
4. Crolla, D.A., El-Razzaz, A.S.A.: A review of the combined lateral and longitudinal force generation of tyres on deformable surfaces. J. of Terramechanics 1987, 24(3), p. 199-225.

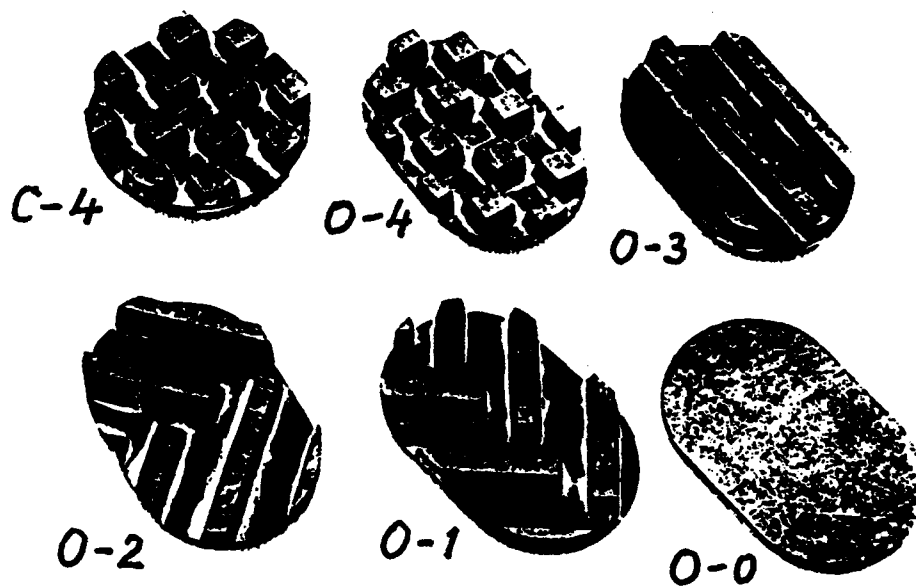
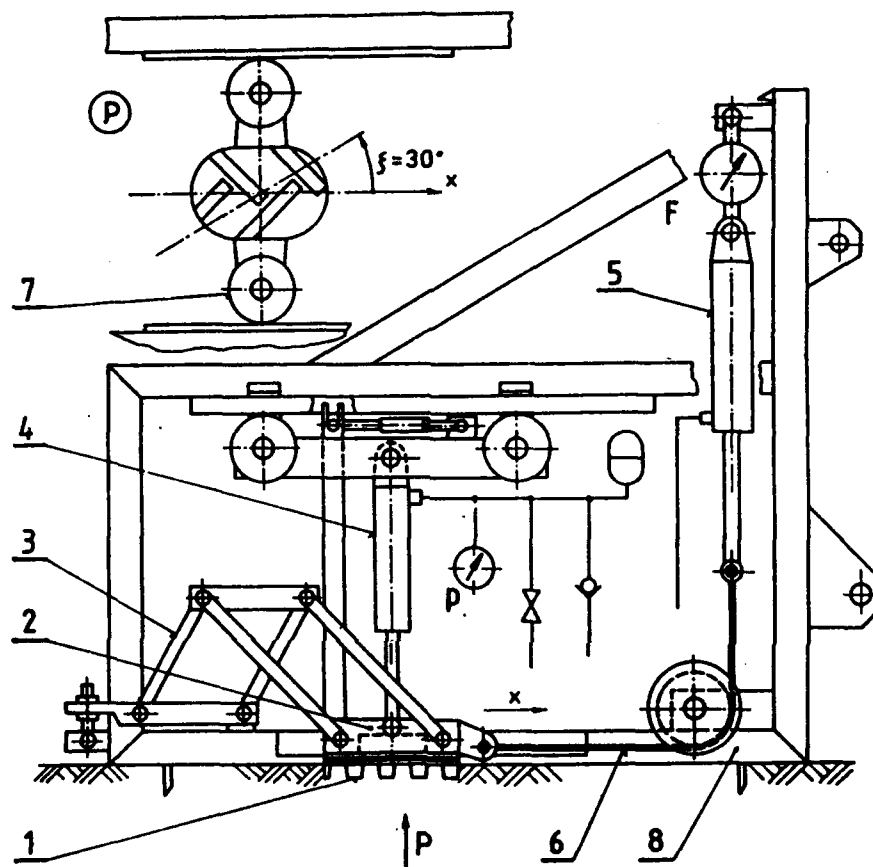


Fig.1



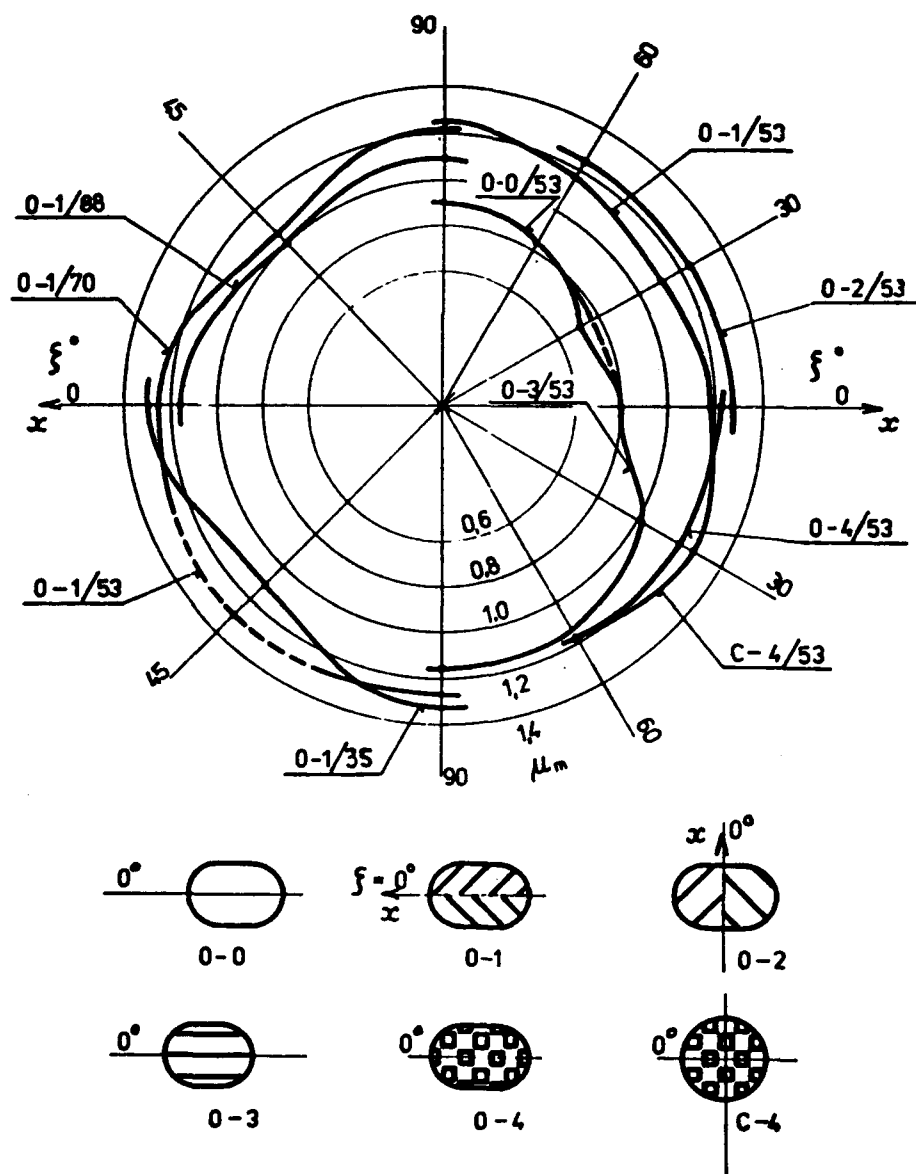


Fig. 3

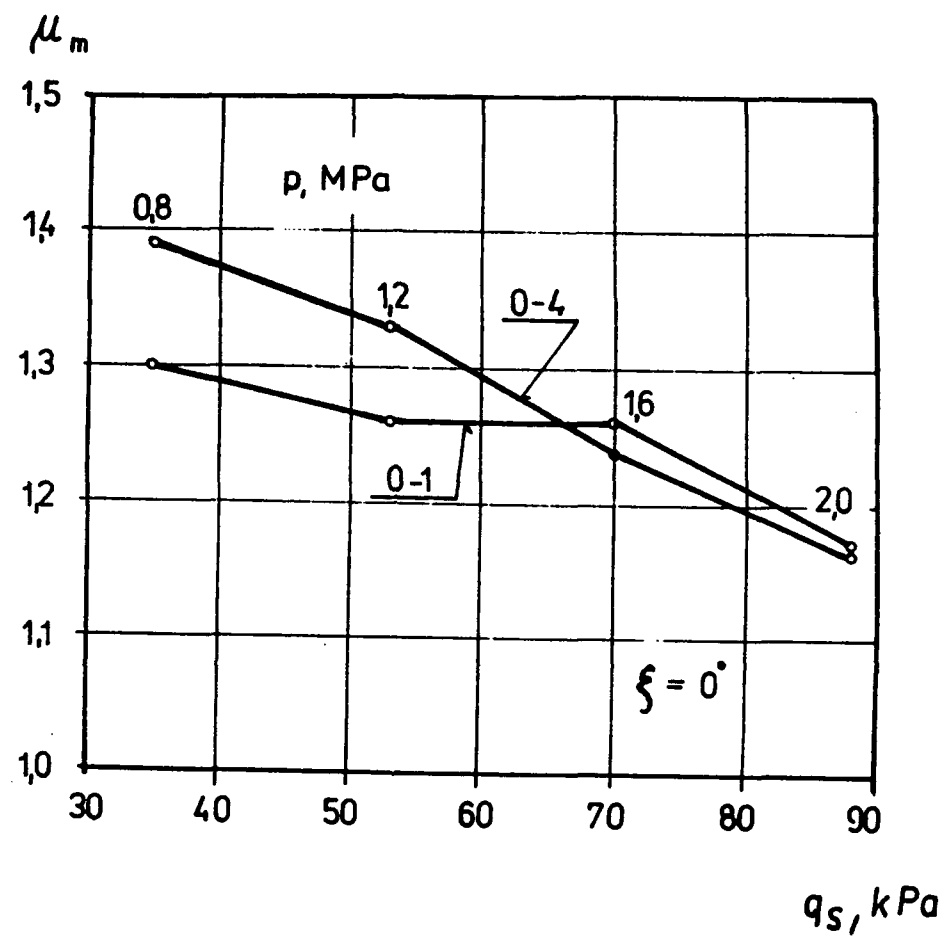


Fig. 4

# SOIL-TRACK INTERACTION RELATION FOR THE MOTION OF TRACKED VEHICLES ON DRY SAND

K. Watanabe\*, M. Kitano\* and H. Murakami\*\*

- \* Department of Mechanical Engineering, The National Defense Academy, Hashirimizu, Yokosuka, Japan 239
- \*\* Department of Applied Mechanics and Engineering Sciences, University of California at San Diego, La Jolla, California 92093-0411, U. S. A.

**Summary** The paper presents a soil-track interaction model for tracked vehicles on dry sand. The kinematics of the model allows for three translational and three rotational degrees-of-freedom. The proposed soil-track interaction relation is characterized by pressure-sinkage and shear force-slippage complemented with sinkage-slippage relations which are in turn measured by both plate penetration and shear tests in a soil bin with dry loose sand. The above basic soil interaction tests and subsequent scale model experimentals revealed that shear force-slippage and sinkage-slippage relations exhibit strong anisotropy in the track longitudinal and lateral directions. The experimentally constructed soil-track interaction model was employed to predict the planar vehicle motion by numerically integrating the spatial rigid-body equations of motion. The predicted data was accurately correlated with the experimental data of scale model tests in the soil bin. The results demonstrate that the spatial vehicle model combined with realistic soil-track interaction models could accurately assess vehicle mobility even on soft ground.

## 1. Introduction

Off-the-road mobility of tracked vehicles depends on track flotation and tractive forces and is achieved with skid steering. Skid steering mechanisms of tracked vehicles in turning motion are complex and differ significantly from wheeled vehicles. For planar motion of tracked vehicles mathematical models of steerability were presented by Kitano and his colleagues together with experimental validation of the models on hard level ground [1, 2] and on soft level ground [3]. For spatial motion on nonlevel ground a rigid-body mobility model was recently developed by the authors [4]. The model describes the vehicle motion on arbitrary terrain by three translational and three rotational degrees-of-freedom. This latter model requires a realistic soil-track interaction model to accurately predict vehicle motion on various terrain; this issue is taken up in this paper.

The paper is concerned with the development of an empirical soil-track interaction relation on dry loose sand. The accuracy of the interaction model was assessed by incorporating the model into the spatial rigid-body vehicle model [4] and comparing the predicted track sinkage and tractive forces with scale-model experimental data. The parameters of the soil-track interaction relations were determined experimentally by conducting plate penetration and shear tests in a soil bin with dry loose sand; the experiments revealed anisotropic shear force-slippage and sinkage-slippage relations in the track longitudinal and lateral directions. Next, the accuracy of the soil-track interaction model was tested by employing it in the spatial mobility model and predicting the track sinkage and slippage under straight motion of a scale vehicle model in the soil bin. The predicted data accurately correlated with the experimental data.

The results of the above procedure demonstrate that the spatial vehicle model combined with realistic soil-track interaction models could accurately assess vehicle mobility even on soft ground. While the soil-track interaction model can be directly applied to the simulation of arbitrary vehicle motion, the experimental validation and the simulation of turning vehicle motion will be deferred for later publications.

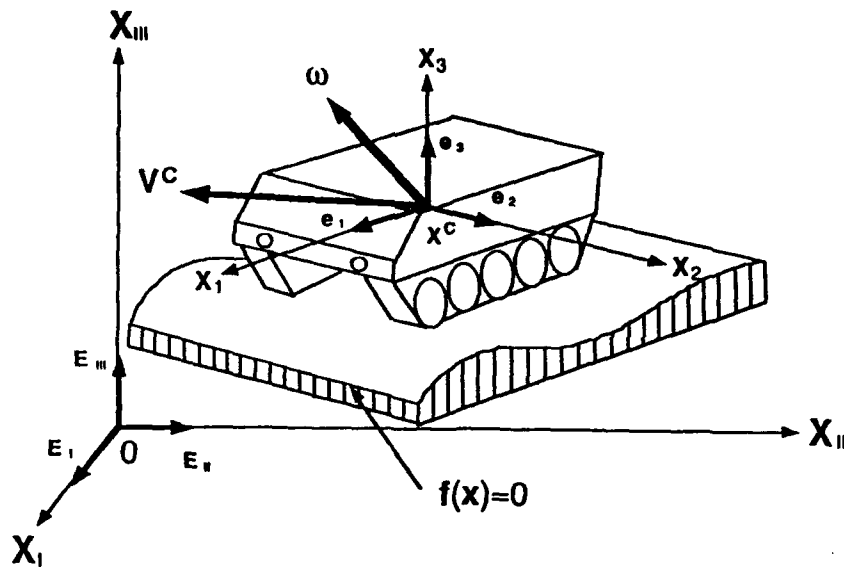


Fig.1 Reference and body-attached coordinate systems

## 2. Mathematical Model for Spatial Motion of Tracked Vehicles

### (1) Kinematics of the vehicle and coordinate systems

A spatial motion of a tracked vehicle represented as a rigid body in a Euclidian 3-space is shown in Fig.1 together with coordinate systems. In the paper only right-handed coordinate systems are employed. A temporal position of the center of mass of the body,  $X^C$ , is described by the coordinates,  $(X_I, X_{II}, X_{III})$ , with respect to a spatial reference frame with unit base vectors,  $\{E_I, E_{II}, E_{III}\}$ . The topology of the ground is represented by a spatially curved surface,  $f(X)=0$ ; the equation for level ground reduces to  $X_{III}=\text{constant}$ .

In addition to the spatial frame, a moving coordinate system  $(x_1, x_2, x_3)$  with unit base vectors  $\{e_1, e_2, e_3\}$  which are rigidly attached to the vehicle, is introduced. The  $x_1$ -axis coincides with the forward longitudinal axis of the vehicle, the  $x_2$ -axis is a lateral principal axis, and the  $x_3$ -axis becomes normal to the  $x_1, x_2$ -plane. The rotations with respect to the  $x_1, x_2$ , and  $x_3$  axis are denoted, respectively, as roll, pitch and yaw angles. At time  $t=0$ , the origin of the moving frame and direction cosines of the base vectors are defined with respect to the spatial frame.

### (2) Equations for motion

The external forces acting on the vehicle include the gravitational force  $-mgE_{III}$  and the resultant forces due to the soil-track interaction,  $Q^{(j,\alpha)}$ , acting on the cell associated with the  $j$ th road wheel ( $\alpha=1$  for the right track and  $\alpha=2$  for the left track), as shown in Fig.2. The cell associated with a road wheel centered with the trackshoe beneath the road wheel, and includes contiguous track shoes — these shoes extend over the semi-span of the adjacent road wheels in both the forward and rear directions. By means of a soil-track interaction model, the interaction force  $Q^{(j,\alpha)}$  at the  $j$ th cell is related to both the sinkage and slip velocity of the  $j$ th cell. The soil-track interaction relation, therefore, reflects inelastic deformation of the soil under the cell.

Newton's second law applied to the present problem yields

$$m\mathbf{A}^C = \sum_{j=1}^n (\mathbf{Q}^{(j,1)} + \mathbf{Q}^{(j,2)}) - mg\mathbf{E}_{III} \quad (1)$$

$$\mathbf{H}^C = \sum_{j=1}^n (\mathbf{x}^{(j,1)} \times \mathbf{Q}^{(j,1)} + \mathbf{x}^{(j,2)} \times \mathbf{Q}^{(j,2)}) \quad (2)$$

where  $\dot{\mathbf{A}}^c$  and  $\dot{\mathbf{H}}^c$  are, respectively, the acceleration vector and the angular momentum at the mass center (the superposed dot on a vector implies a time derivative of the vector). In (2)  $\mathbf{x}(j, \alpha)$  denotes a position vectors of the center of the  $j$ th cell on the right track ( $\alpha=1$ ) and on the left track ( $\alpha=2$ ).

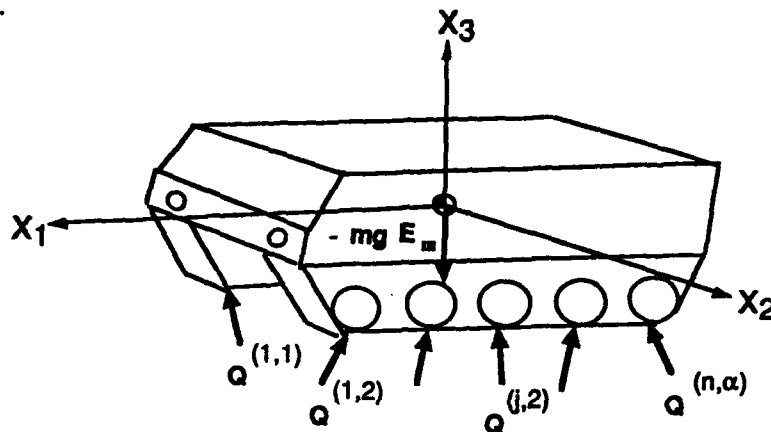


Fig.2 External forces acting on a tracked vehicle

### 3. Soil-Track Interaction Relation

Bekker [5] proposed empirical pressure-sinkage and shear-slippage relations for monotonic loading based upon extensive experimental data. These empirical relations are very useful when experimental measurements of required soil-interaction parameters are available.

In this paper soil responses under cyclic loading, experienced by the soil under the track during the passages of road wheels, are experimentally investigated. The numerical implementation of the resulting soil-track interaction model into the spatial mobility model [4] is also described.

#### (1) Experimental Identification of soil-track interaction relations

The experimental apparatus of plate penetration and shear tests on dry loose sand is shown in Fig.3. Rectangular loading plates with different aspect ratios were first loaded vertically with different weights; the plate were then pulled horizontally to determine shear force-slippage and sinkage-slippage relations. Next, cyclic pressure-sinkage tests were conducted by fixing a supporting frame, Fig. 3; the shear force-slippage and sinkage-slippage relations in the lateral and longitudinal directions were measured by moving the support frame. The latter set of tests was intended to measure the effect of anisotropy between the longitudinal and lateral directions of tracks.

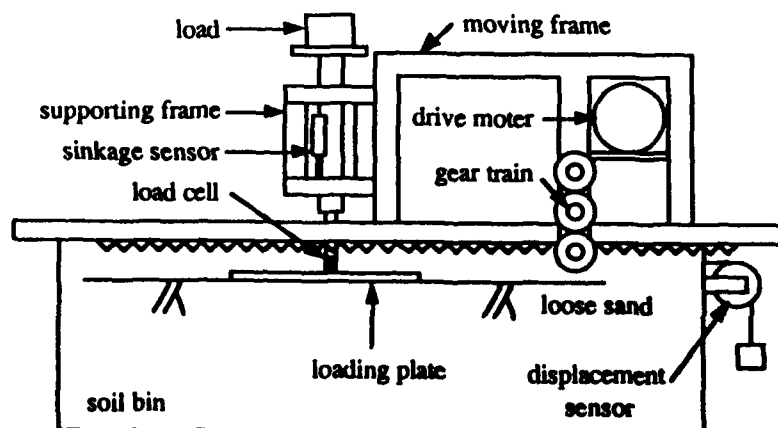


Fig.3 Diagram of the plate penetration and shear test apparatus



## (2) Pressure-sinkage relation

For monotonic loading the pressure-sinkage relation proposed by Bekker [5] is employed. The normal force,  $Q_3$ , is represented by a nonlinear function of the sinkage,  $u_3$ , as follows:

$$Q_3 = \Delta L(k_c + Wk_\phi)u_3^n \quad (3)$$

where  $k_c$ ,  $k_\phi$  and  $n$  are constants,  $\Delta L$  and  $W$  are, respectively, the length of the cell and track width. The constants can be determined from the experimental pressure-sinkage data shown in Fig. 4. For initial loading and plastic loading the rate from of the (3) is employed in the soil-track interaction model.

The pressure-sinkage data, manifesting loading-unloading cycles, are plotted in Fig. 5. After unloading, the irreversible sinkage — termed plastic sinkage,  $u_3^{pl}$  — is observed. During either the unloading process or the reloading below the yield normal force, which is the maximum normal force experienced by the soil, the response becomes elastic as

$$\dot{Q}_3 = K' \dot{u}_3^{el} \quad (4)$$

where  $K'$  is the bulk modulus and  $u_3^{el}$  is the elastic sinkage. In the above plate penetration test the rate of sinkage is, therefore, decomposed into elastic and plastic parts. However, a suite of scale model tests revealed that additional sinkages are necessary to characterize the sand; these are slip-induced sinkage which is observed when a rigid plate slips, and the agitation-induced sinkage observed when the loading plate, assumed flexible, induces settling in the sand.

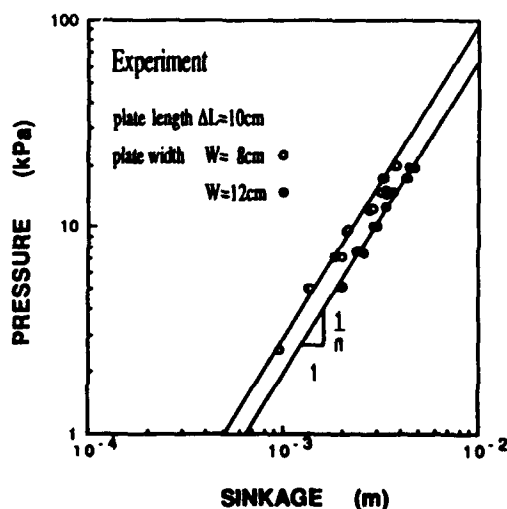


Fig.4 Pressure-sinkage data with different plate width under monotonic loading

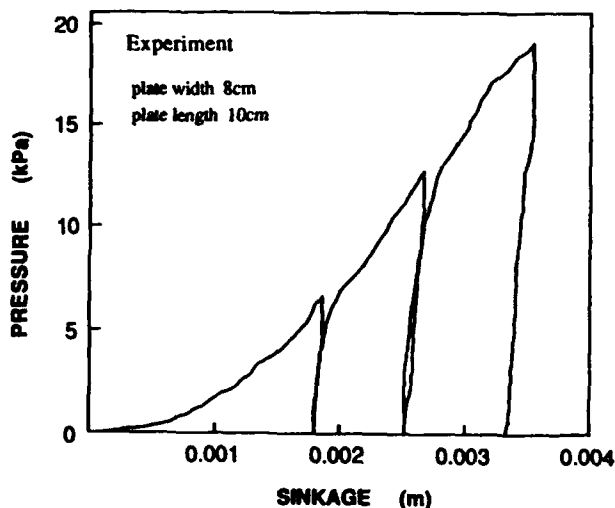


Fig.5 Pressure-sinkage curve under cyclic loading

### (3) Slip-Induced sinkage

The sinkage-slippage data obtained by pulling the loaded plate in the longitudinal and lateral directions are shown in Figs. 6a and 6b. The figures demonstrate notable increase of sinkage due to increasing slippage and the directional dependence (anisotropy) of the slip-induced sinkage in the longitudinal (Fig. 6a) and the lateral (Fig. 6b) directions. The slip-induced sinkage,  $u_3^{sl}$ , and slippage relation is expressed in rate form as

$$\dot{u}_3^{sl} = \gamma(\theta, Q_3) \sqrt{[V_1]^2 + [V_2]^2} \quad (5)$$

where  $\gamma$ , the anisotropy constant, is a function of the direction of slippage,  $\theta$ , and the normal force,  $Q_3$ , and  $[V]$  is the cell slip velocity. In (5), vector components are with respect to the vehicle coordinate system. The anisotropy constant is interpolated from the data for the slippage in the longitudinal direction ( $\theta = 0^\circ = 0$ ) and the lateral direction ( $\theta = 90^\circ = \pi/2$ ) as

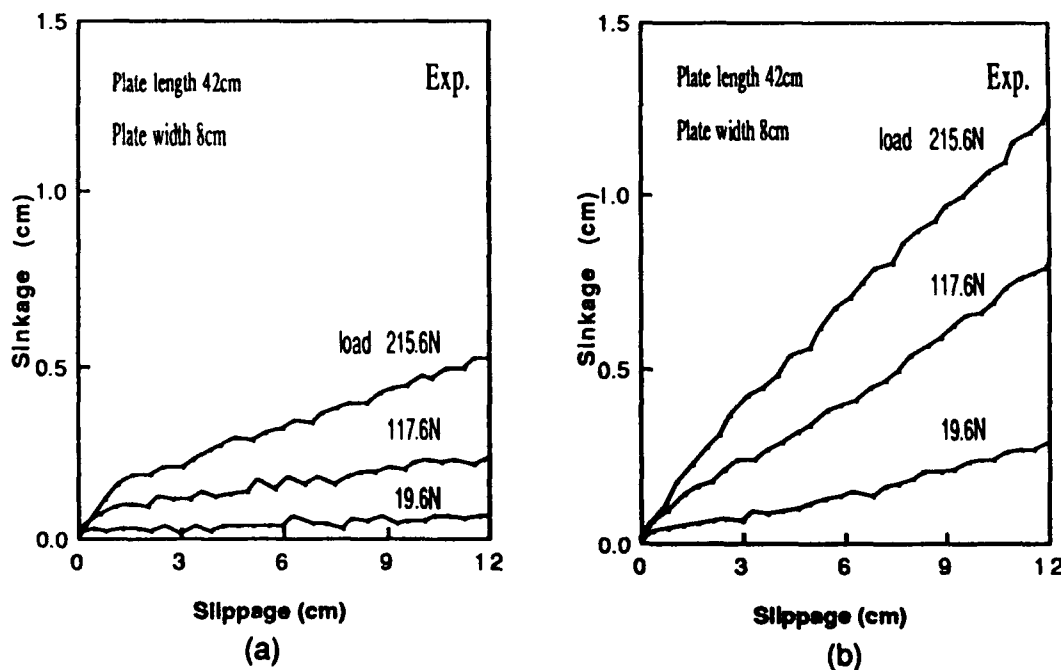
$$\gamma(\theta, Q_3) = \gamma(0, Q_3) \cos|\theta| + \gamma(\pi/2, Q_3) \sin|\theta| \quad (6)$$

where  $|\theta|$  = absolute value of  $\theta$ .

In order to accommodate the slip-induced sinkage in the soil-track interaction relation, the sinkage rate is decomposed into elastic, plastic, slip-induced, and agitation-induced parts as

$$\dot{u}_3 = \dot{u}_3^{el} + \dot{u}_3^{pl} + \dot{u}_3^{sl} + \dot{u}_3^{ag} \quad (7)$$

For the test apparatus shown in Fig. 3, the loading plate is considered to be rigid. Therefore, agitation-induced sinkage is negligible. It is assumed that the slip-induced sinkage occurs whenever the track slips and is independent of the loading and unloading processes of the pressure-sinkage response.



Figs.6 Sinkage-slippage curves with different normal loads: (a) for longitudinal slippage and (b) for lateral slippage

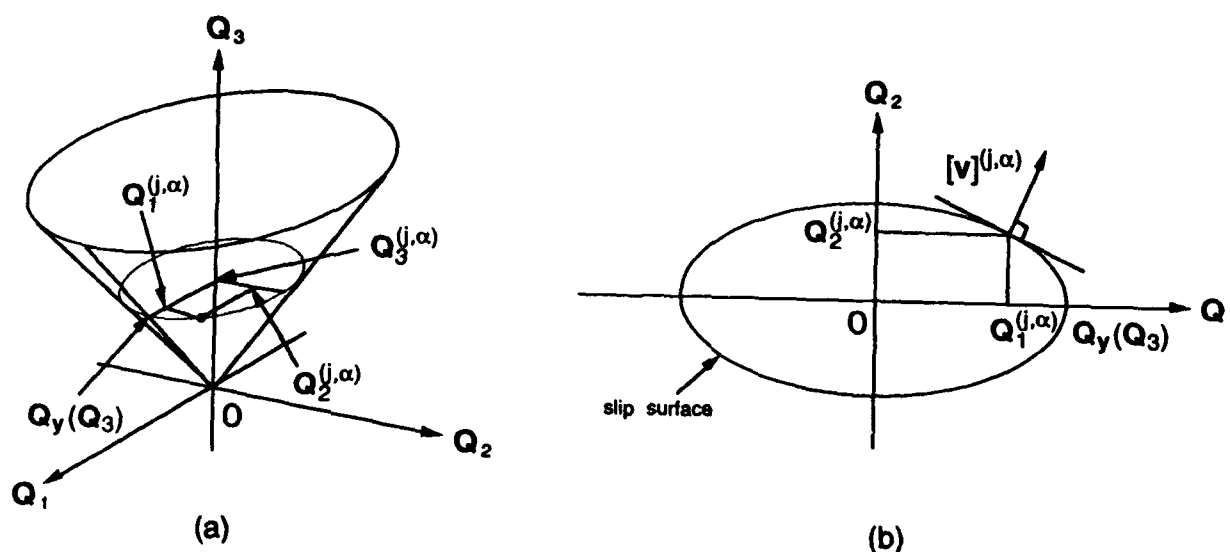
#### (4) Shear force-slippage relation

During the motion of the vehicle, the track slips and the soil under the tracks experiences plastic slippage. Therefore, the stress state of the soil element under the track lies on the failure envelope in the pressure-octahedral shear stress plane. The pressure dependency of the octahedral-shear yield stress has been modeled by the Drucker-Prager model or Cap models [6]. When the above yield criterion in stress space of a soil element is viewed in the interaction force space, the normal force dependent yield shear force is obtained. This yield shear force exhibits directional dependency in the longitudinal and lateral directions. The anisotropy results from the grousers attached to trackshoes and the geometry of the track. The anisotropic yield surface in the space of the interaction force is illustrated in Fig. 7a and expressed as

$$(Q_1)^2 + (\kappa Q_2)^2 = Q_y^2(Q_3) \quad (8)$$

where,  $\kappa$  represents the ratio between the longitudinal yield shear force and the lateral yield shear force, and  $Q_y$  is the longitudinal yield shear force which is a function of the normal force,  $Q_3$ . As a flow rule, an associative flow rule depicted in Fig. 7b is employed.

When the above shear force-slippage relation is employed in the spatial mobility model [4], the track slip velocity is obtained at each time step by integrating the equations of motion. The shear force components are obtained by finding the point on the yield surface at which the slip velocity becomes normal to the yield surface (slip surface) as shown in Fig. 7b.



Figs.7 Yield surface: in the space of the soil-track interaction force and (b) in the shear force plane, and (b) associative flow rule

#### 4. Scale Model Test on Dry Loose Sand

The scale model used for the experiment is shown in Fig.8. The vehicle specifications are included in Table 1. A unique character of scale model is that the mass center, or center of gravity (C.G.), is located at the geometrical center of the projected area of the vehicle onto the  $x_1, x_2$ -plane. The sprockets were driven independently by two DC-motors to control the speed of each track. The sprocket torques were measured by attaching strain gauges on the sprocket axes. Under straight vehicle motion, the sinkage of the center of gravity was measured by an optical method. Figure 9a shows the history of the measured sinkage of the mass center under straight motion. During the course of the experiment excessive plastic sinkage, unexplained by the plastic and slip-induced sinkages was observed. A closer observation of the sinkage data and a suite of experiments using different scale models with

different suspension systems revealed that the excessive sinkage was observed even under negligible slippage, and the excessive sinkage is due to flexible deformation of the trackshoes of a cell during the passage of road wheels. Therefore, the additional sinkage induced without slippage is termed agitation-induced sinkage,  $u_3^{ag}$ , and the sinkage rate was decomposed as shown in (7). Unfortunately, there is no standardized method to characterize this sinkage. Therefore, based upon a suite of scale model experiments the following relation was adopted when the agitation sinkage cannot be neglected:

$$\dot{u}_3^{ag} = a_g(V_1, A_1, Q_3) \quad (9)$$

Here  $a_g$  is a nonlinear function of the vehicle longitudinal velocity,  $V_1$ , the longitudinal acceleration,  $A_1$ , and the normal force  $Q_3$ . For the numerical analyses  $a_g=0.1$  cm was employed. The agitation-induced sinkage occurs *intermittently* as depicted in Fig. 9a. The implementation of the intermittent sinkage may be best explained by considering a square ground surface element (smaller than the cell size); when the first road wheel touches the surface element it experiences the sinkage as shown in (9), the subsequent motion of the first road wheel in the element does not induce any agitation sinkage. However, When the second or other road wheel touches the element it experiences the agitation-induced sinkage according to (9) and is considered the cause of the intermittent settling.

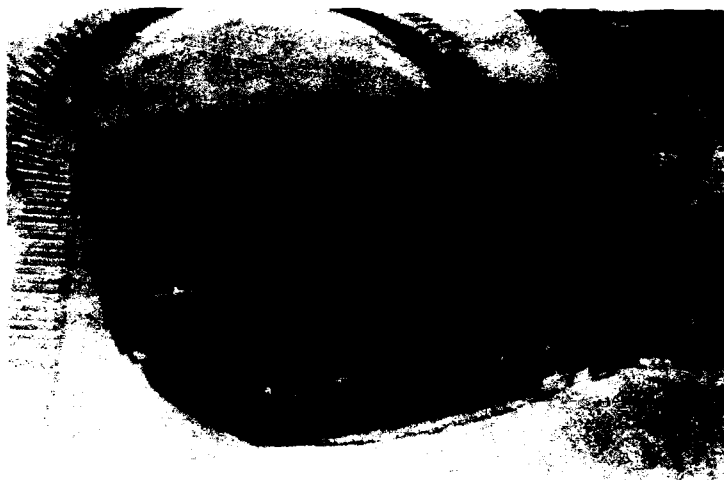
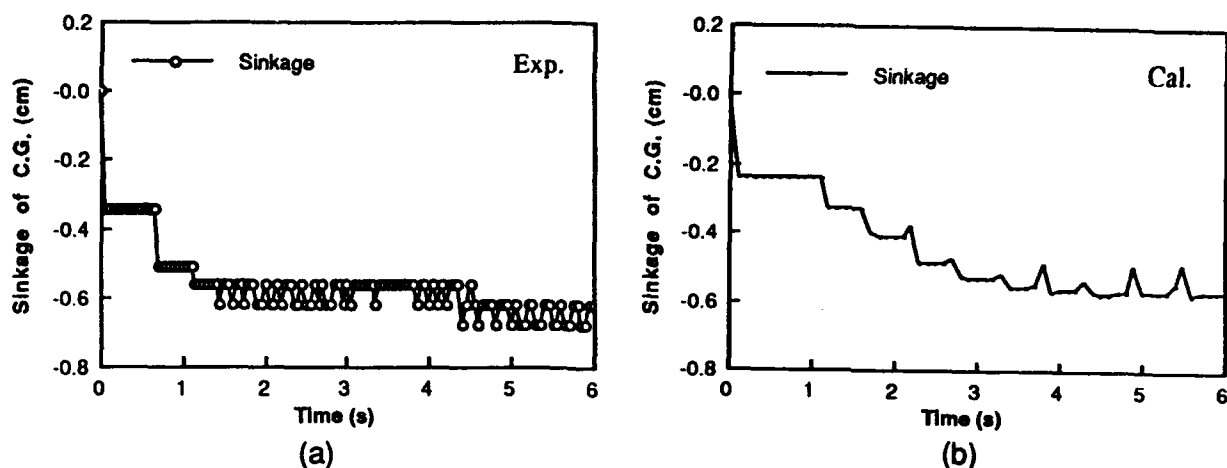


Fig.8 View of the scale model

Table 1 Specifications of the scale model

Mass	50.5 kg
Ground contact length	0.41 m
Tread of track	0.29 m
Height of center of gravity	0.11 m
Width of track	0.08 m
Number of road wheel	5



Figs.9 Evolution of the vertical displacement of the center of gravity:  
(a) experimental data (b) numerical prediction

### 5. Concluding Remarks

The soil-track interaction model was developed to predict the mobility of tracked vehicles on dry loose sand by using the spatial mobility model developed by the authors [4]. The interaction model includes the pressure-sinkage relation, anisotropic shear force-slippage relation, slip-induced sinkage, and agitation-induced sinkage. The slip-induced sinkage and the agitation-induced sinkage without slippage require further careful experimental investigations. In order to fully characterize the terrain for the prediction of vehicle trafficability and steerability, accurate evaluation and characterization of those sinkages become necessary. It is recommended that new field measurement techniques be developed to characterize those sinkages. However, by employing a realistic soil-track interaction model, the spatial mobility model can accurately predict tracked vehicle motion including sinkage and tractive forces.

### References

- [1] M. Kitano and H. Jyozaki, A theoretical analysis of steerability of tracked vehicles, J. of Terramechanics 13(4), p. 241(1976).
- [2] M. Kitano and M. Kuma, An analysis of horizontal plane motion of tracked vehicles, J. Terramechanics 14(4), p. 11(1978).
- [3] M. Kitano, K. Watanabe and O. Akimoto, Track sinkage of tracked vehicles under steering motion, Proc. of 2nd Asia-Pacific Conf. of ISTVS, p. 325(1988).
- [4] H. Murakami, K. Watanabe and M. Kitano, A mathematical model for spatial motion of tracked vehicles on soft ground, Proc. of 10th Conference of ISTVS, p. 635(1990).
- [5] M. G. Bekker, Off-the-road locomotion, Research and development in terramechanics, The University of Michigan Press, Ann Arbor, Michigan (1960).
- [6] W. F. Chen and G. Y. Baladi, Soil plasticity, theory and implementation, Elsevier Science Publishers B. V., Amsterdam, The Netherlands (1985).

## **APPROXIMATION FOR THE TDF-VALUE OF A NEW TIRE-SYSTEM**

**P. Parringer**

**Industrieanlagen-Betriebsgesellschaft m.b.H. (IABG)**

**Ottobrunn, FRG**

### **Summary**

In the Nato-Reference-Mobility-Model (NRMM), which can be used to estimate the mobility of a vehicle, there is a need to calculate the TDF-values for the tires. Unfortunately the WES-method, used in NRMM for the calculation of traction and rolling-resistance, is an empirical approach with an uncertain validity range.

In the last years the new CTS-tires (Conti-Tire-System) have been developed and some investigations have shown, that the TDF-value for this type of tire has to be modified.

Based on the result of a similarity study a modification for the TDF formula in NRMM is suggested.

This modification is varified by test results of field measurements with different tires.

### **Introduction**

In the Nato-Reference-Mobility Model (NRMM) the WES-method is used for the calculation of drawbar pull  $P$  and motion resistance  $R$ . In order to calculate these values for a vehicle with the new CTS-tires (Conti Tire System), there is a need to approximate the TDF-value (Tire Deflection Factor) for the new CTS-tires. The TDF-value is needed to calculate the very important VCI-value (Vehicle Cone Index) of a wheeled vehicle. It should be mentioned that the approximation of the TDF-value for CTS-tires has a big influence to the results of NRMM, as the next chapter will show.

### **Calculation and usage of the Vehicle Cone Index (VCI) in NRMM**

The VCI-value (Vehicle Cone Index) is one of the most important values within NRMM and is calculated from the Mobility Index  $MI$ :

$$VCI = \left( 11.48 + 0.2 MI - \frac{39.2}{MI + 3.74} \right) TDF \quad (1)$$

$$\text{with } TDF = \sqrt[4]{\frac{0.15}{z/h}} \quad (2)$$

$z$  = tire deflection,  $h$  = section height of tire

The Mobility Index MI is calculated from the most important vehicle data like wheel size, wheel load, vehicle clearance and engine and transmission characteristics. The first formulas for the MI and VCI-values were published more than 30 years ago [1]. While for the Mobility Index the formula did not change in the main task, the formula for the Vehicle Cone Index was expanded by the TDF-value.

The TDF-value is 1,0 if  $z/h = 0,15$  (15 % tire deflection), bigger than 1,0 if the tire deflection is less than 15 % and below 1,0 at tire deflections above 15% (Figure 3, highest line). In Figure 3 there are more lines, which show the results of earlier TDF formulas used in NRMM or in predecessor versions [2-7]. The differences between the TDF formulas which are shown by arrows are large. For example, the TDF-value of the formula of 1983 used in [6] is for 35 % tire deflection as small as the TDF-value due to the newest formula [7] at 70 % tire deflection.

The difference between the TDF-values of 1983 and 1985 at 35 % tire deflection is nearly as much as 20 % of the bigger value.

The lines are shown for tire deflections up to 70 % because this is, according to our literature study, the limit of practical usage of the TDF formulas.

The VCI-value, calculated by the formulas shown above, is used together with the soil-related RCI-value (Rating Cone Index) to define the Excess Rating Cone Index  $RCI_x$ :

$$RCI_x = RCI - VCI \quad (3)$$

If the  $RCI_x$ -value is smaller than zero then the vehicle will immobilize. The drawbar pull related to the vehicle weight  $P/W$  is shown in Figure 1 as a function of  $RCI_x$ . This figure is very important to show the large influence of the VCI-value and therefore of the TDF-value in NRMM. Whereas at a  $RCI_x$ -value of zero the vehicle immobilizes, a  $RCI_x$ -value of 3 is enough to overcome a hill with 10 % slope ( $P/W = 0,1$ ). If the  $RCI_x$ -value is

20 the maximum pull P/W becomes bigger than 0,4 which is more than 2/3 of the absolute maximum of P/W (about 0,6).

On the same terrain (same RCI-value) the RCI<sub>x</sub>-value varies in the range of 3 if the VCI-value varies in the range of 3. The VCI-value of a vehicle varies in the range of 3 if, for example, the VCI15-value (VCI-value at 15 % tire-deflection) is 30 and the TDF-value varies in the range of ±5 %. This means that the approximation for the TDF-value for a vehicle with a new tire system is a very sensitive approach with regard to VCI-value and to the calculation of drawbar-pull and motion-resistance.

#### Approximation for the TDF-values of CTS-tires

The new CTS-tire is shown in Figure 2. For this tire no valid formula exists for the TDF-value. For this reason the CTS-tire was compared with a conventional tire. The main criteria were the contact area and the assumption that vehicles with the same contact area, the same configuration and the same weight have to have the same VCI-value.

In Figure 4 the same TDF formula for a vehicle with conventional radial tires 14.00 R20 18PR and for the same vehicle with CTS-tires CT 375/60 R800 is used. The tire deflection is chosen differently in order to get the same numerical value for VCI. In this case the contact areas differ to a large degree which means that these two vehicles will have different drawbar-pulls and different motion resistances. As the VCI-values are the same the method is not consistent. The consistency is realized again if the TDF-value for the CTS-tires is changed.

The following procedure is proposed which results in the same VCI-values if the contact areas are the same:

$$TDF = 4 \sqrt{\frac{a_0}{z/h}} \quad (4)$$

with

$$a_0 = 0.15 \cdot \frac{\text{section height of a comparable 100\% tire}}{\text{section height of tire}} \quad (5)$$

The section height of a comparable 100 % tire is the same as the tire width.

The results are shown in Figure 5.



### Validation with field tests

The field tests in [8] are made in sand. The tests are made with the same vehicle (8x8) but with two different tires. A 85 % conventional tire 17,5 R25 XL and the new CTS-tire CT 405/65 R 775 Keilwulst were used. The drawbar-pull slip lines in the Figures 6 and 7 include the VCI-values as parameters, which are calculated by the newest NRMM-version and the described TDF-formulas. The modified TDF formula in Figure 7 shows a much better correlation between the measured drawbar pulls and the calculated VCI-values. Vehicles with a similar drawbar-pull line have a similar VCI-value, which is not true for the VCI-values in Figure 6, calculated by the original TDF formula. In addition to these field tests, labor tests in a small soil bin have been made with the same tires [9]. These results also confirm the assumptions which are used to modify the TDF-value.

### Conclusion

In order to get a well verified TDF equation, supplementary tests should be made with a single wheel tester [10] with different tires and different tire-sizes. An update of the NRMM with the new TDF formula will be suggested.

### References

- [ 1 ] N.N.: "Soils Trafficability", Department of the Army  
Technical Bulletin TB ENG 37, Washington, USA, 1959
- [ 2 ] N.N.: "The AMC 71 Mobility Model", U.S.Army Tank Automot-  
ive Command, Warren, Michigan, USA, 1973
- [ 3 ] N.N.: "AMC 74 Mobility Model", U.S.Army Tank Automotive  
Command, Warren, Michigan, USA
- [ 4 ] Jurkat, M.P.; Nuttall, C.J.; Haley, P.W.:  
"The U.S.Army Mobility Model (AMM-75)",  
5th International ISTVS-Conference, Detroit, USA, 1975
- [ 5 ] Jurkat, M.P.; Brady P.M.; Haley, P.W.:  
"NATO Reference Mobility Model",  
Technical Report Nr. 12 503, ATAC, Warren, Michigan, 1979

- [ 6 ] Melzer, K.-J.:  
 "Possibilities of evaluating the traction of tires for off-road transportation vehicles",  
 2nd European ISTVS-Conference, Ferrara, Italy, 1983, page 103
  
- [ 7 ] Haley, P.W.:  
 "Correction to module of NRMM since 30.12.84",  
 Department of the army, Warren, Michigan, 1985
  
- [ 8 ] Schlechter, H.P.:  
 "Erprobung Exp.Fahrzeug Rad; Vergleichsuntersuchung CTS-Räder";  
 WTD41-Bericht, 1989
  
- [ 9 ] Parringer P.; Wallisch, W.:  
 "Vergleichende Untersuchungen am CTS-Reifen",  
 IABG-Bericht B-TF 2613, Ottobrunn, 1989
  
- [ 10 ] Parringer P.:  
 "Soil strength measurement at continuous movement",  
 4th European ISTVS-Conference, Wageningen, The Netherlands,  
 1989

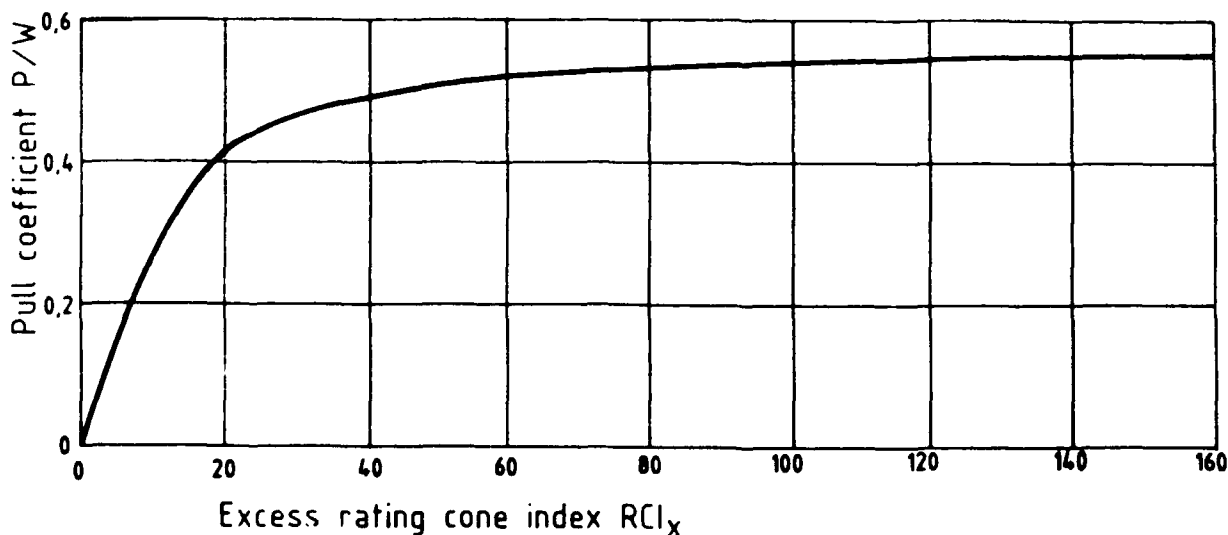


Figure 1: Drawbar pull  $P$  over weight  $W$  as a function of excess rating cone index  $RCI_x = RCI - VCI$

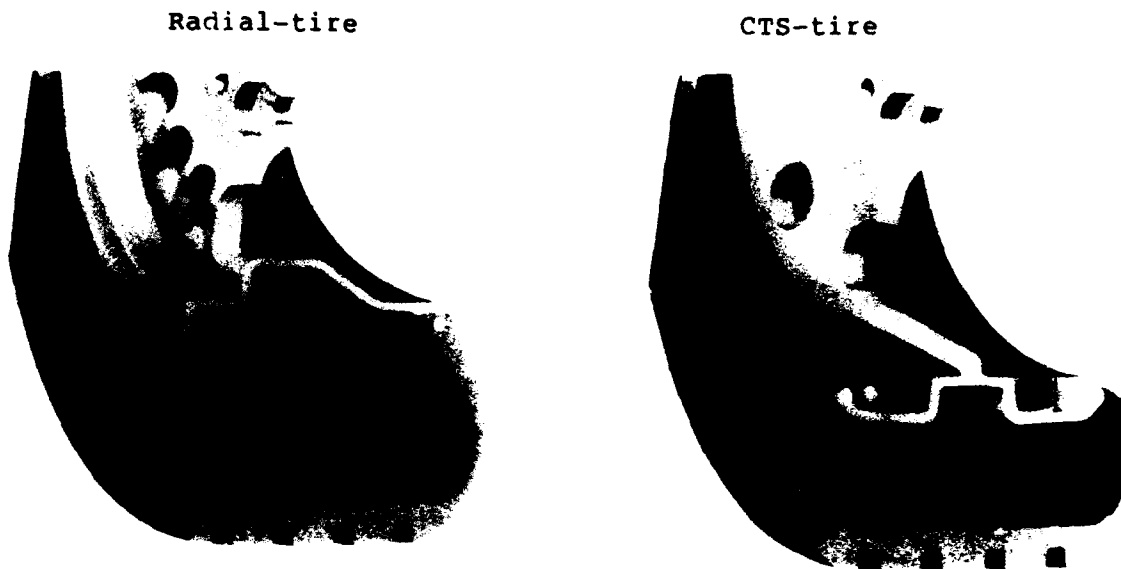


Figure 2: Comparision of the new CTS-tire with a radial-tire

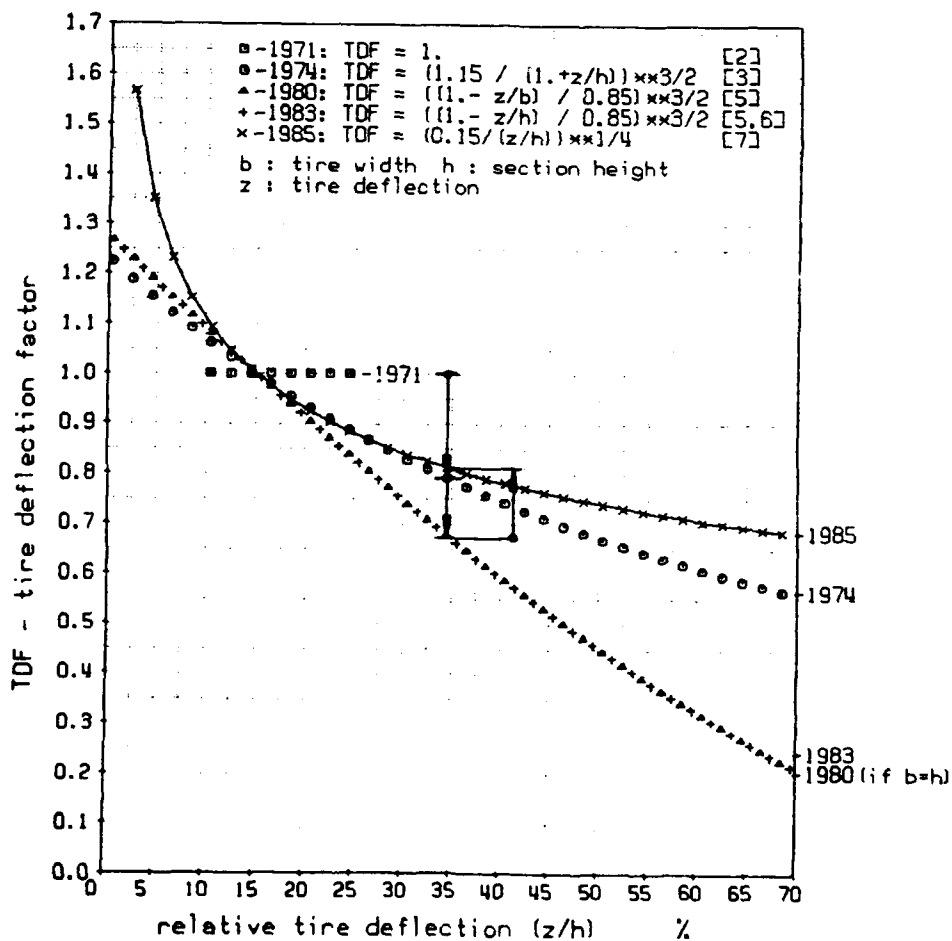


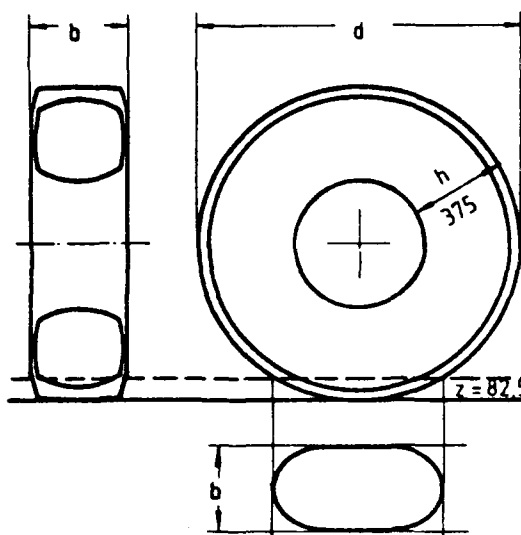
Figure 3: Development of formulas to calculate the Tire Deflection Factor (TDF) with mention of sources used

Radial - tire 14.00 R20 18PR

$$b = 0,375 \text{ m} \quad \text{TDF} = \sqrt[4]{\frac{0,15}{z/h}} = 0,909$$

$$h = b = 0,375 \text{ m} \quad \text{VCI} = 25,8$$

$$d = 1,25 \text{ m}$$



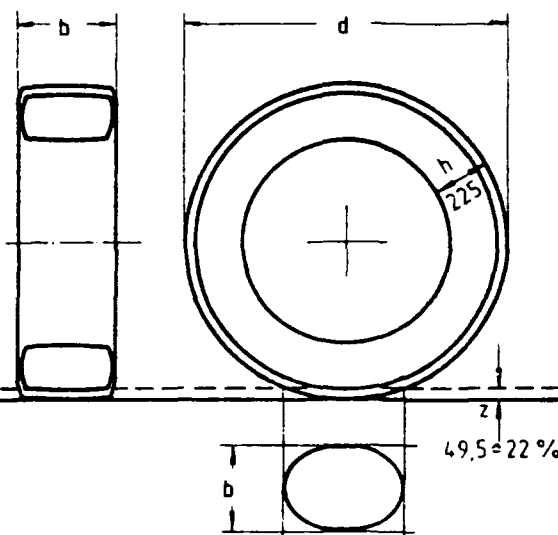
(Contact area : 1875 cm<sup>2</sup>)

CTS - tire CT 375/60 R 800

$$b = 0,375 \text{ m} \quad \text{TDF} = \sqrt[4]{\frac{0,15}{z/h}} = 0,909$$

$$h = 0,225 \text{ m} \quad \text{VCI} = 25,8$$

$$d = 1,25 \text{ m}$$



(Contact area : 1406 cm<sup>2</sup>)

Figure 4: Contact areas of the two tires with the same TDF-value due to NRMM (same VCI-values but different contact areas)

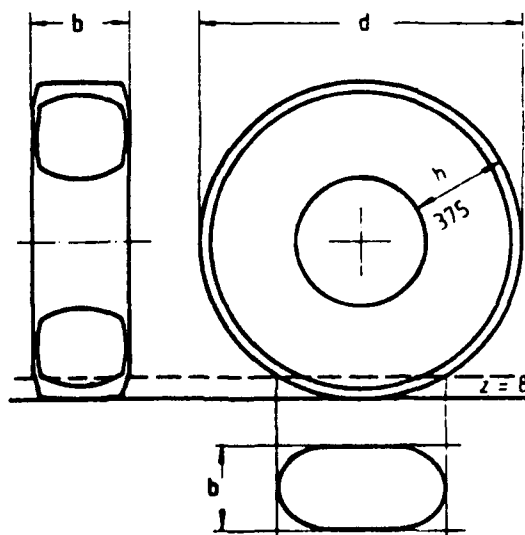
Radial - tire 14.00 R20 18PR

$$b = 0,375 \text{ m} \quad \text{TDF} = \sqrt[4]{\frac{a_0}{z/h}} = 0,909$$

$$h = b = 0,375 \text{ m} \quad \text{VCI} = 25,8$$

$$d = 1,25 \text{ m}$$

$$a_0 = 0,15$$



(Contact area : 1875 cm<sup>2</sup>)

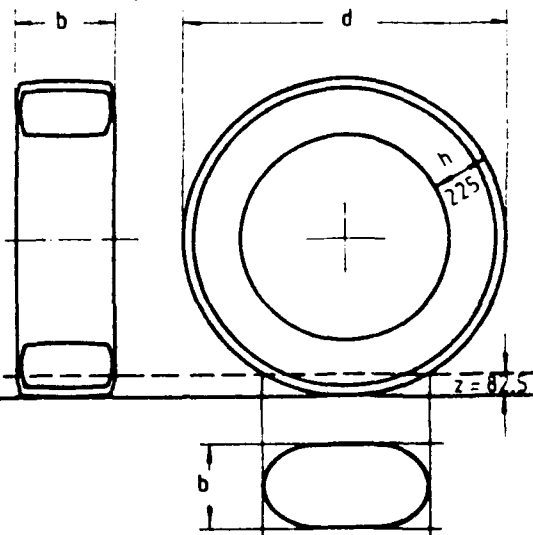
CTS - tire CT 375/60 R 800

$$b = 0,375 \text{ m} \quad \text{TDF} = \sqrt[4]{\frac{a_0}{z/h}} = 0,909$$

$$h = 0,225 \text{ m} \quad \text{VCI} = 25,8$$

$$d = 1,25 \text{ m}$$

$$a_0 = 0,15 \cdot \frac{0,375}{0,225} = 0,25$$



(Contact area : 1875 cm<sup>2</sup>)

Figure 5: TDF- and VCI-values due to modified TDF formula  
(same Vehicle Cone Index VCI and same contact area)

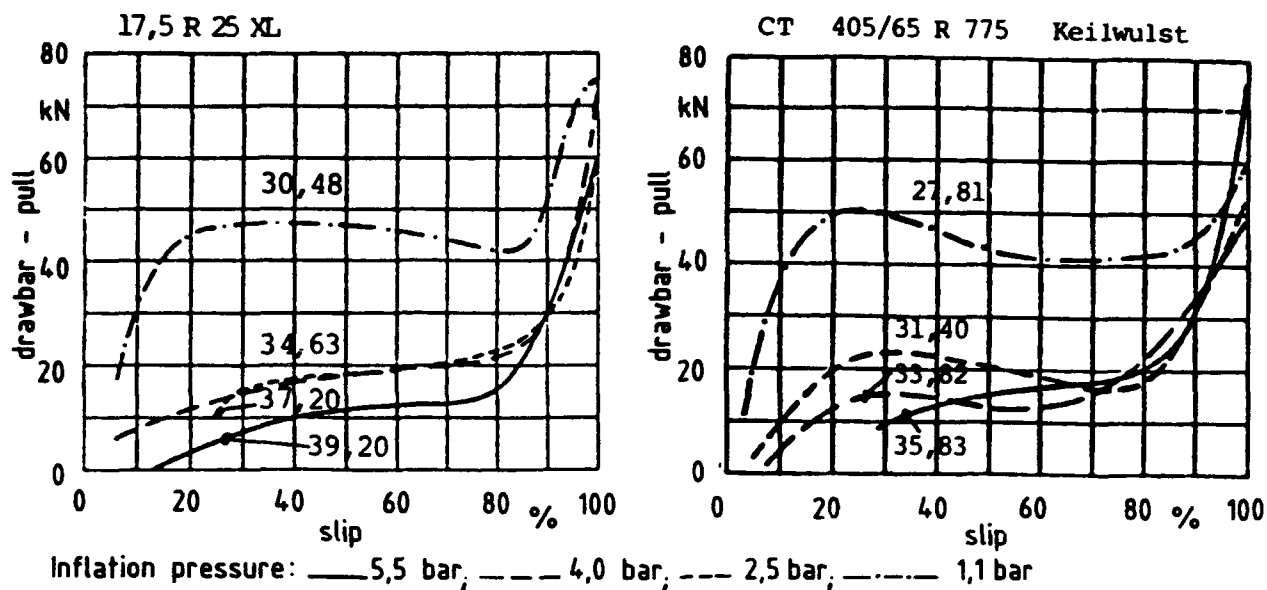


Figure 6: Measured drawbar-pull slip lines for a vehicle with two different tires in the same soil.

VCI-values are parameters at the lines. TDF-values due to NRMM:

$$TDF = 4\sqrt{\frac{0.15}{z/h}}$$

There are contradictory VCI-values at comparable drawbar-pull slip lines.

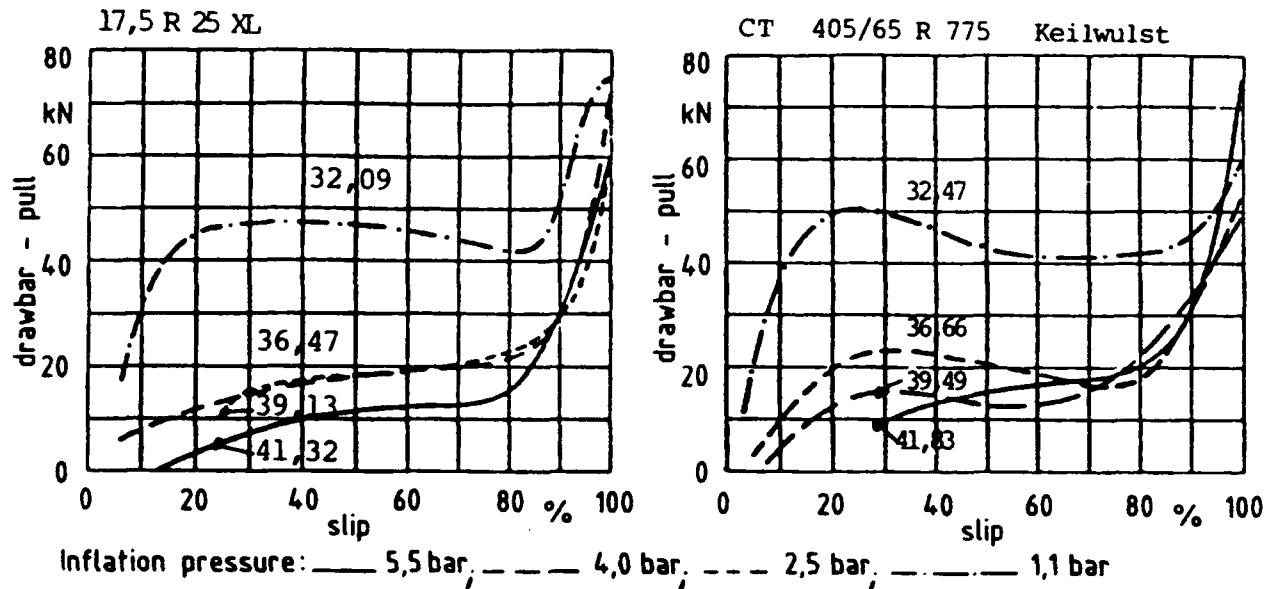


Figure 7: Measured drawbar-pull slip lines for a vehicle with two different tires in the same soil.

VCI-values are parameters at the lines. TDF-value due to modified formula:

$$TDF = 4\sqrt{\frac{a_0}{z/h}}$$

This result shows similar drawbar-pull values at similar VCI-values

# INVESTIGATIONS ON DEPENDENCE OF THE SOIL COMPACTION ON UNIT PRESSURE OF THE TYRE

Dr Z. Błaszczewicz

Agricultural University of Poznań

Institute of Agricultural Mechanization

## Summary

The evaluation of agricultural tyres in respect of their influence upon soil compaction, on the basis of effected unit pressure, is controversial. In literature more often we can find results of investigations on the various quite another effect of unit pressure of wheels upon soil compaction. An attempt to elucidate this relations was undertaken on the basis of elaborated by author, the quite new original method and equipment enabling to project of the contact area of tyres with soft ground for the wheel movement conditions and giving more exact measurement results. In the field investigations, performed on the light texture soil were obtained relations of rut depth and soil bulk density from the contact area and wheel unit pressure. The contact area and unit pressure have changed through change of wheel load and internal pressure in the tyre.

## Introduction

Important for agricultural practice the reduction of soil compaction by agricultural tyres is still an insoluble problem. One of the parameters on whose basis the estimation of agricultural tyres is carried out in respect of the produced changes in the soil compaction is the unit pressure defined as a ratio of the wheel load to the surface of the tyre contact with the soil through which the load is conveyed. The results of the investigations presented in the literature point out more frequently that there is a non-uniform dependence of the soil bulk density on unit pressure of the tyre /2 - 9/. Hence the use of this parameter seems to be controversial.

The results of field investigations carried out on this problem by the author allow to explain some of the accompanied dependencies.

## Experimental method

On the basis of investigations carried out with a light soil it has been acquired the dependence of the rut depth and the soil bulk density in the rut on the unit pressure that has been changed in two ways: through the change of the internal pressure and through application of various loadings of the wheel. The contact area of the tyre with the soil has been established for the dynamic conditions by means of a new original method developed by the author and by using a new original measuring apparatus /1/. The applied measuring apparatus has made it possible to take measurements of the tyre deformations changing dynamically and those of the soil deformation during the wheel movement. At first are made measurements of those deformations during wheel movement by means of following equipment:

- a device for measurement of radial and longitudinal deflections of tyre,
- film camera for measurement of the lateral tyre deflection,
- a device for measurement the cross section of the tyre and rut,
- a device for measurement the height of soil lifting after the tyre.

Obtained results are then the base of calculations with the use of elaborated mathematic models, of the rectangular co-ordinates of this part of tyre surface, which is in contact with soft ground /fig. 1/.

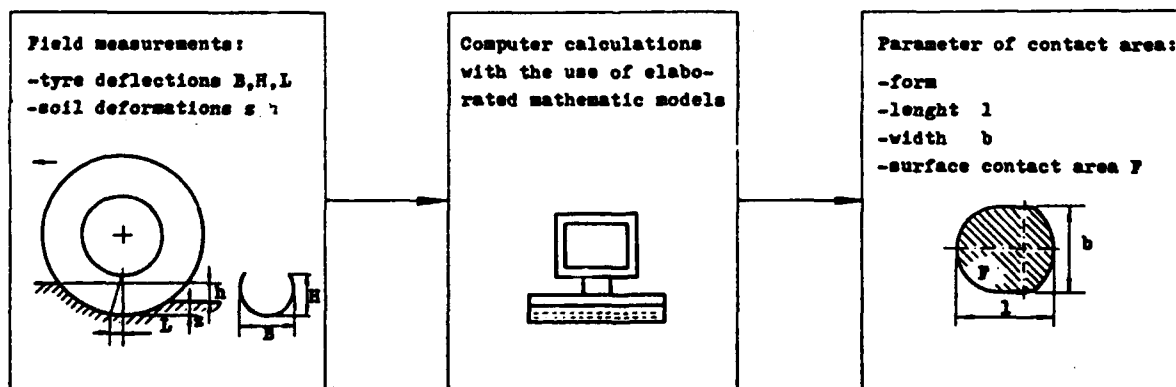


Fig. 1. Scheme of investigations at research of tyres surface contact area with soft ground in dynamic conditions.

The value of rectangular co-ordinates describing are the base of drawing its shape and calculation of the surface contact area. Those operations are made with use of personal computer and elaborated own numerical programme.

## Results

The obtained results of the investigations have demonstrated a lack of a uniform dependence of the soil density and the depth of the rut on unit pressure of the tyre /fig. 2/. The increase of the wheel loading produces a considerable decrease of unit pressure of the tyre, but at the same time it produces an increase of the soil bulk density within the rut and an increase of its depth. On the other hand, the decrease of the internal pressure diminish insignificantly the unit pressure of the tyre and produces a decrease of the soil compaction in the rut and that of its depth. At the same time the decrease of the bulk density and depth of the rut is the greater the greater is the tyre loaded.

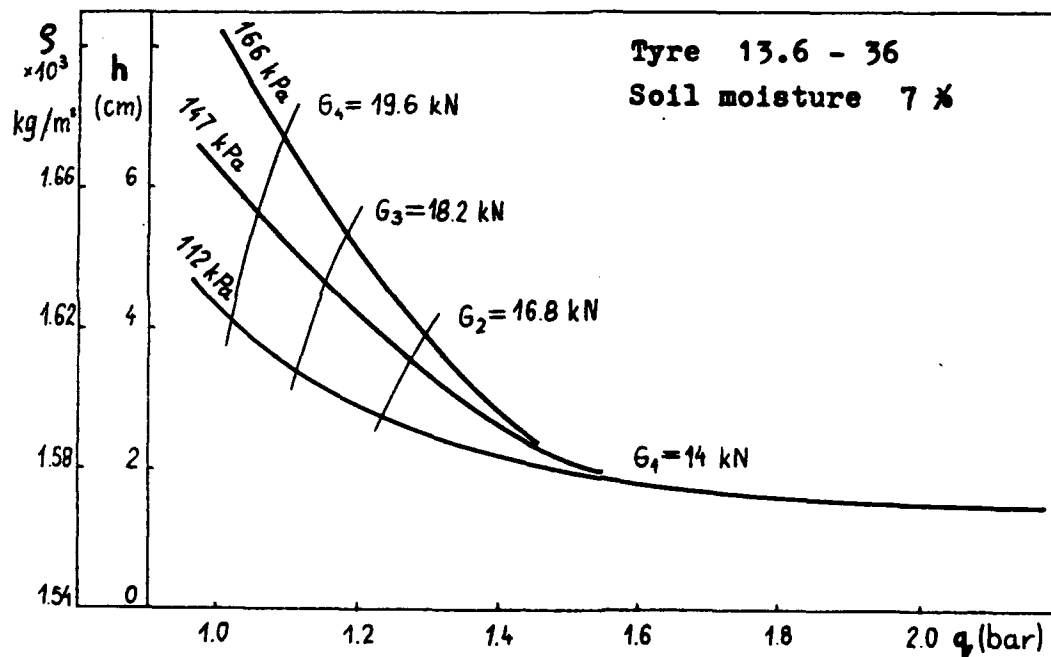


Fig. 2. Dependence of bulk density of the soil and the depth of the rut on the unit pressure  $p$  of the tyre when the unit pressure is changed by various loads  $G$  of the wheel and by change of the internal pressure.

The afore mentioned dependences are understandable if we refer them to the appeared deformation of the tyre and to changes of sizes of the contact area of the tyre with the soil and to the depth of the tyre /fig. 3 and 4/. When there is an increase of the load the tyre undergoes a slight deformation, goes deeper into the soil a deeper rut, on account of which the contact area increases more than the load of the wheel and resulting in decrease of the unit pressure.



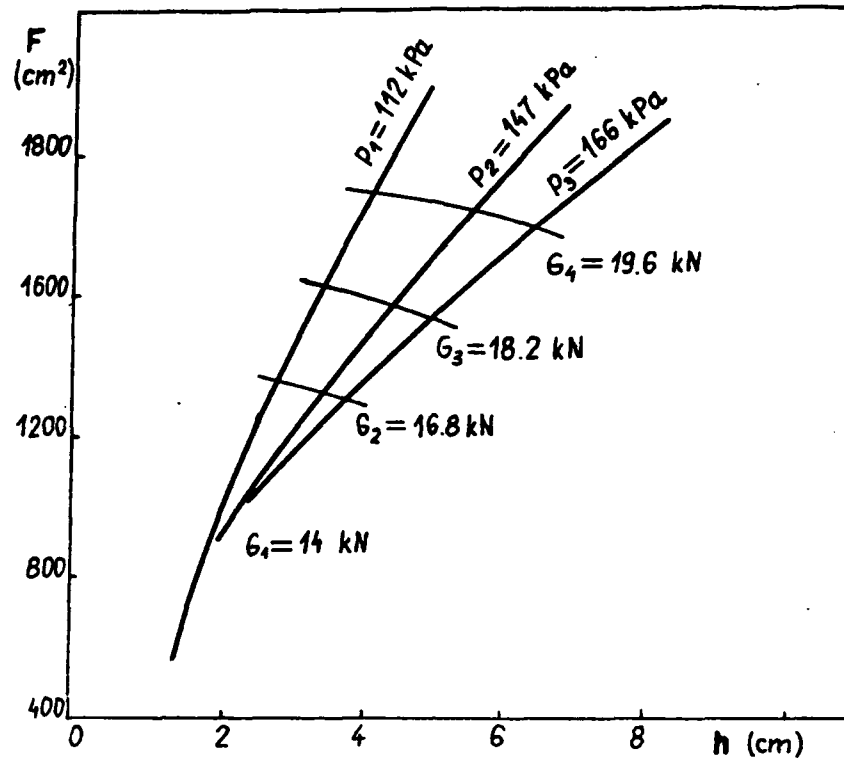


Fig. 3. Variation of the contact area  $F$  between a tyre and the soil with rut depth  $h$  during the wheel passage with load  $G$  and internal pressure  $p$ .

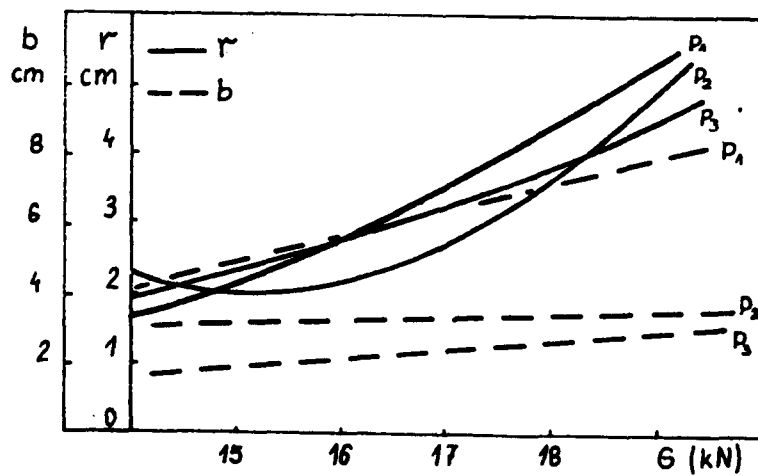


Fig. 4. Dependence of the tyre radial deflection  $r$  and of the tyre lateral deflection  $b$  on the wheel loads  $G$  and on the tyre internal pressure  $p$ .

Whereas the reduction of the internal pressure of the tyre decreases its rigidity, which distorting forms a more flat contact area with the soil and thus producing a less deeper penetration of the wheel and decrease of the soil density. With the same load the increased surface of the contact provides a less unit pressure of the tyre.

When there is a small load of the tyre of an order of 14 kN, the change of the load and that of the tyre internal pressure has a little impact on the depth of the rut and on the bulk density of the soil in the rut. However this is accompanied by considerable changes of the unit pressure, what can be attributed to an inaccuracy of measurements when the measured values of the rut depths, the contact area and the differences in tyre deformation are small.

To summarize, it can be stated on the basis of the unit pressure, defined as a ratio of the wheel loading to the contact area with the soil, there is not possible to presume univocally as regards the changes produced by the tyre in the bulk density of the soil and in the depth of the rut. Hence it is not advisable to use this parameter for the purpose of comparisons and for evaluation of the tyres from the point of view of effected by them the soil compaction.

#### References

1. Błaszczewicz Z. A method for the determination of the contact area between a tyre and the ground. *Journal of Terramechanics*. 1991.
2. Campbell D.J., Dickson J.W., Ball B.C. Effect of under-inflation of Tyres on Seedbed compaction and winter barley establishment and yield. *J. agric. Engng Res*. 1984. 29. 151-158.
3. Fekete A. Some observations on the contact pressure of tyres. *Zeszyty Problemowe Postępów Nauk Rolniczych*. 1977. 183. 125-130.
4. Gameda S., Raghavan G.S.V., Theriault R., McKyes E. High axle load compaction and corn yield. *Transaction of the ASAE*. 1985. Vol. 28. 1759-1765.
5. Gill W.R., Reaves C.A. Compaction Patterns of smooth rubber tyres *Agricultural Engineering*. 1956. 10. 677-680.
6. Koger J.L., Burt E.C., Trowse A.C. Multiple pass effects of skidder tires on soil compaction. *Transaction of the ASAE*. 1985. 11-16.
7. McLeod H.E., Reed I.P., Johnson W.H., Gill W.R. Power efficiency and soil compaction characteristics of single, dual and low-pres-

- sure tyres. Transaction of the ASAE. 1966. 41-44.
8. Taylor J.H., Burt E.C., Bailey A.C. Effect of Total load on sub-surface soil compaction. Transaction of the ASAE. 1980. 568-570.
  9. Taylor J.H., Gill W.R. Soil compaction: state-of-the-art report. Journal of Terramechanics. Vol. 21. No 2. 195-213.1984.

# SOIL PRESSURE AND COMPACTION UNDER AGRICULTURAL TIRES

H. Schwanghart

Institut of Agricultural Machinery, Techn. Univ. München

## 1. Abstract

Because vehicles increase in size and weight, these machines are severely compacting the soil and subsoil in the field of forestry and agriculture. As a consequence, ventilation, root growth and water-infiltration is disturbed in the soil.

Therefore investigations were made to measure the compaction under some agricultural tires. There is reported about measurements of contact area and contact pressure of two tractor tires, a terra tire and an implement tire. The experiments are made in loose soil of a soilbin. There is further shown the soil compaction under the tires in 40 cm deep loosened soil.

While the influence of tire inflation pressure is of no consideration in deeper layers, the total load of the tires is of great importance.

For a certain inflation pressure with rated load the ground pressure is smallest for the terra tire and biggest for the implement tire.

The compaction in the depth of 25 to 40 cm is 13 % less with recent tractor tires than with terra tire and implement tire.

## 2. Introduction

Because in the last decades agricultural vehicles increased in weight and size, there is the risk of compaction of the soils by frequent overrolling. The agricultural yields decrease because the roots cannot penetrate dense soil layers.

The greatest risk however is that rainfall is prevented to penetrate the compacted soil and cannot flow in the subsoil for filling up the reserves of drinking-water. Therefore all over the world investigations are made to study soil compaction. Contact areas of agricultural tires are measured repeatedly on hard and soft soils [3, 9, 13, 18, 19].

In the last time there is frequently reported about measurements and calculations about soil compaction under tires running off road [2, 5, 8, 10, 11, 12, 14, 15, 16, 17].

In [1, 4] a compaction index is proposed for the intensity of compaction from the relation of volume reduction and initial volume respectively porosity. Higher wheel loads cause density increase from 1.3 to 1.45 g/cm<sup>3</sup> in sandy loam and to 1.6 g/cm<sup>3</sup> in clay soil [6, 7].

Number of overrolling changes the condition of upper soil layer whereas heavier loads influence the subsoil.

### 3. Test equipment and experiments.

Experiments about soil compaction were made with four tires (Fig. 1) in a soil bin measuring 20 m in length and 2,5 m in width. The data of the tires shows Table 1. There are two tractor tires with the same diameter but different width. The tire 360/70 R 24 (TM 700) is another version of the tire 12.4 R 24 (TM 200) with greater width. Furtheron a very wide terra tire 38x20.00-16A and a thin implement tire 12.5/80-18 (without tread) is tested

The soil (loamy sand) is 40 cm deep loosened by tillage tools and afterwards 20 cm deep rotary tilled. The moisture content of the medium wet soil was about 15 %.



**Fig 1:** Testtire from left to right: 12.4 R 24 (TM 200)  
360/70 R 24 (TM 700), 38x20.00-16A Terra, 12.5/80-18 (Impl)

**Tabel 1:** Data of the tested tires and rated loads for 20 km/h

Tire	Diameter	Width	0.8	1.2	1.6	2	2.8 bar
12.4 R 24 (TM 200)	1170	340	1212	1451	1673	-	-
360/70 R 24 (TM 700)	1150	386	1341	1599	1845	-	-
38x20.00-16A Terra	993	498	1119	1419	-	1912	2328
12.5/80-18 (Impl)	990	344	-	1367	1623	1880	2380

The non driven tires were towed a few meters with constant load of 1000 - 2500 kg at an inflation pressure of 0.8, 1.2, 1.6 und 2 bar in the loosened soil ( $1.25 \text{ g/cm}^3$ ). After stopping the tire the soil surrounding the tire has been powdered with white calcium carbonite (Fig. 2). After load reduction and lifting the tire (Fig. 3) the projection of the contact area could be drawn on a transparent foil.

The dry bulk density under the 10 to 20 cm deep track was measured down to 40 cm depth with cylindrical soil samples.

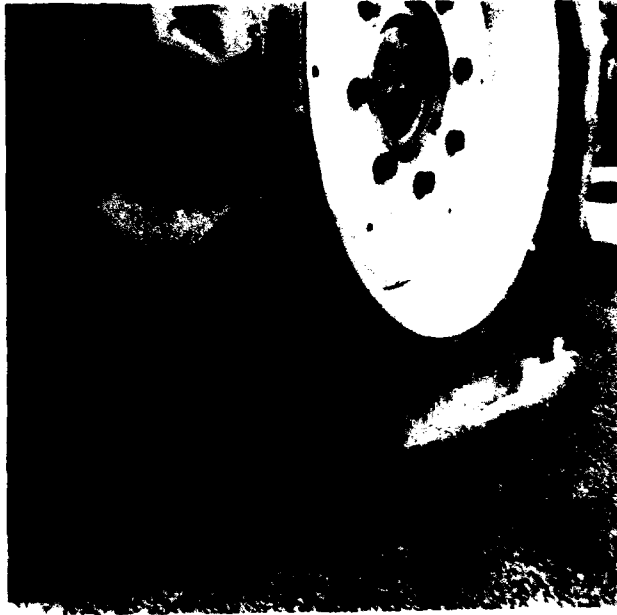


Fig 2: Test tire after the run just before it is lifted.



Fig 3: Track and marking of contact area

#### 4. Results.

Fig. 4 shows for the four tires the tire inflation pressure recommended for the rated loads by the manufacturers. Because for the used terra tire rated loads were known only for a speed of 20 km/h, all inflation pressure values and rated load values are selected for a speed of 20 km/h.

The terra tire and the implement tire 12.5/80-18 require the same inflation pressure for a specific load. The range of inflation pressure is from 0.5 to 2.8 bar for the terra tire and 0.8 to 3 bar for the implement tire. Compared with the terra tire, the rated load for the tire 12.4 R 24 (TM 200) is 5% higher and 15 % higher for the recent tire 360/70 R 24 (TM 700). The rated load of the tire TM 700 is 10 % higher than of the tire TM 200.

The Figures 5 to 8 show the contact area of the four tires in relation to inflation pressure at loads from 1000 to 2500 kg. With decreasing inflation pressure the contact area rises for every load. On the contrary the area decreases with greater inflation pressure. For example in Fig. 5 at the rated load of 1200 kg the decrease is 7 % from 1800 cm<sup>2</sup> and 0.8 bar to 1600 cm<sup>2</sup> and 2 bar inflation pressure.

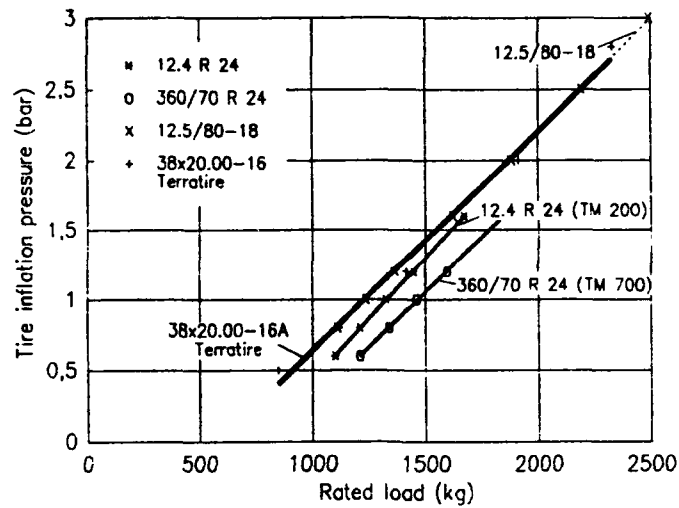


Fig 4: Tire inflation pressure at rated loads at 20 km/h.

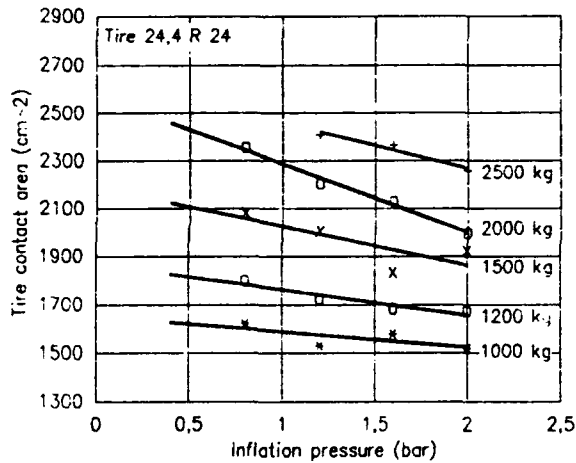


Fig 5: Measured mean contact area.

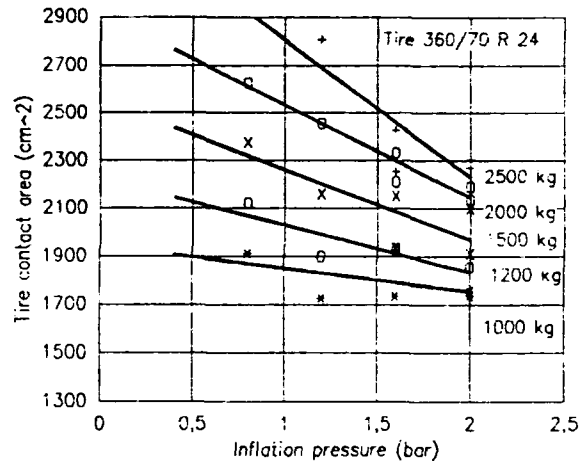


Fig 6: Measured mean contact area.

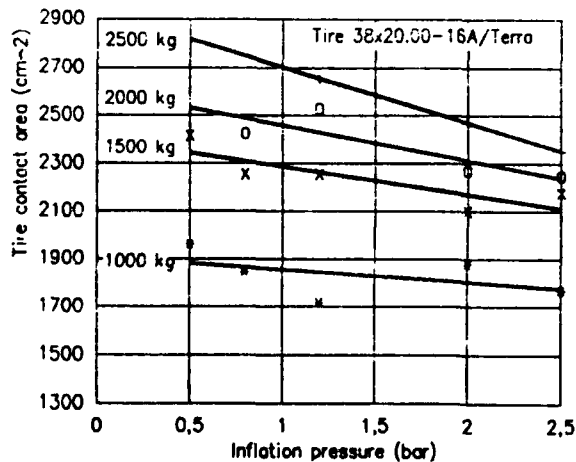


Fig. 7: Measured mean contact area.

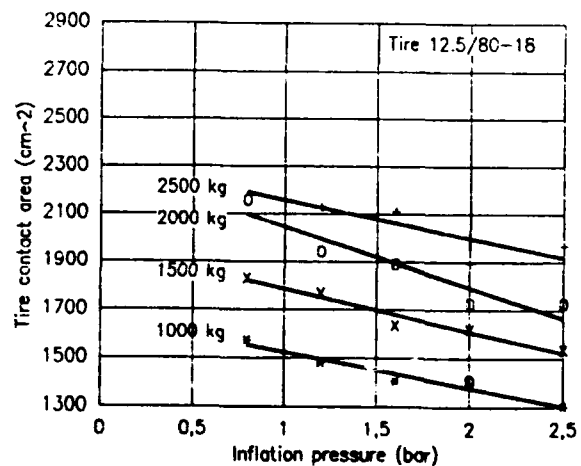


Fig. 8: Measured mean contact area.

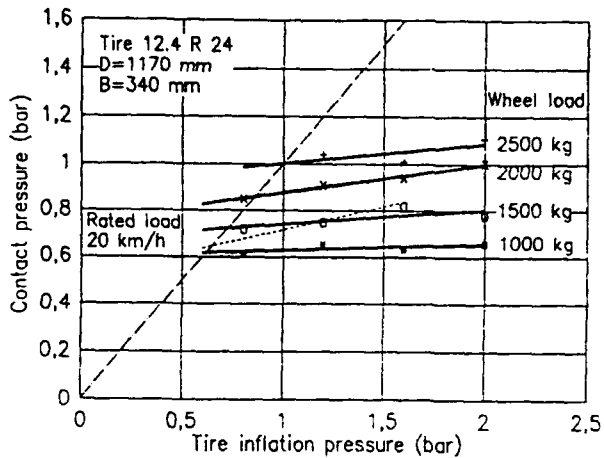


Fig. 9: Contact pressure at different loads.

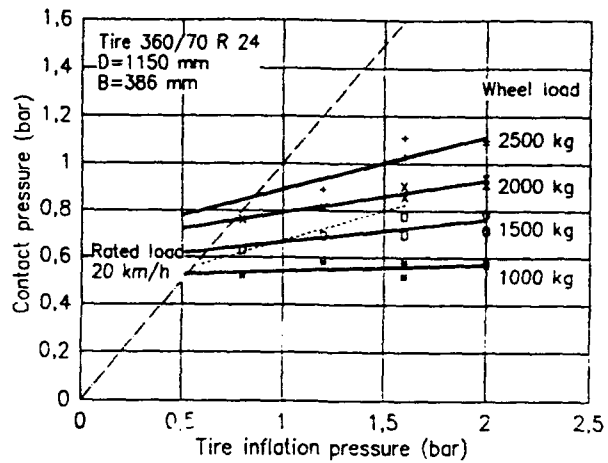


Fig. 10: Contact pressure at diff. loads.

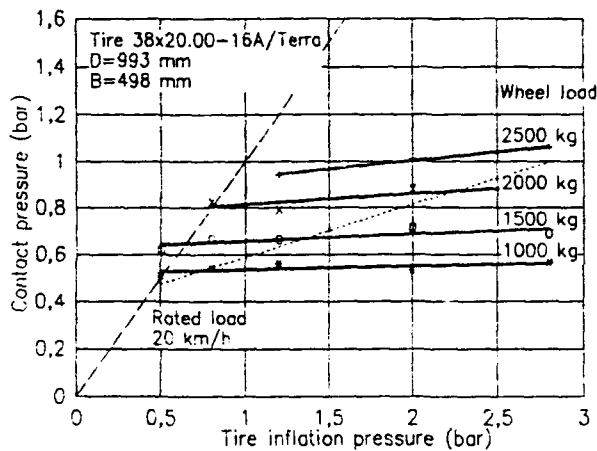


Fig. 11: Contact pressure at different loads.

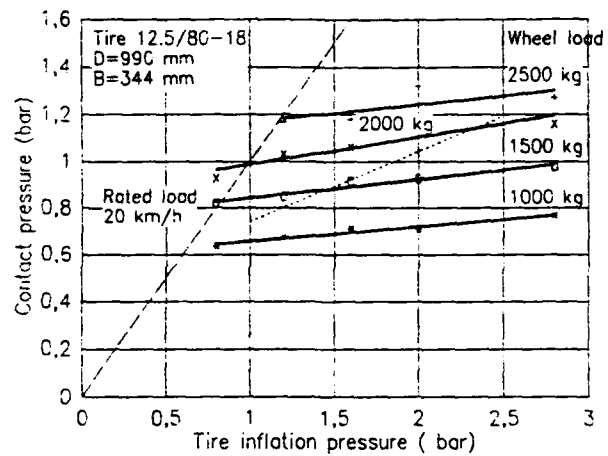


Fig. 12: Contact pressure at diff. loads.

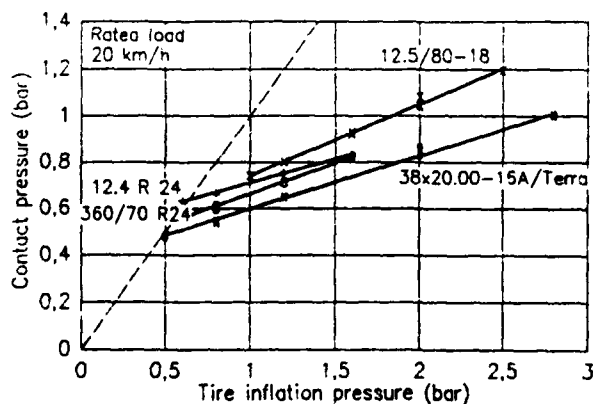


Fig. 13: Contact pressure of the 4 test tires.

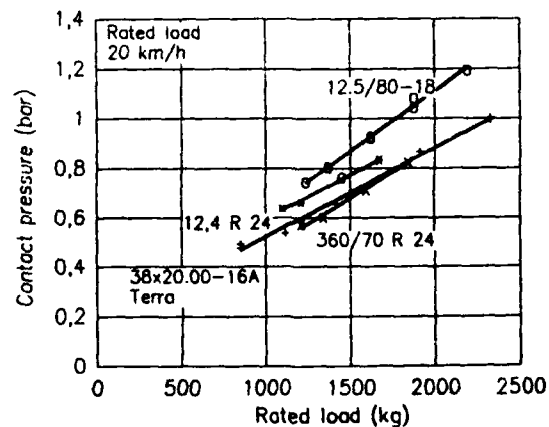


Fig. 14: Contact pressure of the 4 test tires.



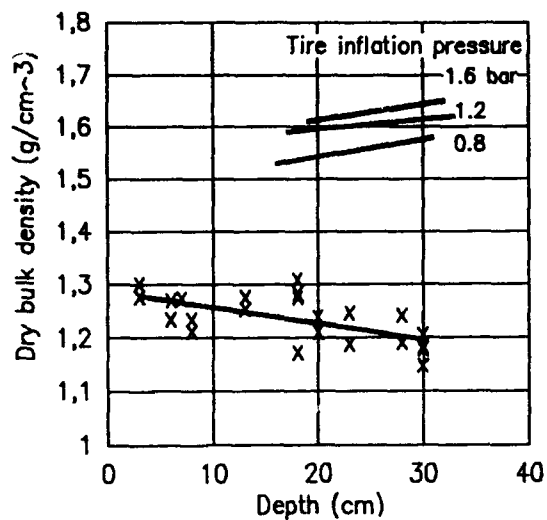


Fig. 15: Bulk density, tire 12.4 R 24.

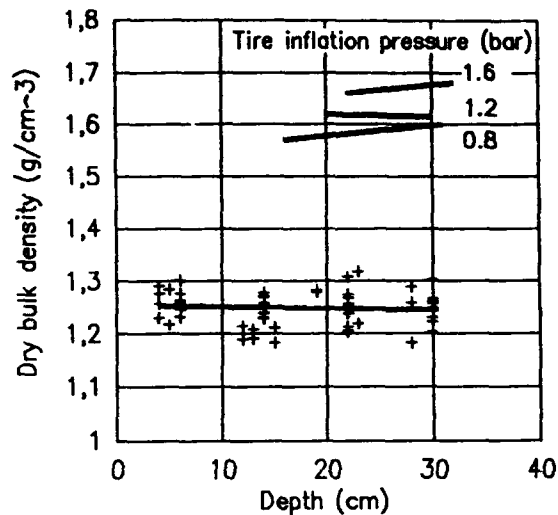


Fig. 16: Bulk density, tire 360/70 R 24.

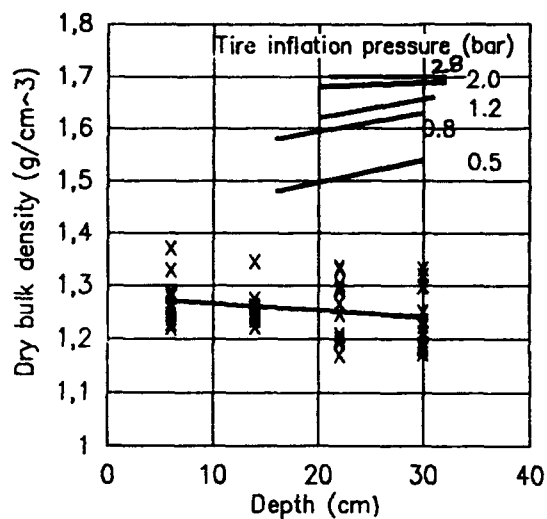


Fig. 17: Bulk density, tire 38x20.00 (Terra).

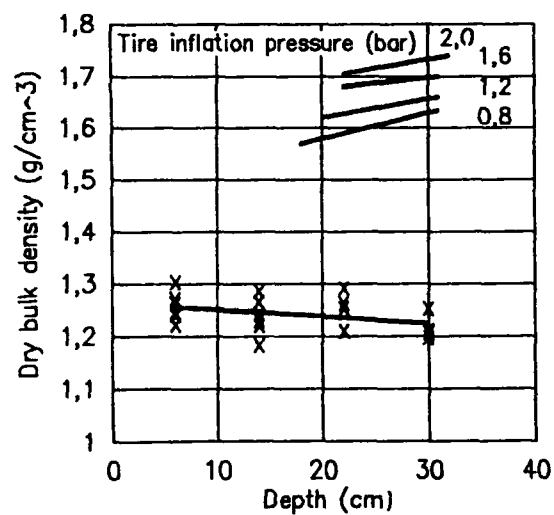


Fig. 18: Bulk density, tire 12.5/80-18.

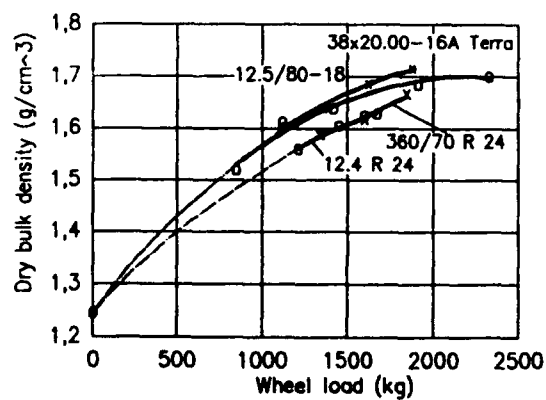


Fig. 19: Bulk density in relation to wheel load for the four test tires.

At 1000 kg rated load and the corresponding inflation pressure the contact area of the tractor tire 12.4 R 24 (TM 200) is 1600 cm<sup>2</sup>, that of the tire 360/70 R 24 (TM 700) is 1900 cm<sup>2</sup>. The contact area of the terra tire 38x20.00-16A is 1900 cm<sup>2</sup> and that of the implement tire 12.5/80-18 is 1600 cm<sup>2</sup>.

The **Figures 9-12** show the mean contact pressure (load/area) in relation to the tire inflation pressure for different loads. The contact pressure increases only slightly with the inflation pressure. The broken lines give the contact pressure of the tires in relation to the inflation pressure at rated load (speed 20 km/h). **Fig. 13** shows these lines for all 4 tires in one graph.

For a certain inflation pressure, the ground pressure is the lowest for the terra tire, the biggest for the implement tire. The range of contact pressure for these 4 tires lies between 0.5 bar (terra tire) and 1.2 bar (implement tire).

**Fig. 14** shows the same result concerning contact pressure, but in relation to rated load. With rated load the tractor tire 360/70 R 24 has the same contact pressure as the terra tire, the contact pressure of the smaller tire 12.4 R 24 is 10 % higher and that of the implement tire 12.5/80-18 is 25 - 30% higher.

The dry bulk density (dry soil mass/ volume) of the soil under the tire loaded with rated load is drawn in the **Figures 15 to 19**. The preparation of the soil produced an initial density of 1.25 g/cm<sup>3</sup> for all experiments. Below the depth of 40 cm there was a very dense subsoil. This may be the reason that the density in some experiments raises slightly with depth. The single lines mark the regression of the measured points.

The bulk density for the rated load and the corresponding tire inflation pressure is 1.55-1.65 g/cm<sup>3</sup> for the tractor tire 12.4 R 24 (TM 200), 1.58-1.68 g/cm<sup>3</sup> for the tractor tire 360 70/ R 24 (TM 700), 1.5-1.7 g/cm<sup>3</sup> for the terra tire 38x20.00-16A and 1.6-1.75 g/cm<sup>3</sup> for the implement tire 12.5/80-18. The greatest density is caused by the implement tire.

Constant wheel load at varying inflation pressure produces only small differences in soil density, but varying wheel load at constant inflation pressure has a great influence on the density.

In **Fig. 20** the soil density caused in 25 cm depth is drawn as a function of rated load. The beginning of the "density curve" is on the point 1.25 g/cm<sup>3</sup> for unloaded loose soil condition.

With 1500 kg load, the terra tire 38x20.00-16A (older model) compacts the soil from 1.25 to 1.65 g/cm<sup>3</sup>, that is about 0.4 g/cm<sup>3</sup>, whereas the two tractor tires compact the soil only from 1.25 to 1.6 g/cm<sup>3</sup>, that is about 0.35 g/cm<sup>3</sup>.

Thus, the same load produces 13 % less compaction with the modern tractor tires compared with the implement tire or the terra tire.

## 5. References

- [ 1 ] **Ashenafi, T.A., T. Tanaka and M. Yamazaki:** Soil compaction by multiple passes of a rigid wheel relevant for optimization of traffic.  
Journal of Terramech. 26 (1989) 2, pp.139/148
- [ 2 ] **Bailey, A., C. Johnson, C.E. Schafer, R.L. Nichols and T.A. Grisso:**  
A compaction model for agricultural soils.  
Proc. Int. Conf. on Soil Dynamics, Auburn (1985) 2, pp. 203/212
- [ 3 ] **Bekker, M.G.:** Prediction of design and performance parameters in agro-forestry vehicles.  
Nat. Res. Council of Canada, Ottawa (1983)
- [ 4 ] **Bolling, I.:** Semi-empirical tire-soil compaction model.  
Proceed. 4th Europ. Conf. ISTVS Wageningen (1989), pp.24/31
- [ 5 ] **Campell, D.J. and J.W. Dickson:** Effect of four alternative front tires on seedbed compaction by a tractor fitted with a rear wheel designed to minimize compaction.  
J. Agric. Engin. Res. (1984) 1, pp.83/91
- [ 6 ] **Gameda, S., G.S. Raghavan, R. Theriault and E.Mc Kyes:** High axle load compaction and corn yield.  
Transactions of ASAE 28 (1985) 6, pp.1759/1765
- [ 7 ] **Henshall, J.K. and D.L.O. Smith:** An improved method of presenting comparisons of soil compaction effects below wheel ruts.  
J. agric. Engng. Res. (1989) 42, pp.1/13
- [ 8 ] **Jakobsen, B.F. and A.R.Dexter:** Prediction of soil compaction under pneumatic tyres.  
Journal of Terramech. 26 (1989) 2, pp.107/119
- [ 9 ] **Perdock, U.D. and W.B. Arts:** The Performance of Agricultural Tyres in Soft Soil Conditions.  
Soil and Tillage Res. 10 (1987) 4, pp.319/330
- [ 10 ] **Rhaghavan, G.S.V., E.Mc Keys and M.Chasse:** Soil compaction patterns caused by off-road vehicles in eastern Canadian agricultural soils.  
J. Terramech. (1976) 2, pp. 107/115
- [ 11 ] **Schwanghart, H.:** Soil compaction under a rolling tire.  
Proceed. 4th Europ. Conf. ISTVS Wageningen (1989), pp.179/186
- [ 12 ] **Schwanghart, H.:** Measurement of contact area, contact pressure and compaction under tires in soft soil.  
Proceed. 10th Intern. Conf. ISTVS Kobe/Japan 1 (1990), pp.193/204.
- [ 13 ] **Sitkei, G.:** Das Verhalten von Ackerschlepperreifen auf nachgiebigem Boden.  
Grundl. Landtechn. 19 (1969) 2, S.33/35.
- [ 14 ] **Smith, D.L. and I.W. Dickson:** The contribution of vehicle weight and ground pressure to soil compaction. Ag. Eng. Intern. Conf. Paper No. 88.260 (1988), Paris
- [ 15 ] **Soane, B.D., P.S. Blackwell, J. Dickson and D.J. Painter:** Compaction by agricultural vehicles.  
Soil and Tillage Res. 1 (1980/81) pp.207/237
- [ 16 ] **Söhne, W.:** Druckverteilung und Bodenverformung unter Schlepperreifen.  
Grundl.d.Landtechn. (1953) 5, S.49/63
- [ 17 ] **Söhne, W.:** Fundamentals of pressure distribution and soil compaction under tractor tires.  
Agric.Engng. 39 (1958) pp.276/281, 290
- [ 18 ] **Vandenberg G.E. and W.E. Gill:** Pressure distribution between a smooth tyre and the soil.  
Transact. of ASAE (1962) 5, pp.105/107
- [ 19 ] **Wong, J.Y.:** Theory of ground vehicles.  
John Wiley and Sons (1978), New York

# WEAR INVESTIGATION ON CRAWLERS OF EARTH MOVING MACHINERY

W. Poppy, C. Segieth  
Technische Universität Berlin; Germany

## Summary

The high degree of wear on all components of the crawler units of bulldozers and crawler loaders results in considerably high costs. With the aid of a comprehensive tribological analysis and tests carried out of a simulation test stand, it was possible to determine the correlation between the structure of the system, loading and wear for bushings and drive wheel that represent one of the main areas of wear.

Studies of parameters involved have shown that the normal force acting between tooth and bushing has a considerable influence on the wear which occurs while the travelling speed does not. Laboratory tests on various materials did not result in any significant reduction in wear. The drive wheel teeth with induction-hardened surfaces and case-hardened bushings which are already standard have been shown to display a high wear resistance. On possible design solution which would enable wear to be reduced consists in increasing the diameter of the drive wheel and the number of teeth.

## 1. Statement of problem and task

The crawler units of construction machinery are subjected to high alternating loads during operation. This results in a considerable degree of wear occurring in all crawler unit components, particularly when abrasive surfaces are driven over. The stress and movement conditions which are a major factor in causing wear in crawler units, especially at the main points of wear - i.e. drive wheel teeth and bushings - largely remain unknown. It was these which formed the subject of a research project which stretched over several years.

The prerequisite for a systematic reduction of wear was the determination of the tribological action to which bushings and drive wheel teeth are subjected, taking into account all those factors which influence wear. By means of tests performed on a recently developed test stand, an attempt was made to analyse the fundamental correlation between the system structure, the stresses involved and the wear process and to deduce from this analysis possibilities for optimizing construction and material with the aim of reducing the wear on bushings and drive wheel teeth.

## 2. Tribological analysis

The type of wear on drive wheel teeth and bushings which contributes most to reducing the service life of crawler units occurs during reverse runs. It is caused by the kinematically determined rotation of the bushings in relation to the teeth when the former engage the latter (fig. 1). Although the forces which occur during the loaded forward run are considerably greater than during the no-load reverse run, the wear occurring on those surfaces which come into contact when crawler units are in operation is far less on forward runs due to the fact that no forced rotation of the bushing takes place. The following values of the mean wear mass for those surfaces which are in contact during reverse runs were determined by measuring the wear on drive wheel teeth and bushings which had been in operation on construction sites:

- for bushings:  $W_m = 1.37 \text{ mg/running-in}$
- for drive wheel teeth:  $W_m = 0.58 \text{ mg/running-in.}$

The sum total of the wear on drive wheel teeth and bushings shows that the wear occurring on reverse runs is around 4 to 5 times greater than on forward runs.

### 3. Test stand for determining wear

The effect of different influencing variables on the wear occurring on bushings and drive wheel teeth can be studied within a reasonable period of time only by performing tests in isolation and under reproducible conditions on a laboratory test stand. A power-assisted hydraulic test stand was therefore developed which was designed to perform tests on the crawler unit size D 6 which is commonly used on bulldozers with an operational mass of 16.5 t and 115 kW motor rating. The force and movement involved when bushings and drive wheel teeth come into contact had to be simulated such that operational conditions and theoretical considerations were taken into account [1].

As a bushing in an unworn condition fits closely against the straight flank of the drive wheel tooth, it was possible to replace the latter by a flat specimen (width: 80 mm). Instead of the bushing, a cylindrical specimen with the same external diameter was used (diameter: 69 mm).

The principle of the test stand is shown in figure 2. A hydraulically operated cylinder (3) pulls the cylindrical specimen (2) against the flat specimen (1). The rotation cylinder (8) then turns the cylindrical specimen. The angle of rotation is equivalent to the angular pitch of the drive wheel teeth. The cylindrical specimen (2) is held in place by means of guide rods (10) to ensure that friction occurs between the cylindrical specimen and the flat specimen by preventing the former from simply rolling over the latter. Sensors (11) located in the guide rods measure the frictional force. An abrasive interfacial medium (14) is fed into the contact zone in measured quantities where it flows downwards. The cylindrical specimen can be moved over the flat specimen in a transverse direction by means of a hydraulic cylinder in order to vary the points of contact.

A test cycle which corresponds to a bushing running into the drive wheel teeth during a reverse run is characterized by the maximum normal force,  $F_N$ , and the time,  $t_e$ , during which the bushing runs into the drive wheel teeth (fig. 3). The latter can be calculated from the travelling speed of the bulldozer and the chain pitch. The normal force is increased linearly as the cylindrical specimen turns and is reduced when it stops turning. The cylindrical specimen is subsequently lifted 3 mm from the flat specimen to allow fresh abrasive material to flow freely into the contact zone. While this is happening, the cylindrical specimen is returned to its initial position after which it is again pulled against the flat specimen. The next cycle begins.

The amount of wear is determined by measuring the specimens with a computer-controlled tracer instrument. The wear mass related to a single turning movement (test cycle), stated in  $W_m/S_w$ , is then calculated from the test results.

### 4. Test parameters

#### 4.1 Materials

The test specimens examined in laboratory tests were either standard components or were constructed from materials used in standard components, materials used by way of trial and/or build-up welds.

The processes and materials used in the production of the original components as well as their structures and surface hardnesses formed a representative cross-section of commercially available crawler unit components for bulldozers.

In order to examine the possibilities of reducing wear, specimens constructed of materials which had already been used successfully in conditions similar to those under which crawler units operate were tested. The wear resistance of build-up welds was examined on a low-alloy

and a high-alloy welding filler, both of which are used in the regeneration of construction machinery components.

## **4.2 Interfacial media**

As crawler units operating on depositing sites are subjected to an especially high degree of wear, the abrasive material chosen was silica sand with a particle size distribution of between 0.1 and 0.4 mm which corresponds to that found on such sites. The silica sand, which was taken from a natural deposit, was fire-dried and sieved. The sand was only used once as it is crushed during the test, causing the particle size distribution to be altered.

## **5. Results**

### **5.1 Applicability of test stand results in practice**

The relative wear masses measured on the test stand were compared with the wear occurring in crawler units during operation in order to examine the applicability of the test stand results in practice (fig. 7). The amount of wear occurring during the laboratory tests was the same order of magnitude as that to be found in bulldozers in operation on the construction site. The types of wear show that abrasion is the predominant wear mechanism involved, both in practice and on the test stand.

The fact that the wear masses observed in the tests and the wear mechanisms involved both correspond to those to be found in practice confirms the suitability of the simulation principle and ensures that the test stand results are applicable in practice.

### **5.2 Influence of normal force and travelling speed on wear**

Three different normal forces and travelling speeds were used, resulting in a test plan with 9 different combinations of parameters. Measurements carried out on bulldozers operating on construction sites have shown that the whole range of operations is covered by normal forces of 10, 30 and 50 kN and speeds of 1, 3 and 5 km/h [2]. During the laboratory tests, each specimen was subjected to 10,000 test cycles.

The relative wear mass for flat specimens ranges from 0.27 to 0.64 mg per bushing rotation (given in mg/Sw, see fig. 5). The travelling speed is of secondary importance for the wear mass as wear is caused primarily by converted frictional energy which is, in theory, independent of the travelling speed. The relative amount of wear occurring in the cylindrical specimen is on average 2.5 times greater than that occurring in the flat specimen and ranges between 0.79 and 1.45 mg bushing rotation, depending on normal force and travelling speed (fig. 6). As with the flat specimens, the influence of the travelling speed is minor, the major factor being the normal force.

### **5.3 Wear on specimen pairs of different materials**

The aim of testing specimens made of different materials was to attempt to discover possibilities of reducing wear. To this end, the results of tests on the most wear-resistant standard pairs of components currently in use were compared (fig. 7). The most wear-resistant pairs of standard components and components made of standard materials are represented by bars while the broken lines indicate those pairs of components which exhibited a higher degree of wear. As for the individual materials shown here, the bars represent the mean value of two separate sets of test results while the broken lines indicate the scatter.

The wear on specimens made of standard materials is of the same order of magnitude as for the standard components, thus providing further confirmation of the test principle. In each case, the scatter is, however, less which is due to the standard heat treatment procedures used.

Owing to its low degree to toughness after exposure to heat, cold-workable steel is not a suitable material for drive wheel teeth. For this reason, a cylindrical specimen made of cold-workable steel was paired with a flat specimen made of a standard material. The high degree of wear resistance due to the primary chromium carbides embedded in the matrix which had been demonstrated under various conditions was not observed in this case. The chromium carbides present in the cold-workable steel do not reduce wear under the loading conditions concerned with here as they are smaller - having a diameter of between 1 and 5  $\mu\text{m}$  - than the peak-to-valley height,  $R_t$ , which ranges from 15 to 25  $\mu\text{m}$  and they are removed from the matrix by the interfacial medium.

The specimen pair made of X 120 Mn 12 high-manganese steel which had been austenitized exhibited an overall degree of wear around 50 % higher than the specimen pair made of the same type of steel but which had not been treated. The normally wear-reducing property of high-manganese steel - i.e. the increase in strength at low temperatures when subjected to impact stress - does not become effective under the loading conditions concerned as these consist primarily of friction.

The combination of a flat specimen and a cylindrical specimen of the same material, both of which had been strengthened with build-up welds of a high-alloy welding filler, resulted in the lowest degree of wear observed in the specimen pairs under examination. The wear on the cylindrical specimen was 34 % less and that on the flat specimen 73 % less than in the case of standard components.

Sections of the extremely brittle and hard welded layer had, however, broken off along the edges of the flat specimen during exposure to wear. The use of build-up welds for drive wheel teeth and bushings is therefore ruled out in practice at the present time on account of the limited durability of the welded layer and the considerable cost of build-up welding.

## **6. Reducing wear by means of a different choice of material and modifications in the design**

As was shown in section 5.3, the laboratory tests carried out on various materials did not result in any significant reduction in wear which would be of interest from an economic point of view.

A possible design solution which would enable the wear on bushings and drive wheel teeth to be reduced consists in increasing the diameter of the drive wheel and the number of teeth [3]. Owing to the smaller angular pitch, the angle of rotation between bushing and tooth during running in is decreased, thus reducing the degree of wear. Based on the laboratory tests, an increase travelled and a reduction in wear-related costs by 60 % and 30 % respectively was forecast if the number of teeth were raised from 25 to 39 (fig. 8). Set against this are the disadvantages such as higher moments of rotation in the drive wheel. In spite of this, the chances of being able to put these changes into practice are considered good as the technologically perfected crawler track and the materials which have been used successfully in practice could be retained without modifications.

## **7. Bibliography**

- [1] Segieth, C.; Poppy, W.: Verzahnungskräfte an Raupenlaufwerken von Baumaschinen. Konstruktion 42 (1990) 4, S. 127-134
- [2] Segieth, C.: Verschleißuntersuchungen an Raupenlaufwerken von Baumaschinen. VDI-Fortschritt-Berichte Reihe 1, Nr. 192, Düsseldorf: VDI-Verlag, 1990
- [3] Poppy, W.; Segieth, C.: Verschleißminderung bei Raupenlaufwerken durch Antriebsräder mit vergrößerter Zähnezahl. Baumaschine und Bautechnik (BMT) 37 (1990) 4, S. 171-176

Fig. 1: Wear on bushing and drive wheel tooth as a result of the different kinematics involved when the bushing engages the drive wheel on forward and reverse runs (Rotation of bushing in relation to the drive wheel tooth on reverse runs; no rotation on forward runs)

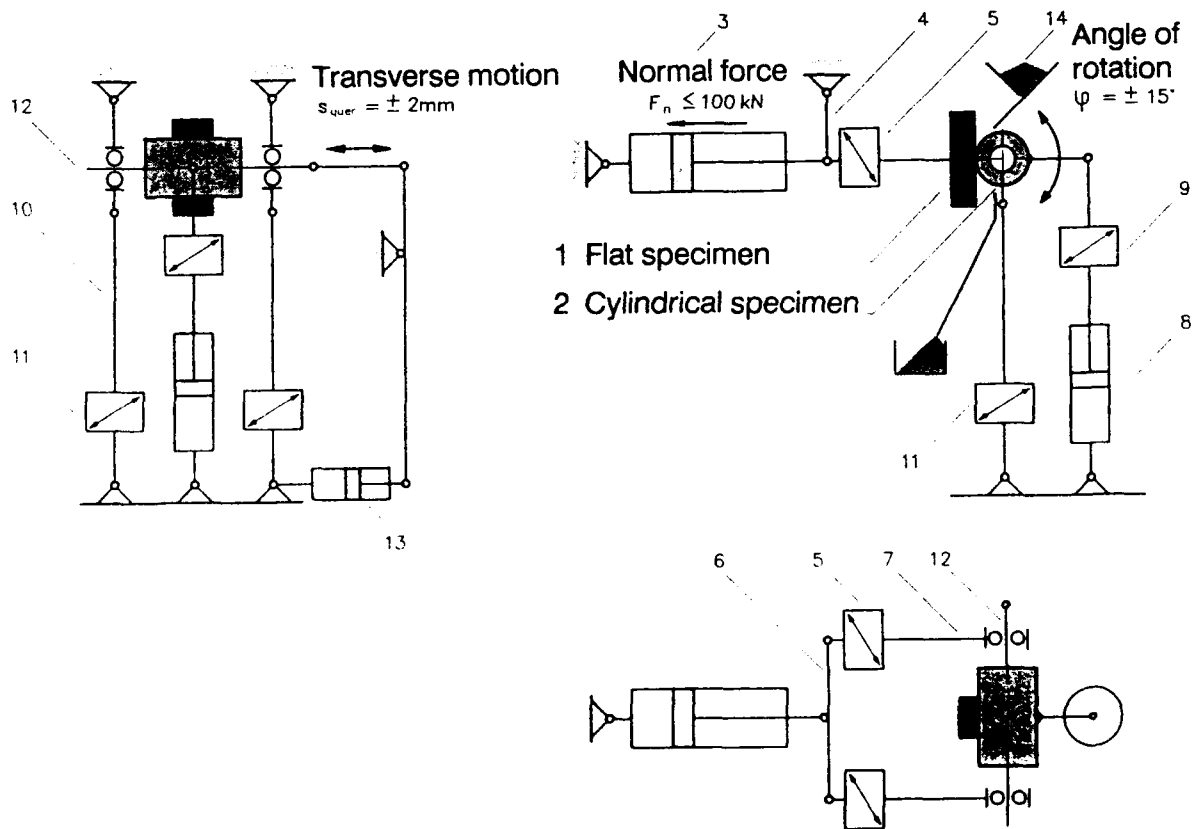
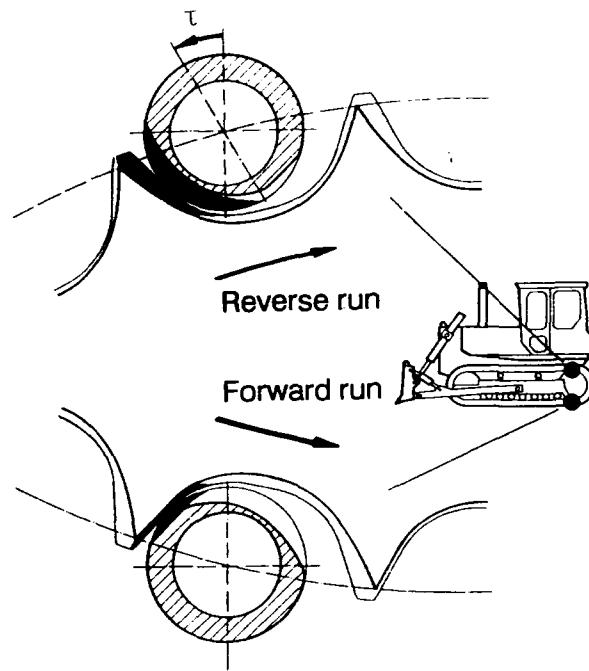


Fig. 2: Principle of the test stand for determining wear

(1) Flat specimen (drive wheel tooth), (2) Round specimen (bushing), (3) Cylinder for producing normal force, (4) Suspension of cylinder, (5) Sensors for measuring normal force, (6) Cross-bar for force transmission, (7) Guide-rod for force transmission, (8) Cylinder for producing rotation, (9) Sensor for measuring rotational force, (10) Guide rod for resisting frictional force, (11) Sensors for measuring frictional force, (12) Mounting of specimen, (13) Cylinder for producing transverse motion, (14) Abrasive materials added in measured quantities



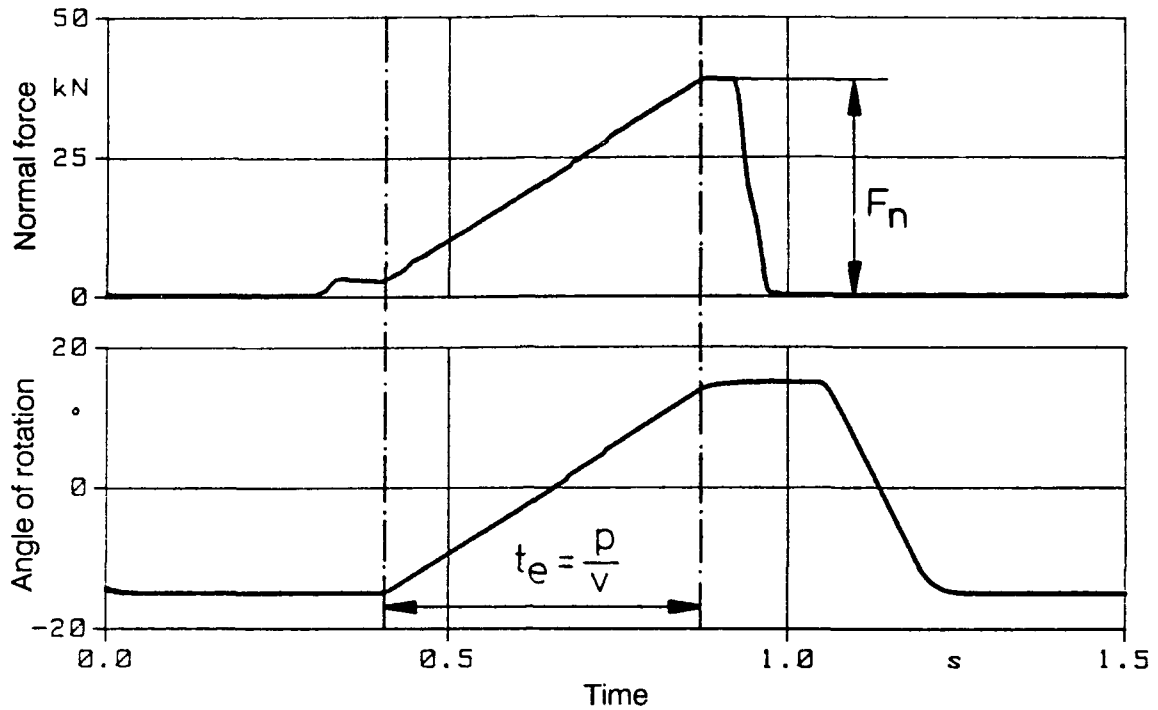


Fig. 3: Test cycle with increasing force to simulate the bushing engaging the drive wheel teeth during reverse runs

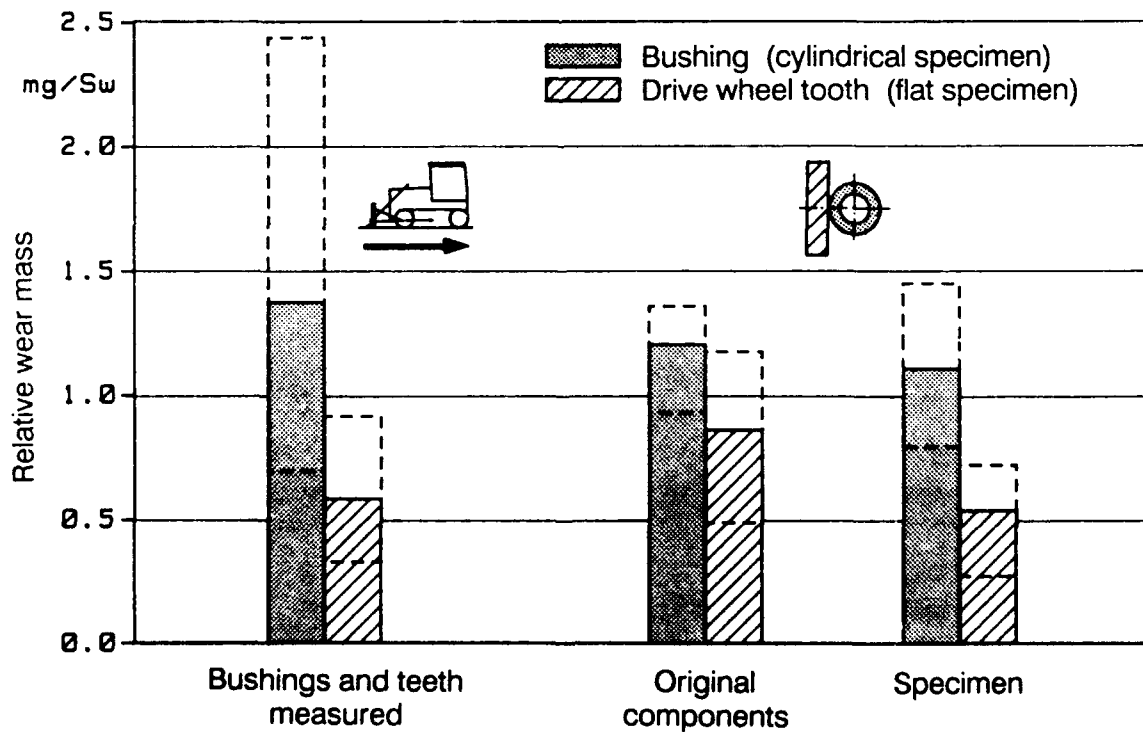


Fig. 4: Relative wear mass occurring in components used on the construction side and in test specimens

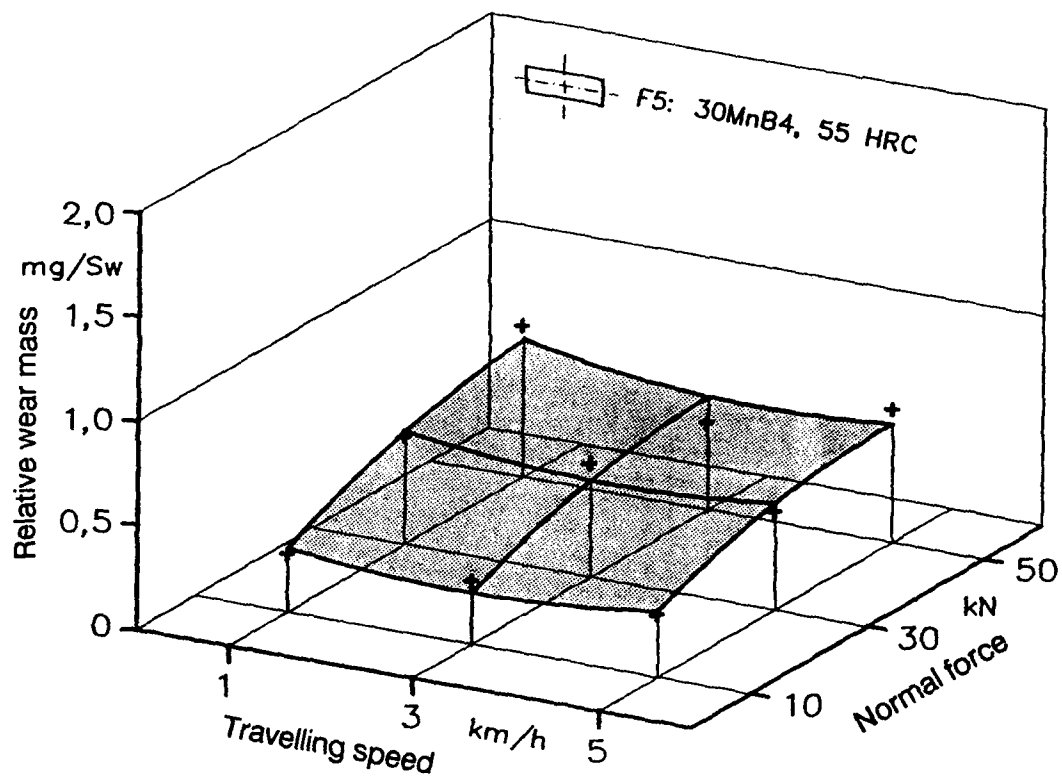


Fig. 5: Wear on flat specimen, in relation to normal force and travelling speed

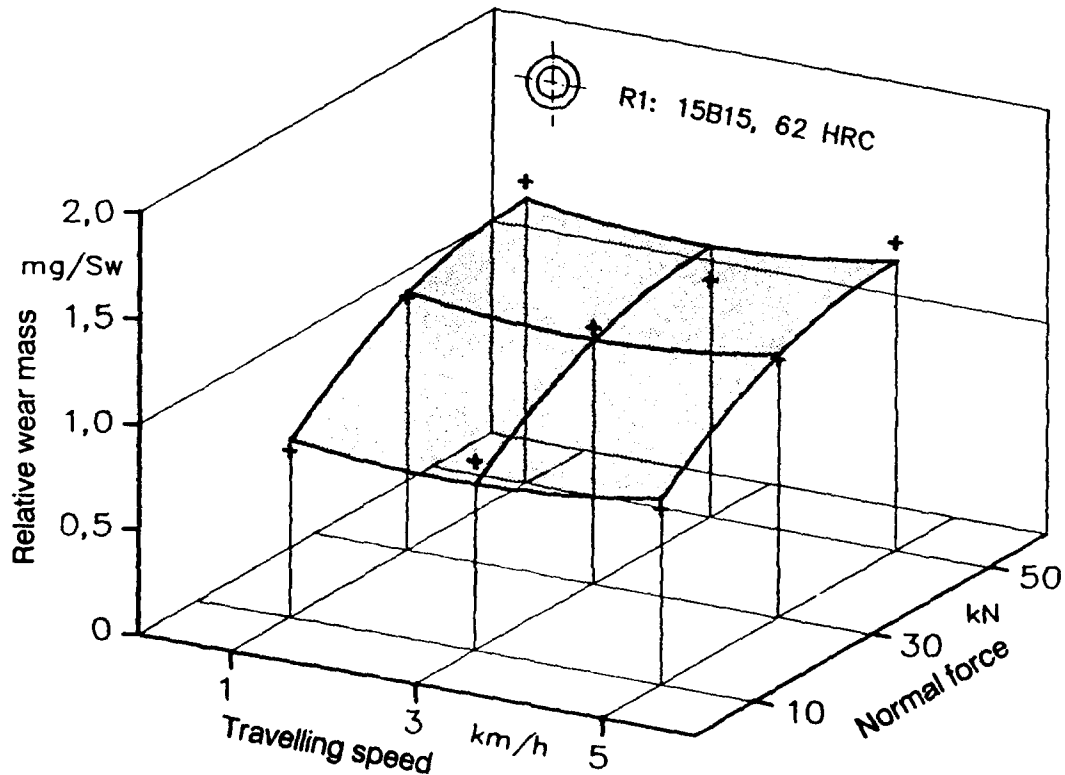


Fig. 6: Wear on cylindrical specimen, in relation to normal force and travelling speed

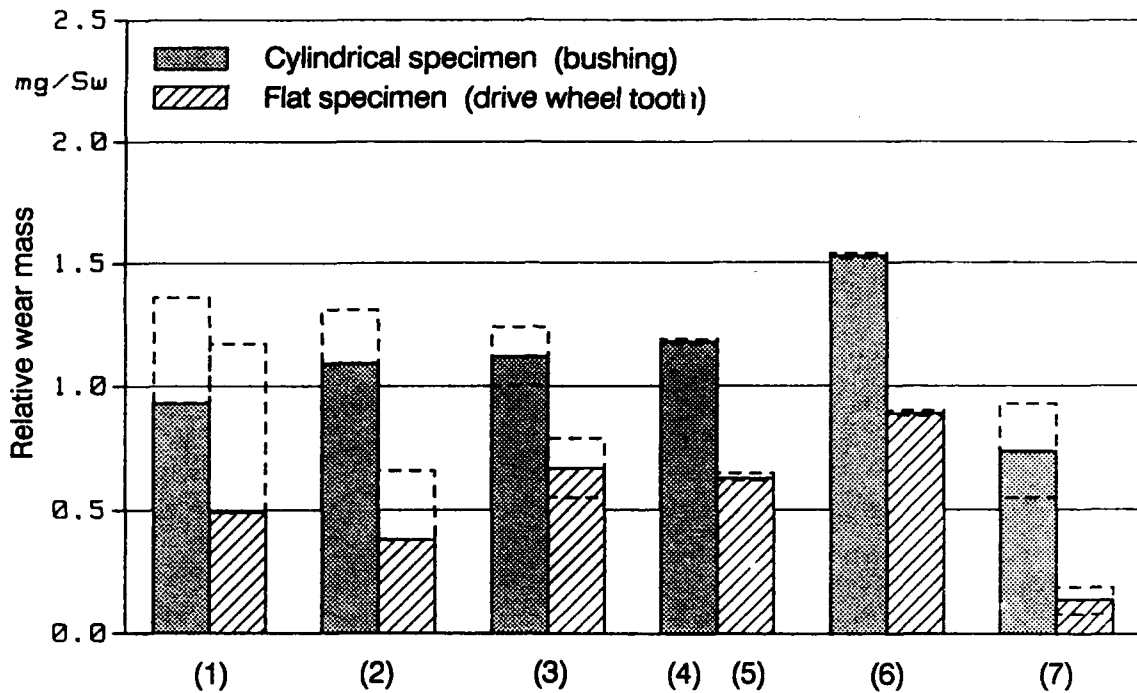


Fig. 7: Wear on specimen pairs made of various materials

(1) Standard bushings and teeth; (2) Specimens made of standard materials; (3) Spring steel 51 CrMoV 4; (4) X 155 CrMoV 121; (5) 30 MnB 4; (6) High-manganese steel X 120 Mn 12; (7) Specimens with build-up welds 30 % Cr

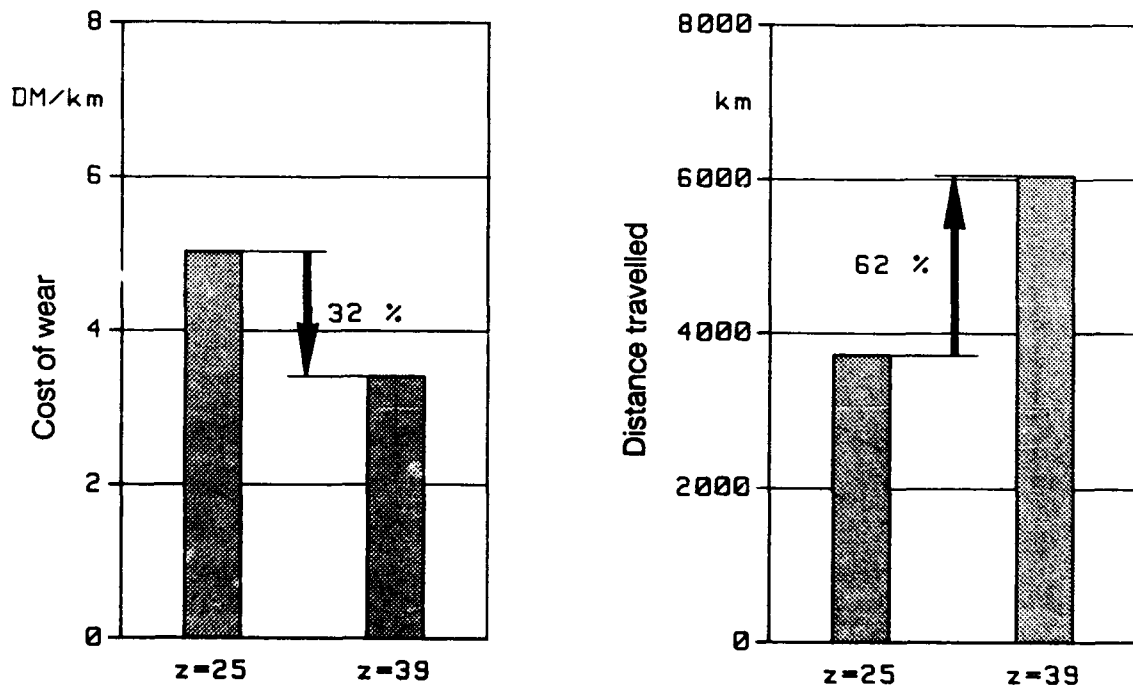


Fig. 8: Travelling distance and cost of wear occurring during the useful life of a standard drive wheel with 25 teeth compared with the optimized drive wheel with 39 teeth

# THE MAXIMUM EFFICIENCY OF THE TRACTOR AND IMPLEMENT COMBINATION

Dr. Andras Fekete  
Hungarian Institute of Agricultural Engineering  
Gödöllő, Hungary

## SUMMARY

The efficiency of the tractor and tillage implement combination is determined as the tractive efficiency of the tractor multiplied by the efficiency of the tillage implement. The efficiency of the tillage implement is expressed by the forward speed and the constants of the exponential equation used to approximate the soil resistance/speed relationship of the tillage implement. A relationship is determined to express the performance of the tractor and tillage implement combination as the function of the forward speed and the slip when the tractor, implement and soil characteristics are constants. Consequently the relationship determined can be used to predict the maximum performance of the tractor and implement combination.

## INTRODUCTION

The tractive efficiency has an important influence on the maximum efficiency of the tractor and implement combination. The tractive efficiency is defined by Sitkei (1986) as the function of the efficiency of the transmission, the slip, the gross traction ratio, the tractive coefficient and the characteristic slip. Consequently the tractive efficiency is dependent on the slip, the tractive coefficient and the coefficient of the rolling resistance. However the slip is principally determined by the soil conditions - moisture content, porosity, etc. - and the tyre parameters.

On the basis of test results and calculations for the workrate (hectars/h) of tractor and implement combinations the conclusion is found (Stroppel, 1980; 1981) that the workrate and the specific fuel consumption (liters/hectar) are determined by the engine performance; the mass of the tractor, the soil conditions, the forward speed and the working width. The maximum workrate is found to occur at a specific fuel consumption that is higher, than the minimum specific fuel consumption.

From the equation for the tractive efficiency of the tractor and from the well known Goriatshkin-formula is concluded (Kománde, 1987) that the forward speed and the slip have significant influence on the ploughing efficiency with given soil conditions, tractor and implement.

The purpose of the work reported here is to determine the gross efficiency of the tractor and implement combination with respect to the tractive efficiency of the tillage implement.

### THE EFFICIENCY OF THE TILLAGE IMPLEMENT

The measured values of the draft of the implement can be shown versus the forward speed and the measured data can be approximated the equation as follows

$$F_r = \beta_0 e^{\beta V} \quad (1)$$

where  $\beta_0$  and  $\beta$  are constants. However the equation cannot be used for zero speed.

The efficiency of the tillage implement is defined as the ratio of the work performed by the implement to the work performed at the drawbar of the tractor:

$$\eta_a = \frac{k \cdot a \cdot b \cdot L}{F_r \cdot V \cdot t} = \frac{k \cdot a \cdot b}{F_r} = \frac{k \cdot a \cdot b}{\beta_0 e^{\beta V}} \quad (2)$$

where:  $k$  - specific draft of the implement,  $N/m^2$   
 $a$  - working depth, m  
 $b$  - working width, m  
 $L$  - the distance, where the work is performed, m  
 $t$  - time, during which the work is performed, s  
 $V$  - forward speed,  $V = L/t$ , m/s

The draft required for the implement at a given forward speed according to the Goriatshkin formula is as follows

$$F_r = F_s + k \cdot a \cdot b + F_d \quad (3)$$

where: - " $k \cdot a \cdot b$ " is the force required for the tillage  
 - " $F_s$ " is the frictional and rolling resistance of the tillage implement  
 - " $F_d$ " is the dynamic component of the force required that is dependent on the forward speed.

Let us suppose that the working depth and width and  $F_s$  are constant with a given soil and implement /Fig. 1/. Therefore

$$k \cdot a \cdot b = \beta_0 - F_s \quad (4)$$

When combining equations (3) and (4) the efficiency of the implement is as follows

$$\eta_a = \frac{\beta_0 - F_s}{e \beta V} = \frac{1}{e \beta V} \left( 1 - \frac{F_s}{\beta_0} \right) = p \frac{1}{e \beta V} \quad (5)$$

where:  $p$  - constant for a given soil and implement,  $p = 1 - \frac{F_s}{\beta_0}$ .

Let us suppose that  $F_s \approx 0$  and  $p \approx 1$ , because it is difficult to determine  $F_s$  in the practice. In this case the efficiency of the implement is as follows

$$\eta'_a = \frac{1}{e \beta V} \quad (6)$$

Some researchers (Söhne, 1960; Perdok and Vermueulen, 1987) use the simplified form of the Goriatshkin formula

$$F_r = F'_s + F_d \quad (7)$$

where:  $F'_s$  - component of the draft required, independent on the speed,

$F_d$  - dynamic component of the draft required, dependent on the speed,

In this case the efficiency of the implement is as follows

$$\eta'_a = \frac{k \cdot a \cdot b \cdot F_s}{F_r} = \frac{\beta_0}{\beta_0 e \beta V} = \frac{1}{e \beta V} \quad (8)$$

The efficiency according to Eqn (8) is equal to the simplified efficiency of Eqn (6).

#### THE TRACTIVE EFFICIENCY OF THE TRACTOR

The measured value of the slip of the tractor is the function of the drawbar pull. The measured values can be approximated by the equation as follows

$$s = \alpha_0 \cdot e^{\alpha F_V} \quad (9)$$

where:  $\alpha$  and  $\alpha_0$  - constants

$F_v$  - drawbar pull, N

The tractive efficiency of the tractor is as follows

$$\eta_v = \eta_h \cdot \eta_g \cdot \eta_s \quad (10)$$

where:  $\eta_h$  - mechanical efficiency between the engine and the drive wheel

$\eta_g$  - efficiency because of the rolling resistance of the tractor

$$\eta_g = \frac{F_v}{F_v + F_g}$$

where:  $F_v$  - pull, N

$F_g$  - rolling resistance, N

$\eta_s$  - efficiency because of the slip,  $\eta_s = 1 - s$

where:  $s$  - slip,  $s = \alpha_0 e^{\alpha F_v}$

$\alpha_0$  and  $\alpha$  - constants

The tractive efficiency can be rewritten in the form as follows

$$\eta_v = \eta_h \cdot \frac{F_v}{F_v + F_g} (1 - \alpha_0 e^{\alpha F_v}) \quad (11)$$

#### THE GROSS EFFICIENCY OF THE TRACTOR AND IMPLEMENT COMBINATION

The efficiency of the tractor and tillage implement combination is defined as the multiplication of the tractive efficiency of the tractor and the efficiency of the implement

$$\eta_{va} = \eta_v \cdot \eta_a = \eta_h \cdot \frac{F_v}{F_v + F_g} (1 - \alpha_0 e^{\alpha F_v}) \frac{1}{e^{\beta V}} \quad (12)$$

The relationship developed for the efficiency of the tractor and implement combination is of two variables, where the efficiency is the function of the forward speed and the drawbar pull. The maximum values of the efficiency in different gears of a given tractor and implement combination are shown in Fig. 2. Consequently the maximum efficiency can be determined as well, when having a given tractor (mass, tyre size), a given implement and given soil conditions where  $\eta_h$ ,  $\alpha$ ,  $\alpha_0$  and  $\beta$  are constants.

## THE PERFORMANCE OF THE TRACTOR AND IMPLEMENT COMBINATION

The performance of the tractor and tillage implement combination can be expressed by the engine performance ( $P_m$ ) and the efficiency ( $\eta_{va}$ ) of the tractor and implement combination, as follows

$$P_{va} = P_m \cdot \eta_{va} \quad (13)$$

The performance of the tractor and implement combination can be expressed as a function of the forward speed and the slip for a given tractor and implement and for given soil conditions, as follows

$$P_{va} = f(V, s) \quad (14)$$

## CONCLUSION

On the basis of the relationship developed conclusions are found, as follows

- with the increase of the inclination of the slip/pull curve, when  $\alpha_c$  and  $\beta$  increase, the maximum efficiency and the maximum performance will occur at a lower value of the pull and at a higher value of the speed,
- with the increase of the inclination of the draft/speed curve, when  $\beta$  increases, the maximum efficiency and the maximum performance will at a higher value of the pull and at a lower value of the speed.

## LITERATURE

1. Fekete, A.: Load control of tractor and implement combinations /in Hungarian/, Akadémia Kiadó, Budapest, 1990. 86 p.
2. Komándi, G.: Optimum connection between the tractor and the tillage implement /in Hungarian/, Járművek, Mezőgazdasági Gépek, 1987/2. 43-47.
3. Sitkei, G.: Modelling of agricultural and forestry vehicles, /in Hungarian/, Akadémiai Kiadó, Budapest, 1986. 83 p.



4. Stroppel, A. : Energie - und Arbeitszeitbedarf für gezogene Geräte der Bodenbearbeitung, Grndl. Landtechnik, 1980/4. 135-139.
5. Stroppel, A. : Arbeitszeit - und Energiebedarf beim Pflügen, Grndl. Landtechnik, 1981/5. 165-171.

# FIGURES

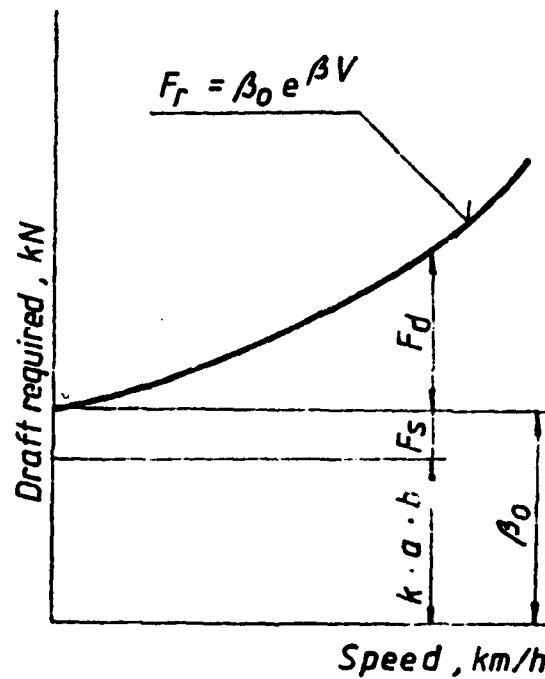


Fig. 1

Draft required versus forward speed for tillage implement

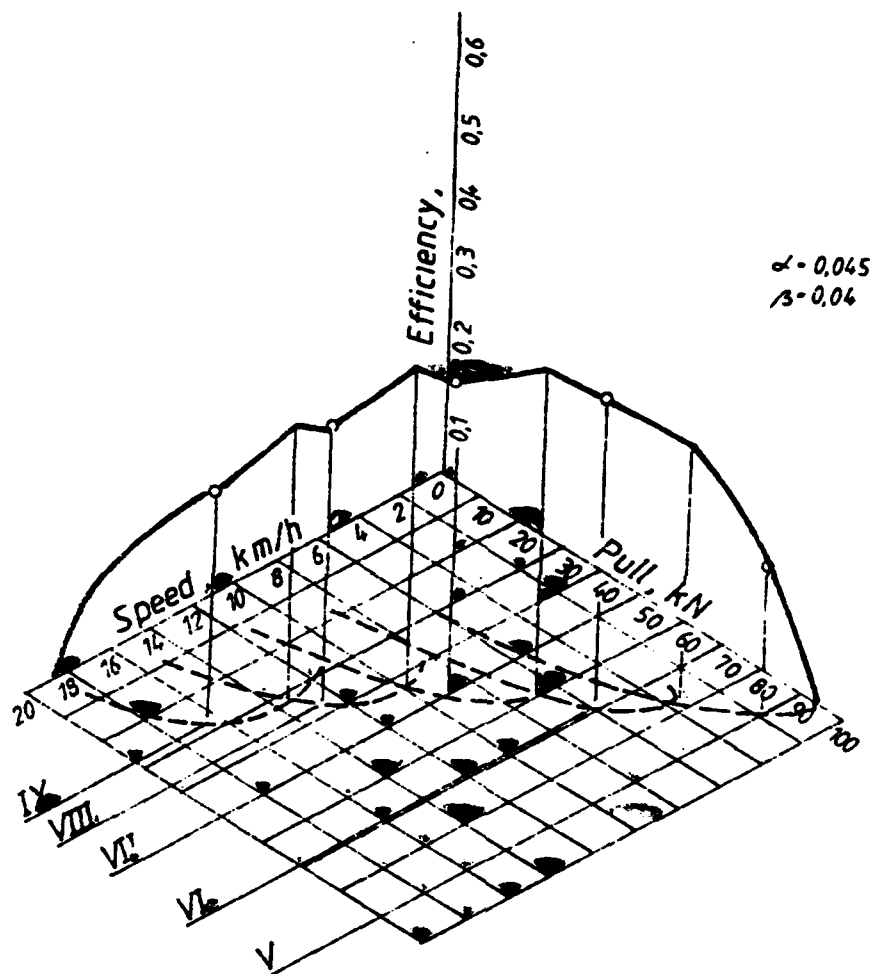


Fig. 2

The gross efficiency of the tractor and implement combination  
 /tractor: Rába 300, implement: Rába-IH-10720 plough, type:  
 20,8 - 34 dual, soil: loam, stubble,  $s = 1,26$  e,  $\beta = 0,04$ /  
 $\alpha = 0,045$

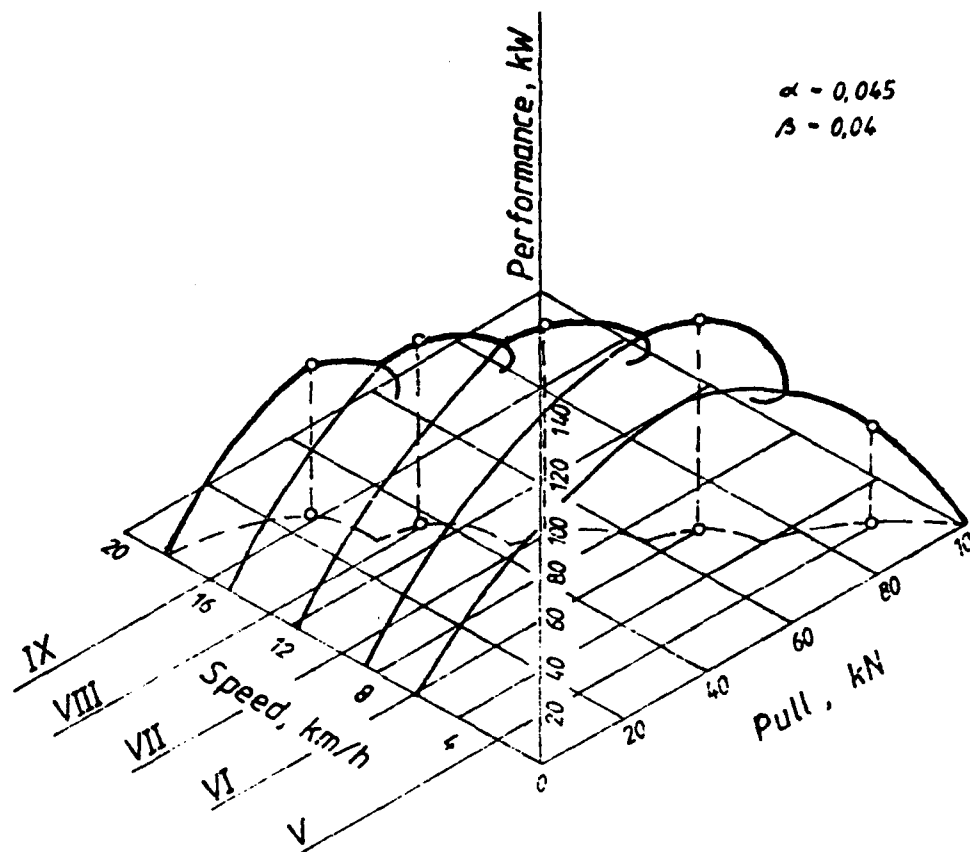


Fig. 3

The performance of the tractor and implement combination  
 tractor: Rába 300, implement: Rába-IH-10720 plough, tyre: 20,8 - 34 dual,  
 soil: loam, stubble,  $s = 1,26 e^{0,045 \cdot F_v}$ ,  
 $\beta = 0,04/$

# MEASUREMENTS OF COMBINED LATERAL AND LONGITUDINAL FORCES GENERATED BY OFF-ROAD TYRES

D.A. Crolla  
Dept. of Mechanical Engineering, The University of Leeds  
Leeds LS2 9JT

A.S.A. El-Razaz  
Dept of Automotive Engineering  
Minia University, Egypt

## Abstract

A tyre force dynamometer capable of measuring lateral and longitudinal forces in soil tank conditions has been designed and built.

A comprehensive set of results obtained for two 6.00 x 16 (8 ply) cross ply tyres with traction and ribbed treads operating on sandy loam soil is presented.

Methods of fitting curves to the data are described which lead to an empirical model of the tyre over the entire range of operating conditions.

## Mathematical Modelling

Much of the background work relating to mathematical modelling of off-road tyres had already been established when this project aimed at the tyre measurements started. A comprehensive review of all previous work on off-road tyre forces is given in Reference 1. The paper includes a summary of existing measured data for tyre forces and a critical appraisal of the previous approaches to tyre modelling, some of which are empirically-based and some an extension of on-road tyre models.

Further work on devising improved mathematical models for off-road tyres on deformable surfaces was carried out partly by El-Razaz (2) and partly during the course of this project by Hockley (3). Two new models were proposed. The first employed a semi-empirical approach and attempted to combine the tyre and soil deformations in the contact regions with empirical relationships for soil shear forces. The second was based on an idealised treatment of the tyre as a series of radial spokes. This approach had already been used successfully for modelling the force generation properties of road tyres (4). Each of the spokes is assumed to have radial, lateral and longitudinal flexibilities and for steady state cornering it must be in equilibrium under the action of tyre/road friction forces at the spoke tip and the restoring forces in the flexible elements.

Some spokes - those at the rear of the contact region - must typically slide across the surface before this condition is satisfied. In the case of a deformable surface, however, these conditions for equilibrium depend also on the elasto-plastic deformation characteristics of the soil and the equations must, therefore be modified to take account of these effects (5). A typical set of 'friction ellipse' curves resulting from this model are shown in Fig. 1.

### Experimental Apparatus

A dynamometer rig was designed and built for use in the soil tank in the Department of Agricultural Engineering, University of Newcastle-upon-Tyne. It enabled the following parameters to be controlled and measured:

- Tractive or braking force
- Wheel torque
- Lateral force
- Self-aligning moment
- Forward speed
- Wheel slip or skid
- Vertical load

It could be fitted with a choice of two 6.00 x 16 (8 ply) cross ply tyres with either a traction or a ribbed tread. A diagram of the rig indicating the linear bearings to allow vertical movement of the tyre and showing the load cell positions is given in Fig. 2. Photographs of the rig in operation in the soil tank are shown in Figs. 3 to 5.

Full details of the design, specification, manufacture and development of the rig are given in reference 6. This report also includes details of the soil processing techniques used, soil measurements (e.g. Figure 5) and of the data collection, processing and subsequent analysis using a programmable data acquisition system (PDAS) developed at the University of Leeds.

### Experimental Results

The range of conditions used for measurements is summarised in Table 1. The results for all these runs (a total of approximately 112) have been analysed and are collected together in Reference 7.

For each, the results are presented as follows:

- (1) Gross tractive (or braking) effort v. wheelslip (or skid)
- (2) Net tractive (or braking) effort v. wheelslip (or skid)
- (3) Side force v. wheelslip.

Curves of the following forms have been fitted to the original data:

$$\text{TFC} = A_1 - B_1 e^{-C_1 s} \quad (1)$$

$$\text{SFC} = A_2 e^{-B_2 s} + C_2 e^{-D_2 s} \quad (2)$$

where     TFC = Thrust (or braking) force coefficient  
              SFC = Side force coefficient  
 $A_1 B_1 C_1 \quad A_2 B_2 C_2 D_2$  = curve fitting coefficients  
 $s$  = wheelslip (or skid)

Two typical sets of results for a tractive and a braking condition are given in Figs. 6 and 7.

Examples of further processing of the results are shown in Figs. 8 to 15. The associated coefficients obtained from fitting curves to the data are listed in Tables 2 to 5. This procedure involved the following stages:

- (1) Collect together the tractive (Table 2, Figs. 8 and 10) and braking (Table 3, Figs. 9 and 11) force coefficient curves against wheelslip for a range of slip angles.
- (2) From these fitted data, generate curves of traction (Table 4, Figs. 12 and 14) and braking (Table 5, Figs. 13 and 15) force coefficients against slip angle for a range of wheelslips. This stage involves fitting another equation of form;

$$\text{SFC} = A_3 - B_3 e^{-C_3 \alpha} \quad (3)$$

to the data derived from Stage (1).

### Conclusions and Suggestions for Further Work

- (1) The original objectives of the project were met and have resulted in:
  - o design and development of a tyre test rig.
  - o series of comprehensive tyre force measurements.
  - o validation and further development of the Leeds tyre model.
- (2) The test rig and measuring facilities are now available to investigate tyre behaviour over a wider range of conditions, e.g. various soil types, tyre tread patterns, extremes of load and inflation pressure etc.
- (3) Further analysis of the existing data should be aimed at simplifying and condensing the tyre force results for use in off-road vehicle dynamics studies.

## References

1. Crolla, D.A.; El-Razaz, A.S.A. A review of the combined lateral and longitudinal force generation of tyres on deformable surfaces. *Journal of Terramechanics*, 1987, 24 3 pp 199-225.
2. Crolla, D.A.; El-Razaz, A.S.A. A model to predict the combined lateral and longitudinal forces on an off-road tyre. *Proc. of the 3rd European I.S.T.V.S. Conference*, Warsaw, Poland, 1986.
3. Crolla, D.A.; El-Razaz, A.S.A.; Hockley, C.; Alstead, C.J. An extended model to predict the combined lateral and longitudinal forces on off-road tyres. *Proc. of the 9th International I.S.T.V.S. Conference*, Barcelona, Spain, 1987, pp 362-372.
4. Sharp, R.S., El Nashar, M.A. A generally applicable digital computer based mathematical model for the generation of shear forces by pneumatic tyres. *Vehicle System Dynamics*, 1986 Vol. 15. No. 4. pp 187-209.
5. El-Razaz, A.S.A.; Crolla, D.A. A multi-spoke model for off-road tyres. *Proc. of the 4th European I.S.T.V.S. Conference*, 1989, pp 44-53.
6. Crolla, D.A.; Hockley, C. Tyre lateral forces on off-road surfaces : Details of rig design and experimental work. *Research Report*, Department of Mechanical Engineering, University of Leeds, 1989.
7. Crolla, D.A.; Hockley, C. Tyre lateral forces on off-road surfaces : Summary of measured results. *Research Report*, Department of Mechanical Engineering, University of Leeds, 1989.

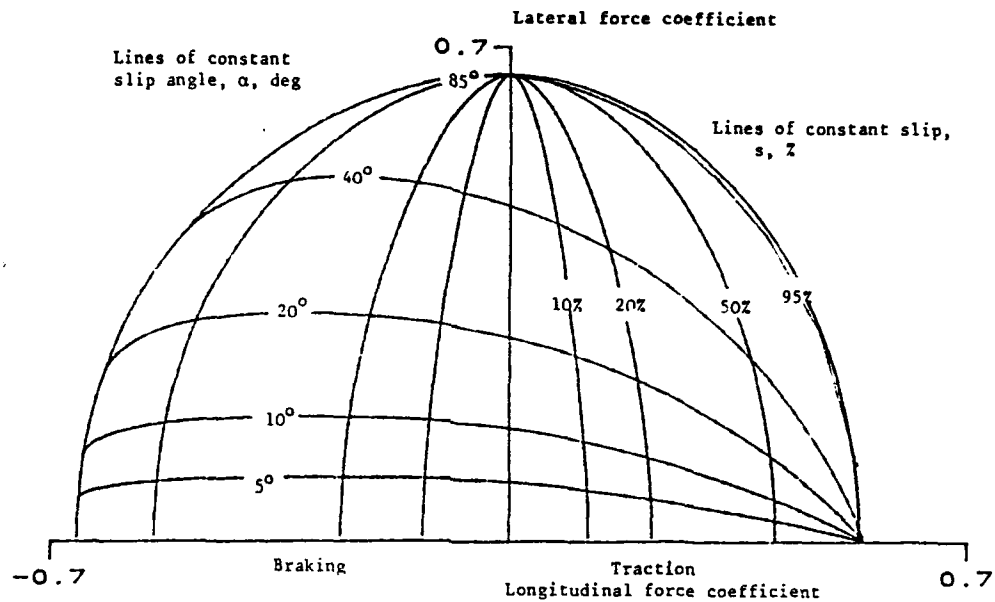


Fig. 1 Tyre force results calculated by the semi-empirical tyre model (3)

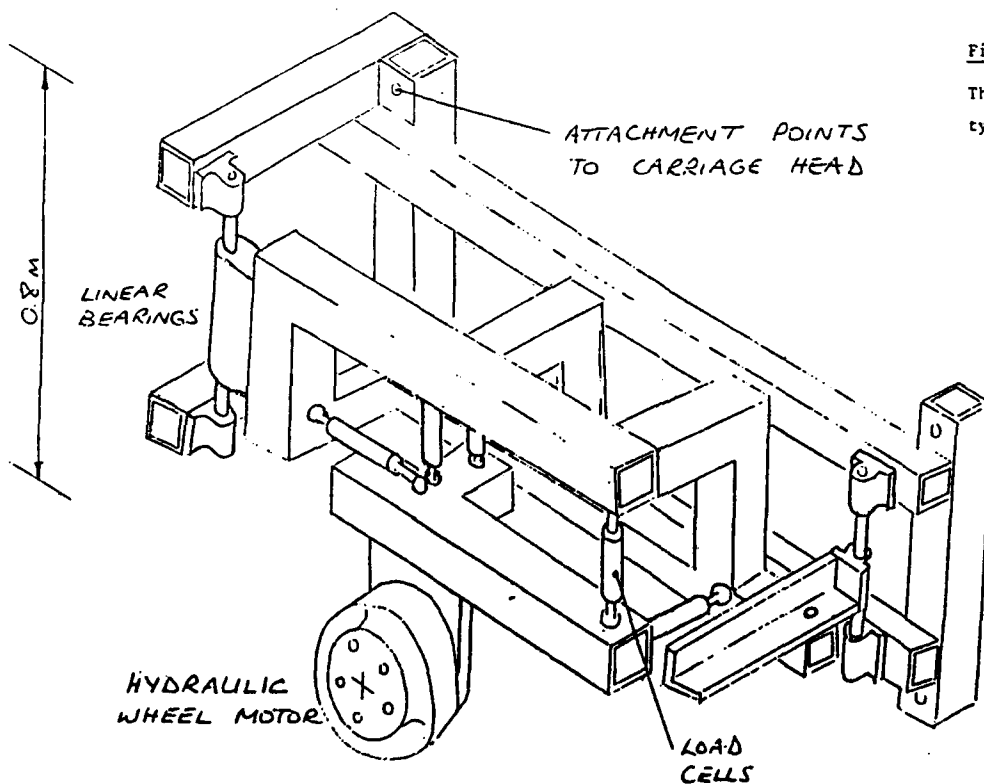


Figure 2

The dynamometer frame for measuring tyre forces in a soil bin



Type of Tyre Tread	Tyre Load kN	Tyre Pressure psi	Range of Slip Angles Degrees	Traction/Braking Conditions
Traction	2.2	12	0 - 30	both
	3	12	0 - 30	both
	3	18	0 - 30	both
	3	6	0 - 30	both
Ribbed	3	15	0 - 30	both
	3	7.5	0 - 30	both
	3	23	0 - 30	both
	2.2	15	0 - 30	both

Table 1 Summary of Conditions for Tyre Tests



Fig. 3 Tyre force dynamometer rig in the soil tank at the University of Newcastle-upon-Tyne

Slip Angle (deg)	Run I/D	Thrust			Side Force			
		A <sub>1</sub>	B <sub>1</sub>	C <sub>1</sub>	A <sub>2</sub>	B <sub>2</sub>	C <sub>2</sub>	D <sub>2</sub>
1.5	00T1	0.5354	0.6837	6.9754	0.0003	-3.2769	0.0592	0.0587
5	05T1	0.6279	0.6635	3.3436	1.4635	2.4649	-1.1503	-2.0962
10	10T1	0.6360	0.6906	3.1747	1.6852	1.4342	-1.3054	-1.0843
15	15T1	1.0907	1.1010	1.1074	2.0683	2.0683	-1.5989	-1.1465
20	20T1	0.7514	0.8100	1.7725	1.3199	1.8282	-0.7989	-1.8282
25	25T1	0.8988	0.9519	1.2588	1.9030	0.6103	-1.3505	-0.3300
30	30T1	0.9675	1.0096	1.1463	2.7198	0.2357	-2.1142	-0.0340
1.5	00B1	18.3810	18.3540	0.0660	1.6713	-3.6276	-1.6119	3.6795
5	05B1	0.6996	0.7097	3.4885	2.8727	0.0838	-2.6167	0.0170
10	10B1	8.6509	8.6689	0.1397	2.2149	-3.8912	-1.9152	4.2569
15	15B1	0.6994	0.6978	2.8726	2.5184	-1.2539	-2.1143	1.5074
20	20B1	4.6638	4.6292	0.2272	1.5538	-0.8162	-1.0578	1.1983
25	25B1	0.7449	0.7136	1.7439	1.4031	0.1704	-0.8454	0.0824
30	30B1	8.0126	8.0793	0.1103	-4.6848	-2.1291	5.1324	2.0051

Table 2

Traction tread; 2.2 kN load; 12 psi pressure

Results for curve fit coefficients for a complete set of traction and braking conditions  
(Curves plotted in Figs. 13 and 14)

Slip Angle (deg)	Run I/D	Thrust			Side Force			
		A <sub>1</sub>	B <sub>1</sub>	C <sub>1</sub>	A <sub>2</sub>	B <sub>2</sub>	C <sub>2</sub>	D <sub>2</sub>
1.5	00TRA1	0.5171	0.5279	7.3221	0.4388	-1.0786	-0.3492	1.2691
5	05TRA1	0.4765	0.4324	4.3941	0.2758	2.5272	0.0502	0.2199
10	10TRA1	0.4333	0.4273	5.2976	2.2914	0.9492	-1.9233	-0.8228
15	15TRA1	0.4252	0.4481	4.0051	-0.0715	23.1516	0.4972	-1.6968
20	20TRA1	0.4465	0.4688	2.8970	2.3309	0.5679	-1.8326	-0.4052
25	25TRA1	0.3704	0.4147	4.2328	2.7937	0.6098	-2.2014	-0.4820
30	30TRA1	0.4102	1.4671	1.3329	-0.0178	-2.4886	0.6683	-0.6689
1.5	00BRA1	4.0584	3.9759	0.2326	2.7289	-3.8636	-2.6066	3.9695
5	05BRA1	0.6825	0.7336	2.4143	1.9559	-2.3799	-1.6762	2.6718
10	10BRA1	0.6442	0.6442	2.3222	-17.8600	-3.4541	17.8502	-3.2841
15	15BRA1	0.4079	0.4011	5.8519	2.7875	-1.7400	-2.4801	1.8594
20	20BRA1	0.4426	0.4281	3.0822	3.3803	-2.3907	-3.0086	2.5396
25	25BRA1	0.5838	0.5855	2.6455	1.9999	-1.7045	-1.6270	1.8656
30	30BRA1	0.3698	0.2429	2.6498	3.6730	-2.1511	-3.1724	2.3233

Table 3 Front Tyre Tread; 3 kN load; 15 psi pressure

Results for curve fit coefficients for a complete set of traction and braking conditions  
(Curves plotted in Figs. 15 and 16)

	Wheel Slip	$A_3$	$B_3$	$C_3$
Run T1 Traction Conditions	0.0	0.594	0.612	0.0957
	0.1	0.679	0.666	0.0513
	0.2	1.311	1.281	0.0148
	0.3	5.186	5.159	0.0027
	0.4	5.186	5.166	0.0023
	0.5	4.626	4.618	0.0022
	1.0	0.004	0.040	18.55
Run B1 Braking Conditions	0.0	0.499	0.513	0.1309
	0.1	0.526	0.532	0.1106
	0.2	0.540	0.524	0.0895
	0.3	0.641	0.605	0.0488
	0.4	9.158	9.177	0.0019

Table 4 Traction tread; 2.2 kN load; 12 psi pressure

Further curve fitting coefficients for the data given in Tables 2 and 3 to obtain side force coefficient v. slip angle relationships

	Wheel Slip	$A_3$	$B_3$	$C_3$
Run TRA1 Traction Conditions	0.0	0.595	0.545	0.1108
	0.1	0.676	0.605	0.0578
	0.2	0.919	0.850	0.0265
	0.3	3.006	2.931	0.0052
	0.4	2.865	2.803	0.0048
	0.5	4.479	4.424	0.0026
	1.0	1.37	1.333	0.0029
Run BRA1 Traction Conditions	0.0	6.674	6.626	0.0018
	0.1	3.734	3.585	0.0034
	0.2	0.774	0.629	0.0317
	0.3	1.046	0.944	0.0236
	0.4	0.946	0.932	0.0351

Table 5 Front tyre tread; 3kN load; 15 psi pressure

Further curve fitting coefficients for the data given in Table 2 and 3 to obtain side force coefficient v. slip angle relationships



Fig. 4 Tyre force dynamometer rig



Fig. 5 Tyre force dynamometer rig mounted on moving head, also showing rotavator used for soil processing

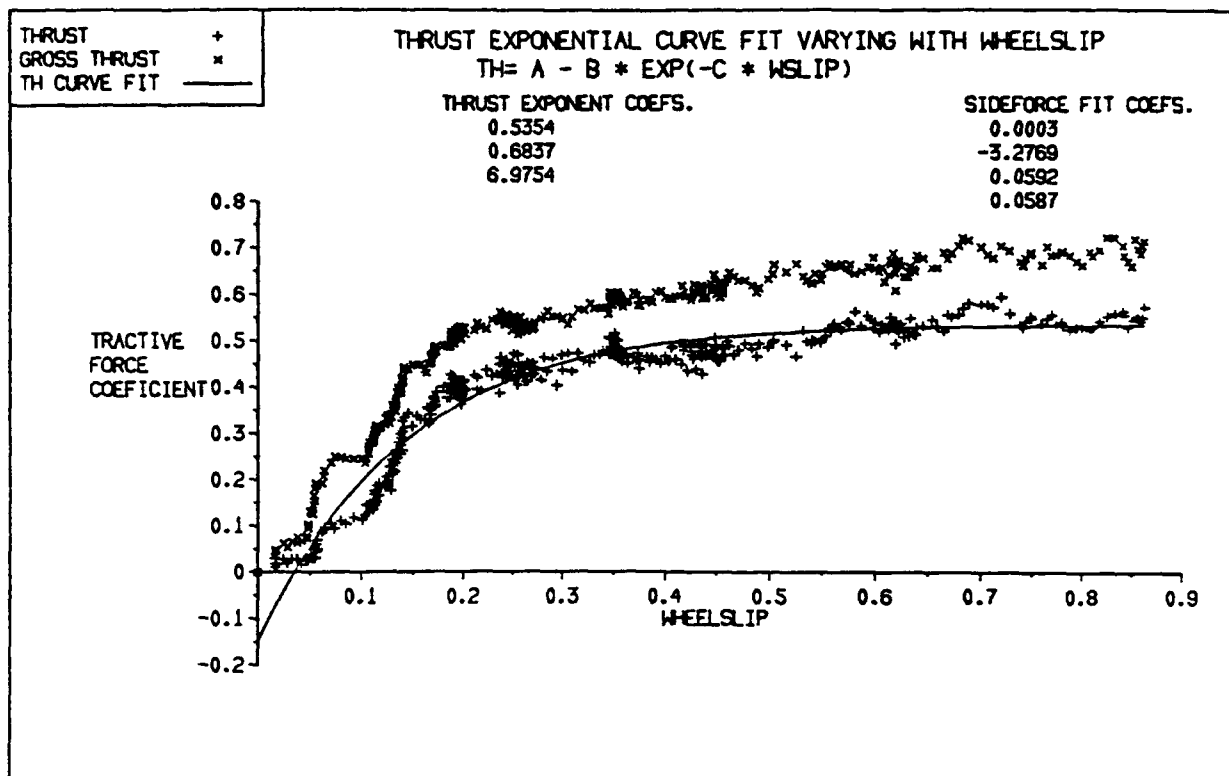
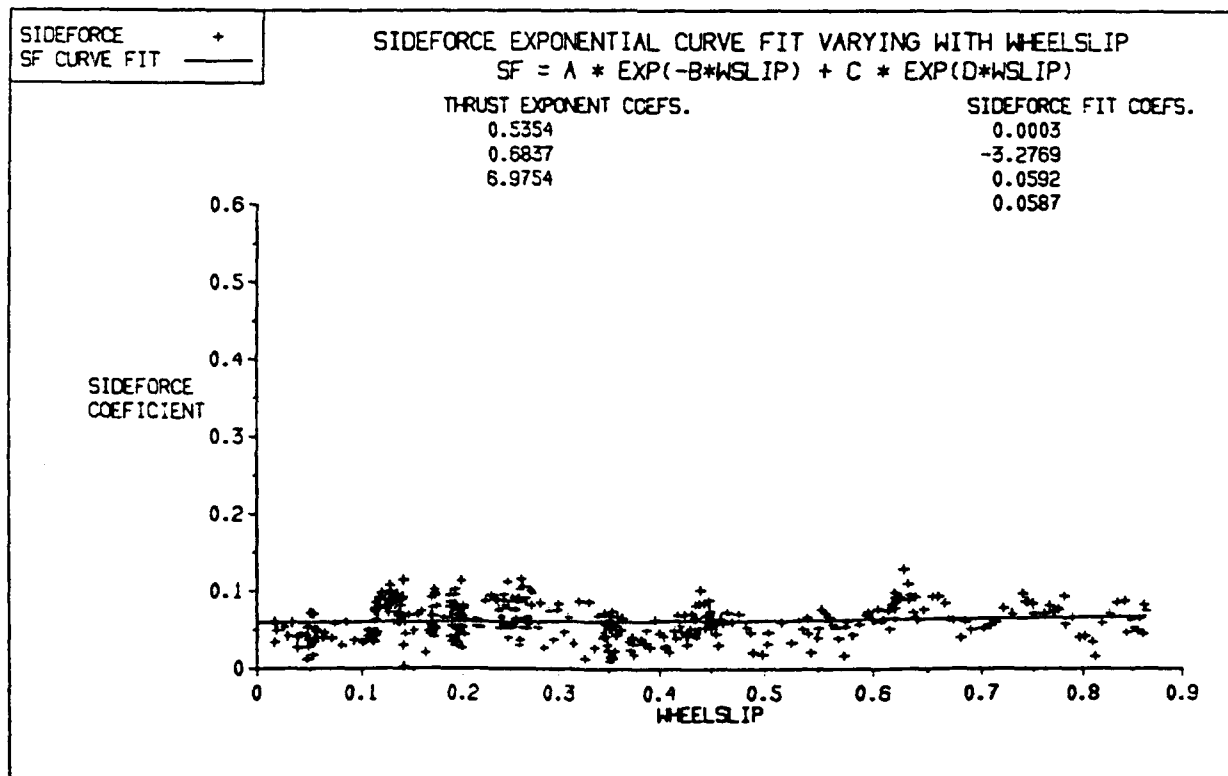


Fig. 6 Typical set of results from a traction experiment



RESULTS FROM RUN 00T1

2.2KN TYRE LOAD  
 12 PSI PRESSURE  
 TRACTION TREAD  
 1.5 DEGREE SLIP ANGLE

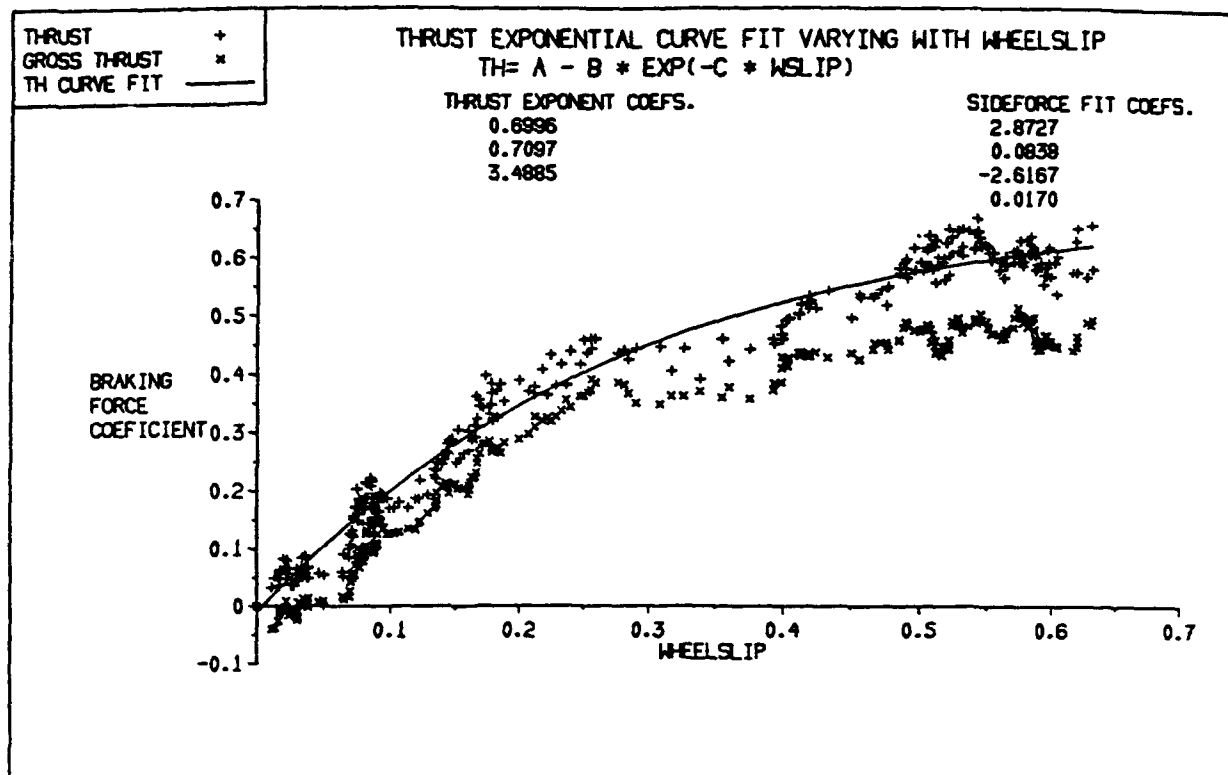
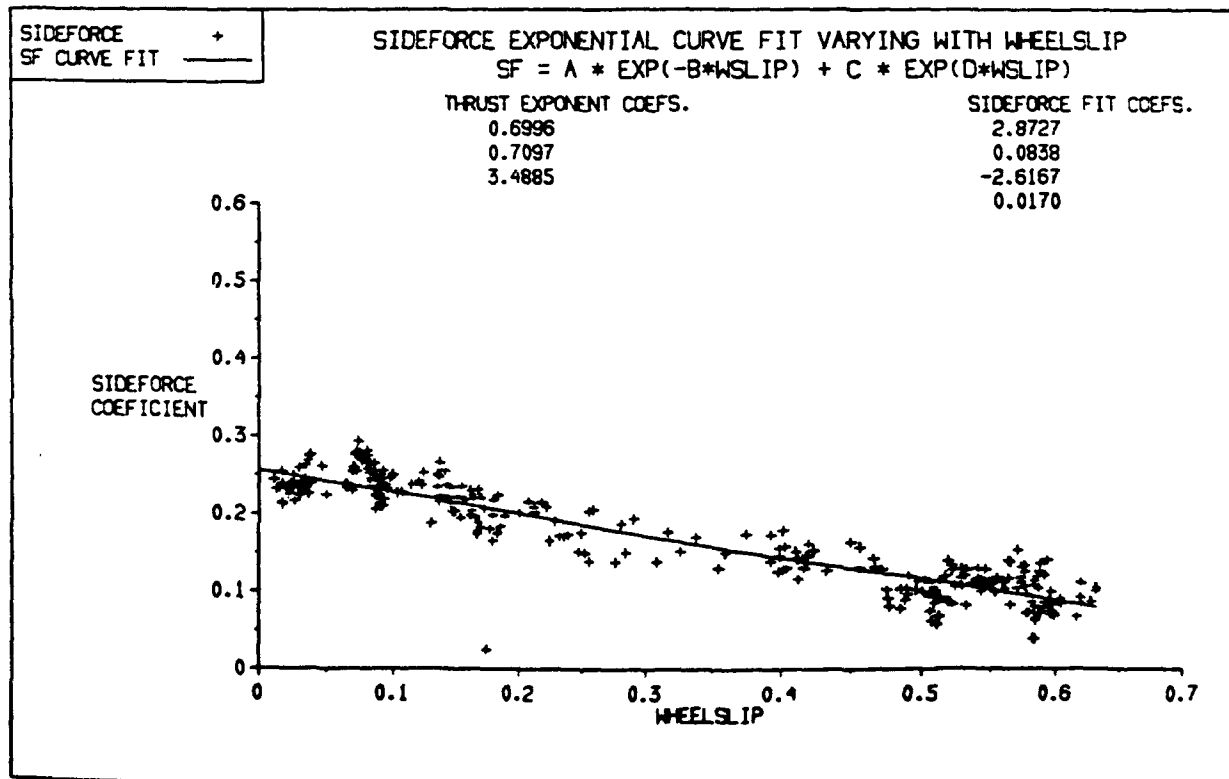


Fig. 7 Typical set of results from braked experiment



RESULTS FROM RUN 05B1

2.2 KN TYRE LOAD  
 12 PSI PRESSURE  
 TRACTION TREAD  
 5 DEGREE SLIP ANGLE

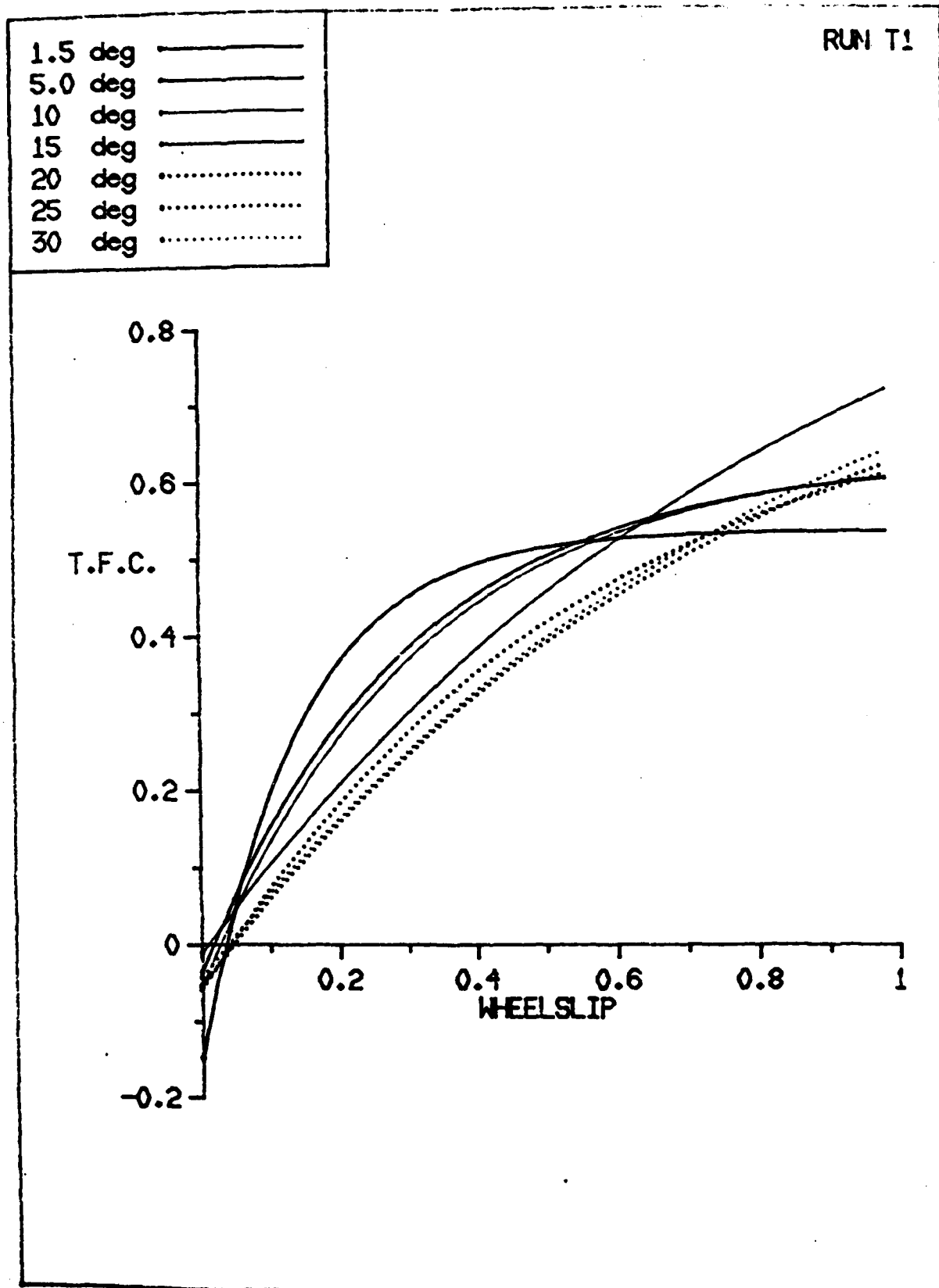


Fig. 8 Tractive tread; traction conditions  
(wheel slip 0 to 1)  
Side force coefficient v. slip angle



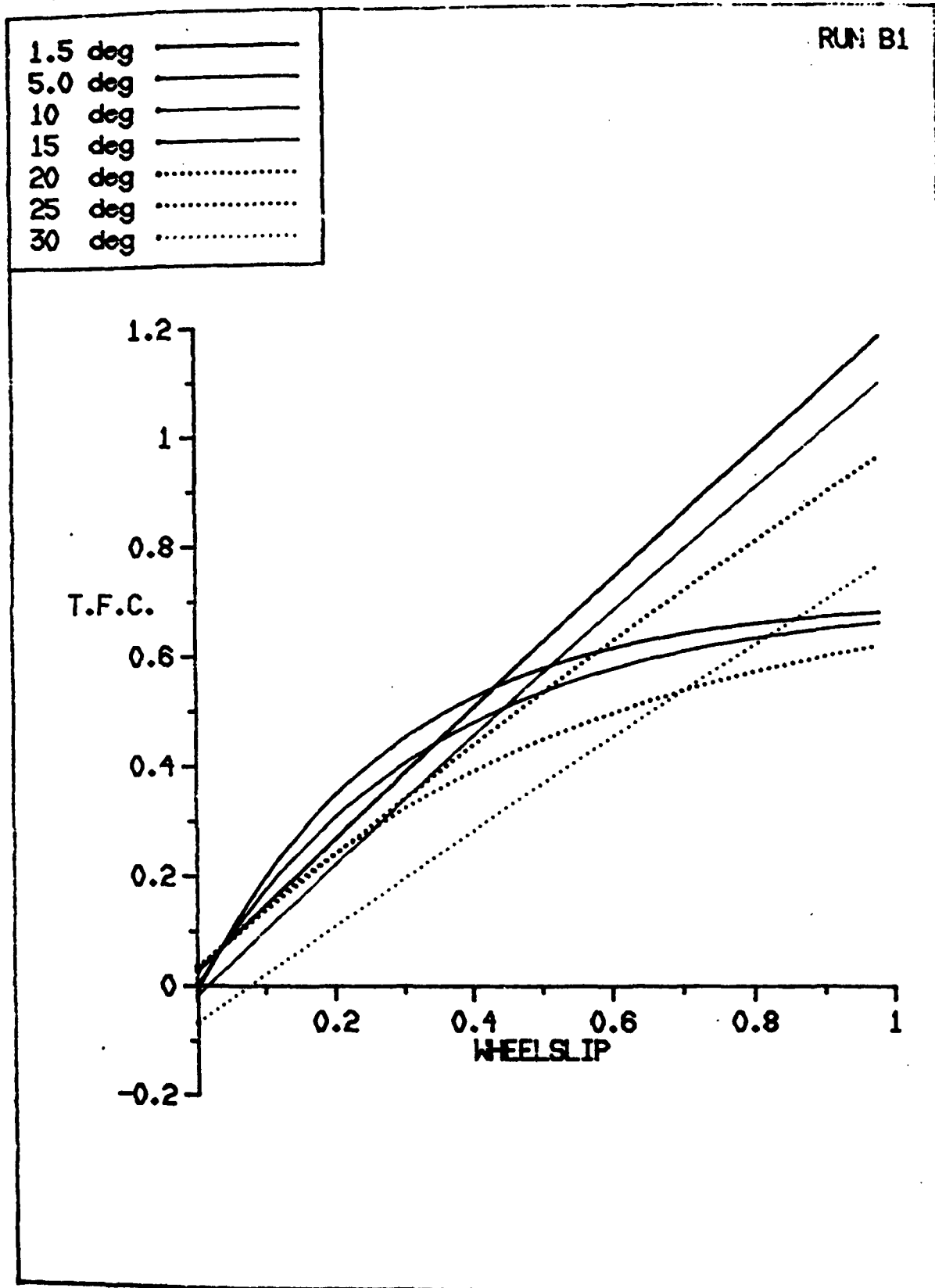


Fig. 9

Tractive tread; braked conditions  
(wheel slip 0 to 0.4)  
side force coefficient v. slip angle

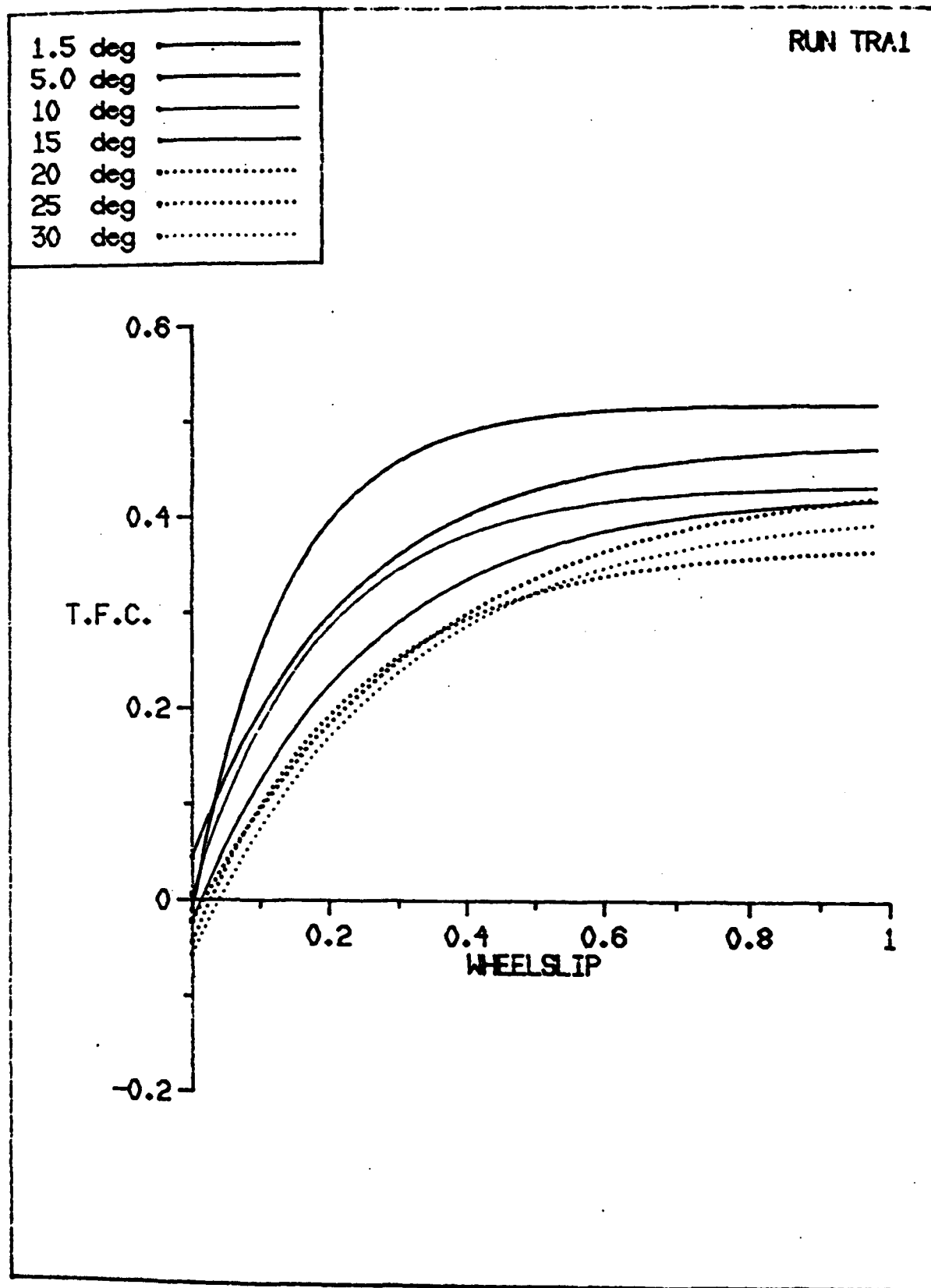


Fig. 10 Front tyre tread; tractive conditions  
(wheel slip 0 to 1)  
side force coefficient v. slip angle

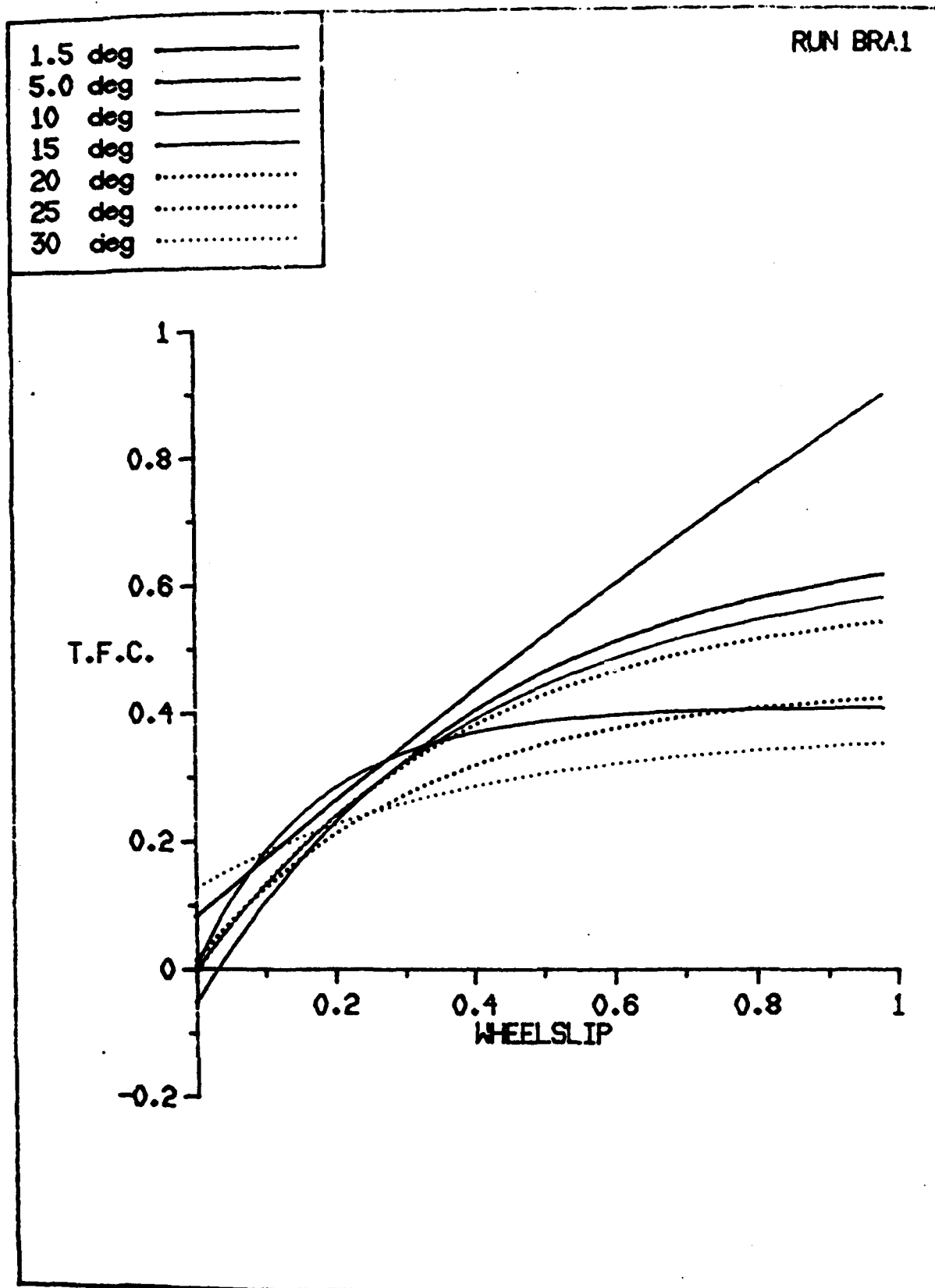


Fig. 11  
202

Front tyre tread; braked conditions  
(wheel slip 0 to 0.4)  
side force coefficient v. slip angle

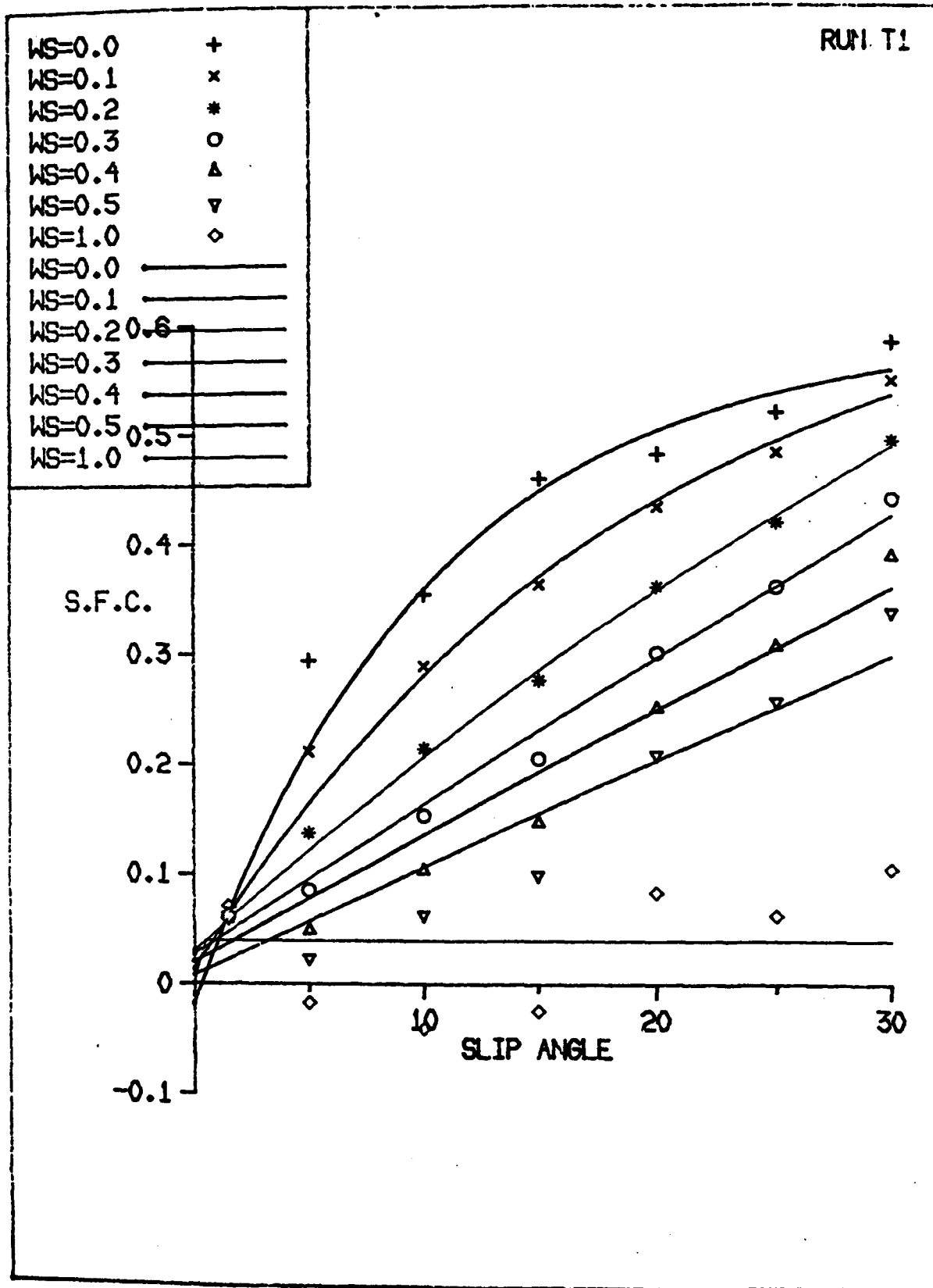


Fig. 12 Tractive tread; traction conditions  
(slip angles ranging from 0 to 30 deg.)  
traction force coefficient v. wheel slip

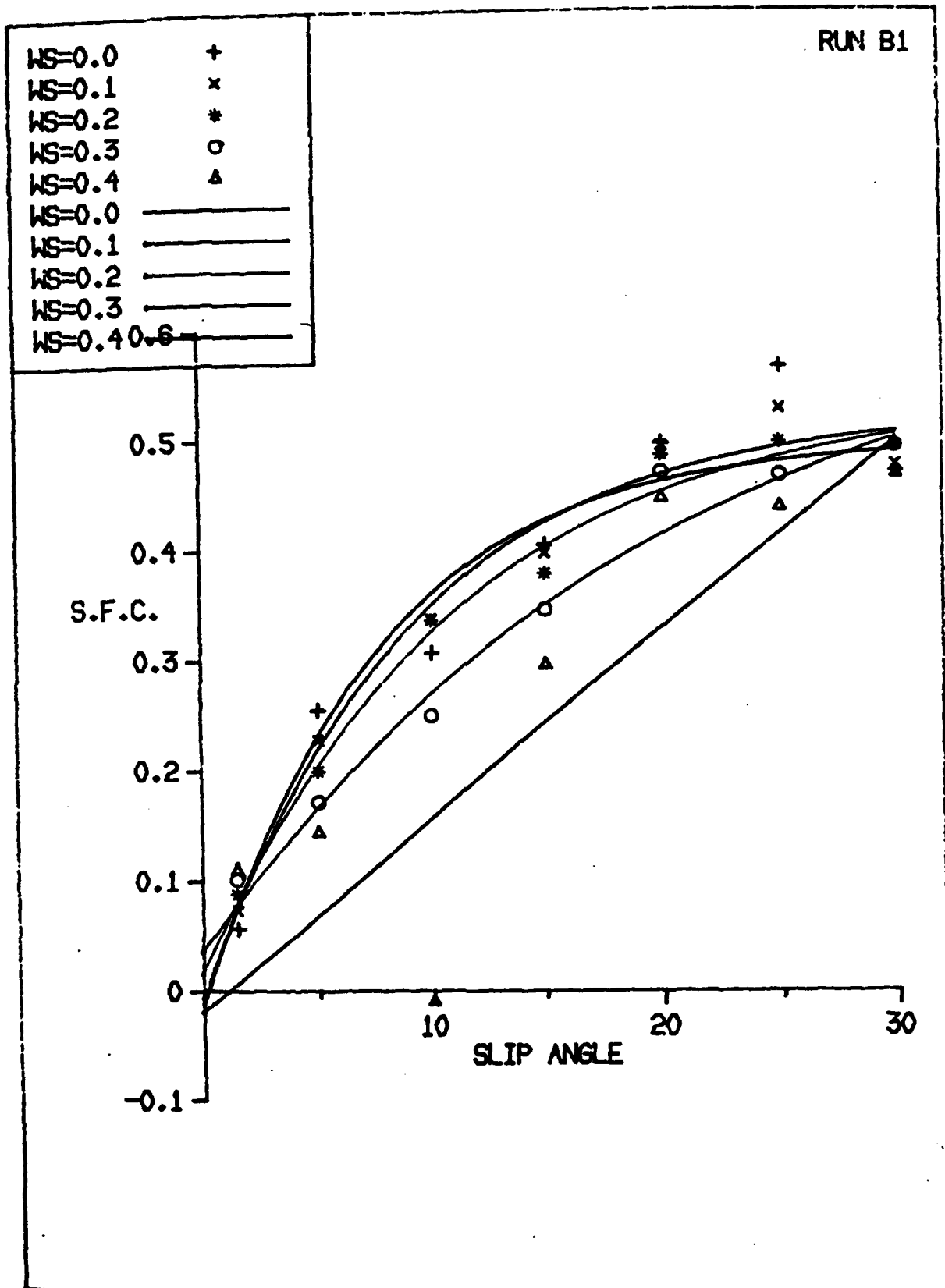


Fig. 13 Tractive tread; braking conditions  
(slip angles ranging from 0 to 30 deg.)  
204: Braking force coefficient v. wheel slip

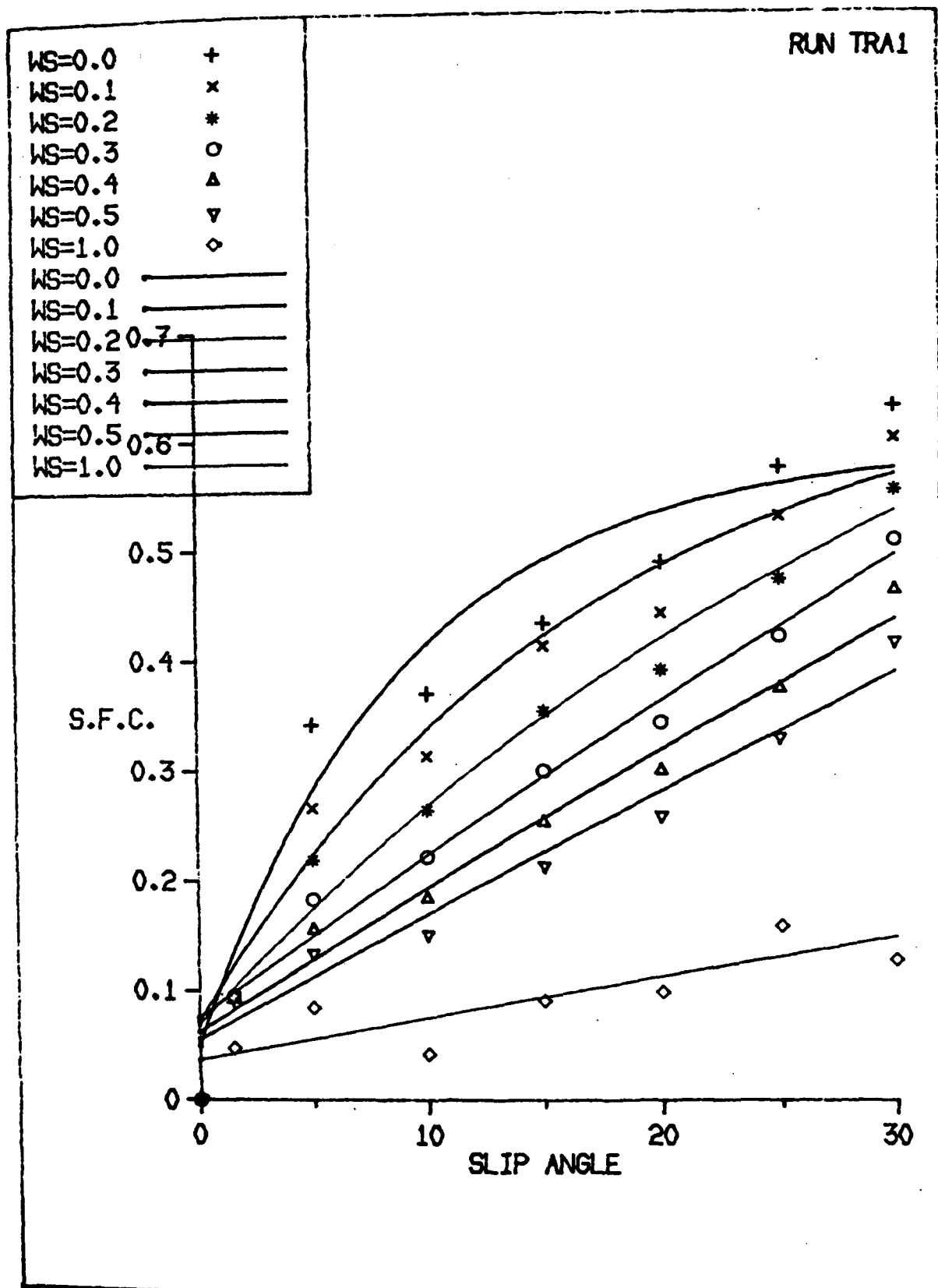


Fig. 14 Front tyre tread; traction conditions  
(slip angles ranging from 0 to 30 deg.)  
traction force coefficient v. wheel slip

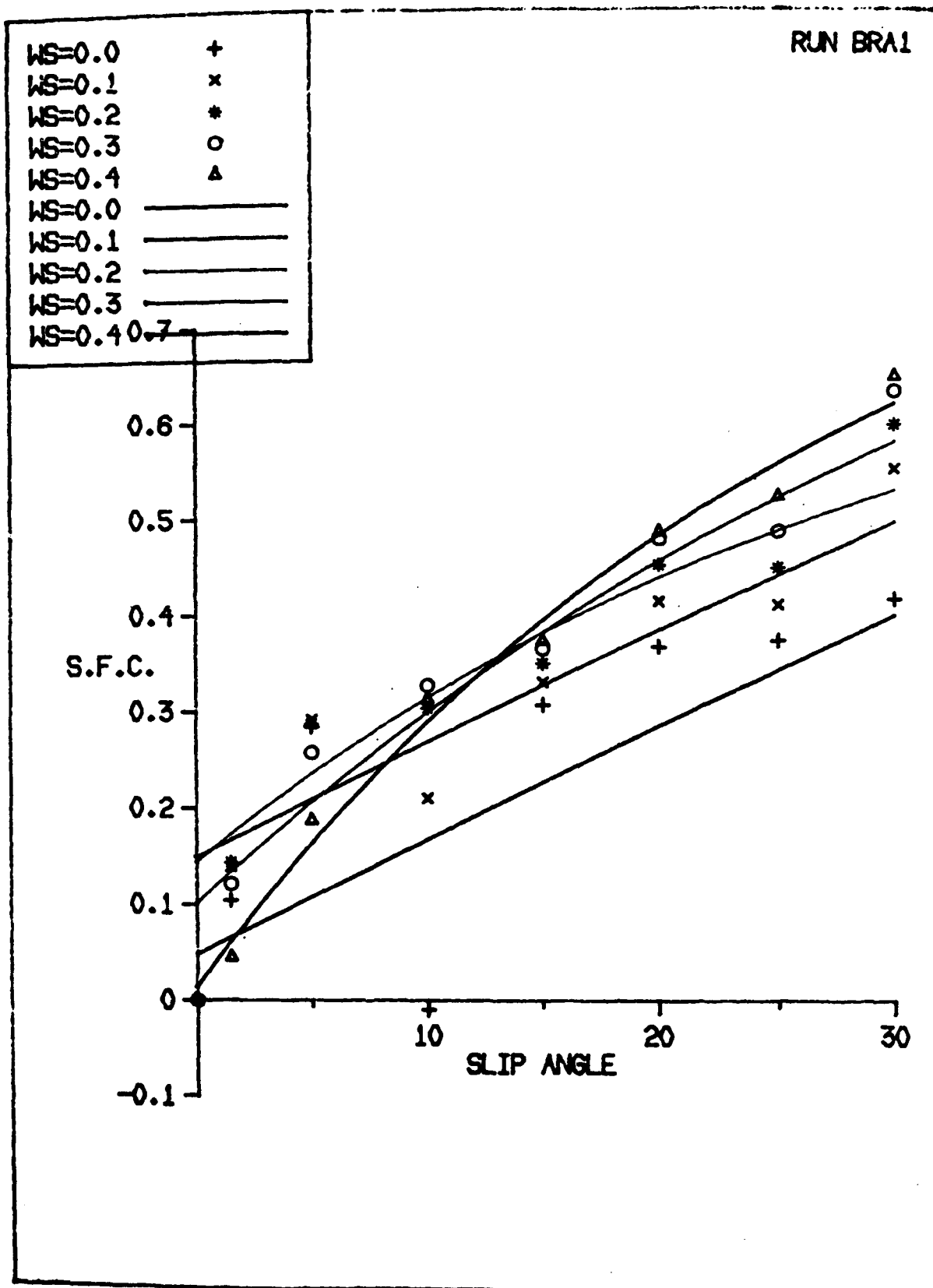


Fig. 15

Front tyre tread; braking conditions  
(slip angles ranging from 0 to 30 deg.  
braking force coefficient v. wheel slip

# CONE RESISTANCE MEASURING SYSTEM FOR GENERATING CONE RESISTANCE DISTRIBUTION MAP

K. OHMIYA

Faculty of Agriculture, Hokkaido University  
Sapporo 060, JAPAN

## Summary

To investigate soil physical properties affected by soil compaction or tillage, a computer controlled cone resistance measuring system and a visualization software for generating cone resistance distribution maps were developed.

A cone resistance measuring system was developed so that coordinates of measuring point was chosen at any location in a 1.5m X 2m horizontal x-y plane. Then, using this system, a series of cone resistance with x,y,z coordinates was measured. A portable computer was selected to measure and acquire series of cone resistance, to set the location of cone, to operate strain amplifier for measuring cone resistance, and to measure location of data. A visualization software generates 2 and 3 dimensional maps. x-z, y-z and x-y cross section are generated in 2 dimensional map. Plane and view point may be selected to 3 dimensional map.

Using this system, cone resistance of 1.5m length X 2.0m width X 0.6m depth in several fields were measured. And cone resistance distribution maps of 2 and 3 dimension were generated by visualization software. It was concluded that 2 and 3 dimensional distribution maps gave us some information that we have not got it from a map of one cross section.

## INTRODUCTION

In order to evaluate soil compaction or effects of tillage, it is necessary to evaluate soil physical conditions. Many investigators have been trying to analyze soil physical conditions, and they have developed equipments or systems for measuring and analyzing soil physical condition.

As Perumpral[1] reviewed, cone penetrometer is frequently used to evaluate soil compaction, off-road vehicle mobility and root impedance. Cone resistance may depend on many factors, radius of cone, water content of soil and penetration rate. However, measurement is quick, easy and economical, and it is easy to understand the data measured in fields. Therefore, cone resistance measured by cone penetrometer was adopted to evaluate soil physical conditions.

Most of cone resistance measuring systems which have been developed before were made for measuring cone resistance at one point or generating cone resistance distribution map of a cross section. Anderson[2], Wells[3] and Morrison[4] made hand-pushed type penetrometer with digital data recording system. Hooks[5] and Sudduth[6] developed recording cone penetrometer with hydraulic cylinder and Riethmuller[7], Olsen[8] and Larney[9] developed portable



cone penetrometer driven with electric motor. Willford[10], Soane[11] and Smith[12] developed recording soil penetrometer to generate cone resistance distribution map, and Clark[13] developed a digital recording cone resistance measuring system with constant rate penetrating system.

Introducing hand-pushed, electric or hydraulic cone penetrometer, cone resistance vs. depth is measured at one location. The data may indicate the maximum cone resistance and its depth, the existence of hard pan. Introducing recording cone resistance apparatus for measuring cone resistance in a cross section, cone resistance distribution map is generated. A cone resistance distribution map may show the area, which indicates the maximum cone resistance in a section, and hard pan.

Investigating soil physical condition under soil compaction, tillage or subsoiling, a part of higher or lower cone resistance exists like a lump, a layer or a tube. Crop has roots in any direction in the soil. Therefore, it is necessary to investigate the soil physical condition in three dimensional analysis. A computer controlled cone resistance measuring system and a visualization software were developed to acquire series of cone resistance and to generalize cone resistance distribution map in two and three dimension.

#### HARDWARE OF THE SYSTEM

A cone resistance measuring system was developed to measure series of cone resistance for generating cone resistance distributing map(Fig.1). Cone penetrating system is mounted on a frame X and the frame X is mounted on a frame Y. The cone penetrating system can be moved laterally and longitudinally on the frame X and the frame Y over a 150cm X 200cm section, and the measuring point may be selected at any position on the section. It has a circular cone with apex of 30 degrees and the base area of  $3.23\text{cm}^2$  and a cone is mounted on a 100cm long shaft of 1.6cm diameter[14]. The maximum stroke of this system is 86cm and the maximum depth is more than 60cm. A penetrating resistance transducer is a strain gage load cell made and calibrated by the author and it is located on the top of the shaft.

A speed controlled 60W AC motor is used to maintain the constant penetration rate and to force the cone into soil. Penetration rate is variable between 0.5cm/s and 3.5cm/s, and the penetrating rate is 3cm/s at measurement[14]. Rotating motion of the motor is transmitted to Ball Screw by chain and transferred to the linear motion by the Ball Screw mechanism. A pair of Linear Way is a guide to maintain the linear motion of the cone.

A portable computer(EPSON PC-286LE) with AD converter and I/O board used to move the cone penetrating system to any location and to acquire cone resistance at every 1/3mm depth. Location of the cone penetrating system is indicated by the count of the pulse of rotary encoders, which are mounted on the frame X and the frame Y. Limit switches are mounted on each end of frames, and the origin of the cone penetrating system is guaranteed by the limit switch. Electric signal of every 1/3mm depth is generated by an approximate switch and chain sprocket. AD converter converts the output of a signal conditioner, cone resistance, to digital number using a depth signal as a timing signal. A surface switch is mounted on the cone penetrating system to sense the surface of terrain. Cone resistance at every 1/3mm, x,y

coordinates of the measured position and the surface height are recorded in a floppy diskette(MS-DOS format, 1.2MB).

The maximum penetration force of this system is about 2,000N. When the penetration rate at no load was 3.5cm/s, the penetration rate was decreased to 2.9cm/s in 1.5s. as the resistance force was increased to 1,900N. However, the penetration force was decreased and the penetration rate was increased as penetrating the cone deeper. In the case that the maximum cone resistance was less than 600N, variation of cone penetration rate was less than 2% of initial penetration rate. Therefore, the apparatus maintains constant penetration rate during the cone penetration into soil.

#### SOFTWARE OF THE SYSTEM

As mentioned above, this system is controlled by a computer in positioning the cone penetrating system and measuring cone resistance. Computer is used to process measured cone resistance and to generate cone resistance distributing map. TURBO PASCAL(V.5.0) for NEC PC9800 series is adopted to develop the software of positioning the cone penetrating system, measuring series of cone resistance, processing the data measured and generating cone resistance distribution map. Table 1 shows functions of the software developed for measuring cone resistance and generating cone resistance distribution map. A software for generating cone resistance distribution map in two dimension was

Table 1. FUNCTIONS OF SOFTWARE FOR GENERATING  
CONE RESISTANCE DISTRIBUTION MAP

MEASURING UNIT	1. Editing data file for locations to measure cone resistance, and saving the file.
	2. Inspecting the system for measurement.
	3. Moving the cone penetrating system to the location by the data file, measuring cone resistance at every 1/3mm depth, and save series of cone resistance.
DATA PROCESSING UNIT	1. Reading sets of cone resistance of every 1/3mm depth from floppy disk.
	2. Adopting linear interpolation, generating a cubic data of 1cmX1cmX1cm with cone resistance in 150cm X 200cm X 80cm(Max.) section.
	3. Writing a set of interpolated data to floppy disk.
GRAPHIC UNIT	1. Generating cone resistance distribution map in 2 dimension, x-z(lateral), y-z(longitudinal) and x-y(horizontal) cross section.
	2. Position of distribution map may be selected in the set of cubic data.
	3. Generating cone resistance distribution map in 3 dimension. It is available to change the view point of the map.
	4. It is available to generate a map in color and monochrome.

developed[15], however, this software has been newly developed for the map for 3 dimensional data.

In order to measure cone penetrating resistance by this system, it is necessary to make a data file for the location measured. The cone penetrating system may move to the position according to the data file, then the cone is penetrated and cone resistance of each 1/3mm is measured. When cone is reached the end of stroke, a series of cone resistance measured is recorded in a floppy disk(2HD,1.2MB). Cone is pulled up and the apparatus moves to next measuring position.

x,y coordinates of location measured, height of surface, the voltage equivalent to zero of penetrating resistance, the voltage equivalent to assumed maximum value of penetrating resistance and cone resistance of every 1/3mm depth are recorded in the data file. To prevent the interaction of probings, it is necessary to keep a distance of measured location in x,y coordinates[13].

Visualization software was developed to aid in the observance of cone resistance distribution in a x-z cross section(lateral plane), a y-z cross section(longitudinal plane), a x-y cross section(horizontal plane) and a three dimensional map. This software was made for a personal computer(NEC 9800 series) with a color display(640 X 400 pixels) and a hard disk or RAM disk.

Series of cone resistance of every 1/3mm depth is measured using the apparatus. Cone resistance distribution map in two dimension and three dimension are generated by using a set of a cube with a value of cone resistance. Size of a cube is 1cmX1cmX1cm in this software. Value of each cube is calculated by a linear interpolation method.

#### FIELD RESULTS AND DISCUSSION

To confirm the functions of the software and to evaluate a map for cone resistance, sample data were collected in a large indoor soil bin and a field. A large indoor soil bin was 4m wide, 48m long and 1m deep. To prepare typical soil condition for soil compaction, a 1,950kg tractor passed over the tilled soil for four times. Series of cone resistance were measured in a field where sweet corns were harvested. Series of cone resistance were processed to cube of 1cmX1cmX1cm with cone resistance. Using this set of cubic data of cone resistance, cone resistance distribution map in any direction may be generated. Fig.2 shows the arrangement of locations measured. Measuring points were arranged so that data for generating map were interpolated properly.

Fig.3 shows a cone resistance distribution map of a x-z cross section in a indoor soil bin. The chart of cone resistance is shown in the right side of the map. "White" means higher cone resistance and "grey" and "black" means low cone resistance. Compared the map of Fig.3 with the chart, part of white color under the surface means that cone resistance was high. This shows that field was compacted by tractor pass. Fig.4 shows a cone resistance distribution map in y-z cross section in a indoor soil bin. A layer of white color is shown in Fig.4 that surface of field and the thickness is about 10cm. This layer indicates that the surface soil was compacted by the traffic and that cone resistance in surface was higher than 2,700kPa.

Fig.5 shows a cone resistance distribution map of y-z cross section in a field. Two sections of black color are shown at the lower left and lower right in the map, and black means that cone resistance is low. It is not recognized that the shape of this black section is like a ball or a shaft from this map. Fig.6 shows a cone resistance

distribution map of x-y cross section. A black section as a strip is shown in the upper and center in the map. Two black sections shown in Fig.5 are recognized as a tube from two maps and they are parallel, so these lower cone resistance sections may be formed by subsoiling.

Fig.7 shows a three dimensional cone resistance map. Three cross sections are shown in this map. Changing view point of the map, it is able to see the outline of cone resistance distribution in soil.

The cone resistance measuring system and the visualization software for generating cone resistance distribution map have been developed. This system and software may be an aid to observe and analyze the state of cone resistance distribution in three dimension.

#### ACKNOWLEDGMENTS

The author wishes to thank Dr. H. Terao for his encouragement and his advice and is pleased to record the assistance received from Mr. T. Masui, Mr. H. Makino and Mr. T. Sato in carrying out this project.

#### REFERENCES

- [1]Perumpral, J.V.: Cone Penetrometer Applications - A Review, Trans. ASAE, 23, 939-944, 1987
- [2]Anderson, G., Pidgeon, J.D., Spencer and Parks, R.: A New Hand-held Recording Penetrometer for Soil Studies, J. of Soil Science, 31, 279-296, 1980
- [3]Wells, L.G., Lewis, C.O. and Distler, R.J.: Remote Electronic Acquisition of Soil Cone Index Measurement, J. of Terramechanics, 18, 201-207, 1981
- [4]Morrison, Jr., J.E. and Bartek, L.A.: Design and Field Evaluation of a Hand-Pushed Digital Soil Penetrometer with Two Cone Materials, Trans. of ASAE, 30, 646-615, 1987
- [5]Hooks, C.L. and Jansen, I.J.: Recording Cone Penetrometer Developed in Reclamation Research, Soil Sci. Soc. AM. J., 50, 10-12, 1986
- [6]Sudduth, K.A., Hummel, J.W. and Levan, M.A.: Widespan Vehicle for Data Collection in Tillage Research, Trans. ASAE, 32, 367-372, 1989
- [7]Riethmuller, G.P., Batchelder, D.G. and Bloome, P.D.: A Microcomputer System for Cone Index Measurement, Trans. ASAE, 26, 96-1005, 1983
- [8]Olsen, H.J.: Electric Cone Penetrometer for Field Tests, J. of Terramechanics, J. of Terramechanics, 25, 287-293, 1988
- [9]Larney, F.J., Huffman, R.L., Schuler, R.T., Taylor, D.R., Kladviko, E.J. and Lowery, B.: A Portable, Self-leveling Constant-rate Cone Penetrometer with Computer-controlled Data Acquisition for Tillage Studies, Soil & Tillage Res., 14, 231-239, 1989
- [10]Willford, J.R., Wooten, O.B. and Fulgham, F.E.: Tractor Mounted Field Penetrometer, Trans. ASAE, 15, 226-227, 1972
- [11]Soane, B.D.: Techniques for Measuring Changes in the Packing State and Cone Resistance of Soil after the Passage of Wheels and Tracks, J. of Soil Science, 24, 311-323, 1973
- [12]Smith, L.A. and Dums, W.T.: A Recording Soil Penetrometer, Trans. ASAE, 21, 12-14, 19, 1978
- [13]Clark, R.L., Radcliffe, D.E. and Tollner, E.W.: Microcomputer-based Instrumentation and Software for Tractor-mounted Penetrometer, ASAE Paper No.86-1040, pp.27, 1986
- [14]ASAE: ASAE S313.1, Soil Cone Penetrometer, 1980
- [15]Ohmiya, K. and Masui, T.: Visualization Software for Cone Resistance Analysis, Proceedings of 2nd Asia-Pacific Conference of ISTVS, 1-11, 1988

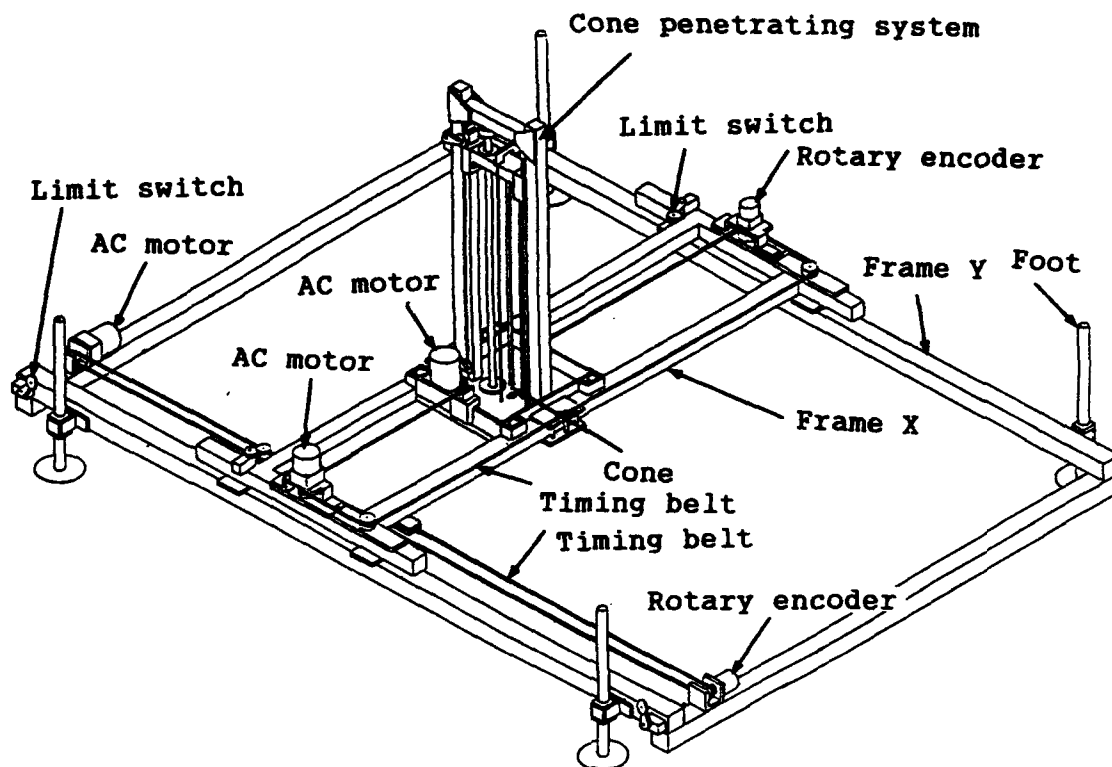


Fig.1 Cone resistance measuring system

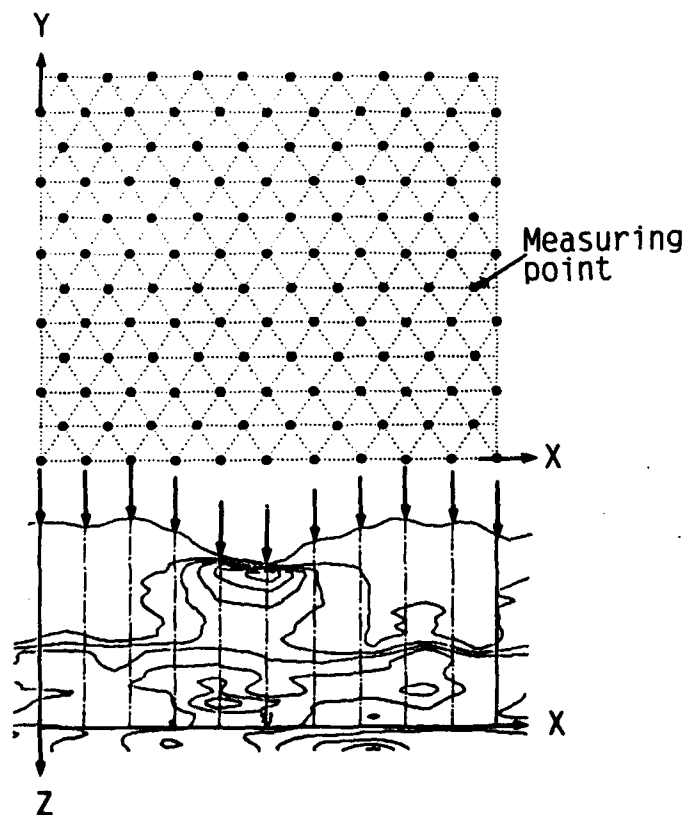


Fig.2 Data sample location for generating cone resistance distribution map

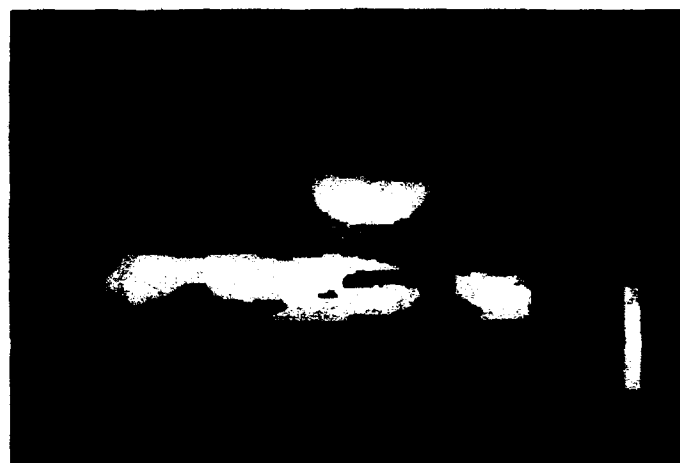


Fig.3 Cone resistance distribution map in x-z cross section (Passage of a tractor wheel)

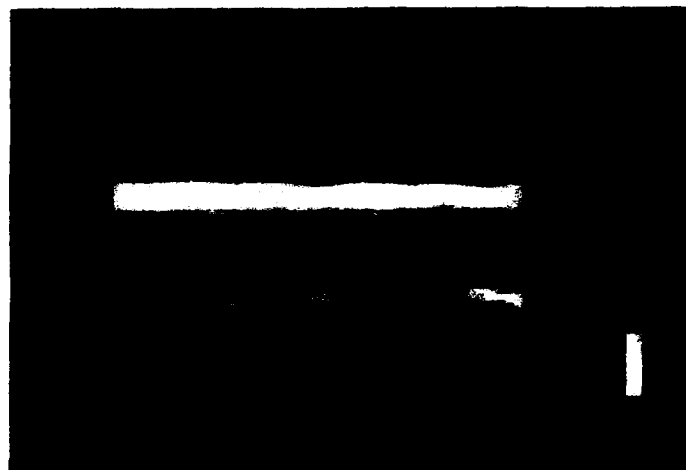


Fig.4 Cone resistance distribution map in y-z cross section (Passage of a tractor wheel)

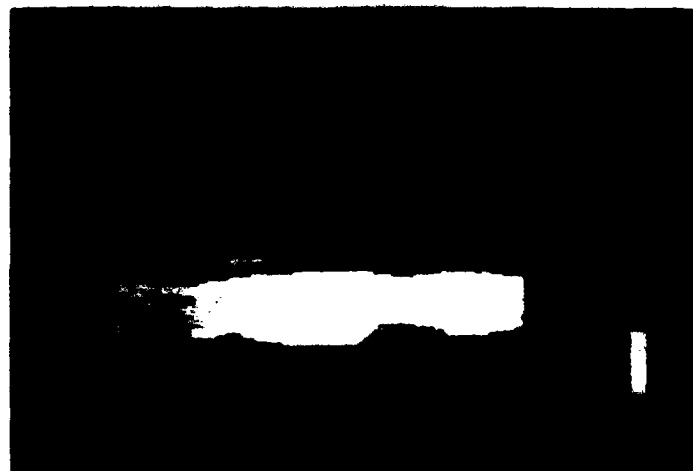


Fig.5 Cone resistance distribution map in y-z cross section (Field where sweet cones were harvested)



Fig.6 Cone resistance distribution map  
in x-y cross section (Field where  
sweet cones were harvested)



Fig.7 Cone resistance distribution map  
in 3 dimension (Field where sweet  
cones were harvested)

# DETERMINING OF DRAWBAR PARAMETERS OF AGRICULTURAL WHEELED TRACTORS

R.I. Nikolić

Faculty of Agriculture, Institute of agricultural technics,  
Trg Dositeja Obradovića 8, 21000 Novi Sad, Yugoslavia

## Summary

The following parameters are treated in this paper: tractive efficiency ( $\eta_v$ ), coefficient of net traction ( $\varphi_n$ ) and the slip ( $\delta$ ) for tractors (4x2)S, (4x4)S and (4x4)Z for the substrates: concrete (P1), dry lucerne-field (P2), stubblefield (P3), stripped soil (P4), soil prepared for sowing (P5) and freshly ploughed soil (P6).

Equations of exponential type and mean values of the parameters are defined in the paper.

## INTRODUCTION

On designing the agricultural tractors and forming the tractorial systems it is necessary to know drawbar parameters defined for various substrates on which the operations are performed. The key parameters determining the success of tractor construction and quality of formed system are as follows: tractive efficiency ( $\eta_v$ ), coefficient of net traction ( $\varphi_n$ ) and the slip ( $\delta$ ).

Several papers have been published concerning this field of research, and the basis of the Off-the Road Wheel Locomotion Theory has been established by Bekker (1) and (2). The problems of relationship tractor - Substrate are dealt with in the paper (5), (8), (10), (18). A considerable amount of research has been carried out on drawbar parameters with different tractor conceptions and on different substrates and the results of the performed measurements are shown in the papers: (3), (6), (7), (13), (+%), (15), (16), (17), (19).

Great number of papers are concerned with predicting of drawbar parameters, but only three of them are cited here (4), (7) and (9). In 1963. Grečenko has defined standard relationship between the slip ( $\delta$ ) and adhesion coefficient ( $\varphi$ ) for three substrates: concrete, stubblefield and laid-down ploughing. He has found out the following relationships:

Concrete

$$\delta = \frac{0,076 \varphi - 0,055 \varphi^2}{0,920 - \varphi}$$

Stubble-field

$$\delta = \frac{0,127 \varphi - 0,095 \varphi^2}{0,890 - \varphi}$$

Laid-down ploughing

$$\delta = \frac{0,194 \varphi - 0,135 \varphi^2}{0,740 - \varphi}$$

This author further defines the expected mean values of parameters for stubble-field for tractors (4x2)S  $\eta_v = 0,58-0,66$   $\varphi = 0,25-0,35$ , (4x4)  $\eta_v = 0,61-0,71$  and  $\varphi = 0,35-0,45$ .

Having analyzing test results for tractors since 1972., Kolobov (9) has established the relationship between coefficient of net traction ( $\varphi_n$ ) and the slip ( $\delta$ ) in the form of exponential equation for stubble-field:

(4x2)S

(4x4)S

(4x4)Z

$$\varphi_n = 0,7-0,75.e^{-8,82. \delta} \quad \varphi_n = 0,6-0,64.e^{-0,82. \delta} \quad \varphi_n = 0,67-0,708.e^{-7,15. \delta}$$

He has established mean values for the stubble-field:

(4x2)S

(4x4)S

(4x4)Z

$$\eta_v = 0,64, \varphi_n = 0,54, \delta = 17-18\% \quad \eta_v = 0,65, \varphi_n = 0,40, \delta = 17-18\% \quad \eta_v = 0,68, \varphi_n = 0,45, \delta = 15\%$$

Dwyer (1987) has performed the analysis of obtained equation for predicting drawbar



parameters of tractors on the hard substrate in France, Germany, United Kingdom and USA. The author concludes that this relationship can be shown in the form of the following equation:

$$\eta_n = 1 - e^{-20 \cdot \delta}$$

Taking into consideration the importance of the treated problems, the aim of this paper was to determine drawbar parameters for wheeled tractors of conception (4x2)S, (4x4)S and (4x4)Z for the six characteristic substrates.

#### WORKING METHOD AND CONDITIONS

Determining the mean values of drawbar parameters and their relationships has been performed on the basis of a number of measured drawbar characteristics of wheeled tractors. The following parameters have been measured or calculated: drawbar pull on pulling device  $F_v$  (daN), weight of tractor  $G$  (daN), motion speed actual  $V_s$  (m/s) and theoretical  $V_t$  (m/s), drawbar power  $P_v$  (kW), motor power  $P_e$  (kW), tractive efficiency of tractor  $\eta_v = P_v/P_e$ , coefficient of net traction  $\eta_n = F_v/G$ , the slip  $\delta = (V_t - V_s) \cdot 100/V_t$  (%).

All measurements have been performed by the mobile laboratory equipped with electronic devices. Field conditions - flat surface, soil humidity from 16-22 weigh. %. Used substrates: (P1) - concrete, asphalt, (P2) - dry lucerne-field, dry stamped stubble-field and the like, (P3) - stubblefield, cornfield, (P4) - stripped substrate, fresh turnipfield, (P5) - soil prepared for sowing, and (P6) - fresh ploughing.

Three conceptions of wheeled tractors have been involved: (4x2)S - standard, rear wheel drive, front wheels smaller, (4x4)S - standard, four-wheel drive, front wheels smaller, (4x4)Z - jointed tractor, four - wheel drive, wheels of identical dimensions.

#### RESEARCH RESULTS

Slipping of the drive wheels and coefficient of net traction are dependant on the type and conditions of pneumatics as well as on the type and condition of substrate. The interrelationship of these two parameters for tractor (4x2)S is shown on diagram Fig.1. With the increase of traction coefficient the curves are becoming steeper and the slip is showing tendency to total slipping. Maximal values for traction coefficient depending in the type of substrate are: 0,94-P1; 0,680-P2; 0,600-P3; 0,560-P4; 0,460-P5 and 0,420-P6. Nominal values range from 0,46 substrate P1 to 0,29 substrate P-6 during maximal  $\eta_v$ . These values decrease from P-1 to P-6 with indexes: 100; 72,34; 63,83; 59,57; 48,94 and 44,68.

For tractors (4x4)S measurement results are shown on diagram Fig.2. It can be seen from the diagram that the same values of traction coefficient are obtained during smaller slips than with tractors (4x2)S.

With maximal efficiency coefficient the following coefficients of net traction have been obtained: 0,47-P1; 0,463-P2; 0,415-P3; 0,360-P4; 0,344-P5 and 0,31-P6 which is from 2,17% to 6,90 % more than with tractors (4x2)S. From these data can be seen that worsw the substrate is according to the ability of takingover tangential forces, the better is the advantage of four-wheel drive tractor. Values of traction coefficients from hard to soft substrate are decreasing slower than those shown with the former tractor conception: 100; 98,51; 88,30; 76,60; 73,19 and 66,00.

On the diagram Fig.3 is shown the relationship between the slip and traction coefficient for tractors (4x4)Z and it can be observed that slip values are smaller than with other tractor conceptions. With maximal efficiency the following coefficients of net traction have been obtained: 0,490-P1; 0,483-P2; 0,450-P3; 0,390-P4; 0,365-P5 and 0,355-P6 with the decrease from substrate P-1 to P-6 as per indexes: 100; 98,57; 91,84; 79,59; 74,49 and 72,45. The values are bigger than with tractor (4x4)S from 4,25 to 14,52 %, i.e. from 6,52 to 22,41 % than with tractor (4x2)S.

Relationship between coefficient of net traction ( $\eta_n$ ) and the slip ( $\delta$ ) is shown in the Table 1 as an equation of exponential form. For the concrete equations have simpler form:

(4x2)S

$$\varphi_{n1} = 1 - e^{-8 \cdot \delta}$$

(4x4)S

$$\varphi_{n1} = 1 - e^{-13 \cdot \delta}$$

(4x4)Z

$$\varphi_{n1} = 1 - e^{-15 \cdot \delta}$$

Table 1

RELATIONSHIP BETWEEN SLIP ( $\delta$ ) AND COEFFICIENT OF NET TRACTION ( $\varphi_n$ )

R. B.	SUBS-TRATE	(4x2)S	(4x4)S	(4x4)Z
1.	P1	$\varphi_{n1}=1,0385-0,9842.e^{-0,0784 \cdot \delta}$	$\varphi_{n1}=0,9554-0,9495.e^{-0,1262 \cdot \delta}$	$\varphi_{n1}=1,0021-0,9272.e^{-0,1494 \cdot \delta}$
2.	P2	$\varphi_{n2}=0,7130-0,7649.e^{-0,0913 \cdot \delta}$	$\varphi_{n2}=0,8333-0,7645.e^{-0,0629 \cdot \delta}$	$\varphi_{n2}=0,7638-0,7950.e^{-0,1403 \cdot \delta}$
3.	P3	$\varphi_{n3}=0,6789-0,7279.e^{-0,0708 \cdot \delta}$	$\varphi_{n3}=1,0470-0,9738.e^{-0,0305 \cdot \delta}$	$\varphi_{n3}=0,6782-0,8356.e^{-0,1433 \cdot \delta}$
4.	P4	$\varphi_{n4}=0,7532-0,7747.e^{-0,0409 \cdot \delta}$	$\varphi_{n4}=1,0736-1,0220.e^{-0,0245 \cdot \delta}$	$\varphi_{n4}=0,5940-0,7838.e^{-0,1394 \cdot \delta}$
5.	P5	$\varphi_{n5}=0,6071-0,6506.e^{-0,0477 \cdot \delta}$	$\varphi_{n5}=0,5548-0,5882.e^{-0,0747 \cdot \delta}$	$\varphi_{n5}=0,610-0,6958.e^{-0,0836 \cdot \delta}$
6.	P6	$\varphi_{n6}=0,5045-0,5623.e^{-0,0546 \cdot \delta}$	$\varphi_{n6}=0,6165-0,6454.e^{-0,0427 \cdot \delta}$	$\varphi_{n6}=0,4995-0,6197.e^{-0,0972 \cdot \delta}$

Dependence  $\eta_v$  on slip for tractors (4x2)S is shown on diagram Fig.4. Maximal coefficient values occur during slipping ranging from 5,6- 18,25 % depending on the substrate.

Maximal values  $\eta_v$  obtained per substrates: P1-0,81; P2- 0,65; P3-0,60; P4-0,56; P5-0,50 and P6-0,46. If we take substrate P1 as index 100 the following ratios are obtained: 80,25-P2; 74,07-P3; 69,14-P4; 61,73-P5 and 56,79-P6. According to these results it is quite obvious that decrease of values of efficiency of traction coefficient depends on the substrate and slip.

On diagram Fig.5 is shown relationship  $\eta_v$  between slips for tractors (4x4)S. With the same slip these tractors perform bigger values  $\eta_v$ . On substrate P-6 the increase of maximal coefficient value  $\eta_v$  would be for 7,03 % more than with tractors (4x2)S. On the same substrate and with the same drawbar pull, the slip will be reduced for 10,14 %. Four-wheel drive has the advantage of obtaining bigger drawbar pulls even when operating on substrate with increased moisture.

Maximal values for  $\eta_v$  are 0,820-P1; 0,670-P2; 0,635-P3; 0,575-P4; 0,540-P5 and 0,485-P6. As it can be seen this coefficient shows rapid decrease from substrate P-1 to substrate P-6 with indexes: 100-P1; 81,71-P2; 77,44-P3; 70,12-P4; 65,85-P5 and 59,15-P6.

For tractors (4x4)Z relationship  $\eta_v$  between slips is given on diagram Fig.6. These tractors with doubled wheels obtain bigger  $\eta_v$  with the same slip which make them more economical. On substrate P-6 maximal value for  $\eta_v$  is bigger for 3,09 % than with tractor (4x4)S and for 8,69 % than with tractor (4x4)S, and the slip is smaller for 6,71 % i.e. 16,16 %, respectively.

Maximal values for  $\eta_v$  are: 0,850-P1; 0,700-P2; 0,670-P3; 0,635-P4; 0,575-P5 and 0,500-P6. Coefficient  $\eta_v$  shows the same tendency of decrease as with other tractor conceptions: 100-P1; 82,35-P2; 78,82-P3; 74,71-P4; 67,65-P5 and 58,82-P6.

In Table T-2 are given slip values and traction coefficient at maximal tractor efficiency as dependant on the substrate. When we compare substrate values P-6 and P-1 it can be observed that  $\eta_v$  is bigger for 76,09 % with conception (4x2)S, 69,07 % with (4x4)S and 70,00 % with (4x4)Z, respectively. Traction coefficient is bigger for 58,62: 51,60 and 38,03 %. With conception (4x4)Z increase is the smallest which means that under normal conditions these tractors are less susceptible to the type of substrate. Starting from substrate P-6 to P-1 the slip is reducing for 69,31 %: 69,51 %: 75,49 % with joint tractors. On the basis of above results it can be concluded that tractors (4x4)Z are more suitable for use under normal conditions than the other conceptions, when the realization of increased drawbar pulls is concerned.

T-2 DRAWBAR COEFFICIENT AND SLIP BY  $\eta_{vmax}$ 

Tractor Conception	Parame- ters	P O D L O G E					
		P1	P2	P3	P4	P5	P6
(4x2)S	$\eta_{vmax}$	0,810	0,650	0,600	0,560	0,500	0,460
	$\varphi_n$	0,460	0,450	0,380	0,340	0,320	0,290
	$\delta$	5,6	12,43	13,13	15,01	17,03	18,25
(4x4)S	$\eta_{vmax}$	0,820	0,670	0,635	0,575	0,540	0,485
	$\varphi_n$	0,470	0,463	0,415	0,360	0,344	0,310
	$\delta$	5,0	11,01	12,04	13,13	15,00	16,40
(4x4)Z	$\eta_{vmax}$	0,850	0,700	0,670	0,635	0,575	0,500
	$\varphi_n$	0,490	0,483	0,450	0,390	0,365	0,355
	$\delta$	3,75	8,31	10,45	11,83	12,84	15,30

## CONCLUSION

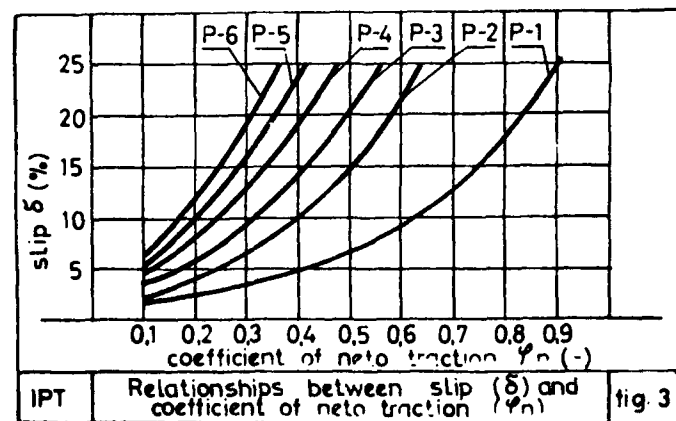
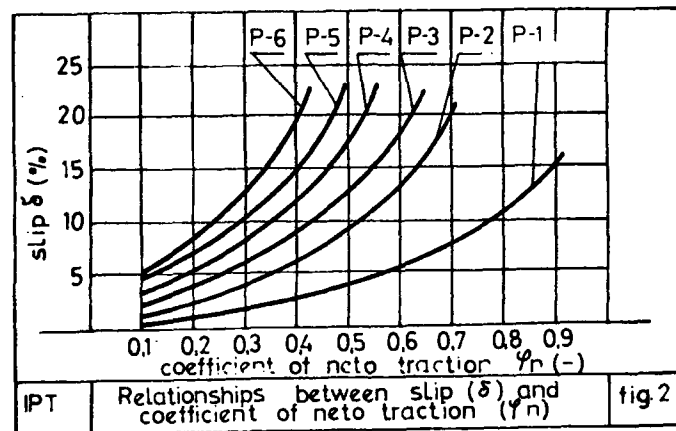
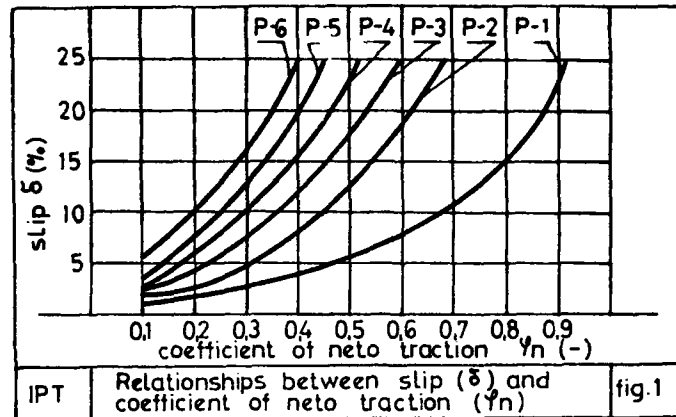
On the basis of performed researches the following conclusion can be made:

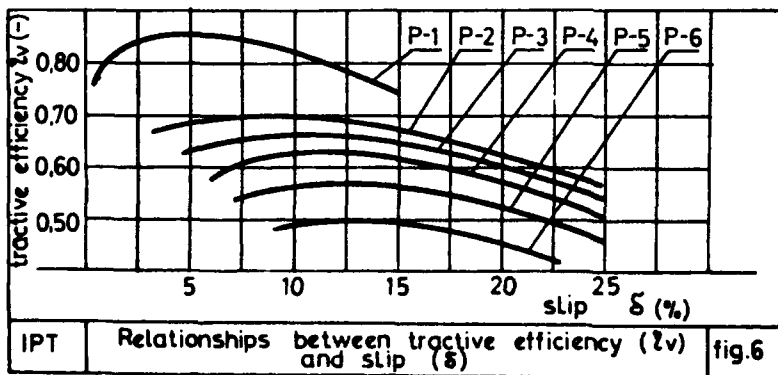
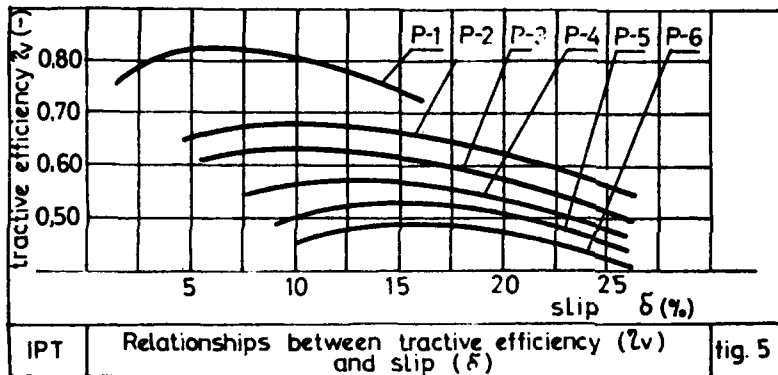
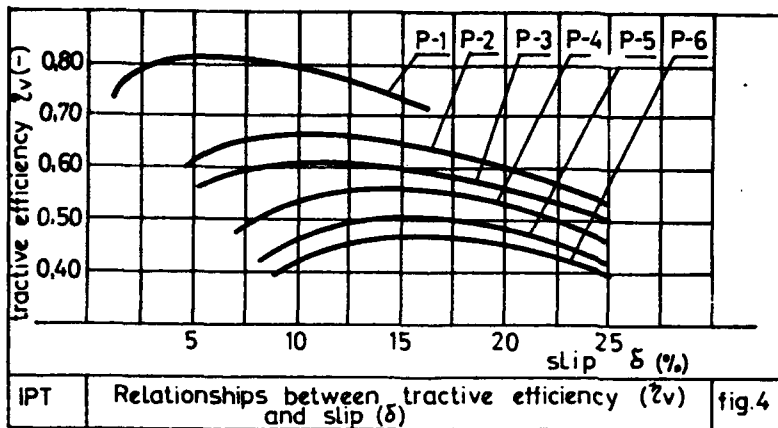
- Values of coefficients  $\eta_v$ ,  $\varphi_n$ ,  $\delta$  change depending on the type of substrate and tractor conception
- More favourable coefficient values are obtained on hard substrates with tractor (4x4)Z, then with (4x4)S and the least favourable with (4x2)S
- Optimal coefficient values for standard substrate - stubblefield - P3 are:  
(4x2)S - 0,600: 0,380 and 13,13 %: (4x4)S - 0,635: 0,415 and 12,04 %: (4x4)Z - 0,670: 0,450 and 10,45 %.
- Maximal values of coefficient of net traction on the identical substrate are: (4x4)S - 0,600: (4x4)S - 0,670 and (4x4)Z - 0,730.

## LITERATURE

1. Bekker G.M.: Theory of land Locomotion, The University of Michigan Press, Ann Arbor 1962.
2. Bekker G.M.: Off-the Road Locomotion, The University Michigan Press, Ann Arbor 1962.
3. Dwyer J.M.: Pearson G.A.: Field Comparison of the Tractive Performance of Two-and Four-Wheel Drive Tractors, The University of Agriculture, Engang Res. (1976), 21,77-85
4. Dwyer J.M.: Prediction of Drawbar Test Performance, Yournal of Terramechanics, vol. 24. No.2, pp.169-177, 1987.
5. Čudakov A.D.: The basis of Theory and Calculations for tractors and Cars, Moscow-Kolos 1972.
6. Frank M.Z.: Predicting Tractor Field Performance Transactions of the ASAE, 1972.
7. Grečenko A.: Kolove a pasove traktory, Prag, 1963.
8. Guskov V.V.: Tractors, Theory II part, Minsk, 1977.
9. Kolobov T.G. and Parfenov P.A.: Drawbar Characteristics of Tractors, Moscow, 1972.
10. Križnar M.: Researches on some Exploitational Parameters of Agricultural Tractors, Dissertation, Zagreb, 1974.
11. Nikolić R.: Optimalization of agricultural Tractors' Parameters for Determining of Rational structure of Motor Pool, Dissertation, Novi Sad, 1983.
12. Obradović D.: Researches on Optimal Parameters of Tractor - Machinery Aggregates for Agricultural Complexes, Dissertation, Belgrad, 1979.

13. Osborne E.L.: A Field Comparison of the Performance of Two-and Four-Wheel Drive and Tracklaying Tractors, University of Agriculture, Engage Res. (1971), 16(1), 46-61.
14. Piria I.: The Impact of Vertical Pull of Carried Tools on the Useful Efficiency Coefficient of traction device of Tractor with Tyred Wheels, Dissertation, Zagreb, 1973.
15. Parfenov P.A.: Razvitie sistemi klassifikacii sel'skohozaistvennih traktorov, Traktori i sel'hozmašini, 10/85.
16. Polak A. and Šupok A.: Exploitation of tractor systems on higher speeds, Moscow, 1974.
17. Sitkei G.: Allgemeine Zusammenhänge zwischen der Leistung, dem Gewicht und den optimalen Getriebsparametern von Schieppern, Grundlagen der Landtechnik, 5/78.
18. Sohne W.: Entwicklungstendenzen und-möglichkeiten bei Allradsschleppern, Landtechnik, 5/80.
19. Surin V.V.: Metodi opredelenii normoobrazuših pokazatelei mašini, Tehnika v s/h, 1/79.





# ANALYTICAL MODELLING OF THE PERFORMANCE OF A SNOW DEPOSIT UNDER COMPRESSION LOADING

R.N. YONG<sup>1</sup>, A.M.O. MOHAMED<sup>2</sup>, AND A.J. MURCIA<sup>3</sup>

## ABSTRACT

An analytical technique for predicting the response of a deep snow under a compression load as might be expected from a stationary vehicle is developed. The model is based on the finite element technique suitably adapted to take into consideration the high compressibility of the material and the progressive shear failure mechanism developed during the loading penetration process. The solution obtained using this model provides the load-sinkage relationship.

The validity of the proposed model is verified through a comparison of predicted and experimentally obtained results. Most results obtained from the finite element model are found to be in reasonably good agreement with the experimental data while some discrepancies are found to exist between specific types of results.

## 1. INTRODUCTION

Properties of the snow-cover such as strength, stiffness and density are of particular interest to transportation engineers concerned with travel over snow. Transportation of supplies and goods to remote communities, mines, construction sites, etc., is heavily dependent on the efficiency of over-snow vehicles. Proper design of such vehicles requires not only a sound mechanical engineering basis but adequate understanding of the response of snow under loading. Since engineering design essentially and inevitably involves a mathematical idealization of thermal problem at hand, the problem of analytically describing the behavior of snow under loading arises.

Various subjects on snow mechanics have been studied over the years in order to develop a methodology to analyze and predict the test ability of a snow mass and its response when subjected to external loading. Respective examples are avalanche prediction, which has been studied by Perla and Marinelli (1976) and Fraser (1978), and over-snow travel problems for which Harrison (1975), Yong (1979) and Brown (1979) have proposed approaches and solution techniques. Strength analyses of snow are difficult because of the nature of the material at hand but a theoretical evaluation has been proposed by Ballard and McGraw (1965).

<sup>1</sup>William Scott Professor, Civil Engineering Department, Director, Geotechnical Research Centre, McGill University, Canada

<sup>2</sup>Research Associate, Geotechnical Research Centre, Adjunct Professor, Civil Engineering Department, McGill University, Montreal, Canada, H3A 2K6

<sup>3</sup>Consultant Engineer, 559 Calle Aragon, Atico 1a, Barcelona, Spain

The purpose of this study is to develop an analytical technique for predicting the responses of a deep snow layer under a compression load-as might be expected from a stationary vehicle. This is considered to be of prime importance since vehicle flotation must be achieved if over-snow mobility is to be obtained. The study is limited in scope to the verification of the validity of the application of an analytical/computer model to simulate the process of load penetration into a deposit of deep snow.

The model is based on the finite element technique suitably adapted to take into consideration the high compressibility of the material and the progressive shear failure mechanism developed during the loading penetration process. The solution obtained using this model provides displacement fields and density distribution beneath the footing, the depth of shear along failure planes as well as the load-sinkage relationship.

## 2. MODELLING

### 2.1 Formulation of the Problem

The simultaneous shear and volume change mechanisms that occur during plate penetration, as experimentally demonstrated by Yong and Metaxas (1985), are schematically illustrated in Fig. 1 showing the shear and compression actions undergone by elements A and B, respectively. The stresses associated with these actions are controlled by the stiffness and strength of the snow material which are a function of snow density. The success of the solution procedure thus relies on the ability to determine the density distribution beneath the plate, from which stiffness and strength values can be correctly assigned to any given point within and along the sides of the pressure bulb as a function of plate penetration. The knowledge of the resulting system stiffness at a given plate sinkage then permits the calculation of incremental reaction forces on the plate from which a load-penetration curve can be constructed.

The problem thus involves the determination of the load-deflection relationship of a non-linear system in which the total stiffness  $K$  is a function of deflection and deflection rate. The mechanics of the system suggest that the reaction force on the plate at a penetration is composed basically of two parts (Fig. 2a): (a) a force  $P_v$  due to the volume change resistance of the snow within the pressure bulb, and (b) a force  $P_s$  resulting from the resistance of the snow to shear along the failure planes.

The nature of the problem thus implies that, in fact, these forces are also a function of the plate penetration  $z$ , as a result of the variation of properties of the material (i.e., stiffening effect due to snow densification and softening effect due to local shear failures along the planes of cutting shear) as plate penetration progresses. In addition, the penetration speed of the plate  $u$  constitutes another parameter to consider since, for a viscous material such as snow, the velocity field generated has a direct effect on material properties and hence, on the reaction force. The total system stiffness can thus be expressed in terms of the volume change and shear components as follows:

$$P(z, u) = P_v(z, u) + P_s(z, u) \quad (1)$$

where:  $P(z, u)$  = total reaction force on the plate as a function of plate penetrations and plate penetration rate  $u$ ;  $P_v(z, u)$  = reaction force on the plate due to volume change resistance of snow, and  $P_s(z, u)$  = reaction force on the plate due to shear resistance of snow.

Differentiating the above expression with respect to plate penetrations and rewriting it in differential form:

$$dP(z, u) = \frac{\partial P_v(z, u)}{\partial z} dz + \frac{\partial P_s(z, u)}{\partial z} dz \quad (2)$$



$$dP(z, u) = (K_v(z, u) + K_s(z, u))dz \quad (3)$$

where:  $K_v(z, u)$  = tangent volumetric stiffness function (Fig. 2b), and  $K_s(z, u)$  = tangent shear stiffness function (Fig. 2b).

Equation (3) is the basic relationship that mathematically represents the process of a rigid plate penetrating into a snow mass at a constant rate.

## 2.2 Solution

The solution of the problem thus requires knowledge of the volumetric and shear stiffness functions  $K_v(z, u)$  and  $K_s(z, u)$  both of which are essentially dependent on the plate penetration  $z$  and the penetration rate  $u$ . The load-penetration relationship can then be determined by integration of equation (3):

$$P(z, u) = \int_0^z (K_v(z, u) + K_s(z, u))dz \quad (4)$$

The following two sections discuss the above functions in more detail.

### 2.2.1 Volumetric Stiffness Function $K_v(z, u)$

Consider an infinitesimal element of snow, of type "B" in Fig. 1, within the pressure bulb, after a plate penetration  $Z_p$  and having a volume  $dV$  in which the density is  $\gamma$  and the instantaneous strain rate is  $\dot{\epsilon}$  (Fig. 3). Also let the compressive modulus, defined herein as the ratio of stress to strain under pure axial deformation conditions, be  $E_c(\gamma, u)$  for the density  $\gamma$  and the strain rate  $u$ . Upon an additional increment of plate displacement  $\Delta Z_p$ , both axial and shearing strains  $\epsilon_x, \epsilon_z, \epsilon_{xz}$  develop, the latter due to the distortion effect of shearing stresses generated along the planes of cutting shear. The strains are then related to stresses through the compressive modulus and the Poisson's ratio of the material. The work done in deforming the given snow element is then:

$$dW = (\sigma_x \epsilon_x + \sigma_z \epsilon_z + \sigma_{xz} \epsilon_{xz})dV \quad (5)$$

Integration of the above expression over the entire pressure bulb yields the total energy spent in compressing and distorting the snow for the given plate incremental displacement. Due to the particular boundary conditions of the present problem and the low Poisson's ratio of the material, the energy involved in the distortion of the snow mass within the pressure bulb is small relative to the volume change energy. It can therefore safely be stated that evaluation of the integral of equation (5) over the volume of the pressure bulb is basically equal to the volume change energy component due to an increment of plate penetration  $Z$ :

$$\Delta E_v = \text{volume change energy} = \int_0^D \int_0^{PW} \int_0^{PL} (\sigma_x \epsilon_x + \sigma_z \epsilon_z + \sigma_{xz} \epsilon_{xz}) dx dy dz \quad (6)$$

Assuming plane strain conditions and realizing that the pressure bulb depth is, in general, a function of plate penetration  $Z_p$ :

$$\Delta E_v = PW \int_0^{D(Z_p)} \int_0^{PL} (\sigma_x \epsilon_x + \sigma_z \epsilon_z + \sigma_{xz} \epsilon_{xz}) dx dz \quad (7)$$

The above quantity is equal to the work done by the incremental force  $P_v$ . Therefore;

$$\Delta E_v = \Delta P_v \Delta Z_p \quad (8)$$

From which the volume change stiffness function evaluated at a plate penetration  $Z_p$  can be obtained:

$$K_v(Z_p, u) = \frac{\Delta P_v}{\Delta Z_p} = \frac{\Delta E_v}{(\Delta Z_p)^2} \quad (9)$$

Substituting for  $E_v$  (eq. 7) in equation (9), the volumetric stiffness function is thus:

$$K_v(z, u) = \frac{PW}{(\Delta Z_p)^2} \int_0^{D(Z_p)} \int_0^{PL} (\sigma_z \epsilon_z + \sigma_z \epsilon_z + \sigma_{zz} \epsilon_{zz}) dx dz \quad (10)$$

The key in the determination of the function  $K_v(Z_p, u)$  thus lies in defining the following functional relationships:

- (1) Distribution of incremental stresses and strains, density, strain rate and pressure bulb depth as a function of plate penetration  $Z_p$ .
- (2) Compressive modulus of snow as a function of density and plate penetration rate.

### 2.2.2 Shear Stiffness Function $K_s(z, u)$

The shear stiffness function  $K_s(z, u)$  is determined by the following analysis. Consider a shear element of surface area  $dA$ , as shown in Fig. 3 in which the snow density and instantaneous strain rate at its centre are  $\gamma$  and  $\dot{\epsilon}$ , respectively, when the total penetration of the plate is  $Z_p$ . If the plate is further displaced downwards by an amount  $\Delta Z_p$ , a shear strain develops, whose value is related to a corresponding shear stress  $\tau$  through the stiffness of the material in shear, which, in general, is a function of density  $\gamma$ , strain  $\epsilon$  and strain rate  $\dot{\epsilon}$

$$K_s = G(\gamma, u) \quad (11)$$

The total shear force developed in the process is:

$$dP_s = \tau dA = \tau dy dz \quad (12)$$

The total area of shearing consists of the two vertical planes of cutting shear passing through the edges of the penetrating plate. Therefore, integrating of the above equation over this area yields the shear force due to an incremental plate displacement  $\Delta Z_p$ :

$$\Delta P_s = 2 \int_0^D \int_0^{PW} \tau dy dz \quad (13)$$

For plane strain conditions and setting the stress bulb depth  $D$  to be a function of the plate penetration  $Z_p$ :

$$\Delta P_s = 2PW \int_0^{D(Z_p)} \tau dz \quad (14)$$

The shear stiffness function evaluated at a plate penetration  $Z_p$  is then

$$K_s(Z_p, u) = \Delta P_s / \Delta Z_p = \frac{2PW}{\Delta Z_p} \int_0^{D(Z_p)} \tau dz \quad (15)$$

Again, as for the volume change stiffness function, the determination of the shear stiffness function thus requires investigation of two types of functions:

- (1) Distribution of shear stresses along the planes of cutting shear as a function of plate penetration  $Z_p$ .
- (2) Parameters describing the shear stress-strain behavior as a function of density  $\gamma$ , strain  $\epsilon$  and strain rate  $\dot{\epsilon}$ .

### 3. MATERIAL PARAMETERS

The components of the proposed model require the following characteristics of the snow material:

- 1) compressibility as a function of density (axial stress-strain relationship for fully confined conditions),
- 2) shear stress-strain response as a function of density.

In view of the above, the experimental program carried out during the course of this study was designed to provide required material input parameters as well as for verification purposes of the proposed model. Consequently, the experimental program consisted of three types of test:

- 1) plate penetration tests performed on snow of two different ages (i.e., different bonding strengths) at a given deformation rate. Results from these tests could then be compared to corresponding predicted values.
- 2) confined compression tests performed on the same types of snow at the same deformation rate as for plate penetration tests.
- 3) vane shear tests performed on the same types of snow and at approximately the same deformation rate as for plate penetration and confined compression tests. These tests were carried out for snow of different density so that results could then be used to represent the snow behavior in shear for the range of densities considered.

Typical results from the three types of tests are shown and discussed in the following sections.

#### 3.1 Confined Compression Response and Results

In a confined compression test, the material undergoes an axial deformation while lateral displacements are prevented. For a material with a relatively high Poisson's ratio, a lateral pressure develops and therefore the confining stress on the sample increases due to the restriction of lateral movement by the rigid wall of the plexiglas container. When a material with a low Poisson's ratio, such as the snow types used in the present study, is tested, lateral deformations are minimal and thus lateral pressure is small in relation to the axial pressure. It can therefore be deduced that for such a material, the effect of confining pressure is insignificant.

Stress-strain relationships under confined compression conditions were obtained from test results simply by dividing the recorded load and piston displacement values by the cross-sectional area and original height of the sample, respectively. An example of a typical curve is illustrated in Fig. 4, showing a generally increasing slope, i.e., characteristic of a stiffening material, and the presence of microfractures also referred to as the "saw-tooth" effect and previously reported by Yong and Fukue (1977). The amplitude of the stress releases observed during tests were seen to be small with respect to the stress values themselves so that, consequently, the "saw-tooth effect due to microfracturing is ignored

as a parameter describing the stress-strain response. An average curve was thus fitted through the center of the recorded peaks and troughs, as shown in Fig. 4a. The resulting stress-strain relationships obtained for the two snow types (i.e., age 4 and 30 days) are shown in Fig. 4b. Ageing of snow increases the degree of bonding and, as expected, the stress corresponding to a particular value of strain increases with the number of ageing days, thus demonstrated in the higher resistance of older snow.

### 3.2 Response in Shear and Results

In a vane shear test, it is assumed that the snow is tested at essentially constant density. The fact that the failure plane is predetermined is consistent with the idealized version of the real situation of plate penetration in which the location of the shear plane is known (i.e., vertical planes through the edges of the plate).

Results from vane shear tests essentially consisted of shear strength-density relationships, corresponding to the given deformation rate, for the two types of snow used. Shear strength of snow was computed from the vane reading and a calibration factor. Results, illustrating the effect of age, are graphically displayed on Fig. 5. A general pattern is observed according to which, as expected, shear strength of snow increases with density as well as with the number of ageing days. During the vane shear tests performed during the study, it was not possible to measure the shear resistance as a function of vane rotation since the recorded vane reading corresponded to the maximum shear stress developed (i.e., the shear strength). This, however, did not cause many problems in the formulation of the present model as the post-peak behavior in shear was actually idealized in this study. Since the proposed model does require a stiffness parameter of snow in shear, which can only be obtained from a shear stress-deformation curve, such a number was thus assumed and considered as an additional parameter in the present study.

### 3.3 Plate Penetration Response and Results

The load penetration curves for ages 4 and 30 days are shown in Figs. 6a and 6b. the "saw tooth" effect, observed in confined compression tests, is also exhibited due to elements of snow within the stress bulb beneath the plate being subjected to a loading condition similar to that of confined compression as a result of the low Poisson's ratio of the material. As the plate penetrates deeper into the snow, more and more of these elements are involved in the volume change process, i.e. the stress bulb extends deeper as penetration progresses. This reasoning seems to be supported by the fact that the amplitudes of stress releases increases with plate sinkage, due to a greater amount of snow material undergoing the bond breaking mechanism. As the plate sinks into the snow, the shear strength of snow at any point along the planes of cutting shear could be exceeded depending on the density of the snow and cumulative shear stress at that point. It is therefore obvious that maximum stress bulb support in terms of side shear action occurs at the beginning of the plate penetration process and decreases as more snow material is stressed beyond its shear strength. Since the stiffness in shear of snow elements located along the planes of cutting shear is reduced to a negligible value after shear failure occurs, it thus becomes evident that the total stiffness of the system in shear decreases with increasing plate penetration.

On the other hand, the volume change mechanism occurs simultaneously during which the density of snow within the stress bulb generally increases. As a result, and referring back to the stiffening behaviour of snow under compression loading, the resistance of the system to volume change increases (i.e., compressibility decreases). The shape of a given plate penetration curve therefore depends on two mechanisms with opposite effects, i.e., softening effect in shear and stiffening effect in volume change. A relatively linear plate load-penetration curve reflects the situation in which both volume change and shear mechanisms participate equally in the vertical support of the pressure bulb and thus tend

to counteract onto another. The validity of the above statements is demonstrated by the results of the plate penetration tests. The load-penetration curves from a test performed on 4 day old snow (Fig. 6a) show that the response is essentially linear whereas results from the tests performed on older snow, aged 30 days, shows a strain softening behavior (Fig. 6b). The curves fitted through the experimental plots in Figs. 6a and 6b serve as reference for comparative purposes with analytical predictions.

## 4. PREDICTION AND COMPARISON

### 4.1 Load-Penetration Curves

The plate penetration curves are expressed in terms of stress on the plate as a function of penetration. Plate stress is obtained by dividing the reaction load by the area of the plate. The stress-penetration relationships for 4 day old snow obtained from the plate test and predicted by the finite element model are depicted on the plot in Fig. 7a for comparison purposes. The experimental curve shown in the same figure is the same as that fitted through the experimental graph (Fig. 6a) which passed approximately half-way between the mean of the band of the test curve and the lower boundary of the same curve. The reason for the selection of such a reference curve is due to the fact that the finite element model predicts the plate load after stress releases caused by failing shear elements. In the actual case, the stress vibrations observed are produced by both the microfracturing of snow while compressed and the stress release effect mentioned above. It is therefore difficult to affirm that the lowest boundary of the plate penetration curve represents the behaviour after shear element stress releases since the microfracturing effect is also incorporated into the response with the result that it is impossible to separate the two components. Similarly, the means of the same curve does not necessarily represent the response that can be compared to the finite element prediction because of the stress release effect although the latter is not suspected to cause large drops in plate stress. Therefore, due to the above arguments, a curve in the middle of the mean of the band and the lower boundary was selected as the reference experimental curve.

In the predicted response, the effect of shear stiffness is included. For the values of  $K_s$  considered, the agreement between experimental and finite element results is reasonable (Fig. 7a). The shape of both experimental and predicted curves is similar in that the relationships are characterized by a bi-linear type of behaviour such that the response is essentially linear, starting at a given slope, and then followed by a decrease in slope. It should also be noted that the predicted stress-penetration responses is somewhat sensitive to the value of shear stiffness  $K_s$ , and thus, that different values of  $K_s$  generate different curves. In the set of curves shown in Fig. 7a, the relationships pertaining to  $K_s = 4500$  and  $K_s = 6000$  seem to give the best results or closest agreement with the experimental curve. The curve corresponding to  $K_s = 3000$  overestimates the response whereas that for  $K_s = 15000$  tends to underestimate it. In general, the plot on Fig. 7a implies that an increase in  $K_s$  lowers the predicted curve whereas a decrease in  $K_s$  tends to raise it.

The reaction of the curve to a change in shear stiffness can be explained as follows; a low value of  $K_s$  implies a "ductile" behavior of snow in shear so that elements of the material along the failure planes, and thus acting principally in shear, tolerate relatively large displacements before mobilizing the full shear strength. In such a case, if the value of  $K_s$  is too low in the model, the total shear stiffness of the system (i.e., the stiffness contributed by the shear elements along the planes of shear) changes too slowly, as compared to the real situation, since few elements have failed for a given plate penetration. Conversely, a high value of shear stiffness results in a "brittle" behaviour in shear such that failure occurs at a small shear deformation. A high value of  $K_s$  in the model causes a rapid progressive failure of shear elements resulting in a low value of the shear stiffness of the system starting at a small value of plate penetration and thus applying for most of

the penetration process.

The corresponding plate stress-penetration curves for 30 day old snow are shown in Fig. 7b. The agreement between experimental and predicted curves is not as good as for the 4 day old snow especially for the higher values of  $K_s = 4500$  yields relatively good results. Again, the predicted curves are bi-linear, but to a lesser degree than those for 4 day old snow. The analytical model is consistent in that its sensitivity parameters is similar to that for 4 day old snow; an increase in  $K_s$  results in a lower plate stress-penetration response and vice versa. It is also interesting to note that, as for 4 day old, predictions are quite good when the shear stiffness parameter  $K_s$  is 4500.

## 5. CONCLUSIONS

On the basis of the tests performed and the results of the developed predicting analytical model, the following conclusions may be drawn:

1. the compressive modulus of snow, as shown in by confined compression tests, increased with density. A stiffening type of curve was obtained for all tests on both types of snow used. As expected, the response for 30 day old snow was stiffer due to the higher degree of sintering.
2. the shear strength of snow increased with age, due to the greater strength of bonds between particles, and with density, as demonstrated by results of vane shear tests.
3. the experimental plate stress-penetration curves were essentially bi-linear with a change of slope occurring relatively early in the penetration process. Significant stress vibration due to microfracturing was observed.
4. a method to model a highly compressible non-linear material which failed according to a punching shear type of mechanism was developed. The model includes the effect of non-linearity and strain hardening behaviour in compression as well as the effect of shear stresses generated along the vertical sides of the pressure bulb. The maximum shear stress tolerated by a shear element was limited by its shear strength which in turn depended on density. Provision were made to simulate this effect so that the model includes an algorithm by which excess shear stress in failing joint elements are redistributed within the snow mass. In so doing, the shear stress in any shear element never exceeds the value corresponding to shear strength.
5. the plate resistance-penetration curves as predicted by the analytical model compared rather well with the experimentally obtained ones. The predicted response was somewhat sensitive to the single value of shear stiffness employed in the model but a value of 4500 for this parameter gave satisfactory results for both types of snow used. As expected, the predicted value for 30 day old snow is higher than that for 4 day old snow.

The good agreement between predicted and experimental plate stress-penetration curves demonstrates the ability of the proposed model to simulate the plate penetration mechanism.

## ACKNOWLEDGMENTS

The work performed in this study was in partial fulfillment of the study requirements for Defence Research Establishment Suffield (DRES) under contract arrangement with Department of Supply and Services (DSS), Canada.

## REFERENCES

Ballard, G.E.H., and McGraw, R.W., (1965) "A theory of snow failure" U.S. Cold Regions Research and Engineering Laboratory. Research Report 137.

Brown, R.L. (1979) "Applications of Energetics to Vehicle Trafficability Problems" Proceedings of International Society of Terrain Vehicle Systems Workshop on Snow Traction Mechanics, Alta, Utah, 1979.

Fraser, C. (1978) "Avalanches and Snow Safety" Scribner and Sons, New-York, N.Y.

Harrison, W.L. (1975) "Vehicle Performance over Snow: Mathematical Model Validation Study" CRREL, Technical Report 268.

Perla, R.L., and M. Martinelli Jr. (1976) "Avalanche Handbook" Agricu. Handbook. No. 489, U.S. Govt. Printing Office, Washington, D.C.

Yong, R.N. and Fukue, M. (1977) "Performance of Snow in Confined Compression" Journal of Terramechanics, Vol. 14, No. 2, pp. 59 - 82.

Yong, R.N. and Metaxas, I. (1985) "Influence of Age Hardening and Strain Rate on Confined Compression and Shear Behaviour of Snow" J. Terramechanics, Vol., 2, No. 1, pp. 37-49.

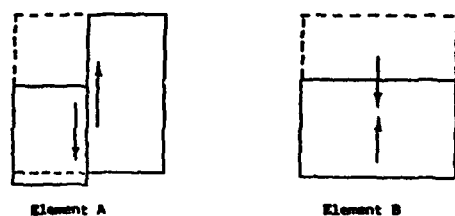
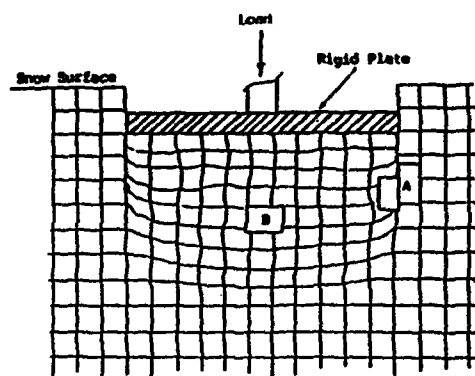


Fig. 1 Volume Change and Cutting Shear Mechanisms Under Plate Loading Condition

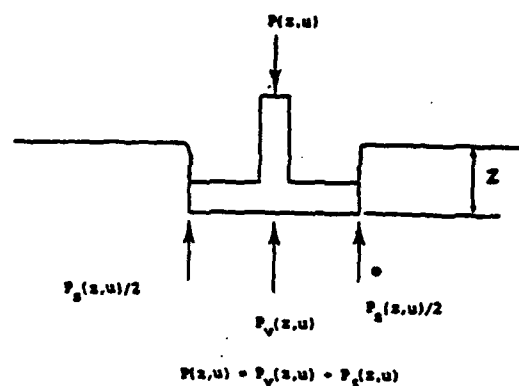


Fig. 2a forces on Plate Due to Volume Change and Cutting Shear Mechanisms

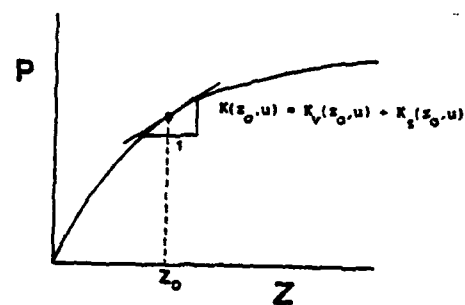


Fig. 2b Schematic Representation of Stiffness Function

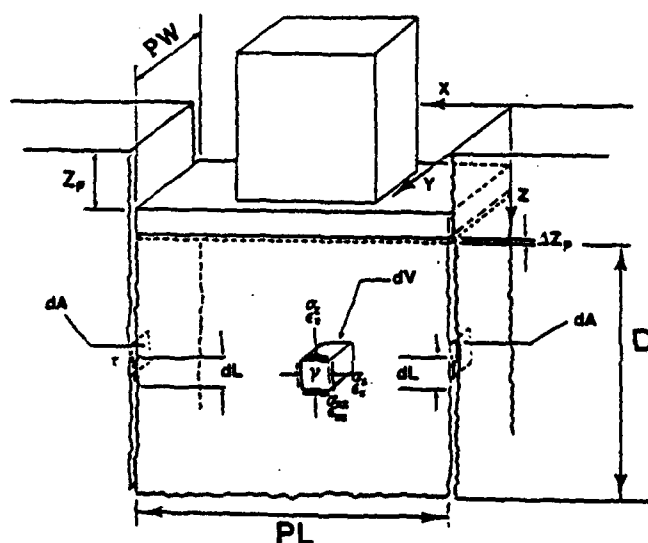


Fig. 3 Stresses Induced in Snow Mass Due to Incremental Plate Displacement



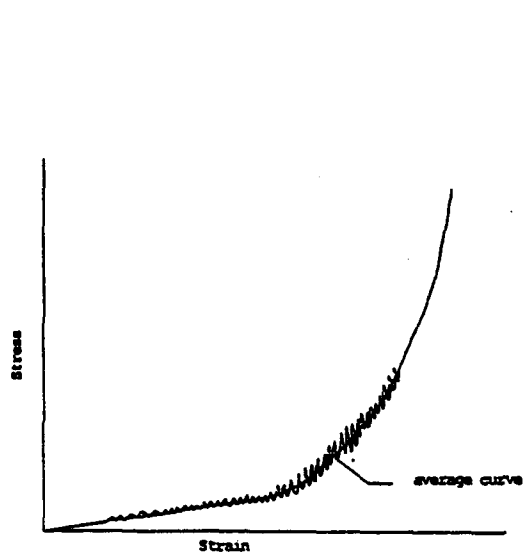


Fig. 4a Typical Curve From a Confined Compression Test

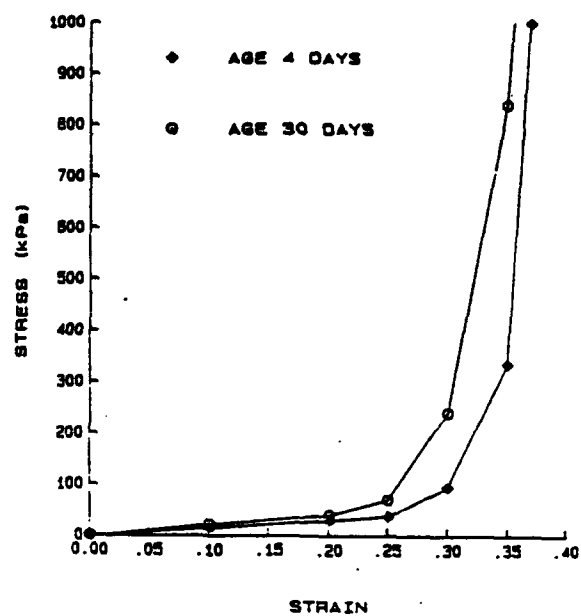


Fig. 4b Confined Compression Test Results

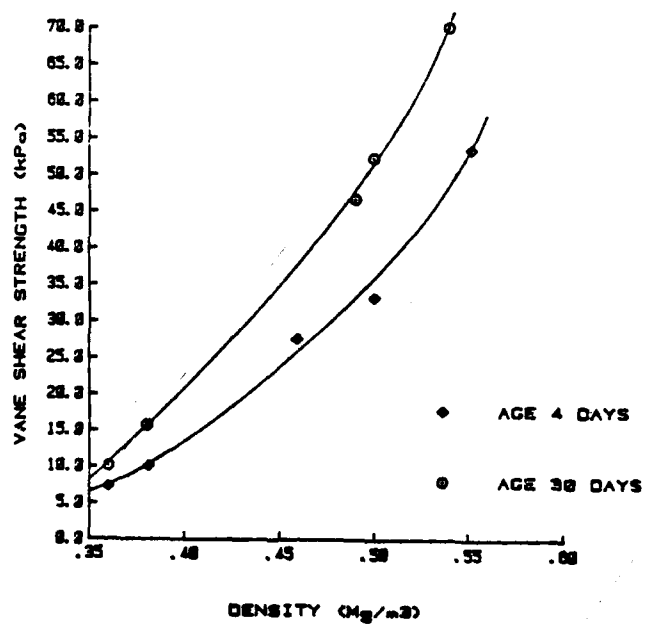


Fig. 5 Vane Shear Strength Results

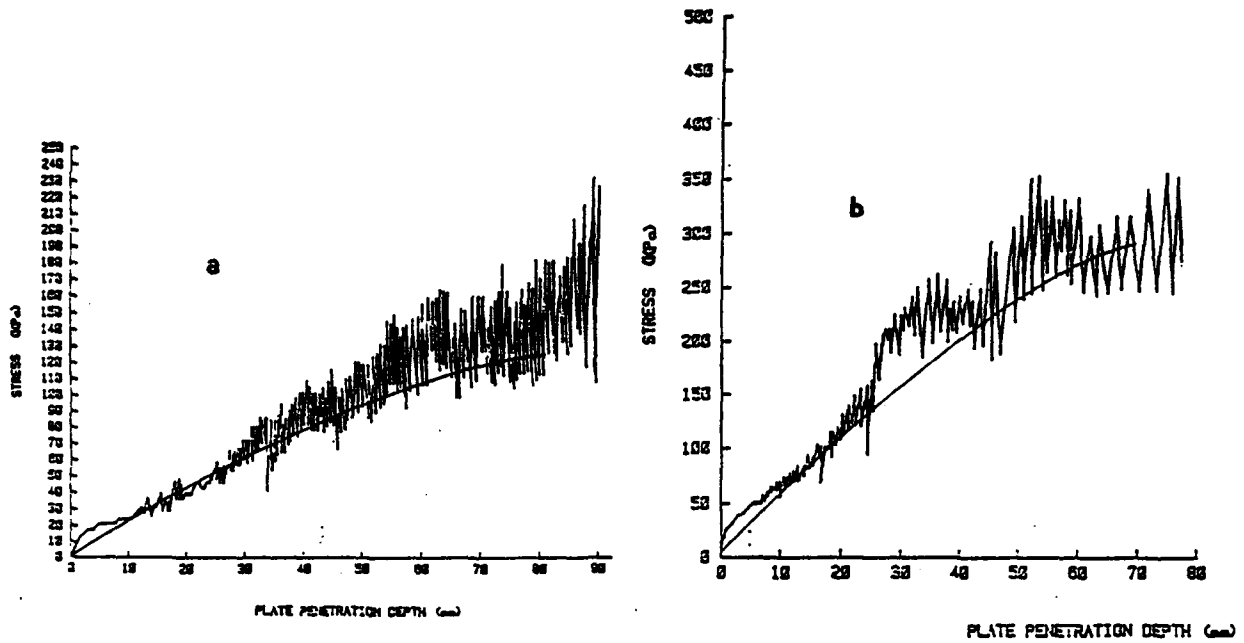


Fig. 6 Plate Penetration Test Results with Different Ageing (a) 4 days; (b) 30 days

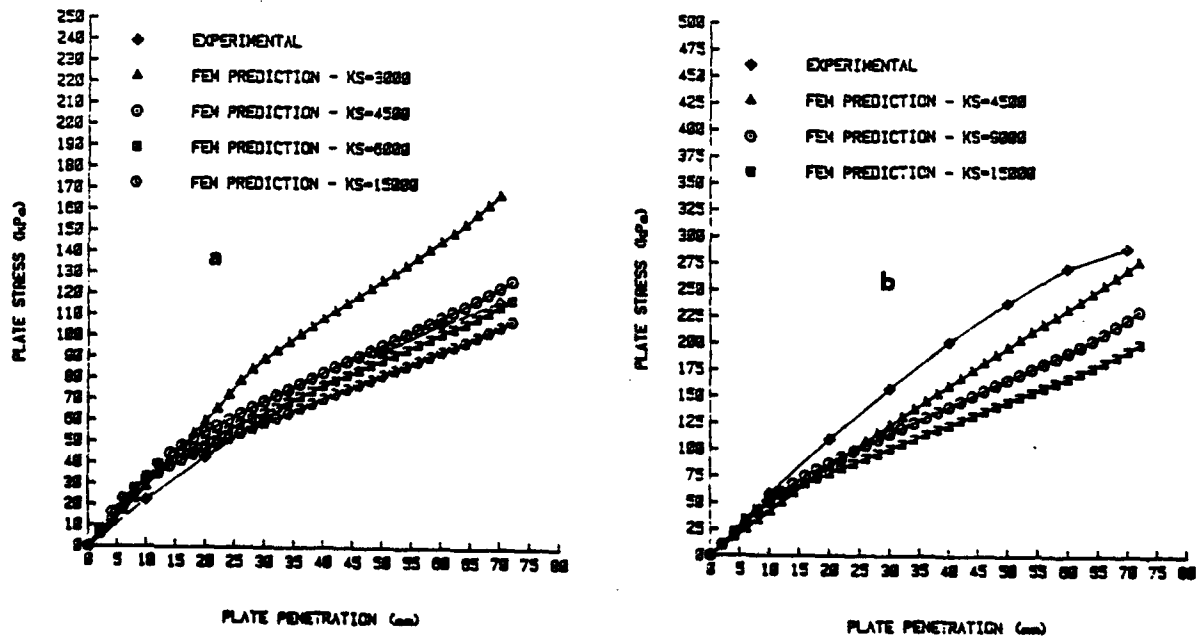


Fig. 7 Experimentally Obtained and Predicted Plate Penetration Curves with Different Ageing. (a) 4 days, (b) 30 days

# ONE SIMPLE LABORATORY METHOD FOR RELATIVE ESTIMATIONS OF TRACTOR TYRES PERFORMANCES

Dr Dj.M.Ronai, Institute for mechanization, Novi Sad, YU  
Mr V.Muzikravic, Institute for mechanization, Novi Sad, YU

## Summary

A definition of agricultural tractor tyre's performances is often bound by very expensive laboratory equipment or time lasting field experiments. At the same time, there are requirements for fast and inexpensive experiments which could be able to give reasonable answers about choices between two or more of types of tyres with similar traction characteristics.

In order to find a way to answer the mentioned requirement, a simplified method for tractor tyres traction performance estimation has been developed at the Institute for mechanization in Novi Sad, and applied to the pneumatic industry.

According to the applied method, based on Bekker's theory, the necessary measuring devices have been developed, and adequate measuring and computing system has been adapted.

The presented paper includes the description of the method and developed measuring equipment, and discussion of some of the obtained results, which, as mentioned, have been accepted by Yugoslav tyre industry.

## THEORETICAL APPROACH

The main theoretical source for present investigation has been known as Bekker's theory for motion of elastic tyre under the soft soil conditions or more precisely, the fact that the differences in traction potentials between the two of the observed tyres could lie in the differences in their motion resistance. This statement is even more correct if the observed tyres are of similar dimensions and protector characteristics.

Starting from the known equation for net traction (P) as the difference between gross traction (H) and motion resistance force (R),

$$P = H - R \quad \dots\dots\dots(1)$$

and assuming that gross traction (which depends on torque and rolling radius) is close to equal for observed tyres, the possible conclusion could be that net traction and draw bar pull depend only on the value of the tyre motion resistance.

The lowest level of motion resistance is in the case of elastic tyre running over the deformable soil, which is usual exploitation conditions in agricultural production. According to the Bekker's theory, the motion resistance (R) for mentioned case (if bulldozing and dragging resistance are small) is equal to:

$$R = R_c + R_f \quad \dots\dots\dots(2)$$

where (R<sub>c</sub>) is motion resistance caused by soil compaction, and (R<sub>f</sub>) is tyre's deflection resistance.

Compaction resistance for elastic tyre and deformable soil is equal to 1/:

$$R_c = \frac{[b(p_i + p_c)]^{\frac{n+1}{n}}}{(n+1)(k_c + b k_\phi)} \quad \dots\dots\dots(3)$$

where (b) is the width of the contact area, (p<sub>i</sub>) tyre inflation pressure (p<sub>c</sub>) carcass stiffness and (k<sub>c</sub>, k<sub>φ</sub>, n) Bekker's soil parameters.

Assuming that tests could be run under the same soil conditions then compaction resistance depend on

$$R_c = f(b, p_i, p_c) \quad \dots\dots\dots(4)$$

In addition, parameters written in equation (4) become the subjects of testing and analyzing.

Deflection resistance (R<sub>f</sub>), mainly caused by hysteresis, according to the Bekker's theory could be defined as:

$$R_f = F_n \frac{u}{p_i^a} \quad \dots\dots\dots(4)$$

where (F<sub>n</sub>) is a vertical load, and (u, a) empirical equation parameters depending on tyre's stiffness. This part of the equation (1) could be measured and the relation for observed tyres found..

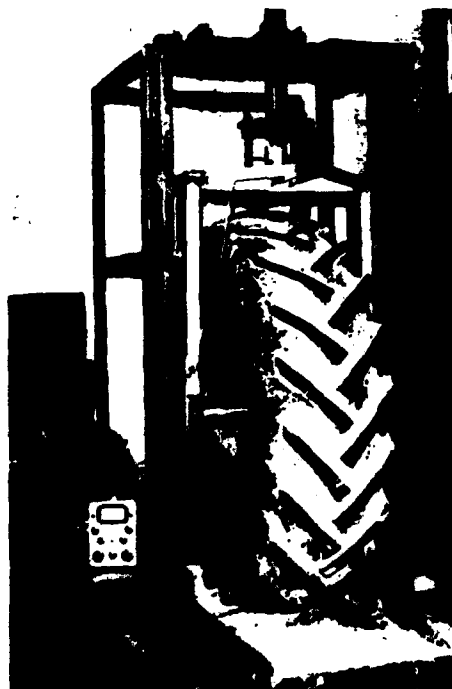
As a partial conclusion which could be derived from the previous discussion are the next:

- There are possibility for relative observation of traction performances of tractor tyres through analysis of their motion resistance.

- Analysis of tyre's motion resistances could be done through measuring of tyre's carcass stiffness, parameters of the contact area between tyre and soil, and tyre's deflection resistance for variations of dynamic load and inflation pressure;

## MEASURING EQUIPMENT

According to the well known methods for measuring parameters of the contact area on deformable soil and hard surface [2], specific testing device has been developed.



In Figure 1. picture of contact area parameters testing device is given. The device consists of the main frame and the inbuilt measuring frame which carries tested tyre.

In case when contact area on soft soil is observed, a small soil bin becomes a part of the measuring device. Mentioned soil bin is equipped with four wheels so, the dynamic tyre footprint could be taken by moving soil bin instead of rolling of the tested tyre.

Footprint parameters for hard surface which are necessary for carcass stiffness definition could be simply taken from the steel basement of the device without soil bin movement.

The measuring device is equipped with precise instruments for registering forces (strain gauge transducer), and displacements (inductive transducers).

Fig.1. Measuring device for the footprint parameters of the tested tyre

Also, the device given in Fig.1 has been used for defining the global stiffness parameters of tested tyres.

For deflection resistance investigations, also, special testing device is developed. The picture of mentioned device is given in Fig 2.

Testing device (Fig.2.) is an added part of a large soil bin equipment consisting of the main frame which carries tested tyres and the measuring frame connected to the power drive part of the soil bin.

During the test the towing force could be registered by the strain gauge transducer. Also the device is equipped by instruments for speed and overrun distance measuring.

Using the two of the described simple devices, all of necessary parameters could be taken for the analysis of total tyre's motion resistance.

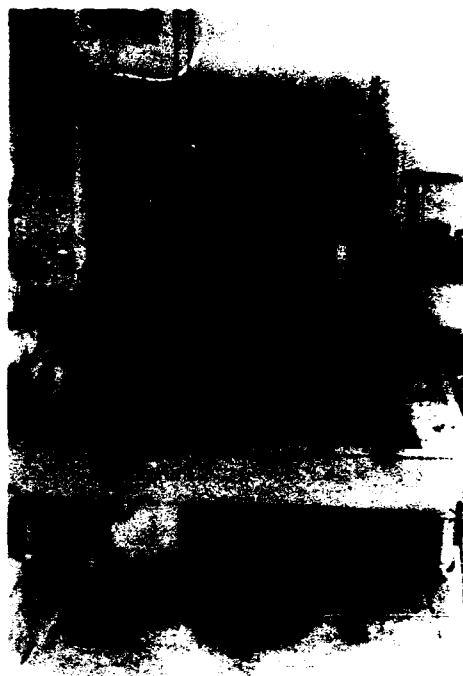


Fig.2. Testing device for deflection resistance definition

#### TYRE'S CONTACT AREA PARAMETERS ANALYSIS ON SOFT SOIL SURFACE

Tyre contact area parameters from 12.4-28 radial and bias ply tyres (different manufacturers) are taken according to the known method /2/ in sand. Tested tyre has been loaded, and after unloading the plaster of Paris was poured in the print until its depth exceeded the highest of the lugs by 1/cm/. The reason for using this method lies in the fact that the high lugs prevented the use of "hard surface and paint" technique.



Measuring of taken footprints was made by taking the photographs (slides) and projecting them for measuring purposes. During the tests inflation pressure was varied from 50 to 175/kPa/ and vertical load from 500 to 1500/daN/

An example a of taken footprint is given in Fig.3.

Relative footprint area data for two 12.4-24 bias ply tyres (I and II) are given in Table I.

Table I: Footprint area

p/kPa/	Footprint area /cm <sup>2</sup> /					
	500 daN		1000 daN		1500 daN	
	I	II	I	II	I	II
75	394	517	488	662	552	741
125	383	452	472	597	522	652
175	326	352	423	487	476	544

Fig.3. Photograph of tyre's footprint

From Table I is visible that footprint area for Tyre I is greater relative to Tyre II for all loads and inflation pressures. This leads to the conclusion that Tyre II could have better traction characteristics.

At the same time, footprint length of Tyre II is longer, which could be assumed as good, but wider footprint (3.6%) for this tyre could produce a little bit greater motion resistance.

#### ANALYSIS OF CARCASS STIFFNESS

Carcass stiffness is defined from a known relation [1] between the total ground pressure ( $p_g$ ) and inflation pressure ( $p_i$ ), i.e:

$$p_g = p_i + p_c = F/A \quad \dots\dots\dots(5)$$

where (A) is a footprint area on soft soil.

Knowing the footprint areas for different vertical loads and inflation pressures, carcass stiffness can be easily calculated.

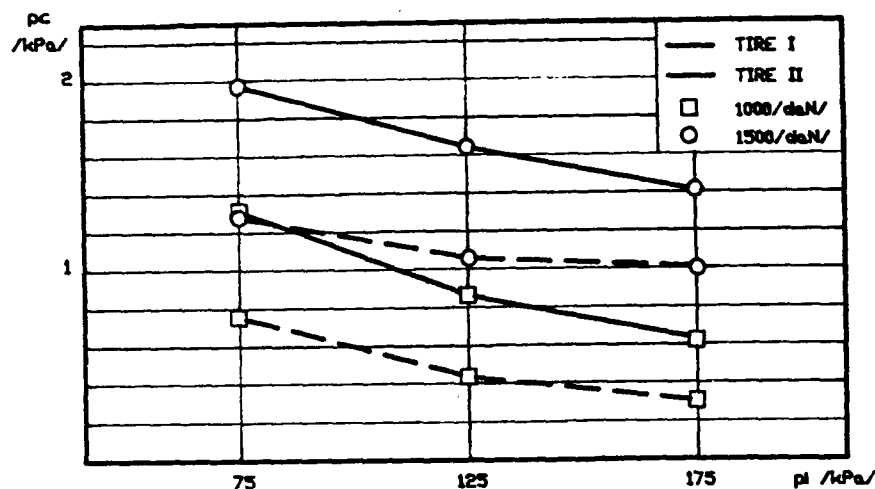


Fig.4. Lines for carcass stiffness for two tested tyres and variation of inflation pressure and vertical load

Calculated carcass stiffness for the two bias ply tractor tyres are given in Fig.4. relating to variations of the tyres inflation pressures of 1000 and 1500 /N/ vertical loads. It is clearly visible the from shown lines that carcass stiffness for Tyre I is much greater for both applied vertical loads over the range of inflation pressures, than for Tyre II.

In addition, the fact that values of carcass stiffness for Tyre I is greater relating to Tyre II leads to the conclusion that Tyre II has a lower level of motion resistance and a better potential traction characteristics.

At the same time, more intensive increase of carcass stiffness for Tyre I with increase of inflation pressure is visible from Fig 4. The same is also given in Table II.

Table II. Relative increase of carcass stiffness

	Tyre I		Tyre II	
	1000 /N/	1500 /N/	1000 /N/	1500 /N/
$p_{c_{125}} - p_{c_{75}}$ /kPa/	0.43	0.33	0.34	0.22
$p_{c_{125}} - p_c$ /kPa/	0.26	0.22	0.12	0.08

Concluded behavior of tyres carcass stiffness shows more intensive increase of footprint area of Tyre I with changes in inflation pressure caused by global tyre's side and radial stiffness behavior. Anyway this gives some advantages to Tyre II.

#### ANALYSIS OF DEFLECTION RESISTANCE

As it was mentioned before, measuring of tyre's deflection resistance has been done on a specially developed device enabled to register towing forces and overrun distances.

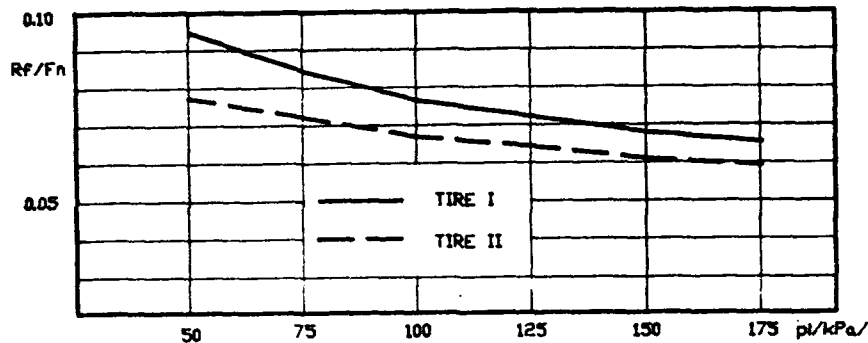


Fig.5. Specific deflection resistance as a function of inflation pressure for tested tyres

Graphical interpretation of measured and fitted data is given in Fig.5. Taken ( $R_f$ ) values for different tyre's inflation pressures are divided by vertical load ( $F_n$ ), giving specific deflection resistance values ( $f_f$ ). Values obtained on described way have been fitted by equation:

$$f_f = \frac{u}{p_i a} \quad \dots\dots\dots (6)$$

Rough analysis of shown lines in Fig.5. leads to the conclusion that Tyre I produces higher values of deflection resistance over the whole range of tested inflation pressures.

On the other hand, smaller total footprint area for Tyre I, leads to the conclusion that smaller deflection resistance for this tyre could be expected. It means that there could be some more reasons for the observed behavior of Tyre I. One possible explanation lies in protector rubber characteristics or total tyre's hysteresis characteristics which give more deflection resistance.

In addition, knowing that increase of deflection resistance, according to equation (2) leads directly to increase of total motion resistance of observed tyres, the conclusion of this analysis is positively clear: Tyre II has lower value of deflection resistance and better potential traction characteristics than Tyre I.

#### ANALYSIS OF GLOBAL TYRE'S STIFFNESS

Analysis of global tyre's stiffness characteristics is no part of motion resistance evaluation, but it could be helpful in trying to explain obtained behavior of tested tyres. Better to say, the conclusion connected to the statement "what is better" without trying to find "why is better", could be too poor especially for presented tests. The purpose to present tests lied in the effort to define the tyre prototype (Tyre I) characteristics relating to parameters of one commercial tyre (Tyre II) with reasonable good characteristics, and explain the reasons for eventual differences.

So, analysis of global stiffness characteristics could explain, for example, why wider (under unloaded condition) Tyre I gives smaller footprint area related to Tyre II, or why carcass stiffness values for Tyre I are higher for a whole range of tested inflation pressures.

Bar chart given in Fig 6. shows calculated values of radial and side stiffness coefficients, which are taken using devices given in Fig.1 where footprint characteristics have been evaluated. The device has been adapted for stiffness measuring purposes, i.e., soil bin has been moved out and inductive displacement transducer have been added. Also vertical load and tyre inflation pressure have been registered during the tests.

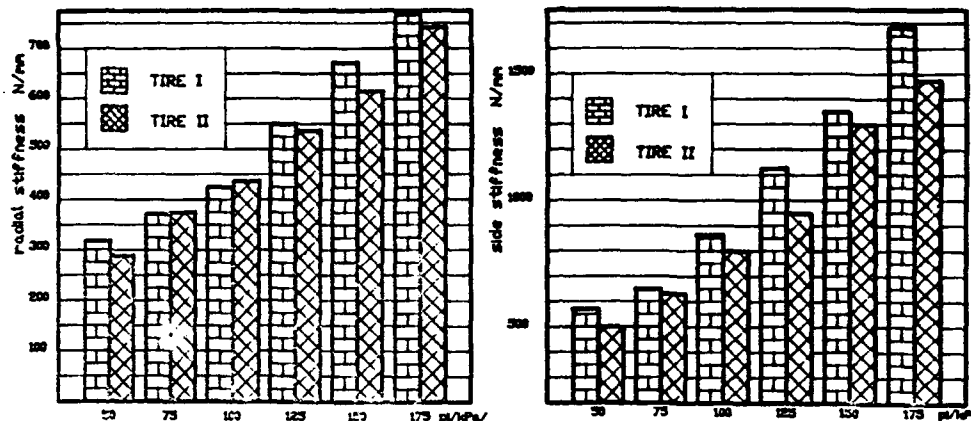


Fig.6. Radial and side stiffness characteristics for tested tyres

Some conclusions can be taken from Fig.6. As a first, the side and radial stiffness of Tyre I is greater related to Tyre II over the whole range of applied tyre's inflation pressure. Also, the differences in side wall stiffness are greater in relation to radial stiffness.

Knowing the stiffness behavior of Tyre I, higher values of carcass stiffness taken for this tyre could be understandable.

More intensive stiffness of Tyre I prevents growing of footprint area with increasing of the applied load, which leads to increase of total ground pressure, higher level of motion resistance and, probably, soil compaction problems becomes more serious.

Lower level of radial stiffness of Tyre II enabled longer footprint area, what gave some advantage in total traction possibilities.

## CONCLUSION

From presented discussion two types of conclusions could be made, one related to suggested methods, and second one related to taken test results.

- 1 Suggested method, based on known theoretical background, can be successfully applied for quick, and inexpensive tyre tests, when global relative tyre performances are in question;
2. Taken results unquestionable give advantage in energy balance to Tyre II, showing, at the same time, the reasons for such a behavior.

Also, simple and inexpensive measuring equipment gives excellent opportunity for small laboratories to include themselves to problems of tyre's traction.



# LITERATURE

1/ M. G. Bekker

INTRODUCTION TO TERRAIN-VEHICLE SYSTEMS  
Ann Arbor, The University of Michigan  
Press, 1969;

2/ Z. Janosi

AN ANALYSIS OF PNEUMATIC TIRE PERFORMANCE  
ON DEFORMABLE SOILS

Proceedings of the 1st International Con-  
ference on the mechanics of Soil-Vehicle  
Systems, Torino, 1961;

# BASIC ENERGY ANALYSIS IN SOIL-CRAWLER INTERACTION

K.Kogure and Y.Ohira

Department of Civil Engineering, National Defense Academy  
1-10-20 Hashirimizu, Yokosuka, Kanagawa, 239 Japan

## SUMMARY

In studies concerned with soil crawler interaction, it is known that there exist interdependent relationship between soil and crawler. This paper deals with a method of basic energy analysis for crawler motion on the ground. Six types of motion resistances acting on the running gear of a crawler are considered and the relationships between the driving force, drawbar pull and motion resistances are investigated. The conservation of energies between the input energy, drawbar pull energy, compaction resistance energy, bulldozing resistance energy, two slip energies and track rotation resistance energy are analysed for unit travelling and unit time.

## INTRODUCTION

The principle of energy conservation is one of the basic laws of physics. Based on the principle, some investigations on the analysis between the running gear of vehicle and soil were reported[1,2,3]. Authors considered on the soil thrust and motion resistance exerted by tracked vehicle[4,5]. Based on the past investigations as mentioned above, the paper is practically considered the basic ideas of the energy conservation between a crawler type tractor with rigid track and soil. Six types of motion resistance acting to running gear of a crawler tractor motion on soil are introduced into the analysis and the energy equilibrium equation between the input, output and motion resistance energies for the motion of running gear is considered.

The performance of running gear with rigid track is evaluated in terms of the output energy that can be developed in view of the track contact surface characteristics and soil properties. The amount of input energy that can be developed for production of drawbar pull is intimately tied into the properties of soil and slippage of track. The input energy per unit travelling distance of crawler tractor increases with the increasing slippage. The output energy(drawbar pull energy) per unit time of crawler tractor decreases with slippage and the maximum output energy occurs at no slippage.

## SLIPPAGE AND FORCES ACTING RUNNING GEAR

The slippage occurs between the running gear and soil when the crawler is travelling under pulling load. The slip ratio  $i$  at pulling state is given as

$$i = \frac{V_t - V}{V_t} = 1 - \frac{V}{V_t} \quad (1)$$

where,  $i$ :slip ratio,  $V_t$ :rotation speed of track belt,  $V$ :horizontal vehicle travelling speed. The slip ratio can be considered as the ratio of horizontal deformation  $j$  to the contact distance  $x$ . Therefore, the soil deformation  $j$  under slipping track can be represented by  $j=ix$ , where,  $j$ :soil deformation,  $x$ : contact distance from front of track contacted ground. The total slippage of the running gear is  $iL$  when the crawler is travelling with slip ratio  $i$ , where,  $L$  is the contact length.

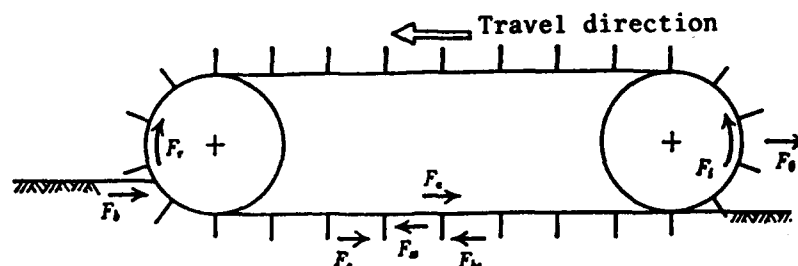


Fig.1 Forces acting on running gear

Fig.1 shows the forces acting on the running gear. In Fig.1,  $F_i$ :driving force,  $F_o$ :drawbar pull,  $F_{bs}$ :soil shear force under one track belt,  $F_{ss}$ :soil shear force on one side of track belt,  $F_c$ :compaction resistance for one track belt,  $F_b$ :bulldozing resistance for one track belt,  $F_a$ :adhesion resistance on one side of running gear,  $F_r$ :rotation resistance of one track belt.

The total driving force of a crawler tractor is the sum of  $2F_r$ ,  $2F_{bs}$  and  $4F_{ss}$ . The balance of the forces is given as follows

$$2 F_i = 2 F_{bs} + 4 F_{ss} + 2 F_r \quad (2)$$

The soil thrust exerted by the tractor is given as  $(2 F_{bs} + 4 F_{ss})$  and the motion resistance is represented by  $(2 F_c + 2 F_b + 4 F_a)$ . The relationship between the forces acting on travelling tractor on horizontal plane is given as

$$2 F_{bs} + 4 F_{ss} = F_o + 2 F_c + 2 F_b + 4 F_a \quad (3)$$

Equation (3) shows that the drawbar pull is defined by subtracting the motion resistances from the soil thrust.

#### ENERGY CONSERVATION FOR RUNNING GEAR MOTION

The energy equilibrium for running gear motion can be represented based on the acted forces as follows

$$E_i = E_o + E_c + E_b + E_{bs} + E_{ss} + E_a + E_r \quad (4)$$

where,  $E_i$ :input energy,  $E_o$ :drawbar pull energy,  $E_c$ :compaction energy,  $E_b$ :bulldozing energy,  $E_{bs}$ :bottom slip energy,  $E_{ss}$ :side slip energy,  $E_a$ :adhesion resistance energy,  $E_r$ :rotation resistance energy.

#### Input Energy $E_i$

The input energy  $E_i$  is defined as the effective input energy and is inputted

to the sprocket by the driving force  $2F_i$ . The input energy for track motion of tractor is expressed as follows

$$E_i' = 2 F_i L \quad (\text{kgf}\cdot\text{cm}) \quad (5)$$

where,  $E_i'$ :input energy when the track belt rotates the distance  $L$ ,  $L$ :contact length. The tractor travelling distance  $L'$  when the track belt rotates  $L$  is  $L'=(1-i)L$ . Therefore

$$\bar{E}_i = \frac{E_i'}{L'} = \frac{2 F_i L}{(1-i)L} \left( = \frac{2 F_i}{1-i} \right) \quad (\text{kgf}\cdot\text{cm}/\text{cm}) \quad (6)$$

where,  $\bar{E}_i$ :input energy when the tractor is advanced unit distance(input energy per unit travelling distance). The input energy can be expressed as follows

$$\dot{E}_i = 2 F_i V_t \quad (\text{kgf}\cdot\text{cm}/\text{sec}) \quad (7)$$

where,  $\dot{E}_i$ :input energy when the tractor travels per unit time(input energy per unit time).

#### Drawbar Pull Energy $E_o$

For the tractor motion over the distance  $L'$  with the slip ratio  $i$ , the drawbar pull energy  $E_o'$  will be defined as

$$E_o' = F_o L' = F_o (1-i)L \quad (\text{kgf}\cdot\text{cm}) \quad (8)$$

Therefore

$$\bar{E}_o = \frac{E_o'}{L'} = \frac{F_o (1-i)L}{(1-i)L} \left( = F_o \right) \quad (\text{kgf}\cdot\text{cm}/\text{cm}) \quad (9)$$

$$\dot{E}_o = \frac{E_o'}{L/V_t} = F_o (1-i) V_t \quad (\text{kgf}\cdot\text{cm}/\text{sec}) \quad (10)$$

where,  $\bar{E}_o$ :drawbar pull energy per unit travelling distance,  $\dot{E}_o$ :drawbar pull energy per unit time.

#### Compaction Energy $E_c$

The compaction energy  $E_c$  identifies the energy required to compact the soil as a result of track motion. Here, it is assumed that the relation between the contact pressure  $p$  and sinkage  $z$  of the track plate can be represented as follows[6]

$$p = k z^n \quad (11)$$

where,  $k$ ,  $n$ :experimental constants. The mean contact pressure between track and soil is written as

$$p = \frac{W}{2 B L} \quad (12)$$

where,  $W$ :tractor weight,  $B$ :contact width. The compaction energy of soil per track contact area( $2BL$ ) CE may be expressed as

$$CE = 2 B L \int_0^{z_o} p dz = \frac{W}{n+1} \left( \frac{W}{2 B L k} \right)^{1/n} \quad (\text{kgf}\cdot\text{cm}) \quad (13)$$

where,  $z_0$ : sinkage of track which is obtained from equations (11) and (12).  
The compaction energy CE can be equated to the work done in overcoming compaction resistance  $F_c$  and from  $CE=2F_cL$ ,

$$F_c = \frac{W}{2L(n+1)} \left( \frac{W}{2BLk} \right)^{1/n} \quad (14)$$

When the compaction resistance force  $F_c$  is obtained from equation (14), the compaction energy is given as

$$E'_c = 2F_c L' = 2F_c (1-i)L \quad (\text{kgf}\cdot\text{cm}) \quad (15)$$

and

$$\bar{E}_c = \frac{E'_c}{L'} = \frac{2F_c(1-i)L}{(1-i)L} (= 2F_c) \quad (\text{kgf}\cdot\text{cm}/\text{cm}) \quad (16)$$

or

$$\dot{E}_c = \frac{E'_c}{L/V_t} = 2F_c(1-i)V_t \quad (\text{kgf}\cdot\text{cm}/\text{sec}) \quad (17)$$

where,  $E'_c$ : compaction energy when the track belt rotates the distance  $L$ ,  $\bar{E}_c$ : compaction energy per unit travelling distance,  $\dot{E}_c$ : compaction energy per unit time.

#### Bulldozing energy $E_b$

The problem of bulldozing resistance  $F_b$  is considerably difficult to solve in theoretically. In predicting the bulldozing resistance, it is assumed that it is equivalent to the horizontal force of the passive earth pressure acting on a vehicle front. Here, the bulldozing resistance  $F_b$  was estimated using the passive earth pressure theory. The bulldozing energy can be estimated when the force  $F_b$  can be obtained as follows

$$E'_b = 2F_b L' = 2F_b(1-i)L \quad (\text{kgf}\cdot\text{cm}) \quad (18)$$

and

$$\bar{E}_b = \frac{E'_b}{L'} = \frac{2F_b(1-i)L}{(1-i)L} (= 2F_b) \quad (\text{kgf}\cdot\text{cm}/\text{cm}) \quad (19)$$

or

$$\dot{E}_b = \frac{E'_b}{L/V_t} = 2F_b(1-i)V_t \quad (\text{kgf}\cdot\text{cm}/\text{sec}) \quad (20)$$

where,  $E'_b$ : bulldozing energy when track belt rotates the distance  $L$ ,  $\bar{E}_b$  and  $\dot{E}_b$ : bulldozing energies per unit travelling distance and per unit time respectively.

#### Bottom Slip Energy $E_{bs}$

The bottom slip energy  $E_{bs}$  refers to the energy loss due to slippage between the bottom of track and soil. The force by bottom slippage  $F_{bs}$  may be estimated as follows

$$F_{bs} = BL(c + p \tan \phi) \quad (21)$$

where,  $c$ : cohesion of soil,  $\phi$ : internal friction angle of soil. Therefore, the bottom slip energy  $E_{bs}$  is obtained as

$$E'_{bs} = 2F_{bs} i L \quad (\text{kgf}\cdot\text{cm}) \quad (22)$$

and

$$\bar{E}_{bs} = \frac{E'_{bs}}{L'} = \frac{2F_{bs} i L}{(1-i)L} (= 2F_{bs} \frac{i}{1-i}) \quad (\text{kgf}\cdot\text{cm}/\text{cm}) \quad (23)$$

or

$$\dot{E}_{bs} = \frac{E'_{bs}}{L / V_t} = 2 F_{bs} i V_t \quad (\text{kgf}\cdot\text{cm}/\text{sec}) \quad (24)$$

where,  $E'_{bs}$ :bottom slip energy when track belt rotates the distance  $L$ ,  $\bar{E}_{bs}$  and  $\dot{E}_{bs}$ :bottom slip energies per unit travelling distance and per unit time respectively.

#### Side Slip Energy $E_{ss}$

The side slip energy  $E_{ss}$  refers to the energy loss due to slip between the side of track and soil. The side slip force  $F_{ss}$  may be estimated as follows

$$F_{ss} = H L (c + \sigma \tan \phi) \quad (25)$$

where,  $H$ :grouser high,  $\sigma$ :normal stress. The side slip energy is given as

$$E'_{ss} = 4 F_{ss} i L \quad (\text{kgf}\cdot\text{cm}) \quad (26)$$

and

$$\bar{E}_{ss} = \frac{E'_{ss}}{L'} = \frac{4 F_{ss} i L}{(1 - i) L} (= 4 F_{ss} \frac{i}{1-i}) \quad (\text{kgf}\cdot\text{cm}/\text{cm}) \quad (27)$$

or

$$\dot{E}_{ss} = \frac{E'_{ss}}{L / V_t} = 4 F_{ss} i V_t \quad (\text{kgf}\cdot\text{cm}/\text{sec}) \quad (28)$$

where,  $E'_{ss}$ :side slip energy when track belt rotates the distance  $L$ ,  $\bar{E}_{ss}$  and  $\dot{E}_{ss}$ :side slip energies per unit travelling distance and per unit time respectively.

#### Adhesion Energy $E_a$

When the sinkage of tractor is considerably large, the adhesion resistance force  $F_a$  may be acted between the tractor body and soil. If the adhesion  $\tau_a$  between the tractor body and soil is known, the adhesion resistance force  $F_a$  may be expressed as

$$F_a = z_o L \tau_a \quad (29)$$

and the adhesion energy is given as follows

$$E'_a = 4 F_a L' = 4 F_a (1 - i) L \quad (\text{kgf}\cdot\text{cm}) \quad (30)$$

and

$$\bar{E}_a = \frac{E'_a}{L'} = \frac{4 F_a (1 - i) L}{(1 - i) L} (= 4 F_a) \quad (\text{kgf}\cdot\text{cm}/\text{cm}) \quad (31)$$

or

$$\dot{E}_a = \frac{E'_a}{L / V_t} = 4 F_a (1 - i) V_t \quad (\text{kgf}\cdot\text{cm}/\text{sec}) \quad (32)$$

where,  $E'_a$ :adhesion energy when track belt rotates the distance  $L$ ,  $\bar{E}_a$  and  $\dot{E}_a$ :adhesion energy per unit travelling distance and per unit time respectively.

#### Rotation Energy $E_r$

The force due to rotation of track belt is the rotation resistance force  $F_r$ . The force  $F_r$  is measured as a part of the driving force of sprocket, but it is does not distribute to the thrust of tractor. The force  $F_r$  is one of the resistance force. The rotation energy was given as follows

$$E'_r = 2 F_r L \quad (\text{kgf}\cdot\text{cm}) \quad (33)$$

$$\text{and } \bar{E}_r = \frac{E'_r}{L'} = \frac{2 F_r L}{(1-i)L} \left( = 2 F_r \frac{1}{1-i} \right) \quad (\text{kgf}\cdot\text{cm}/\text{cm}) \quad (34)$$

$$\text{or } \dot{E}_r = \frac{E'_r}{L / V_t} = 2 F_r V_t \quad (\text{kgf}\cdot\text{cm}/\text{sec}) \quad (35)$$

where,  $E'_r$  : rotation energy when track belt rotates the distance  $L$ ,  $\bar{E}_r$  and  $\dot{E}_r$ : rotation energies per unit travelling distance and per unit time respectively.

#### Energy Conservation for Running Gear

Based on the definitions of the energies mentioned above, the energy equilibrium of the running gear of crawler tractor motion can be written from equation (4) as follows

$$E'_i = E'_o + E'_c + E'_b + E'_{bs} + E'_{ss} + E'_a + E'_r \quad (\text{kgf}\cdot\text{cm}) \quad (36)$$

$$\text{or } \bar{E}_i = \bar{E}_o + \bar{E}_c + \bar{E}_b + \bar{E}_{bs} + \bar{E}_{ss} + \bar{E}_a + \bar{E}_r \quad (\text{kgf}\cdot\text{cm}/\text{cm}) \quad (37)$$

$$\text{or } \dot{E}_i = \dot{E}_o + \dot{E}_c + \dot{E}_b + \dot{E}_{bs} + \dot{E}_{ss} + \dot{E}_a + \dot{E}_r \quad (\text{kgf}\cdot\text{cm}/\text{sec}) \quad (38)$$

#### DISCUSSIONS

Some discussions will be made the proposed energy conservation based on the calculated results for a tractor and soil conditions. The characteristics of crawler tractor used in the calculation of the energies are shown in Table 1 and the properties of soil for calculation of the energies are shown in Table 2.

Table 1 Characteristics of crawler

Total weight $W$	16000	kgf	—
Contact length $L$	280	cm	
Track width $B$	50	cm	
Grouser height $H$	5	cm	
Contact pressure $p$	0.571	kgf/cm <sup>2</sup>	

Table 2 Soil properties

	Cohesive soil	Frictional soil
Cohesion $c$ (kgf/cm <sup>2</sup> )	0.4	0
Internal friction angle $\phi$ (deg.)	0	33
Adhesion $\tau_a$ (kgf/cm <sup>2</sup> )	0.2	0.1
Constant $k$	0.06	0.6
Constant $n$	0.9	1.2

It is assumed that the tractor speed  $V_t$  is 100 cm/sec (about 4 km/hr). The horizontal force of passive earth pressure is used as the bulldozing resistance.

Figs. 2 and 3 show the relationships between slip ratio  $i$  and energies  $E$  per unit travelling distance. It is evident that  $E_i$ ,  $E_{bs}$ ,  $E_{ss}$  and  $E_r$  rapidly increase according to the increasing slip ratio. When  $i = 1.0$ , the tractor is perfectly slipping and the most of input energy is spented for  $E_{bs}$ ,  $E_{ss}$  and  $E_r$ .

Figs. 4 and 5 show the relationships between slip ratio  $i$  and energies  $\dot{E}$  per

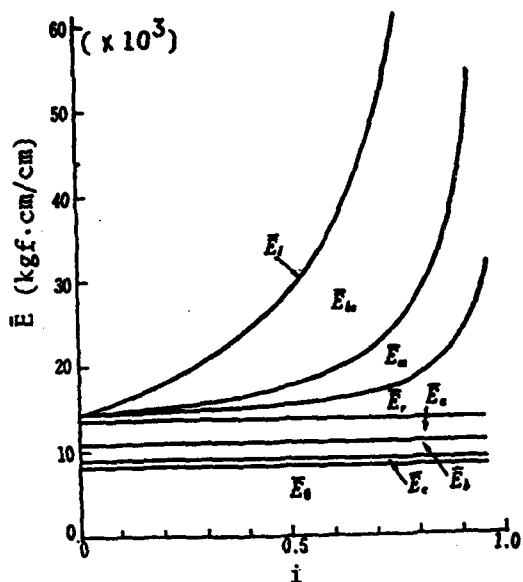


Fig.2 Relationship between slip ratio  $i$  and energy  $\bar{E}$  (cohesive soil)

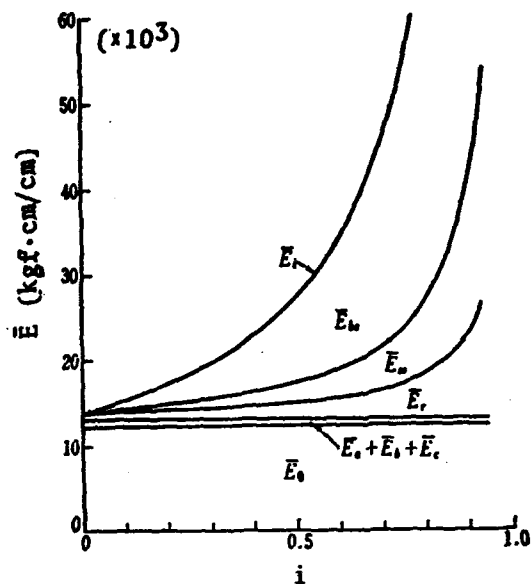


Fig.3 relationship between slip ratio  $i$  and energy  $\bar{E}$  (frictional soil)

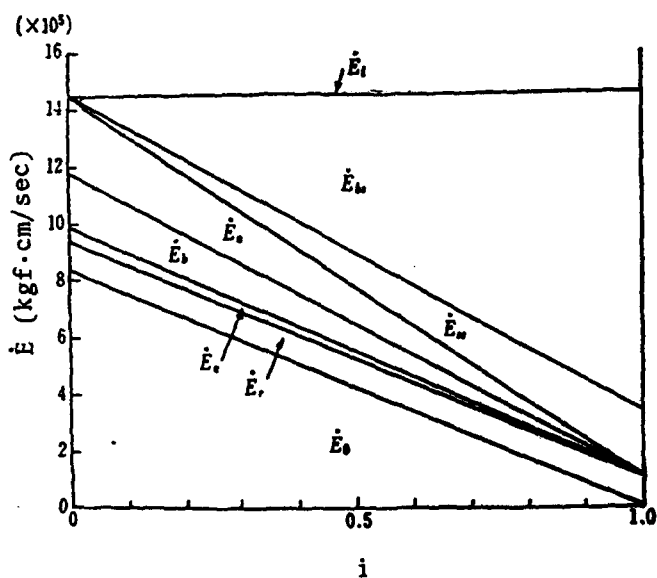


Fig.4 Relationship between slip ratio  $i$  and energy  $\dot{E}$  (cohesive soil)

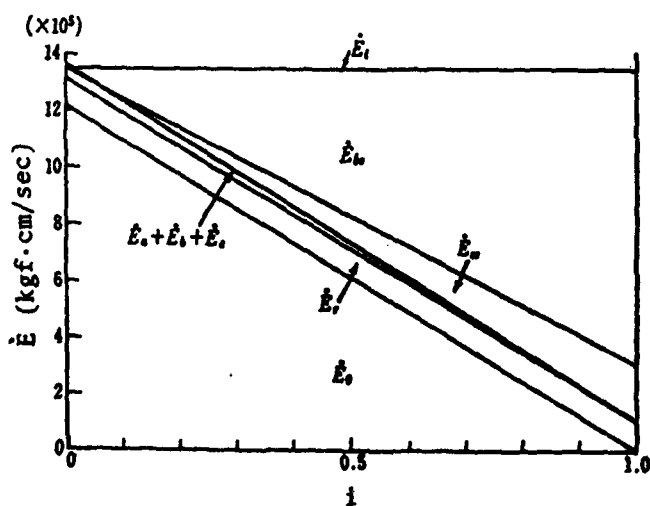


Fig.5 relationship between slip ratio  $i$  and energy  $\dot{E}$  (frictional soil)



unit time. The input energy  $\dot{E}_i$  per unit time is constant regardless of slip ratio. When the slip ratio is small, the most of input energy changes to the drawbar pull energy, but when large the most of input energy is lost as the bottom slip energy  $\dot{E}_{bs}$ , the side slip energy  $\dot{E}_{ss}$  and others. The drawbar pull energy  $\dot{E}_o$  is linearly decreased according the increasing the slip ratio.

## CONCLUSIONS

From the analysis of energy conservation between running gear and soil and the discussions on the results calculated, we can conclude as follows;

The six types of motion resistance acting on running gear of crawler tractor are introduced into the energy conservation. The performance of running gear is evaluated in terms of output energy that can be developed in view of the track contact surface characteristics and soil properties.

The energy conservation between running gear and soil can be represented in terms of the energy per unit travelling distance  $\bar{E}$  and per unit time  $\dot{E}$ .

The input energy per unit travelling distance  $\bar{E}_i$ , bottom slip energy  $\bar{E}_{bs}$ , side slip energy  $\bar{E}_{ss}$  and rotation energy  $\bar{E}_r$  rapidly increas according to the increasing slip ratio. When crawler tractor is perfectly slipping, the most of input energy  $\bar{E}_i$  is spend for the bottom slip energy  $\bar{E}_{bs}$ , side slip energy  $\bar{E}_{ss}$  and rotation energy  $\bar{E}_r$ .

The input energy per unit time  $\dot{E}_i$  is constant regardless of slip ratio. The most of input energy  $\dot{E}_i$  changes to the drawbar pull energy  $\dot{E}_o$  for small slip ratio. The drawbar pull energy  $\dot{E}_o$  is linearly decreased according to the increasing slip ratio. When the slip ratio is large, the most of input energy per unit time  $\dot{E}_i$  is lost in the bottom slip energy  $\dot{E}_{bs}$ , side slip energy  $\dot{E}_{ss}$  and others.

## REFERENCES

- [1] Yong, R.N. and Webb, G.L. (1969): Energie dissipation and drawbar pull prediction in soil-vehicle interaction, Proc. of 3rd Int. Conf., ISTVS, Vol.1, pp.93-142.
- [2] Yong, R.N. and Fattah, E.A. (1975): Influence of contact characteristics on energy transfer and wheel performance on soft soil, Proc. of 7th Int. Conf., ISTVS, Vol.2, pp.291-310.
- [3] Muro, T., Omoto, K. and Nagira, A. (1989): Traffic performance of a bulldozer running on a weak terrain-Energy analysis-, Proc. of JSCE, No.403/6-10, pp. 103-110 (in Japanese).
- [4] Kogure, K., Ohira, Y. and Yamaguchi, H. (1983): Prediction of sinkage and motion resistance of a tracked vehicle using plate penetration test, Jour. of Terramechanics, Vol.20, No.3/4, pp.121-128.
- [5] Kogure, K., Ohira, Y. and Yamaguchi, H. (1982): A simplified method for the estimation of soil thrust exerted by a tracked vehicle, Jour. of Terramechanics, Vol.19, No.3, pp.165-181.
- [6] Bekker, M.G. (1960): Off-The-Road Locomotion, Research and Development in Terramechanics, The Univ. of Michigan Press, pp.32-35.

# TRAFFICABILITY OF DEEP-SEA FLOOR

Dipl.-Ing. G. Dörfler

Institut für Maschinenwesen im Baubetrieb  
University of Karlsruhe  
Am Fasanengarten, 7500 Karlsruhe, Germany

## SUMMARY

In cooperation with several French and German partners the Institut für Maschinenwesen im Baubetrieb (IMB) is developing a manganese nodule mining system. The essential part of this mining system is a mobile collector to pick up manganese nodules in sea-depth of 5000 m and more.

To guarantee high mobility, the collector is running on crawlers. The goal of the research is to work out guidelines for the optimal shape of caterpillar tracks for most effective traction of the self-propelled manganese nodule miner. With the attention to the ecological system of the deep-sea floor, large sinkage and slip of the caterpillar chains have to be avoided.

For this purpose extensive experiments with a testing vehicle are carried out. Different types of crawlers and grousers can be assembled to be tested. The soil of the floor used for testing consists of a bentonite-water-mixture to simulate deep-sea floor conditions.

## 1. INTRODUCTION

Environmental protection as a basic requirement for all industrial activities is becoming a global principle. This is a particular must in future ocean mining. Bearing this in mind, the German Ministry for Research and Technology is sponsoring a research and development program in industry and universities to develop environmentally acceptable methods /1/.

Special attention must be paid to the tractive system of a future mining vehicle. The technically and environmentally best traction method is caterpillar drive. It provides high load bearing and traction forces on very soft soils. Caterpillar chains destroy the seafloor less than alternative traction methods such as Archimedean Screw, which was tested by a different ocean mining group. It apparently worked technically (with some difficulties), but it destroyed the deep-sea floor to a considerable extend.

This article gives a survey, including first results, of the research on the trafficability of the deep-sea floor.

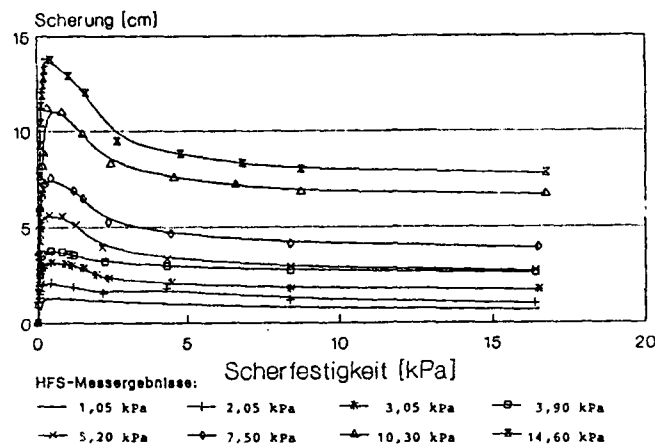
## 2. DEEP-SEA SOIL

A suitable substitute for the soil predominant on deep-sea floors had to be found to carry out the tests. In experiments a mixture of bentonite and water proved to be the best assimilation to the natural properties of the deep-sea soil, particularly with regard to shear strength and the property of liquifying under dynamic strain /2/. The shear strength of the substitute can be varied by the proportions of bentonite and water. Shear strength measurements on deep-sea soil samples and in-situ gave values of about 3.5 kPa /3/. Various other tests, e.g. load-plate and the

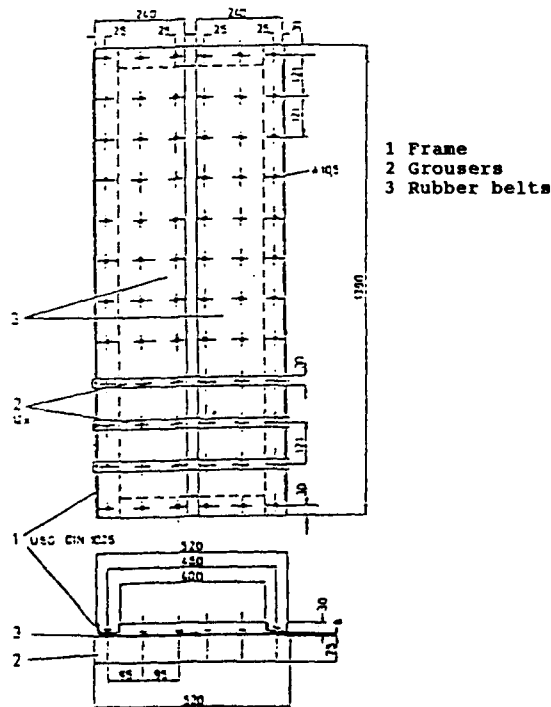
- mineralogy: Montmorillonite(60%), Illite(20%), Kaolinite(10%)
- grain density: 2,806 t/m<sup>3</sup>
- liquid limit: W<sub>L</sub>=104%
- plasticity limit: W<sub>P</sub>=34%
- plasticity index: I<sub>P</sub>=70

## Automatische Flügelsonde

### Ergebnisse der autom. FS-Messungen



### 3. GROUSERBOARD TESTS



The so-called grouserboard test works in such a way, that a board which is armed with grousers, is pulled across the floor while tractive force and displacement are measured. The goal of these tests was to prove a potential correlation of measuring results of shear vane tests and grouserboard tests. .

The board was equipped with grousers of 5.5 cm or 7.6 cm in height. The spacing of the grousers was 12 cm or 24 cm. In this way either 12 or 6 grousers could be mounted. Fig. 3 shows some results of measured tractive forces dependent on the shear strength of the soil consisting of bentonite and water. The shear strength was determined by shear vane (GEONOR A/S, 25.4\*50.8 mm). All results are valid within the range of 2 kPa to 10 kPa.

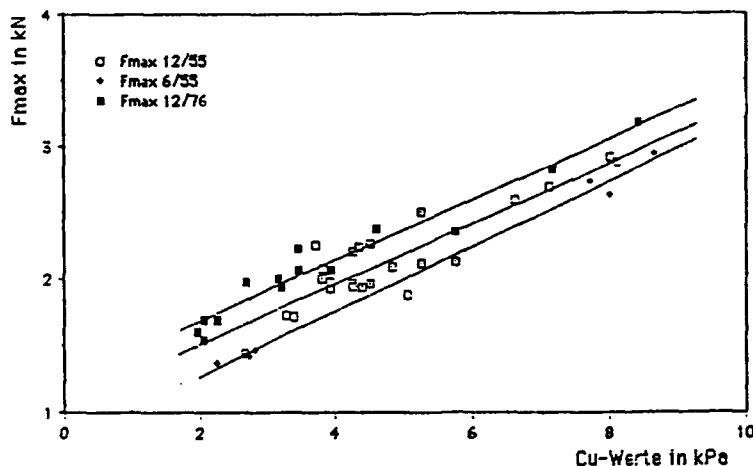


Fig. 3: Effect of height and spacing of grousers and shear strength of soil ( $c_u$ )

Following correlation of grouserboard tests and shear vane tests could be proved:

SPACING / HEIGHT OF GROUSERS / MAX. TRACTIVE FORCE		
12 cm	/ 7.6 cm	/ $F=1.225+0.228 \cdot c_u$
12 cm	/ 5.5 cm	/ $F=1.048+0.228 \cdot c_u$
24 cm	/ 5.5 cm	/ $F=0.866+0.228 \cdot c_u$

#### 4. TEST VEHICLE AND EQUIPMENT

The test vehicle is an original undercarriage of a snowmobile, normally used to prepare ski runs. The length of the vehicle is about 3 m and with the track type used it is about 2 m wide. It can be equipped with several types of caterpillar tracks of different width and grousers of different height and spacings.

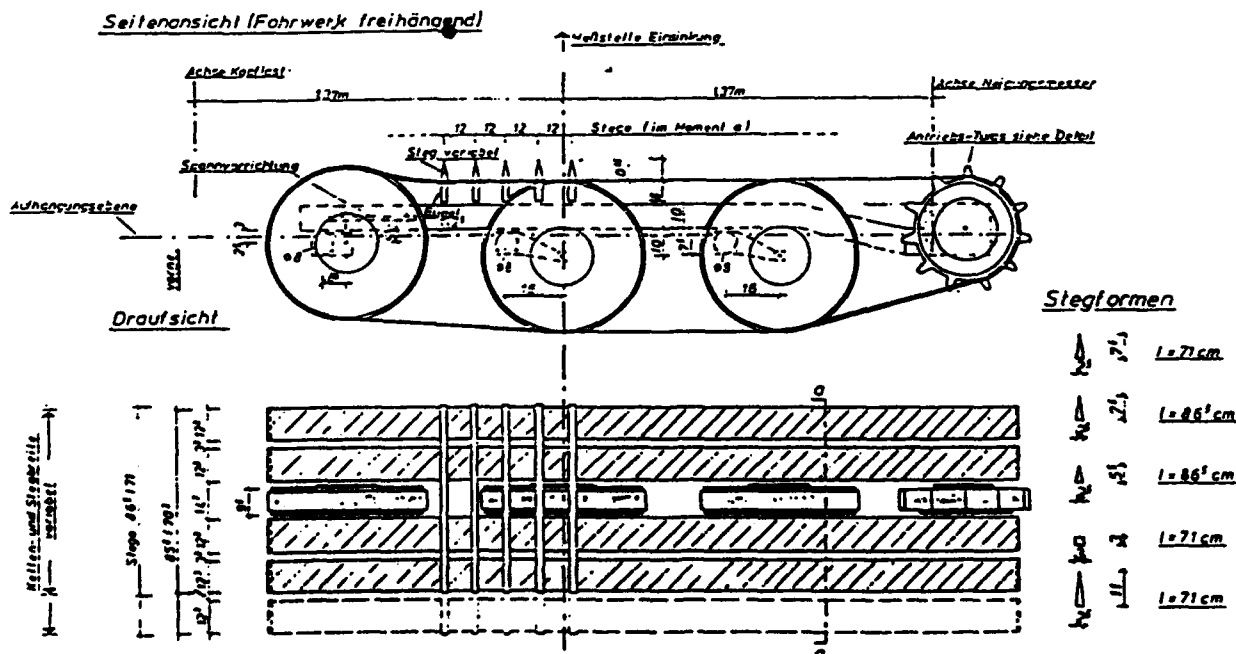


Fig. 4: Test vehicle

By loading ballast the ground pressure is variable. Load distribution along the longitudinal axis can be varied as well. The caterpillar tracks are of modular structure. The traction is transmitted into the floor by aluminum grousers, interconnected by several reinforced rubber belts. The energy conversion operates hydrostatically. Tests were performed in three stages:

- Research using a single caterpillar chain
- Testing the complete vehicle
- Manoeuvrability and overcoming of obstacles

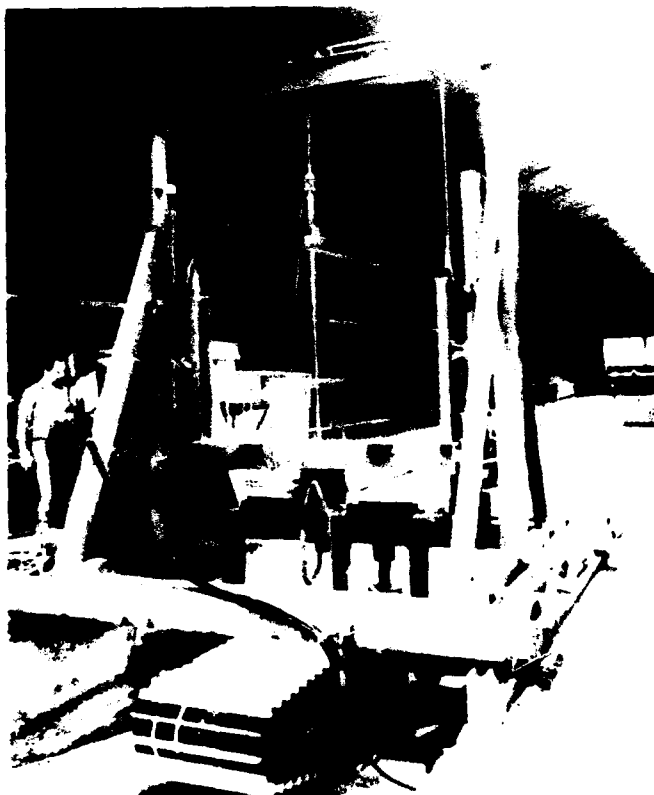


Fig. 5: Bollard-pull test with a single caterpillar track

The test program with a single caterpillar track has taken place in a test channel of 36 m length (Fig. 5). Here the main installation is a frame system, which can be moved vertically and horizontally. The vehicle under test is fixed to this frame in such a way, that it can swing around its lateral axis. Surcharges on the frame produce pre-determined ground pressures underneath the contact area of the crawler belt. The sinkage of the vehicle is determined at two points. The traction is measured by using a pressure cell. This set-up is mainly used to carry out bollard-pull tests. Both bollard-pull tests and drawbar-pull tests with the entire vehicle, e.g. both caterpillar chains mounted, are carried out in a test channel of 63 m in length.



Fig. 6: Crawler test in the large test channel

The mechanism of the installation is designed in such a way, that driving forward of the vehicle causes lifting of several ballast weights. Thus the vehicle can be exposed to pre-determined traction resistances.

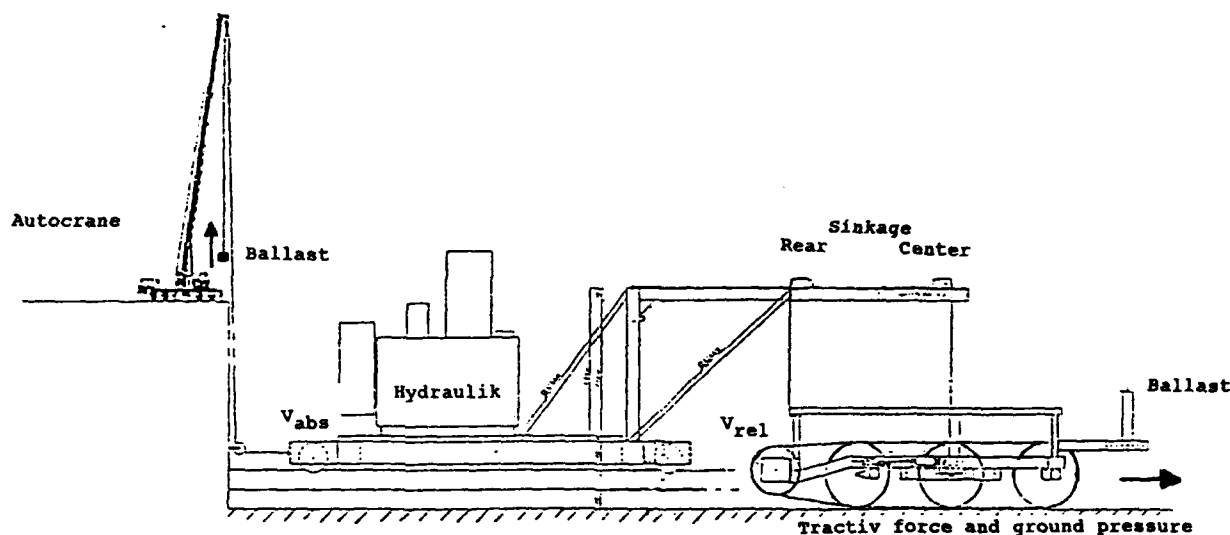


Fig. 7: Mechanism of drawbar-pull tests

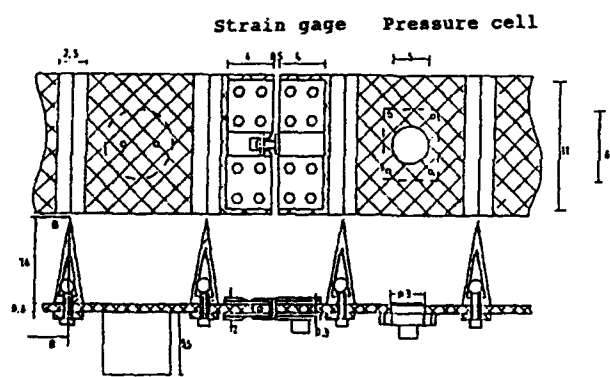


Fig. 8: Strain gages and pressure cells integrated to caterpillar belt

The vehicle is connected to a rail mounted trailer, carrying the power unit, data printer etc. The tractive force of a single grouser is determined by using a double set of strain gages, installed in the spacings in front and behind the grouser. This is done continuously on the grouser travelling around. Pressure cells integrated into the rubber belts measure the actual ground pressure distribution (Fig. 8). Sinkage and slip of the caterpillar chains, velocity and reserve power in the driving unit are also recorded.

Thus the travelling resistances caused by chain deformations and displacing the soil can be determined. Lateral track stability can be investigated by inducing lateral forces.

## 5. FIRST RESULTS

The most important results of the experiments to date are summed up as follows:

For driving on soft soil (shear strength 3.5 kPa) the ground pressure should be within the range of 3 to 5 kPa depending on the height of the grousers. With the area of contact designed accordingly, the grousers will penetrate completely into the floor, so that the most effective plane of shear will be activated for power transmission, whereas the vehicle is not sinking too deeply into the floor. Thus the travelling resistances are small and the destruction of the sea-bottom is minimized. Fig. 9 shows the trend of the resulting traction force dependent on shear strength of the soil and ballast.

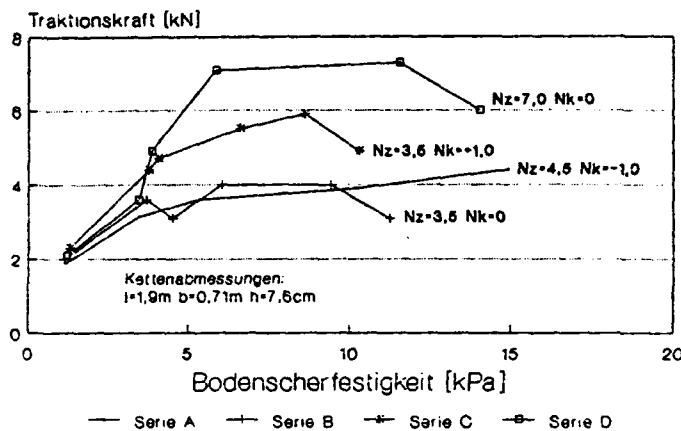


Fig. 9: Bollard-pull  
 $N_z$  = center ballast  
 $N_k$  = front ballast

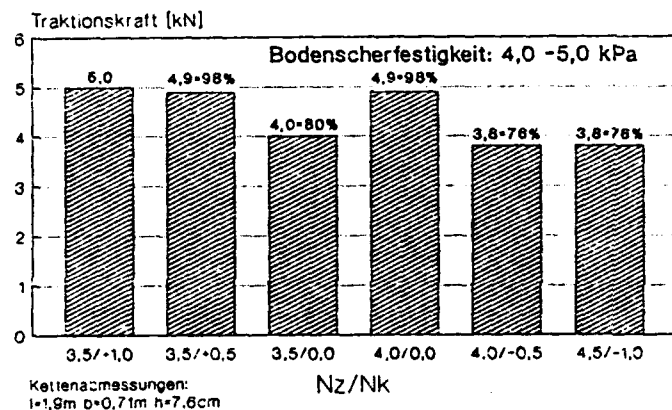


Fig. 10: Bollard-pull  
 $N_z$  = center ballast  
 $N_k$  = front ballast  
 Shear strength = 4 - 5 kPa

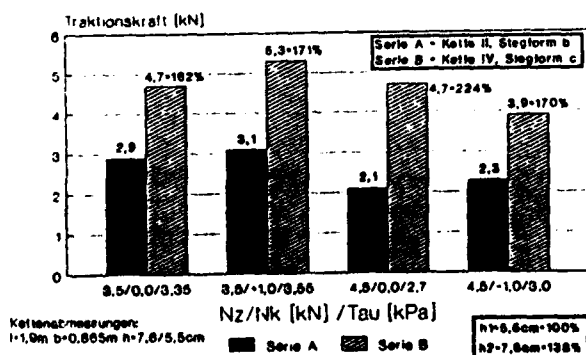


Fig. 12: Bollard-pull  
 Series A: height = 5.5 cm  
 Series B: height = 7.6 cm

The distribution of the dead weight should be designed in such a way, that the center of gravity is in the front half of the contact area. This results in steady distribution of ground pressure along the longitudinal axis when driving forward and it prevents the rear from sinking too much into the ground. Fig. 10 obviously reproduces the influence of the distribution of the dead weight on the resulting traction force.

The following three figures give some results of investigations of width (Fig. 11), height (Fig. 12) and spacing (Fig. 13) of grousers.

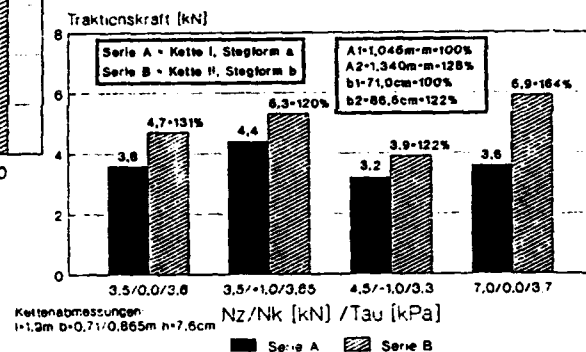


Fig. 11: Bollard-pull  
 Series A: contact area = 1.37 m<sup>2</sup>  
 Series B: contact area = 1.93 m<sup>2</sup>

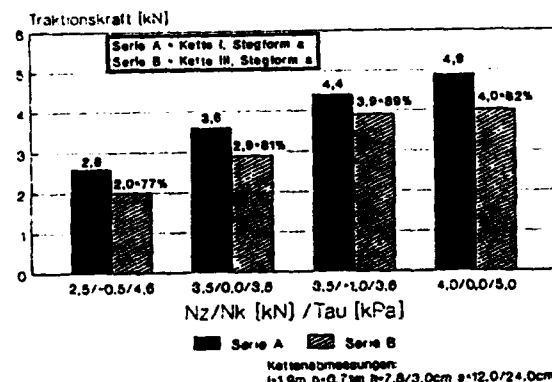


Fig. 13: Bollard-pull  
 Series A: spacing = 12 cm  
 Series B: spacing = 24 cm

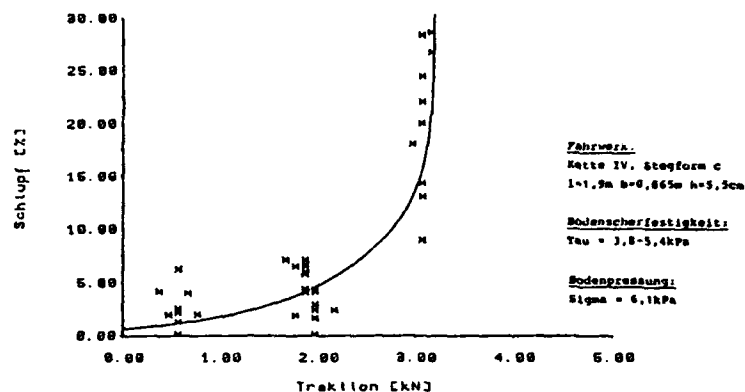


Fig. 14: Drawbar-pull [kN] and slip [%]

Fig. 14 reproduces several drawbar-pull tests, carried out with the entire vehicle. The average shear strength of the soil was about 4.5 kPa, the ground pressure underneath the caterpillar chains was 6.1 kPa. The width of the grousers was 86.5 cm, the height 5.5 cm. The velocity of the vehicle was 0.5 m/s. Maximum traction force is reached with a slip of the caterpillar tracks of about 15%.

A higher amount of slip leads to increased destruction of the floor and driving energy losses, without improved traction force.

With regard to an alternative improved concept of undercarriage and tracks the following can be mentioned:

To get steady distribution of ground pressure even when passing obstacles or ground deformations, a concept of roller suspensions with oscillating axles should be used.

Special attention should be given to the design of the grousers. Plate shaped grousers destroy the sea-floor already when being pressed into the soil at the front-end of the track. The degree of destruction depends on the radius of the sprocket wheel and the height of the grousers (Fig. 15). Caused by this effect valuable reserves of traction force are lost. A different design of grousers, e.g. involute grousers (Fig. 16), prevent the vehicle from "just digging" into the floor, because involute grousers have a compaction effect and do not shear away the soil.

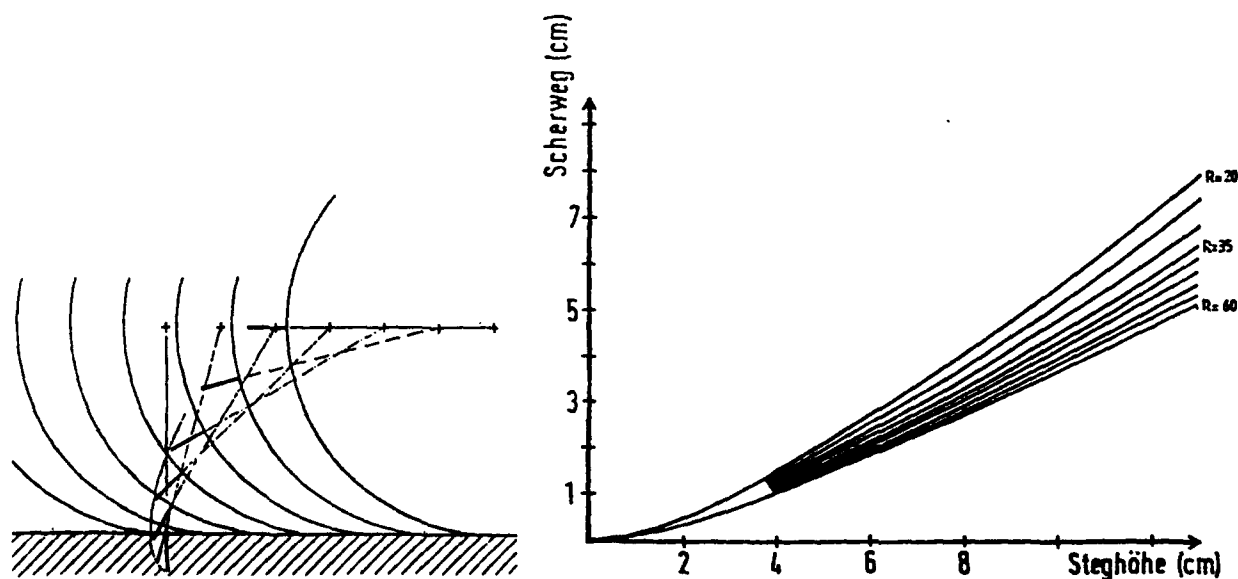


Fig. 15: Destruction of the soil (Scherweg) depending on sprocket radius  $R$  [cm] and height of the grousers (Steghöhe)



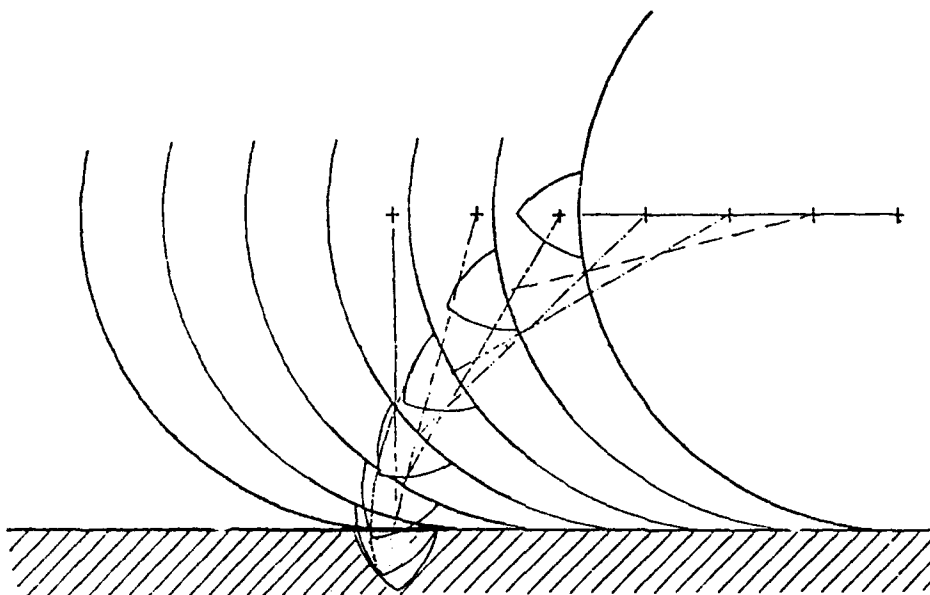


Fig. 16: Involute grouser

## 6. FINAL REMARKS

Research and principle design of the underwater mining vehicle is going on. Therefore this paper contains just first results of the research in the field of trafficability of deep-sea floor. The goal is the development of an algorithm to predict the performance of such a vehicle on very soft ocean soil. Further research should comprise the investigation and testing of both the new types of caterpillar tracks and the new concepts of roller suspensions with special attention to the ecological system of the deep-sea floor.

However, it was found worth-while to present this research project in the context of this conference as an example for the development of a mining vehicle, a special type of crawler in a very delicate and difficult environment.

## REFERENCES

- /1/ H. Amann, F. Gehbauer, H. Oebius, W. Schwarz, R. Weber  
SOFT OCEAN MINING  
Paper, presented at the 23rd Annual Offshore Technology  
Conference in Houston, Texas, May 6-9, 1991
- /2/ Groupement pour la mise au point des moyens necessaire à  
l'exploitation des nodules polymetalliques (Gemonod)  
POLYMETALLIC NODULE DEEP-SEA MINING COOPERATION PROGRAM -  
LOCOMOTION MINER STUDIES  
1987 (unpublished)
- /3/ A. Bath, B Greger - Preussag AG  
ENTWICKLUNG VON MANGANKNOLLENABBAU- UND - GEWINNUNGSVERFAHREN  
1988 (unpublished)
- /4/ G. Dörfler - Universität Karlsruhe  
ENTWICKLUNG VON MANGANKNOLLENABBAU- UND - GEWINNUNGSVERFAHREN  
1990 (unpublished)

# COMPACTION OF AGRICULTURAL SOILS WITH VISCOELASTIC BEHAVIOR UNDER CONFINED AND UNCONFINED CONDITIONS

G. Sitkei, University of Sopron, Hungary

## S u m m a r y

Compaction of agricultural soils plays an important role at tillage and traction operations. The compaction increases the load carrying capacity of soils and gives also a better traction capability. At the same time, soil compaction is unfavourable for plant growth and water household properties.

Because the theory of soil mechanics supplies no accurate solution to the compaction problems, therefore, the experimental method is the only possible way to clear the fundamental and general relationships of the soil compaction. Measurements were taken under confined and unconfined conditions with different soil moisture contents considering also the loading velocity effect. For describing dynamic compaction behavior a quasi-linear rheological method was suggested.

## i n t r o d u c t i o n

The compaction behavior of agricultural soils reflects a very complicated process. Unsaturated soils under loading can be compacted considerably. The compaction has in principle two types of appearance. First, stress may cause compaction that is elastically recovered when the stress is removed. Secondly, the compaction is not recovered when the stress is removed. In general, the non recoverable compaction is much larger than the recoverable one. Under footings or tires the compaction process is associated with plastic flow of the soil in unconfined three-dimensional space. The plastic flow field has always and everywhere a velocity gradient and with this a shear stress distribution. The shear stresses are the greatest near at the tip of the soil body adnering to the footing surface where the soil flow gradients are the greatest. According to the experimental observations the compaction is determined by the mean normal stress at first and by the shear strain to a certain extent [1].

The role of shear stresses or shear strains in the compaction mechanism is questionable. It may however be assumed that the shear strains play the more important role in the compaction process making easier the packing of soil particles in a well-ordered form. In structural soils the shear stress causes failure destroying the skeleton of the soil mass and hereby the cohesion. This circumstance will cause more compaction under the same mean normal stress.

In the case of confined compression shear stresses and shear strains occur near the wall at first. Their role in the compaction process is not essential. In unconfined compression, however, the shear strains influences the local compaction considerably.

An other problem of soil compaction is the varying modulus of elasticity which makes the use of linear viscoelasticity impossible. In order to overcome these difficulties a quasi-linear method is suggested and experimentally verified.

## Confined Compression of Soils.

The most common experimental method for studying compression and compaction characteristics of soils is the confined compression in a cylindrical container. If the container height is shallow compared to its diameter, the vertical stress varies not too much in the soil mass and soil can be considered a volume element.

SÖHNE has carried out systematic measurements for determining soil compaction [2,3] and his results are suitable for further processing. We have conducted similar experiments to study the effect of loading velocity on the stress-strain relationship.

The pressure-strain relation may be described in the following form:

$$p = K \cdot \left[ e^{A \gamma_0 \frac{\epsilon}{1-\epsilon}} - 1 \right] \quad (1)$$

where  $\gamma_0$  - the initial volume weight,  
K, A - constants.

The instantaneous modulus of elasticity is given by

$$E = \frac{\partial p}{\partial \epsilon} = \frac{KA \gamma_0}{(1-\epsilon)^2} \cdot e^{A \gamma_0 \frac{\epsilon}{1-\epsilon}} \quad (2)$$

and the initial value of E becomes

$$E_0 = K \cdot A \cdot \gamma_0 \quad (2a)$$

The more simple relationship

$$p = C \cdot \left( \frac{\epsilon}{1-\epsilon} \right)^n \quad (3)$$

may also be used with values of 1.8-2.0 for the exponent n. However, Eq.(3) has the drawback, in which the initial modulus of elasticity becomes zero.

The effect of loading speed on the stress-strain relationship is to be seen in Fig.1. The constant K in Eq.(1) can now be given as a function of loading velocity in the following form:

$$K = K_0 \left[ 1 + 0.95(1 - e^{-v/V}) \right]$$

where v - loading velocity

$K_0, V$  - constants.

A similar approach can be made in Eq.(3).

The values of constants in Eqs.(1) and (3) for a loam soil are summarized in the following table.

U, %	$K_0$	V	A	$\gamma_0$	$C_0$	n
16	0.24	0.09	5.15	1.16	14.0	1.9
22	0.155	0.11	5.13	1.36	10.0	1.9

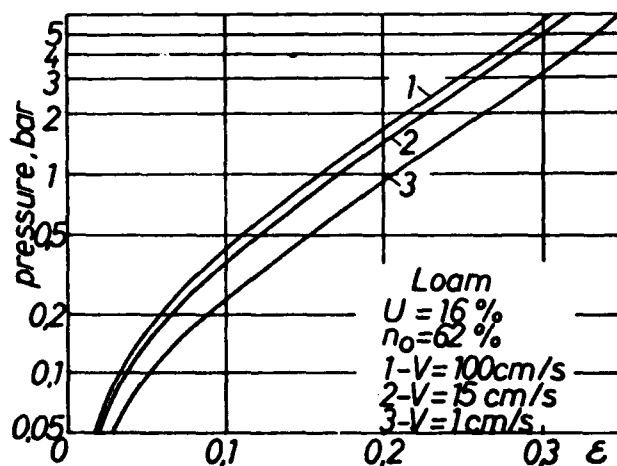


Fig. 1. Effect of loading velocity on the stress-strain relationship

The stress-strain-time relationship for the above problem may also be described with rheological equations. The compression process is strongly non-linear, therefore, the equations of linear viscoelasticity can not be used. In order to overcome these difficulties a quasi-linear viscoelastic method is suggested.

The viscoelastic model used is to be seen in Fig. 2. The spring  $E_0$  exhibits elastic response and the Kelvin-elements in series represent delayed elasticity with multiple retardation times. The non-linear behavior of the material may be taken into account in such a way that the E-moduli will be given and used as a function of strain. The retardation times must also be given as a function of strain or elastic modulus. Formulation and use of the above functions require special considerations.

In the case of a constant deformation rate  $v_0$ , the instantaneous strain is

$$\varepsilon = (v_0/L) \cdot t = a \cdot t \quad \text{and} \quad d\varepsilon/dt = a$$

Solving the governing differential equation of the model given in Fig. 2 for the linear case, the stress-time equation will be

$$\begin{aligned} \sigma(t) = & E_{\infty} a t + T_1 a (E_0 - E_{\infty 1}) (1 - e^{-t/T_1}) + \\ & + T_2 a (E_{\infty 1} - E_{\infty 2}) (1 - e^{-t/T_2}) + \\ & + T_3 a (E_{\infty 2} - E_{\infty}) (1 - e^{-t/T_3}) \end{aligned} \quad (4)$$

where  $1/E_{\infty} = \sum 1/E_i$ ;  $E_{\infty 1} = \frac{E_0 \cdot E_1}{E_0 + E_1}$ ;  $E_{\infty 2} = \frac{E_0 \cdot E_1 \cdot E_2}{E_0 E_1 + E_0 E_2 + E_1 E_2}$

Eq.(4) is valid in the time interval  $0 \leq t < t_1$ , where  $t_1$  denotes the end of the loading period. The subsequent relaxation under constant deformation occurs according to the equation:

$$\begin{aligned} \sigma(t) = & E_{\infty} a t_1 + T_1 a (E_0 - E_{\infty 1}) (e^{-(t-t_1)/T_1} - e^{-t_1/T_1}) + \\ & + T_2 a (E_{\infty 1} - E_{\infty 2}) (e^{-(t-t_1)/T_2} - e^{-t_1/T_2}) + \\ & + T_3 a (E_{\infty 2} - E_{\infty}) (e^{-(t-t_1)/T_3} - e^{-t_1/T_3}) \end{aligned} \quad (5)$$

Eqs.(4) and (5) are normally valid for the linear case with constant E-moduli. As a first approximation, variable E-moduli may also be used if their functions are correctly defined. The modulus of elasticity for a curved line can generally be defined either the instantaneous modulus ( $E = d\sigma/d\varepsilon$ ) or the secant modulus ( $E_s$ ). The difference in their use may be demonstrated in Hook's law:

$$\sigma = \int E(\varepsilon) d\varepsilon \quad \text{and} \quad \sigma = E_s(\varepsilon) \cdot \varepsilon$$

Because Eqs.(4) and (5) are obtained by integration, therefore, the secant moduli of elasticity must here be used. The same consideration is related to the multiple relaxation times.

The secant modulus of elasticity will be calculated by dividing Eq.(1) or (3) with the strain  $\varepsilon$ . This means that the E-moduli in the rheolo-

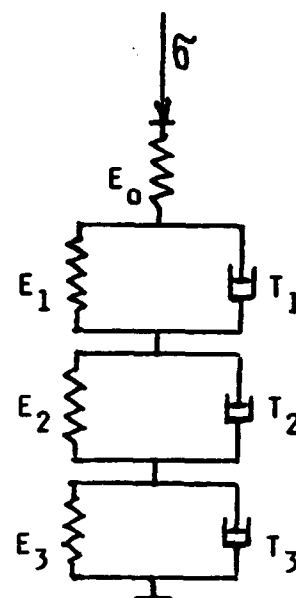


Fig. 2. Rheological model used

gical model have the form (using Eq.(3) with exponent  $n$ )

$$E_0 = C_0 \frac{\epsilon^{n-1}}{(1-\epsilon)^n} \quad E_1 = C_1 \frac{\epsilon^{n-1}}{(1-\epsilon)^n} \quad \text{etc.} \quad (6)$$

where  $C_0$ ,  $C_1$ ,  $C_2$  and  $C_3$  must be determined experimentally.

The averaged functions of relaxation times may be given in the form

$$T_i = \text{const.}/E_\infty^m \quad (7)$$

showing decreasing relaxation times with increasing modulus of elasticity.

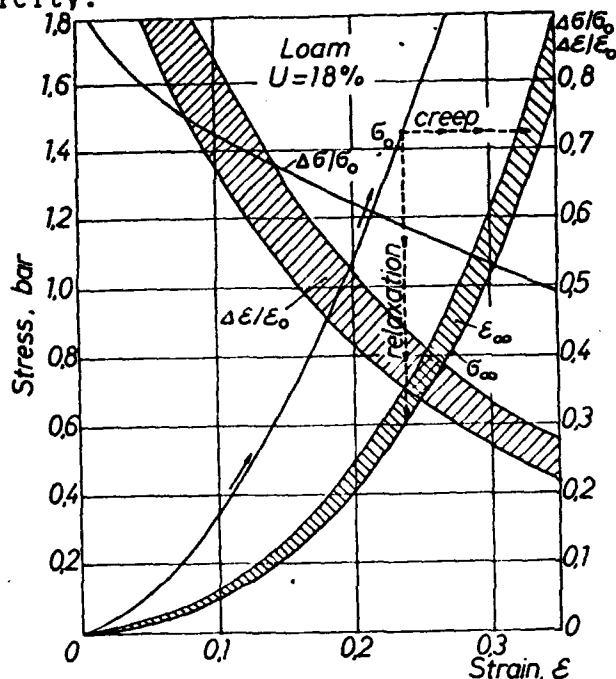


Fig.3. Confined compression of a loam soil.

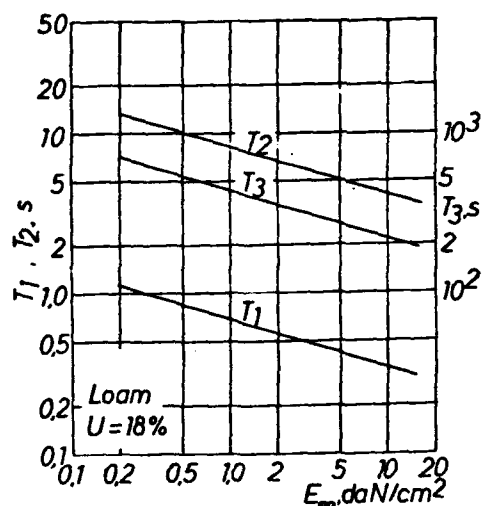


Fig.4. Multiple relaxation times for a loam soil.

The experimental results for confined compression are to be seen in Fig.3. The constants in Eq.(6) have the following values:  $C_0 = 12.1$ ,  $C_1 = 11.8$ ,  $C_2 = 41$ ,  $C_3 = 35.4$ . The compression curves have always a parabolic form. The curves  $G_0$  and  $G_\infty$  describe the compression for infinitely high and infinitely low loading velocities respectively. The relative stress relaxation ( $\Delta\epsilon/\epsilon_0$ ) decreases with increasing strains.

The relaxation times for several compaction rates and moisture content were obtained by the successive residual method. The experimental results for a moisture content of 18% are plotted in Fig. 4.

In Fig.3 the asymptotic creep values are also plotted. These values show a definite scattering (dotted zone) with some regularities: after a sudden load the end creep value is always somewhat smaller than those after a low velocity loading. This behavior may be explained by the different packing of soil particles as a function of loading velocity.

The calculations made have shown that the proposed quasi-linear model gives sufficient accuracy for different loading velocities using multiple relaxation times according to Fig.4. The subsequent creep shows a small systematic difference for high loading velocities, however, this discrepancy at practical loading velocities may be neglected.

A more rigorous examination shows that the exponent  $n$  varies with loading velocities. With increasing loading velocities the exponent  $n$  decreases.

## Unconfined Compression of Soils.

The most common case in the agricultural practice is the unconfined compression of soils. The soil exists as a semi-infinite three-dimensional medium. Since semi-infinite volumes of soil are loaded over small portions of their boundaries, distributions of forces must exist in the soil mass. However, this distribution is influenced and distorted by the facts that the soil has a special three-phase structural system and, therefore, it is compactable and practically always plastic flow occurs. Shear strains contribute to a rapid consolidation of soil volume elements giving more compaction at the same mean normal stress.

In respect to the above difficulties an experimental study was undertaken for determining basic regularities of the deformation zone under loading plates. Under deformation zone we understand here a volume within which a perceptible displacement of soil layers occurs. This displacement is a result of compaction and plastic flow. The perceptible stress zone must be much greater than the perceptible deformation zone. It may be assumed that outside of the perceptible deformation zone only elastic deformations occur at first. Furthermore, it may also be assumed that compaction of soil occurs only within the perceptible deformation zone.

The shape of the deformation zone and the relative displacement of layers in the center line are plotted in Fig. 5. The relative displacement of layers defined as

$$RD = \frac{l_i}{z_0} = \frac{z_0 - \sum \epsilon_i L_i}{z_0} = 1 - \sum \epsilon_i L_i / z_0$$

where

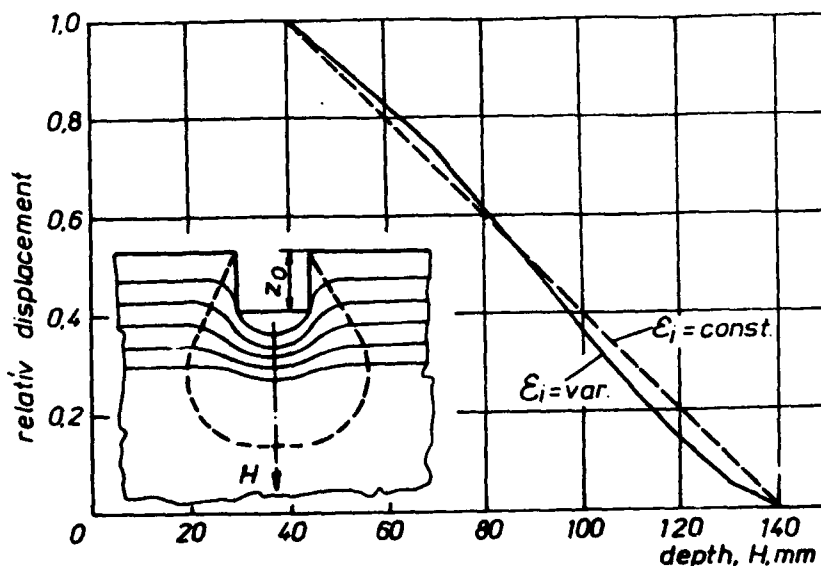
$l_i$  - displacement of a given layer,  
 $\epsilon_i$  - strain in a given layer including plastic flow,  
 $L_i$  - thickness of a given layer.

If the strain in all layers would be constant, so a straight line becomes valid. In practice the greatest strains are to be seen under the wedge of the soil body adhered to the plate surface.

The relative depth of the deformation zone as a function of relative plate-sinkage is plotted in Fig. 6.

The relationship may be described by the equation

$$\frac{H}{D} = 3.33 \left( \frac{z_0}{D} \right)^{0.67}$$



(7) Fig. 5. Relative Displacement of Soil Layers under Footings.

The relative width of the deformation zone is to be seen in Fig. 7. The relative width depends also on the plate diameter and the rela-

tionship can be given as

$$\frac{B}{D} = \frac{4.876}{0.55} \cdot \left(\frac{z_0}{D}\right)^{0.3} + 1$$

where  $D$  is the plate diameter taken in cm.

Knowing the main sizes of the deformation zone, the volume and other related values of the deformation zone can be calculated.

One of the related values is the ratio of the displaced soil volume to the total deformed volume,  $\Delta V_0/V$ . This relationship is plotted in Fig. 8 and may be described in the following manner (for  $z_0/D = 0.05 - 0.1$ ):

$$\Delta V_0/V = 0.0322 \cdot D^{0.35}$$

There is more interesting to study the load bearing capacity of the deformed volume. This relationship is given in Fig. 9, which may be approximated as

$$\frac{P}{V} = \frac{0.1086}{D^{0.65}}$$

From this Figure two important conclusions may be drawn. At first, the load bearing capacity of soils with increasing footing diameters decreases because the decreasing support action of soil masses located outside of the footing perimeter. Secondly, the relative sinkage of footing has a given influence only at smaller footing diameters. Tires have print diameters of 40 to 60 cm and, therefore, the influence of relative sinkage may be neglected. At the same time, The evaluation of footing measurements for bearing capacity determination may require to take the above statement into account.

The above measurement results and considerations are valid for a homogeneous semi-infinite medium. If in a given depth a firm layer acts then the deformation zone will be distorted and the stress distribution as a function of depth will be more equalized.

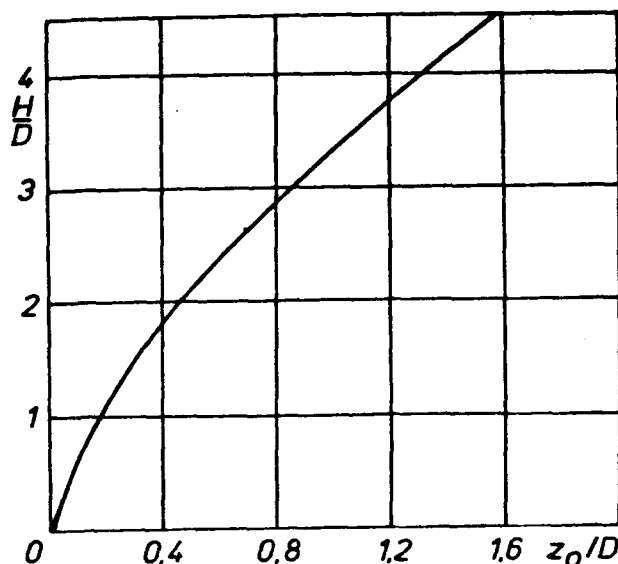


Fig. 6. The relative depth of the deformation zone.

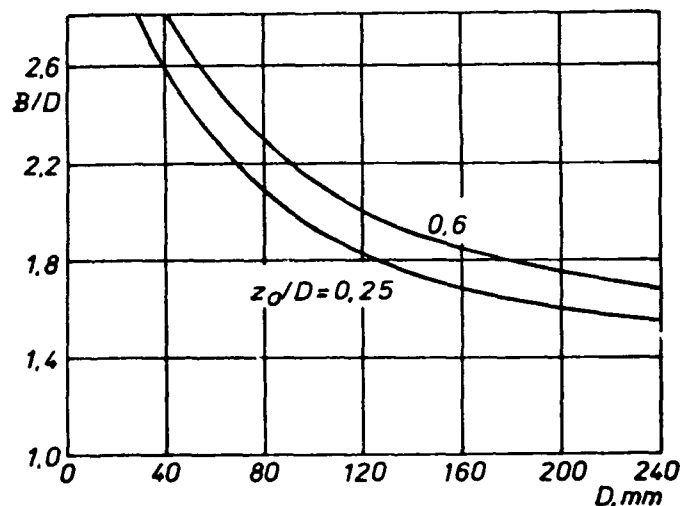


Fig. 7. The relative width of the deformation zone

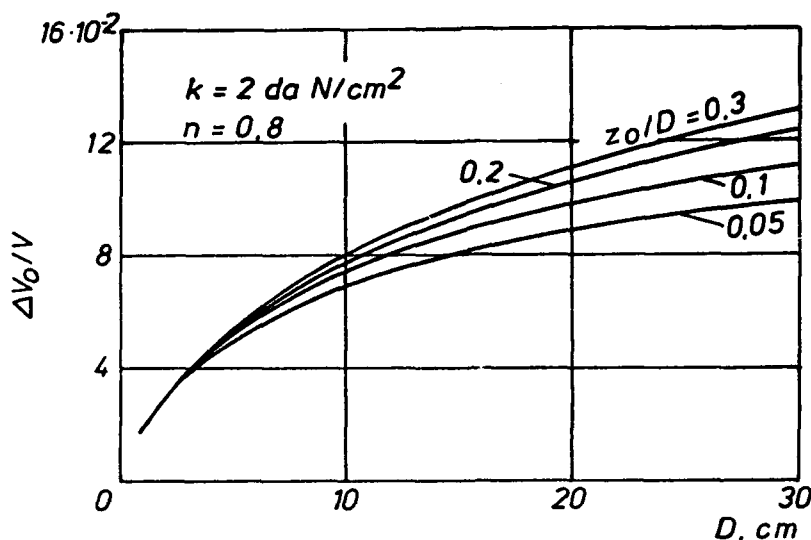


Fig. 8.  $\Delta V_0/V$  as a function of the footing diameter.

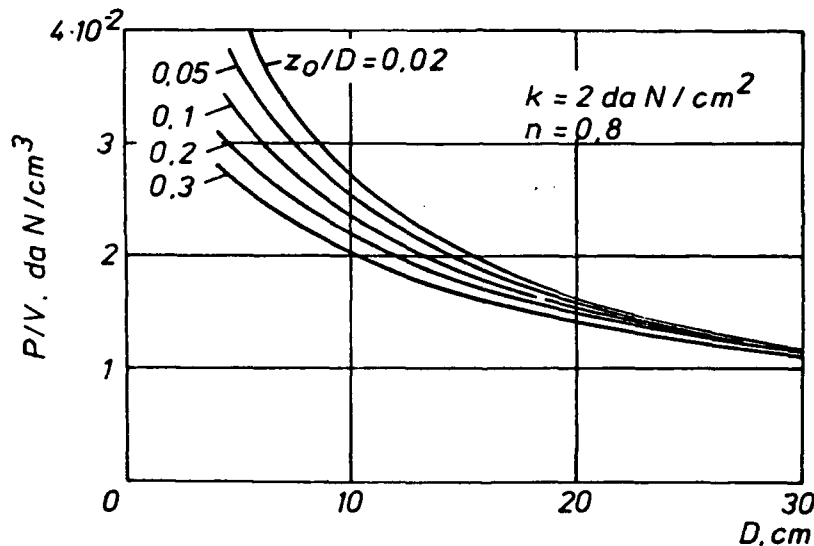


Fig. 9. The load bearing capacity of soil as a function of footing diameter.

### Conclusions

From the above theoretical and experimental investigations the following conclusions may be drawn:

- 1) The compaction process may be described only with the use of variable E-moduli in the rheological models,
- 2) The unconfined compression process of soils is a complicated phenomenon and the experimental methods take priority at that time,
- 3) The perceptible deformation zone under footing depends on the footing diameter and on the relative sinkage of the footing to a certain extent,
- 4) The load carrying capacity of soils decreases with increasing footing diameters and the influence of the relative sinkage, at the same time, will be negligible.



## L i t e r a t u r e

1. GILL, W. and G. VANDENBERG, Soil Dynamics in Tillage and Traction. ARS USDA, 1967.
2. SOHNE, W., Die Verformbarkeit des Ackerbodens. Grundlagen der Landtechnik, Heft 3, 1952.
3. SÖHNE, W., Einige Grundlagen für eine Landtechnische Bodenmechanik. Grundlagen der Landtechnik, Heft 7, 1956.

# THE RELATIONSHIP BETWEEN THE TECHNICAL, AGROTECHNICAL AND ENERGY PARAMETERS OF MEDIUM-DEEP TILLAGE IMPLEMENTS

*Dr. István J. Jóri - Dr. Sándor Soós*

*Hungarian Institute of Agricultural Engineering  
Gödöllő, Hungary*

## SUMMARY

The detrimental compacting effect of agricultural vehicles, including tractors, harvesting machinery, transport vehicles and tillage implements, rises parallel with any increase in the capacities and the weight of the vehicles. Today, the detrimental effects can be noted not only in the top layers of the soil but in other layers as well deeper down.

One of the methods to eliminate detrimental soil compacting is medium-deep tillage which is becoming more and more widespread these days. Due to variations in the locations of operation and the jobs to be performed, different tillage implement and engine parameters are required. Therefore, research is aimed at selecting the most favourable tillage angle ranges and implement widths. At the same time, a medium-deep tillage implement has been developed in which the clearance between the gusset plates is continuously adjustable in the 425 - 700 mm range. The new implement is capable of fully satisfying varying agrotechnical and energy requirements.

## INTRODUCTION

It is becoming more and more difficult to perform the most important soil tillage function, i.e. the provision of optimum conditions for crops. Increasing the intensity of crop production implies that the number of machinery in the production areas would also increase. The greater weight of tractors, combine harvesters and transport vehicles means that axle load is increasing which in turn means that soil compacting is intensified. The increase in density falls gradually as we go deeper, although it may still be noticeable at a depth of one meter. The other cause for the increase in density is in soil tillage itself due to the extensive use of disk-harrows, known to have a serious compacting effect, and ploughing done repeatedly at the same depth.

Consequently, there are compacted layers at the soil surface and immediately below (at 15-20 cm) and at the limit of primary cultivation (at 30-35 cm). These layers hinder the flow of water, air and nutritive matter and the development of roots and ultimately reduce the volume of crops. Deterioration in water percolation is indicated by the fact that pools and rivulets appear on the surface from time to time. Soils with compacted layers can be cultivated only with increased energy consumption and heightened wear and tear on tillage implements with undercuts the profitability of crop production.

Considering the above statements, the assignment to be addressed is clear: detrimental soil compacting has be eliminated and its development has to be precluded.

Several procedures are known and available to preclude soil compacting. Some of them are actually used, some have been forgotten and some are described only in technical literature:

- optimum crop production systems (crop rotation),
- minimum soil cultivation (pressure on soil and detrimental impact on soil can be reduced via the combination of tillage operations and by cutting the number of runs),
- rational machinery operation (appropriate timing of operations and choice of tillage implements best matched to soil conditions, the application of running gear types that help reduce compacting, tillage path or controlled run cultivation).

Detrimental soil compacting can be eliminated by proper primary tillage operations. Primary tillage operations include the methods that change the physical properties of deep soil layers. One of the typical features of primary tillage is that the impact last for relatively long periods of time. Primary tillage can be achieved by using any of the following three methods:

- turning by plough,
- loosening without turning,
- combining the above two methods.

Our research efforts have been concentrated in the following fields in order to identify and discover the relationship between the technical, work quality and energy parameters of medium-deep tillage implements working in the 26-50 cm range:

- the identification of the most favourable angle for medium-deep tillage implement blades and the definition of the best value to the tillage blade width;
- the development of a frame to ensure the most appropriate geometric and energy-intensive connection between the tractor and the tillage implement.

## TEST METHODS AND CONDITIONS

We have been using a frame for testing, made of a RABA-IH-10-14 medium-deep tiller, taken from serial production. Implement blades, developed for the purposes of the experiment with different angles and width, were mounted on the middle gusset plate which was the only one left on the medium-deep tiller. This way, we could ensure identical adjustability and identical positioning of the various tillage blades which was a core requirement for comparisons. The different tillage blades were compared on the basis of their impact on the soil surface, the cross section of the cores obtained and the traction resistance. Measuring was performed at a nominal working depth of 40 cm at three speeds ( $5-9 \text{ km.h}^{-1}$ ) with six re-runs.

In order to map all the possible applications of the VFK-5 medium-deep tiller with adjustable working width, tests were conducted under given conditions with all the versions in every speed range. Work quality and energy-intensity parameters were specified at a nominal working depth of 40 cm with three different gusset plate clearances (minimum, medium and maximum), using three different working depths (30, 40 and 50 cm) with the medium clearance of the gussets. Measurements were performed six times.

The tillage implement tests were conducted at the "Vörös Csillag" Agricultural Co-operative of Balatonszárszó in 1987. The testing area was a flat wheat stubble field with sandy clay soil. In the 0-50 cm range, the moisture content of the soil was between 12.5 - 17.0%. The measuring frame was mounted on a FIAT 1880 DT tractor.

Tests with the VFK-5 medium-deep tiller were conducted at the Kimle Unit of the Lajta-Hanság State Farm in 1989.

The testing area was flat hybar stubble field with clay soil. In the 0-55 cm range, the moisture content of the soil was between 17.2 - 22.5%. The medium-deep tiller was operated with a Tba-245 tractor.

## TEST RESULTS

When testing the tiller blades, we wished to find out what is the impact of

- the angle (20-25°) and
- the adjustment of the tiller blades (60-300 mm)

on work quality and energy-intensity parameters. Tillage implements were evaluated by comparing work quality and energy-intensity features.

Work done with tillers with four different angles, identical settings and speed ranges was evaluated on the basis of the sketches drawn about the cross sections of the cores. Considering the findings it is evident that settings below 20° and above 30 must not be taken into account as the impact of the implements is much smaller than in the 25-30° range. When reviewing the change in the cross section of the soil, which is the most tell-tale feature of tillers, we found that in soils with medium hardness the 30° was the most favourable.

When reviewing the effects of increasing the tiller blade width on work quality we found that, contrary to our expectations, increasing the width of the tiller wedge produced unfavourable changes. The performance of the winged wedges was clearly better than that of the simple ones which was reflected in the combined growth of the cross section cultivated and the working width. However, increasing the

wing width failed to bring about significant changes that would be comparable with those produced by the replacement of the loosening wedge by the winged blade. Considering this, it seems that the most appropriate wing width should be specified on the basis of energy-intensity and design aspects.

When reviewing the energy-intensity data of the various tillers subject to working speed we found that angles should be increased only up to the point until proper loosening effect is achieved. With a view to tiller performance it is evident that a  $30^{\circ}$  angle is the most favourable considering traction resistance both for working width and the cross section cultivated, to be followed by  $25^{\circ}$  and  $35^{\circ}$  blades.

When analyzing the effects of changing the implement width we found that there is a definitive sequence of the specific features in which tiller performance is also taken into account. Winged blades were found to be more advantageous in every aspect. The difference between the 200 - 300 mm width is not crucial therefore actual values should be selected on the basis of considerations concerning tensile strength.

Following the definition of the tiller blade parameters and the selection of the most favourable shapes and sizes, we have turned our attention to the connection between the tractor and the tillage implement. If identical tillage implements are used, this connection has the most crucial impact upon the conditions of using the medium-deep tillers.

Wide-ranging field tests have proven that suspended medium-deep tillers cannot be properly used with staggered steering tractors (these types are most wide-spread in Hungarian agriculture), as steering maneuvers place an unavoidably detrimental load on the tillage implement.

While at work, some parts of the tractor, such as the hinge and the suspension bars, or the gusset plates of the medium-deep tiller may be deformed or get broken.

Within a given range (30-50 cm), the depth of loosening may change subject to soil conditions and the needs of the crops grown in the field. Whenever working at a certain depth, the type of the tiller or the clearance among the gusset plates have to be correctly chosen in order to achieve the necessary loosening effect.

In the case of the traditional devices, blade replacement or changing the gusset plate clearance is a limited, time-consuming and difficult operation. Assembly work is required if the traction requirements of the tractor used and the traction resistance of the medium-deep tiller are not harmonized. More often than not, harmony could be established by adjusting the clearance among the gusset plates or by changing the working width of the machine.

To overcome these problems, we have developed a medium-deep tiller with adjustable working width. The articulated attachment of the gusset plates allows for diagonal movement during steering thereby precluding the development of detrimental loads.

The adjustment of the angle between the two stems of the V-shaped frame and the self-adjusting gusset plates enable us to adjust the clearance between the gusset plates. The adjustability of the gusset plate clearance is of vital importance concerning the harmonization of working depth and loosening effect which is well-known from several publications. Another advantage of the new solution is that in addition to achieving a loosening effect, proper energy harmonization can be achieved between the tractor and the tillage implement.



The work quality features of the implement were specified at three different working depths while the gusset plates were positioned in the two extreme and the one middle positions. The analysis of the work quality features at the different positions has substantiated the view in that gusset plate clearance and working depth are interrelated values. Under given conditions the following pairs of clearance (mm) x working depth (cm) values prevail: (a) 425 x 30; (b) 600 x 40; and (c) 700 x 50.

Energy-intensity features were specified in settings which were identical with those used in the case of the work quality features. On the basis of the results it was found that adjustment parameters exert considerable influence on the traction resistance of the medium-deep tillers. Parallel with increasing the clearance between the gusset plates, traction resistance per unit of working width and capacities required decreases.

However, in response to increasing the working width, both the absolute and the specific values of traction resistance increase. The conclusion is that loosening must be done at the depth as required strictly in accordance with the agro-technical requirements. The highest possible gusset plate clearance should be selected to go with the working depth which would still ensure the best necessary loosening in a profitable way.

In addition to ensuring a practical and quick adjustment of working width and depth, another advantage of the new medium-deep tiller is that it can be adapted to the staggered steering tractors, the constraints on public road transport (max. 2.5m) can be met and the danger of congestion can be reduced.

## CONCLUSIONS

Considering the results and the findings of the tests, the following conclusions can be drawn:

(1) about tiller design (loosening wedge and wing):

- \* The angle of the loosening wedge has an optimum value in the range under review, considering its impact on the cross section of the soil loosened and the size of the specific traction resistance. On a medium-hard soil, the optimum angle is  $30^{\circ}$ .
- \* The soil cross section loosened by the tiller blades can be increased by using the loosening wings. The loosening angle of the winged blade is greater than that of the traditional blades. As a result, the critical depth of the blade increases therefore the clearance between the gusset plates (the working width of the tiller) can be increased while the loosening effect will remain the same.
- \* The loosening wings increase the lowering effect of the tiller component. In a medium-hard soil, this effect produces a 1-2 cm increase in working depth.
- \* The traction resistance of the winged blades is lower in the range under review than that of the simple blades across the loosened soil cross section.
- \* The most favourable width range of the winged blade from a work quality and energy-intensity aspect in medium-hard soil is 200 - 300 mm.

(2) about the VFK-5 medium-deep tiller with variable working width:

- \* The new frame and the arrangement used to attach the gusset blades enables the use of suspended medium-deep tillers with staggered-steering tractors without deformations or component breakage.
- \* In the new medium-deep tiller, the gusset plate clearance is continuously adjustable between 425 - 700 mm.

Consequently:

- \*\* Blade clearance can be adjusted simply, quickly and easily to match the loosening depth, required in accordance with agro-technical requirements.
- \*\* Desired loosening effect can be achieved without implement replacement or re-assembly by adjusting the gusset plate clearance to match changing soil types and conditions.
- \*\* The traction capacity of the tractor and the traction resistance of the medium-deep tiller can be harmonized despite changing conditions which ensures the maintenance of the optimum loosening depth and speed.

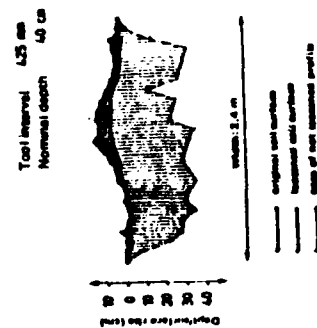


Fig. 2.: Transverse profile of the soil with minimum tool intervals

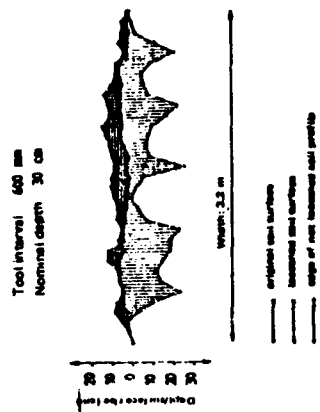


Fig. 4.: Transverse profile of the soil with maximum working depth

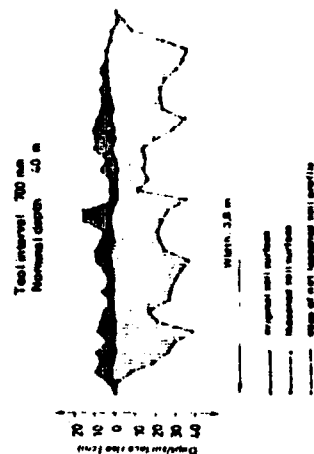


Fig. 3.: Transverse profile of the soil with maximum tool intervals

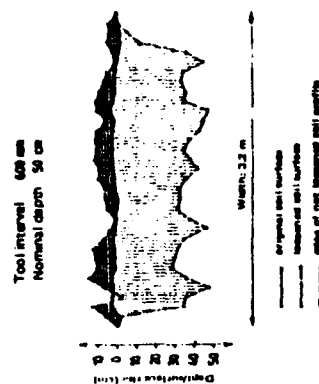
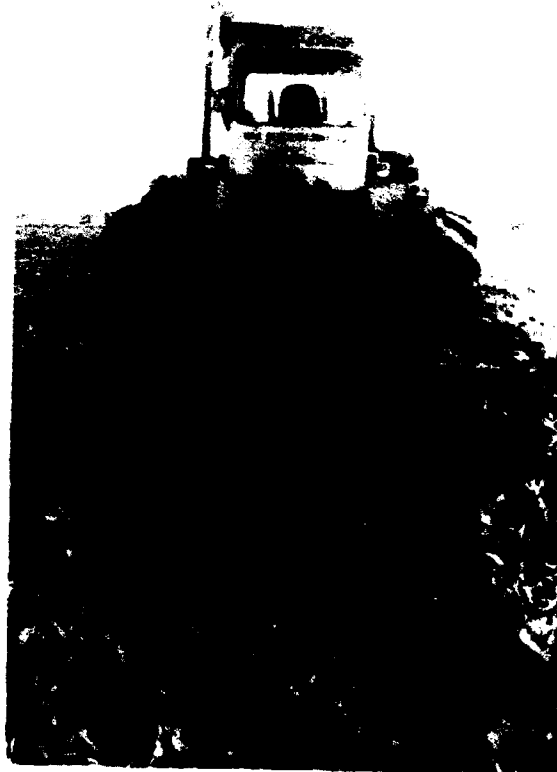
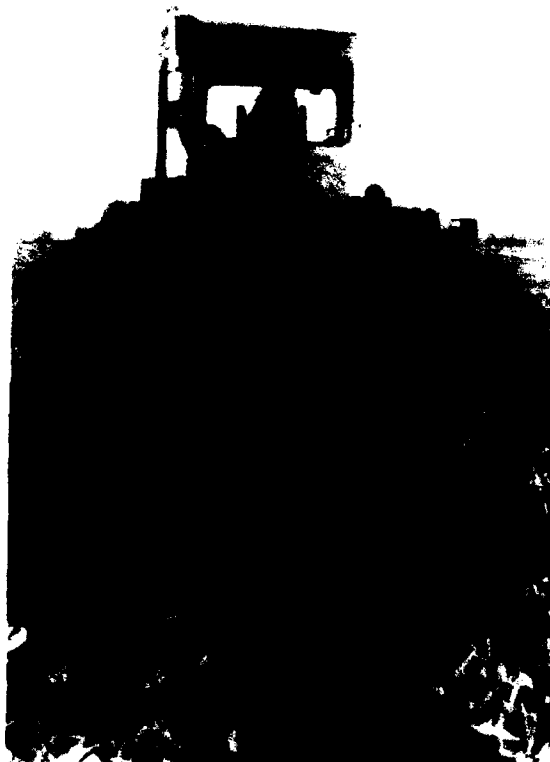


Fig. 5.: Transverse profile of the soil with maximum working depth

## List of figures

1. Figure: VFK-5 medium-deep tiller
2. Figure: Transverse profile of the soil with minimum tool intervals
3. Figure: Transverse profile of the soil with maximum tool intervals
4. Figure: Transverse profile of the soil with maximum Working depth
5. Figure: Transverse profile of the soil with maximum Working depth
6. Figure: VFK-5 medium-deep tiller in position with minimum tool intervals
7. Figure: VFK-5 medium-deep tiller in position with maximum tool intervals



# THE EFFECTS OF VARIOUS DESIGN PARAMETERS ON THE TRACTIVE PERFORMANCE OF RUBBER TRACKS

M J Dwyer, J A Okello and F B Cottrell

Silsoe Research Institute (formerly AFRC Engineering), England

The tractive performance of an experimental rubber track unit was compared with that of a 16.9 R34 tractor driving wheel tyre, in six different field conditions, using a single wheel tester. Tractive performance was assessed in terms of coefficient of rolling resistance, maximum coefficient of traction, maximum tractive efficiency and coefficient of traction and slip at maximum tractive efficiency. The track unit was fitted in turn with two rubber tracks having different tread patterns. Tests were carried out with vertical loads of 1700 kg and 2000 kg. The results of the comparison between the tractive performance of the tracks and the tyre confirmed the results from a previous investigation and showed that the tracks gave a higher coefficient of traction with less slip, but also had a higher rolling resistance, which resulted in similar values for tractive efficiency. The differences between the tread patterns of the two rubber tracks had no statistically significant effect on their tractive performance.

## 1. INTRODUCTION

For many years rubber tracks have held out the promise of obtaining improved tractive performance from off-road vehicles by combining the better field performance of steel tracks with the road-going capability of pneumatic tyres<sup>1</sup>. The Bonmartini pneumatic track was found to be very successful technically<sup>2</sup>, but it was not adopted commercially, presumably because of its complexity and cost of manufacture. The most notable recent development in the application of rubber tracks to agricultural vehicles has been the introduction of the Caterpillar Challenger rubber-tracked tracklayer<sup>3</sup>.

Initial work on rubber tracks at Silsoe Research Institute attempted to use a friction drive to the rubber track from a pneumatic tyre<sup>4,5</sup>. This proved to be impracticable and the first satisfactory comparative data between the tractive performance of a tyre and rubber track were obtained using a small rubber-tracked dumper and a two-wheel drive agricultural tractor having the same weight on its driving axle<sup>6</sup>. The rubber track of the dumper was positively driven from a sprocket on the axle. The comparison showed that the rubber-tracked vehicle gave more drawbar pull with less slip than the wheeled tractor, but had a higher rolling resistance, resulting in similar values of tractive efficiency.

A more detailed comparison of the tractive performance of a rubber track and a tractor driving wheel tyre<sup>7</sup> was carried out using the Silsoe Research Institute single wheel tester<sup>8</sup>. This confirmed the results of the previous experiments using the dumper, showing the potential of the rubber track, but emphasising the need to reduce internal rolling resistance losses, if the full potential was to be realised. However, the rubber track used in this experiment was not one which was designed to be positively driven and it had been necessary to drive onto the guide horns, which were only normally intended to provide lateral guidance, in a way which may have caused higher than normal power losses.

The work described here was carried out to provide further comparative data between the tractive performance of a rubber track and a tyre, using a more appropriate drive to the track, and to compare two tracks with different tread patterns.

## 2. EXPERIMENTAL EQUIPMENT

The rubber tracks used in the experiment were made by the Japanese Bridgestone company, primarily for earthmoving equipment. They are reinforced longitudinally with steel wire and transversely with steel plates which engage with the teeth of the driving sprocket. One track had straight transverse lugs and the other had lugs set at an angle, as shown in Fig. 1. The main dimensions of the tracks are shown in Table 1.



Fig. 1 Rubber track tread patterns

Table 1 Track dimensions, mm

	Straight lugs	Angled lugs
Track width	375	375
Track length	5040	5040
Track thickness	27.5	27
Lug height	35	25
Lug width at tip	12	14
Lug pitch	90	90
Sprocket and idler diameter	387	387
Sprocket to idler centre distance	1750	1750
Roller diameter	200	200

The tractive performance of the tracks was compared with that of a conventional 16.9 R34 radial ply tractor driving wheel tyre with R1 tread pattern. Both were tested with vertical loads of 1700 kg and 2000 kg. The inflation pressure of the tyre was 1.0 bar for the lower load and 1.3 bar for the higher load.

## 3. EXPERIMENTAL PROCEDURE

The single wheel tester is fitted with two independent hydrostatic transmissions, one of which drives the test wheel or track and the other of which drives the main vehicle. A traction test is carried out by maintaining the test wheel or track rotational speed approximately constant whilst gradually reducing the forward speed of the vehicle. This causes the torque input to the test wheel or track, the forward thrust produced and the slip to increase. These parameters are all recorded continuously.

In the tests described here the rolling resistance of the tyre or track was first measured by driving the tester forward, with zero torque in the driveline to the test carriage, and measuring the towing force required. This was then divided by the vertical load on the test carriage to calculate the coefficient of rolling resistance.

Wheel or track slip was derived from the rotational speed of the drive to the test carriage and the forward speed of the vehicle measured by a small trailing track unit. Zero slip was defined as occurring when just sufficient input torque was applied to overcome the rolling resistance, but the forward thrust was zero.



Tractive efficiency was defined as follows:

$$\eta = \frac{COT(1-S)}{COT + CORR} \quad \dots\dots\dots(1)$$

where  $\eta$  = tractive efficiency  
 COT = coefficient of traction (forward thrust/vertical load)  
 S = slip  
 CORR = coefficient of rolling resistance

Each test for the tyre or track at either vertical load consisted of six separate runs in different places in the field to minimise the effect of variations in soil conditions within the test area. Data from the six runs were then put together to comprise a single set of test results. Tests were started with a no-slip speed of approximately 5 km/h.

Soil conditions were defined by particle size classification, plastic limit, moisture content and the average cone penetrometer resistance measured through the top 225 mm depth.

#### 4. FIELD CONDITIONS

Tests were carried out in 1990 in the 6 field conditions described in Table 2.

Table 2. Field conditions

Field No.	Month	Surface	Soil type	Plastic limit, %	Moisture content, %	Cone index, kPa
1	Jan	Ploughed and rolled	SCL	18	17	560
2	Jan	Ploughed and rolled	SCL	18	16	391
3	June	Grass	Clay	27	18	2029
4	July	Discd	Clay	27	5	1263
5	July	Stubble	SCL	*	6	1650
6	Sept	Ploughed	SCL	*	10	196

SCL = Sandy clay loam      \*Too sandy to record

#### 5. RESULTS

Examples of relationships between coefficient of traction and slip and between tractive efficiency and coefficient of traction for the tyre and track respectively with a vertical load of 1700 kg, in Field 5, are shown in Figs. 2-5. Curves were fitted to all the coefficient of traction/slip relationships, by a least squares method, assuming the relationship to be of the following form, derived from Bekker<sup>9</sup> and Janosi and Hanamoto<sup>10</sup>.

$$COT = A (1 - B/S(1 - e^{-a/B})) \quad \dots\dots\dots(2)$$

where A and B are constants derived from the curve fitting technique.

The curves for the tractive efficiency/coefficient of traction relationships were derived from equations (1) and (2) and the measured value of coefficient of rolling resistance.

The measured values of coefficient of rolling resistance and the values of maximum coefficient of traction, maximum tractive efficiency and coefficient of traction and slip at maximum tractive efficiency obtained from the curve fitting technique are shown in Tables 3, 4, 5, 6 and 7 respectively.

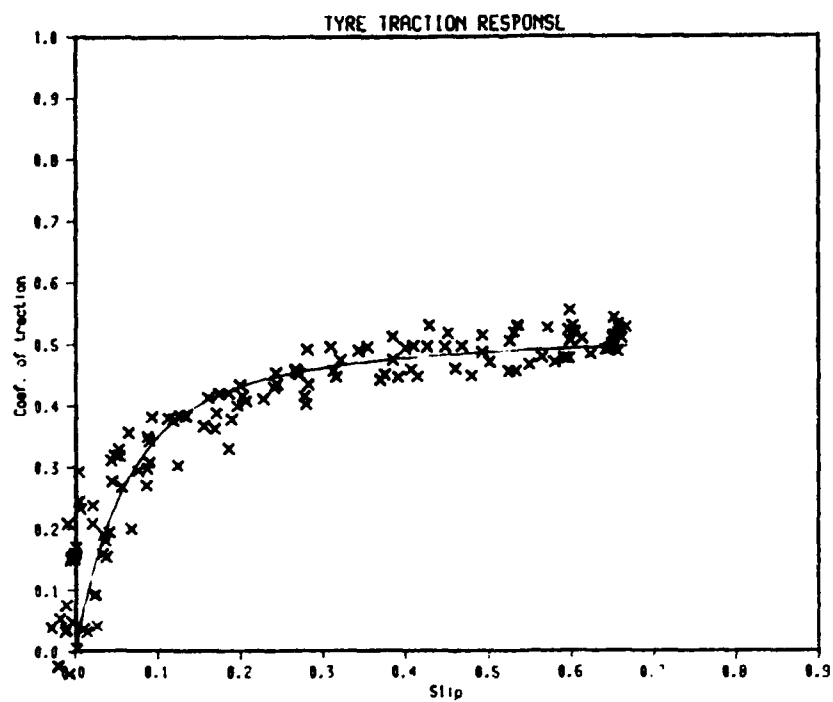


Fig 2 Relationship between coefficient of traction and slip for tyre

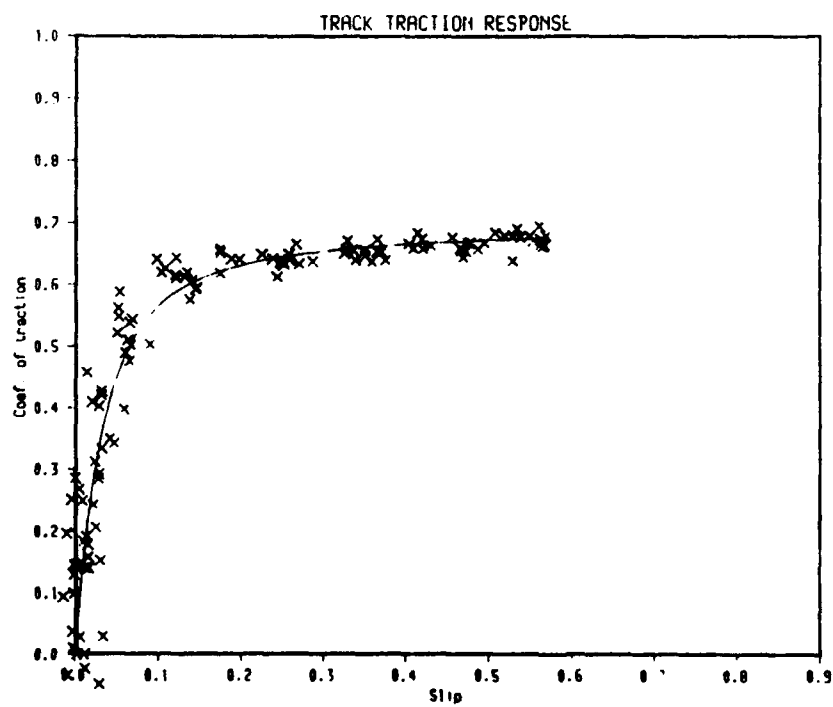


Fig 3 Relationship between coefficient of traction and slip for track

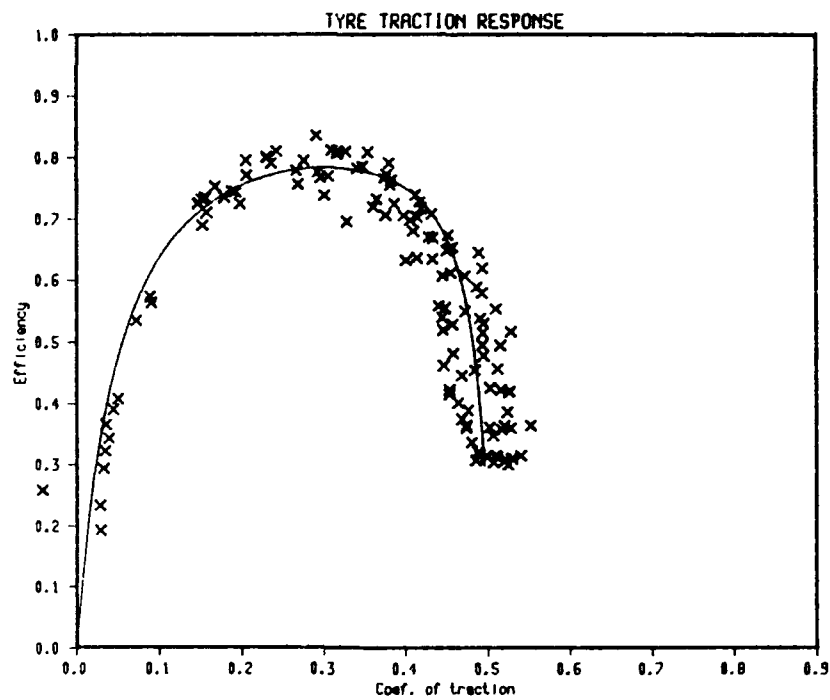


Fig. 4 Relationship between tractive efficiency and coefficient of traction for tyre

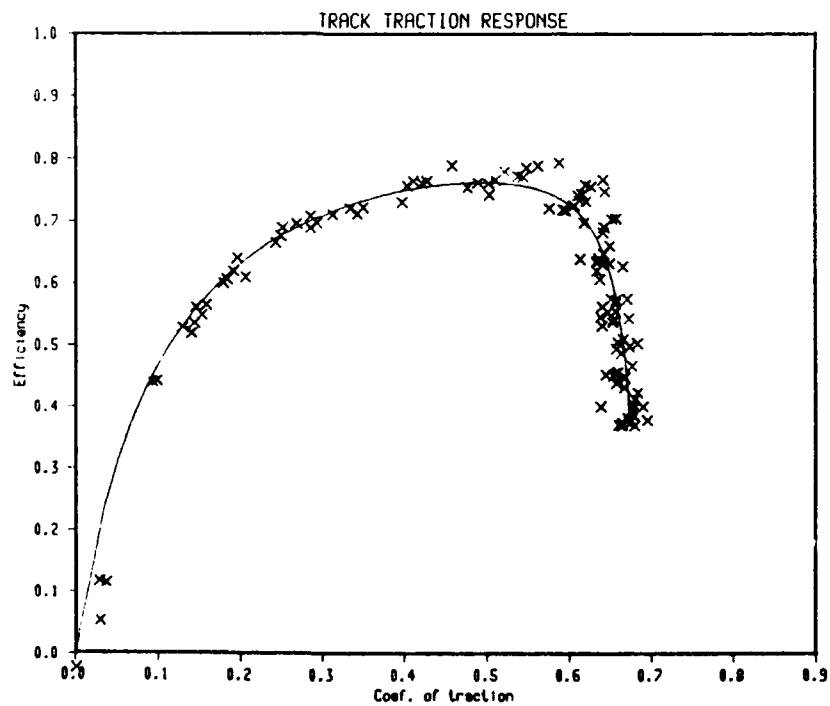


Fig. 5 Relationship between tractive efficiency and coefficient of traction for track

Table 3 Coefficient of rolling resistance

Field No.	1700 kg			2000 kg		
	Tyre	Track		Tyre	Track	
		Straight lugs	Angled lugs		Straight lugs	Angled lugs
1	0.09	0.19	0.21	0.11	0.19	0.19
2	0.11	0.21	0.20	0.13	0.20	0.19
3	0.07	0.16	0.17	0.08	0.16	0.12
4	0.08	0.16	0.19	0.08	0.16	0.16
5	0.06	0.11	0.12	0.05	0.10	0.11
6	0.13	0.20	0.20	0.13	0.19	0.19
Mean	0.09	0.17	0.18	0.10	0.17	0.16

Table 4 Maximum coefficient of traction

Field No.	1700 kg			2000 kg		
	Tyre	Track		Tyre	Track	
		Straight lugs	Angled lugs		Straight lugs	Angled lugs
1	0.52	0.68	0.67	0.40	0.65	0.58
2	0.50	0.68	0.68	0.48	0.66	0.65
3	0.83	0.83	0.75	0.78	0.78	0.77
4	0.68	0.61	0.62	0.74	0.64	0.62
5	0.52	0.67	0.64	0.54	0.64	0.63
6	0.58	0.70	0.67	0.48	0.69	0.66
Mean	0.61	0.70	0.67	0.57	0.68	0.65

Table 5 Maximum tractive efficiency, %

Field No.	1700 kg			2000 kg		
	Tyre	Track		Tyre	Track	
		Straight lugs	Angled lugs		Straight lugs	Angled lugs
1	72	67	66	66	68	65
2	68	66	67	64	66	66
3	79	74	72	77	74	77
4	72	67	65	73	69	67
5	78	76	76	82	77	77
6	64	65	64	63	65	64
Mean	72	69	68	71	70	69

Table 6 Coefficient of traction at maximum tractive efficiency

Field No	1700 kg			2000 kg		
	Tyre	Track		Tyre	Track	
		Straight lugs	Angled lugs		Straight lugs	Angled lugs
1	0.34	0.52	0.52	0.30	0.51	0.46
2	0.33	0.53	0.53	0.34	0.51	0.50
3	0.44	0.58	0.56	0.41	0.57	0.54
4	0.34	0.45	0.46	0.36	0.47	0.45
5	0.30	0.49	0.49	0.32	0.47	0.48
6	0.35	0.49	0.48	0.32	0.48	0.47
Mean	0.35	0.51	0.51	0.34	0.50	0.48

Table 7 Slip at maximum tractive efficiency, %

Field No	1700 kg			2000 kg		
	Tyre	Track		Tyre	Track	
		Straight lugs	Angled lugs		Straight lugs	Angled lugs
1	9	8	8	9	7	8
2	10	8	8	10	8	8
3	8	6	6	9	5	5
4	11	8	9	11	8	8
5	7	6	6	6	6	5
6	12	9	10	12	10	9
Mean	10	8	8	10	7	7

## 6. DISCUSSIONS

The results were analysed statistically to determine significant differences. The coefficient of rolling resistance of the rubber tracks was higher than that of the tyre, with 99% probability. Also, the coefficient of rolling resistance of the tracks when carrying a vertical load of 1700 kg was higher than when carrying a vertical load of 2000 kg, with 99% probability. The ruts formed by the tracks were, however, shallower than those caused by the tyre. Therefore, the major part of the rolling resistance of the tracks must have been due to internal power losses and, therefore, independent of the vertical load. These power losses could be caused by friction at the teeth of the driving sprocket, hysteresis in the rubber, as it flexed around the sprocket and idler, or friction in the bearings of the sprocket, idler and rollers. These power losses were slightly less than those measured with a previous rubber track<sup>7</sup>, when there was clearly a lot of friction at the sprocket. No other differences in coefficient of rolling resistance were statistically significant.

The maximum coefficient of traction of the rubber tracks was higher than that of the tyre with 99% probability. No other differences in maximum coefficient of traction were statistically significant. It was apparent, however, that in Fields 3 and 4, which both had a more slippery or loose surface, overlying firmer

soil, the tyre produced higher maximum coefficients of traction than the rubber tracks. This may have been because the higher contact pressure or more aggressive lugs on the tyre enabled it to bite through the surface cover and dig down more easily to the stronger soil below. There were insufficient data in these conditions, however, to have statistically significant evidence for this.

Because of the lower rolling resistance of the tyre, its maximum tractive efficiency was higher than that of the rubber tracks, with 99% probability. No other differences in tractive efficiency were statistically significant.

The coefficient of traction at maximum tractive efficiency was higher for the rubber tracks than for the tyre, with 99% probability. This confirms the results of previous work and the potential for rubber tracks to reduce the weight of vehicles without reducing tractive performance. The coefficient of traction at maximum tractive efficiency was also higher for the rubber tracks when carrying a 1700 kg vertical load than when carrying a 2000 kg vertical load, with 95% probability. This is probably due to the higher coefficient of rolling resistance at 1700 kg. No other differences in coefficient of traction at maximum tractive efficiency were statistically significant.

The slip at maximum tractive efficiency was lower for the rubber tracks than for the tyre, with 99% probability. This is a function of the better tractive performance of the tracks, particularly in the mid-range of coefficients of traction. The slip at maximum tractive efficiency was higher for the rubber tracks when carrying a 1700 kg vertical load than when carrying a 2000 kg vertical load, with 95% probability. This is consistent with the higher coefficient of traction at maximum efficiency and higher coefficient of rolling resistance. No other differences in slip at maximum tractive efficiency were statistically significant.

## 7. CONCLUSIONS

The rubber tracks had higher rolling resistances than the tractor driving wheel tyre. This appeared to be due to internal power losses in the track unit.

The rubber tracks produced generally higher values of coefficient of traction than the tyre.

Because of the higher rolling resistance of the rubber tracks, their maximum tractive efficiency was lower than that of the tyre.

The coefficient of traction of the tracks at maximum tractive efficiency was consistently higher than that of the tyre and the slip at maximum tractive efficiency was consistently lower.

The differences between the tread patterns of the two rubber tracks had no statistically significant effect on their tractive performance.

## REFERENCES

1. Culshaw, D.W. Rubber tracks for traction. J. Terramech. 1988, 24,1,69-80
2. Taylor, J.H. Burt, E.C. Track and tire performance in agricultural soils. Trans. Am. Soc. Agric. Engrs., 1975, 18,3-7
3. Evans, W.C. and Gove, D.S. Rubber belt track in agriculture. Am. Soc. Agric. Engrs., 1986, Paper No. 86-1061
4. Mickelson, P.I. Rubber tracks for machinery and vehicles in forestry and agriculture. Proc. 8th Int. Conf. of ISTVS, Cambridge, 1984
5. Culshaw, D.W. and Dawson, J.R. The performance of a simple rubber track for an agricultural vehicle. Div. Note DN 1382, Silsoe Research Institute, 1987
6. Culshaw, D.W. Tractive performance of a small rubber-tracked vehicle. Div. Note DN 1389, Silsoe Research Institute, 1987
7. Dwyer, M.J., Okello, J.A. and Cottrell, F.B. A comparison of the tractive performance of a rubber track and a tractor driving wheel tyre. Proc. 9th Int. Conf. of ISTVS, Kobe, 1990
8. Billington, W.P. The Mk II Single wheel tester. J. Agric. Engng. Res., 1973, 18,67-70
9. Bekker, M.G. Off-the-road locomotion. University of Michigan Press, Ann Arbor, 1960
10. Janosi, Z. and Hanamoto, B. Analytical determination of drawbar pull as a function of slip for tracked vehicles in deformable soils. Proc. 1st Int. Conf. of ISTVS, Turin, 1981

ON THE KINEMATICALLY ADMISSIBLE SOLUTIONS FOR  
SOIL-TOOL INTERACTION DESCRIPTION IN THE CASE  
OF HEAVY MACHINES WORKING PROCESS

W. Trampczyński, J. Maciejewski

Institute of Fundamental Technological Research  
Polish Academy of Sciences  
Świetokrzyska 21, 00-049 Warsaw, Poland

Summary

The paper concerns simplified theoretical analysis of such complex soil shoving processes, as for example process of moving walls in the way similar to such heavy machine tools as the loading machine bucket, the excavator bucket and so on. Assuming material to be rigid perfectly plastic with strain behavior governed by the modified Coulomb-Mohr yield criterion, kinematically admissible solutions were found. It was shown that using this technique one can study this process as and soil-tool interactions. Such results can not be obtained using the characteristics methods or any other simple method of theory of plasticity. Characteristic scale-shaped rigid zones generated during cohesive soil cutting process were predicted, without any additional assumptions about crack initiations and energetic criterions of propagation. Theoretical results were compared, in qualitative manner, with experimental data.

Although it is difficult to estimate this way the complete solutions for such problems, some advices how to find the more efficient ways of the tool moving process can be pointed out.

1. Introduction

It is well known that earth moving process due to construction works etc. realized by heavy machines such as loaders and excavators is energetically very ineffective and its optimization

can save a lot of energy. Although it is the earth cutting process itself which is the most important for this problem, it has no proper theoretical description until now. In this paper, the model based on mathematical theory of plasticity is applied to describe it. Within this theory the earth cutting process is considered as the problem of passive pressures exerted by a granular material on a rigid wall shaped similarly to heavy machine tools.

The problem of passive and active pressures exerted by a granular medium on a rigid wall in a plane strain conditions has a quite broad literature. Several theoretical solutions (as well for statics as for kinematics) were obtained within theory of plasticity under the assumption of the rigid-perfectly plastic behavior of a granular material [1,2,3]. Quite often the method of characteristics was used to solve full set of static and kinematic equations. Although a lot of boundary value problems were solved this way, several limitation in obtaining complete solutions and kinematically admissible solutions were observed [4,5]. It was shown that it is not possible to follow this way more complex processes, as for example process of moving walls in the way similar to such heavy machines tools as bulldozer blades or loader buckets. Since theoretical description of such processes can have quite great practical importance, a simplified technique was used to describe it in [6]. The rigid-perfectly plastic behavior of material with cohesion was assumed and kinematically admissible mechanisms, for associated flow rule, were used to solve the problem of the tool, similar to the loading machine bucket, filling process. It was shown that effects similar to that observed experimentally can be described this way. It was also found that, because of considerable dilatation predicted on slip lines by associated flow rule assumption, for some cases material behavior far from experimentally observed was predicted. Although, according to the limit load theorems [3], such solutions give only the upper bound for forces necessary to process realization, obtained results are quite promising for its theoretical description. More detailed discussion of kinematically admissible solutions for different problems and different flow rules (non associated) is presented in [7].

In the present paper the process of the wall shaped similar to



the tools of different heavy machines, while movement in a way similar to the loading machine tools was studied using kinematically admissible mechanisms for non associated flow rule. It is shown that using this technique one can describe this way observed soil cutting mechanisms itself (in qualitative manner) as well as force -time relation.

## 2. Statics and kinematics of the process

Let us discuss a soil movement due to the process of a plane rigid wall movement, as it is schematically shown in Fig.1. Perpendicular rigid wall of height  $h$  moves horizontally with velocity  $v$  within soil having horizontal free boundary AB. It is assumed that the wall is so wide that all the process can be considered as a plane strain process.

### 2.1 Statics

It is assumed that material behavior can be described by rigid-perfectly plastic model. The stress equilibrium state is described by two following equations:

$$\frac{\partial \sigma_x}{\partial x} + \frac{\partial \tau_{xy}}{\partial y} = 0, \quad \frac{\partial \tau_{xy}}{\partial y} + \frac{\partial \sigma_y}{\partial x} = \gamma \quad 1$$

and modified Coulomb-Mohr yield criterion for plane strain conditions (Fig.2):

$$\begin{cases} \frac{1}{2}(\sigma_1 - \sigma_2) + \frac{1}{2}(\sigma_1 + \sigma_2)\sin\phi - c_0\cos\phi = 0 & \text{dla } \sigma_1 \leq St_0 \\ \sigma_1 - St_0 = 0 & \text{dla } \sigma_1 = St_0 \end{cases} \quad 2$$

where:  $c_0$  - material cohesion,  $St_0$  - material strength to uniaxial tension,  $\phi$  - internal friction angle.

### 2.2 Kinematics

To describe material strain behavior the non-associated flow rule was taken in following form:

$$\dot{\epsilon}_{1j} = \lambda \frac{\partial G(\sigma_{1j})}{\partial \sigma_{1j}} \quad 3$$

where  $G(\sigma_{1j})$  represents a plastic potential which is described in similar way to the yield criterion (eq.2) putting only instead of internal friction angle  $\phi$  dilatation angle  $\psi$  ( $0 \leq \psi \leq \phi$ ). So, for principal strain rate:

$$\dot{\epsilon}_1 + \dot{\epsilon}_2 + \dot{\epsilon}_3 = \dot{\lambda} \sin \psi \quad 4$$

It means that material volume increase is related to plastic strain for  $\psi > 0$ . In present paper it was assumed that  $\psi = 0$ .

### 2.3 Forces acting on velocity discontinuity line

In plasticity of granular media the velocity discontinuity line is interpreted as a finite thin layer  $\Delta n$ , across which the velocity experience rapid change (Fig.3a). Material, moving from zone 1 to zone 2, undergoes velocity jump  $\Delta V$  which is inclined at an angle  $\delta$  to discontinuity line. This line moves with velocity  $V_p$ . For  $\delta=0$  material within mentioned above layer doesn't change its density. It was assumed that because of a slip line crossing  $c_0$  and  $St_0$  material parameters drop its values to residual ones  $c_r$  and  $St_r$  (described by  $Fr(\sigma_{1j})$  surface - Fig.2) in a way shown in Fig.3d (line 1). A particular case of discontinuity line is a slip line where  $V_p = V_1$  and all the time this same material is sheared (Fig.3c, Fig.5 - OB). For such a case the way of  $c$  and  $St$  parameters change is represented by line 2 in Fig.3d as a linear function of material displacement ( $\Delta s$ ) along the discontinuity line.

Forces acting on velocity discontinuity line can be presented as a sum of two components (Fig.4c - OA line):  $\vec{R}$  i  $\vec{C}$ . Force  $\vec{C}$  is due to material cohesion on a slip line and its direction is opposite to the velocity increment  $\Delta V$  along discontinuity line. Reacting force  $\vec{R}$  is inclined at an angle  $\psi_k$  to the normal to the line. Mentioned factors are defined by following equations:

$$\vec{C} = c \cdot l \cdot \frac{\cos \phi \cos \psi}{1 - \sin \phi \sin \psi}$$

5

$$\operatorname{tg} \psi_k = \frac{\sin \phi \cos \psi}{1 - \sin \phi \sin \psi}$$

where  $l$  is discontinuity line length.

It was assumed that on the contact between rigid wall and soil the cohesion force  $\vec{C}$  doesn't appear and the reaction force  $\vec{R}$  is inclined at an angle  $\delta_*$  to the normal to the wall- where  $\delta_*$  is the friction angle between soil and wall.

#### 2.4 Kinematically admissible mechanisms

The soil cutting process modeling is based on simplified mechanisms of soil movement due to rigid wall pushing. Assumed mechanism can be arbitrary chosen since it is kinematically admissible. Such a mechanism is shown in Fig.4a. The region OAB moves as a rigid body with velocity  $V_1$ . The velocity  $V_1$  is parallel to the OA line and is inclined at an angle  $\alpha$  to horizontal. The discontinuity line OA moves with velocity  $V_0$ . As it was described above the cohesion  $c$  and parameter  $St_0$  of virgin material, which undergoes shear as moving through the slip line, drops respectively to residual  $c_r$  and  $St_r$  values.

The force acting on the rigid wall value is calculated from the equilibrium state where:

- on the discontinuity lines there are cohesion ( $\vec{C}$ ) and reaction ( $\vec{R}$ ) forces described by eq.5
- the force ( $P$ ) on the contact line between rigid wall and medium is inclined at an angle  $\delta_*$  and there are not cohesion forces from the following equation (Fig.4a):

$$\vec{P} + \vec{Q} + \vec{C} + \vec{R} = 0 \quad 6$$

The graphical way of forces determination for more complicate kinematically admissible mechanism is shown in Fig.5.

Then the optimal kinematically admissible mechanism defined as minimum work of P force on  $\Delta s$  displacement is claimed:

$$W(\alpha) = \int_0^{\Delta s} P(\alpha) ds \quad 7$$

During the rigid wall movement process material surface, or some parts of material surface, can achieve the equilibrium state. So, as a result, three different material damage mechanisms can appear (Fig.6):

- stiff material rotation connected to continuous displacement zone (Fig.6a)
- stiff material rotation with tear along straight line (Fig.6b)
- shear of stiff zone (Fig.6c).

As a result of such mechanisms material transformation takes place as it is shown in Fig.6d and 6e.

In Fig.7 it is shown theoretical solution for the rigid wall movement of 0.5 m. for following material parameters:

$$\begin{array}{lll} c_0 = 5 \text{ KN/m}^2 & c_r = 0.25 \text{ KN/m}^2 & St_0 = 1 \text{ KN/m}^2 \quad St_r = 0.05 \text{ KN/m}^2 \\ \phi = 23.4^\circ & \gamma = 18 \text{ KN/m}^3 & h = 0.1 \text{ m} \end{array}$$

It was obtained as a sum of following kinematically admissible solutions. The material strained zone consists of several regions with different cohesion. It is due to jump changing of slip mechanisms. This effect is schematically shown in Fig.8. In Fig.8a it is shown the beginning of the pushing wall process. All the material is a virgin one and assuming kinematically admissible mechanism similar to that presented in Fig.4 the slip line angle  $\alpha_1$  was found to be optimal (eq.7). Situation after  $\Delta s$  wall displacement is presented in Fig.8b. Region ABC and ODM consist of virgin material while, due to shear along slip line, material cohesion in ODAC zone is equal  $c_r$  and  $St = St_r$ . The optimal slip line is not longer inclined at an angle  $\alpha_1$ , but its inclination is  $\alpha_2$  (Fig.8b). This way, up to wall displacement shown in Fig.8c, the slip line angle  $\alpha_3$  value diminishes. Then it appears that optimal inclination of the slip line is this same as for virgin material. In this moment the discontinuity line inclination jumps from  $\alpha_3$

value to  $\alpha_0$  value. Described above process repeats periodically. Force necessary to realize such a process versus wall displacement and slip line inclination versus wall displacement diagram is shown in Fig. 7g.

### 3. Theoretical solutions for different models of heavy machines tools

In following Fig. 9 - 11 they are shown theoretical solutions, obtained using described above technique, for different heavy machine tools. Although this same technique was applied, different kinematically admissible mechanisms were assumed to get best solutions from energetical point of view. The force necessary to realize such mechanisms versus tool displacement diagrams are also shown.

### 4. Conclusions

It was shown that using quite simple kinematically admissible mechanisms one can study such a complicated process as that similar to the heavy machine tools working process. Such solutions can't be obtained using other methods of plasticity.

Using such simplified approach characteristic scale-shaped rigid zones generated during cohesive soil cutting process were predicted. Also unstable character of force necessary to realize such a process was predicted quite well (at least from qualitative point of view).

Although application of non associated flow rule gives much more realistic prediction of material behavior (no material dilatation on a slip line is predicted - comparing with continuous dilatation for associated flow rule) it is not possible to estimate what is the possible error range (limit theorems doesn't apply to non-associated flow rule).

### Literature

1. W. Szczepiński, Stany graniczne i kinematyka ośrodków sypkich, PWN 1974
2. W. Sokołowski, Statyka ośrodków sypkich, PWN 1958
3. R. Izbiński, Z. Mróz, Metody nośności granicznej w mechanice gruntów i skał, PWN 1976
4. W. Trampczyński, Mechanika procesów urabiania gruntów jako zagadnienie teorii plastyczności (PhD Thesis), IPPT PAN 1976
5. W. Trampczyński, Experimental study of kinematics of soil shoving, Bull. Acad. Polon. Sci., vol. XXV, No 11, 1977
6. W. Trampczyński, A. Jarzębowski, On the kinematically admissible solution application for theoretical description of shoving processes, Eng. Transactions (in press).
7. J. Maciejewski, Analiza przyrostowa mechanizmów urabiania gruntów, (MSc Thesis), Pol. Warszawska, 1987.

## FIGURE CAPTIONS

Fig.1 The plane rigid wall movement problem.

Fig.2 The modified Coulomb-Mohr yield criterion for plane strain conditions.

Fig.3 A discontinuity line relations

a. velocity discontinuity line

b. velocity hodograph

c. velocity discontinuity line where  $V_p = V_1$

d. material parameters relations

Fig.4 Kinematically admissible mechanism for plane wall movement

a, b velocity relations

c, d equilibrium state forces

Fig.5 The graphical method for forces determination

Fig.6 Material damage mechanisms for free surface

Fig.7 Theoretical solution for the rigid wall movement of 0.5 m.

Fig.8 A different cohesion material zone evolution

Fig.9 Theoretical solution for the wall shaped as a short loading machine bucket horizontal movement.

Fig.10 Theoretical solution for the wall shaped as a medium loading machine bucket horizontal movement.

Fig.11 Theoretical solution for the wall shaped as a long loading machine bucket horizontal movement.

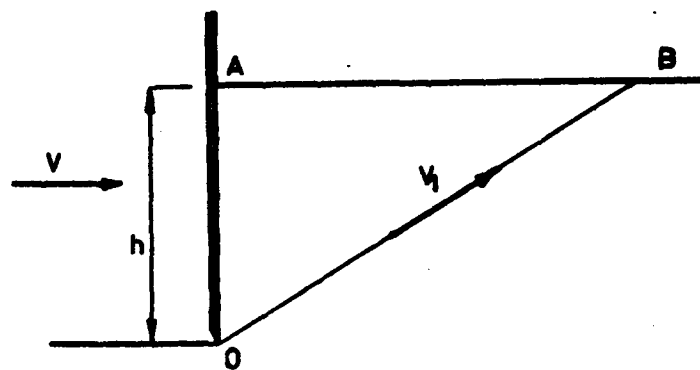


Fig.1

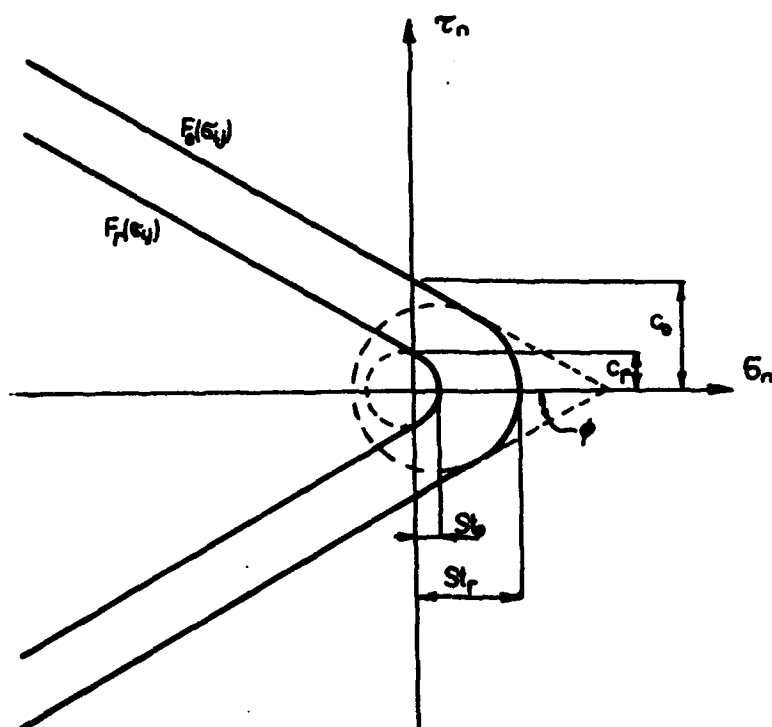


Fig.2



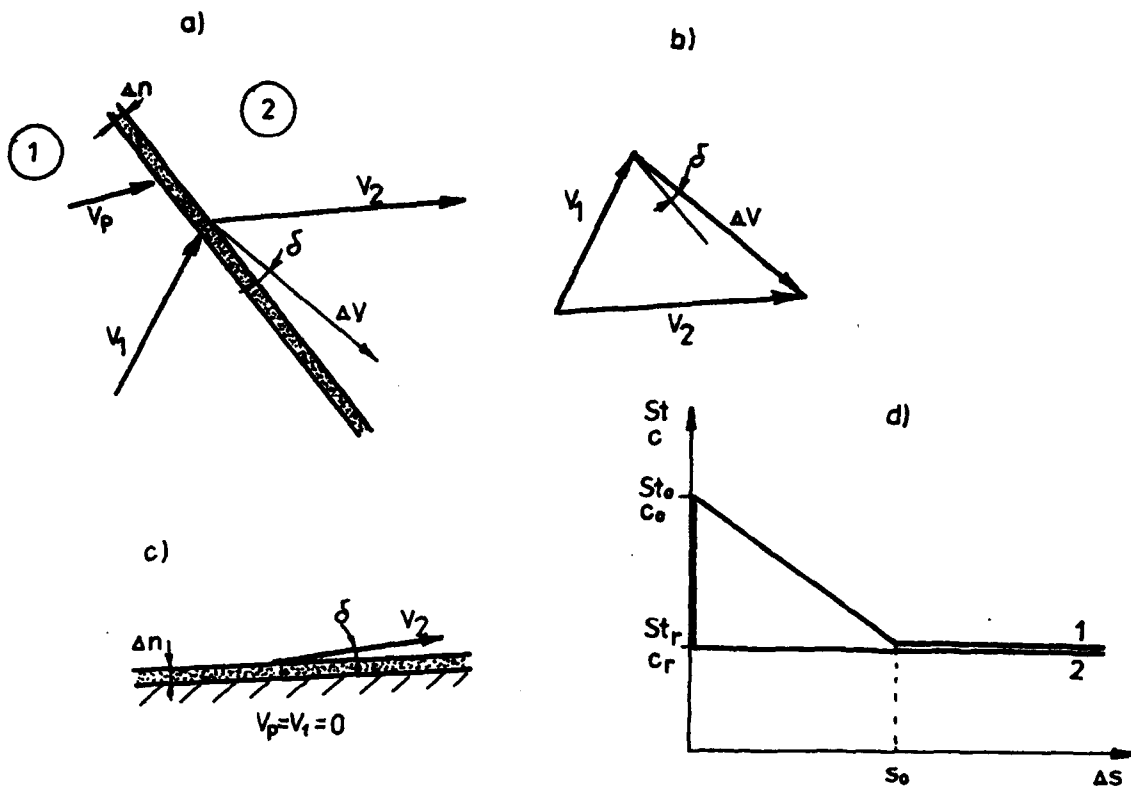


Fig.3

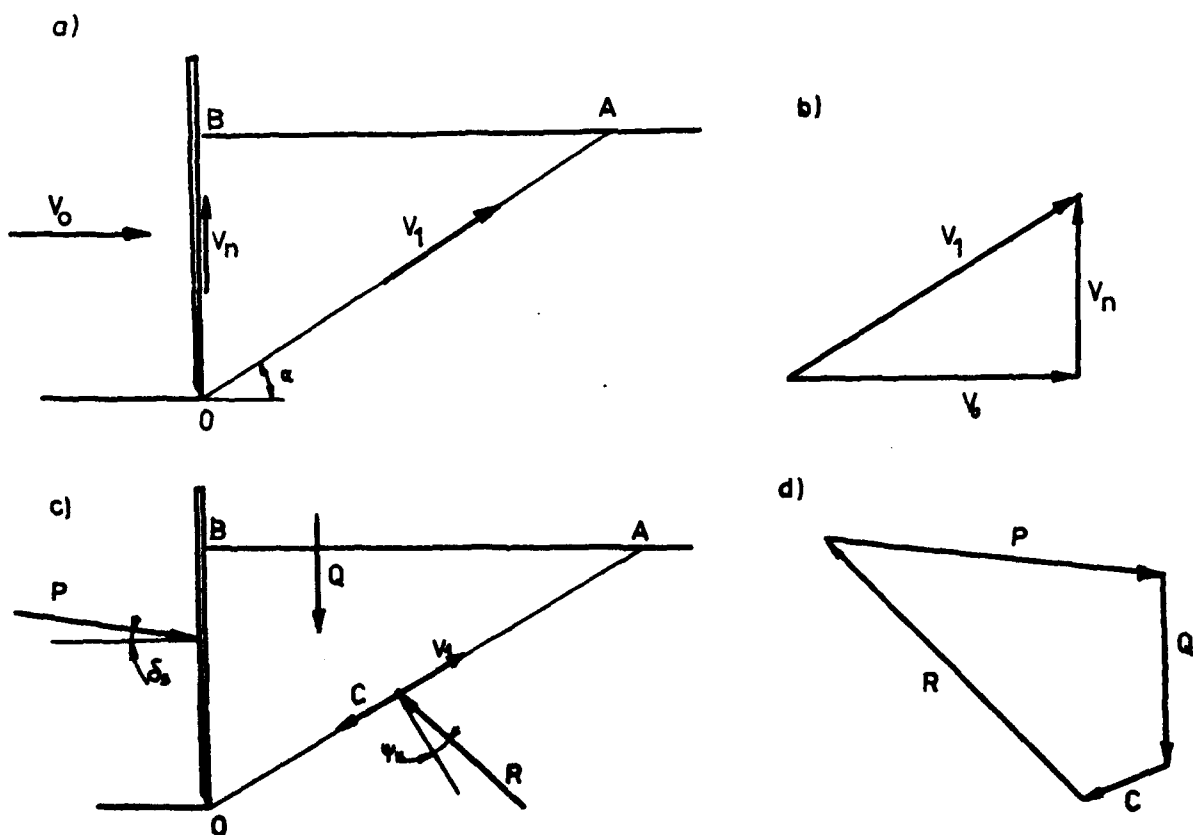


Fig 4

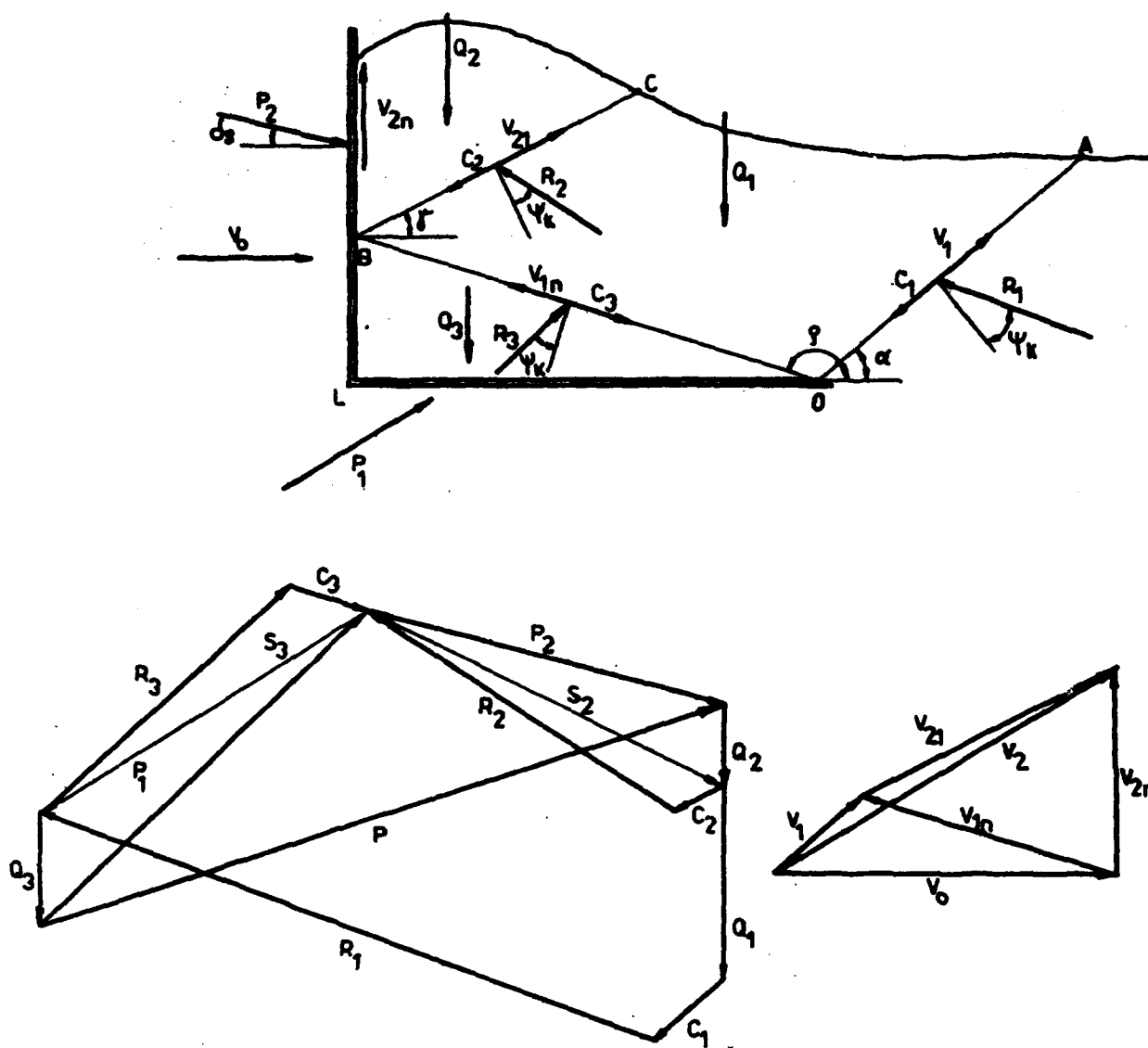


Fig. 5

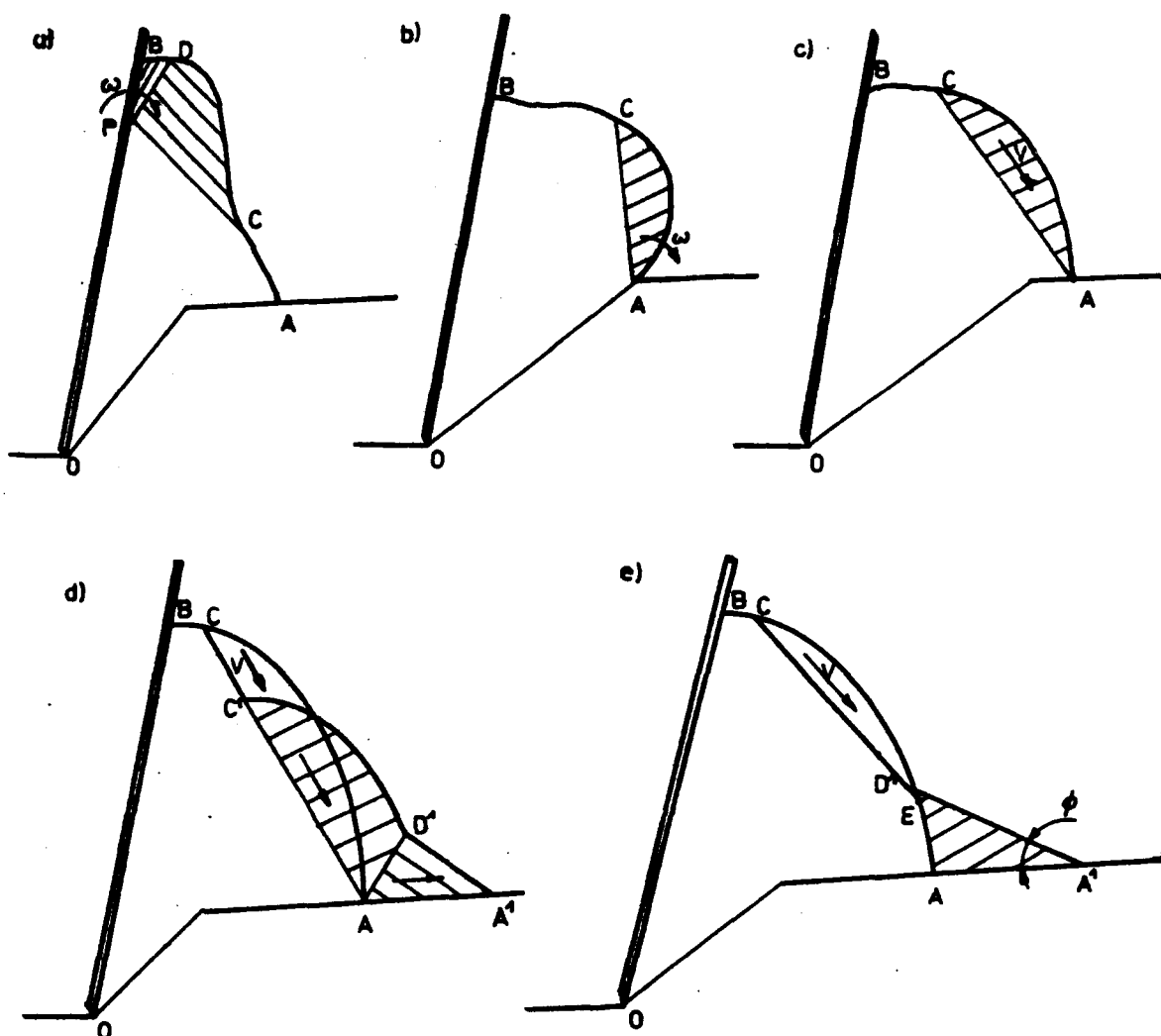


Fig. 6

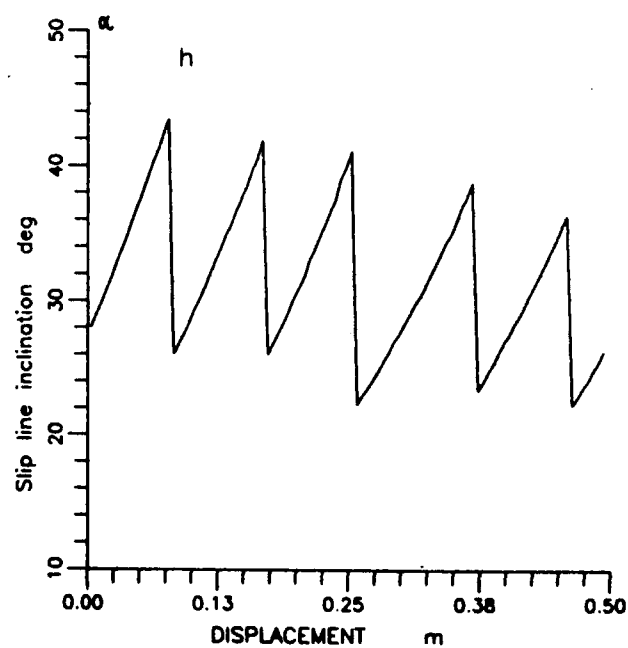
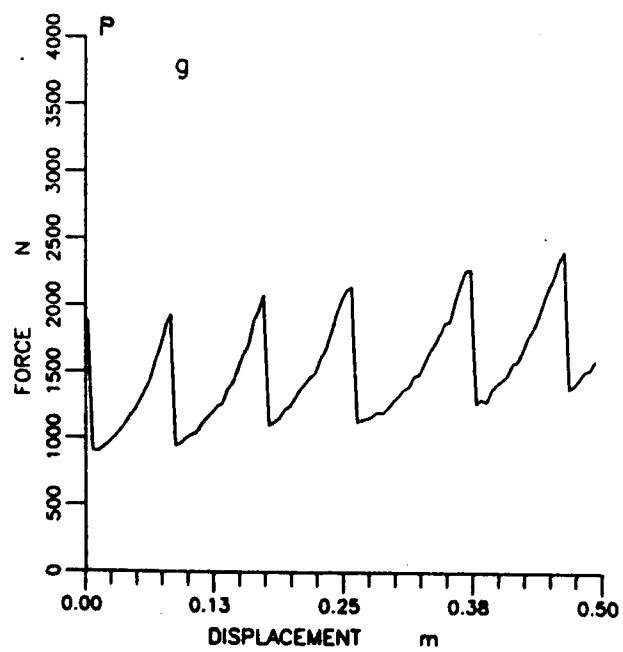
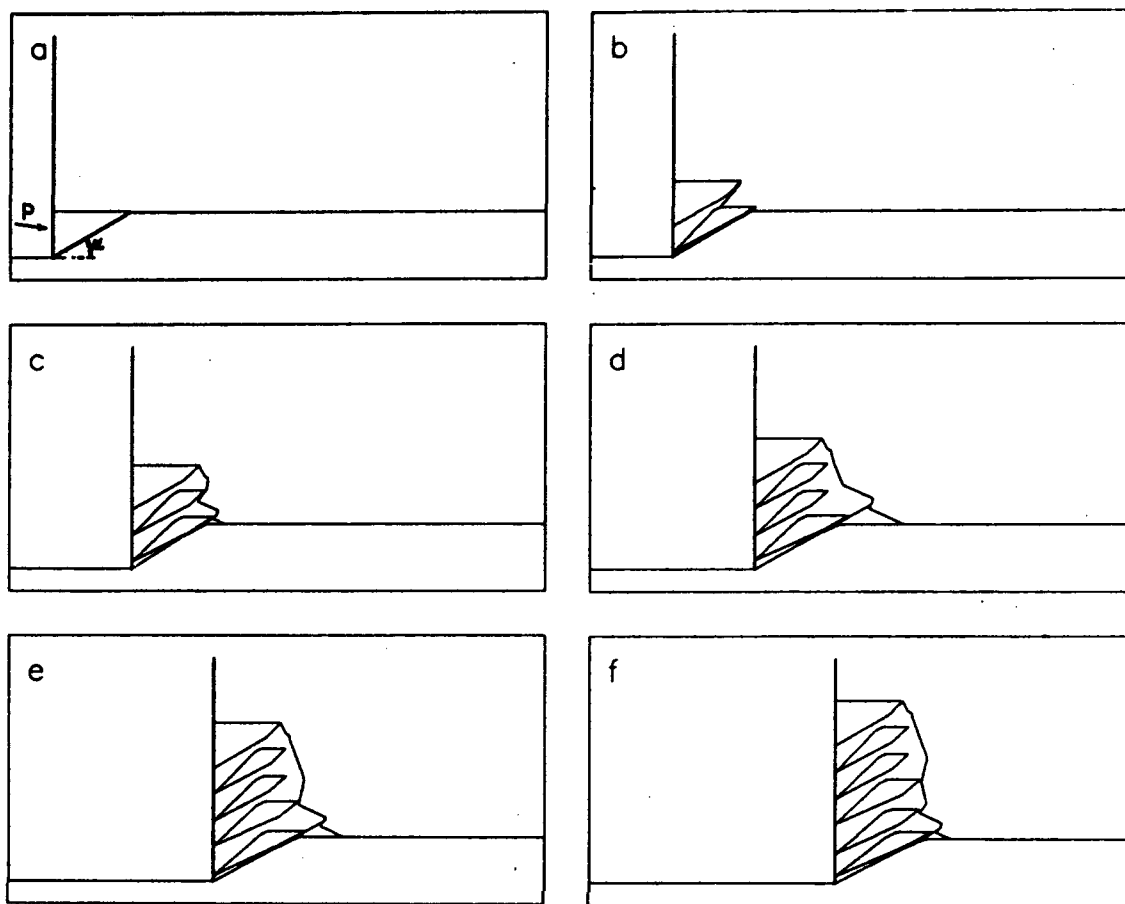


Fig. 7.

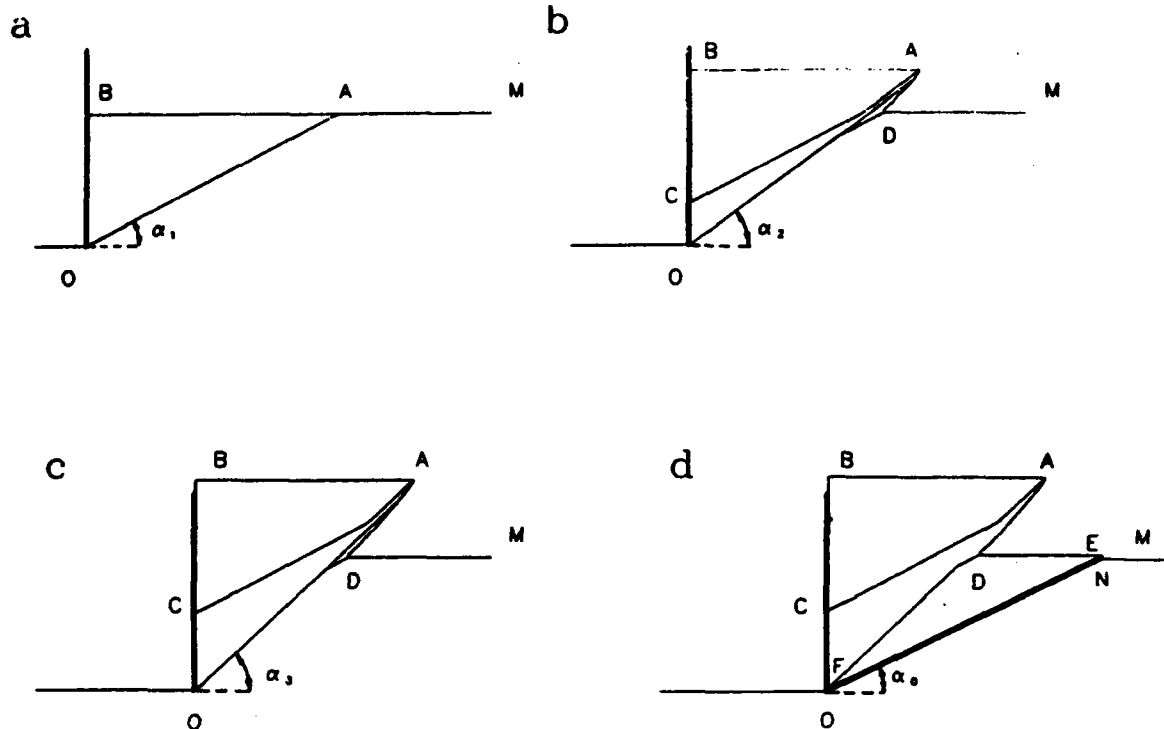


Fig. 8.

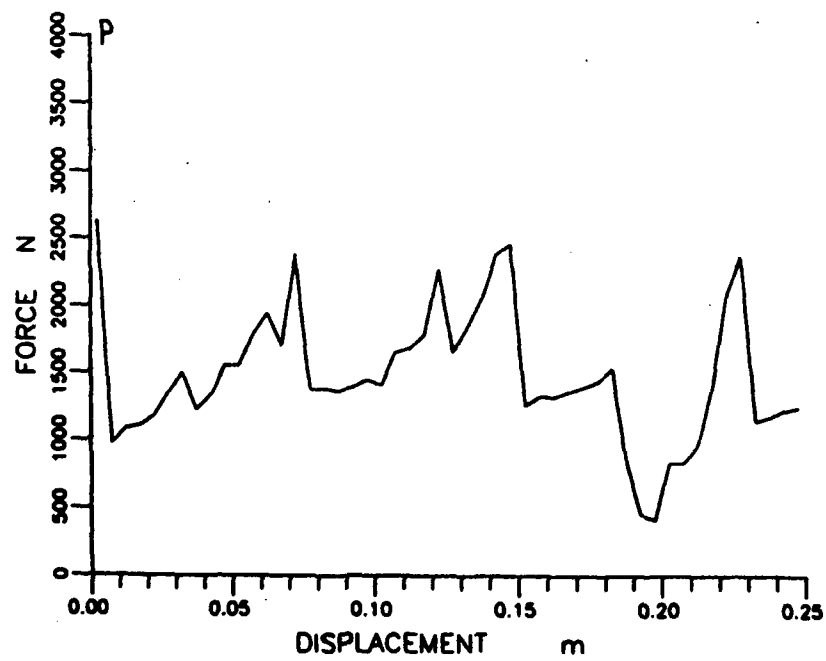
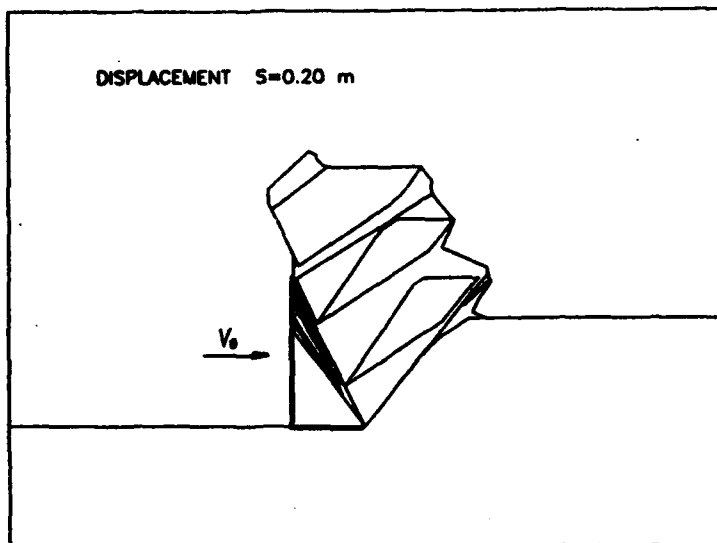


Fig.9

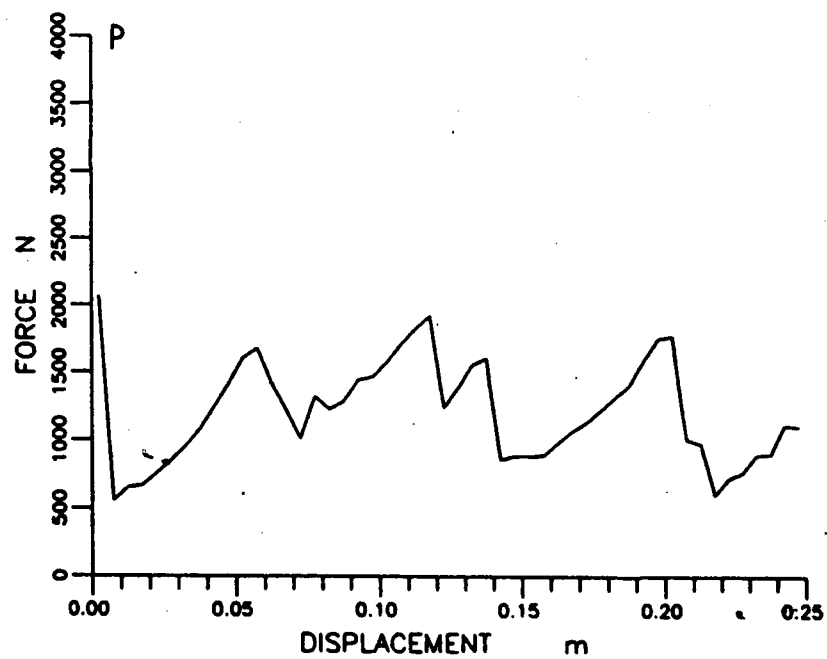
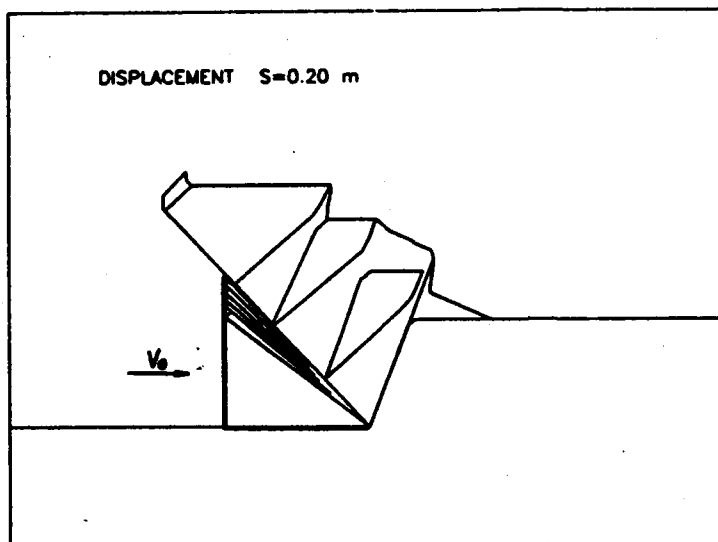


Fig.10

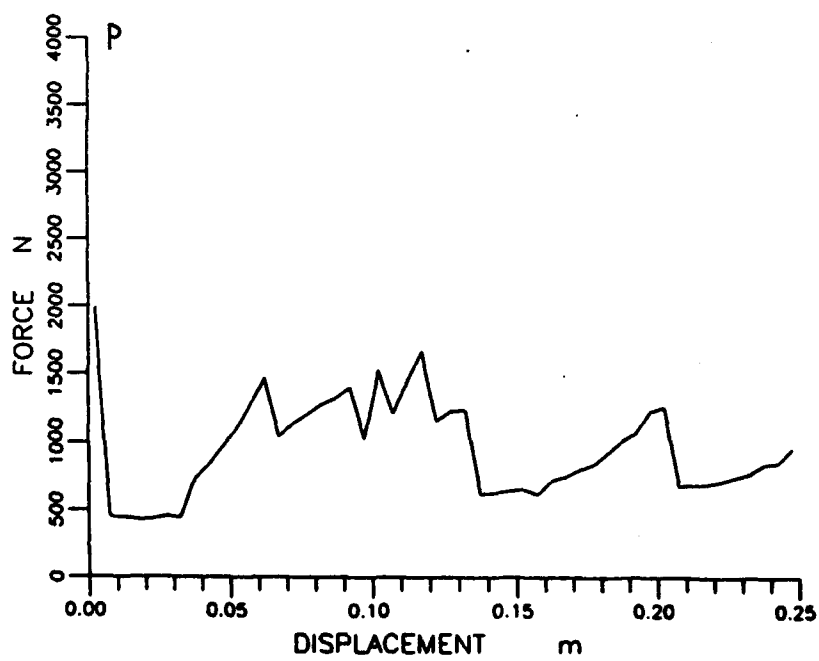
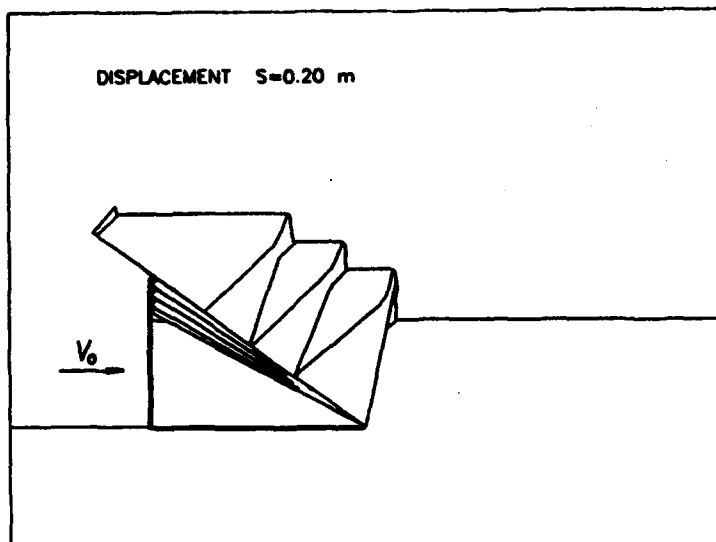


Fig.11



## **SHEAR STRENGTH PROPERTIES FROM CONE INDEX TESTS**

by

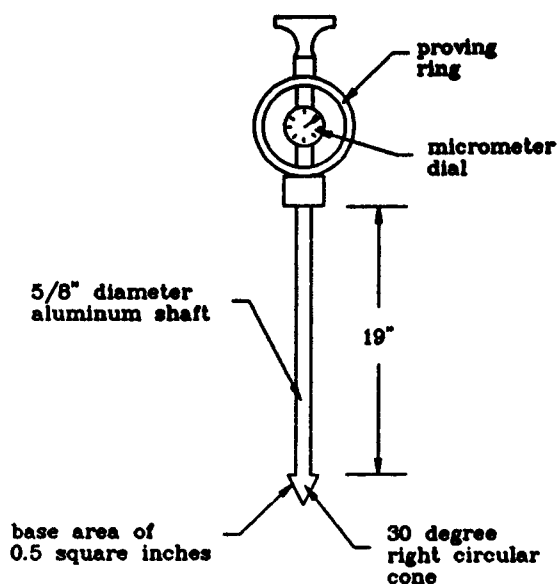
**J. V. Farr**

**Geotechnical Laboratory, U.S. Army Engineer  
Waterways Experiment Station (WES), Vicksburg, Mississippi, USA**

**SUMMARY -** The military cone penetrometer (MCPT) has been used as a descriptor of soil strength by the United States Armed Forces since the 1950s. However, the device is less than ideal for obtaining classical soil mechanical properties such as cohesion, friction angle, elastic shear modulus, and total unit weight because the properties must be implied from the tip resistance using either empirical or theoretical relations. As vehicle terrain interaction models become more complicated, these detailed properties are needed to characterize the three dimensional response of the soil. A direct or triaxial shear device would provide a direct measure of the soil properties needed. However, numerous vehicle studies have been performed over the last 30 years using the MCPT. Also, many digital terrain data bases exist that are used for vehicle studies for areas throughout the world with cone index (i.e., the tip resistance from the MCPT) as the principal indicator of soil strength, the device is man portable, simple, and easy to operate. Thus, relationships must be developed that translate cone index into classical soil properties.

**INTRODUCTION -** Many of the complex vehicle terrain interaction models in existence require numerous physical and mechanical properties for the soil to represent the complex interaction between the vehicle and terrain. In addition, a simple technique is needed to characterize large areas from which detailed soil properties can be determined for vehicle tests and evaluation studies. The cone index (CI) value obtained from the MCPT shown in Figure 1 can be used for this purpose.

Numerous solutions exist in the literature relating shear strength to cone penetration test results for foundation engineering. Unfortunately, limited research has been directed towards the more complex problem of characterizing surficial soils. Several theoretical based solutions (Karafiath and Nowatzki, 1976, Rohani and Baladi, 1981, and Meier and Baladi, 1988) have been developed to obtain soil strength properties from the MCPT for mobility problems (usually the upper 24 in.) with limited success. The technique presented by Karafiath and Nowatzki (1976) treated the soil as a rigid plastic material but did not account for the stiffness characteristics of the soil. The methodology presented by Rohani and Baladi (1981) used cavity expansion to account for the stiffness of the soil. Unfortunately, the cavity expansion relationships use cohesion, friction angle, shear modulus, and unit weight to predict CI. Thus, if the CI is known, four unknowns exist.



The solution presented by Meier and Baladi (1988) was an attempt to use this same cavity expansion methodology to obtain mechanical properties from a CI profile. Essentially, that methodology makes estimates of shear modulus and total unit weight and calculates cohesion and friction angle using two adjacent CI readings. This implies that the material is homogeneous and the methodology seems to work for granular materials. However, the solutions obtained for cohesive materials are not representative of the in situ shear strength because of the rapidly changing strength profiles (i.e., nonhomogeneity) caused by changes in density, over consolidation ratio, water content, etc.

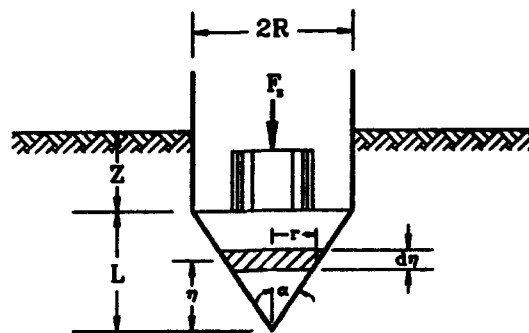
Figure 1. Standard military cone penetrometer

The solution contained herein is based upon the work presented by Rohani and Baladi (1981) and Meier and Baladi (1988). Simplistically, estimates are made of three of the four unknowns (shear modulus, total unit weight, and friction angle) used in the cavity expansion equation based on knowledge of soil type. Cohesion is then calculated using the measured CI. For most soil types, two of the four variables, density and friction angle have limited ranges of variation. The technique seems to work for all of the soil types used in validation. In addition, the numbers obtained from sensitivity analysis of partially saturated surficial soils seem representative.

**SHEAR STRENGTH PROPERTIES FROM CI** - The MCPT consists of a right circular cone with a base area of 0.5 square in. attached to an aluminum shaft. A proving ring and micrometer dial is attached to the top of the shaft to measure axial load. The basic geometry of the cone tip is shown in Figure 2 and is characterized by its diameter  $D$  (equal to twice the radius  $R$ ), length  $L$ , and apex angle  $2\alpha$ . Using the vertical force  $F_z$ , on the cone, CI at any depth is calculated as

$$CI = \frac{4F_z}{\pi D^2} \quad (1)$$

For the WES version of the MCPT,  $L = 1.48$  in.,  $D = 0.799$  in., and  $2\alpha = 30$  deg.



a. Geometry of the problem.



b. Stresses on a finite frustum of the cone

Figure 2. The cone penetration problem

If the soil is assumed to satisfy Mohr-Coulomb failure criteria, cavity expansion can be used to determine the magnitude of the vertical force  $F_z$  required to penetrate the soil. Vesic (1972) first solved this problem.

It has been observed in practice that the cone has a tendency to shear the surrounding material during penetration and flow around the cone tip and towards the surface. This indicates that the entire shearing strength of the soil is mobilized. Therefore, assuming Mohr-Coulomb failure is applicable, the shear stress  $\tau$  can be expressed as

$$\tau = c + \sigma \tan \phi \quad (2)$$

where  $c$  = Mohr-Coulomb cohesion parameter,  $\sigma$  = normal stress, and  $\phi$  = Mohr-Coulomb angle of internal friction. By integrating the stress over the surface of the cone, the vertical force  $F_z$  can be determined if the normal stress can be assumed to be equivalent to the internal pressure required to expand a spherical cavity in an unbounded elastic-plastic soil. Cavity expansion theory relates fundamental soil properties to this internal pressure.

The basic premise of using cavity expansion is the assumption that the cone penetration process can be viewed as the expansion of a series of spherical cavities (simulating the geometry of the cone) in an unbounded elastic-plastic medium. The normal stress (normal to the surface of the cone) resisting the penetration of the cone is therefore equivalent to the internal pressure required for expansion of a spherical cavity. Using this expression for internal pressure, the vertical force resisting penetration of the cone is computed from the geometry of the cone and conditions of static equilibrium.

The expression for an expanding spherical cavity in an unbounded elastic-plastic medium is given as

$$\sigma = 3(q + c \cot \phi) \left( \frac{1 + \sin \phi}{3 - \sin \phi} \right) I_{rr} - c \cot \phi \quad (3)$$

where

$$m = \frac{4 \sin \phi}{3 (1 + \sin \phi)}$$

$$I_{rr} = \frac{I_r}{(1 + \Delta I_r)}$$

$$I_r = \frac{G}{q \tan \phi + c}$$

$$q = \gamma (z + L - \eta)$$

and  $m$  = constant to simplify equations,  $G$  = elastic shear modulus,  $q$  = total overburden stress along the tip of the cone,  $\gamma$  = total unit weight of the soil,  $I_{rr}$  = reduced rigidity index,  $\Delta$  = plastic volumetric strain, and  $I_r$  = rigidity index.

For purely cohesive soils (i.e.,  $\phi = 0$ ), the expression for  $\sigma$  can be written as

$$\sigma = \frac{4}{3} c \left( 1 + \ln \frac{I_r}{1 + \Delta I_r} \right) + q \quad (4)$$

From the condition of static equilibrium and the geometry of the problem

$$F_r = 2\pi \tan \alpha \int_0^L c f_c d\eta + 2\pi \tan \alpha (\tan \alpha + f_\phi \tan \phi) \int_0^L c_\eta d\eta \quad (5)$$

where  $f_c$  and  $f_\phi$  are reduction factors to account for soil-steel interaction in lieu of soil-soil for the cohesion and friction angle, respectively.

Substituting Equation 3 into 5 and completing the integration

$$CI = \frac{C}{\tan \alpha} (f_c - f_\phi) - c \cot \phi + \frac{2 \tan \alpha (1 + \sin \phi) G}{\left( \frac{\gamma D}{2} \right)^3 \tan^3 \phi} \left[ \frac{3 (\tan \alpha + f_\phi \tan \phi)}{3 - \sin \phi} \right] \Omega \quad (6)$$

where

$$\Omega = \frac{(\Phi - \gamma L \tan \phi)^{3-m} - \Phi^{3-m}}{3-m} +$$

$$\frac{(\Phi + \Delta G)^{2-m} - (\Phi - \gamma L \tan \phi)^{2-m}}{2-m} + \frac{\Phi \Delta G ((\Phi - \gamma L \tan \phi)^{1-m} - \Phi^{1-m})}{1-m}$$

$$\Phi = \gamma (z + L) \tan \phi + c + \Delta G$$

and  $\Omega$  and  $\Phi$  are simply constants to simplify the mathematics.

Also, substituting Equation 4 into 5 and completing the integration

$$CI = 2 f_c \frac{LC}{D} + \frac{4}{3} c \left( 1 + \ln \frac{G}{c + \Delta G} \right) + \gamma \left( z + \frac{L}{3} \right) \quad (7)$$

the equation for frictionless materials can be determined. If the assumption that  $f_c = f_\phi = 1$  and  $\Delta = 0$ , the equations will reduce to those presented by Rohani and Baladi (1981). These assumptions were used for all calculations.

The methodology previously presented to obtain soil properties from CI will consist of estimating typical values for  $\gamma$ ,  $\phi$ , and  $G$  and back-calculating  $c$  from CI measurements. Listed below are discussions that provide the basis for these empirical relationships for these three soil properties.

Rohani and Baladi (1981) and Meier and Baladi (1988) presented detailed discussions of the existence of a free surface effect. The cavity expansion equations used to derive the CI equations are based upon the assumption that the cavity expands in an unbounded medium. The process of cone penetration, however, takes place in a medium which is bounded by a free surface. The existence of this free boundary will result in an upward flow of the near-surface materials in the vicinity of the cone that consequently reduces the penetration resistance of the cone. The free-surface effect is most pronounced for granular materials and becomes less important as the cohesive strength of the material increases. Also, its effect on cone penetration resistance decreases with depth and eventually becomes negligible. In the case of the standard WES cone it appears that at the depth of about  $6L$  the effect of the free surface on the penetration resistance in sand becomes negligible. To account for the free-surface effect for granular materials it is postulated that the apparent shear modulus  $G^A$  which controls the shearing flow of the material varies with depth according to the following relationship

$$G^A = 0.5 \left[ A + \frac{(1 - B \exp^{(-\beta z)})}{1 + B \exp^{(-\beta z)}} \right] G \quad (8)$$

where  $A$ ,  $B$ , and  $\beta$  are constants that must be evaluated experimentally and related to the geometry of the cone of interest. The constant  $G$  is the elastic shear modulus and depends on soil type and the initial state of compaction of the soil. In the case of cohesive or mixed soil, free-surface effect is negligible. In this case the constants in Equation 8 become  $A = 1$ ,  $B = 0$ , and  $\beta = 0$  (i.e.,  $G^A = G$ ). The numerical values of the three constants  $A$ ,  $B$ , and  $\beta$  have been determined for granular materials (for the standard WES cone) and are  $A = 0.986$ ,  $B = 100$ , and  $\beta = 0.55/\text{in.}$

The elastic shear modulus can be calculated using

$$G = 1,230 \frac{(2.973 - e)^2}{1 + e}$$

where  $e$  is equal to the void ratio of the soil.

Meier and Baladi (1988) stated that this equation tended to overestimate the shear modulus of some surficial soils. In an attempt to adjust the elastic shear modulus and account for the effects of density and moisture content, the above equation was modified to include the measured CI

$$G = 1,230 \frac{(2.973 - e)^2}{1 + e} \left( \frac{CI + 25}{500} \right) \quad (9)$$

Based upon the void ratio values presented in Table 1, Equations 8 and 9 can be used to estimate the shear modulus for the CI equations. The values presented in Table 1 were taken from Meier and Baladi (1988) and Lade and Lee (1976) and are classed according to the Unified Soil Classification System (USCS).

Table 1. Typical Values of Void Ratio, Total Unit Weight, and Undrained Friction Angle

USCS Soil Classification	Void Ratio, $e$	Total Unit Weight, $\gamma$ (pcf)	Max Friction Angle, $\phi$ (deg)
SW	0.45	120	38
SP	0.55	110	37
SM	0.70	105	35
SC	0.80	110	32
SM-SC	0.75	107	33
CL*	1.05	110	25
ML*	0.85	93	32
CL-ML*	0.95	102	28
CH*	1.20	95	19
MH*	1.00	90	28
OL*	1.50	90	10
OH*	2.00	90	10
GW	0.20	135	40
GP	0.35	125	38
GM	0.50	130	36
GC	0.60	130	33
PT*	2.00	90	10

\* For these soils, the free surface effects on shear modulus should be ignored (i.e.,  $G^A = G$ ).

The CI equations are fairly insensitive to total unit weight. The values recommended in Table 1 are based upon a relative density of 75 percent and are loosely based upon tables presented by Lade and Lee (1976).

Most soil types have a well defined range of friction angles. Table 1 also contains a listing of recommended values for friction angle and values also correspond to a relative density of 75 percent. These values are used to limit the maximum value for friction angle. If the calculated CI is greater than the measured value, the friction angle is incrementally reduced from this maximum value until the measured and calculated CI are equal. If the calculated value is less than that measured, cohesion is included.

**VALIDATION OF METHODOLOGY** - The methodology and equations presented above were translated into a computer code to determine soil properties. The code is titled (S)trength (E)stimates from (C)one (I)ndex (T)esting or SECIT and is written in FORTRAN for an IBM PC computer or compatible.

The main menu for the code contains three menu selections. Choice 1 lets the user calculate a single CI value for inputted values of cohesion, friction angle, shear modulus, and unit weight. This choice was included in the code to allow for parametric analysis. Choice 2 lets the user input a unique CI value, USCS soil type, and depth and calculate the soil shear strength properties. Choice 3 allows the user to process a cone index profile and obtain estimates along with probabilistic values for cohesion, friction angle, and shear modulus.

A literature survey revealed very little reliable data. Complete CI profiles and the corresponding in situ direct shear results are normally not measured for surficial soils because they are normally discarded for construction and replaced with compacted materials. Some data are presented by Meier and Baladi (1988), Perkins (1988), and Farr, et. al. (1990). These data were used to provide validation of the methodology presented.

Validation was accomplished by comparing the model predicted values using Choice 3 of the SECIT program of cohesion, friction, shear modulus, and total unit weight against the field measured values. A single, statistically determined value representative of the average properties over the depth of the CI profile was compared against a single laboratory value and are summarized in Table 2. Of the 17 soil types presented in Table 1, the model was validated for only 6 soils.

Table 2. Validation Data for the Mechanical Properties from CI Prediction Methodology

		Laboratory Measured					Model Predicted								Reference
Site	USCS	$\gamma$	$c$	$\phi$	$G$	$\gamma$	$c$	$\sigma_c$	$\phi$	$\sigma_\phi$	$G$	$\sigma_G$	No.		
		(g)	(pcf)	(psi)	(deg)	(psi)	(pcf)	(psi)	(psi)	(deg)	(deg)	(psi)	(psi)		
7B, Redwood, MS	CH	60	101.0	1.6	23	-	95	1.1	0.2	19.0	0.0	373	55	3	
White Sands	SM-SC	-	88.1	1.4	36	-	110	2.2	2.0	33.0	0.0	526	546	3	
Reid Bedford	SP	-	100.5	0	34	-	110	0.3	0.3	37.0	0.7	651	748	3	
Chattahoochee	SP-SW	-	95.9	0	43	1150	110	0.0	0.1	33.9	2.5	2617	2112	6	
LeTourneau 2	CL	-	105.3	2.6	30	1563	107	2.2	0.9	25.0	0.0	1276	455	7	
LeTourneau 3	CL	-	119.5	5.0	37	1250	107	2.2	1.1	25.0	0.0	1294	552	7	
Duckport	CH	-	120.0	13.0	22	1250	95	6.6	0.8	19.0	0.0	1345	44	7	
Duckport	CH	-	113.2	4.3	25	1150	95	4.0	1.4	19.0	0.0	880	227	7	

**SUMMARY AND RECOMMENDATIONS FOR FUTURE RESEARCH** - A methodology has been presented to determine classical Mohr-Coulomb shear strength properties. The methodology is based upon the cavity expansion theory and estimation of some soil properties. For the limited validation efforts presented, the methodology seems to work.

Presently, at the U.S. Army Military Academy, West Point, New York, an effort is underway to develop an rule based expert systems to better estimate values of total unit weight, shear modulus, and friction angle as a function of the measured CI. An example of how this system would work is shown in Figure 3. Simplistically, based upon laboratory and field testing, the measured value of cone index would be used to adjust density and friction angle to account for density effects.

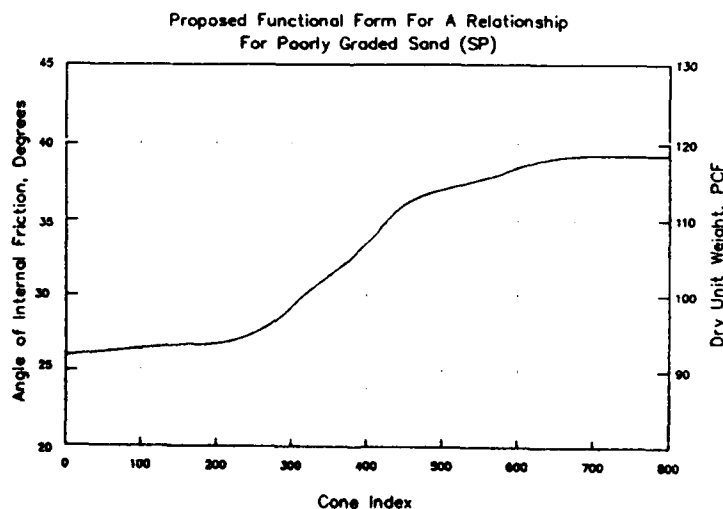


Figure 3. Example relationship for poorly graded sand

**ACKNOWLEDGEMENT** - The methodology and data described herein was obtained from research conducted under the **MILITARY RESEARCH DEVELOPMENT TEST AND EVALUATION PROGRAM** of the U.S. Army Corps of Engineers and under a program for the Deputy Under Secretary of the Army-Operations Research. Permission was granted by the Chief of Engineers to publish this information.

#### **REFERENCES**

1. Karafiath, L. L. and Nowatzki, E. A. 1976, "Soil Mechanics in Off-Road Vehicle Engineering," Trans Tech Publications, Bay Village, Ohio.
2. Rohani, B., and Baladi, G. Y. 1981. "Correlation of Mobility Cone Index with Fundamental Engineering Properties of Soil," Technical Report SL-81-4, U.S. Army Engineer Waterways Experiment Station, Vicksburg, Mississippi.
3. Meier, R. W. and Baladi, G. Y. 1988. "Cone-Index-Based Estimates of Soil Strength: Theory and User's Guide For Computer Code CIBESS," Technical Report SL-88-11, U.S. Army Engineer Waterways Experiment Station, Vicksburg, Mississippi.
4. Vesic, A. S. 1972. "Expansion of Cavities in Infinite Soil Masses," Journal of the Soil Mechanics and Foundation Division, ASCE, Vol 98, No. SM3.
5. Lade, P. V., and Lee, K. L. 1976. "Engineering Properties of Soils," UCLA-ENG-7652, Soil Mechanics Laboratory, University of California, Los Angeles, California.
6. Perkins, W. E. 1988. "Development and Initial Testing of the Automated Military Cone Penetrometer," Miscellaneous Paper GL-88-5, U.S. Army Engineer Waterways Experiment Station, Vicksburg, Mississippi.
7. Farr, J. V., Rabalais, C. P., Underwood, R. P., III, and Ahlvin, R. B. 1990. "Mobility and Plowing Capabilities of the Combat Mobility Vehicle," Technical Report GL-90-\_\_, currently under review, U.S. Army Engineer Waterways Experiment Station, Vicksburg, Mississippi.



## **ANALYSIS OF SOIL-TRACK INTERACTION FOR TANK STEERABILITY**

by

John F. Peters and Newell R. Murphy

Geotechnical Laboratory, US Army Engineer Waterways Experiment Station  
Vicksburg, Mississippi, USA, 39180

### **Summary**

The computer code TVSTEER for predicting steering performance of tracked vehicles was found to over-estimate turning resistance for large radius turns. A detailed analysis indicated that the turning resistance could be directly linked to the amount of track-soil slip needed to mobilize traction. The TVSTEER slip-traction model was based on soil strength parameters determined from a direct shear test which ignored soil-track interaction effects. An analysis of drawbar pull test results showed that the direct shear test data significantly underestimated the slip required to mobilize traction; thus, the overestimation of turning resistance is a result of using the direct shear test rather than being an error in TVSTEER.

### **Introduction**

The computer code TVSTEER (Baladi et. al. 1986) was developed to predict steering performance of tracked vehicles. Initial comparisons between measured and predicted performance by Baladi and Rohani (1979) validated the model's ability to predict some aspects of steering tests. However, the focus of these tests was the turning capabilities of tracked vehicles in tight turns rather than large radius turns. More recently an analysis for large radius turns (Spreitzer, 1989) showed that turning resistance values predicted by TVSTEER are too large. The over prediction of turning resistance is a direct result of the soil-track interaction model which predicts virtually full mobilization of traction under very small values of slip. The ultimate traction was predicted well by the model thus explaining the ability to predict performance under small radius turns for which the slip is expected to be greatest.

This paper presents a brief description of TVSTEER then addresses two issues in predicting turning resistance. First, the accuracy of the TVSTEER soil model is considered for two dimensional slip paths to determine if the simple model used is a direct cause of the large turning resistance. It is noted that while two-dimensional slip paths should lead to a smaller turning resistance than predicted by the TVSTEER model, directional effects should not be great enough to account for the overestimation of turning resistance. Second, the behavior of the model for one-dimensional slip (straight-ahead motion) is compared to measured performance in drawbar pull tests. Test results showed that more slip is required to mobilize traction than is predicted by the TVSTEER model. Thus the key to predicting turning performance actually lies in the ability in predicting straight-ahead motion.

### **Overview of TVSTEER**

TVSTEER models the turning process in terms of three elements; 1) three equations of motion which define the interrelationships of applied forces; 2) three kinematic variables which can be used to define the motions of all points on the tank and the relative slip between the track and soil, and; 3) the traction-slip relationship which relates forces in the three equations of motion to the

three kinematic variables. The first and second elements are the result of well defined physical and geometric laws and are valid for all tracked vehicles in all terrains. The third element cannot be defined without recourse to measurements.

The slip traction relationship is depicted in TVSTEER as a hyperbolic relationship between the track-soil slip  $\Delta$  and the traction  $\tau$  as given by Equation (1).

$$\tau = \tau_f \frac{G\Delta}{1 + G\Delta}. \quad (1)$$

Two parameters are needed to define the relationship; a stiffness parameter  $G$  and the ultimate slip resistance  $\tau_f$ . The ultimate slip resistance is not a parameter but depends on the normal force on the track and the rate of slip. The stiffness  $G$  and the various parameters defining  $\tau_f$  are determined by a direct shear test described by Baladi and Rohani (1979); thus the slip-traction relationship, as used in TVSTEER, is a characteristic of the soil that does not depend on the effects of soil-track interaction.

## Turning Resistance

The equations of motion for flat ground are as follows:

$$\int_0^L [t_1(x) + t_2(x)] dx - \mathcal{F}W_T = f_{CX}, \quad (2)$$

$$\int_0^L [q_1(x) + q_2(x)] dx = f_{CY}, \quad (3)$$

$$\begin{aligned} - \int_0^L [q_1(x) + q_2(x)](x - d_x) dx + \frac{b}{2} \int_0^L [t_1(x) - t_2(x)] dx \\ + \frac{b}{2} \mathcal{F} \int_0^L [r_2(x) - r_1(x)] dx = \frac{I_z}{LW_T} \frac{d^2\omega}{dt^2}. \end{aligned} \quad (4)$$

The relevant quantities are defined in Figure 1. For uniform turning the right hand side of Equation (4) is zero. Also, for large radius turns the dynamic forces  $f_{CX}$  and  $f_{CY}$  are small and  $r_1 \approx r_2$ . From the equations of motion that result from these simplifications it can be seen that the track forces  $t_i$  are related to  $q_i$ ; therefore, it can be concluded that an overestimate in  $t_1 - t_2$  comes from an overestimation in  $q_1$  and  $q_2$ . This observation gives rise to questions concerning the directional dependance of the slip on the forces: are the  $q_i$ 's overestimated because of an oversimplified traction-slip model?

A typical path taken by a track during a turn is shown in Figure 2 where it is seen that there is a change in direction of the lateral component of the track velocity. The two components are determined in TVSTEER by assuming that the tractions  $t_i$  and  $q_i$  act in the same direction as the velocities  $v_x$  and  $v_y$ ; the resultant  $\tau_f = \sqrt{t_i^2 + q_i^2}$  is computed from Equation (1). Thus the resistance in the  $y$ -direction will be predicted to reach its maximal value of  $\tau_f \sin \gamma$  even if most of the slip has occurred along the  $x$ -direction. A more reasonable result is obtained by a model which accounts for the slip history, such as those given by Equations (5) and (6).

$$t_i = \int_0^{\Delta_i} \rho(\Delta_i - \Delta') \tau_f \cos \gamma d\Delta', \quad (5)$$

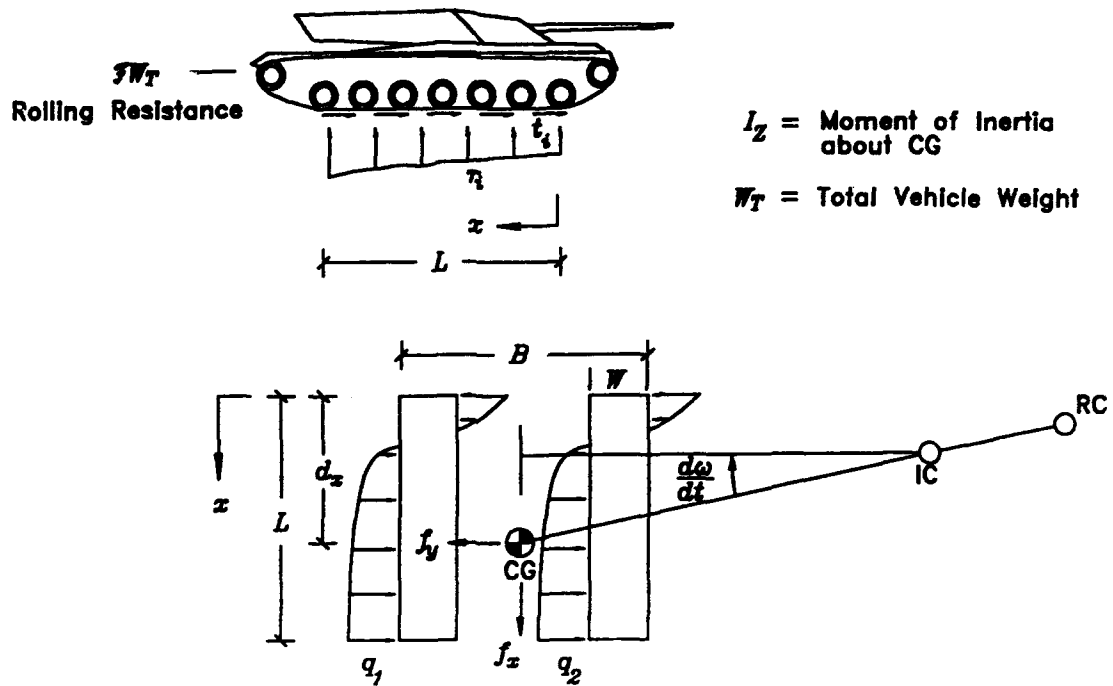


Figure 1: Tracked vehicle model definition

$$q_i = \int_0^{\Delta_s} \rho(\Delta_s - \Delta') \tau_f \sin \gamma d\Delta', \quad (6)$$

where  $\Delta_s = \Delta/\tau_f$ . These equations describe a kinematic hardening process whereby the resultant force direction lags behind the resultant velocity; as a result, the magnitude of  $q_i$  is reduced when the slip is predominately in the  $x$ -direction or when there is a reversal in slip direction. The response function  $\rho(\Delta_s)$  is determined such that Equation (1) is recovered for straight ahead motion (i.e.  $d\Delta_x = d\Delta$  and  $d\Delta_y = 0$ ). The appropriate response function is given by

$$\rho(\Delta_s) = \frac{G}{(1 + G\Delta_s)^2}. \quad (7)$$

For large values of  $G$ , history-dependence is essentially lost and Equations (5) and (6) and (7) describes the same slip-traction response as Equation (1). It was found by computation that for  $G$  values actually used by Spreitzer (1989), Equations (5) and (6) gave a turning resistance that was only five percent less than that determined by Equation (1); thus multi-dimensional effects alone do not account for the over estimation of turning resistance.

Although alternative models may be proposed, it is important to recognize that the possible responses of the multi-dimensional slip model must include that for straight-ahead motion. Thus, for any model to give a lower turning resistance and still be consistent with the direct shear test it would have to permit a stiff response to one dimensional loading (straight-ahead motion) but a significantly softer response to multidirectional loading (turning). The only source for such an anisotropic response comes from the track pad which implies that the traction-slip relationship is a product of the track soil-interaction which cannot be measured from a soil test alone. From this

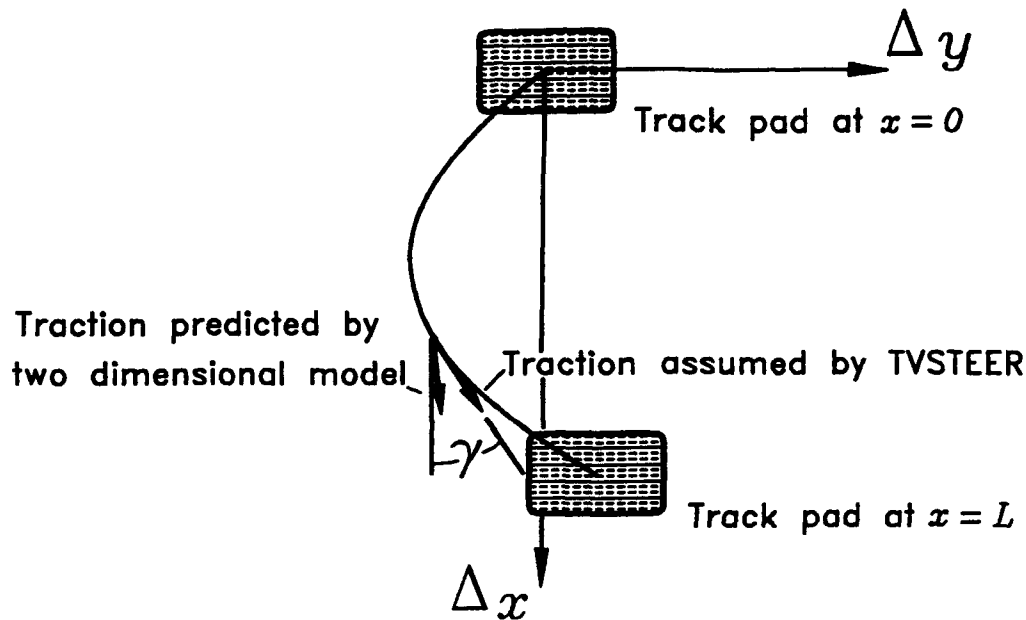


Figure 2: path taken by track pad during turn

reasoning, it was decided that rather than explore a more complicated multidimensional traction-slip model, the ability of the present model to depict straight-ahead motion should be investigated.

### Evaluation of Mobilization Slip

To evaluate the performance of the TVSTEER slip-traction relationship a model was developed for the drawbar pull test. The drawbar pull relationships were derived for the case where the tank is traveling straight ahead at velocity  $V$  with both tracks traveling at  $V_T$ . The slip velocity is therefore constant and equal the difference  $V_T - V$ . The slip at a point  $x$  under the track is thus given by

$$\Delta = S_L x, \quad (8)$$

where  $S_L$  is the slip ratio given by  $S_L = 1 - V/V_T$ . By using Equation (1) in conjunction with the assumption that the limiting shear stress is distributed uniformly along the length of the track, the drawbar pull can be expressed as

$$P = 2LW\tau_m \left[ 1 + \frac{\tau_m}{LGS_L} \log \frac{\tau_m}{\tau_m + LGS_L} \right]. \quad (9)$$

As the slip ratio becomes large the drawbar pull reaches its limiting value given by

$$P_{\max} = 2LW\tau_m. \quad (10)$$

By setting  $S_L = 2.515\tau_m/GL$ , a value of drawbar pull equal to 50 per cent of the ultimate value is obtained. Accordingly, the stiffness parameter can be computed from the values of drawbar pull

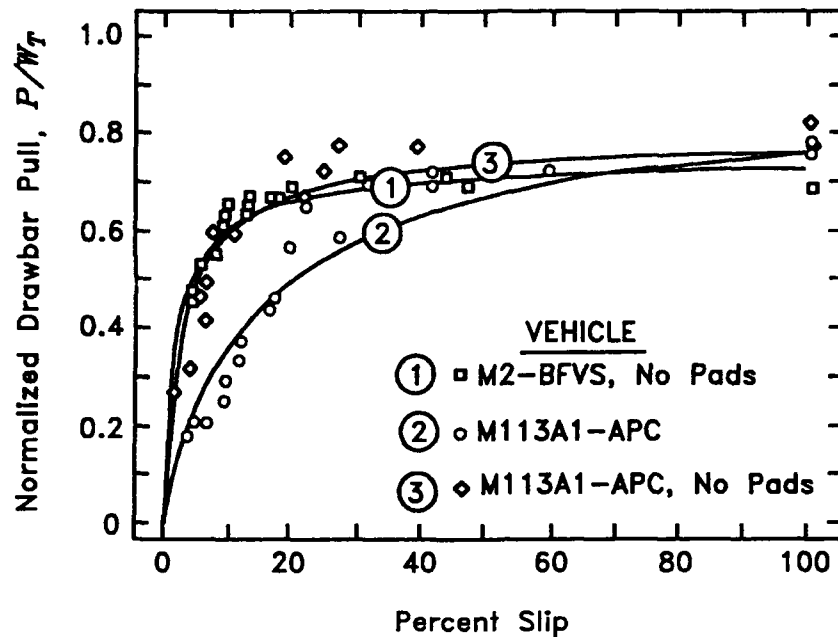


Figure 3: Test results and predictions from drawbar pull tests

and slip ratio at fifty percent mobilization as

$$G = 2.515 \frac{\tau_m}{LS_{L50}} \quad (11)$$

In Figure 3 are results of drawbar pull tests performed by Willoughby et. al. (1990) on three vehicles under essentially the same conditions. The limiting shear stress computed from Equation (10) corresponds to friction angles ranging from 35 to 41 degrees which are somewhat higher yet still consistent with direct shear tests by Baladi and Rohani (1979) (20 to 35 degrees) and Spreitzer (1989), (25 degrees). It should be noted that the smaller values of friction angle reported by Baladi and Rohani (1979) were accompanied by cohesion which would bring the limiting shear stress in line with the drawbar pull test results.

Curves 1 and 3 were generated with  $G = 5.0$  psi/in and curve 2 was generated with  $G = .92$  psi/in. Baladi and Rohani (1979) gave typical values of  $G$  ranging from 20 to 50 psi/in while Spreitzer used a value of 150 psi/in. These results indicate that parameters derived from the direct shear test underestimate the slip needed to mobilize traction by factors ranging from 10 to 100.

## Discussion of Results

The analysis of the previous section indicate that the overestimate of turning resistance by TVSTEER may be caused by using a value of  $G$  that is too large. The relatively small values of  $G$  inferred from the drawbar pull test clearly indicate that the direct shear test is not appropriate for a direct determination of the slip-traction relationship. In fact it is expected that the slip-traction relationship is a product of the complex interaction between the road wheel, track, and soil and depends on both vehicle and soil characteristics. Influence of vehicle characteristics is indicated by

by drawbar pull tests whereby different vehicles display different slip-traction relationships even for the same soil. Therefore, while the TVSTEER model is simple and convenient for preliminary analysis, its accuracy depends on obtaining a value of  $G$  that is suitable for both the vehicle and soil under consideration.

## Conclusions

Traction-slip relationships were derived for straight-ahead motion from the TVSTEER model permitting data from drawbar pull tests to be used to evaluate predicted slip-traction relationships directly. Slip measurements from drawbar pull tests indicate that the parameters derived from soil tests greatly underestimated mobilization slip with a result that turning resistance is overestimated. By contrast, the maximum traction derived from the drawbar pull test is comparable to those inferred from the direct shear test. Thus, it appears that the principal error introduced by using the direct shear test occurs for large radius turns for which only a fraction of the full traction is mobilized.

These conclusions must still be considered tentative because they are based on a comparison between results of selected drawbar pull tests and "typical" soil parameters. Research is currently directed under way to obtain field measurements for verification of the TVSTEER model.

## Acknowledgements

The methodology and data described herein was obtained from research conducted under the MILITARY DEVELOPMENT TEST AND EVALUATION PROGRAM of the U. S. Army Corps of Engineers. Permission was granted by the Chief of Engineers to publish this information. Special thanks to Cadet Jeffery S. Simpson, U. S. Army Military Academy, West Point, New York, who assisted in analyzing the field drawbar pull tests.

## References

1. Baladi, G. Y. and Rohani, B. (1979) "A Terrain-Vehicle Interaction Model for Analysis of Steering Performance of Track-Laying Vehicles," Technical Report GL-79-6, US Army Engineer Waterways Experiment Station, Vicksburg, Mississippi.
2. Baladi, G. Y., Barnes, D. E. and Berger, R. P. (1986) "Steerability Analysis of Tracked Vehicles: Theory and User's Guide for Computer Program TVSTEER," Technical Report SL-86-30, US Army Engineer Waterways Experiment Station, Vicksburg, Mississippi.
3. Spreitzer, F. (1989) "Analyse des Programms TVSTEER der WES," Report B-TF2428, Industriean-Betriebsgesellschaft mbh, West Germany.
4. Willoughby, W., Green, C., Temple, R. and Grimes, K. (1990) "Drawbar Pull Test Results," Personal Notes, US Army Engineer Waterways Experiment Station, Vicksburg, Mississippi.

# IMPROVED CALCULATION OF SINKAGE OF A WHEEL ON SOFT GROUND

I.C. Schmid, J. Ludewig

University of the Federal Armed Forces Hamburg, Germany

Institute of Automotive Engineering

## SUMMARY

Sinkage of a wheel is a most interesting parameter of soft ground mobility. Usually it is calculated with the well-known equations by BEKKER. However, this method accepts simplifications. Higher accuracy is obtained by considering series expansions in the basic formulas. Another way, proposed in the paper, using a parabolic approach for the contact-area contour, leads to higher accuracy and simpler mathematical handling. It also encloses evaluation of the elastic wheel on soft ground.

### 1. BEKKER'S APPROACH FOR A RIGID WHEEL

BEKKER [1] describes the contour of penetration of the rigid wheel as an undeformed circle, see fig. 1. Sinkage  $z_0$  is calculated from the equilibrium of wheel-load  $F_z$  and the vertical ground reaction force resulting from pressure distribution. Using Cartesian coordinates  $(x, z)$  the mathematical procedure leads to complications, because the expression for the pressure distribution cannot be integrated in closed form. In order to get integrability, BEKKER replaces the expression by a series expansion of which only zero and first order terms are considered. This simplification is valid for  $z_0/D \ll 1$ . The result is the well-known BEKKER formula for sinkage

$$z_{0B} = \{F_z / [\sqrt{(D)} * B * k * (1 - n/3)]\}^{2/(2n+1)}, \quad (1)$$

where  $k$  and  $n$  are the soil parameters;  $D$  and  $B$  are wheel dimensions.

### 2. IMPROVEMENT BY SERIES EXPANSION

To improve accuracy, LUDEWIG considers also terms of higher order. This results in

$$z_{0L} = \{F_z / [\sqrt{(D)} * B * k * (1 - n/3 - E_L)]\}^{2/(2n+1)} \quad (2)$$

which differs from the BEKKER formula in the additional expression

$$E_L = n(1-n)/10 + n(1-n)(2-n)/42 + (z_0/D) * [1/2 - 3n/10 - 3n(1-n)/28] + (z_0/D)^2 * [1/8 - 5n/56] . \quad (3)$$

For practical cases  $E_L > 0$ ; therefore  $z_{0L} > z_{0B}$ . This means, that the BEKKER formula underestimates the sinkage of the wheel.

### 3. APPLICATION TO ELASTIC WHEEL

Eqs. (1) and (2) are valid for a rigid wheel, however normally the sinkage of an elastic wheel is of interest. A simple method to consider an elastic wheel is, to replace the elastic wheel (D) by a rigid wheel with a diameter  $D^* > D$ . Thereby the length of the contact-area is considered to be equal for the elastic and for the surrogate rigid wheel. Accordingly, in order to obtain the sinkage of an elastic wheel, in eqs. (1) and (2) the diameter D has to be replaced by  $D^*$ . The problem in this procedure is, how to get the surrogate diameter  $D^*$ .

### 4. PROPOSED MODEL

#### 4.1 Length of contact-area

The following consideration uses a new method to calculate the sinkage of an elastic wheel. The model proposed is based on the assumption [1], that the contour of the contact-area of the elastic wheel consists of a flatted part  $L_f$  and an undeformed circular arc ( $L_K$ ), fig. 2a. Therefore the length of contact-area is

$$L = L_f + L_K \quad (4)$$

Application of the general equation for the chord of a circle, fig. 2b,

$$l = 2 * (d*h - h^2)^{1/2} = 2 * \epsilon_h * (d*h)^{1/2}, \text{ where } \epsilon_h = (1 - h/d)^{1/2},$$

leads to

$$L_f = 2 * \epsilon_f * [D*f]^{1/2} \quad (5)$$

$$L_K = \epsilon_{z,f} * [D*(z_0+f)]^{1/2} - \epsilon_f * [D*f]^{1/2} \quad (6)$$

with  $\epsilon_{z,f} = [1 - (z_0+f)/D]^{1/2}$  and  $\epsilon_f = (1 - f/D)^{1/2}$  at the present case of an elastic wheel with tire deflection  $f$  and sinkage  $z_0$  in soft ground. Considering eqs. (4), (5) and (6) one obtains

$$L = \epsilon_{z,f} * [D*(z_0+f)]^{1/2} + \epsilon_f * [D*f]^{1/2} \quad (7)$$

On the other hand the surrogate circle ( $D^*$ ) yields

$$L = \epsilon^* * (D^* * z_0)^{1/2} \quad (8)$$

with  $\epsilon^* = (1 - z_0/D^*)^{1/2}$ .

#### 4.2 Surrogate wheel diameter

Eqs. (7) and (8) lead to

$$(D^*/D)^{1/2} = \epsilon_{z,f}/\epsilon^* * (1 + f/z_0)^{1/2} + \epsilon_f/\epsilon^* * (f/z_0)^{1/2} \quad (9)$$



From eq. (9) the diameter  $D^*$  can be calculated. As  $\epsilon_{zf}$ ,  $\epsilon_f$  and  $\epsilon^*$  are all close to the value 1, if  $z_0 \ll D$  and  $f \ll D$ , the ratios  $\epsilon_{zf}/\epsilon^*$  and  $\epsilon_f/\epsilon^*$  tend to be 1.0. For this case, fig. 3 shows the ratio  $D^*/D$  dependent on sinkage  $z_0$  and tire deflection  $f$ .

#### 4.3 Parabolic approach for contact-area contour

The shape of the real contact-area contour determines sinkage of the elastic wheel. As mentioned above the contour was approximated by

A : circular arc of surrogate wheel ( $D^*$ )

B : flatted area and circular arc of original wheel ( $D$ ).

Another possibility used in this paper consists in

C : parabolic curve.

As can be seen in fig. 4, the calculated contour C (example) is quite close to the contour A. It will be proved in the following, that the parabolic course (C) leads to a simple equation for sinkage. With the origin of the coordinates ( $x, z$ ) in point  $P_1$ , fig. 4, the parabolic course formulation is

$$z = C * x^{1/2} = z_0 * (x/L)^{1/2} \quad (10)$$

according to the boundary conditions in the fixed points  $P_1$  and  $P_3$ . With the well-known pressure-sinkage relation  $p = k * z^n$  the distribution of pressure is

$$p(x) = k * z_0^n * (x/L)^{n/2} \quad (11)$$

Integration of pressure distribution over the contact area  $A = B * L$  yields

$$F_z = B * L * k * z_0^n / (1 + n/2) \quad (12)$$

Using eq. (8)

$$F_z = B * \epsilon^* * (D^* * z_0)^{1/2} * k * z_0^n / (1 + n/2) \quad (13)$$

is obtained, from where

$$z_0 = \{F_z / [D^{1/2} * (D^*/D)^{1/2} * \epsilon^* * B * k * (1/(1+n/2))]\}^{2/(2n+1)} \quad (14)$$

Eq. (14) can be applied also to the rigid wheel, for which  $D^*/D = 1$ .

With eqs. (1), (2) and (14), there are three possibilities to calculate sinkage  $z_0$  of a wheel.

## 5. RESULTS

Figs. 5 and 6 show the sinkage for a rigid wheel on loam and on sand, respectively, as a function of wheel-load  $F_z$ . Thereby the three methods of calculation are compared. As mentioned before, eq. (1) provides too low values for the sinkage, due to the simplifications accepted. This is expressed also in the plots. The results from eq. (1) are close to those obtained with eq. (14) in case  $\epsilon^* = 1$ . That is to say, that the simplifications in eq. (1) are comparable with the simple case  $\epsilon^* = 1$  in eq. (14). Higher accuracy is obtained with eq. (2) as well as with eq. (14), when in the latter the true value for  $\epsilon^*$  is used.

Fig. 7 shows the sinkage  $z_0$  for a wheel on loam, calculated from eq. (14). Thereby the elasticity of the wheel is varied by different ratios of tire deflection  $f$  to ground deformation  $z_0$ . This illustrates the effect of tire elasticity on sinkage which can be influenced by inflation pressure.

It should be reminded to the fact, that the amount of sinkage  $z_0$  is decisive for the rolling resistance of a wheel:  $F_{RR} = B \cdot k \cdot z_0^{n+1} / (n+1)$ . Better accuracy is expected when using eq. (2) or eq. (14) for  $z_0$ .

## 6. MAXIMUM AND MEAN GROUND PRESSURE

Sometimes the mean ground pressure  $p_m = F_z/A = F_z/(L \cdot B)$  is used to characterize the mobility of a vehicle on soft ground. However, for sinkage and rolling resistance the maximum ground pressure  $p_{max} = k \cdot z_0^n$  is responsible. Therefore the ratio  $p_{max}/p_m$  is of interest. Using eq. (8) for  $L$  and eq. (14) for  $z_0$ , this ratio can be obtained:

$$p_{max}/p_m = 1 + n/2 \quad (15)$$

It can be seen, that the ratio is independent from tire data, but dependent on the exponent  $n$  for soil deformation, only.

## REFERENCES

- [1] BEKKER, M.G. : "Introduction to Terrain-Vehicle Systems", Ann Arbor, The University of Michigan Press, 1969

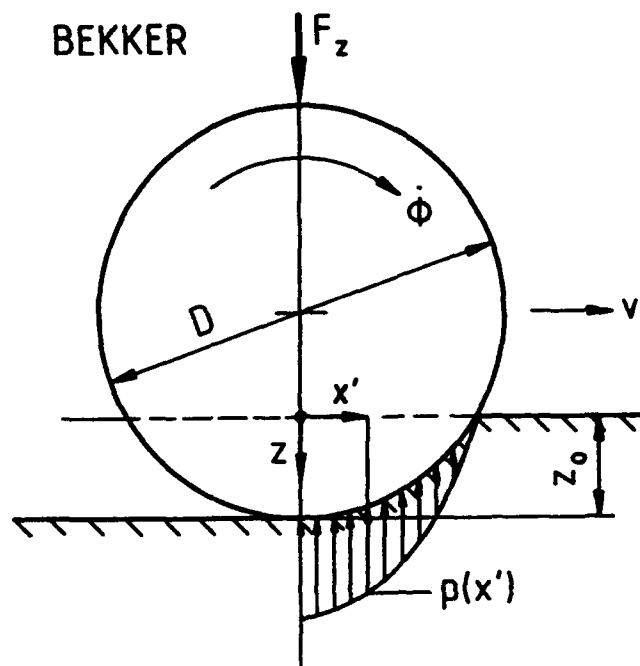


Fig. 1: Model of a rigid rolling wheel (BEKKER)

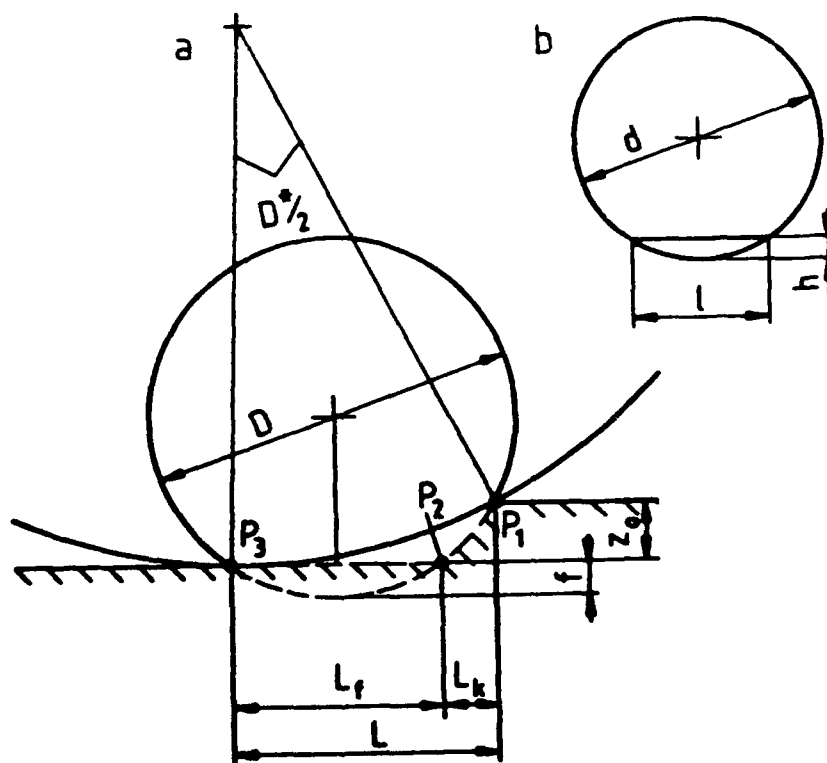


Fig. 2: a) Elastic wheel ( $D$ ) and surrogate circle ( $D^*$ )  
b) Circle and chord

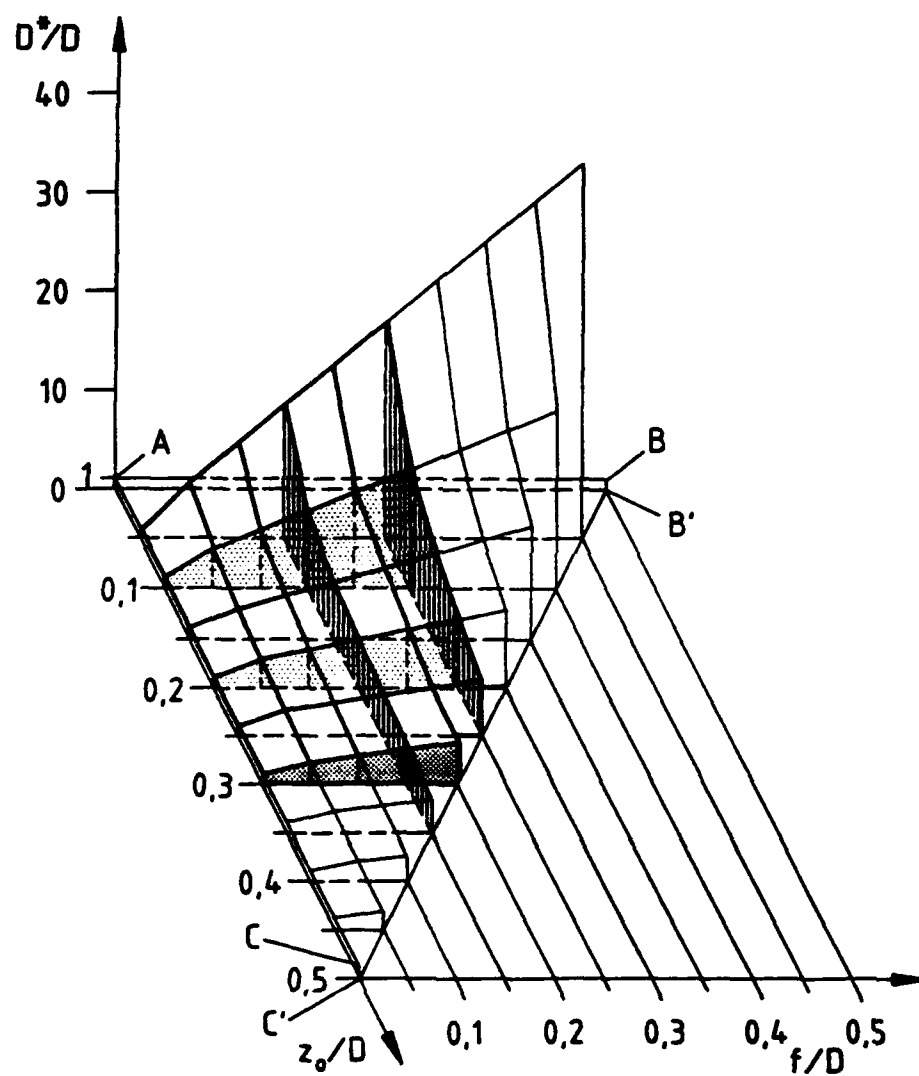


Fig. 3:  $D^*/D$  calculated as a function of  $z_0/D$  and  $f/D$

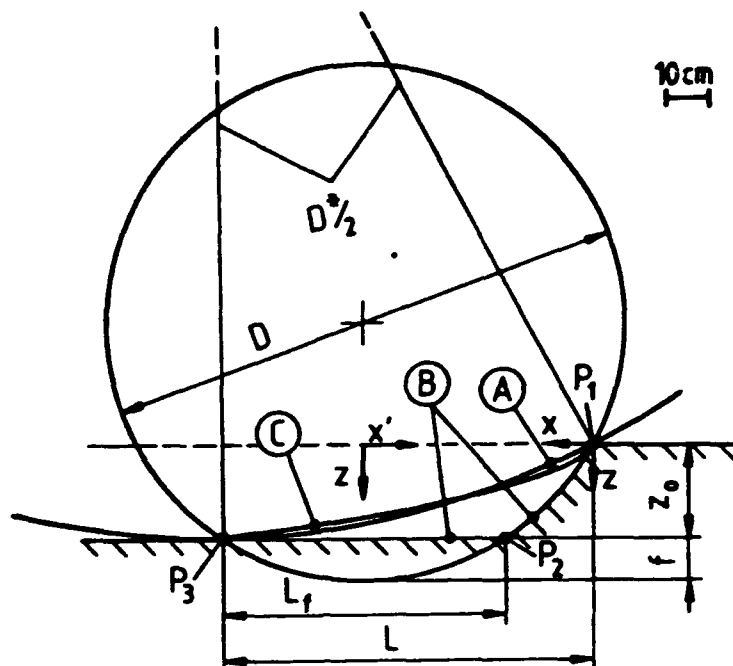


Fig. 4: Comparison of 3 different shapes of a wheel contour according to  $D=120$  cm,  $z_0=20$  cm,  $f=10$  cm; A) surrogate wheel  $D^*$ , B) proposed by BEKKER, C) parabolic approach

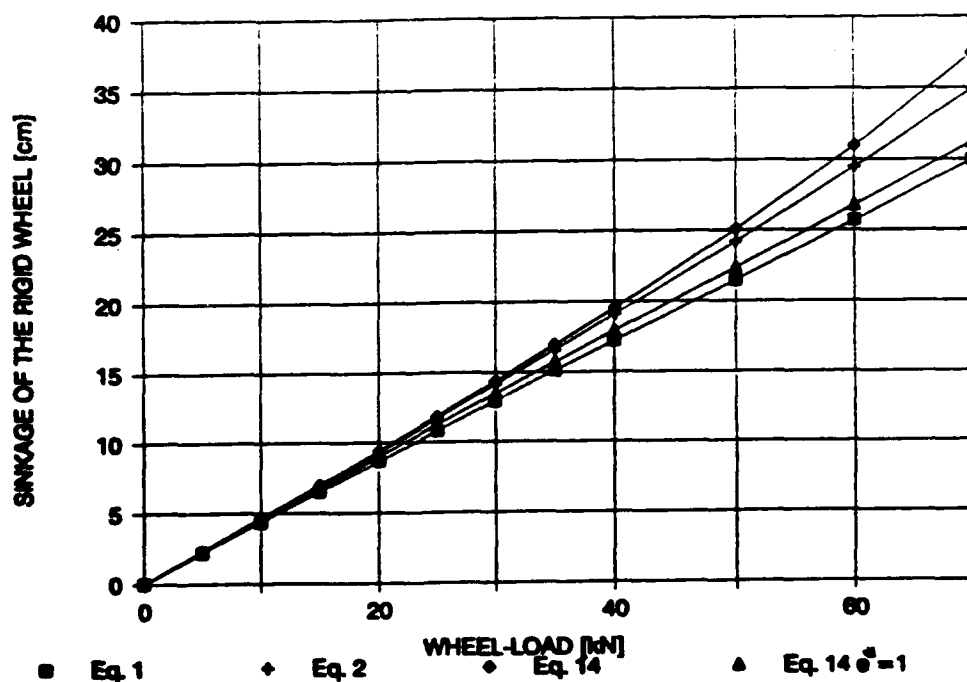


Fig. 5: Sinkage of a rigid wheel ( $D=121.7$  cm,  $B=37.2$  cm) on loam ( $k=6.627$  N/cm $^{n+2}$ ,  $n=0.51$ ), calculated with different formulas as a function of wheel-load

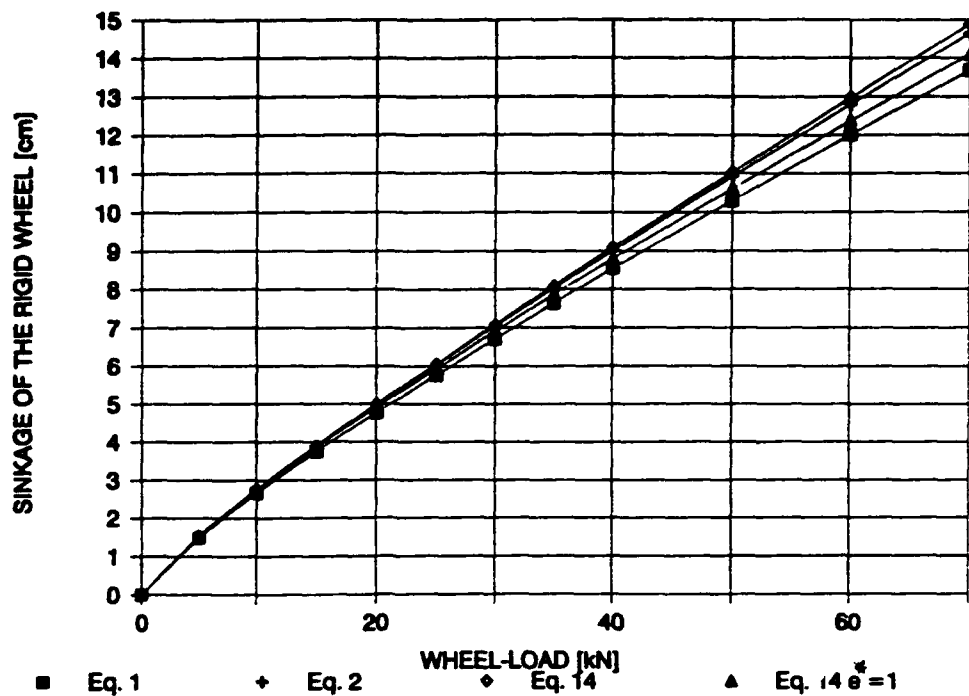


Fig. 6: Sinkage of a rigid wheel ( $D=121.7$  cm,  $B=37.2$  cm) on sand ( $k=9.850$  N/cm<sup>n+2</sup>,  $n=0.69$ ), calculated with different formulas as a function of wheel-load

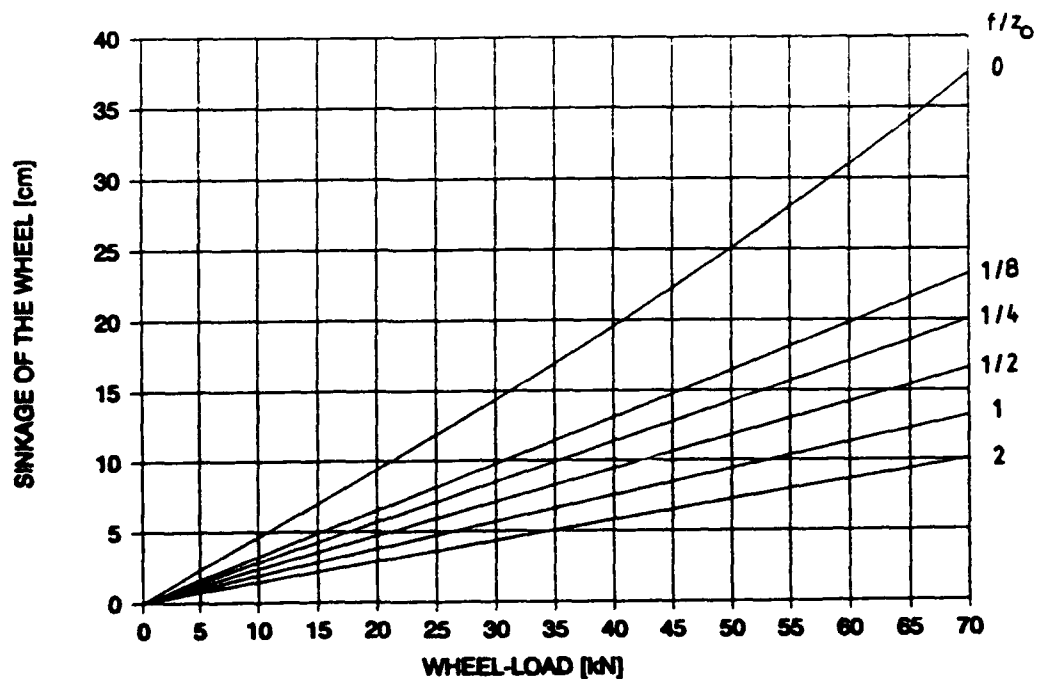


Fig. 7: Sinkage of an elastic wheel ( $D=121.7$  cm,  $B=37.2$  cm) on loam ( $k=6.627$  N/cm<sup>n+2</sup>,  $n=0.51$ ), calculated with eq. (14) as a function of wheel-load for different  $f/z_0$  values

MATHEMATICAL MODELS FOR PREDICTING THE TRACTIVE  
CHARACTERISTICS OF TRACTOR TIRES

I: TRACTIVE EQUATIONS MODEL

ELSAID ELASHRY

Agr. Eng. Dept. Faculty of Agriculture  
Alexandria University, Egypt

Abstract

Development a mathematical model for predicting the tractive characteristics (net traction ratio, gross traction ratio, tractive efficiency and rolling resistance ratio) as a function of soil cone index, tire parameters, and tire load, by using dimensionless numerics. The accuracy of prediction was checked by experiments. This model may be used to predict the performance of any tire under any soil conditions.

I. Introduction

The efficient use of energy in farming operations becomes increasingly important as the cost of energy increases world wide. On the farm, a large part of tractor power is used for field work which requires traction through the use of traction devices, mainly lugged tires.

The tractive characteristics of a tire depend on the type and condition of the soil, the tire parameters, and tire loading. The effect of soil type and condition on tractive performance is complex and interrelated with the other parameters such as, dynamic load, lug configuration, inflation pressure etc... The most important factor affecting tractive performance is the weight on the driving wheels, which must match the power available, therefore, the tractor and machine manufacturers increased the weight on the driving wheels and increased tire size as tractor weight increased.

Wisner and Luth (1973) developed a relationship to formulate a method for predicting the traction characteristics of towed and driven wheels. The equation for net traction ratio of the driven wheel was:

$$\frac{P}{W} = 0.75 (1 - e^{-0.3 C_n S}) - \left( \frac{1.2}{C_n} + 0.04 \right) \quad (1)$$

Where: P is pull force and, C<sub>n</sub> is wheel numeric = CI b d/W.

This formula was determined experimentally for the tires that were commonly used seventian 1972. The highest values for b, d and W investigated were 840 mm, 1650 mm, and 3000 kg, (29.43 kN) respectively, and CI varied from 20 to 500 psi (138 to 3447 kPa).

Equation (1) is the most common use today and its given in the ASAE standard (Agricultural Machinery Management Data, ASAE D 230.4). This empirical equation is limited to bias ply tire performance at 20 % slip and 20 % tire deflection, in the range of soil conditions for which Wismer and Luth (1973) were developed, therefore the effect of tire dimensions, inflation pressure and soil shear properties are not explicitly included.

Sitkei (1986) developed that, the empirical equation for predicting the gross traction ratio. This relationship was as:

$$GTR = GTR_{max} (1 - e^{-S/S^*}) \quad (2)$$

where: GTR = gross traction ratio

GTR<sub>max</sub> = the maximum value of gross traction ratio

$$GTR_{max} = (0.85 - 26Mc^3) \frac{d}{1.7} \quad (3)$$

where: Mc = soil moisture contact wet basic (decimal) d = tire diameter (m) S = slip (%) S\* = character value of slip

S\* = character value of slip

$$S^* = (6 + 1000 Mc^3) \left( \frac{1.7}{d} \right) \left( \frac{1.72}{\gamma d} \right) \quad (4)$$

Macnab et. al. (1977) developed a computer model using the emperical models developed by Wismer and luth (1973). this model determined tractor drawbar pull by summing results for each wheel, whether towed or driven. They obtained reasonably accurate predictions for field tests of six tractors. The exception was on test plots containing surface vegetation, where the actual cone index values were three to four times larger then values that best fit measured raults. This was attributed to the higher wheel slips on the vegetative surface.



Leviticus and Reyes (1983a and 1983b) used a generalized form of the Wismer and Luth, to model the tractive characteristics of tractors tested on concrete. They used iterative regression analysis along with five years worth of data from the Nebraska Tractor Tests to determine best fit values of the equation constants.

The objective of this study was to develop empirical equations to predict the tractive characteristics of the tire as the function of the slip, for different tire sizes and soil conditions.

## II. Equipments and Methods

The measurements of the tires tractive performance were made in twenty different fields during the investigation. In order to determine the soil condition, soil samples covering a depth 0-20 cm were taken to determine soil classification, soil bulk density and soil moisture content. Also cone index was measured. The field conditions range were:

- Soil type: Sandy, Loam, Silty loam, Silty, Clay loam and Clay
- Soil Moisture content: 6.8 to 18.5 %
- Soil bulk density: 1.12 to 1.75 g/cm<sup>3</sup>

Twenty-three tires were available for this study. Tire size range from 11.2R28 to 30.5R32, where the range of the tire width was 0.268 to 1.092 m and the range of tire diameter 1.2 to 1.835 m. A Zetor 160.45 tractor and a Rába 245 tractor were used for the tire investigation.

Before each test the vertical static load on tire was measured. Then the tire inflation pressure was adjusted according to the operators manual. For each test condition several load test with different values of the pull and one no-pull test (to determine the zero-pull tire rolling radius) were conducted by recording the number of driving wheel revolutions and the calculation of travelled distance by means of a fifth wheel. The drawbar pull was applied by pulling a trailed tractor. Drawbar pull was gradually increased by controlling the towed tractor brakes. The drawbar pull was measured using a dynamometer. For each test run, pull, axle torque and the number of revolutions of the driving wheels and the fifth wheel were recorded along the test pass.

The measuring instrument used for tire performance field tests

were designed, constructed and calibrated in the Hungarian Institute of Agricultural Engineering, Gödöllő, Hungary.

The results obtained were subjected to statistical analysis (F-test, regression analysis and multilinear regression analysis) and simulation technique, whenever it seemed necessary. The first part from result analysis was included the development the dimensionless numerics "Pi-term" affecting tire tractive performance by using the dimensional analysis method and Buckingham theorem. A computer program was written and run to analyse the data and calculated the Pi-terms and traction parameters and to perform a multilinear regression of the traction equations and determined the true zero slip rolling radius.

### III. Results and Discussion

The principal objective of this work was the development of dimensionless numerics (groupings of Pi-terms) for the prediction of tractive performance of tires under different soil conditons. These correlations were to account for the effect of tire load, geometry, flexibility and soil strength on traction. Tire performance depends on tire geometry, physical properties of both the tire and the soil and on the loading applied. Dimensional analysis can be used to reduce the number of experimantal variables. The Pi terms were derived by a combination of inspection and matrix solution techniques (Freitag 1965). As constituted , the Pi terms are conventional in form, physically meaning ful and could be tested conveniently:

$$\pi_1 = P/W = \text{The net traction ratio (NTR)}$$

$$\pi_2 = Q/Rr.W = \text{The gross traction ratio (GTR)}$$

$$\pi_3 = CI.b.Rr/W = \text{Soil-tire coefficient}$$

$$\pi_4 = P_1.b.Rr/W = \text{Tire coefficient}$$

$$\pi_5 = b/Rr = \text{Width - rolling radius ratio}$$

$$\pi_6 = b/d = \text{Width-diameter ratio, and}$$

$$\pi_7 = S = \text{Slip}$$

where P is Pull, (kN) , W is Dynamic load, (kN), Q is Axle torque, (kN.m), Rr is Tire rolling radius at zero pull force, (m),  $P_i$  is Inflation pressure, (kPa); b is Tire width, (m), d is Tire diameter, (m), CI is Cone index, (kPa) and S = Slip, (%).

An iterative non-linear regression procedure was developed to fit curves to the traction data, as the following:

$$\text{Net traction ratio "NIR"} = \frac{P}{W} = f_1(S) \quad (5)$$

$$\text{Gross traction ratio "GTR"} = \frac{Q}{Rr.W} = f_2(S) \quad (6)$$

The correlation coefficient values for net traction ratio equation and gross traction ratio equation ranged from 0.94 to 0.999 ( $n \geq 25$ ;  $P = 0.1\%$ ).

A general empiric relationship is determined by the means of dimensional analysis, on the basis of the results of traction experiments for tires of  $b/d = 0.168$  to  $0.652$  and for different soil conditions. The relationship can be used to predict the net traction ratio of the tire as a function of the slip (S) and as a function of parameters " $\alpha$ ", " $\mu$ " and " $\beta$ ", where " $\alpha$ " and " $\mu$ " are a function of  $(\pi_3)$  and  $(\pi_4)$ , and " $\beta$ " is a function of  $(\pi_3)$  and  $(\pi_5)$ . The net traction ratio is as follows:

$$\text{NTR} = \frac{P}{W} = \alpha (1 - \mu e^{-\beta S}) \quad (7)$$

The net traction ratio increases when parameter " $\alpha$ " increases, and " $\alpha$ " increases non linear way with respect to  $P_i$ -term  $(CI.b.Rr/W)$  and/or  $P_i$ -term  $(p_i.b.Rr/W)$ . A general empiric relationship is determined to predict parameter " $\alpha$ " as a function of the terms  $(CI.b.Rr/W)$  and  $(p_i.b.Rr/W)$ :

$$\alpha = 0.451 + 0.01 \left( \frac{CI.b.Rr}{W} \right) \left( \frac{p_i.b.Rr}{W} \right) \quad (8)$$

the correlation coefficient value was 0.839. ( $n=51$ ,  $P=0.1\%$ ).

From Equation 8 is concluded that, when the value of  $(CI.b.Rr/W)$  increase the value of " $\alpha$ " parameter at constant value of  $(p_i.b.Rr/W)$  increase. However the effect of  $(CI.b.Rr/W)$  on parameter " $\alpha$ " is stronger at a lower  $(p_i.b.Rr/W)$  ratio than at a higher one.

The net traction ratio increases when the parameter " $\beta$ " increases, however the parameter " $\beta$ " follows a non-linear function versus Pi-term ( $CI.b.Rr/W$ ) or/and Pi-term ( $b/Rr$ ). A general empiric relationship is determined to predict parameter " $\beta$ " as a function of the term ( $CI.b.Rr/W$ ) and ( $b/Rr$ ):

$$\begin{aligned} \beta = & 0.106 + 0.001 \left( \frac{CI.b.Rr}{W} \right) - 0.025 \left( \frac{b}{Rr} \right) \\ & + 0.002 \left( \frac{CI.b.Rr}{W} \right) \left( \frac{b}{Rr} \right) \end{aligned} \quad (9)$$

the correlation coefficient value was 0.85 ( $n=51$ ,  $P=0.1\%$ ).

From Equation 9 is concluded that, when the value of ( $CI.b.Rr/W$ ) increase the value of " $\beta$ " parameter at a constant value of ( $b/Rr$ ) increases. However the effect of ( $CI.b.Rr/W$ ) on parameter " $\beta$ " is stronger at a higher ( $b/Rr$ ) ratio than at a lower one.

The net traction ratio decreases when parameter " $\mu$ " increase, which the parameter " $\mu$ " follows a non linear function with respect to change in Pi-term ( $CI.b.Rr/W$ ) and/or Pi-term ( $pi.b.Rr/W$ ):

$$\begin{aligned} \mu = & 0.216 + 0.0022 \left( \frac{CI.b.Rr}{W} \right) - 0.026 \left( \frac{pi.b.Rr}{W} \right) \\ & - 0.001 \left( \frac{CI.b.Rr}{W} \right) \left( \frac{pi.b.Rr}{W} \right) \end{aligned} \quad (10)$$

the correlation coefficient value was 0.427 ( $n=51$ ,  $P=1\%$ ).

From Equation 10 is concluded that, when the value of ( $CI.b.Rr/W$ ) increase the value of " $\mu$ " parameter at constant value of ( $pi.b.Rr/W$ ) decreases. However the effect of ( $CI.b.Rr/W$ ) is stronger at a higher ( $pi.b.Rr/W$ ) ratio than at a lower, also at ( $pi.b.Rr/W$ ) ratio equal to 2 the value of " $\mu$ " is constant and equal to about 1.164.

In general for any conditions the values of " $\alpha$ ", " $\beta$ " and " $\mu$ " predicted from the Equations 8, 9 and 10 and by using generalized form for net traction ratio equation (Equation 7) we can predict the net traction ratio as a function of slip.

On the basis of the test results and the dimensional analysis the gross traction ratio (GTR) was determined as a function of the slip,

and as a function of the parameters " $\sigma$ " and " $\epsilon$ ", where " $\sigma$ " is a function of  $(\pi_3)$  and " $\epsilon$ " is a function  $(\pi_3)$  and  $(\pi_5)$ .

The gross traction ratio is as follows:

$$GTR = \frac{Q}{RrW} = \sigma (1 - e^{-\epsilon S}) \quad (11)$$

The gross traction ratio (Equation 11) indicates, that an increase in parameter " $\sigma$ " increases GTR, and parameter " $\sigma$ " follows a non linear function with respect to changes in Pi-term  $(CI.b.Rr/W)$ .

$$\sigma = 0.926 - 0.58 \left( \frac{CI.b.Rr}{W} \right)^{-1} \quad (12)$$

the colleration coefficient value was - 0.58 (n=51, P=0.1 %).

When increase  $(CI.b.Rr/W)$ , the " $\sigma$ " parameter increases. In Wismer and Luth equation (1973) the value of parameter " $\sigma$ " is constant and equal to 0.75.

A general empiric relationship is determined to predict parameter " $\epsilon$ " as a function of the term  $(CI.b.Rr/W)$  for different  $(b/Rr)$  ratios.

$$\begin{aligned} \epsilon = & 0.085 + 0.002 \left( \frac{CI.b.Rr}{W} \right) - 0.013 \left( \frac{b}{Rr} \right) \\ & + 0.001 \left( \frac{CI.b.Rr}{W} \right) \left( \frac{b}{Rr} \right) \end{aligned} \quad (13)$$

the correlation coefficient value was 0.91 (n=51, P=0.1 %).

From Equation 13 is concluded that the increase of the term  $(CI.b.Rr/W)$  increases parameter " $\epsilon$ ". At constant value of  $(CI.b.Rr/W)$  the increase of  $(b/Rr)$  the value of parameter " $\epsilon$ " increases.

For any conditions the values of " $\sigma$ ", and " $\epsilon$ " one can be predict from the Equation 12 and 13 respectively and by using the Equation 11, we can predict the gross traction ratio as a function of slip.

From the definition of tractive efficiency "TE" and by using the net traction ratio equation (Equation 7) and gross traction ratio equation (Equation 11) "TE" is determined as follows:

$$T E = \frac{\alpha(1 - M e^{-\beta S})}{\sigma(1 - e^{-\epsilon S})} (1 - SL) \quad (14)$$

where SL is slip (decimal)

Also, From Equations 7 and 11, the coefficient of motion resistance value (CMR) is given as:

$$CMR = \rho + (\gamma e^{-\beta S} - \sigma e^{-\epsilon S}) \quad (15)$$

where:

$$\rho = (\sigma - \alpha)$$

$$\gamma = \alpha \mu$$

#### IV. Conclusions

A mathematical model was developed to describe the performance of tire under different conditions.

The net traction ratio equation, the gross traction ratio equation, the tractive efficiency equation and rolling resistance equation were developed as a function of soil one index, tire parameters, tire load and slip. The accuracy of prediction was checked by experiments.

#### REFERENCES

- ASAE. 1983. "Agricultural Machinery Management Data" ASAE. D.230.4 Agricultural Engineer Yearbook. Amer. Soc. Agr. Engr., St. Joseph MI 49085.
- Freitag, D.R. 1965. "A Dimensional Analysis of the Performance of Pneumatic Tires on Soft Soils." Army Corps of Engineers Waterways Experiment Station. Technical Report, pp 3-688. U.S.
- Leviticus, L.I. and J.F. Reyes 1983a "Traction on concrete: I. Dynamic ratio and tractive quotient." ASAE. paper No. 83-1558. Amer. Soc. Agr. Engrs. St. Joseph, MI 49085.
- Leviticus, L.I. and J.F. Reyes 1983b "Traction on Concrete: II. Tractive Efficiency. ASAE paper No. 83-1559. ASAE, St. Joseph, MI 49085.
- Macnab, J.E., R.B. Wensink, and D.E. Booster. 1977. "Modeling Wheel Tractor Energy Requirements and Tractive Performances." Transactions of the ASAE. 20(4):602-605, 609.
- Sitkei 1986. "Mezőgazdasági és erdészeti járművek modellezése" Budapest, Akadémiai Kiadó 1986. 83.P.
- Wismer R.D. and H.J. Luth 1973. "Off-Road Traction Prediction for Wheeled Vehicles" J. of Terramech., 10, 49.